AD_____

Award Number: W81XWH-04-2-0012

TITLE: Core Development Integration and Demonstration of the DARPA Virtual Soldier

PRINCIPAL INVESTIGATOR: Brian D. Athey, Ph.D.

CONTRACTING ORGANIZATION: University of Michigan
Ann Arbor, MI 48109-1274

REPORT DATE: September 2006

TYPE OF REPORT: Final

PREPARED FOR: U.S. Army Medical Research and Materiel Command
Fort Detrick, Maryland 21702-5012

DISTRIBUTION STATEMENT: Approved for Public Release;
Distribution Unlimited

The views, opinions and/or findings contained in this report are those of the author(s) and should not be construed as an official Department of the Army position, policy or decision unless so designated by other documentation.

REPORT DOCUMENTATION PAGE

Form Approved
OMB No. 0704-0188

Public reporting burden for this collection of information is estimated to average 1 hour per response, including the time for reviewing instructions, searching existing data sources, gathering and maintaining the data needed, and completing and reviewing this collection of information. Send comments regarding this burden estimate or any other aspect of this collection of information, including suggestions for reducing this burden to Department of Defense, Washington Headquarters Services, Directorate for Information Operations and Reports (0704-0188), 1215 Jefferson Davis Highway, Suite 1204, Arlington, VA 22202-4302. Respondents should be aware that notwithstanding any other provision of law, no person shall be subject to any penalty for failing to comply with a collection of information if it does not display a currently valid OMB control number. **PLEASE DO NOT RETURN YOUR FORM TO THE ABOVE ADDRESS.**

1. REPORT DATE *(DD-MM-YYYY)*	2. REPORT TYPE	3. DATES COVERED *(From - To)*
01-09-2006	Final	1 Dec 2003 – 31 aug 2006

4. TITLE AND SUBTITLE

Core Development Integration and Demonstration of the DARPA Virtual Soldier

5a. CONTRACT NUMBER

5b. GRANT NUMBER
W81XWH-04-2-0012

5c. PROGRAM ELEMENT NUMBER

6. AUTHOR(S)

Brian D. Athey, Ph.D.

E-Mail:

5d. PROJECT NUMBER

5e. TASK NUMBER

5f. WORK UNIT NUMBER

7. PERFORMING ORGANIZATION NAME(S) AND ADDRESS(ES)

University of Michigan
Ann Arbor, MI 48109-1274

8. PERFORMING ORGANIZATION REPORT NUMBER

9. SPONSORING / MONITORING AGENCY NAME(S) AND ADDRESS(ES)
U.S. Army Medical Research and Materiel Command
Fort Detrick, Maryland 21702-5012

10. SPONSOR/MONITOR'S ACRONYM(S)

11. SPONSOR/MONITOR'S REPORT NUMBER(S)

12. DISTRIBUTION / AVAILABILITY STATEMENT
Approved for Public Release; Distribution Unlimited

13. SUPPLEMENTARY NOTES – Original contains colored plates: ALL DTIC reproductions will be in black and white.

14. ABSTRACT

See next page for abstract.

15. SUBJECT TERMS
Holomer, electrophysiology, auto-segmentation, anatomy, diagnosis

16. SECURITY CLASSIFICATION OF:			17. LIMITATION OF ABSTRACT	18. NUMBER OF PAGES	19a. NAME OF RESPONSIBLE PERSON
a. REPORT	b. ABSTRACT	c. THIS PAGE			USAMRMC
U	U	U	UU	332	19b. TELEPHONE NUMBER *(include area code)*

Abstract

Two demonstrations of the capabilities developed under Cooperative Agreement Contract W81XH-04-0012, "Core Development Integration and Demonstration of the DARPA Virtual Soldier" (The Virtual Soldier Project) were performed as final deliverables. The March 17th 2005 Demonstration targeted 5 areas: Statistical Reasoning, Multiscale Modeling, Causal Reasoning, P-Tag-CODEC-Holomer Displays-Hotbox, and Autostereoscopic / Holographic Display. The 14 June 2005 Demonstration targeted 3 areas: 1. An End-to-End Demonstration of Statistical Reasoning, 2. Multiscale Modeling and Anatomy from Anatomy Forecasts with Autopsy Results and a Report of Statistical Findings, and 3. a Causal Reasoning demonstration using the Virtual Soldier Knowledge Base, simulated physiology data, and ballistic modeling. The 7 Tasks of the project: 1. Global Architecture, 2. Organ-tissue systems, 3. Property-levels model, 4. Automatic segmentation of organ-tissue systems, 5. Holomer display and interface, 6. Holomer storage, retrieval and interface, and, 7. Demonstration; have been met in fulfillment of the main contract demonstration goal of statistical prediction of outcomes to an accuracy > 0.80. Subcontractors developed the software and model systems to achieve the required degree of faithfulness to physiology, anatomy, physical properties, and anatomy information hierarchy to statistically predict wounding outcomes from minimal post-wound experimental data, and to separately describe post-wound effects from initial wound states.

TABLE OF CONTENTS

Introduction	04
Body	05
Key Research Accomplishments	13
Reportable Outcomes	22
Conclusions	43
References	44
Appendices	Briefing Books: March 17, 2005 Demonstration June 14, 2005 Demonstration DVD of June 14, March 17 2005 Demonstrations. Publications

Introduction

Two demonstrations of the capabilities developed under Cooperative Agreement Contract W81XH-04-0012, "Core Development Integration and Demonstration of the DARPA Virtual Soldier" (The Virtual Soldier Project) were performed as final deliverables. The first demonstration on March 17th, 2005, targeted 5 areas: Statistical Reasoning, Multiscale Modeling, Causal Reasoning, P-Tag-CODEC-Holomer Displays-Hotbox, and Autostereoscopic/Holographic Display. The second demonstration on June 14th, 2005, targeted 3 areas: An End-to-End Demonstration of Statistical Reasoning, Multiscale Modeling and Anatomy from Anatomy Forecasts with Autopsy Results, a Report of Statistical Findings, and a Causal Reasoning demonstration using the Virtual Soldier Knowledge Base, simulated physiology data, and ballistic modeling.

The 7 Tasks of the Project: 1. Global Architecture, 2. Organ-tissue systems, 3. Property-levels model, 4. Automatic segmentation of organ-tissue systems, 5. Holomer display and interface, 6. Holomer storage, retrieval and interface, and, 7. Demonstration; have been met in fulfillment of the main contract demonstration goal of statistical prediction of outcomes to an accuracy > 0.80.

Goals Demonstrated

- Diagnose heart wounds w/ accuracy >= 80%
- Predict likelihood of mortality, 93%
- Forecast time to death, 85%
- Estimate injury location, 83%. Correctly identified injury location (LV vs. RV) for 5 cases with one ambiguous result (83%)
- Examined the utility of variables other than LVP and RVP including multivariate approaches
- Compared baseline data to post-injury data
- Make anatomy from anatomy forecast and compare to autopsy results
- Demonstrate organ and system level integration
- Extend and use global architecture
- Develop and use automatic segmentation

Display results in visualizations simultaneously and synchronized with respect to time

While this report summarizes the Phase I results, readers are encouraged to consult the two briefing books and video summaries from the March 17th and June 14th demonstrations, the quarterly reports, and the more than 15 published papers that give a more complete and detailed view of the work.

Body

Participating Institutions, PIs and Development Areas:

- University of Michigan: Dr. Brian Athey. Demonstration project integration and management, Holomer display and interface, holomer storage retrieval and interoperability, statistical reasoning. Tasks 7, 6, 5, 2, 1.
- University of Washington Bioengineering (UWB): Dr. James Bassingthwaighte. Highly Integrated Physiology (HIP) models. Tasks 2, 1.
- University of Utah Scientific Computing and Imaging Institute (SCI): Dr. Chris Johnson: The SCIRun Modeling and Visualization platform and Heart Electrophysiology. Tasks 2, 3.
- General Electric Global Research (GE), Harvard University subcontractor: Mr. Bill Lorensen and Dr. Peter Ratiu: Segmentation, Anatomy Label Maps and CT processing. Task 4.
- University of California San Diego (UCSD), University of Auckland (UA) subcontractor: Dr. Andrew McCulloch, UCSD, and Dr. Peter Hunter, UA. Heart Finite Element Modeling. Tasks 2, 3.
- Stanford University (Stanford): Drs. Mark Musen and Parvati Dev. Anatomy Reasoning and Tasks 1, 2.
- Federation of American Scientists (FAS): Dr. Henry Kelly. Digital Human.
- Case Western Reserve University (CWRU): Dr. Cenk Cavusoglu. Medical Robotics.
- University of Washington Structural Informatics Group (UWSIG): Dr. Cornelius Rosse with Dr. Dan Cook. Virtual Soldier Knowledge Base (VSKB). Extended FMA. Tasks 3, 5.
- TATRC: Dr. Gerry Moses. Task 7.
  TATRC Contractors:
  1. ATK-Mission Research Corporation (ATK-MRC): Mr. Robert Eisler. Ballistics, wound modeling, and tissue loading. Task 3.
  2. Brooke Army Medical Center Institute for Surgical Research (ISR): CPT Eric Ansorge. Animal experimental protocols and data collection.
  3. Crowley Davis Research (CDR): Mr. Tom Menten. Compression algorithms. Task 6.
  4. Xtria, LLC: Mr. John Monville. Ptag Holomer dog tag, adaptor for HP Ipaq handheld. Task 6.
  5. Oak Ridge National Laboratory (ORNL): Dr. Richard Ward. The Hotbox reasoning interface, web services. Task 1.

The following Overview Figure I, from the original proposal, shows the work areas to be discussed below.

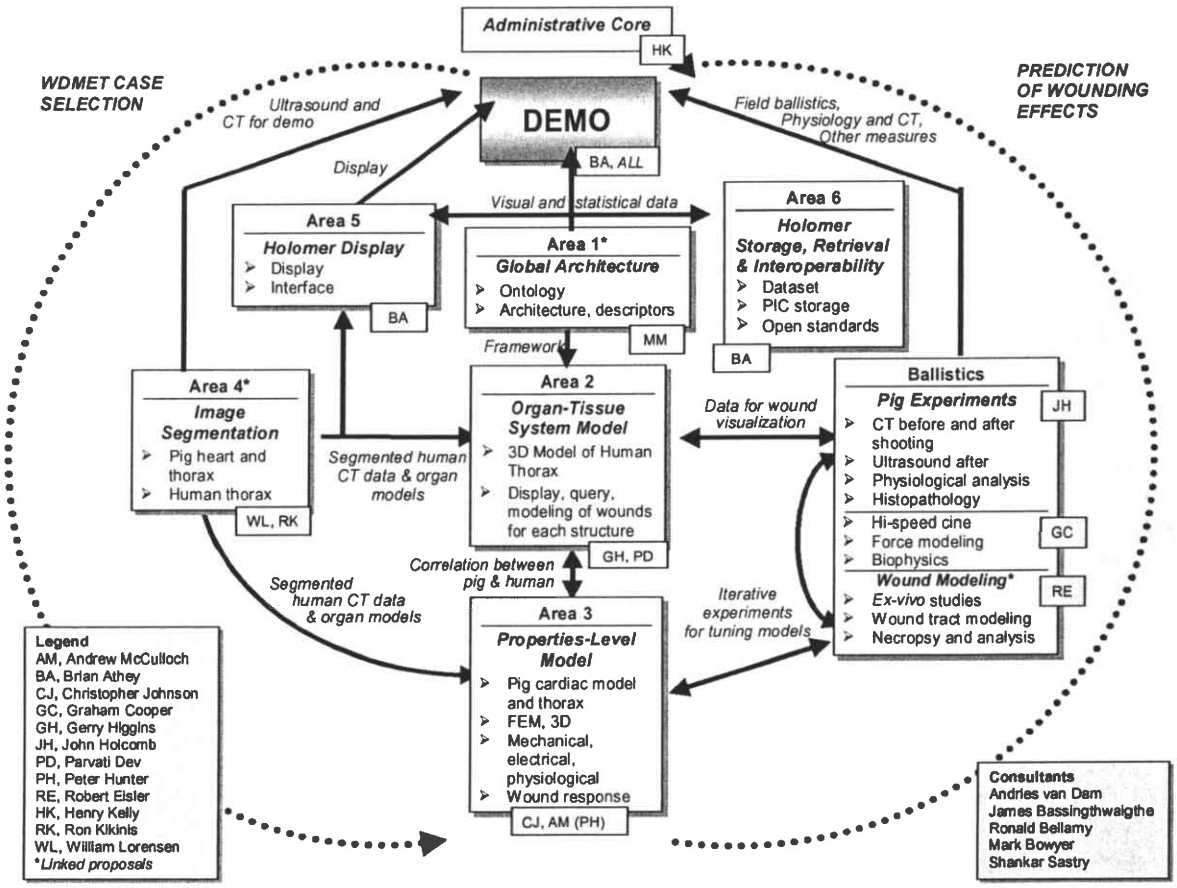

Overview Figure: Work Areas to be discussed in the report. Legend on bottom left gives table of abbreviations of key Investigators, which are related to Work Areas defined by the original Statement of work published by the sponsor, DARPA, in its orginal Statement of Work (SOW). The "Demo" task is work area 7, led by the University of Michigan and PI Brian Athey.

Phase I of the Virtual Soldier Project started at a pre-kickoff meeting held in Ann Arbor, MI on August 22-23, 2003. A kickoff meeting was held in Alexandra, VA on October 14, 2003. The contract between the U.S. Army and the University of Michigan as prime contractor was signed on December 24, 2003 with an effective date of December 1, 2003. The majority of work on the project was completed between December 1, 2003 and June 30, 2005. Results were reported in quarterly reports; at quarterly meetings; in papers, posters, and presentations delivered at MMVR 2005; at two demonstrations held in Ann Arbor on March 17, 2005 and June 14, 2005; in a series of video presentations summarizing the demonstrations; and in more than 15 published papers.

Definitive progress was made on all seven tasks of the project: (1) global architecture, (2) organ-tissue models, (3) property-levels model, (4) automatic segmentation of organ-tissue systems, (5) holomer display and interface, (6) holomer storage, retrieval and interoperability, and (7)

demonstrations showing project integration and statistical prediction of outcomes to an accuracy > 0.80. (See Overview Figure, above).

The main deliverables for Phase I were the demonstrations held in Ann Arbor on March 17, 2005 and June 14, 2005. The March 17th demonstration included five components covering (i) statistical reasoning; (ii) multiscale modeling and simulation; (iii) causal reasoning, (iv) P-Tag, CODEC, holomer displays and hotbox, and (v) autostereoscopic/holographic display.

On March 18th the DARPA Program Manager, Rick Satava, said he was pleased with what he saw during the demonstration, felt the project participants had done a good job, had done what was expected, and that the project was on track. Dr. Satava also asked for some additional work including (i) analysis of additional experiments to be conducted by ISR; (ii) statistical analysis of the data already collected as well as new data that had only recently become available or which was expected to become available over the next few weeks; (iii) work, primarily at GE, on forecasting post-injury anatomy from baseline and post-injury CT scans; and (iv) a second much shorter demonstration focused much more on the statistical work needed to identify alarms and forecast survival or time to death.

The June 14th demonstration included (i) a more integrated end-to-end demonstration of statistical reasoning, multi-scale modeling, and comparison of anatomy from anatomy forecasts against autopsy results; (ii) a report of statistical findings; and (iii) a causal reasoning video presentation using the Virtual Soldier Knowledge Base (VSKB), simulated baseline and post injury physiology data, and ballistic modeling to automatically generate the multiple holomer instances necessary to accommodate uncertainties in baseline conditions, damage assessment, pathological response, and alternative interventions.

Following the demonstration on June 14th, Dr. Satava declared Phase I to be a success and focused our remaining Phase I work on summarizing and presenting the results within DARPA and the White Paper development for potential Phase II activities (submitted to DARPA).

Dr. Brian Athey, Dr. Fred Bookstein and Mr. Jeff Ogden have been the driving forces in the overall project coordination and intellectual leadership, assessing progress and directing the efforts of the subcontractors. They served as the primary liaisons between University of Michigan subcontractors, TATRC, and TATRC subcontractors.

THE DARPA Virtual Soldier Project created mathematical modeling approaches to develop an information representation (a holographic medical electronic representation or holomer) of an individual soldier that can be used to augment medical care on and off the battlefield with a new level of integration. The Virtual Soldier is based upon complex models derived from biologically driven principles and populated with properties extracted from evidence-based data. The Phase 1 effort addressed all 7 Task Areas and provided three-dimensionally displayed models with an Organ-tissue System model component and a Properties Level model component and two reasoning mechanisms (Statistical and Causal). The VSP demonstrations showed the project deliverables can provide multiple capabilities, including but not limited to diagnosis of battlefield injuries. In order to develop the VSP, integrated inter-disciplinary teaming occurred where all researchers collaborated

extensively throughout the development toward the two demonstrations to integrate the technologies and meet the program goals. The following areas were addressed to construct the Holomer, to provide wound diagnosis and forecasts of wound outcomes >0.8, and to conduct the Phase 1 demonstrations:

1. Global Architecture. The University of Washington (UW), Stanford University, Oak Ridge National Laboratories (ORNL), University of Utah and University of Michigan collaborated to develop a generalizable, scalable ontology to characterize the holomer and provided the architecture to integrate the organ-tissue system model and properties-level models. The UW Foundational Model of Anatomy (FMA), UW Virtual Soldier Knowledge Base (VSKB) and Causal Reasoning component, Stanford Protégé, UM Statistical Reasoning component, ORNL HotBox, UW HIP modeling, and U. Utah SciRun software components were integrated and physical properties added as descriptors. The heart and circulation was the major organ system targeted. This milestone architecture with descriptors for the heart and circulation assigned attributes to the system and can in principle incorporate all levels of properties (genetic, molecular, biochemical, cellular, physiologic, organ, tissue and whole body).
2. Organ-tissue system model component. The organ systems modeled in Phase 1 were certain organs of the chest cavity, specifically the chest wall, heart, great vessels, lung and aorta. The milestone of a full 3-D representation of the chest cavity with segmented heart, great vessels, lung and aorta of the Visible Human Male model fully interactive for display, query, and modeling of a penetrating injury was demonstrated. Phase II White Papers were prepared to address other organs and tissues (e.g., liver, kidney, hemopoetic, lymphatic, etc.) systems.
3. Properties-levels model. These models consisted of the different levels of representation modeled within the organ-tissue system. For Phase 1 (heart only) the levels modeled included the cellular and molecular by the myocyte modeling of the University of Auckland and UCSD, physiologic (including electrophysiology, mechanics, hemodynamics, etc.) via the UCSD electrophysiology modeling based on ISR experimental EKG data, the University of Washington HIP models, and total organ structure from General Electric / Brigham and Women's Hospital geometric representations and University of Michigan Edgewarp morphometric modeling. The modeling dynamics responded to a penetrating wound of the heart by predicting the expected response at each level to the wounding forces. Material properties derived from ATK-MRC experiments provided input for the analytical simulation of the projectile trajectory and the wound tract model, and modeling by the University of Utah.
4. Automatic segmentation of organ-tissue systems. The individual organ-tissue system models (e.g., heart, lung, great vessels, etc.) on the whole-organ level were derived (segmented) from a volume-labeled Visible Human Male dataset atlas and experimental subject's Computed Tomography (CT) and visually displayed in three dimensions. Additional imaging modalities such as Magnetic Resonance Imaging (MRI), Positron Emission Tomography (PET) were not included in this Phase I effort but extension of the developed techniques to these modalities is possible. General Electric and Brigham and Women's Hospital were the main collaborators in this effort. In addition, the database that provided the storing and displaying of segmented images of the heart was linked to the Task

Area 1 general architecture and was capable of storing the data for every property of the heart.

5. Holomer display and interface. The display of the Virtual Soldier must bear a high-fidelity resemblance to the real data. For Phase 1, the image of the heart was a full 3D volume rendered representation. Segmentations from Task Area 4, a Holographic Optical Element (HOE) display, the University of Utah SCIrun software environment, and the ORNL Hotbox all integrated by the University of Michigan demonstrated this capability. Interaction with the 3-D display representation provided rotation, scaling and translation. Physiology measurements computed by University of Washington HIP modeling followed the 500Mhz data collected by ISR. A separate display system (the All-in-One demonstration of June 17th, 2005) integrated the Task 1 global architecture, Task 2 and Task 3 model components, Task 4 automatic segmentation, and Task 6 holomer storage areas. The software driving both display systems was jointly developed by the University of Michigan, the University of Utah, and ORNL.
6. Holomer storage, retrieval and interoperability. The CT dataset and all segmented models used for the March 17 demonstration was stored on a 2Gigabyte P-Tag (e.g. U.S. Army Personnel Information Carrier) provided by Xtria Corporation. Compression algorithms provided by Crowley Davis Research Corporation allowed the full dataset to be placed on the P-Tag and demonstrated a reduced transfer time from the P-Tag for appropriate Regions of Interest. Investigation of the BMIS-T software architecture and general medical record database architectures suggests transfer of this data to other medical records platforms will be feasible.
7. Demonstration. The March 17th and June 14th Demonstrations showed the integration of the individual project tasks and the work of the participating institutions in a unified program. The successful prediction of outcomes by statistical reasoning with an accuracy of >0.8 was shown. Data flow between each component was shown; The demonstration proved the validity of the virtual soldier (holomer) concept by a porcine model of wounding of the heart by a fragment, an event paralleling a similar event documented in the Wound Data and Munitions Effectiveness Team (WDMET) database. After a CT scan of the porcine chest, the anatomic model of the heart (and representational models of the chest wall, lung, great vessels and aorta) was derived through automatic segmentation and properties added to only the heart database. The imagery and data were stored on a P-Tag. Continuous monitoring of the experimental subjects occurred until completion of the protocol.

Two model comparisons made must have at least a $p > 0.80$ correlation: The best predictor of survivorship uses the average of ABP and LVP power drop. The accuracy begins at 13/14 and dwindles with the passage of time to 8/9 as the pool of non-survivors shrinks. Accuracy of the assessment of side of wound: five correct classifications and one ambiguity for a set of 6 animals; Time to Death (TTD) and recognition of an alarm state were additional comparison states.

The following passage from the Statistical Findings Report of Dr. Fred Bookstein provides a summary of the results and methods used. For expanded information on the techniques, see the Appendix - Briefing Book #2 - Report of Statistical Findings, pp.40-61.

Summary of Statistical Findings

The hearts of 25 open-chest experimental pigs (anesthetized, respirated) were injured by projected fragments to the left or right ventricular wall. Fourteen of these animals survived for at least 10 minutes while continuously generating valid data 500 times per second in seven instrumented channels. Six of the fourteen were "survivors" that survived at least 120 minutes; we compared these to the 8 "non-survivors" that died before 120 minutes had elapsed. Gross effects of heart rate variation and respiratory cycle were removed from the original time series to produce smoothed resampled waveforms for each original instrument channel except for ECG. From singular-value analysis of these waveforms over one-minute intervals, were extracted predictors of survival minute by minute, predictors of time-to-death (TTD) for the non-survivors, and an estimate of the side of the heart that was injured (LV or RV). The channels contributing to these computations besides ECG included LVP, RVP, and ABP individually and in multivariate combinations. Other available data include various blood chemistries from draws at long intervals.

The best predictor of survivorship that we could find used the average ABP and LVP power drop, minute by minute. This estimator accrues a total of one error, always for the same animal (a non-survivor), at any time after four minutes post-wound. The accuracy thus begins at 13/14 and dwindles with the passage of time to 8/9 as the pool of survivors shrinks. Classification is by the leave-one-out method, in which no animal's data contributes to the formula by which itself is classified, using a standard maximum-likelihood classification rule on Gaussian normal models of different means and variances.

Rise in blood lactate levels, a chemical consequence of lowered cardiac output, tracks the power drop quite well, and so separates survivors form non-survivors nearly as well, although with much lower temporal resolution.

Levels of ABP alone predicts time of death (TTD) in non-survivors by an essentially linear regression TTD ~ 2(ABP-9), with a correlation of 0.65. An "alarm" triggered by a comparison of ABP with its lagged and led values significantly improves the accuracy of the TTD forecast at the lowest range of ABP amplitudes. We believe that alarm makes considerable physiological and bio-mathematical sense, and we look forward to opportunities to extend its logic in later studies of cardiopulmonary instabilities.

All experiments using fragments to cause RV injuries resulted in TTD of less that 10 minutes, and so no such injuries were available for analysis. Prediction of injury location relied on data collected earlier that included probe experiments as well as fragment experiments. Accuracy of the assessment of side of wound is five correct classifications (and one ambiguity) for the set of 6 animals gathered after March 17, 2005 using the actual formulas already demonstrated on March 17.

This combination of signal detection demonstrations substantially fulfills the statistical requirements of the original BAA under which we proceeded.

In the first quarter of 2005, the 7 task areas were addressed by the creation of 4 Working Groups: Statistical Reasoning, Multi-scale Modeling and Simulation, Causal Reasoning, and Infrastructure. The following bullet points highlight the successes of each Working Group.

Statistical Reasoning Goals Demonstrated:

- Diagnose heart wounds w/ accuracy >= 80%
- Compare baseline data to post-injury data
- Accuracy >0.8 for structural abnormalities
- Accuracy >0.8 for physiologic response
- Predict likelihood of battlefield mortality
- Predict outcomes
- Forecast time to death (TTD)
- Demonstrate organ and system level integration
- Extend and use global architecture
- Develop and use automatic segmentation
- Develop and use Holomer display and interface

Multi-scale Modeling and Simulation Goals Demonstrated:

- Compare baseline data to post-injury data
- Demonstrate organ and system level integration
- Extend and use global architecture
- Develop and use automatic segmentation
- Develop and use Holomer display and interface

Causal Reasoning Goals Demonstrated:

- Diagnose heart wounds
- Compare baseline data to post-injury data
- Predict outcomes
- Demonstrate organ and system level integration
- Extend and use global architecture
- Develop and use automatic segmentation
- Develop and use Holomer display and interface

Infrastructure Goals Demonstrated:

- Extend and use global architecture
- Develop and use automatic segmentation
- Develop and use Holomer display and interface
- Store baseline anatomy & physiology on P-Tag
- Data on P-Tag transferable to other systems
- Data compression via CODEC

Table 1: Summary of Phase I Project Goals Demonstrated

✔ Primary Goal of Demonstration
✔ Work Used in Demonstration

	Statistical	Multiscale Modeling	Causal Reasoning	Infrastructure: P-Holomer, P-Tag, CODEC,
Diagnose heart wounds	✔		✔	
Accuracy >= 80%	✔			
Compare baseline data to post-injury data	✔	✔	✔	
Accuracy >0.8 for structural abnormalities	✔			
Accuracy >0.8 for physiologic response	✔			
Predict likelihood of battlefield mortality	✔			
Predict outcomes	✔		✔	
Forecast time to death	✔			
Demonstrate organ and system-level integration	✔	✔	✔	
Extend and use global architecture	✔	✔	✔	✔
Develop and use automatic segmentation	✔	✔	✔	✔
Develop and use Holomer display and interface	✔	✔	✔	✔
Store baseline anatomy and physiology on P-Tag				✔
Data on P-Tag transferable to other systems				✔
Data compression via CODEC				✔

Key Research Accomplishments

Key research accomplishments are listed using the End-to-End Demonstration with a description of the All-in-One Display with contributions from each institution.

The End-to-End Demonstration of June 14th 2005 showed statistical reasoning from effects to causes and created predictive multiscale anatomical and physiologic models

- Using data from two test subjects
    - baseline porcine CT and instrumentation data from ISR
    - post-injury porcine instrumentation data from ISR
    - segmented and labeled anatomy from GE
    - simulated physiology data from UW's HIP model
    - functionally integrated models of circulatory physiology, anatomically and biophysically detailed 3D models of electromechanics of ventricles and torso from UCSD, Auckland, and Utah
    - the Virtual Soldier Knowledge Base (VSKB) from UW
- Statistically forecast survival or death, time to death, the location of the injury, and detected "alarms"
- Model physiologic signals not easily measured in the field
- Validate model output against experimental data
- Display information simultaneously synchronized with respect to time

Allows creation of a database that covers more cases than is possible with experimental data alone

The All in One Display End-to-End Demonstration, June 14th, 2005
University of Michigan

The integrated display of the June 14th demonstration shown in Figure 1 has 8 separate screen components. The Visualization working group, composed primarily of members from the University of Michigan, The University of Utah, and Oak Ridge National Labs, created the All in One software application for the visualization of all data, forecasts, and simulations simultaneously in a single display environment (SCIRun) synchronized with respect to time. All displays show baseline and post-injury data for comparison and can be played in real-time, faster or slower than real-time, and can be paused, rewound, or fast-forwarded to specific points in time. The displays showing three-dimensional data can be viewed on standard monitors or stereo-capable display systems such as the holographic display demonstrated at UM. The combination of displays integrated data from diverse sources in a wide variety of formats including physiological data from ISR, HIP data, mechanical and electrical FE results, GE segmentations, ATK-MRC strain values and wound tracks, the Foundational Model of Anatomy, the Stanford injury list, and wound forecast data.

All of the displays, except for the movies (H and I), are synchronized with respect to time. All of the displays will display baseline and post-injury information. They can be played in real-time,

faster than real-time, slower than real-time, paused, rewound, and fast forwarded to specific points in time.

In the Research Outcomes section, each institution provides further explanation of their contribution.

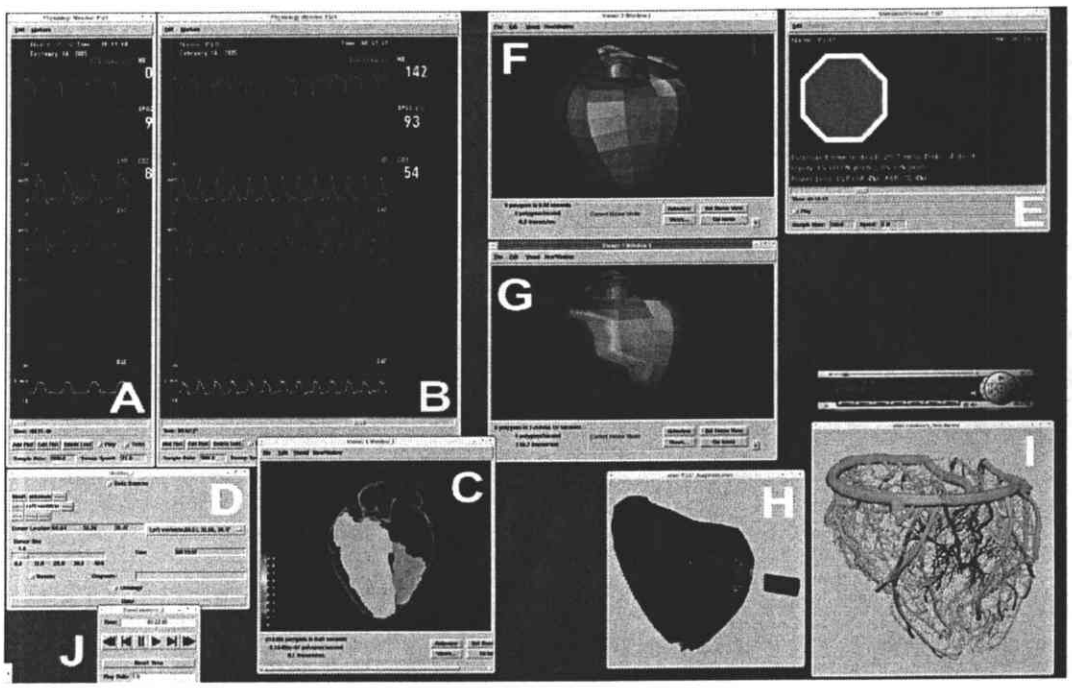

Figure 1: All-in-One Display

There are several displays in the All-in-One Demonstration (Fig. 1) and each separate screen of this display is summarized below.

Figure 1 A and B. Physiology Display

Physiology Waveform data from ISR (real) and University of Washington (HIP simulated) are shown. This display resembles a monitor that one might see in a hospital room. It can display time dependent waveforms and individual values. The display can run at various rates, be paused, scrolled forward or backward or jumped to previously marked points of interest (the Time Control, J, shown above). Negative times are baseline while positive times are post-injury. Multiple displays can be run to allow comparisons of past and present data. These side-by-side physiology displays allowing comparison of different times of the real time-dependent waveforms, and individual values were run at various rates, paused, scrolled forward or back, or jumped to previously marked points of interest. Multiple displays were run to allow comparisons of past and present data. As used during the demonstration the Physiology Display shows both experimental data waveforms from ISR and simulated data that is intermediate or final output from the HIP or FE models. (University of Washington HIP Modeling, pg XX, this report), the real and calculated waveforms can also be shown separately. The figure below displays the HIP model simulated data as grey tracings super-imposed on the ISR recorded data.

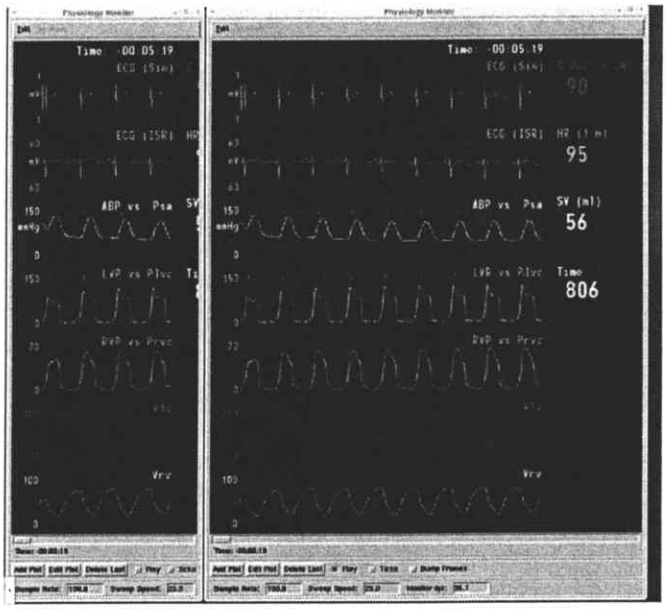

Physiology Display

Figure 1C and 1D: Anatomy Display and Hotbox

1C: Anatomy display showing probability of LV or RV injury. The Anatomy Display shows a 3D view that can be rotated, translated, and scaled to show the anatomical model that has been created from an individual's baseline CT scan. To this baseline image other post-injury information such as the wound track or an indication of specific injuries can be added based on either statistical or causal reasoning.

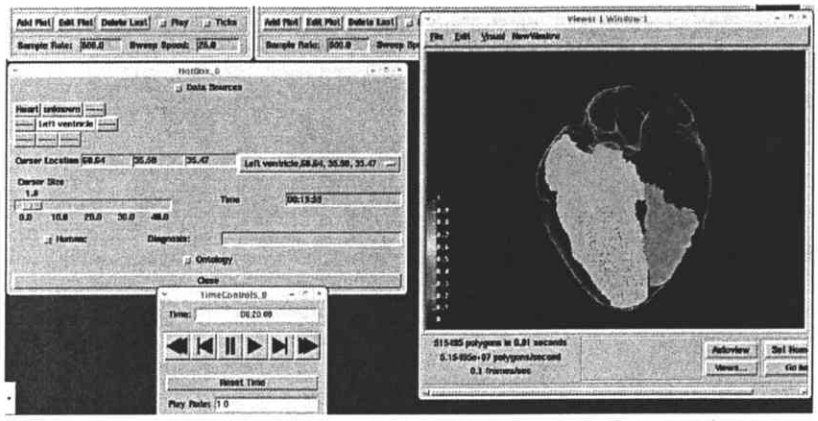

Figure 2: 1 D - Hotbox (left) and 1C - Anatomy Display (right)

1D: Hotbox shows information from the VSKB and physiology data related to anatomical structures selected in the anatomy display (C). The HotBox is a user interface into the 3D anatomy and physiology providing connection between the anatomy and associated physiology and other information of a specific individual (a porcine or a virtual human subject). The HotBox highlights tissue at the location of the 3D probe and adjacent tissues; provides hotlink to select locations; connects the anatomy to the Virtual Soldier Knowledge Base (VSKB) displaying parent/child relationships; connects to the UW injury list description of the wound, connects the visual

anatomical model created from the CT to the Foundational Model of Anatomy, the wound's strain map, and the HIP model results. It works in combination with other SCIRun modules, the Physiology Display, and the 3D probe widget to display specific information selected by the medic, nurse, physician, or researcher.

Figure 1E. Statistical Prediction Display Forecast Display

Forecast display showing information on survival vs. death, time to death, and location of injury

The simplified display of statistical results (Green, Yellow, Red indicators) with short text describing the predicted state and future probabilities is an extensive modification of the March 17th demonstration graphs depicting rates of change of ventricular and aortic pressures (Appendix - Briefing Book #1). The simple schema shown is the most useful for interpretation by a field medic under battlefield conditions. This display has two parts. At the top is the summary area that displays graphics and text to give a quick overview of the current forecast. At the bottom is a more detailed text summary of important forecasts and related information. Both parts are time dependent and are updated once per minute of wall clock time. The display can be set to run in real-time, faster than real-time, can be paused, or moved forward or backward in time to skip or review portions of the forecast.

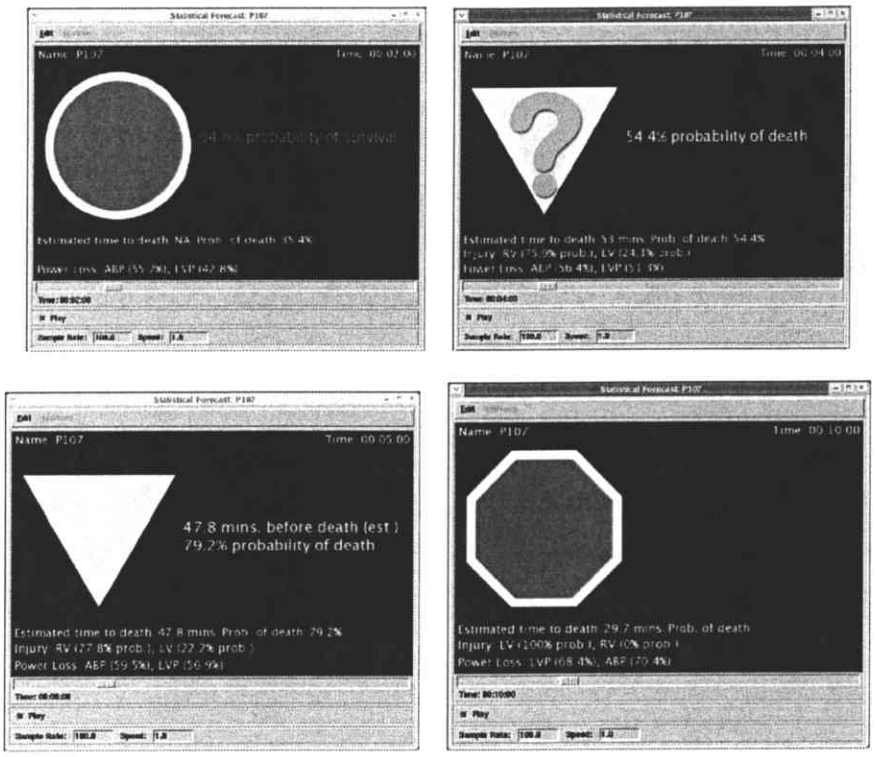

Figure 3: Forecast Display

The graphical portion of the display uses three icons with text to the right to summarize the current forecast:

- A green circle indicates that the subject is expected to survive.
- A red octagon indicates that the subject is expected to die within a relatively short period of time and there is no time for interventions to change the outcomes.

- A yellow triangle indicates that the subject is expected to die, but there is time to intervene to change the outcome.
- To the right of the icons text gives the percentage probability of survival or death and if death is the forecast an estimate of time to death in minutes.

The icons, text, and more detailed text summary are only displayed when there is sufficient data available to make a forecast. A survival vs. death forecast can be made before a time to death forecast. The display is controlled by three user settable thresholds (probability of survival, probability of death, and minimum time to death). A large question mark (?) is added in the center of the icons when the probability of death falls between the survival and death thresholds. These icons and text are a simple distillation of a complex series of statistical reasoning dataflows and processes shown in Fig. 4

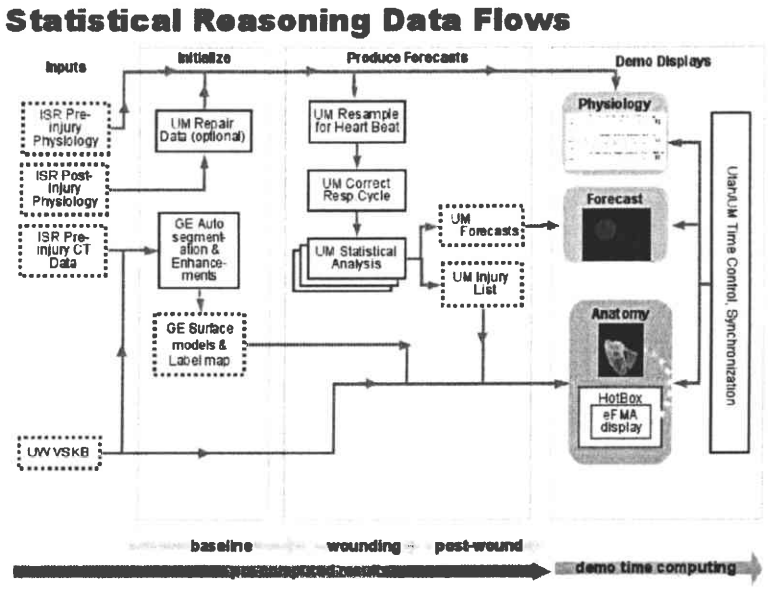

Figure 4: Statistical Reasoning data flow

For more in-depth analysis of the Statistical Reasoning process, see the Statistical Summary pp 21-2X of this report, and Appendix Briefing Book #2 - Report of Statistical Findings, pp.40-61.

Figures 1F, 1G, 1H, 1I - Multiscale Modeling

The Multiscale Modeling dataflow diagrammed in figure 5 reflects this section describing the University of Washington HIP modeling, University of California San Diego, University of Auckland, University of Utah contributions to the All-in-One Demonstration.

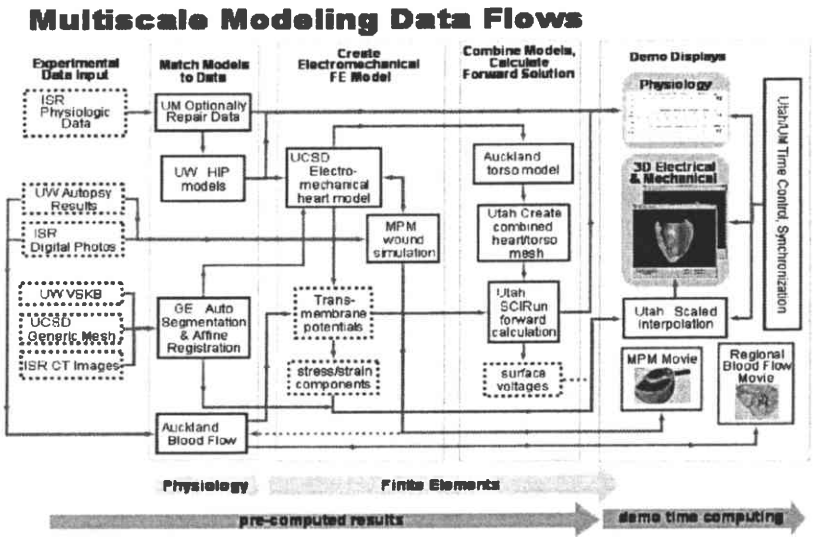

Figure 5: Multiscale Modeling data flow

Highly Integrated Physiology (HIP) Modeling - University of Washington

Outputs of HIP Model

- Pressures, volumes, forward flow and radial flow in:
  - Left atrium, Left ventricle, Proximal aorta, Distal aorta, Systemic arteries, Systemic arterioles, Systemic capillaries, Systemic veins, Vena cava, Right atrium, Right ventricle, Proximal pulmonary artery, Distal pulmonary artery, Small pulmonary arteries, Pulmonary capillaries, Pulmonary shunt, Pulmonary veins, Epicardial arteries, Coronary arteries, Coronary capillaries, and Coronary veins.
- Pressures, volumes, forward flow, and radial flow in:
  - Upper airways
  - Collapsible airways
  - Alveoli
- Heart and respiratory rates
- Heart chamber elastances
- Injury specifications
  - Blood lost from circulation
- Presently 150 variables, 40 ODEs are used in the current HIP modeling.

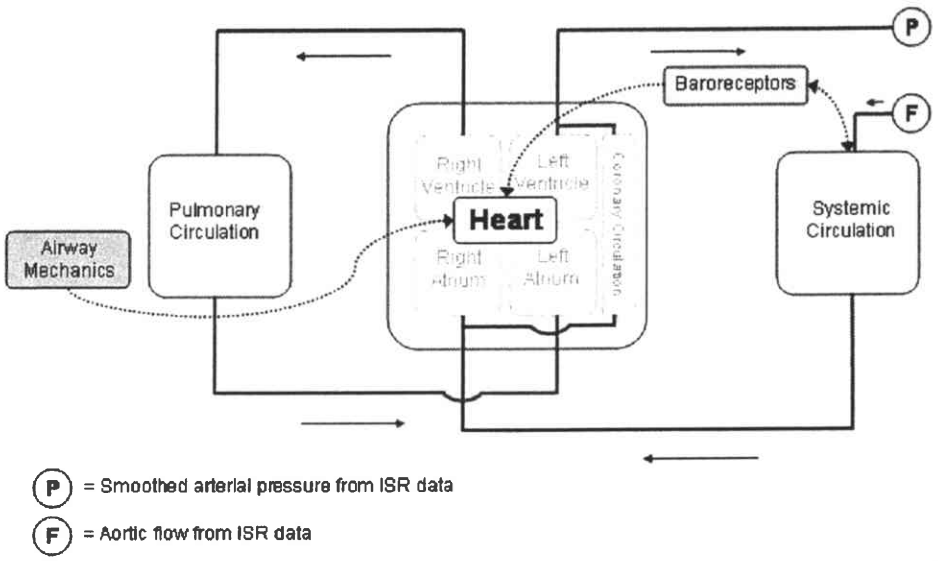

Figure 6: Highly Integrated Physiology (HIP) structure: open loop used for multiscale modeling

3D Finite Element Model of Cardiac Electromechanics - University of California, San Diego, University of Auckland, University of Utah

- Geometry of porcine left and right ventricles scaled to match specific subjects acquired from porcine CT scans (ISR)
- Realistic myofiber architecture
- Nonlinear, anisotropic 3D passive and active material properties
- Local cellular properties based on detailed ionic-currents and realistic excitation-contraction coupling mechanisms
- Ventricular hemodynamics determined by highly integrated circulatory model initialized from and tuned to empirical data (ISR)
- Penetration wound modeled based on MPM results and coronary perfusion model (Auckland) by decoupling cells electrically, altering ionic currents and inhibiting active contraction around site of wound
- Reduction of contractility based on regional perfusion measurements (ISR)
- Real-time visualization done using a unique multi-mesh interpolation scheme triggered by the highly integrated circulatory model
- ECG simulated by solving the bioelectric forward solution in a 3-component model of the torso, heart, and lungs

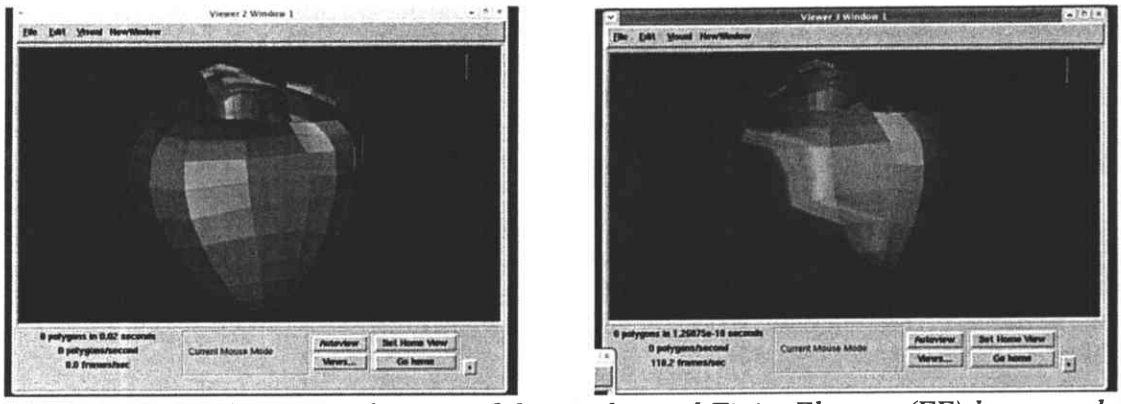

F: *(left panel) 3D visualization of the Mechanical Finite Element (FE) heart model results*
G: *(right panel) 3D visualization of the Electrical Finite Element (FE) results*

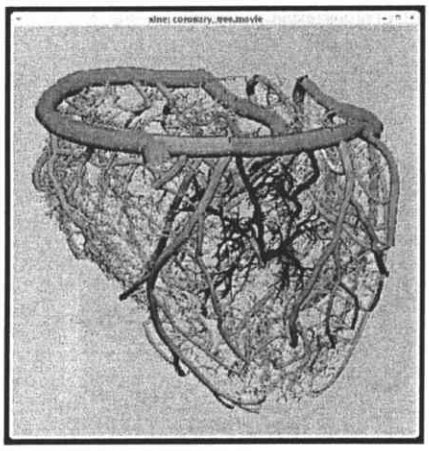

I: *Regional coronary blood flow movie. An animation of the University of Auckland simulation showing changes in regional coronary blood flow at the time of injury*

Material Point Method - University of Utah

- General particle-based multiphysics model
- Handles large deformations/tearing automatically
- Capable of modeling large scale penetrating injuries in arbitrarily complex geometries e.g. torso prototype
- Hi-fidelity/resolution tissue damage simulations
- Leverages 10yr DOE code investment
- Allows detailed validation of coarse-grain models
- Parallel computation of wound database possible

MPM Penetration Trauma of the Heart

- Heart
  - anatomically accurate porcine heart
  - discretized into ~1.5 mil material particles
  - modeled as a transversely isotropic hyperelastic material: an isotropic matrix reinforced by an elastic fiber family (fiber directions vary through the wall thickness)
  - a two-surface strain failure criteria is embedded in the model
- Projected fragment (or shell casing)
  - modeled to experiment specific geometry
  - elasto-plastic (metallic) material model
  - 76 ft/s initial speed
  - frictional contact enforced between tissue and probe

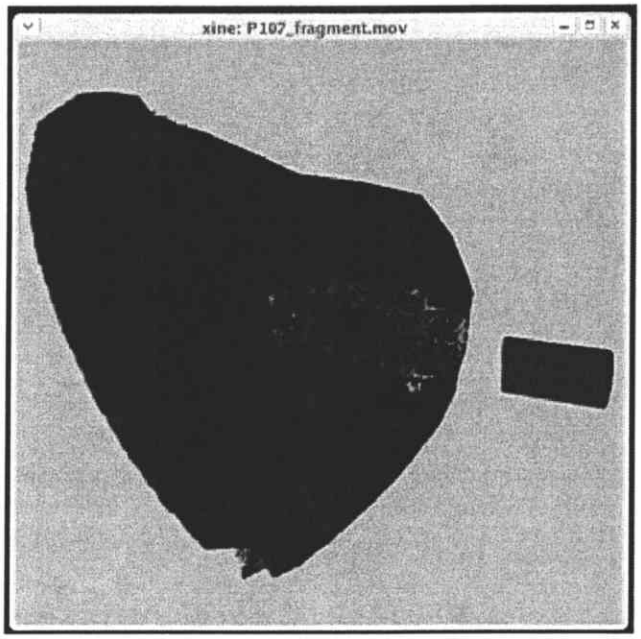

H: Material Point Method (MPM) movie showing a shell casing fragment injury.

Reportable Outcomes

1A. Statistical Analysis Summary - University of Michigan

An analyzable experiment is one with a time-to-death (TTD) longer than 10 minutes and relatively complete data collection. Death is defined as a sustained Mean Arterial Pressure (MAP) of 20 mmHg or less. Survival is defined as a time to death greater than 120 minutes. The survival or time to death in minutes post-injury is given in the title over each plot. The times of any alarms, also in minutes post-injury, are listed toward the bottom of the plot. The plots start with baseline data generally in the upper right quadrant. A "W" indicates the point of wounding (see Figure 1 below). Alarms, when they occur, are indicated by a small solid circle.

For the class of animals surviving more than 10 minutes post-injury:

- At five minutes post injury, death or survival can be forecast accurately for 12 out of the 13 experiments. Percentage loss of LVP amplitude has been shown to be a very sound early prognosticator of ultimate (120+ minute) survival. All of the animals that lost more than 37% of baseline LVP amplitude at five minutes post-wound died; all but one of the animals that lost less than 37% of baseline LVP amplitude at five minutes post-wound lived. Given this sample of experimental results the number 37% can be replaced by any value between 31% and 45% and the statement remains true.
- The fraction of drop of ventricle pressure amplitude, LVP vs. RVP, in the first few minutes is a very highly reliable discriminator of the chamber hit.
- Even absent knowledge of baseline physiology (and thus absent knowledge of the severity of that LVP amplitude loss), there is an indicator of incipient death, the scaled second-difference we have called "the alarm." Of the six test subjects that never showed this alarm, five survived to 120 minutes. Of the seven test subjects that showed the alarm, all died before 120 minutes elapsed. The sixth non-alarm test subject can be shown to have an alarm using an adapted algorithm.
- For the class of 11 test subjects surviving more than 30 minutes post-wound, TTD can be predicted quite well from the time of the alarm. From the first alarm to the ultimate declaration of death is 34 minutes (range, 22 to 48 minutes). These same test subjects all set off a second alarm as well, at times from 3 to 16 minutes before death.

Within the set of 14 non-quarantined analyzable open chest fragment experiments the Statistical Analysis:

- Detected an alarm in all 8 non-survivors and no alarm in all 6 survivors (100%)
- Correctly forecast death or survival for 13 of 14 (93%) at 4 minutes post-injury
- Forecast a TTD correlating 0.75 with actual TTD for the 7 non-survivors still alive at 20 mins. post-injury
- Forecast a TTD of 21 mins. ±9 mins. at 20 mins. before actual death for 6 non-survivors that lived >25 mins.
- Forecast a median TTD of 30 mins. from first alarm for all 8 non-survivors vs. the actual median TTD of 24 mins.

Within a test subset of 6 non-quarantined analyzable open chest fragment experiments:

- Correctly identified injury location (LV vs. RV) for 5 cases with one ambiguous result (83%)

Additional data items were examined for usefulness in making multivariate forecasts, and the forecast criteria changed to include ABP.

Model Development, Training, and Test Sets:

Sets of experimental data are often divided into model development, training, and test sets for statistical analysis. Dividing the Virtual Soldier Project's experimental data in this fashion is not always possible or appropriate. The alternative approaches used are described here.

The 31 model development experiments ISR conducted before November 30th constitute the "model development" set used to develop and refine procedures and gain familiarity with the data.

The 46 experiments ISR conducted between November 30, 2004 and April 28, 2005 were divided into the following three groups:

25 analyzable open chest experiments (regular ECG and full instrumentation);
3 analyzable closed chest experiments (60+ lead ECG and limited instrumentation); and
18 experiments un-analyzable according to criteria established in advance (incomplete or missing data, time to death of 10 minutes or less).

Data from the closed chest experiments were used by the University of Utah to help validate their cardiac electrical models, but were not used for the statistical analysis.

For the June 14th demonstration, only data from the experiments conducted using fragments were used. Omitting the probe experiments left one quarantined experiment and 14 other analyzable open chest fragment experiments. The quarantined experiment could be considered the "test set" and the 14 other experiments as the "training set." However, the 14 available analyzable experiments were too few to be split into statistically meaningful "training" and "test" sets. Instead, we used the technique of leave-out-one cross-validation, a well-known, well-accepted alternative to separate "training" and "test sets" when data are scarce. This technique provided 14 cross-validations, where each experiment is treated as the "test subject" in turn and the remaining 13 subjects become the "training set". In a sense this gives a "test set" of 14 and a "training set" of 182, and because each cross-validation is done independently the required separation of "test" and "training" sets is maintained.

Even without the leave-out-one cross-validation, the statistical results as represented in a standard scatterplot smoothing (appendix - Report of Statistical Findings, final figure section 6) for the dependence of time to death against its principal predictor (amplitude of ABP), along with an adjustment for the observance of the "alarm" are very strong and both powerful and suggestive without additional validation.

The discussion to this point applies to the statistical work done to detect "alarms", and to make survival or death and time-to-death forecasts. Because the fragment only "training set" included no RV injuries, the forecasts of the location of the injury (LV vs. RV) were done using the same criteria used for the March 17th demonstration, using all the analyzable experiments for which

experimental data from ISR had been received on or before January 31, 2005 and including both fragment and probe experiments. Due to the lack of analyzable data from the RV fragment experiments, there was no choice but to use data from the probe experiments to make a statistical forecast of anatomy (injury location) from physiology.
(see Appendix, Briefing Book #2, pp 25 - 27, Use of Experimental Data, Summary of ISR Experiments, Model Development, Training, and Test Sets)
Anatomy-from-Anatomy forecasts included in the June 14th demonstration were based on the CT images from fragment experiments and did not use data from probe experiments.

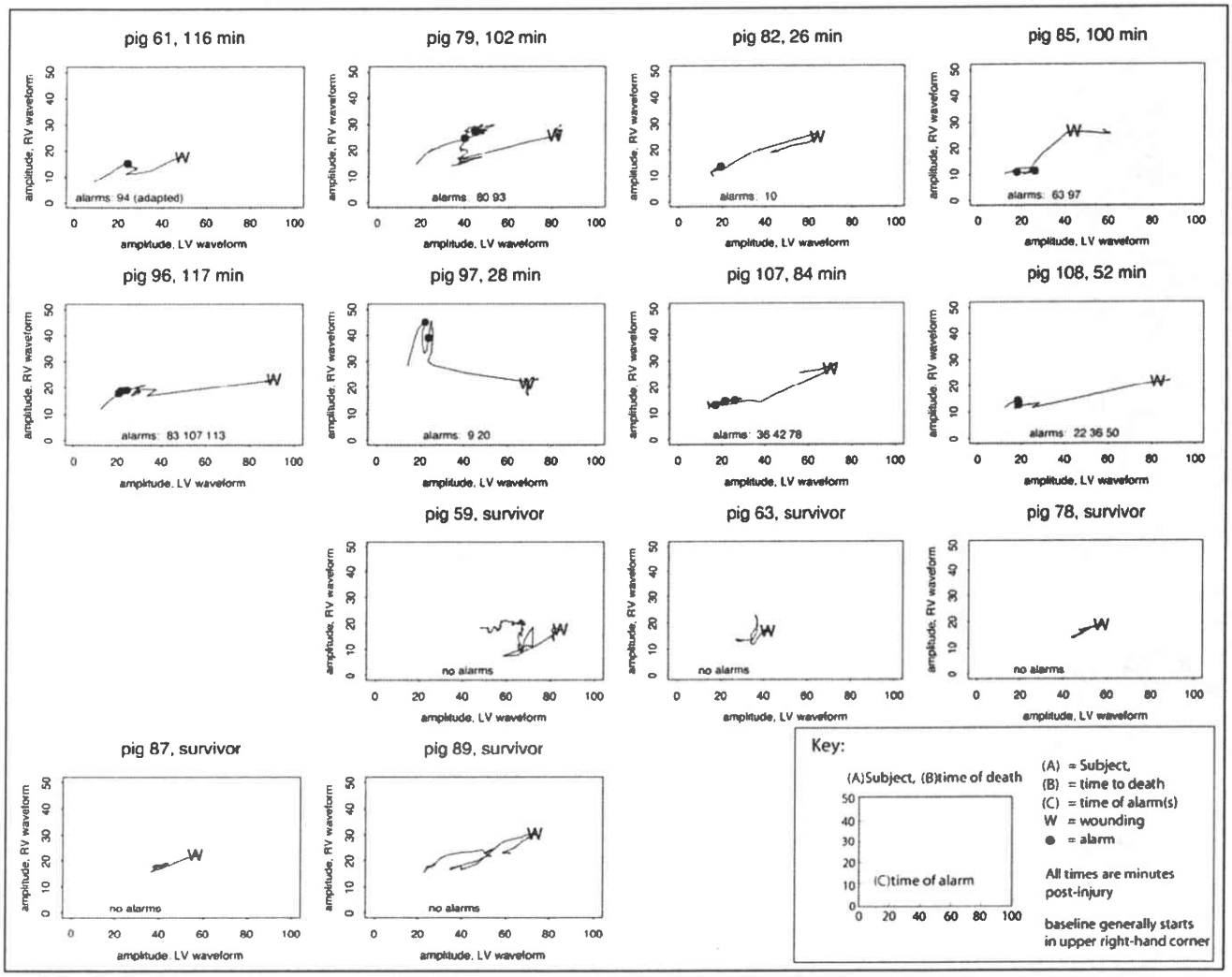

Figure 1. RV vs. LV Amplitude Waveform Graphs

1B. Lactate Analysis University of Michigan

After the March 17th demonstration, Dr. Satava asked for a review of the experimental data collected to search for potential predictors of survival vs. death. The review of the data collected at 500 Hz (14 animals) is included in Dr. Bookstein's Report of Statistical Findings.

Data items collected at less frequent intervals (baseline, 5, 15, 30, 60, 90, and 120 minutes post-injury or at death) were then evaluated: Temperature corrected pH (pHt), Hematocrit (Hct), White Blood Cell (WBC), Platelets (Plt), Prothrombin time (PT), Activated Partial Thromboplastin Time (aPTT), Creatine (Creat), Blood Urine Nitrogen (BUN), Total Protein, Albumin, Glucose, Lactate, Weight, and Blood Loss as a percent of total body weight.

16 animal data sets were used. The two additional animals had incomplete data collected at 500 Hz, but sufficient blood samples were collected to perform this analysis. Blood samples were drawn for all values at baseline (approximately 15 to 30 minutes before injury) and at 5, 15, 30, 60, 90, and 120 minutes, or at death. For some values there is a screening measurement performed days before the experiment, and a pre-baseline measurement taken early in the morning of the experiment. Of the 16 animals, 7 survived for more than 120 minutes and 9 died within 120 minutes of injury. One non-surviving animal, died at exactly 15 minutes, so analysis of the lab values at 15 minutes are not included for this animal.

The most promising value showing separation between survival and death was lactate. The difference between baseline lactate and lactate at 5 and 15 minutes after injury showed perfect discrimination between survivors and subjects who died.

While lactate showed differences, pHt did not help discriminate between the survivors or the non-survivors.

Total Protein showed initial promise in discriminating survivors and non-survivors. Curiously, using the protein values collected before the experiment also allowed discrimination between survivors and non-survivors. Albumin, the most abundant protein in the blood, did not demonstrate the same discriminating pattern. There was no difference in survivor and non-survivor weight, indicating malnourishment was not a factor. Upon analysis of the animals wounded using probes rather than fragments the trend of protein as a discriminator disappeared.

While most trauma protocols are concerned with total fluid loss of the individual, comparing measured total blood loss at the end of the experiment as a percentage of animal body weight was not a good discriminator between survivors and non-survivors.

The other values examined, Hematocrit (Hct), White Blood Cell (WBC), Platelets (Plt), Prothrombin time (PT), Activated Partial Thromboplastin Time (aPTT), Creatine (Creat), Blood Urine Nitrogen (BUN), and Glucose, did not provide useful discrimination between survivors and non-survivors.

2. University of Washington HIP Modeling

Technical Elements:
The Highly Integrated Physiology (HIP) Model outputs were expanded to the:

- Pressures, volumes, forward flow and radial flow in the:

Left atrium, Left ventricle, Proximal aorta, Distal aorta, Systemic arteries, Systemic arterioles, Systemic capillaries, Systemic veins, Vena cava, Right atrium, Right ventricle, Proximal pulmonary artery, Distal pulmonary artery, Small pulmonary arteries, Pulmonary capillaries, Pulmonary shunt, Pulmonary veins, Proximal epicardial arteries, Distal epicardial arteries, Large coronary arteries, Small coronary arteries, Coronary capillaries, Small coronary veins, Large coronary veins, Epicardial veins, and Pericardium (injury flow)

- Pressures, volumes, forward flow, radial flow, [O2], [CO2], and [N2] in:
  Upper airways, collapsible airways and alveoli
- pO2, pCO2, pH, [HCO3] and [Carbaminohemoglobin] in the aorta and pulmonary artery
- Diffusion capacity of O2, CO2 and N2 across the alveolar membrane
- Heart and respiratory rates
- Heart chamber elastances
- Injury specifications:
  Conductances of penetrating "wounds"
  Blood in pericardial space
  Blood lost from circulation

363 variables and 75 Ordinary Differential Equations were included in the HIP models.

Objectives

- Create ordinary differential equation (ODE)-based whole body models for simulating clinically relevant human and porcine physiology.
- Use UW's JSim simulation system to code models, provide system and models to other institutions (ORNL, UCSD, U. Michigan, Stanford).
- Parameterize model to reflect normal resting human physiology.
- Enable simulation of cardiovascular penetrating injuries to the heart
- Parameterize model to match specific baseline and post-injury data gathered from porcine experiments at ISR.
- Use model simulations in conjunction with statistical methods at the University of Michigan to aid in prediction/simulation of battlefield wounds.
- Support UW knowledge representation team by providing HIP model as a collection of entities that will help inform the structure of the VSKB

Deliverables

7 HIP models of varying complexity were created over the course of Phase I, the most advanced of which contains all components listed under Technical Elements.

- Most advanced HIP model (VS001) tuned for textbook normal human physiology
- VS001 tuned to subject P87 baseline and post-injury data: datasets corresponding to a single representative respiratory cycle were created and stored.
- Datasets providing boundary conditions for 3D finite element models were delivered to UCSD.
- Two injury simulations using the textbook human parameterization were created for 1) a pericardium/LV penetrating injury that causes a 0.78 mm diameter hole in the heart and a 20% contractility loss and 2) a pericardium/LV penetrating injury that causes a 0.78 mm

diameter hole in the heart and severs a coronary artery, resulting in a larger contractility loss and a significant amount of blood in the pericardial cavity.

- An array of simulations was used by the statisticians U Michigan statisticians to match ISR data curves.

Impact

The HIP modelling played a key role in three of the four virtual soldier working groups: statistical reasoning, multiscale modelling, and causal reasoning. The HIP model can be tuned to represent a particular subject's unique physiology. Once tuned, the HIP model provides outputs that can be used by other models as surrogates for empirical measurements. HIP results provided the needed boundary conditions for UCSD's models used in the University of Utah torso. Post-injury time-courses can be simulated using the HIP model. Reasoning services developed by UW's knowledge representation team and Stanford U. were used to call HIP model runs for simulating post-injury physiology.

HIP models were also used in conjunction with U. Michigan's statistical methods for matching empirical data curves in order to compare physiological states.

For the June 14th demonstration, the HIP models were fit to the entirety of data pre and post injury for two experimental subjects. The HIP models were also altered to allow the models to be driven by the empirical data.

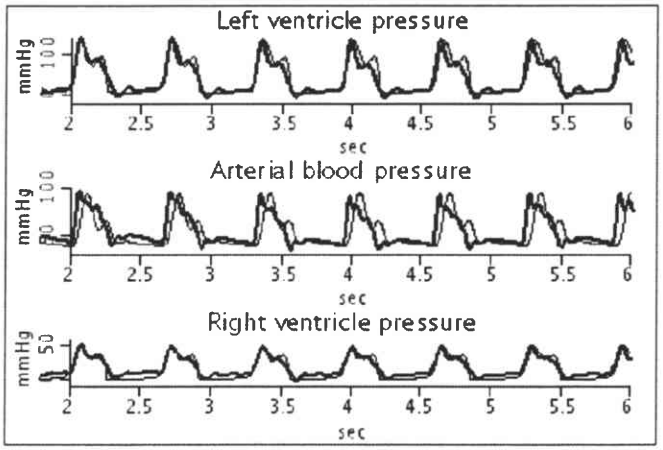

Subject P87 data curves (thick) and corresponding HIP model fits (thin)

3. University of Utah

- Perfusion fields and Material Point Method (MPM) data were used to model mechanical and electrophysiology. MPM simulations of experimental specifics were generated for two experiments. Simulation of cardiac electrophysiology and ECG were performed by applying high order finite element meshes. The FE mechanical and electrophysiologic simulation

results were visualized in their entirety through development of an extremely novel scaled interpolation scheme (Utah, UCSD).

- The Material Point Method is a general particle-based multiphysics model handled the large deformations/tearing automatically, modeled the large scale penetrating injuries in arbitrarily complex geometries (e.g. torso prototype) and provided hi-fidelity/resolution tissue damage simulations. The MPM leverages 10yr DOE code investment and allows detailed validation of coarse-grain models. Parallel computation of wound database(s) are possible.
- The MPM penetration trauma of the heart was performed on an anatomically accurate porcine heart which had been discretized into ~1.5 mil material particles. This modeling was performed as a transversely isotropic hyper-elastic material - an isotropic matrix reinforced by an elastic fiber family (fiber directions varying through the wall thickness). A two-surface strain failure criteria was embedded in the heart model.
- The projected fragment (or shell casing) was modeled to experiment-specific geometry using an elasto-plastic (metallic) material model. The fragment initial velocity was 76 ft/s, with frictional contact enforced between the tissue and probe on subsequent penetration.

	Deliverable Schedule
Q1	First MPM Model was developed from heart geometry Higher Order Design (HOE) in SCIRun Closed chest experiment planning
Q2	Developed close chest experimental ECG protocol – equipment (ISR) Proof of concept simulation of bullet wound to porcine heart with MPM Posted first SCIRun net for visualization of human data SCIRun implementation to MRC
Q3	Assisted in closed chest experiments (on-site) (ISR/UMich) First run of MPM model with high speed fragment Implemented HOE in SCIRun to support UCSD/Auckland models Aided in development of HotBox as a SCIRun module (ORNL) Began project management role in Multi-Scale Modeling demo preparation
Q4	Prototype visualization of visible human within SCIRun (GE/ORNL/UMich) Prototype visualization of UCSD heart model (strain/currents) (UCSD) Story-board of demo for Multi-Scale modeling group (UCSD/UWash/UMich) Created physiology monitor module (UMich/UWash/ORNL)
Q5	Meshed the UCSD heart model into Auckland torso model (UCSD/Auckland) Calculated electrical field in the torso Ran a successful demo with SCIRun as part of 3 of 4 demos (UMich/UWash/UCSD/ORNL/GE)

New Technical Ideas

- Beginning of a Holomer Display
- Injury Modeling on the Porcine Torso
- Injury due to Penetration or Blast could be Modeled for Porcine and Human Torso using MPM
- Integrative Software System for Multiple Organ Systems through Multiple Scales

Impact

Created Software Environment for: HotBox, Physiology display, Model display, Anatomy display
Injury Modeling on the Porcine Heart
Simulated Torso (surface + volume) ECG: based on bidomain model of cardiac electrophysiology.

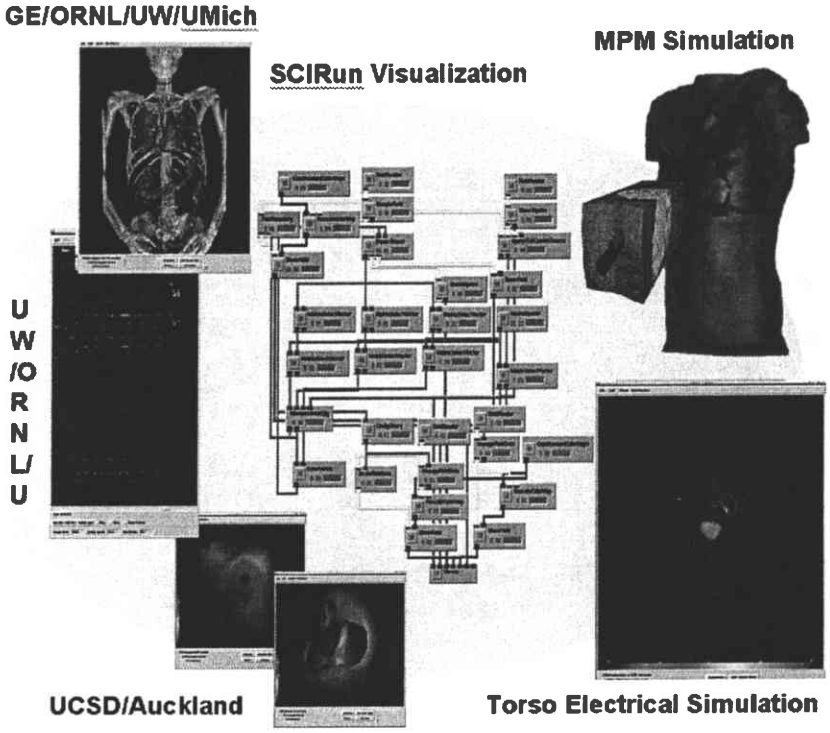

4. ATK-MRC

Developed analytic models describing tissue damage from ballistic impact by low velocity fragments penetrating human heart. Tissue damage included descriptions of projectile trajectory through heart and tissue damage lateral to projectile trajectory (*wound tract*) (Fig. 1). Predicted anatomical tissue disruptions were used as input to physiological models to predict casualty outcome.

Observed that penetration depth, $\delta(v)$, as function of striking velocity, v, of a spherical projectile into materials like soft tissue have sigmoidally shaped curves bounded by low velocity and high velocity asymptotes. Retarding force on spherical projectile derived from $\delta=\delta(v)$. More complicated projectile geometries represented as ensemble of spherical projectiles where retarding forces derived by integrating resultant forces from constituent spheres about projectile geometry. For unknown material (e.g., Human Tissue) Taylor series expansion of asymptotes were rigorously derived. Limits of asymptotes as $v\rightarrow 0$ and $v\infty\rightarrow$ have dominate leading terms expressed in terms of independently measured material properties. This information was used to construct $\delta=\delta(v)$ for unknown materials. Intermediate velocity $\delta=\delta(v)$ was established by matching slopes of high and low velocity asymptotes (Fig 2.). This allowed the determination of projectile retarding forces in unknown materials where quasi-static properties were available. Projectile rotational kinematics and trajectory were determined

by continuum techniques once retarding forces specified facilitated the development of analytical models of wounding state simulations (Figs. 3 and 4).

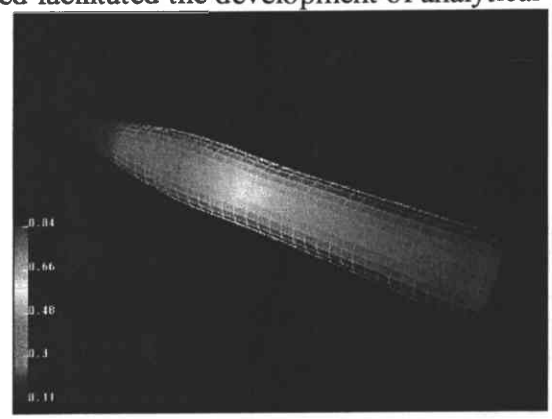

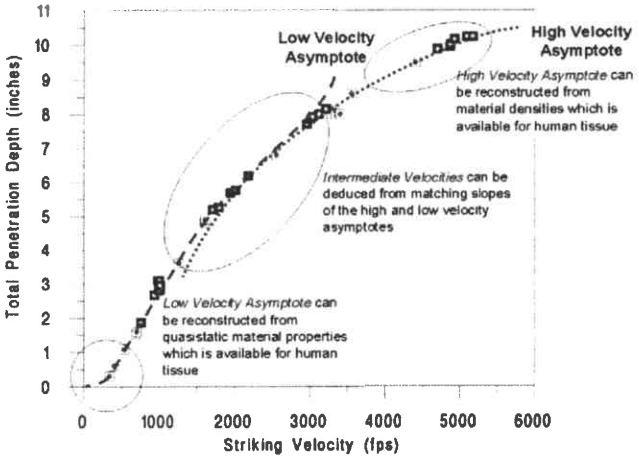

Fig 1. ATK-MRC circumferential strain model of wound tract *Fig 2. Total Penetration Depth vs Striking Velocity*

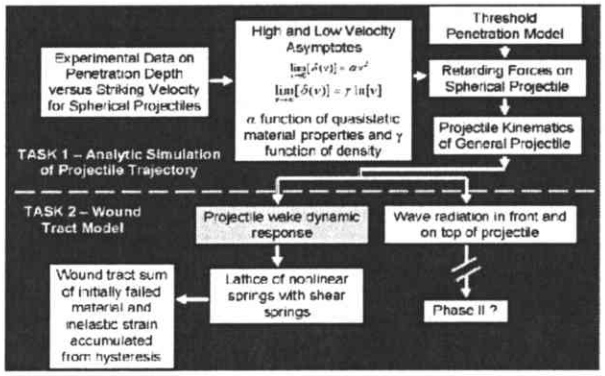

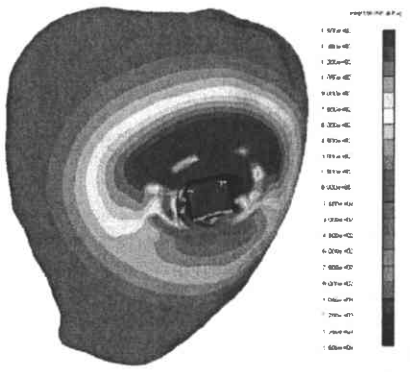

Fig. 3. Schema of Analytical Simulation of Projectile Trajectory and Wound Tract Model

Fig.4. Stress Contours on LV Surface at 95 milliseconds after impact. Peak stress is 20 bars.

ATK-MRC Injury Device Characterization
GLB, Inc. in cooperation with ATK-MRC performed a preliminary characterization of the Modified Nail Gun (MNG) being used at ISR. GLB determined the MNG probe travels at a velocity of between 76 and 92 feet per second (+-7%) and they estimate that a fragment would be released at a velocity of approximately 100 feet per second. The device characterization suggests it is possible the ISR MNG delivers a fragment with a velocity and energy similar to .32 and .60 caliber projectiles.

5. Crowley Davis

Impact
Efficient compression of image data provides potentially life-saving transmission time reductions. Compression allows required data to fit onto the current P-Tag models.

Such transmissions between a soldier's P-Tag and field data stores provide medical personnel with access to critical information in time to affect immediate field response. Until such compression is available, field personnel will either have to make vital decisions without little or no relevant information.

New Technical Ideas
Development and adaptation of compression algorithms into a single CODEC to process different file types for the most efficient compression.

- Enhancement and application of emerging image compression technologies with features (e.g., ROI) to further reduce size and increase transmission speed.
- Optimization for fast decompression even at the sacrifice of compression speed.
- Use of developmental processes to rebuild the original file.
- Invention of a lossy VTK model compression using a constrained step size quantization.
- Adaptation of Generalized Partial Significant Bitplanes Shift (GPSBS) theory for later application to preserve image fidelity.

	Milestones	Deliverables
Q1	CODEC Version 1. Standard Compression, Part 1 - Basic Functionalities	CODEC Requirements Document; CODEC Framework; Basic Functionalities of the reference software. (JPEG2000)
Q2	CODEC Version 2. Standard Compression, Part 2 - Extended Functionalities	Support for DICOM format; Programmatic access (Function Call); Batch processing of multiple files; Lossless image compression; GUI Demo of CODEC
Q3	CODEC Version 2. Standard Compression, Part 2 - Extended Functionalities (Continued)	Enhancements on GUI Demo of CODEC; Region Of Interest (ROI) coding, Part 1; Lossless text coding; Initial analysis and report on coding of VTK models.
Q4	CODEC Version 3. Advanced	Report on GPSBS method for ROI coding; ROI

	Compression System	coding for GUI; Edgebreaker, Part 1: compression for geometry data;
Q5	CODEC Version 3. Advanced Compression System (Continued)	Support for PNG file format; Edgebreaker, Part 2: VTK binary compressed format, Compression for points data, VTK compression tutorial
Q6	Phase I demo	Software testing; Final CODEC wrap-up; Delivery of the CODEC; Final report

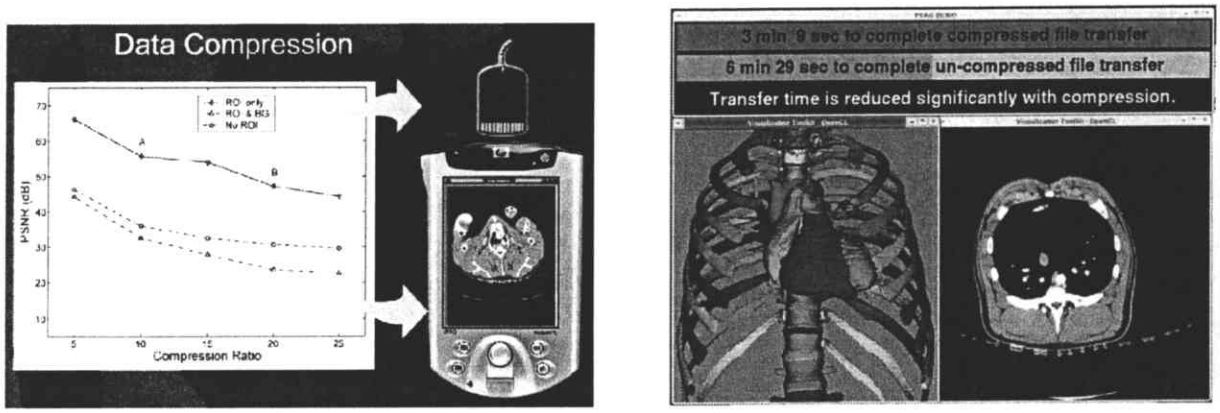

Data Compression and Transfer Rates for CDR processed data

6. General Electric Global Research (GE)

Description / Objectives / Methods

- Automatically generate patient-specific models from computed tomography data. Use of high resolution Visible Human anatomy atlases to generate automatic segmentations of individual data. Integration of anatomical data with modeling and physiology. Adaptation of baseline data to multi-scale modeling.
- Technically, software techniques are maturing and there is a rich set of techniques available for automatic segmentation and registration of radiological data. The main challenge is combining multiple approaches into a robust, automatic processing pipeline. There are still challenges to produce consistent high quality CT data for the baseline.
- Militarily, augmenting medic decision support with patient specific anatomical data and linking to integrated models and battlefield measurements will enhance triage and increase the fraction of potentially avoidable battlefield casualties supporting medics. Augmentation of baseline data with field deployable imaging sensors should be explored as they become available.

Project Integration for Holomer and Trauma Demonstrations

- Global Architecture – coordinated atlas labeling with the ontology
- CT Quality Control – processed all CT data through automated smoothing process

- Automatic Segmentation – registered human/porcine atlases to patient-specific radiology
- Geometric Modeling – provided implicit and geometric models of segmented structures for both human and porcine data
- Holomer storage – optimized storage requirements
- Holomer display – provide realistic models suitable for interactive display

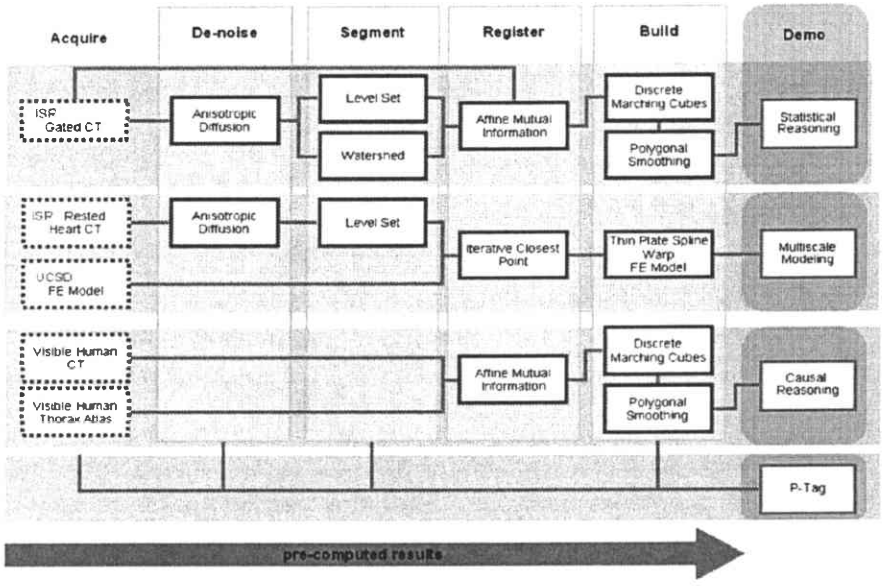

Milestones and Deliverables Schedule

	Milestone(s)	Deliverable(s)
Q1	Preliminary geometry models for human atlas	Discrete geometric models.
Q2	Register cryo-section atlas to Visible Human Male CT Data. Refine geometric models for human atlas.	Transformed geometry. Discrete, smoothed, decimated and colored geometric files.
Q3	Create initial porcine atlas. Porcine CT Data Quality control. Automatic registration of Visible Human atlas to novel data.	Initial Porcine label maps. Labeled novel CT data.
Q4	Refined porcine atlas. Porcine CT Data smoothing	Higher fidelity porcine label maps. Smoothed porcine CT data.
Q5	Phase I Demonstration Automatic segmentation of porcine data. Refined Visible Human Thorax Atlas	Labels for all porcine data. Geometric models for all porcine data. Refined Visible Human geometry data.
Q6	Anatomy/Anatomy wound validation Refined registration/segmentation algorithms	Qualitative assessment of CT for wound assessment. Enhanced automatic segmentation pipeline.

7. Anatomy from Anatomy Forecast and Comparison to Autopsy Findings
General Electric, ISR, University of Washington

- Analyze postmortem image data, including:
  - porcine CT images from ISR,
  - postmortem isolated heart CT images from ISR
  - manual segmentation by UW
  - smoothed, segmented, and labeled anatomy from GE
  - the Virtual Soldier Knowledge Base (VSKB) from UW, and
  - autopsy reports from UW
- Determine which anatomical structures are injured
- Display information for use by the medic/physician
- Compare forecast and autopsy results

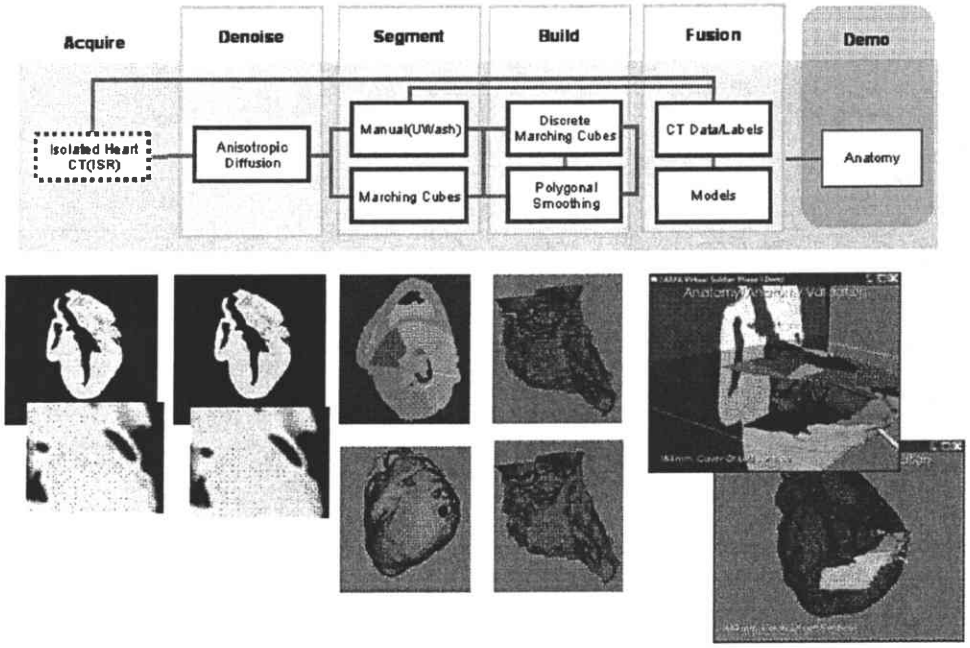

Anatomy from anatomy data flow diagram

8. University of Washington, Causal Reasoning

Development of the Virtual Soldier Knowledge Base (VSKB) containing anatomy relationships and physical/physiology properties (U. Washington, Stanford, ORNL).

New Technical Ideas

- Used **symbolic representations**, such as the Injury List, to automatically amend simulation models according to the outcomes of symbolic reasoning processes.
- Extend the **Foundational Model of Anatomy** (eFMA) to represent zones of myocardium and other cardiac parts for labeling the Visible Human data set.

- Create a **Pathology Reference Ontology** (PathRO) to link injuries (e.g., tissue ablation, added conduit) to eFMA entities.
- Create a **Physiology Reference Ontology** (PRO) with a Physical Attribute Taxonomy (PAT) to represent attributes such as mass and pressure.
- Create **Injury Lists** as XML data structures to symbolically represent instances of cardiac injuries in terms of eFMA, PathRO and PRO entities.

Impact

- The VSKB demonstrated that ontologies of **anatomy, physiology** and **pathology** can integrate **all** components of the VSP project.
- VSKB was required for **Holomer display, reasoning** and **simulation** of pathophysiological outcomes of wounds.
- VSKB-based **label maps** (fig 1) of Visible Human were used to navigate anatomical displays and automate reasoning about cardiac injuries (fig 2).
- VSKB-based **Injury Lists** (fig 1) represented causal reasoning outcomes (fig 2; e.g., *added conduit* in *wall of left ventricle*) and were used to amend math models to simulate pathophysiology.

Deliverables

- Created the **VSKB** ontology that includes **eFMA, PRO** and **PathRO**.
- We prototyped the **Injury List** used to communicate causal reasoning results to displays and simulations.
- Extended the **FMA** to model detailed anatomy of the myocardium.
- Led the design, implementation and scripting of the **Causal Reasoning Demo.**

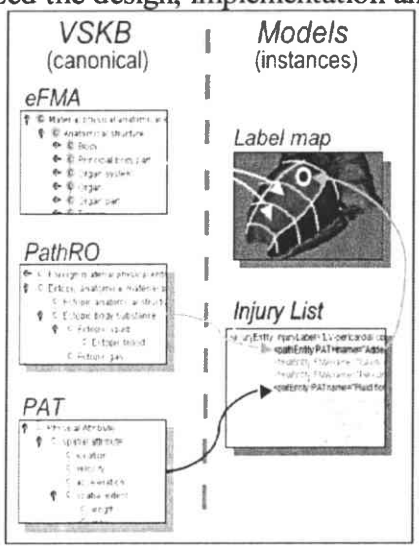

Figure 1.

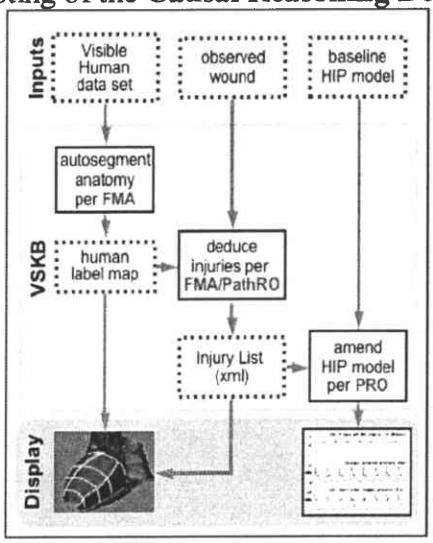

Figure 2.

9. Oak Ridge National Laboratory (ORNL) and University of North Carolina (subcontractor)

The HotBox user interface was used to explore the 3D anatomy and physiology of a specific subject (in the March 17th demonstration, a porcine subject or a virtual human). The Hotbox connected the visual anatomical model created from CT imagery to: the Foundational Model of Anatomy, the wound's strain map, the injury list description of the wound, and the results of the high-level integrative physiological simulation. The Hotbox worked in combination with SCIRun modules, the Physiology Display, and the 3D probe widget to display specific information from the available resources listed above.

The web services created by the University of South Carolina team with appropriate web service client and server software was not completed by the second demonstration. Subsequent additional work has brought this task to near completion.

New Technical Ideas – Features

- HotBox provides connection between the anatomy and associated physiology and other information
- Highlights tissue at the location of the 3D probe
- Shows the tissues adjacent to the location of 3D probe
- Provides hotlink to select locations
- Highlights injured tissue as determined from Injury List
- Visualizes strain map at the proper location
- Launches Physiology Display for location-specific variables
- Connects the anatomy to the Virtual Soldier Knowledge Base (VSKB) displaying parent/child relationships
- Displays time-dependent data supplied by the Injury List
- ORNL/USC provided support in creating Injury List and physiology data files for the Causal Reasoning Demonstration of June 14, 2005

Impact

- HotBox is critical user interface for implementation of the Holographic Medical Electronic Record (Holomer)
- HotBox implements the "deep voxel" concept, locations in the anatomical space provide location-specific physiology information and wound geometry
- HotBox was used in all the demos, providing a user interface to unique features of the Holomer
- By connecting to the VSKB, the HotBox implements the integration of ontological information and geometry
- HotBox connects to the VSKB using the C++ client stubs for the OQAFMA interface (developed by our subcontractor the University of South Carolina)

	Schedule -- Deliverables
Q1	Decision made to use SCIRun for the Holomer Display. Prototype HotBox created by coupling to SCIRun 3D probe widget.
Q2	HotBox prototype integrated into SCIRun. Created SCIRun field files from the VTK surface models provided by GE.

Q3	C++ client Web service developed for the OQAFMA interface to the VSKB. Access to VSKB integrated into the HotBox.
Q4	Incorporated XML parser into the HotBox. Provided capability to read the prototype Injury List provided by UW and Stanford.
Q5	Added capability to display time-dependent information from Injury List (Statistical Reasoning Demo). Hotlink feature added, gives quick access to locations. HotBox readied for 1st demo
Q6	HotBox tested with refined Injury Lists for three injury scenarios for the Causal Demo. Movement of 3D probe to center of selected tissues refined by utilizing proper transform of volume space into the label map and bounding box space.

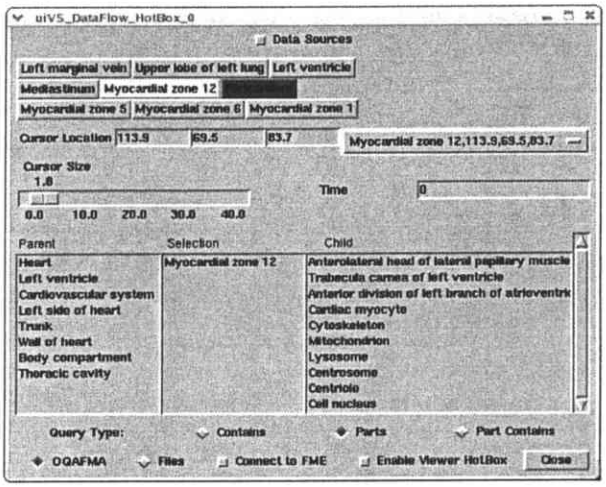

Figure 1. HotBox Interface

10. Stanford University

- Inference of damaged anatomic structures (both primary injuries and injury propagation) based on a wound description or spatially-oriented patterns of tissue strains. Raw data tell the field medic little about the war fighter's internal injuries. Stanford reasoning services provide the field medic with needed insights.
- Developed a software platform to integrate anatomic knowledge with geometry data from image label maps. We created reasoning services using OWL, an emerging standard in knowledge representation that permits automatic classification, to deduce primary and propagated injuries.
- Created a system to demonstrate our reasoning capability. A user specifies the trajectory of the projectile, and the application infers the anatomic structures that are directly injured as well as secondary injuries.
- These reasoning services can be used to provide the field medic decision support, and they can be combined with patient physiological and anatomical data to enhance triage and increase survivability of battlefield casualties.

Impact of Symbolic Reasoning in Final Demonstration

- **Demonstration of automated reasoning.** We delivered capability for automated determination of (1) the size of geometric injury based on inference from strain data, (2) identification of directly injured anatomic structures, (3) likely secondary injuries, including consequences of coronary-artery injury and of wounds in left ventricle causing hemopericardium and hemothorax.
- **Development of XML schema** to transmit results of reasoning to VSP team, permitting integration of reasoning with other services.
- **Prototype global software architecture**, including all data structures and reasoning services for causal reasoning in the Phase I demo.
- **Enhancement of image-based geometry** by our creation of image-processing code to segment heart into regions corresponding to functional anatomic zones and to reconstruct invisible structures, such as the pericardium.
- **Numerous tight collaborations** with other VSP contractors—including GE, MRC, UW, UM, and ORNL—which made the Phase I demo possible

	Milestone(s)	**Deliverable(s)**
Q1	Models of geometry and creation of these models in ITK/VTK derived from GE label maps	
Q2	Design of software architecture for reasoning (the Patient Specific Model) and implementation of API to the PSM. Create representation of cardiac anatomy in OWL and reason about myocardial ischemia after coronary artery damage.	API to the PSM OWL ontology of heart anatomy and coronary supply to myocardium.
Q3	Creation of views of FMA specific to cardiac anatomy and linking this to models of geometry to the VSKB.	FMA view of cardiac anatomy.
Q4	Creation of additional geometry needed for reasoning based on knowledge in FMA. Create prototype application showing links between VSKB and geometry and reasoning based on these models.	New label maps augmented with additional geometry delivered to remainder of project
Q5	Develop reasoning service to interpret MRC strain map data and deduce shape/size of projectile injury. Update reasoners to infer direct injury. Create XML file format to serve as output of reasoning and file exchange of data.	Complete demonstration of reasoning capability running on GE label map data and MRC strain map data, with XML output of reasoning results to be used by remainder of VSP team.
Q6	Update reasoning services according to the needs of the final demo. Added additional reasoning services.	Demonstration of all components of reasoning services and integration with other groups' activities.

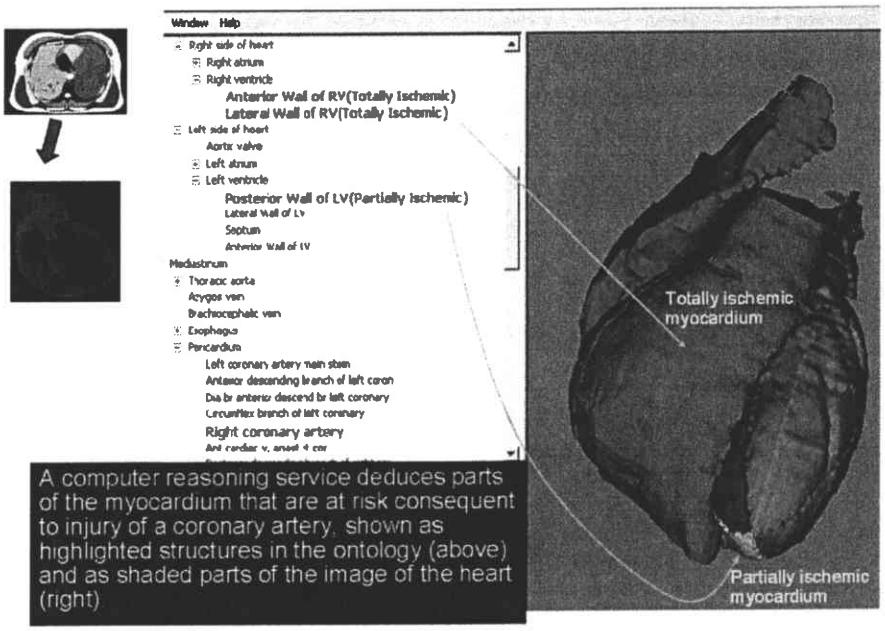

Figure 1. Stanford Reasoning Service

11. UCSD and University of Auckland (subcontractor)

3D Finite Element Model of Cardiac Electromechanics

- Geometry of porcine left and right ventricles scaled to match specific subjects acquired from porcine CT scans (ISR)
- Realistic myofiber architecture implemented
- Nonlinear, anisotropic 3D passive and active material properties
- Local cellular properties based on detailed ionic-currents and realistic excitation-contraction coupling mechanisms
- Ventricular hemodynamics determined by highly integrated circulatory model initialized from and tuned to empirical data (ISR)
- Penetration wound modeled based on MPM results and coronary perfusion model (Auckland) by decoupling cells electrically, altering ionic currents and inhibiting active contraction around site of wound
- Two new regional coronary blood flow simulations – University of Auckland
- Reduction of contractility based on regional perfusion measurements (ISR)
- Real-time visualization done using a unique multi-mesh interpolation scheme triggered by the highly integrated circulatory model
- ECG simulated by solving the bioelectric forward solution in a 3-component model of the torso, heart, and lungs

For the June 14th demonstration, the electrophysiology model had diffusion set to zero at the site of the wound; around the wound hyperkalemia was modeled and a 35% reduction in the sodium-potassium pump added.

Description / Objectives / Methods

- Scientific: Developed and validated anatomically and biophysically detailed 3D models of ventricular electromechanics in interaction with functionally integrated comprehensive models of circulatory physiology to model trauma.
- Technical: Decreased computation time and memory requirements by new hardware (parallel Linux cluster) and by improving parallelization/solver algorithms.
- Militarily: augmenting medic decision support with patient specific physiological and anatomical data and linking to integrated models. Numerical models provide a framework of supplying non-measurable physiologic signals and a variety of injury mechanisms. Numerical and measurable results serve as input for algorithms that forecast survival and/or time to death, developed at University of Michigan.

Project Integration for Trauma Demonstration

- An accurate finite element geometry of porcine left and right ventricle with a realistic myofiber orientation from Auckland University was used to solve cardiac electromechanics. General Electric provided porcine-specific geometries.
- Modeling of excitation-contraction and mechano-electrical feedback by coupling cellular ionic models to models of myofilament activation and crossbridge formation in combination with a mono- or bidomain formulation of propagation.
- Simulated transmembrane potentials were used by University of Utah to calculate potentials on the porcine torso. Torso potentials are measurable and served as a means of tuning and validation.
- Complete integration of ventricular electromechanics and circulatory model from University of Washington, such that the FE model is the driving force of the circulation.

	Milestone(s)	Deliverable(s)
Q1	Auckland porcineheart FE mesh and accompanying porcinefiber and sheet angles converted to UCSD's FE environment. Received porcine torso mesh from Auckland University.	Heart anatomy and torso models delivered to University of Utah.
Q2	Implemented and tested simplified canine cellular ionic model (Fox et al) and coupled it with a modified myo-filament activation model (Rice et al). Implemented new fast solver (SuperLU). Stress and strain were obtained from passively inflating the FE geometry.	Preliminary data for passive deformation of the normal heart was sent to Utah
Q3	Implemented models for human ventricular myocyte ionic currents (ten Tusscher et al), calcium handling, myo-filament activation, crossbridge interactions. Switched FE package from SGI Unix to Linux cluster, reducing computation time and memory.	Preliminary data for transmembrane potential of the normal heart model was sent to Utah for visualization
Q4	Depolarization, stress and strain obtained from simulation of systolic porcine electromechanics. Preliminary injury calculations.	Deformation, strain and fiber angles of the normal heart for whole cardiac cycle was sent to Utah for visualization

Q5	Normal and injured electromechanics computed for pig. Injury based on measurements from ISR. Hemodynamical boundary conditions for FE model set by HIP model. Parallel Linux cluster installed, which reduced simulation of a cellular ionic model and propagation in the porcine mesh from 12 hours to ~10 minutes.	Deformation, strain, and fiber angles for injured and normal heart sent to Utah for visualization in SCIRun. Trans-membrane potentials sent to Utah for forward calculations on torso.
Q6	Refined porcine mesh. Use of tricubic basis functions. Complete integration of FE and HIP model, introducing mutual interaction of both.	Deliverables as in Q5 for the refined model.

Algorithm for 3-D Electromechanical integration

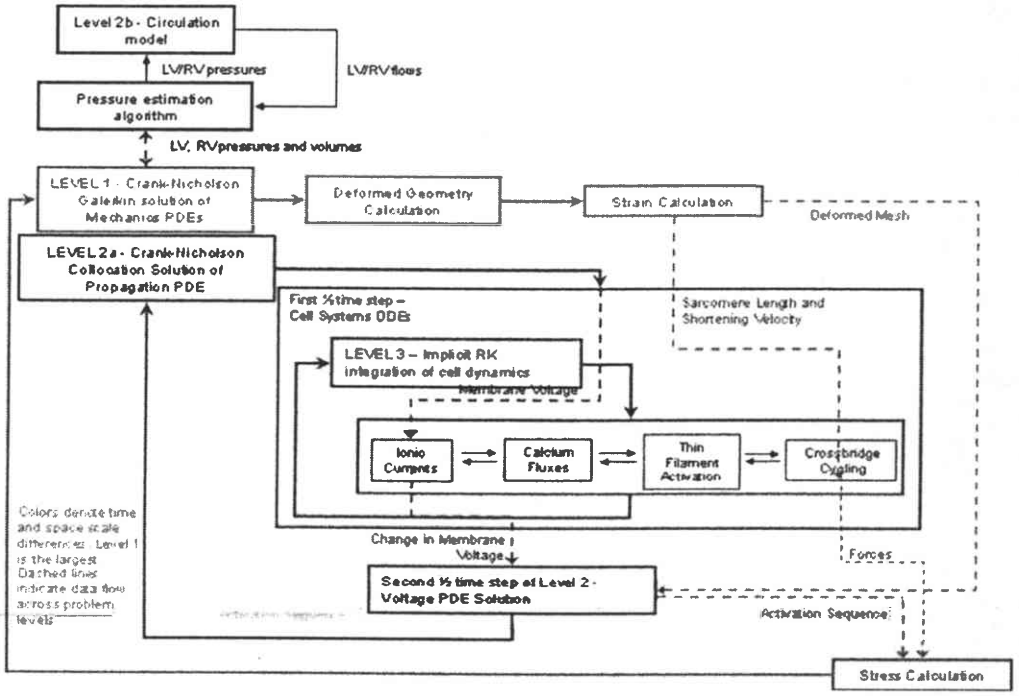

12. ISR

In support of the entire Virtual Soldier Project the U.S. Army Institute for Surgical Research (ISR) performed experiments and data collection.

The porcine animal experiments were performed according to DoD Animal Use Protocol number A-04-004: *Virtual Soldier Porcine Heart Injury Physiology Model* which was originally approved in May, 2004 and amended in September 2004, October 2004, and March 2005.

The following data items were collected for the open chest experiments:

- Aortic Flow in l/min @ 500 Hz
- Pulmonary Artery Flow in l/min @ 500 Hz
- Time Step Coronary Perfusion Studies @ baseline, 5 and 30 mins. post-injury (4 experiments)
- Blood Volume @ baseline, 5 and 30 mins. post-injury (4 experiments)

The following data items were collected for the closed chest experiments:

- ECG 60+ leads @ 1000 Hz using equipment loaned to ISR by Utah
- Cardiac Gated CT Scan pre-injury, post-instrumentation, 0.5mm slices, w/ contrast, reconstructions at systole and diastole, zoomed and unzoomed

The following data items were collected for both open and closed chest experiments:

- Body Weight in kg @ start of experiment
- Sex (always Female)
- Times of Baseline CT Scan, Hemodynamic Data Collection Start, Injury, Blood Sample Collection, Death
- Cardiac Gated CT Scan pre-injury, pre-instrumentation, 0.5mm slices, w/ contrast, reconstructions at systole and diastole, zoomed and un-zoomed
- Heart Rate (bpm) 5 sec.
- Body temp. in deg. C @ 5 sec.
- RV Pressure in mmHG @ 500 Hz
- LV Pressure in mmHG @ 500 Hz
- Central Venous Pressure in mmHG @ 500 Hz
- Arterial Blood Pressure in mmHG @ 500 Hz
- Pulse Oximetry (SPO2) in % @ 500 Hz
- Plethysmograph (Pleth) @ 500 Hz (some experiments)
- Respiratory Cycle @ 500 Hz (some experiments starting January 31, 2005)
- Ventilator Settings including tidal volume (ml), breaths per min. @ 15 mins.
- Respiratory CO2 in mmHg @ 500 Hz (not synchronized with other 500 Hz data)
- ECG one lead @ 500 Hz
- CT Scan postmortem isolated heart 0.5mm slices, w/o contrast (some experiments)
- CT Scan postmortem in situ 0.5mm slices, w/o contrast (some experiments)
- Blood Collection standard laboratory analysis @ baseline, 5, 15, 30, 60, 90, and 120 mins., or at death
- Blood loss estimated by weight at the end of experiment
- Description of injury (size, location, angle), cause of death, time to death
- Digital photos of isolated heart w/ marker pins inserted at the end of experiment
- Heart autopsy (conducted at University of Washington for some experiments)

After the March 17th Demonstration, ten additional animal experiments where performed by ISR for use in the June 14th Demonstration.

Conclusions

- A new statistical methodology to predict injury progression. Best predictor of survivorship using the average of ABP and LVP power drop.
- The indication of a simple measurable physiology parameter, lactate concentrations, can assist in determining an injury state and its progression.
- Mapping of atlas-based imagery and volume data to individuals by semi-automated segmentation and registration.
- Communication protocols between anatomy ontology databases, medical imagery, and mathematical physiology models.
- Extension of the Highly Integrated Physiology, Finite Element and Electrophysiology models to more closely mimic human medical conditions.
- Compression algorithms for rapid retrieval of regions of interest.
- A Virtual Soldier Knowledge Base which integrated the functionalities of the Foundational Model of Anatomy, the new HotBox display concept, and Protégé.

Software Listing Developed/Enhanced for the Virtual Soldier Project by the University of Michigan, University of Utah, and ORNL.

SCIRun Module modifications

1. Physiology Monitor
2. Electrical/Mechanical Heart Viewer
3. Statistical Forecast Display
4. Executive State Display
5. Hotbox
6. Causal Modeling/Wound Track Display

University of Michigan - Edgewarp
University of Washington - JSim
ATK-MRC - Ballistics Modeling software
Oak Ridge National Laboratories - OQAFMA Web Service
Crowley David Research - Compression/decompression software
General Electric Global Research - Segmentation software
University of California, San Diego - Continuity/Modeling software (modifications)
Stanford University - Protege Ontologies
University of Utah - Material Point Method (MPM) software

References:

MMVR 2005 Papers

- Challenges of Presenting High Dimensional Data to aid in Triage in the Virtual Soldier Project. A. D. Boyd, Z.C. Wright, A.S.Ade, F. Bookstein, J.C. Ogden, W. Meixner, B.D. Athey and T. Morris
- Computational Simulation of Penetrating Trauma in Biological Soft Tissues using the Material Point Method. Irina Ionescu, Jameus Guilkey, Martin Berzins, Robert M. Kirby and Jeffrey Weiss
- Linking Human Anatomy to Knowledgebases: A Visual Front End for Electronic Medical Records. Stewart Dickson, Line Pouchard, Richard Ward, Gary Atkins, Martin Cole, Bill Lorensen and Alexander Ade
- Compressing Different Anatomical Data Types for the Virtual Soldier. Tom Menten, Xiao Zhang, Lian Zhu and Marc Footen
- Using an Ontology of Human Anatomy to Inform Reasoning with Geometric Models. Daniel L. Rubin, Yasser Bahir, David Grossman, Parvati Dev and Mark Musen
- Three Dimensional Electromechanical Model of Porcine Heart with Penetrating Wound. Taras Usyk and Roy Kerchoffs

MMVR Abstracts

- "Analytical Simulation of Penetrating Wounds to the Heart". R. D. Eisler, S. F. Stone, A. K. Chatterjee
- "A Biologically Derived Computational Approach to Tissue Modeling". Tim Andersen, Tim Otter, Cap Petschulat, Tom Menten
- "Representing the Holomer on Digital Media: Challenges and Opportunities for Data Representation and Compression". Thomas G. Menten, Xiao Zhang, Lian Zhu. Abstract and Poster.
- "Creating Models from Segmented Medical Images". Bill Lorensen, Jim Miller, Dirk Padfield, James Ross
- "Linking Human Anatomy to Knowledgebases: A Visual Front End for Electronic Medical Records". Stewart Dickson, Line Pouchard, Richard Ward, Gary Atkins, Martin Cole, Bill Lorensen, Alexander Ade
- "A Middleware-based Computing Architecture for Virtual Medicine". Line C. Pouchard, Richard C. Ward, Michael N. Huhns, Laura Zavala, Karthik Iyer
- "A Web-Service Based Computational Environment for Biomedical Computing
- Line C. Pouchard". Richard C. Ward, Michael N. Huhns, Laura Zavala, Karthik Iyer. Abstract and Poster.
- "Using an Ontology of Human Anatomy to Inform Reasoning with Geometric Models". Daniel L. Rubin, Yasser Bashir, David Grossman, Parvati Dev, and Mark A. Musen
- "Three Dimensional Electromechanical Model of Porcine Heart with Penetrating Wound Injury". Roy Kerckhoffs, Taras P. Usyk
- "Challenges of Presenting High Dimensional Data to aid in Triage in the Virtual Soldier Project". Boyd AD, Wright ZC, Ade AS, Bookstein F, Ogden JC, Meixner W, Athey BD

- "The Cardiac Morphometric Markup: a Template for Experimental Cardiology". Fred L. Bookstein, Ameed Raoof, William Green
- "Tracking Physiological Models by Kalman Filters", Fred L. Bookstein, Daniel Cook, Jim Bassingthwaighte. Abstract and Poster.
- "Advanced Modeling and Visualization of Cardiothoracic Electrical Fields". F. B. Sachse, M. Cole, R. M. Kirby, X. Tricoche, C. Johnson. Abstract and Poster.
- "Ontologies of Anatomy and Physiology - Basis for Causal Modeling Standards". Daniel Cook
- "Computational Simulation of Penetrating Trauma in Biological Soft Tissues using the Material Point Method". I Ionescu, J Guilkey, M Berzins, RM Kirby, J Weiss
- "Knowledge-based Anatomical Dynamic Scene Generation in XJ3D". Wayne V. Warren, James F. Brinkley
- "Amending Dynamic Physiological Models to Represent Pathophysiological States". Daniel Cook
- "A Highly Integrated Physiology (HIP) Cardiovascular/respiratory Model used to Simulate Cardiac Injury". Maxwell Neal, James Bassingthwaighte, Taras Usyk, Andrew McCulloch, Roy Kerckhoffs

Journal/Conference Publications

- Functionally and Structurally Integrated Computational Modeling of Ventricular Physiology. Andrew D. McCulloch, Ph.D. Japanese Journal of Physiology, 2004 Dec; 54(6):531-9.
- Linking Ontologies with Three-Dimensional Models of Anatomy to Predict the Effects of Penetrating Injuries. Rubin DL, Bashir Y, Grossman D, Dev P, Musen MA. 26th Annual International Conference IEEE Engineering in Medicine and Biology, San Francisco, CA 2004. Conf Proc IEEE Eng Med Biol Soc. 2004;5:3128-31
- Using Ontologies with geometric models to reason about penetrating injuries. Rubin DL, Bashir Y, Grossman D, Dev P, Musen MA. Intelligent Data Analysis in Medicine and Pharmacology, Stanford, CA 2004.
- Integrating Ontologies with Three-Dimensional Models of Anatomy. Rubin DL, Bashir Y, Grossman D, Dev P, Musen MA Eleventh International Protégé Conference, Bethesda, MD, 2004
- An Acoustic Model for Wave Propagation in a Weak Layer. Michael El-Raheb, ATK-MRC Journal of Applied Mechanics. An Acoustic Model for Wave Propagation in a Weak Layer. Journal of Applied Mechanics --September 2005. Volume 72, Issue 5, pp. 744-751.

Other Posters and Conference Presentations

- 'Computational and Informatics Approaches to Understanding Physiological and Anatomical Changes During Acute Ballistic Trauma.' Presentation and research discussion to the Dept. of Anesthesiology, University of Michigan. May 16, 2007.
- 'Cardiopulmonary Circuit Models for Predicting Injury to the Heart.' Richard Ward. Presentation at Southeast Section of the American Physical Society in Oak Ridge, November 11, 2004.

- 'A Web-based Computer Architecture for the Virtual Soldier.' Line Pouchard, Richard Ward, Michael N. Huhns, Laura Zavala, Karthik Iyer presentation to InterLab 2004 at Oak Ridge National Laboratory, Oct. 28, 2004.
- 'The Development of Sophisticated Cardiac Models for Use in the Virtual Soldier Project.' Sarah Wing (ORNL student intern) poster at ORNL, presented on August 11, 2004
- 'Computational Modeling of Tissue Damage from Penetrating Trauma: Linking Geometric Models to Anatomic and Biomechanical Knowledge.' Rubin DL, Bashir Y, Grossman D, Dev P, Musen MA. Invited presentation, abstract, and poster. InfoRad. Ninetieth Annual Scientific Meeting of the RSNA, Chicago, IL, 2004.

Appendices:

Briefing Books: March 17, 2005 Demonstration
June 14, 2005 Demonstration
DARPA Virtual Soldier Phase I Final Demonstration of June 14, 2005. Hybrid Video and Data DVD Version 2 containing:
Causal Reasoning Video
Supplemental Materials

- Demonstration 2 June 14, 2005:
- Causal Reasoning Slides, Causal Reasoning Photos.
- Posters from Demonstration
- Anatomy from Anatomy Slides
- Causal Reasoning Prototype (Fall, 2004)
- Demonstration 1, March 17, 2005 Materials
  - Slides
  - Photos
  - Posters
    - Five Parts of the Main Demonstration
    - Statistical Reasoning
    - Experimental and Statistical Summary
    - Multiscale Modeling
    - Causal Modeling
    - P-TAG, CODEC, Holomer Displays
    - Holomer Display and HotBox
    - Virtual Soldier Phase I Goals

References

- MMVR 2005 Papers
- MMVR Abstracts
- Journal / Conference Publications
- Other Posters and Conference Presentations

Appendices

Briefing Books: March 17, 2005 Demonstration
June 14, 2005 Demonstration
DARPA Virtual Soldier Phase I Final Demonstration of June 14, 2005. Hybrid Video and Data DVD Version 2 containing:
Causal Reasoning Video
Supplemental Materials

- Demonstration 2 June 14, 2005:
- Causal Reasoning Slides, Causal Reasoning Photos.
- Posters from Demonstration
- Anatomy from Anatomy Slides
- Causal Reasoning Prototype (Fall, 2004)
- Demonstration 1, March 17, 2005 Materials
  - Slides
  - Photos
  - Posters
    - Five Parts of the Main Demonstration
    - Statistical Reasoning
    - Experimental and Statistical Summary
    - Multiscale Modeling
    - Causal Modeling
    - P-TAG, CODEC, Holomer Displays
    - Holomer Display and HotBox
    - Virtual Soldier Phase I Goals

References

- MMVR 2005 Papers
- MMVR Abstracts
- Journal / Conference Publications
- Other Posters and Conference Presentations

Virtual Soldier Project
Phase I Demonstration
March 17, 2005

Dr. Richard Satava, Defense Advanced Research Projects Agency, Program Manager
Dr. Gerald Moses, Telemedicine and Advanced Technology Research Center, COR

Prime Contractor, University of Michigan:

Brian D. Athey, VSP Principal Investigator
Jeff Ogden, VSP Project Manager
Fred Bookstein, Statistical Reasoning Lead

Co-Principal Investigators:

CPT Eric Ansorge and LTC James Fudge
Brooke Army Medical Center Institute for Surgical Research
Jim Bassingthwaighte, University of Washington Bioengineering
William Crowley, Crowley Davis Research
Bob Eisler, ATK-Mission Research Corporation
Chris Johnson, University of Utah Scientific Computing and Imaging Institute
Henry Kelly, Federation of American Scientists
Bill Lorensen, General Electric Global Research
Andrew McCulloch, University of California San Diego
John Monville, Xtria LLC
Mark Musen, Stanford University
Cornelius Rosse, University of Washington Structural Informatics Group
Richard Ward, Oak Ridge National Laboratory

Table of Contents

Letter of Introduction 3
Introduction 4
Part 1: Statistical Reasoning 5
Part 2: Multiscale Modeling and Simulation 13
Part 3: Causal Reasoning 18
Part 4: Infrastructure: P-Tag, CODEC, Holomer Display 23
Part 5: Autostereoscopic Holographic Optical Element (HOE) Display 31
Summary of Phase I Project Goals Demonstrated 32
Virtual Soldier Project Team Members 33
Appendix 34
- Use of Experimental Data 34
- Summary of ISR Experiments 34
- Data Collected at ISR 35
- Preliminary Injury Device Characterization 38
- Summary of Experimental Data Including Statistical Forecasts 42
- Fred Bookstein's Time-to-Death Memo (2-14-2005) 45
- Virtual Soldier Project Publications 48

University of Michigan
Michigan Center for Biological Information
Brian D. Athey, Ph.D., Director
Phone: 734-615-5914
Email: bleu@umich.edu

Letter of Introduction

March 17, 2005

Dr. Richard Satava
Program Manager
Defense Advanced Research Projects Agency
3701 North Fairfax Drive
Arlington, VA 22203-1714

Dr. Gerald Moses
Director, Clinical Applications Division
Telemedicine and Advanced Technology Research Center
U. S. Army Medical Research and Materiel Command
504 Scott Street
Fort Detrick, MD 21702-5012

Dear Rick and Gerry,

It is with great pride and pleasure that I present to you the status of the Virtual Soldier Phase I demonstration as a part of our 5th Quarter team meeting. The team has worked very hard to produce an integrated set of demonstrations that address the required Phase I deliverables as specified in BAA 03-02 Addendum 4.

The results you will see are in many ways truly amazing and I believe this has the potential to form the basis of a new standard of care for injured warfighters and the medics who care for them. Additionally, it appears that important new scientific breakthroughs relating to our understanding of the physiological and anatomical sciences are beginning to emerge, which hold great future promise for 21st century Digital Human Capabilities to emerge. This long term goal, coupled with the first realization of the "Holomer" vision as a Personal Health Record (PHR), as presented over these next two days, only begin to tap the future of defense healthcare as envisioned by the "Virtual Soldier" concept.

Respectfully,

Brian D. Athey, Ph.D.
Associate Professor, Biomedical Informatics (Medical School)
Director, Michigan Center for Biological Information (Office of the Vice President of Research)
Interim Director, University of Michigan Biomedical Informatics Center
Principal Investigator, DARPA Virtual Soldier Project

Introduction

This handbook provides a status report on the DARPA Virtual Soldier Project Phase I progress and deliverables, focused on the demonstration. We have chosen to present this demonstration and this report in five components:

1. Statistical Reasoning
   - Reasoning backward from effect to cause using experimental data provided by ISR

2. Multiscale Modeling and Simulation
   - Creating and implementing multiscale physiologic and anatomic predictive models by integrating MPM, FE, and HIP models

3. Causal Reasoning
   - Reasoning forward from cause to effect using the Virtual Soldier Knowledgebase, Visible Human Data, and ballistic modeling results

4. P-Tag, CODEC, Holomer Displays, and Hotbox
   - Demonstrating infrastructures to support reasoning, modeling, and visualization

5. Autostereoscopic / Holographic Display
   - Developing the hardware and software for interactive and realistic holography-based autostereoscopic display of Virtual Soldier volume data

The following table summarizes the uses being made of the experimental data by each portion of the demonstration list above.

Portion of Demo	Image/CT Data	Physiology Data
Statistical Reasoning	Porcine	Porcine
Causal Reasoning	Visible Human	Simulated data only
Multiscale Modeling and Simulation	Porcine	Porcine
P-Tag, CODEC, Holomer Display	Porcine and Visible Human	Porcine and Simulated Human
Autostereoscopic / Holographic Display	Porcine and Human	None

Part 1: Statistical Reasoning

Help save soldiers' lives by:

- Reasoning backward from effect to cause, using:
  - baseline porcine CT and instrumentation data from ISR
  - post-injury porcine instrumentation data from ISR
  - segmented and labeled anatomy from GE
  - morphometric markup from UMich
  - simulated physiology data from UW's HIP model
  - the Virtual Soldier Knowledge Base (VSKB) from UW
- Forecast survival and/or time to death
- Estimate the location and severity of the injury
- Provide this information to the medic or physician

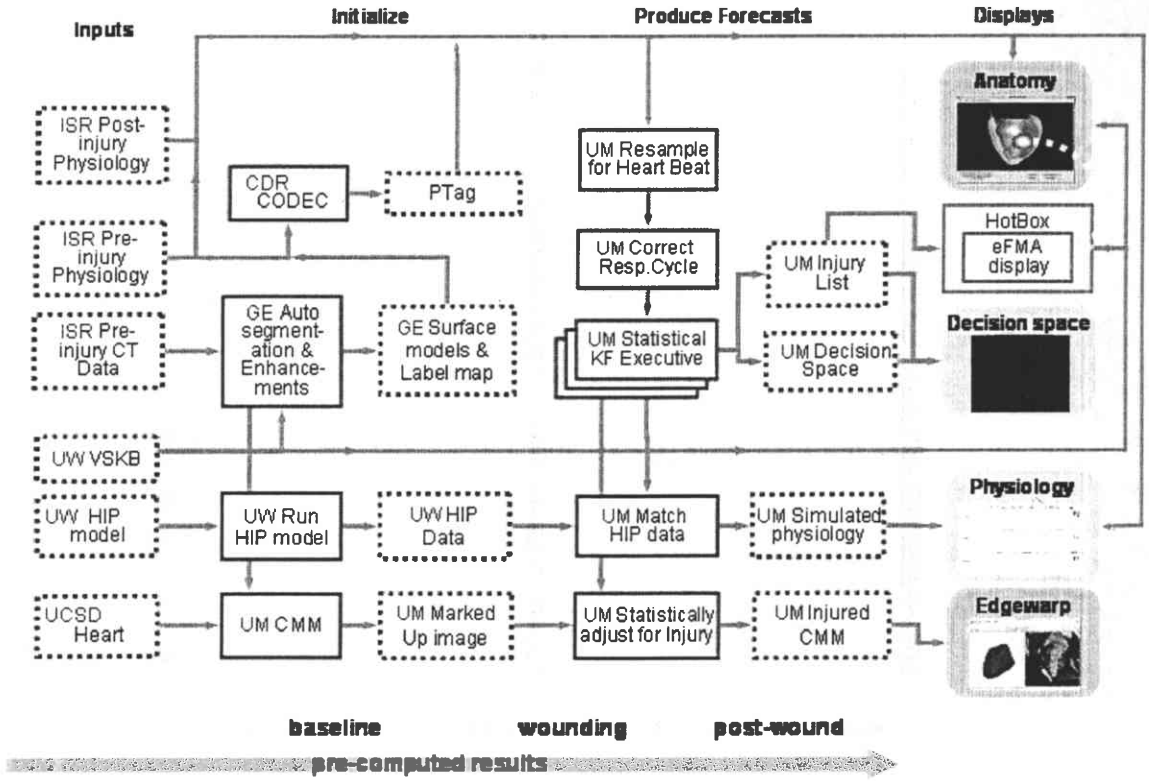

Figure 1: Statistical Reasoning data flow

Four main displays:

- Decision Space
- Physiology
- Anatomy
- Edgewarp

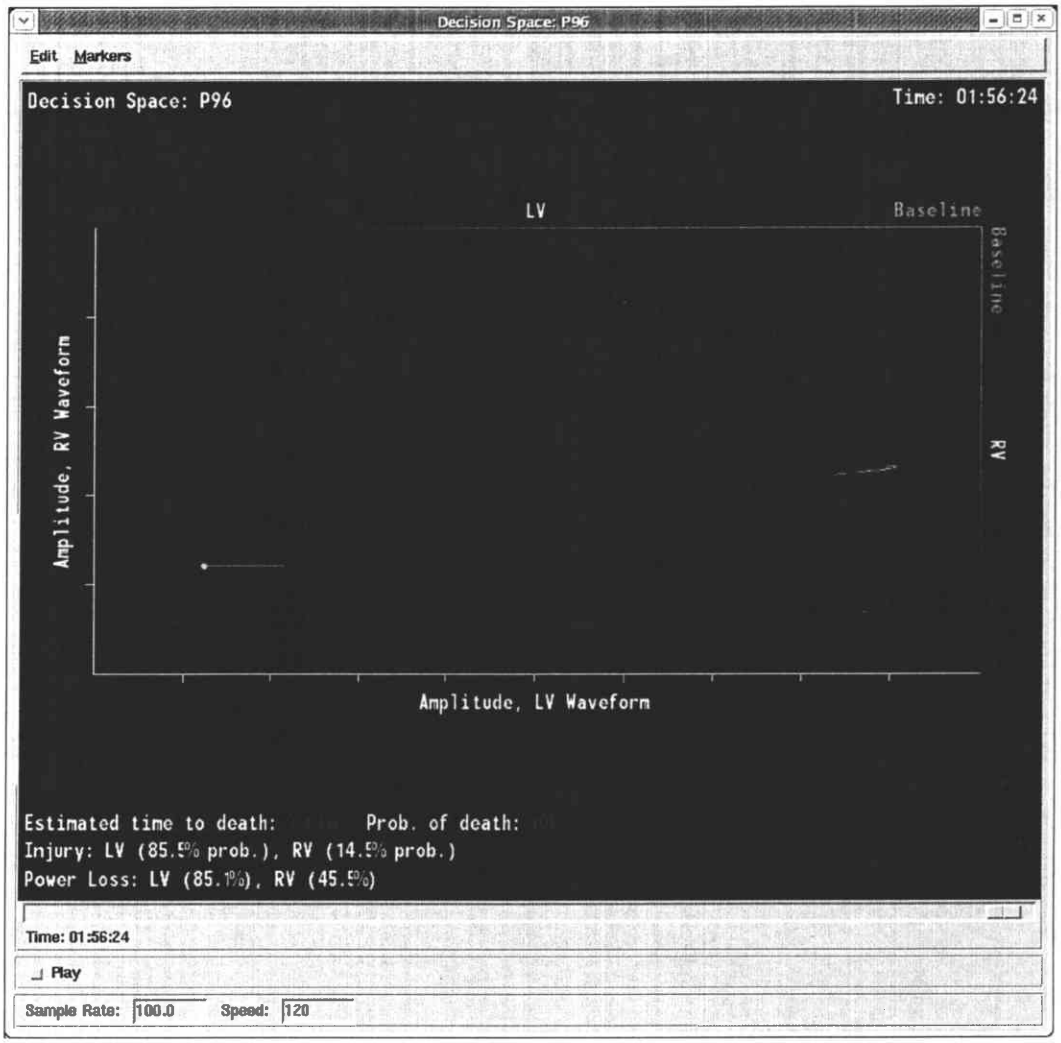

Figure 2: Decision Space Display

Decision Space Display

This display has two parts. At the top is the decision space plot and at the bottom is a summary of important forecasts and related information. Both parts are time dependent and are updated once per minute of wall clock time, although the display is usually set to run at 60 or 120 times faster than real-time.

The decision space plot generally starts out in the upper right quadrant. Baseline information is plotted in green. This is followed by a blue plot from the time of injury until the first alarm, if there is an alarm for this individual. The plot changes to red after the first alarm.

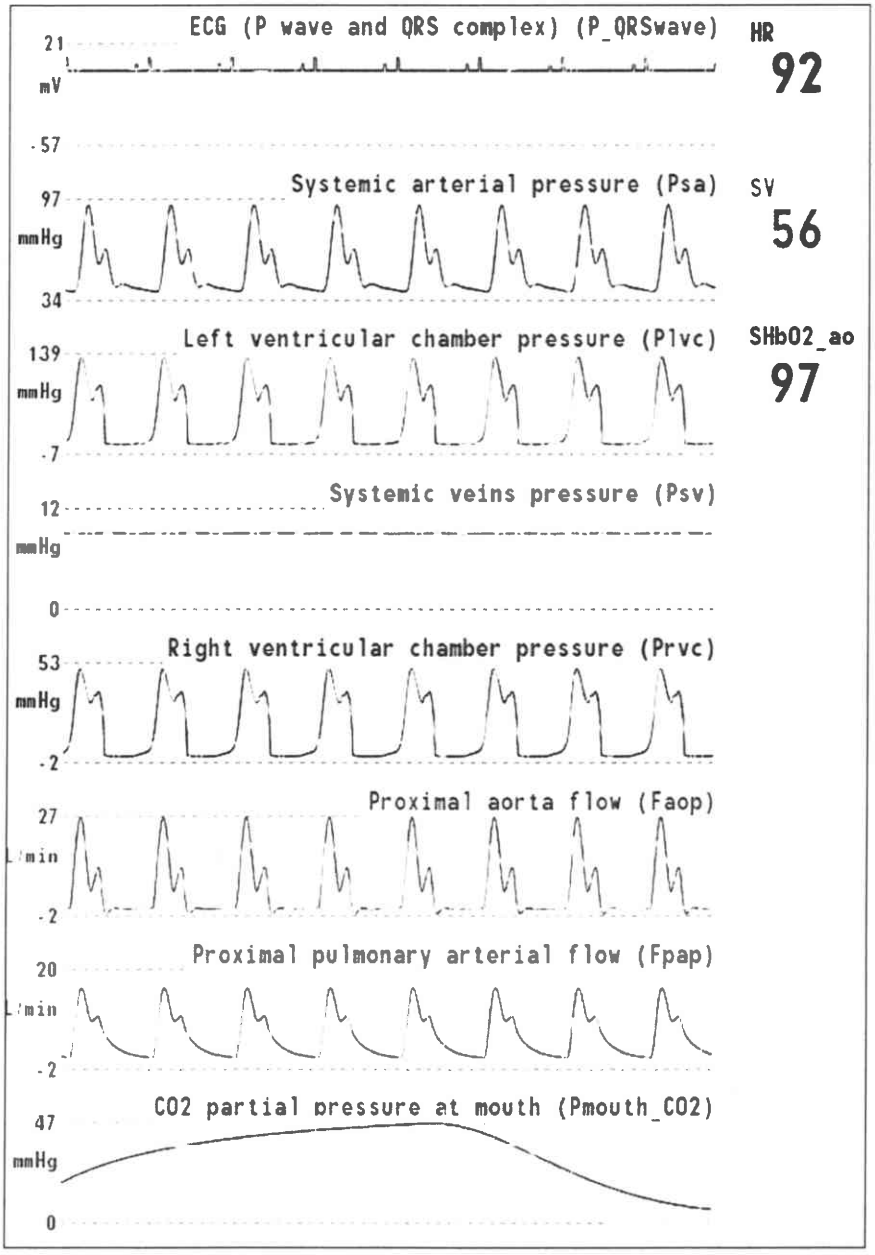

Figure 3: Physiology Display

Physiology Display

This display resembles a monitor that one might see in a hospital room. It can display time dependent wave forms and individual values. The display can run at various rates, be paused, scrolled forward or backward or jumped to previously marked points of interest. Negative times are baseline while positive times are post-injury. Multiple displays can be run to allow comparisons of past and present data.

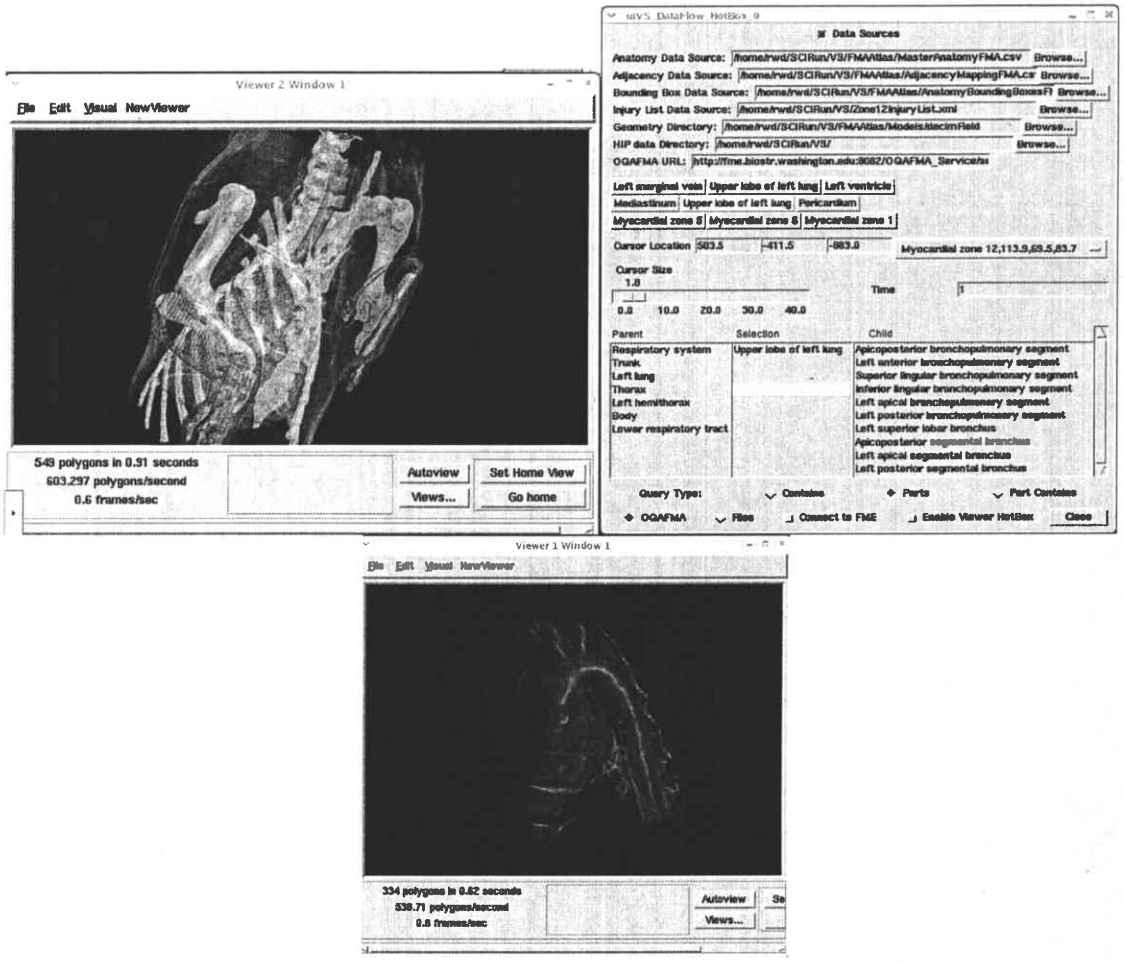

Figure 4: Anatomy Display and Hotbox

Anatomy Display and Hotbox

The Anatomy Display shows a 3D view that can be rotated, translated, and scaled to show the anatomical model that has been created from an individual's baseline CT scan. To this baseline image other post-injury information such as the wound track or an indication of specific injuries can be added based on either statistical or causal reasoning.

The HotBox is a user interface into the 3D anatomy and physiology of a specific individual (in this portion of the demo, a porcine subject, in other portions, a virtual human or porcine subject). It connects the visual anatomical model created from the CT to the Foundational Model of Anatomy, the wound's strain map, the injury list description of the wound, and the results of the high-level integrative physiological simulation. It works in combination with other SCIRun modules, the Physiology Display, and the 3D

probe widget to display specific information selected by the medic, nurse, physician, or researcher.

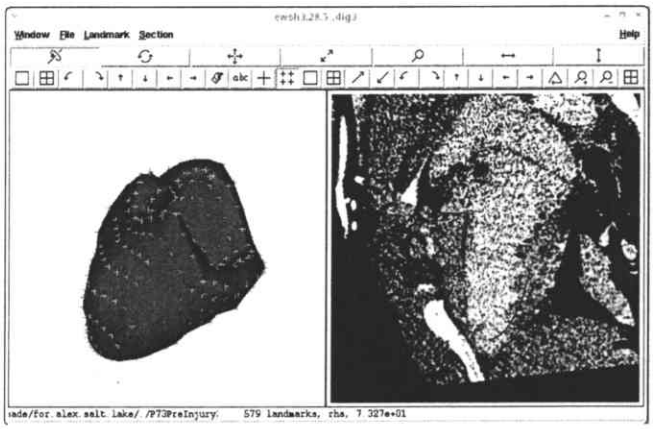

Figure 5: Edgewarp Display showing morphometrically marked-up heart

Edgewarp Display

In Figure 5 above, the Edgewarp Display consists of two windows: on the left, a 3D view, and on the right, a 2D view of a plane through the 3D model.Shows a beating heart (from diastole to systole) with contractility adjusted from baseline based on a statistical estimate of the injury.

Decision Space Plots and Experimental Results Summary

Shown below are the decision space plots for each of the 13 "analyzable" open chest experiments completed through January 31, 2004.

An analyzable experiment is one with a time to death longer than 10 minutes and relatively complete data collection. Death is defined as a sustained Mean Arterial Pressure (MAP) of 20 mmHg or less. Survival is defined as a time to death greater than 120 minutes. The survival or time to death in minutes post-injury is given in the title over each plot. The times of any alarms, also in minutes post-injury, are listed toward the bottom of the plot. The plots start with baseline data generally in the upper right quadrant. A "W" indicates the point of wounding (see Figure 6 below). Alarms, when they occur, are indicated by a small solid circle.

The plots and the table of "Analyzed Open Chest Experiments" show that for this class of animals surviving more than 10 minutes post-injury:

- At five minutes post injury, death or survival can be forecast accurately for 12 out of the 13 experiments. Percentage loss of LVP amplitude has been shown to be a very sound early prognosticator of ultimate (120+ minute) survival. All of the animals that lost more than 37% of baseline LVP amplitude at five minutes post-

wound died; all but one of the animals that lost less than 37% of baseline LVP amplitude at five minutes post-wound lived. Given this sample of experimental results the number 37% can be replaced by any value between 31% and 45% and the statement remains true.

- The fraction of drop of ventricle pressure amplitude, LVP vs. RVP, in the first few minutes is a very highly reliable discriminator of the chamber hit.

- Even absent knowledge of baseline physiology (and thus absent knowledge of the severity of that LVP amplitude loss), there is an indicator of incipient death, the scaled second-difference we have called "the alarm." Of the six test subjects that never showed this alarm, five survived to 120 minutes. Of the seven test subjects that showed the alarm, all died before 120 minutes. The sixth non-alarm test subject can be shown to have an alarm using an adapted algorithm.

- For the class of 11 test subjects surviving more than 30 minutes post-wound, time to death can be predicted quite well from the time of the alarm. From the first alarm to the ultimate declaration of death is 34 minutes (range, 22 to 48 minutes). These same test subjects all set off a second alarm as well, at times from 3 to 16 minutes before death.

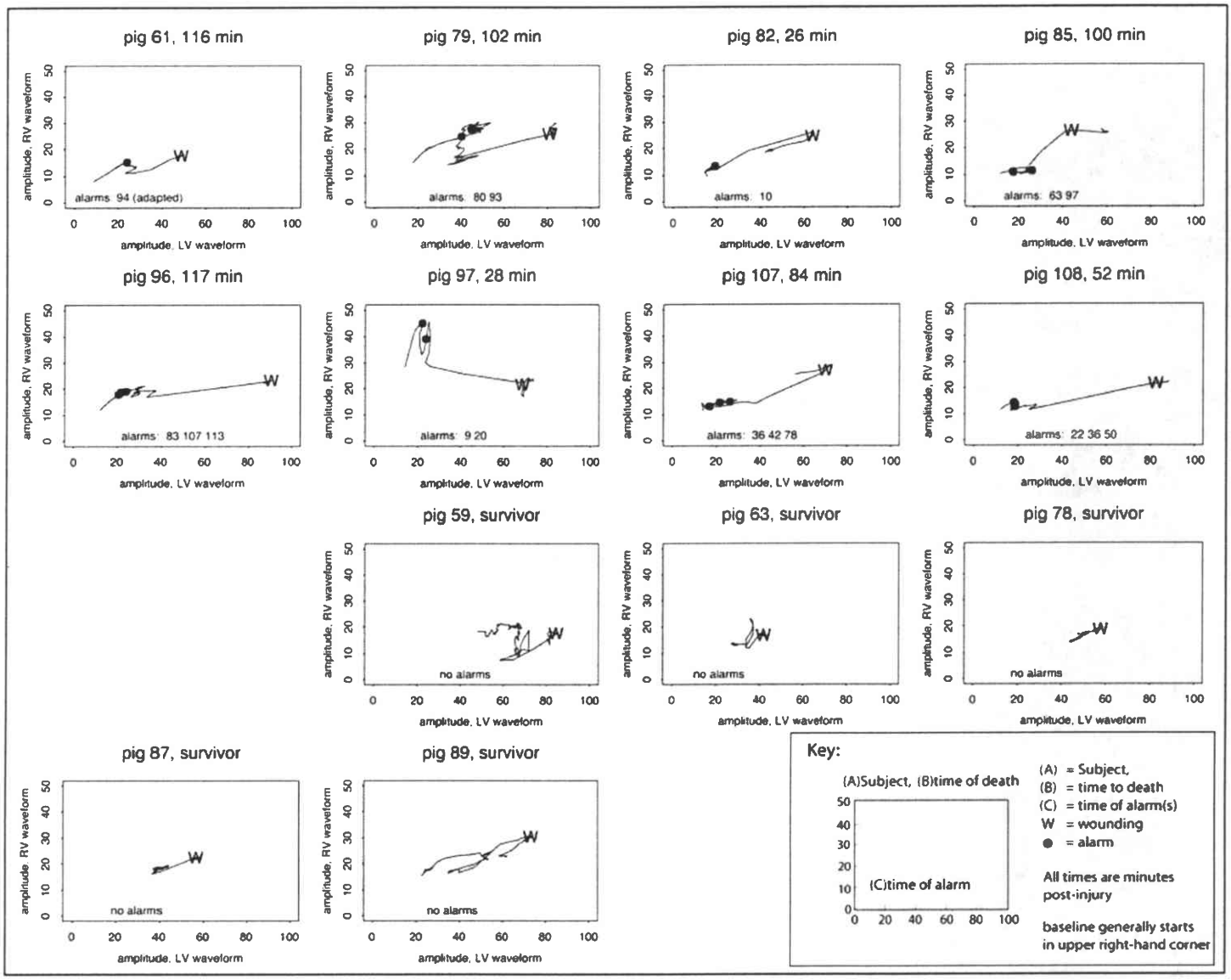

Figure 6: Decision Space plots of analyzed experiments

Virtual Soldier Project: Summary of Experimental Data including Statistical Forecasts-- 15 March 2005

Status: Quarantined (Q), Short TTD (S), Death prior to injury (D), Incomplete data (I) Available for use during March 17th demo (A)

Injury Method: Blunt Probe (PR), Pointed Probe (PP), ISR Fragment (IF), MRC Fragment (MF)

Location: Closed Chest (CC), otherwise Open Chest plus RV or LV

Status	Date of Experiment	Data Received	Tag No.	Injury Method	Size (mm)	Loc.	Cause of Death	Time of Death ISR / UM (mins)	Forecast @ 5 mins. Post-injury: Survival or Average Time of Death (mins.)	Forecast of Time of Death (mins.) @ 1st alarm	Number of Alarms	Time of 1st Alarm	Time of 2nd Alarm	Time of 3rd Alarm
Analyzed Open Chest Experiments:														
	30Nov2004	8Dec2004	63	MF	7	LV	Euthanized	120+	Survival	--	0			
	2Dec2004	8Dec2004	59	PR	7	RV	Euthanized	120+	Survival	--	0			
	7Dec2004	6Jan2005	61	PR	7	LV	hemorrhage	90 / 116	Survival*	128	1*	94		
	* 5 min. forecast of survival is not correct. Recognition of an alarm for this subject requires an adapted algorithm.													
	16Dec2004	20Dec2004	78	PP	10	LV	Euthanized	120+	Survival	--	0			
	4Jan2005	12Jan2005	79	IF	11	LV	hemorrhage	104 / 102	74	114	2	80	93	
	10Jan2005	14Jan2005	89	PP	10	LV	Euthanized	120+	Survival	--	0			
	Two injuries, 1st unsuccessful or minor. Microsphere, blood volume, and isolated heart CT.													
A	11Jan2005	14Jan2005	87	PP	10	LV	Euthanized	120+	Survival	--	0			
	Microsphere, blood volume, and isolated heart CT.													
	12Jan2005	14Jan2005	82	IF	11	LV	hemorrhage	27 / 26	74	60	1	26		
	Microsphere, blood volume, and isolated heart CT.													
A	13Jan2005	26Jan2005	85	PR	7	RV	hemorrhage	113 / 100	74	97	2	63	97	
	Microsphere, blood volume, and isolated heart CT.													
A	18Jan2005	26Jan2005	96	IF	11	LV	hemorrhage	115 / 117	74	117	3	83	107	113
	19Jan2005	26Jan2005	97	IF	11	LV	hemorrhage	26 / 28	74	43	2	9	20	
	25Jan2005	31Jan2005	108	MF	7	LV	hemorrhage	52 / 52	74	56	3	22	36	50
	26Jan2005	31Jan2005	107	MF	7	LV	hemorrhage	85 / 84	74	70	3	36	42	78
	The notes for this experiment report a 124 minute time to death, when the more detailed marker annotations show an 85 minute time to death. 85 minutes is correct.													

*incorrect forecast at this point in time

Figure 7: Statistical Summary of Analyzed Open Chest Experiments (see Appendix for the additional experiments)

Statistical Reasoning Goals Demonstrated

- ✓ Diagnose heart wounds w/ accuracy >= 80%
- ✓ Compare baseline data to post-injury data
  - ✓ Accuracy >0.8 for structural abnormalities
  - ✓ Accuracy >0.8 for physiologic response
- ✓ Predict likelihood of battlefield mortality
  - ✓ Predict outcomes
  - ✓ Forecast time to death
- ✓ Demonstrate organ and system level integration
- ✓ Extend and use global architecture
- ✓ Develop and use automatic segmentation
- ✓ Develop and use Holomer display and interface

Part 2: Multiscale Modeling and Simulation

Create Multiscale Physiologic Predictive Models:

- Create Multiscale Anatomical and Physiologic Predictive Models, using:
  - baseline porcine CT and instrumentation data from ISR,
  - post-injury porcine instrumentation data from ISR,
  - segmented and labeled anatomy from GE,
  - morphometric markup from UMich,
  - simulated physiology data from UW's HIP model
  - functionally integrated models of circulatory physiology combined with anatomically and biophysically detailed 3D models of ventricular electromechanics
- To model physiologic signals that are not directly measurable in the field
- To match experimental data with multiscale model output and validate the models for eventual field use
- To build a database that covers more cases than is possible with experimental data alone

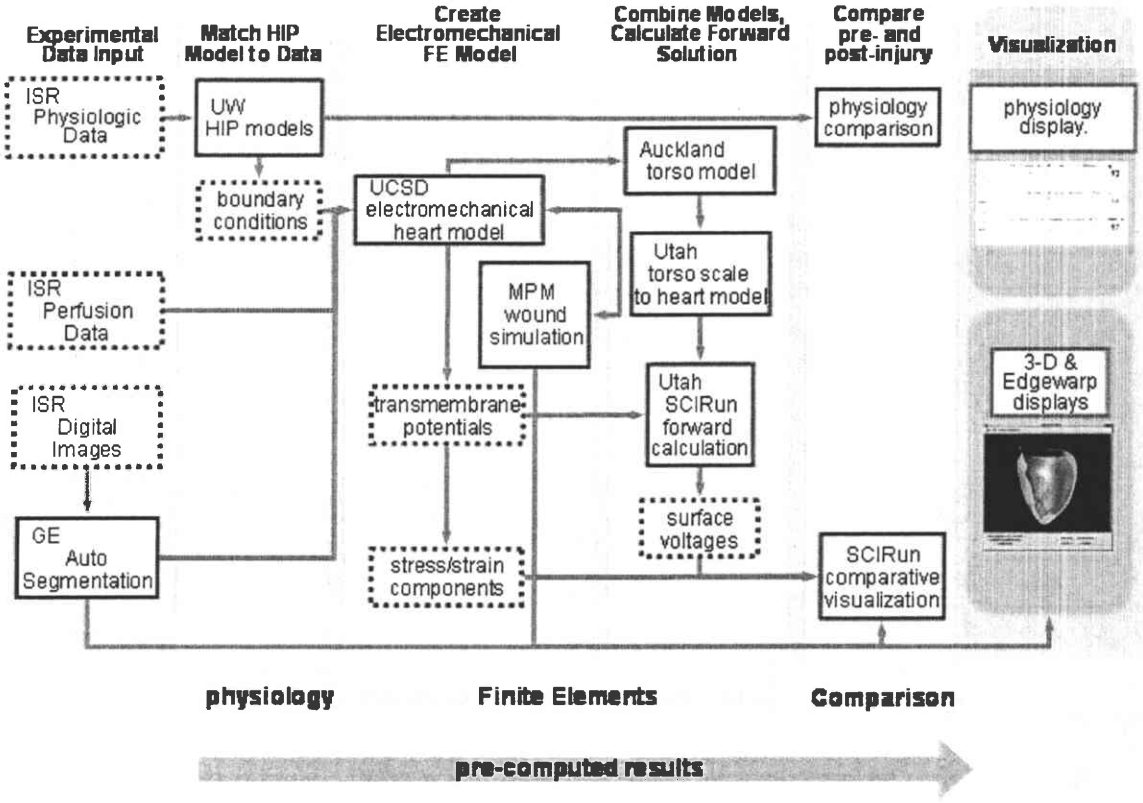

Figure 8: Multiscale Modeling and Simulation data flows

Highly Integrated Physiology (HIP) Modeling

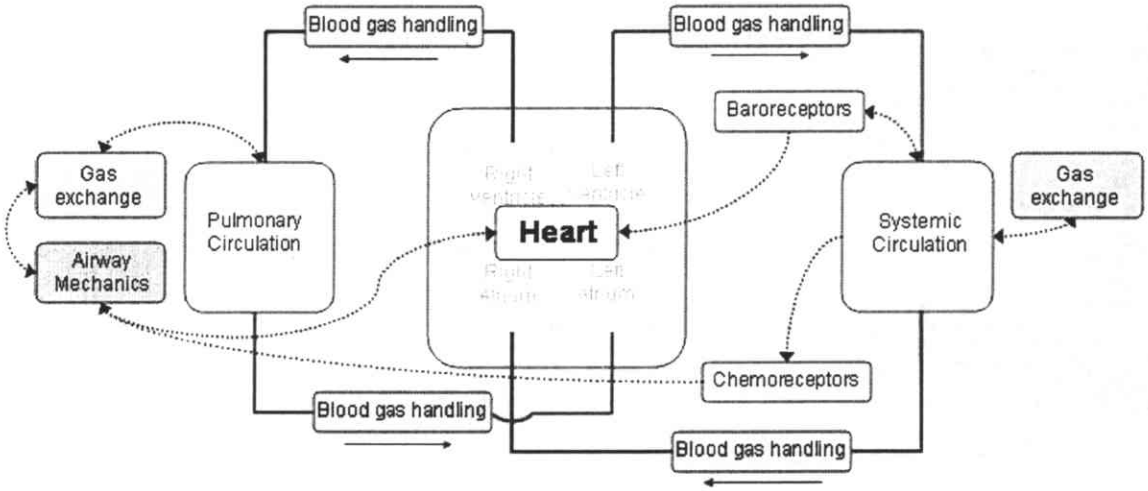

Figure 9: Highly Integrated Physiology (HIP) structure

Outputs of HIP Model

- Pressures, volumes, forward flow and radial flow in:
  - Left atrium, Left ventricle, Proximal aorta, Distal aorta, Systemic arteries, Systemic arterioles, Systemic capillaries, Systemic veins, Vena cava, Right atrium, Right ventricle, Proximal pulmonary artery, Distal pulmonary artery, Small pulmonary arteries, Pulmonary capillaries, Pulmonary shunt, Pulmonary veins, Proximal epicardial arteries, Distal epicardial arteries, Large coronary arteries, Small coronary arteries, Coronary capillaries, Small coronary veins, Large coronary veins, Epicardial veins, Pericardium (injury flow)
- Pressures, volumes, forward flow, radial flow, [O2], [CO2], and [N2] in:
  - Upper airways
  - Collapsible airways
  - Alveoli
- pO2, pCO2, pH, [HCO3] and [Carbaminohemoglobin] in aorta and pulmonary artery
- Diffusion capacity of O2, CO2 and N2 across alveolar membrane
- Heart and respiratory rates
- Heart chamber elastances
- Injury specifications
  - Conductances of penetrating "wounds."
  - Blood in pericardial space
  - Blood lost from circulation

- ***Presently 363 variables, 75 ODEs***

3D Finite Element Model of Cardiac Electromechanics

- Accurate geometry of porcine left and right ventricle, acquired from porcine CT scan (ISR)
- Realistic myofiber orientation
- Passive and active material properties
- Local depolarization activates contraction
- Boundary conditions set by highly integrated circulatory model initialized from and tuned to empirical data (ISR)
- Penetration wound modeled by preventing depolarization and active contraction at site of wound
- Reduction of contractility based on regional perfusion measurements (ISR)

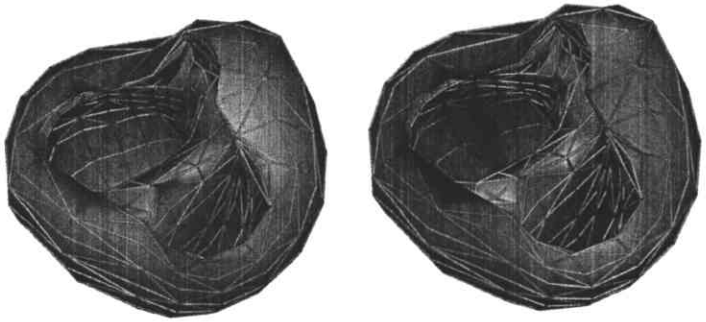

Figure 10: Finite Element heart models showing pre-injury (left) and post-injury (right) myofiber strain

Material Point Method

- General particle-based multiphysics model
- Handles large deformations/tearing automatically
- Capable of modeling large scale **(non) penetrating injuries** in arbitrarily complex geometries e.g. torso prototype
- Hi-fidelity/resolution tissue damage simulations
- Leverages 10yr DOE code investment
- Allows detailed validation of coarse-grain models
- Parallel computation of wound database possible

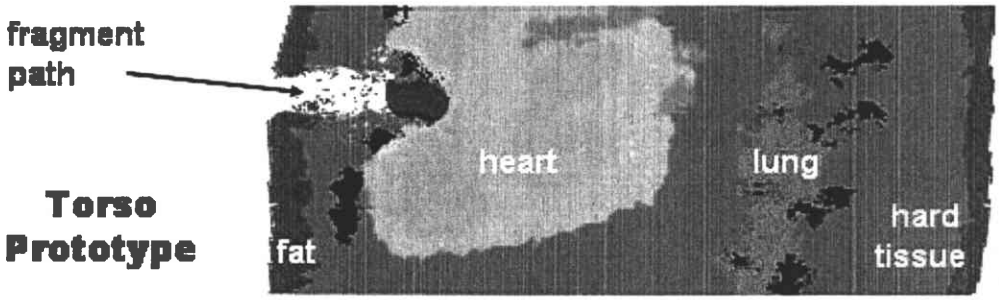

MPM Penetration Trauma of the Heart

- **Heart**
  - anatomically accurate porcine heart
  - discretized into ~1.5 mil material particles
  - modeled as a transversely isotropic hyperelastic material: an isotropic matrix reinforced by an elastic fiber family (fiber directions vary through the wall thickness)
  - a two-surface strain failure criteria is embedded in the model
- **Probe**
  - 10 mm pointed, probe (as in experiments)
  - elasto-plastic (metallic) material model
  - 76 ft/s initial speed
  - frictional contact enforced between tissue and probe

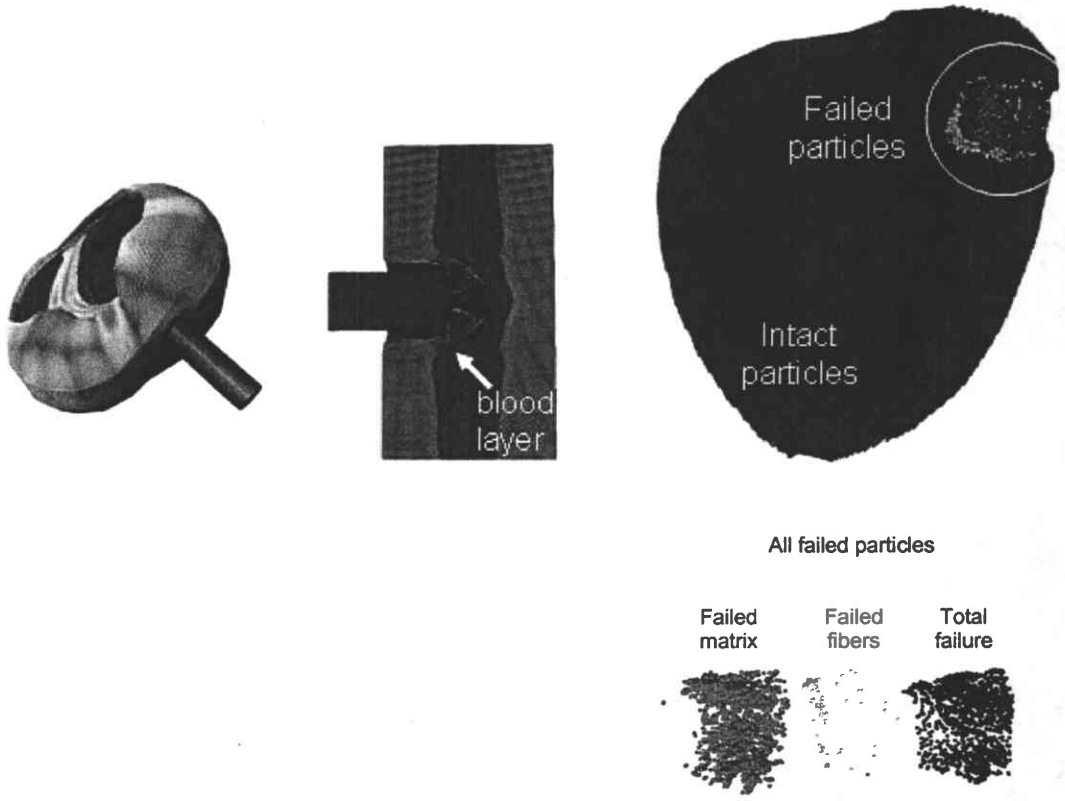

Figure 11: MPM Modeling with material failure due to wound

Multiscale Modeling and Simulation Goals Demonstrated

- ✓ Compare baseline data to post-injury data
- ✓ Demonstrate organ and system level integration
- ✓ Extend and use global architecture
- ✓ Develop and use automatic segmentation
- ✓ Develop and use Holomer display and interface

Part 3: Causal Reasoning

Help the medic make triage decisions:

- Given two anatomically similar fragment wounds:
  - LV wall penetration, *vs.*
  - LV wall penetration with a severed coronary artery
- Reason from cause to effect, using:
  - the Virtual Soldier Knowledge Base (VSKB) from UW
  - segmented and labeled Visible Human Male from GE,
  - ballistic damage simulated by ATK-MRC,
  - symbolic causal reasoning from Stanford University,
  - pathophysiology simulated using UW's HIP model.
- To deduce differences in pathological consequences
- To simulate differences in pathophysiological outcomes

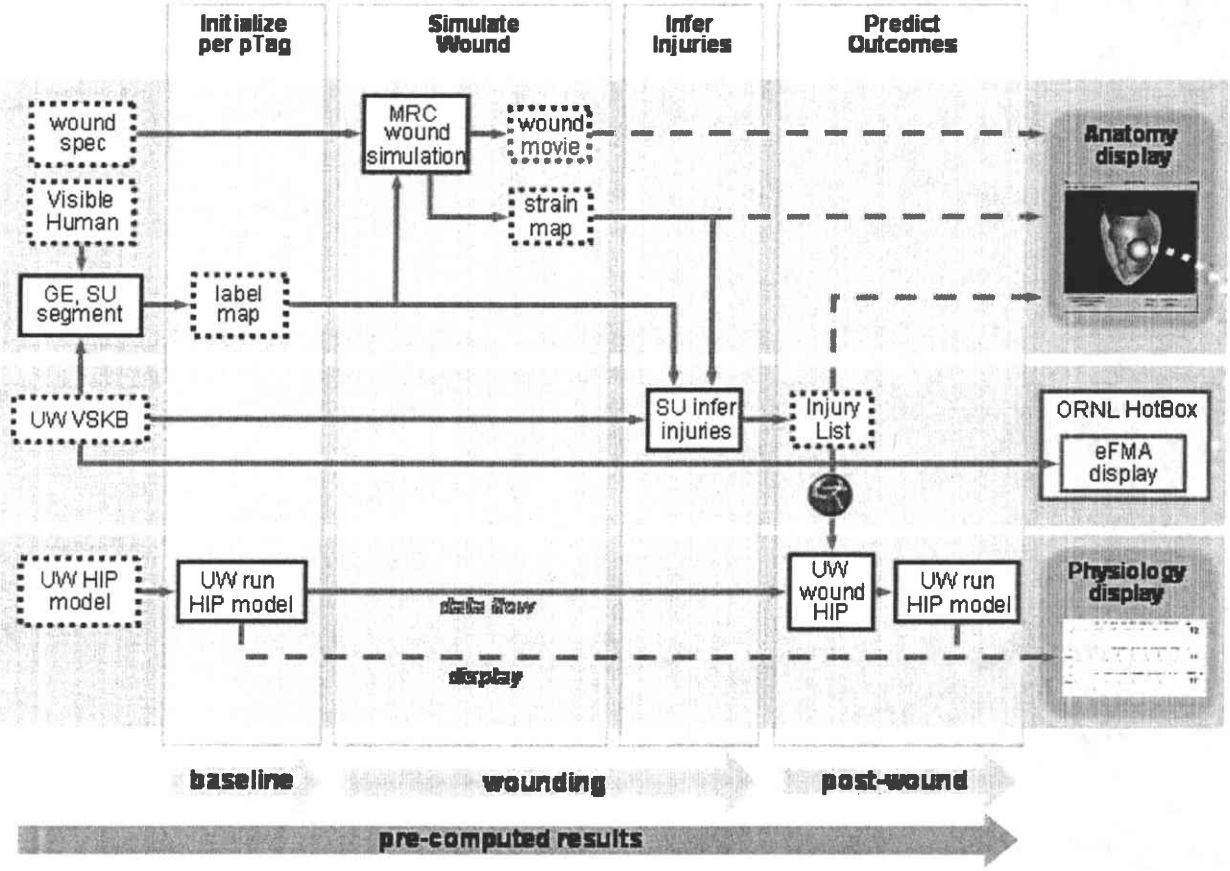

Figure 12: Causal Modeling data flow

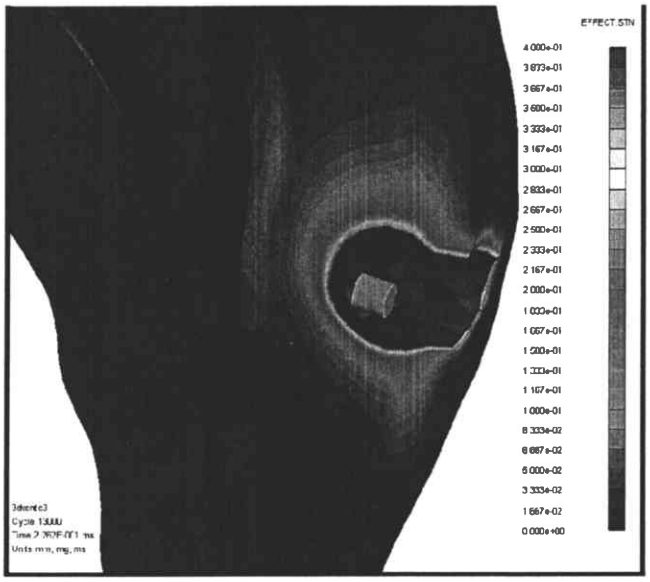

Figure 13: ATK ballistic model of LV wound

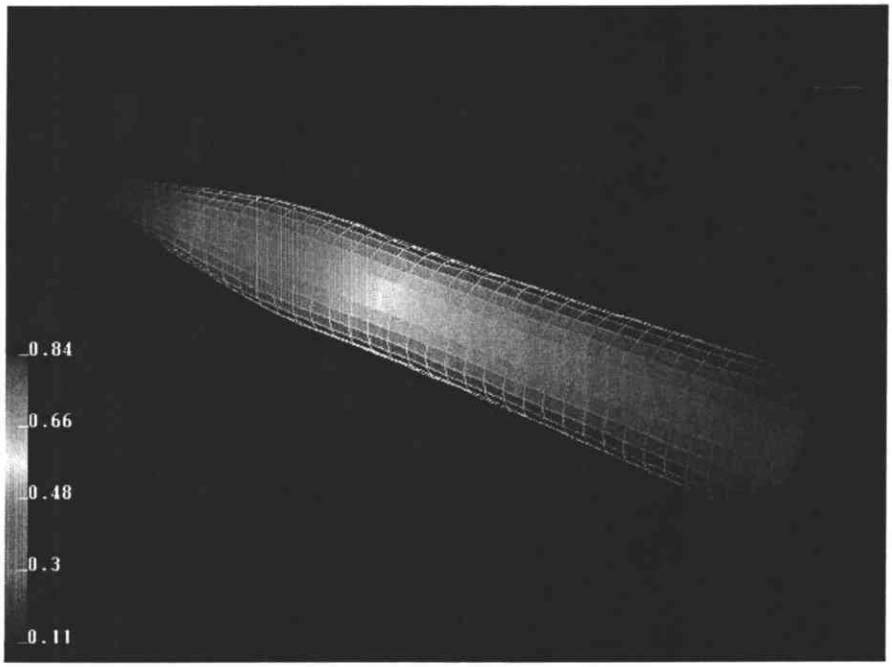

Figure 14: ATK-MRC circumferential strain model of wound track

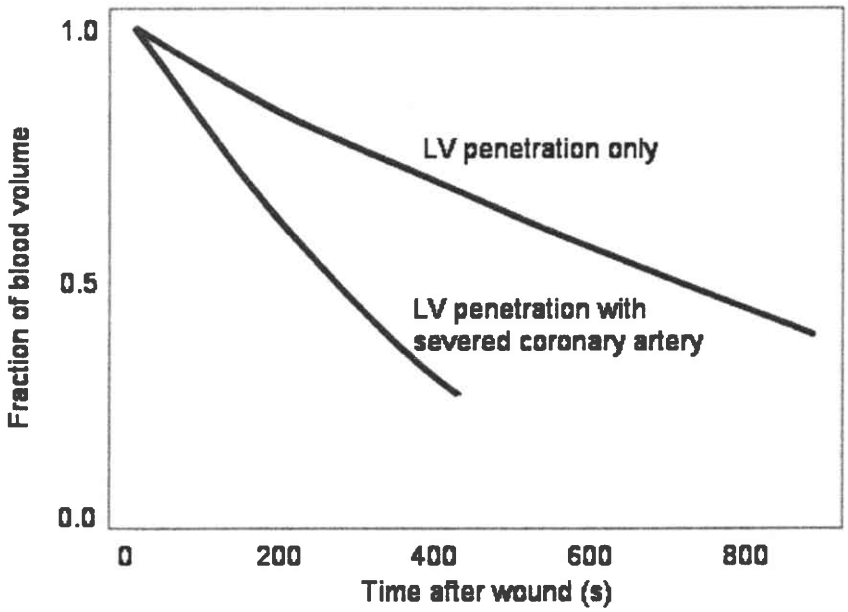

Figure 15: Blood loss differences

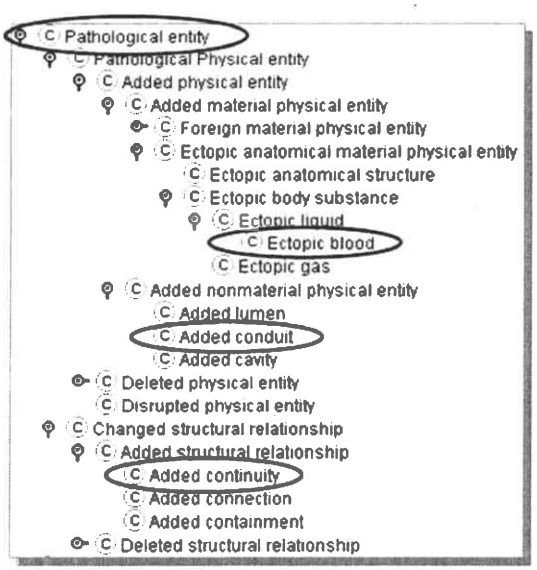

Figure 16: Wound added to VSKB

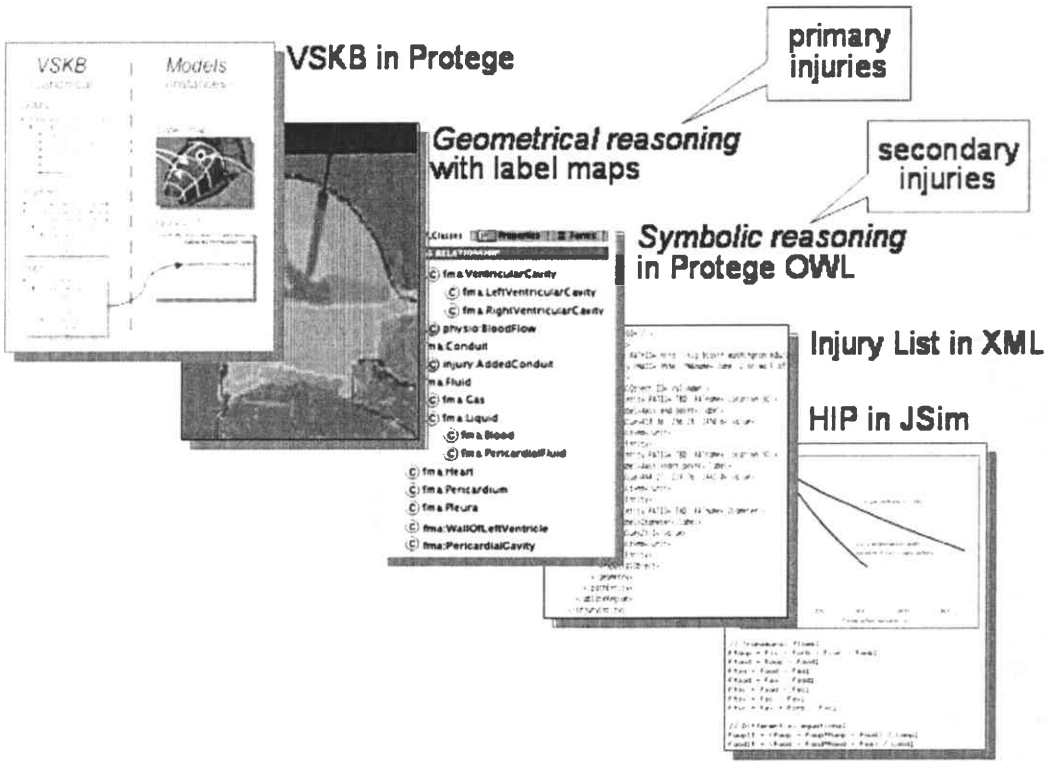

Figure 17: Causal Modeling components

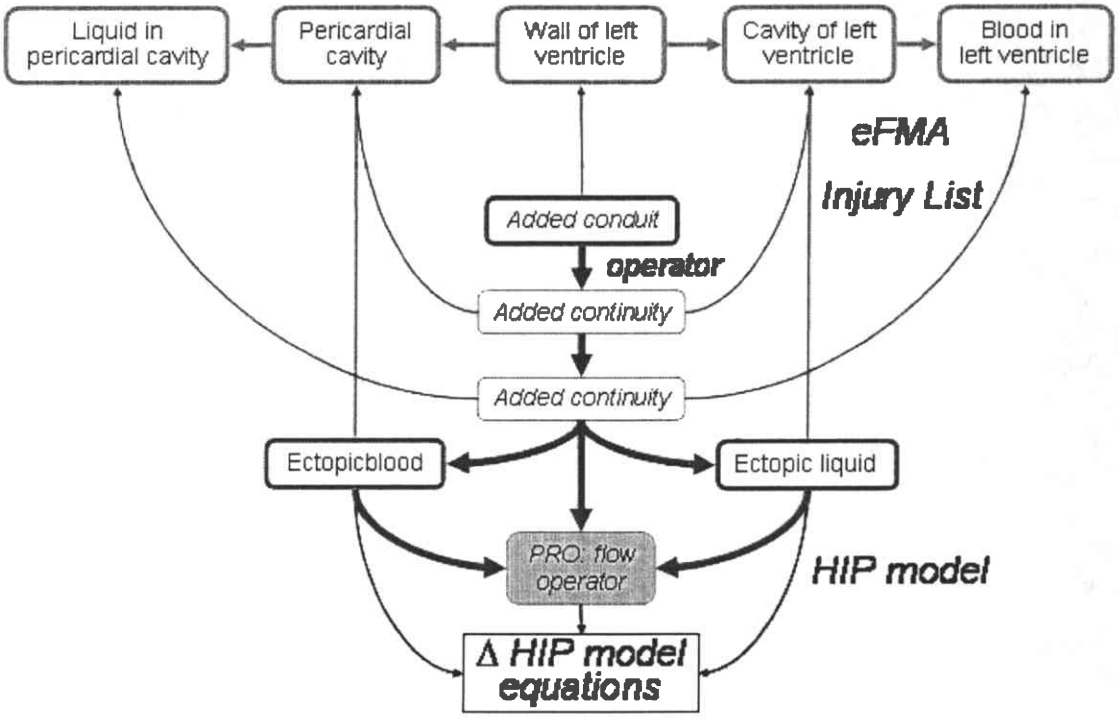

Figure 18: Injury propagation

Causal Reasoning Goals Demonstrated

- ✓ Diagnose heart wounds
- ✓ Compare baseline data to post-injury data
- ✓ Predict outcomes
- ✓ Demonstrate organ and system level integration
- ✓ Extend and use global architecture
- ✓ Develop and use automatic segmentation
- ✓ Develop and use Holomer display and interface

Part 4: Infrastructure: P-Tag, CODEC, Holomer Display

Infrastructure to support the project, by:

- Using baseline image data from the Visible Human
- Using baseline & post-injury image & physiology from ISR
- Compressing datasets using the CODEC from CDR
- Storing baseline images and physiology on 2 GB P-Tag
- Creating or extending the Global Symbolic Knowledge Architecture as represented by the VSKB
    - Foundational Model of Anatomy (FMA)
    - Physiological Reference Ontology (PRO)
    - Pathological Reference Ontology (PathRO)
- Automatic segmentation and labeling from human and porcine CT data by GE via ISR
- Visualization of human and porcine pre- and post-injury anatomy and physiology data with linkages to the VSKB
    - anatomy displays: Thorax, Heart, Hotbox, Edgewarp
    - Decision Space display, Physiology display

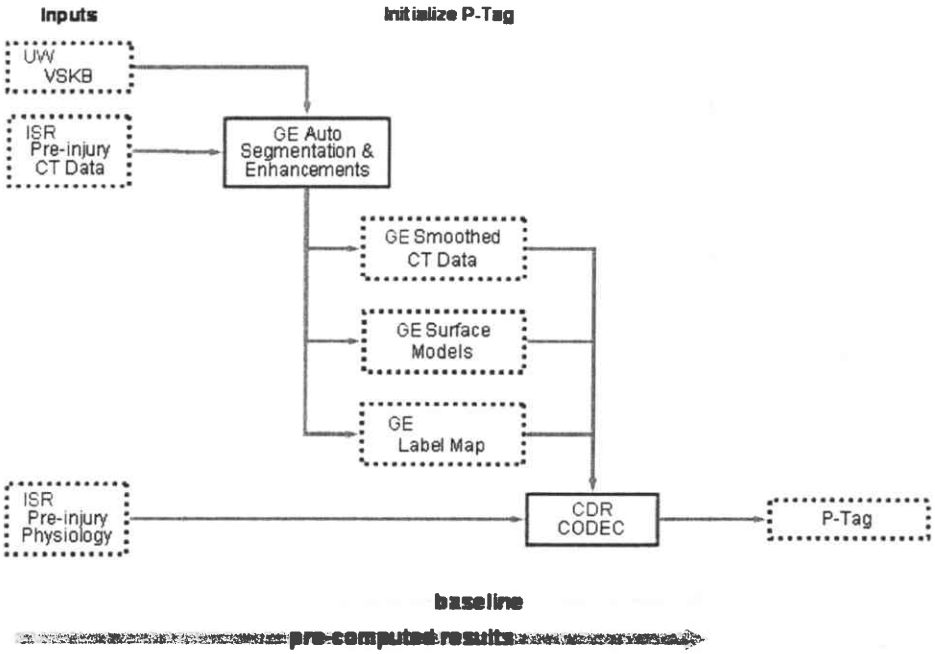

Figure 19: P-Tag data flow

Imaging and Segmentation

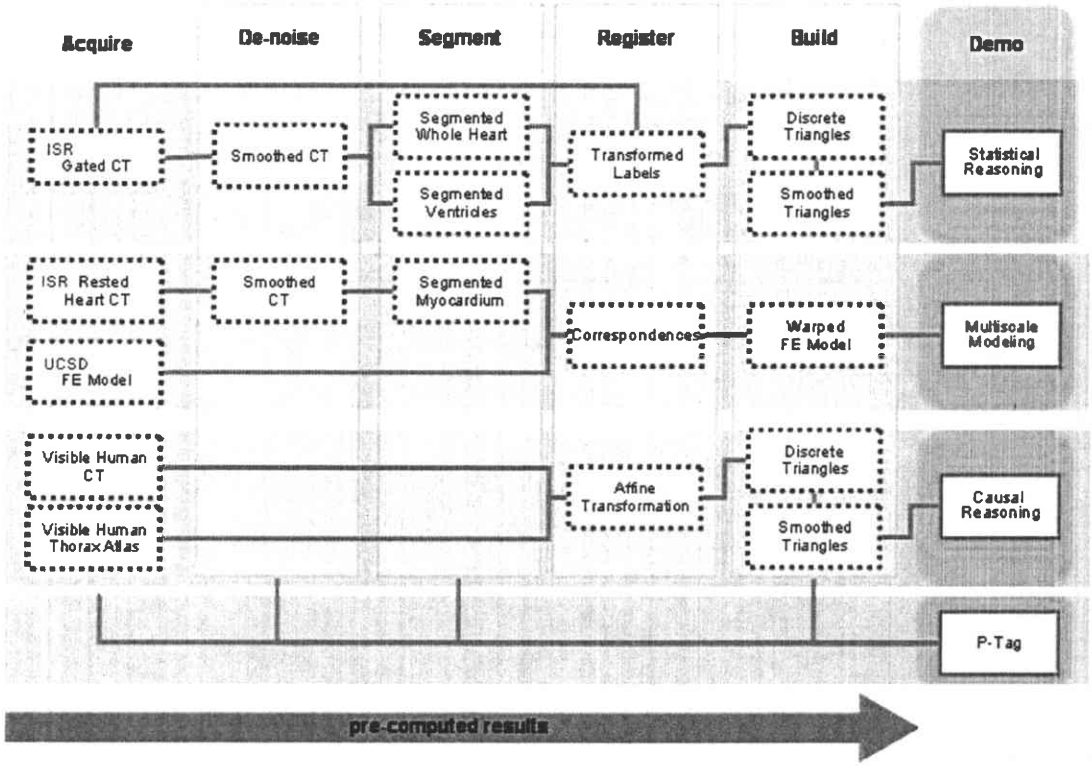

Figure 20: GE imaging and segmentation data flow

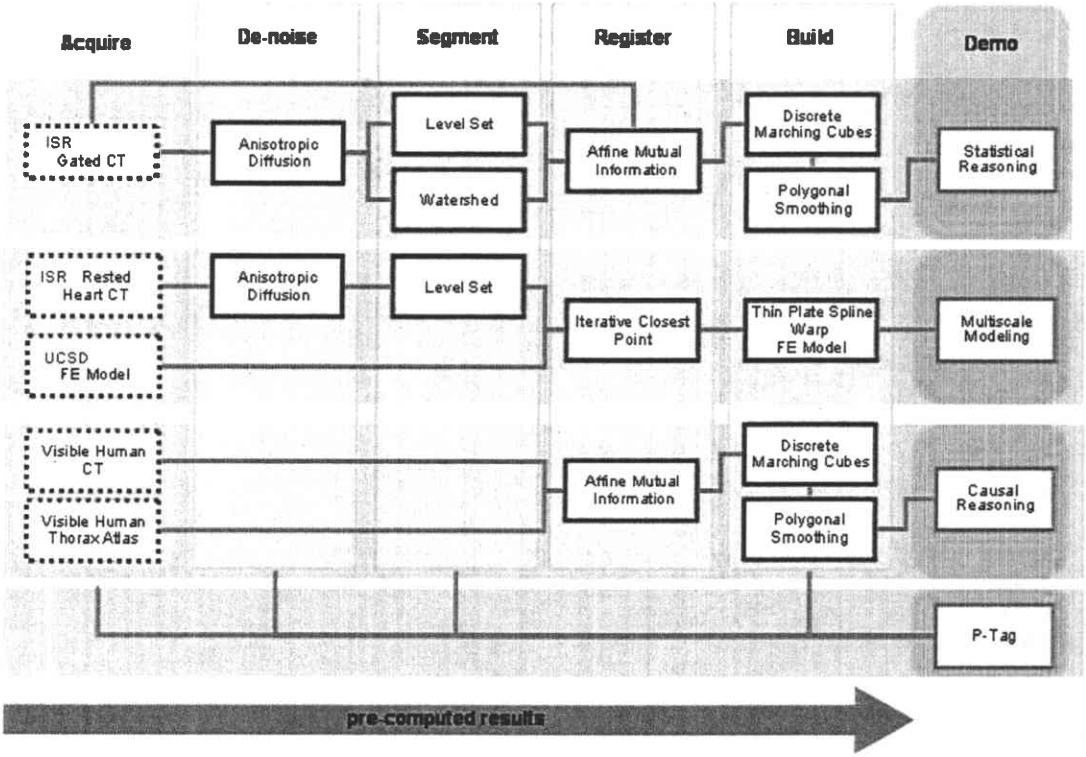

Figure 21: GE imaging and segmentation process flow

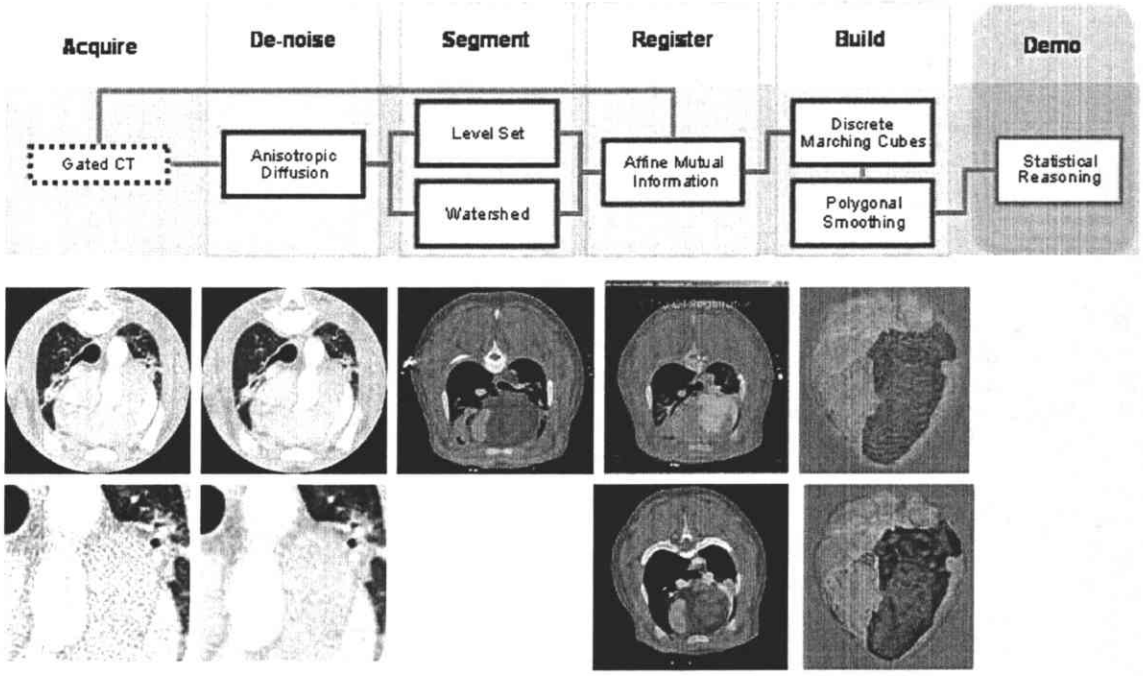

Figure 22: GE imaging and segmentation for Statistical Reasoning

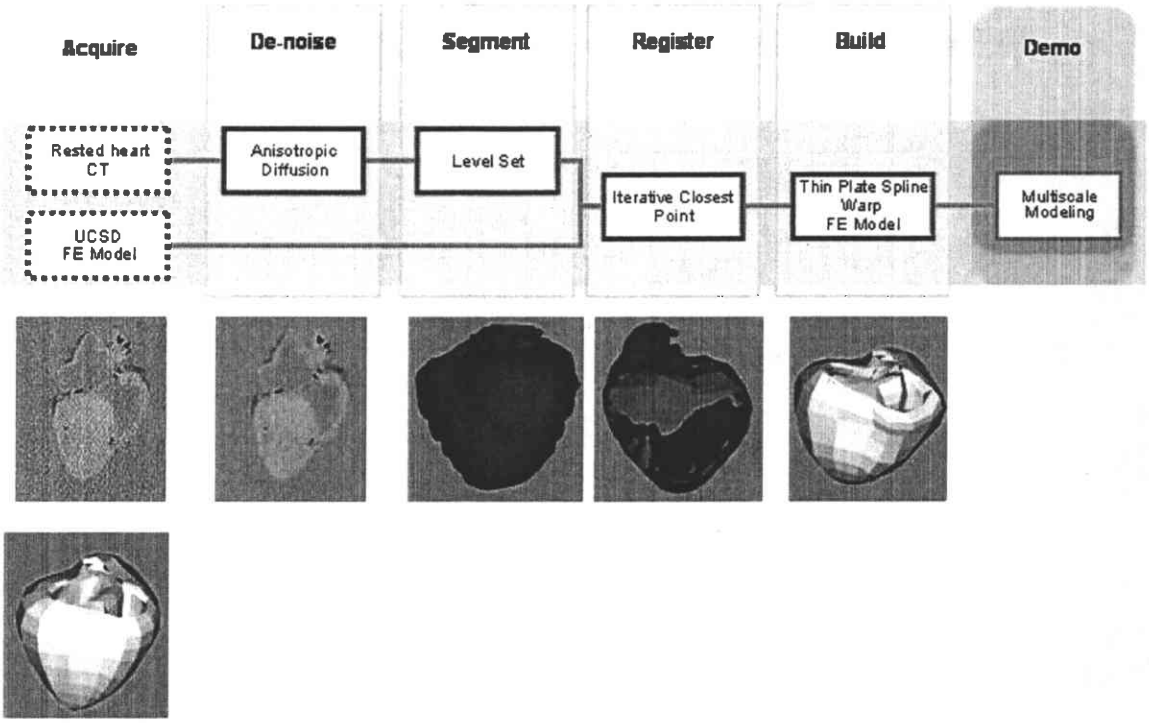

Figure 23: GE imaging and segmentation for multiscale modeling and simulation

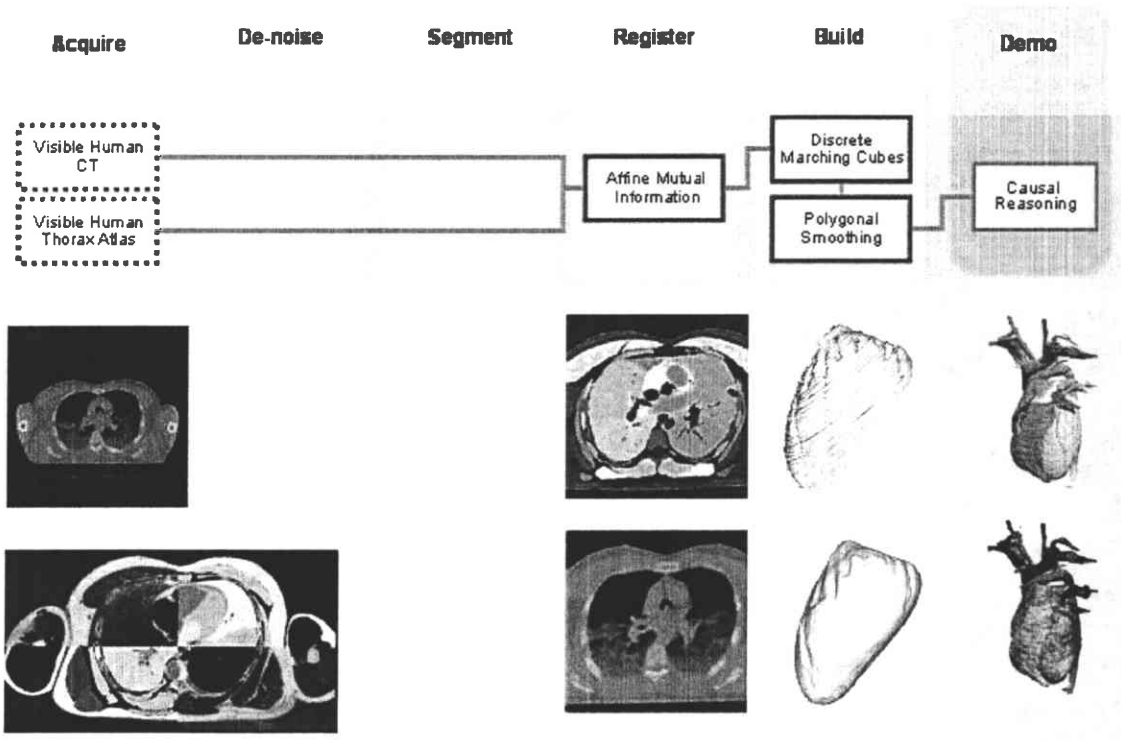

Figure 24: GE segmentation and imaging for causal reasoning

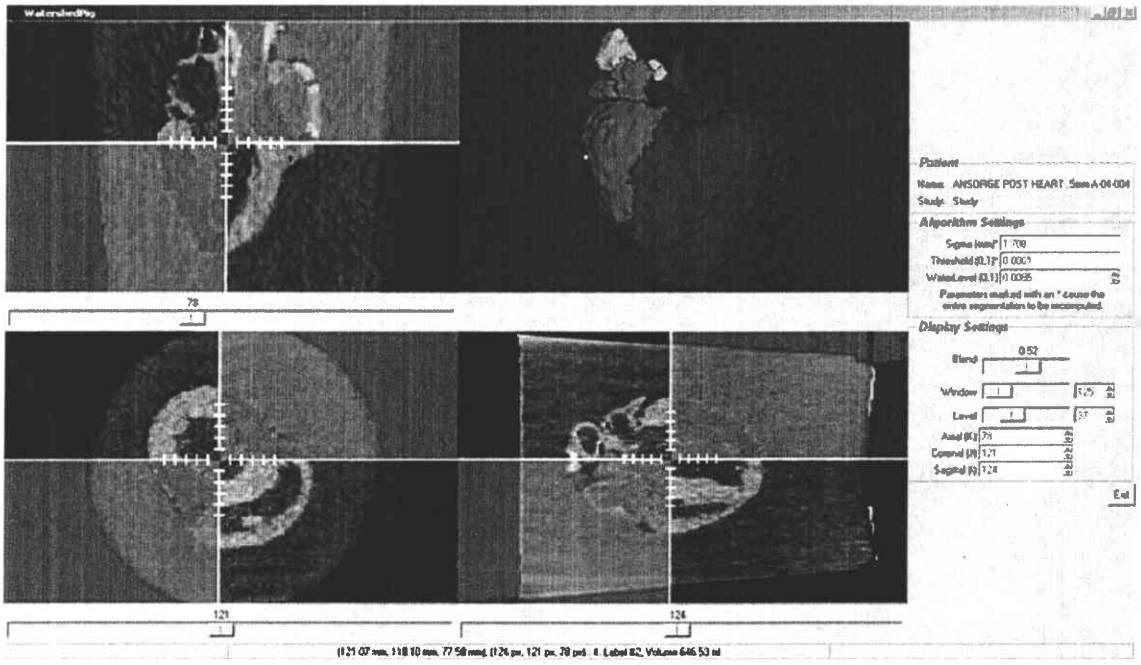

Figure 25: GE imaging and segmentation of isolated heart

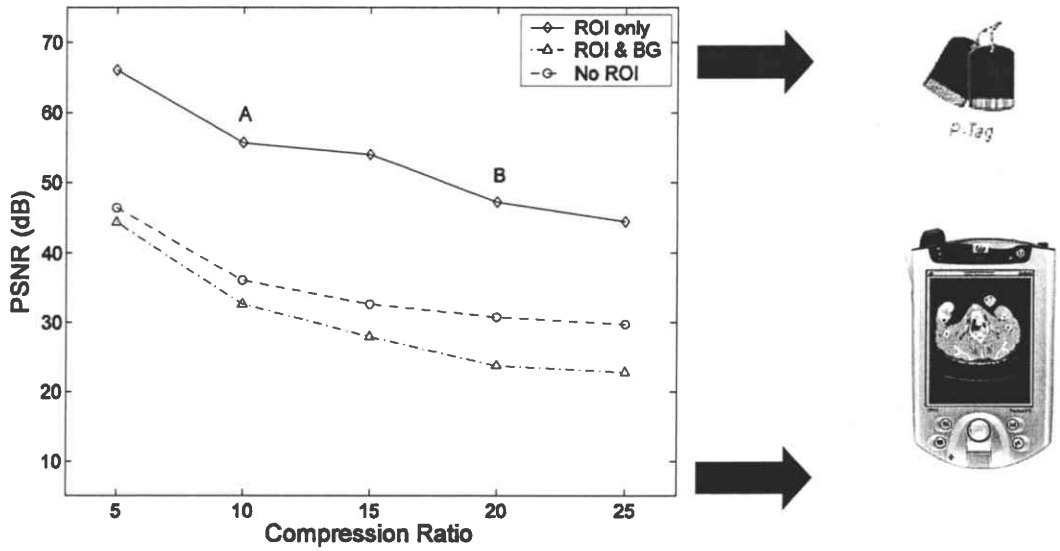

Figure 26: Data compression, P-Tag, and iPaq

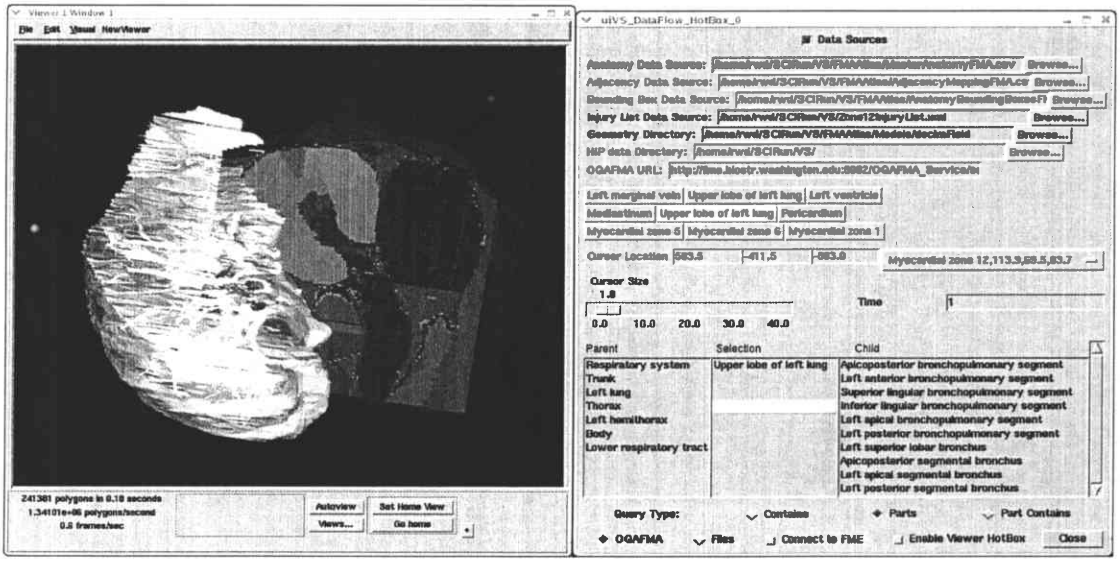

Figure 27: Anatomy display (left) and Hotbox (right) showing location of probe and surrounding structures

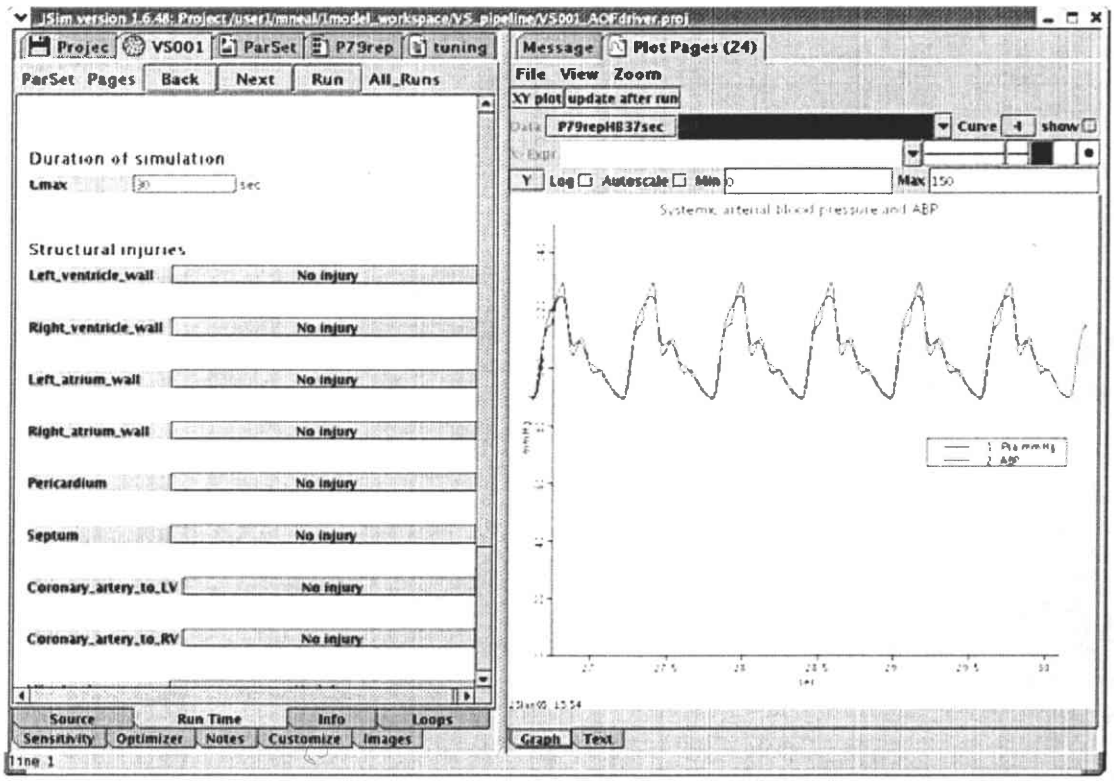

Figure 28: JSIM screenshot showing match between baseline HIP-generated and real data (black = simulated, red = observed)

Collaboration Support Tools

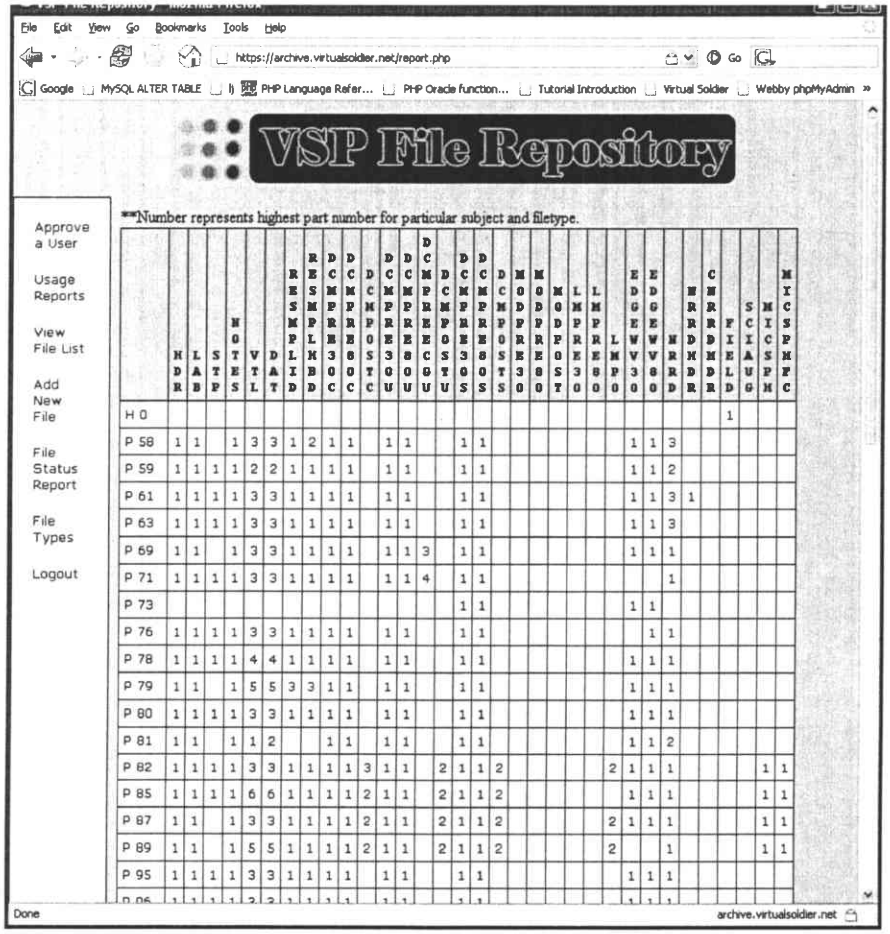

Figure 29: VSP File Repository File Report Page

Above is a screenshot of the VSP Web Repository. This web application allows the VSP team to upload, download, and keep track of data as it is received or created.

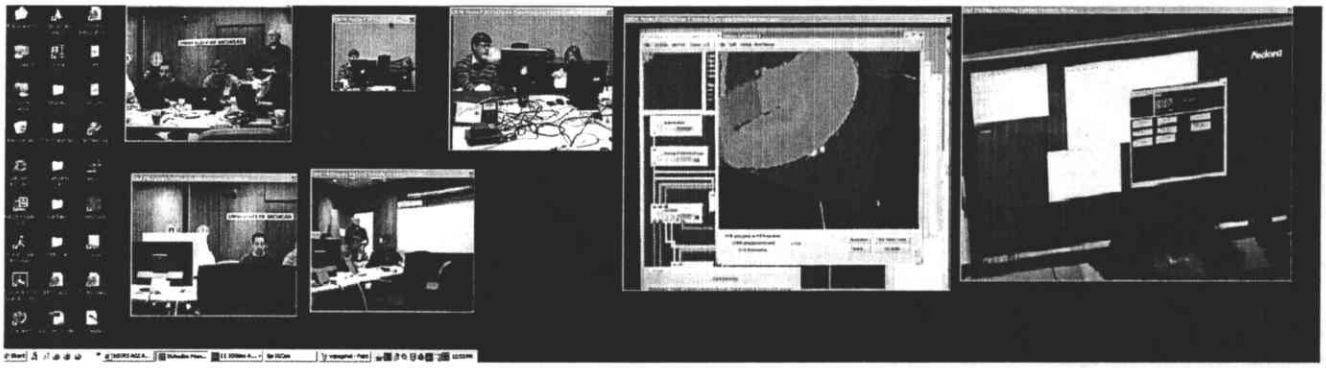

Figure 30: VSP Access Grid Session between UM and ORNL

This is a screenshot of an Access Grid session during the Feb. 28 2005 Final demo rehearsal. The VSP team members in Ann Arbor were able to interact with ORNL.

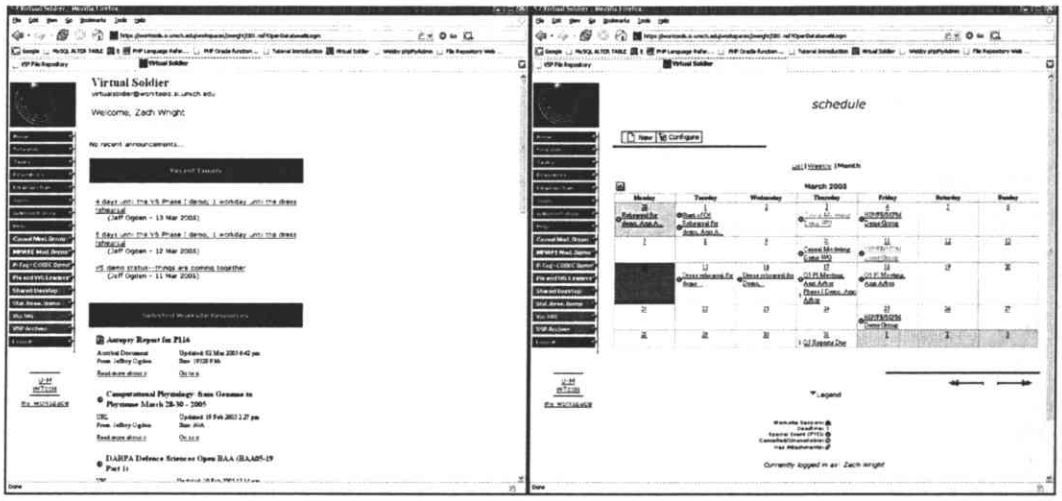

Figure 31: Virtual Soldier Worktools Site showing homepage (left) and schedule (right)

The Virtual Soldier Worktools site has been an essential tool for sharing documents, scheduling, and managing email groups since the beginning of the project.

Infrastructure Goals Demonstrated

- ✓ Extend and use global architecture
- ✓ Develop and use automatic segmentation
- ✓ Develop and use Holomer display and interface
- ✓ Store baseline anatomy & physiology on P-Tag
- ✓ Data on P-Tag transferable to other systems
- ✓ Data compression via CODEC

Part 5: Autostereoscopic Holographic Optical Element (HOE) Display

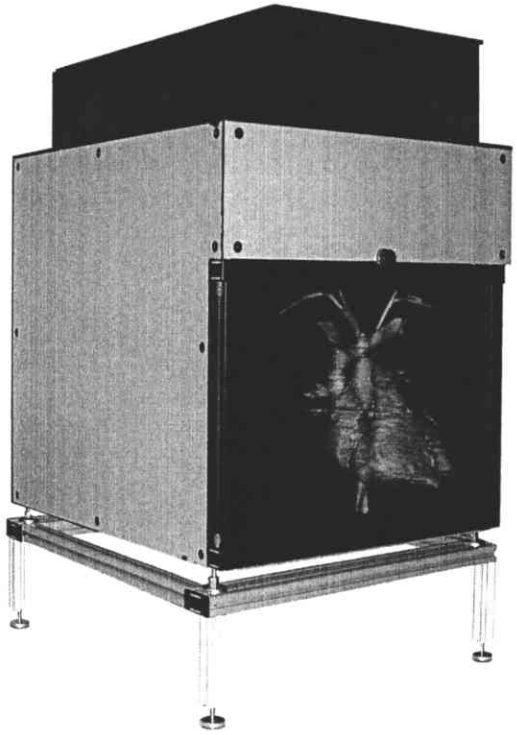

Figure 32: Moss Optics Stereo Display

The Moss Optics Autostereoscopic display is a fourth-generation prototype display based on a patented Holographic Optical Element (HOE) screen and several novel and patentable optical path improvements. The device utilizes two projectors that are controlled by a Commercial Off The Shelf (COTS) computer and stereo graphics card. The software providing the imagery is a standard DARPA Virtual Soldier package, built on top of the SCIRun (University of Utah) software framework. The Moss Optics Autostereoscopic Display represents over 3 years of partnership between the University of Michigan and Moss Optics, LLC (Marina del Rey, CA).

To date, this system has the largest "sweet spot" (viewable area) in the industry. Future plans include repackaging into a smaller ruggedized rack mount (feasible, earlier prototype) and low-cost head tracking capability. Discussions are underway with Dr. Kevin Montgomery (Stanford University) to incorporate haptic feedback capabilities.

Summary of Phase I Project Goals Demonstrated

✔ Primary Goal of Demonstration
✔ Work Used in Demonstration

	Statistical	Multiscale Modeling	Causal Reasoning	Infrastructure: P-Tag, CODEC, Holomer
Diagnose heart wounds	✔		✔	
Accuracy >= 80%	✔			
Compare baseline data to post-injury data	✔	✔	✔	
Accuracy >0.8 for structural abnormalities	✔			
Accuracy >0.8 for physiologic response	✔			
Predict likelihood of battlefield mortality	✔			
Predict outcomes	✔		✔	
Forecast time to death	✔			
Demonstrate organ and system-level integration	✔	✔	✔	
Extend and use global architecture	✔	✔	✔	✔
Develop and use automatic segmentation	✔	✔	✔	✔
Develop and use Holomer display and interface	✔	✔	✔	✔
Store baseline anatomy and physiology on P-Tag				✔
Data on P-Tag transferable to other systems				✔
Data compression via CODEC				✔

Virtual Soldier Project Team Members

Academic

University of Michigan (Prime Contractor)
Stanford University Medical School
University of Washington, Bioengineering
University of Washington, Structural Informatics Group
University of Utah, Scientific Computing and Imaging Institute
University of California San Diego
    Subcontractor: University of Auckland
Case Western Reserve University

Government

Defense Advanced Research Projects Agency
Telemedicine and Advanced Technology Research Center
Brooke Army Medical Center Institute for Surgical Research
Oak Ridge National Laboratory
    Subcontractor: University of South Carolina

Corporate

General Electric Research
    Subcontractor: Brigham and Women's Hospital, Harvard University
ATK- Mission Research Corporation
Crowley Davis Research
    Gerry Higgins, Ph.D. (consultant)
    Howard Champion, M.D. (consultant)
    Lou D'Alecy, M.D., Ph.D (consultant)
Xtria

Not-for-Profit

Federation of American Scientists

Appendix

Use of Experimental Data

The following table summarizes the uses being made of the experimental data by each portion of the demonstration:

Portion of Demo	Image/CT Data	Physiology Data
Statistical Reasoning	Porcine	Porcine
Causal Reasoning	Visible Human	Simulated data only
Multiscale Modeling and Simulation	Porcine	Porcine
P-Tag, CODEC, Holomer Display	Porcine and Visible Human	Porcine and Simulated Human
Autostereoscopic / Holographic Display	Porcine and Human	None

Summary of ISR Experiments

Through March 10, 2005 a total of sixty seven porcine animal experiments have been conducted at the U.S. Army's Institute for Surgical Research in San Antonio, Texas. Model development ended on November 12, 2004. The first experiment was conducted on November 30, 2004.

	Open Chest		Closed Chest		
Outcome	**LV**	**RV**	**LV**	**RV**	**Total**
TTD 10–120 mins.	7	1	0	0	8
TTD >120 mins.	4	1	1	2	8
Quarantined	4		0		4
Analyzable Sub-total	**17**		**3**		**20**
TTD <10 mins.	2	4	0	0	6
Death before injury	2		0		2
Incomplete data	2		1		3
Data not yet received	5		0		5
Model development					31
Total					**67**

Death is defined as a sustained MAP of 20 mmHg or less. Survival is defined as a time to death of more than 120 minutes. An "analyzable" experiment is an experiment with a time to death of 10 mins. or longer and relatively complete data collection.

All deaths have been due to hemorrhage. No deaths due to ventricular fibrillation were observed. Death due to tamponade is not possible since during the open chest procedures much of the pericardium is removed before injury.

If three or more of the five experiments for which no data have yet been received from ISR prove to be analyzable, there will be 20 or more analyzable open chest experiments available for future statistical and other analysis. Some of the experiments for which data have yet to be received may replace some of the quarantined experiments, if these experiments prove to be more appropriate for demonstration purposes as determined by the Program Manager.

There are three analyzable closed chest experiments, but none of the three resulted in a particularly severe injury. A decision needs to be made regarding whether additional closed chest experiments will be conducted during the remainder of Phase I.

Data Collected at ISR

The porcine animal experiments are performed according to DoD Animal Use Protocol number A-04-004: *Virtual Soldier Porcine Heart Injury Physiology Model* which was originally approved in May, 2004 and amended in September 2004, October 2004, and March 2005.

The following data items are collected for just the open chest experiments:

1. Aortic Flow in l/min @ 500 Hz
2. Pulmonary Artery Flow in l/min @ 500 Hz
3. Time Step Coronary Perfusion Studies @ baseline, 5 and 30 mins. post-injury (4 experiments)
4. Blood Volume @ baseline, 5 and 30 mins. post-injury (4 experiments)

The following data items are collected for just the closed chest experiments:

1. ECG 60+ leads @ 1000 Hz using equipment loaned to ISR by Utah
2. Cardiac Gated CT Scan pre-injury, post-instrumentation, 0.5mm slices, w/ contrast, reconstructions at systole and diastole, zoomed and unzoomed

The following data items are collected for both open and closed chest experiments:

1. Body Weight in kg @ start of experiment
2. Sex (always Female)
3. Times of Baseline CT Scan, Hemodynamic Data Collection Start, Injury, Blood Sample Collection, Death
4. Cardiac Gated CT Scan pre-injury, pre-instrumentation, 0.5mm slices, w/ contrast, reconstructions at systole and diastole, zoomed and unzoomed
5. Heart Rate (bpm) 5 sec.

6. Body temp. in deg. C @ 5 sec.
7. RV Pressure in mmHG @ 500 Hz
8. LV Pressure in mmHG @ 500 Hz
9. Central Venous Pressure in mmHG @ 500 Hz
10. Arterial Blood Pressure in mmHG @ 500 Hz
11. Pulse Oximetry (SPO2) in % @ 500 Hz
12. Plethysmograph (Pleth) @ 500 Hz (some experiments)
13. Respiratory Cycle @ 500 Hz (some experiments starting January 31, 2005)
14. Ventilator Settings including tidal volume (ml), breaths per min. @ 15 mins.
15. Respiratory CO2 in mmHg @ 500 Hz (not synchronized with other 500 Hz data)
16. ECG one lead @ 500 Hz
17. CT Scan postmortem isolated heart 0.5mm slices, w/o contrast (some experiments)
18. CT Scan postmortem in situ 0.5mm slices, w/o contrast (some experiments)
19. Blood Collection standard laboratory analysis @ baseline, 5, 15, 30, 60, 90, and 120 mins., or at death
20. Blood loss estimated by weight @ end of experiment
21. Description of injury (size, location, angle), cause of death, time to death
22. Digital photos of isolated heart w/ marker pins inserted @ end of experiment
23. Heart autopsy (conducted at University of Washington for some experiments)

Blood Collection Laboratory Analysis

Samples collected at baseline, 5, 15, 30, 60, 90, 120 mins. or at death.

Name	Abbreviation	Units
CBC		
White Blood Cell Count	WBC	10 3/mm3
Red Blood Cell Count	RBC	
Hemoglobin	HGB	g/dl
Hematocrit	HCT	%
Mean Corpuscular Volume	MCV	um3
Mean Corpuscular Hemoglobin	MCH	pg
Mean Corpuscular Hemoglobin Concentration	MCHC	g/dl
Platelet	PLT	10 3/mm3
Lymphocytes	LYM	%
Monocytes	MON	%
Neutrophils	NEU	%
Eosinophils	EOS	%
Basophils	BAS	%
Coagulation		
Prothrombin Time	PT	sec.
Activated Partial Thromboplastin Time	aPTT	sec.
Fibrinogen	FIB	mg/dl
Chemistry		

Name	Abbreviation	Units
Urea Nitrogen		mg/dL
Creatine		mg/dL
Total Protein		g/dL
Albumin		dg/dL
Blood Gases		
Temperature At Time of Sample Collection	Temp	deg. C
Hydrogen Ion Activity	pH	
Partial Pressure of Carbon Dioxide	PCO2	mmHg
Partial Pressure of Oxygen	PO2	mmHg
pH Temperature Corrected	pHt	
PCO2 Temperature Corrected	PCO2t	mmHg
PO2 Temperature Corrected	PO2t	mmHg
Hematocrit	HCT	%
Total Hemoglobin Concentration	ctHb	g/dl
Oxyhemoglobin	O2Hb	%
Carboxyhemoglobin	COHb	%
Methemoglobin	MetHb	%
Sulfhemoglobin	SulfHb	%
Deoxyhemoglobin	HHb	%
Oxygen Concentration	ctO2	vol %
Oxygen Capacity	BO2	vol %
Functional Oxygen Saturation	SO2	%
Sodium	Na	mmol/l
Potassium	K	mmol/l
Chloride	Cl	mmol/l
Glucose	Glu	mmol/l
Lactate	Lac	mmol/l
Bicarbonate Concentration	cHCO3	mmol/l
Total Co2 Concentration in Blood	ctCO2(B)	mmol/l
Base Excess in Blood	BE	mmol/l
Base Excess In Vivo	BEecf	mmol/l
Standard Bicarbonate	cHCO3st	mmol/l
Functional Oxygen Saturation	SO2	%
Half Saturation Tension of Oxygen in Partial Pressure of Oxygen	P50	mmHg

Preliminary Injury Device Characterization

GLB, Inc. in cooperation with ATK-MRC performed a preliminary characterization of the Modified Nail Gun (MNG) being used at ISR. A more complete characterization of the wounding device to be carried out by ISR was not funded.

GLB determined that the MNG probe travels at a velocity of between 76 and 92 feet per second (+-7%) and they estimate that a fragment would be released at a velocity of approximately 100 feet per second. See the table below. The device characterization may be too preliminary to draw firm conclusions, but it is possible that the ISR MNG delivers a fragment with a velocity and energy that is similar to .32 and .60 caliber projectiles.

Table 4 from *Physics of Penetrating Trauma*: *Examples of Missile Kinetic Energies on Different Tissues*, updated to include data on ISR MNG

Projectile	Mass (gm)	Velocity (ft/sec)	Impact Energy (Joules)	Tissue	Size of Temporary Cavity	Result
ISR 11mm fragment	**5.0**	**~100**	**--**	**Heart**	**N/A**	**Varies by location of wound**
ATK-MRC 7 mm fragment	**4.1**	**~100**	**--**	**Heart**	**N/A**	**Varies by location of wound**
.32 caliber	0.27	87.4	1.0	Heart	None, only permanent cavity	Survived
.60 caliber	2.27	100.7	11.5	Liver	63.5 mm	Survived
40 mm Multi Pellet fragment	14	105.2	77.6	Heart	27mm	Cardiac avulsion - death
.25 Remington Rimfire	42	1180	154	Heart	N/A	Cardiac death
12 gage shot bag	40.8	87.9	157.6	Heart	N/A	Ventricular avulsion - death
M16	3.6	3094	1416	Toe	2 mm	Minor wound repair
44 magnum	125	2340	1660	Heart	Not measurable as in solid tissue	Death
3006 Rifle	150	3779	2820	Heart	N/A	"Exploded thorax"
405 Winchester	75	3500	4489	Heart	N/A	Cardiac avulsion - death

References for the preceding table:

1. *Ballistic Trauma* (1997). (Eds. J.M. Ryan, N.M. Rich, R.F. Dale, B.T. Morgans and G.J. Cooper) Arnold Publishing, London.

2. *Textbook of Military Medicine, Part I, Warfare, Weaponry, and the Casualty, Volume 5 - Conventional Warfare: Ballistic, Blast and Burn Injuries.* (1990, *new update draft – 2004*) (R. Zajtchuk, D.P. Jenkins, R.F. Bellamy and M. Quick) Published by the Office of the Surgeon General, Department of the Army, United States of America.

3. Lyon, D.H., C.A. Bir and D. DuBay (1998) *Injury Evaluation Techniques for Non-Lethal, Kinetic Energy Munitions*. NTIS AQI98-11-2308.

4. Memo GBL-04-081 dated December 2, 2004 reporting qualified results of preliminary characterization of ISR MNG.

5. E-mail from Bob Eisler, ATK-MRC dated December 3, 2004, subject: *Quick and Dirty Checkout tests on ISR MNG.*

6. E-mail from Cpt. Eric Ansorge, USAISR dated January 7, 2005, subject: *fragment weights.*

Figure 33: Modified Nail Gun with tip attached

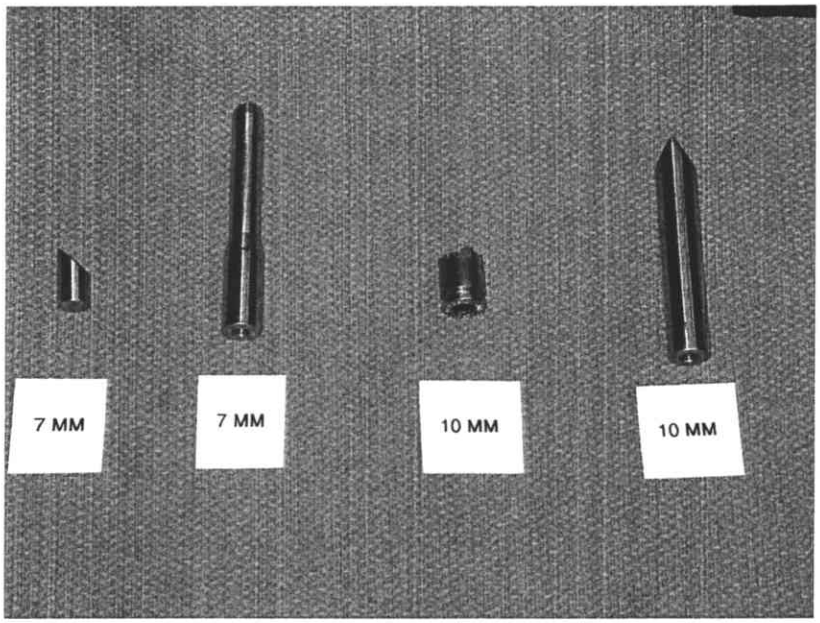

Figure 34: 7mm MRC fragment, 7mm blunt probe, 11mm ISR fragment, 10mm pointed probe

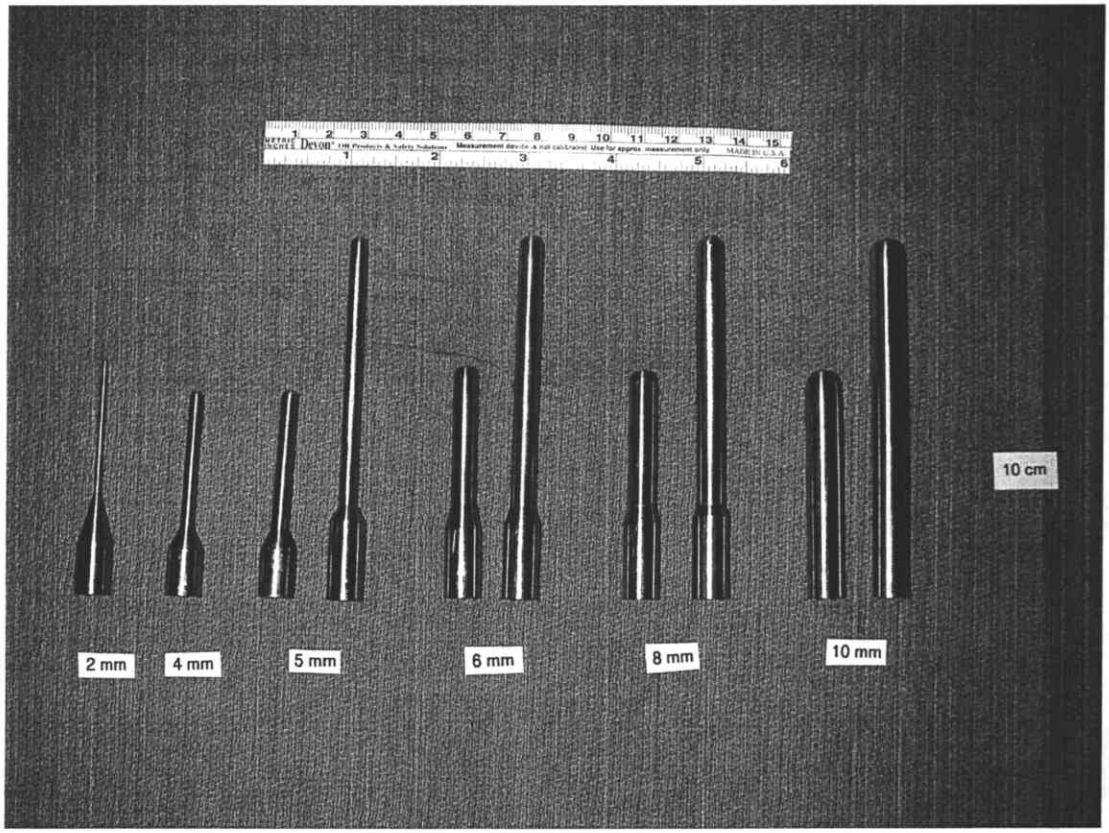

Figure 35: Blunt probes, long and short

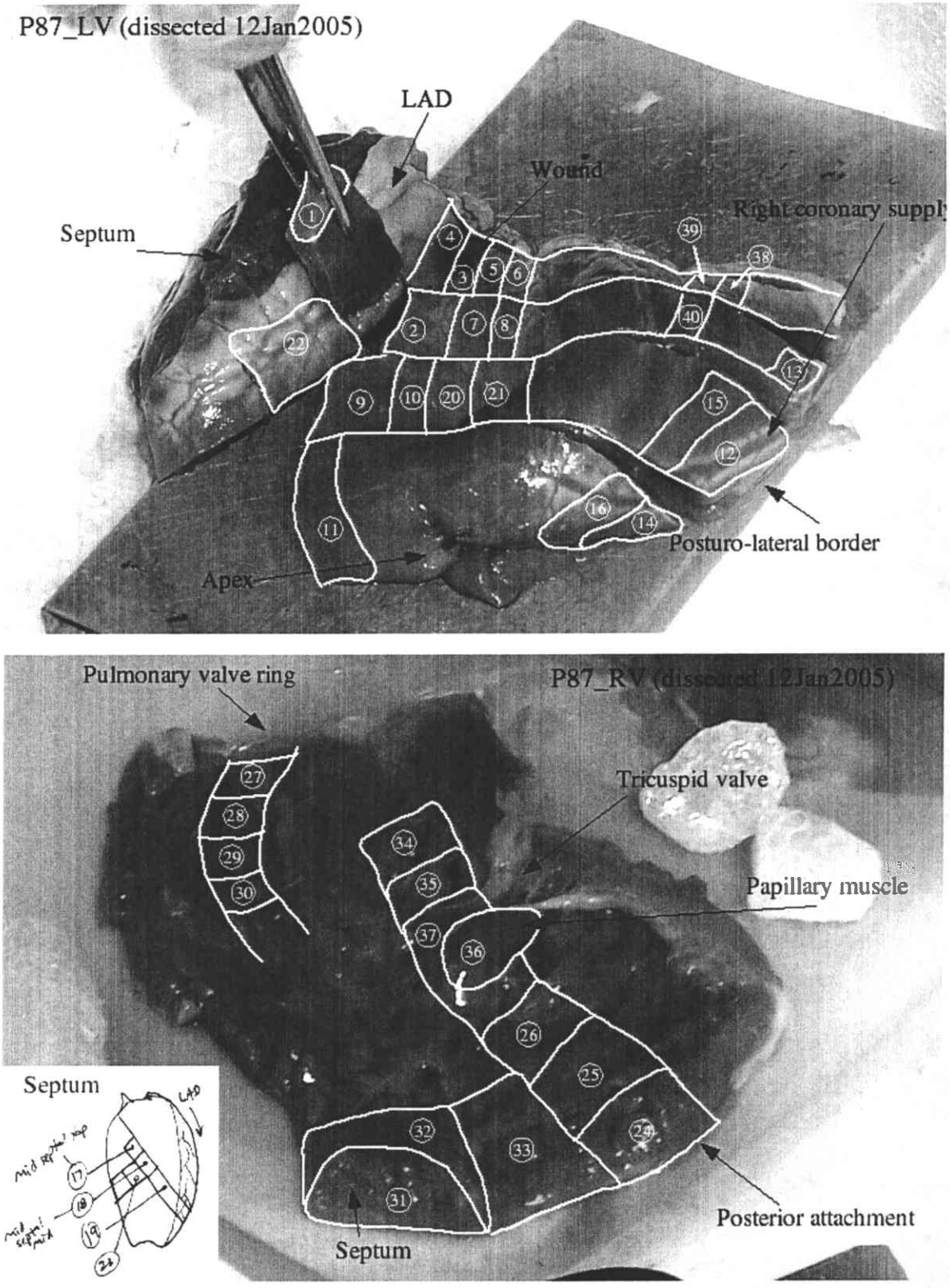

Figure 36: Perfusion analysis

Summary of Experimental Data Including Statistical Forecasts

Virtual Soldier Project: Summary of Experimental Data including Statistical Forecasts-- 15 March 2005

Status: Quarantined (Q), Short TTD (S), Death prior to injury (D), Incomplete data (I) Available for use during March 17th demo (A)

Injury Method: Blunt Probe (PR), Pointed Probe (PP), ISR Fragment (IF), MRC Fragment (MF)

Location: Closed Chest (CC), otherwise Open Chest plus RV or LV

Status	Date of Experiment	Data Received	Tag No.	Injury Method	Size (mm)	Loc.	Cause of Death	Time of Death ISR / UM (mins)	Forecast @ 5 mins. Post-injury: Survival or Average Time of Death (mins.)	Forecast of Time of Death (mins.) @ 1st alarm	Number of Alarms	Time of 1st Alarm	Time of 2nd Alarm	Time of 3rd Alarm
Analyzed Open Chest Experiments:														
	30Nov2004	8Dec2004	63	MF	7	LV	Euthanized	120+	Survival	--	0			
	2Dec2004	8Dec2004	59	PR	7	RV	Euthanized	120+	Survival	--	0			
	7Dec2004	6Jan2005	61	PR	7	LV	hemorrhage	90 / 116	Survival*	128	1*	94		
		* 5 min. forecast of survival is not correct. Recognition of an alarm for this subject requires an adapted algorithm.												
	16Dec2004	20Dec2004	78	PP	10	LV	Euthanized	120+	Survival	--	0			
	4Jan2005	12Jan2005	79	IF	11	LV	hemorrhage	104 / 102	74	114	2	80	93	
	10Jan2005	14Jan2005	89	PP	10	LV	Euthanized	120+	Survival	--	0			
		Two injuries, 1st unsuccessful or minor. Microsphere, blood volume, and isolated heart CT.												
A	11Jan2005	14Jan2005	87	PP	10	LV	Euthanized	120+	Survival	--	0			
		Microsphere, blood volume, and isolated heart CT.												
	12Jan2005	14Jan2005	82	IF	11	LV	hemorrhage	27 / 26	74	60	1	26		
		Microsphere, blood volume, and isolated heart CT.												
A	13Jan2005	26Jan2005	85	PR	7	RV	hemorrhage	113 / 100	74	97	2	63	97	
		Microsphere, blood volume, and isolated heart CT.												
A	18Jan2005	26Jan2005	96	IF	11	LV	hemorrhage	115 / 117	74	117	3	83	107	113
	19Jan2005	26Jan2005	97	IF	11	LV	hemorrhage	26 / 28	74	43	2	9	20	
	25Jan2005	31Jan2005	108	MF	7	LV	hemorrhage	52 / 52	74	56	3	22	36	50
	26Jan2005	31Jan2005	107	MF	7	LV	hemorrhage	85 / 84	74	70	3	36	42	78
		The notes for this experiment report a 124 minute time to death, when the more detailed marker annotations show an 85 minute time to death. 85 minutes is correct.												

*incorrect forecast at this point in time

Virtual Soldier Project: Summary of Experimental Data including Statistical Forecasts-- 15 March 2005

Status: Quarantined (Q), Short TTD (S), Death prior to injury (D), Incomplete data (I) Available for use during March 17th demo (A)

Injury Method: Blunt Probe (PR), Pointed Probe (PP), ISR Fragment (IF), MRC Fragment (MF)

Location: Closed Chest (CC), otherwise Open Chest plus RV or LV

Status	Date of Experiment	Data Received	Tag No.	Injury Method	Size (mm)	Loc.	Cause of Death	Time of Death ISR / UM (mins)	Forecast @ 5 mins. Post-injury: Survival or Average Time of Death (mins.)	Forecast of Time of Death (mins.) @ 1st alarm	Number of Alarms	Time of 1st Alarm	Time of 2nd Alarm	Time of 3rd Alarm
Quarantined Open Chest Experiments:														
Q, A	14Feb2005	25Feb2005	124											
Q	15Feb2005	25Feb2005	125											
Q, A	16Feb2005	25Feb2005	127											
		Note from ISR: Some of the CT images have been skipped due to an irregular heart beat present at the time of the scan. The gated procedure cannot correctly process scans when the patient has an abnormal heart beat or rhythm. These results were also taken with a different filter convolution than normal. I tried to change it back to the normal filter convolution when I reconstructed the data, but I'm not sure if it will look the same.												
Q	17Feb2005	8Mar2005	129											
		Note from ISR: In the .dat, .vtl. and notes file the second marked time point that reads 15 min. is actually the 30 min time point.												
Open Chest Experiments for which data has not yet been received:														
I	2Mar2005		132											
I	3Mar2005		138											
I	8Mar2005		146											
I	9Mar2005		143											
I	10Mar2005		145											
Closed Chest Experiments:														
	8Dec2004	20Dec2004	71	MF	7	CC-LV	Euthanized	120+						
		Note from ISR: The fragment did not pierce / nor penetrate the pericardium or the LV, essentially there was no injury to the LV.												
	9Dec2004	15Dec2004	69	PR	10	CC-RV	Euthanized	120+						
	23Feb2005	8Mar2005	136	PP	10	CC-RV	Euthanized	120+						

Virtual Soldier Project: Summary of Experimental Data including Statistical Forecasts-- 15 March 2005

Status: Quarantined (Q), Short TTD (S), Death prior to injury (D), Incomplete data (I) Available for use during March 17th demo (A)

Injury Method: Blunt Probe (PR), Pointed Probe (PP), ISR Fragment (IF), MRC Fragment (MF)

Location: Closed Chest (CC), otherwise Open Chest plus RV or LV

Status	Date of Experiment	Data Received	Tag No.	Injury Method	Size (mm)	Loc.	Cause of Death	Time of Death ISR / UM (mins)	Forecast @ 5 mins. Post-injury: Survival or Average Time of Death (mins.)	Forecast of Time of Death (mins.) @ 1st alarm	Number of Alarms	Time of 1st Alarm	Time of 2nd Alarm	Time of 3rd Alarm
Unsuccessful or short time to live (<10 mins.) experiments:														
S, I	1Dec2004	8Dec2004	58	MF	7	RV	hemorrhage	4						
		LVP and AOF not measured.												
S	15Dec2004	20Dec2004	76	PR	10	RV	hemorrhage	3						
S	5Jan2005	12Jan2005	80	IF	11	RV	hemorrhage	7						
D	6Jan2005	12Jan2005	81	n/a	n/a	n/a	n/a	n/a						
		Died during instrumentation												
I	20Jan2005	26Jan2005	95	IF	11	F-LV	hemorrhage	15						
		Problems with anesthesia, RVP, AOF--see nts file for details.												
S	27Jan2005	31Jan2005	106	MF	7	RV	hemorrhage	6						
I	1Feb2005	10Feb2005	105	MF	7	F-LV	Euthanized	120+						
		Note from ISR: RVP trace appears to be consistent with CVP, suspect it has floated out of the ventricle. Data collection suspended from approx 1230 hrs until approx 1310hrs due to a hard drive failure. Hard drive recovered at approx 1310 hrs and data set continued as pig #105A.												
D	8Feb2005	10Feb2005	117	n/a	n/a	n/a	n/a	n/a						
		Died during instrumentation												
S	9Feb2005	14Feb2005	120	MF	7	LV	hemorrhage	7						
S	10Feb2005	14Feb2005	116	MF	7	LV	hemorrhage	4						
I	22Feb2005	4Mar2005	126	PP	10	CC-RV	hemorrhage	5						
		Problems with pre-injury post-instrumentation CT.												

Fred Bookstein's Time-to-Death Memo (2-14-2005)

Executive summary: To date, eleven experimental animals have lived past thirty minutes post-wound. Among these 11, all six of those in which net LV pressure waveform amplitude dropped by 30% or more died within 120 minutes, versus none of the other five. Of those that died, five (of six) signaled death by one specific alarm, a sudden deceleration of 2.5% or more in relative LV amplitude; but none of the surviving test subjects ever showed this alarm. Most of the nonsurviving test subjects produced the alarm twice, once around 30 minutes before death and again within about ten minutes of death. These findings demonstrate the substantial fulfillment of the BAA criteria of 0.80 accuracy and adequate statistical significance for this domain of deliverables.

This memo summarizes a very promising time-to-death analysis for the eleven animals that survived at least thirty minutes after injury, in the open-chest condition, as of February 1.

Tag numbers for these animals are:

61 79 85 96 107 108

59 63 78 87 89

The first six of these died after at least thirty minutes survival post-wound; the last five survived to the full 120 minutes of the experimental design.

All data were subsampled to 32nds of a heartbeat, using Jim Rees's resampler, as demonstrated before.

The powerful effects of the respiratory cycle were removed as described in the test subject 61 memo or my MMVR poster.

Average waveforms were computed for derespirated LVP and RVP per heartbeat, minute by minute. ("Average" here is in the sense of the singular-value decomposition, which is least-squares in terms of multiples of a single prototype form; it is, however, indistinguishable from the ordinary phase-by-phase average.) AMPLITUDE of a waveform is quantified as its root-mean-square around zero.

For this subset of animals, there is a perfect discrimination of long-term survival/nonsurvival, and a nearly perfect alarm for TTD of the nonsurvivors, as follows:

The percentages of drop in the LVP from baseline to the maximum average (over a ten-minute window) post-injury are:

43 43 58 65 59 78

17 31 6 26 15

This supplies a PERFECT DISCRIMINATOR for ultimate survival within this group of 11 animals. A convenient cutpoint is 35%, or "one-third of baseline function."

Out of a wide range of quantifications of the stability of the heart post-wound, one stands out for its accuracy: the _relative_ second difference of LV amplitude at lag 3 minutes. This means the change of LV amplitude from the (i-3)-rd minute to the i-th minute, minus the change from the (i-6)-th minute to the (i-3)-rd, divided by that amplitude averaged over the later interval.

THE ALARM IS SET OFF WHEN this relative second difference first falls below -0.025 (i.e. a 2.5% downward acceleration in net LV output over some six-minute clock interval) after the period during which the test subject has had an opportunity to stabilize (to survive beyond thirty minutes).

Of the test subjects that survived, NONE (out of 5) ever had a relative second difference of LV output below this threshold. In other words, there are NO "false alarms" from this indicator.

Of the test subjects that did not survive, all but one (i.e. five out of six) DID have at least one episode of relative second difference below -0.025 in the second half of their post-wound history. The one exception, test subject 61, shows a remarkable consistently negative FIRST difference that permits a prediction simply from negative trend. We are not counting it as a success for the second-difference filter, but we can effectively anticipate its death nevertheless; perhaps someday we shall receive a second test subject that dies this way.

The association between alarm and survival is certainly significant. Fisher's exact test on the 2 x 2 table

5 0 (rows: alarm vs. no alarm;
1 5 columns: live vs. die)

yields a p-value of 0.015.

The proportion of test subjects with the alarm is 5/6 > 0.80; the proportion of alarmed test subjects that died is 5/5 > 0.80.

Two test subjects survived more than 10 minutes but less than 30: test subjects 82 and 97. One of these (97) has the same alarm signal as the five others; it comes at 20 minutes into the survival period of 28 minutes, hence giving only 8 minutes' warning.

The time of the relative second difference alarm, in minutes before animal death, is as follows, for the six test subjects that made it to 30 minutes but not to 120:

-- 22 37 34 48 30

Superimpose the strong signal from test subject 61 at 32 minutes before death, after which time every consecutive minute has lower LV than it had three minutes earlier:

32 22 37 34 48 30

These are on denominators equal to total postwound life in minutes:

116 102 100 117 84 52

Of the five pigs that set off a first alarm, all but one (test subject 97, the one with the shortest survival time among the alarmed test subjects) set off an alarm at least once more, at intervals before death as follows: test subject 79, 9 minutes before death; test subject 85, 3 minutes before; test subject 96, 10 minutes before; test subject 107, 6 minutes before; test subject 108, 16 minutes before.
Of course no surviving test subject had a second alarm, as none had a first alarm. It might make sense to count test subject 97's alarm as a "second alarm" predicting an imminent death, rather than a first alarm allowing half an hour's grace.

These alarm times are certainly nonrandom over the lifespans of the test subjects. The alarms cluster in the second half of the test subjects' post-wound life with $p<0.01$ (i.e. they do indeed foreshadow death).

In my view, the combination of findings here substantially satisfies the requirements of the BAA, and also Dr. Satava's personally expressed expectations, regarding TIME TO DEATH.

Virtual Soldier Project Publications

MMVR 2005 Abstracts and Posters

"Analytical Simulation of Penetrating Wounds to the Heart". *R. D. Eisler, S. F. Stone, A. K. Chatterjee*

"A Biologically Derived Computational Approach to Tissue Modeling". *Tim Andersen, Tim Otter, Cap Petschulat, Tom Menten*

"Representing the Holomer on Digital Media: Challenges and Opportunities for Data Representation and Compression". *Thomas G. Menten, Xiao Zhang, Lian Zhu. Abstract and Poster.*

"Creating Models from Segmented Medical Images". *Bill Lorensen, Jim Miller, Dirk Padfield, James Ross*

"Linking Human Anatomy to Knowledgebases: A Visual Front End for Electronic Medical Records". *Stewart Dickson, Line Pouchard, Richard Ward, Gary Atkins, Martin Cole, Bill Lorensen, Alexander Ade*

"A Middleware-based Computing Architecture for Virtual Medicine".
Line C. Pouchard, Richard C. Ward, Michael N. Huhns, Laura Zavala, Karthik Iyer

"A Web-Service Based Computational Environment for Biomedical Computing
Line C. Pouchard". Richard C. Ward, Michael N. Huhns, Laura Zavala, Karthik Iyer. Abstract and Poster.

"Using an Ontology of Human Anatomy to Inform Reasoning with Geometric Models".
Daniel L. Rubin, Yasser Bashir, David Grossman, Parvati Dev, and Mark A. Musen

"Three Dimensional Electromechanical Model of Porcine Heart with Penetrating Wound Injury". *Roy Kerckhoffs, Taras P. Usyk*

"Challenges of Presenting High Dimensional Data to aid in Triage in the Virtual Soldier Project". *Boyd AD, Wright ZC, Ade AS, Bookstein F, Ogden JC, Meixner W, Athey BD*

"The Cardiac Morphometric Markup: a Template for Experimental Cardiology". *Fred L. Bookstein, Ameed Raoof, William Green*

"Tracking Physiological Models by Kalman Filters", *Fred L. Bookstein, Daniel Cook, Jim Bassingthwaighte. Abstract and Poster.*

"Advanced Modeling and Visualization of Cardiothoracic Electrical Fields". *F. B. Sachse, M. Cole, R. M. Kirby, X. Tricoche, C. Johnson. Abstract and Poster.*

"Ontologies of Anatomy and Physiology - Basis for Causal Modeling Standards". Daniel Cook

"Computational Simulation of Penetrating Trauma in Biological Soft Tissues using the Material Point Method". *I Ionescu, J Guilkey, M Berzins, RM Kirby, J Weiss*

"Knowledge-based Anatomical Dynamic Scene Generation in XJ3D". *Wayne V. Warren, James F. Brinkley*

"Amending Dynamic Physiological Models to Represent Pathophysiological States". *Daniel Cook*

"A Highly Integrated Physiology (HIP) Cardiovascular/respiratory Model used to Simulate Cardiac Injury". *Maxwell Neal, James Bassingthwaighte, Taras Usyk, Andrew McCulloch, Roy Kerckhoffs*

MMVR 2005 Papers

Challenges of Presenting High Dimensional Data to aid in Triage in the Virtual Soldier Project. *A. D. Boyd, Z.C. Wright, A.S.Ade, F. Bookstein, J.C. Ogden, W. Meixner, B.D. Athey and T. Morris*

Computational Simulation of Penetrating Trauma in Biological Soft Tissues using the Material Point Method. *Irina Ionescu, Jameus Guilkey, Martin Berzins, Robert M. Kirby and Jeffrey Weiss*

Linking Human Anatomy to Knowledgebases: A Visual Front End for Electronic Medical Records. *Stewart Dickson, Line Pouchard, Richard Ward, Gary Atkins, Martin Cole, Bill Lorensen and Alexander Ade*

Compressing Different Anatomical Data Types for the Virtual Soldier. *Tom Menten, Xiao Zhang, Lian Zhu and Marc Footen*

Using an Ontology of Human Anatomy to Inform Reasoning with Geometric Models. *Daniel L. Rubin, Yasser Bahir, David Grossman, Parvati Dev and Mark Musen*

Three Dimensional Electromechanical Model of Porcine Heart with Penetrating Wound. *Taras Usyk and Roy Kerchoffs*

Journal/Conference Publications

Functionally and Structurally Integrated Computational Modeling of Ventricular Physiology.
Andrew D. McCulloch, Ph.D.
Japanese Journal of Physiology, Submitted 21 July, 2004, accepted.

Linking Ontologies with Three-Dimensional Models of Anatomy to Predict the Effects of Penetrating Injuries. *Rubin DL, Bashir Y, Grossman D, Dev P, Musen MA*
26th Annual International Conference IEEE Engineering in Medicine and Biology, Bethesda, MD, San Francisco, CA 2004.

Using Ontologies with geometric models to reason about penetrating injuries. *Rubin DL, Bashir Y, Grossman D, Dev P, Musen MA.*
Intelligent Data Analysis in Medicine and Pharmacology, Stanford, CA 2004.

Integrating Ontologies with Three-Dimensional Models of Anatomy. *Rubin DL, Bashir Y, Grossman D, Dev P, Musen MA*
Seventh International Protégé Conference, Bethesda, MD, 2004

Linking Ontologies with Three-Dimensional Models of Anatomy to Predict Physiological Effects of Penetrating Injuries.
Rubin DL, Bashir Y, Grossman D, Dev P, Musen MA
NASA Workshop on the Knowledge Integrating Virtual Iron Bird, Monterey, CA, 2004.

An Acoustic Model for Wave Propagation in a Weak Layer. *Michael El_Rahib, ATK-MRC*
Journal of Applied Mechanics, provisional acceptance pending revision.

Transient Waves in an Inhomogeneous Hollow Infinite Cylinder. *Michael El-Raheb,* ATK-MRC
International Journal of Solids and Structures, Accepted with Revision, Feb. 7, 2005

Wave Propagation in a Hollow Cylinder Due to Prescribed Velocity at the Boundary. *Michael El-Raheb*, ATK-MRC
International Journal of Solids and Structures, Accepted March 8, 2005

Transient Respose in a finite Hollow Cylinder from Time-delayed Prescribed Motion at the Boundary. *Michael El-Raheb*, ATK-MRC
Journal of Sound and Vibration, Accepted March 11, 2005

Other Posters and Conference Presentations

Computational Modeling of Tissue Damage from Penetrating Trauma: Linking Geometric Models to Anatomic and Biomechanical Knowledge.
Rubin DL, Bashir Y, Grossman D, Dev P, Musen MA. Invited presentation and poster, InfoRad Theater, Ninetieth annual scientific meeting of the RSNA, Chicago, IL, 2004.

Using 3-Dimensional Models as a Front End for Knowledge. *Gary Atkins (ORNL student intern)* Poster presented on Aug 11, 2004

The Development of Sophisticated Cardiac Models for Use in the Virtual Soldier Project. *Sarah Wing (ORNL student intern)* Poster at ORNL, presented on Aug 11, 2004

Cardiopulmonary Circuit Models for Predicting Injury to the Heart.
Richard Ward presentation at Southeast Section of the American Physical Society in Oak Ridge, November 11, 2004

A Web-based Computer Architecture for the Virtual Soldier
Line Pouchard, Richard Ward, Michael N. Huhns, Laura Zavala, Karthik Iyer
presentation to InterLab 2004 at Oak Ridge National Laboratory, Oct. 28, 2004

Visualization in the DARPA Virtual Soldier Project.
Stewart Dickson, Richard Ward, Alex Ade, Chris Johnson, Greg Jones, Martin Cole, Tom Menten
Abstract Submitted to Digital Human Modeling for Design and Engineering (DHM) meeting in Iowa City June 14-16, 2005

Virtual Soldier Project
Phase I Final Demonstration
June 14, 2005

Dr. Richard Satava, Defense Advanced Research Projects Agency, Program Manager
Dr. Gerald Moses, Telemedicine and Advanced Technology Research Center, COR
Mr. Edward Monachino, Strategic Analysis, Inc., Senior Biomedical Engineer

Prime Contractor, University of Michigan:
Brian D. Athey, VSP Principal Investigator
Jeff Ogden, VSP Project Manager
Fred Bookstein, Chief Statistician

Co-Principal Investigators:
CPT Eric Ansorge and LTC James Fudge, U.S. Army Institute for Surgical Research
Jim Bassingthwaighte, University of Washington Bioengineering
William Crowley, Crowley Davis Research
Bob Eisler, ATK-Mission Research Corporation
Chris Johnson, University of Utah Scientific Computing and Imaging Institute
Henry Kelly, Federation of American Scientists
Bill Lorensen, General Electric Global Research
Andrew McCulloch, University of California San Diego
John Monville, Xtria LLC
Mark Musen, Stanford University
Dan Cook and Cornelius Rosse, University of Washington Structural Informatics Group
Richard Ward, Oak Ridge National Laboratory

Table of Contents

Letter of Introduction 3
Overview 4
End-to-End Demonstration 6
    Forecasts 9
    Multiscale Modeling 12
    Anatomy from Anatomy Forecast and Comparison to Autopsy Findings 15
    Goals Demonstrated 16
Causal Reasoning Video 17
Appendix 24
    Virtual Soldier Project Team Members 24
    Use of Experimental Data 25
    Summary of ISR Experiments 25
    Data Collected at ISR 27
    Preliminary Injury Device Characterization 30
    Summary of Statistical Results 34
    Report of Statistical Findings 40
    Response to Comments on Report of Statistical Findings 59
    Review of Additional Experimental Data Items 62
    Virtual Soldier Project Publications 65

University of Michigan
Michigan Center for Biological Information
Brian D. Athey, Ph.D., Director
Phone: 734-615-5914
Email: bleu@umich.edu

Letter of Introduction

June 13, 2005

Dr. Richard Satava
Program Manager
Defense Advanced Research Projects Agency
3701 North Fairfax Drive
Arlington, VA 22203-1714

Dr. Gerald Moses
Director, Clinical Applications Division
Telemedicine and Advanced Technology Research Center
U. S. Army Medical Research and Materiel Command
504 Scott Street
Fort Detrick, MD 21702-5012

Dear Rick and Gerry,

I am pleased to present to you the Briefing Book for the Phase I Final Demonstration that will be given on June 14th. This Briefing Book includes the Report of Statistical Findings, together with information on the June 14th demonstration and the Causal Reasoning Video. Taken together, the demo, briefing book, and the Causal Reasoning Video will give you the current the status of the Virtual Soldier Project as we approach the end of Phase I. The team has worked very hard to produce this final integrated demonstration that addresses the required Phase I deliverables as requested by the Program Manager and as specified in BAA 03-02 Addendum 4.

As you know the June 14th Final Demonstration is a follow-up to the pre-demonstration that you saw on March 17th. We have done our best to address the desires of the Progam Manager to time-synchronize and integrate the material as requested. Not all of the elements from the March 17th demonstration are repeated here and you may wish to refer to the March 17th Briefing Book for additional information.

The results you saw on March 17th and the results you will see during the June 14th demonstration are in many ways truly amazing. I believe this work has the potential to form the basis of a new standard of care for the injured warfighter. Additionally, it appears that important new scientific breakthroughs relating to our understanding of the physiological and anatomical sciences are beginning to emerge, which hold great promise for the development of 21st century Virtual Soldier Capabilities.

Respectfully,

Brian D. Athey, Ph.D.
Associate Professor, Biomedical Informatics (Medical School)
Director, Michigan Center for Biological Information (Office of the Vice President of Research)
Principal Investigator, DARPA Virtual Soldier Project

Overview

This briefing book provides a status report on the DARPA Virtual Soldier Project Phase I progress and deliverables, focused on the final demonstration that will be given on June 14th. Included are:

1. End-to-End Demonstration, including:

    a. All-in-One Demonstration: Statistical Reasoning and Multiscale Modeling. The Statistical Reasoning demonstrates reasoning backward from effects to causes using experimental data provided by ISR. The Multiscale Modeling demonstrates the results from HIP and 3D FE modeling displayed simultaneously with each other and with the statistical forecasts, as well as the results from MPM and Regional Coronary Blood Flow simulations

    b. Anatomy from Anatomy forecasts: use post-injury CT data to determine which anatomical structures have been injured

    c. A comparison of the anatomy from anatomy forecast with autopsy results

2. Report of Statistical Findings

3. Causal Reasoning Video

    Reasoning forward from causes to effects using the Virtual Soldier Knowledge Base (VSKB), Visible Human Data, simulated physiologic data from the HIP model, and ballistic modeling results to automatically generate multiple Holomer instances

A number of elements that were included in the initial March 17th demonstration are not being repeated during the June 14th demonstration, including the P-Tag, CODEC, Hotbox, Holomer and Stereo Displays, Auto Segmentation, Edgewarp, collaboration and other infrastructure. These capabilities were used to prepare for, are used during, or are available to support the demonstration, but are not emphasized during the demonstration.

Accomplished since March 17th:

1. Ten additional animal experiments – ISR
2. Visualization of all data, forecasts, and simulations simultaneously in a single display synchronized with respect to time – Utah, UMich, ORNL
3. Statistical analysis including only fragment experiments plus additional analyzable animal experiments – UMich
4. New Forecast Display – UMich
5. Additional data items examined for usefulness in making multivariate forecasts, forecast criteria changed to include ABP – UMich

6. FE element meshes matched to experimental subjects using affine transform method including mesh correction, image processing, mesh to image registration– GE, UCSD, Utah
7. HIP models fit to entirety of data pre and post injury for two experimental subjects. HIP models altered to allow the models to be driven by the empirical data
8. In depth analysis of empirical data for qualification for demo – GE, UCSD, UW
9. Repair of empirical data – UMich, UW
10. Two new regional coronary blood flow simulations – Auckland
11. Perfusion fields and MPM data used to model mechanical and electrophysiology – UCSD, Utah

    For the electrophysiology, at the site of the wound the diffusion was set to zero, and around that hyperkalemia was modeled and a 35% reduction in the sodium-potassium pump.

12. Material Point Method Simulations – experimental specifics generated for two experiments – Utah
13. Simulation of cardiac electrophysiology and ECG applying high order finite element meshes– Utah
14. FE mechanical and electrophysiologic simulation results visualized in their entirety through development of an extremely novel scaled interpolation scheme – UCSD, Utah
15. Torso model with three compartments (heart, lung, others) instead of one (body), resolution of the model improved by a factor of ~10
16. Anatomy from anatomy forecasts including changes in postmortem CT procedures, segmentations, image processing, autopsies, and comparison of results – ISR, UW, GE
17. Tamponade scenario added to Causal Reasoning demo – UW, Stanford, ORNL
18. Produced Causal Reasoning Video – UW, UMich

End-to-End Demonstration

Reason statistically from effects to causes and create predictive multiscale anatomical and physiologic models

- Using data from two test subjects
  - baseline porcine CT and instrumentation data from ISR
  - post-injury porcine instrumentation data from ISR
  - segmented and labeled anatomy from GE
  - simulated physiology data from UW's HIP model
  - functionally integrated models of circulatory physiology, anatomically and biophysically detailed 3D models of electromechanics of ventricles and torso from UCSD, Auckland, and Utah
  - the Virtual Soldier Knowledge Base (VSKB) from UW
- Statistically forecast survival or death, time to death, the location of the injury, and detect "alarms"
- Model physiologic signals not easily measured in the field
- Validate model output against experimental data
- Display information simultaneously synchronized with respect to time
- Allow creation of a database that covers more cases than is possible with experimental data alone

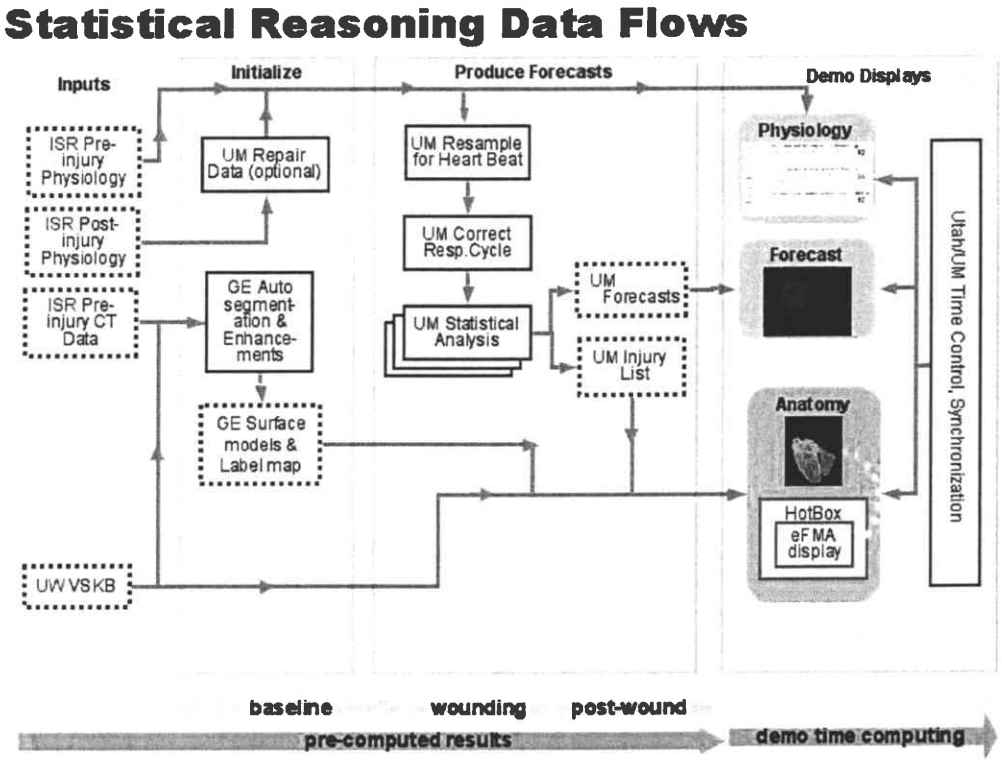

Figure 1: Statistical Reasoning data flow

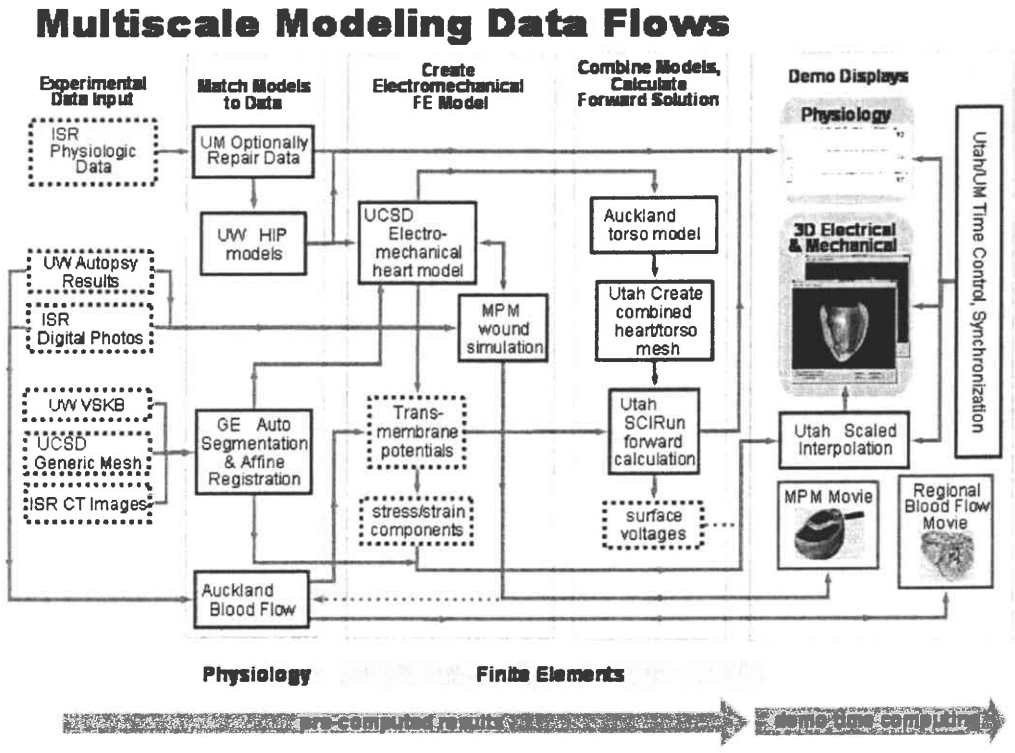

Figure 2: Multiscale Modeling data flow

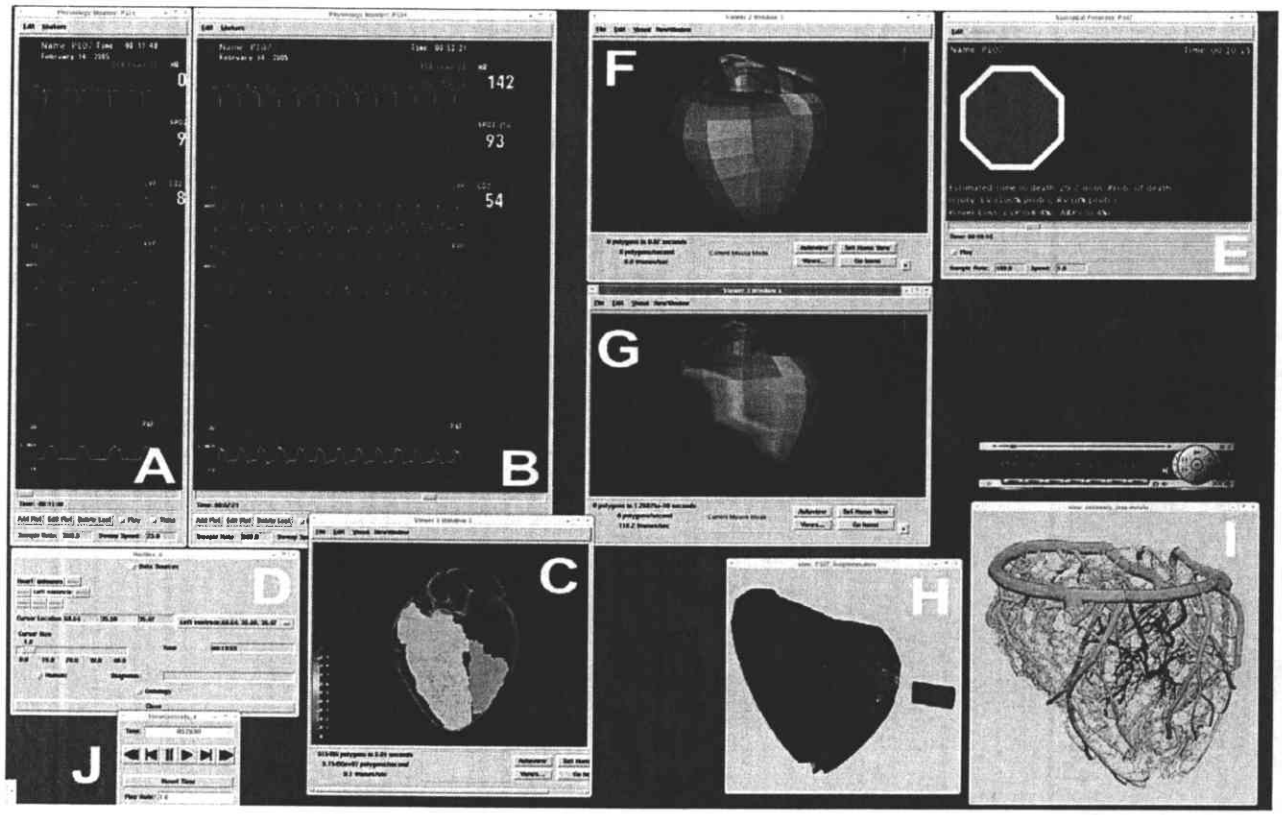

Figure 3: All-in-One Display

There are several displays in the All-in-One Demonstration (shown above):

A and B: Side-by-side physiology displays allowing comparison of different times
C: Anatomy display showing probability of LV or RV injury
D: Hotbox shows information from the VSKB and physiology data related to anatomical structures selected in the anatomy display (C).
E: Forecast display showing information on survival vs. death, time to death, and location of injury
F: 3D visualization of the mechanical Finite Element (FE) results
G: 3D visualization of the electrical Finite Element (FE) results
H: Material Point Method (MPM) movie
I: Regional coronary blood flow movie
J: Time Control

All of the displays, except for the movies (H and I), are synchronized with respect to time. All of the displays will display baseline and post-injury information. They can be played in real-time, faster than real-time, slower than real-time, paused, rewound, and fast forwarded to specific points in time.

Forecast Display

This display has two parts. At the top is the summary area that displays graphics and text to give a quick overview of the current forecast. At the bottom is a more detailed text summary of important forecasts and related information. Both parts are time dependent and are updated once per minute of wall clock time. The display can be set to run in real-time, faster than real-time, can be paused, or moved forward or backward in time to skip or review portions of the forecast.

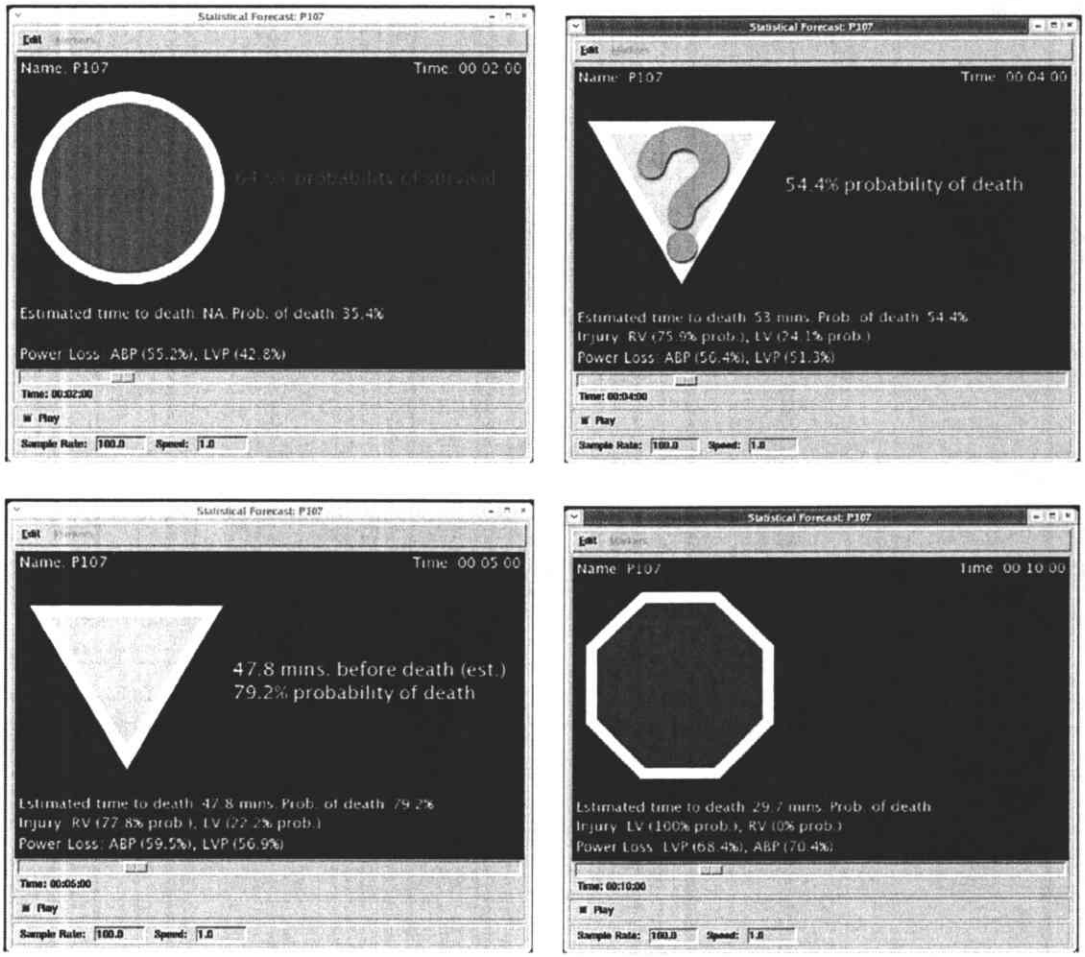

Figure 4: Forecast Display

The graphical portion of the display uses three icons with text to the right to summarize the current forecast:

- A green circle indicates that the subject is expected to survive.
- A red octagon indicates that the subject is expected to die within a relatively short period of time and there is no time for interventions to change the outcomes.

- A yellow triangle indicates that the subject is expected to die, but there is time to intervene to change the outcome.

- To the right of the icons text gives the percentage probability of survival or death and if death is the forecast an estimate of time to death in minutes.

The icons, text, and more detailed text summary are only displayed when there is sufficient data available to make a forecast. A survival vs. death forecast can be made before a time to death forecast. The display is controlled by three user settable thresholds (probability of survival, probability of death, and minimum time to death). A large question mark (?) is added in the center of the icons when the probability of death falls between the survival and death thresholds.

Physiology Display

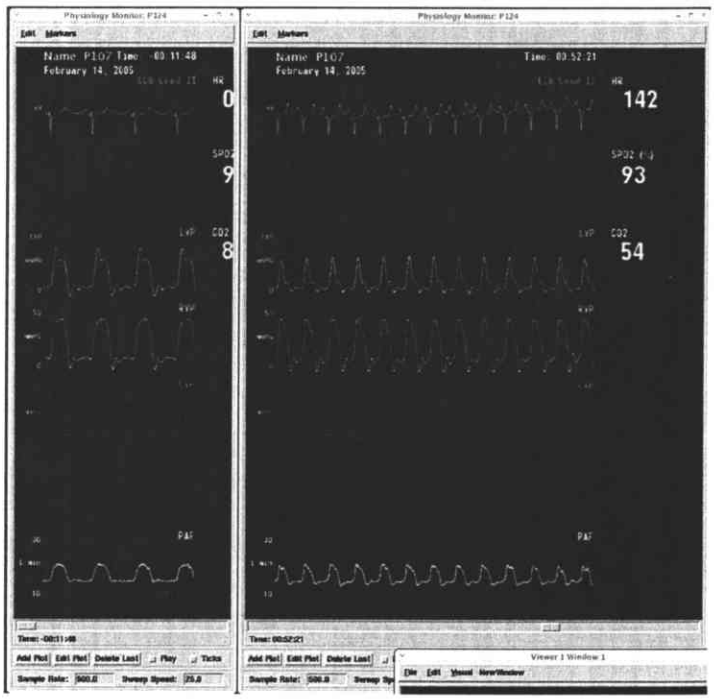

Figure 5: Physiology Display

This display resembles a monitor that one might see in a hospital room. It can display time dependent wave forms and individual values. The display can run at various rates, be paused, scrolled forward or backward or jumped to previously marked points of interest. Negative times are baseline while positive times are post-injury. Multiple displays can be run to allow comparisons of past and present data. As used during the demonstration the Physiology Display shows both experimental data from ISR and simulated data that is intermediate or final output from the HIP or FE models.

Anatomy Display and Hotbox

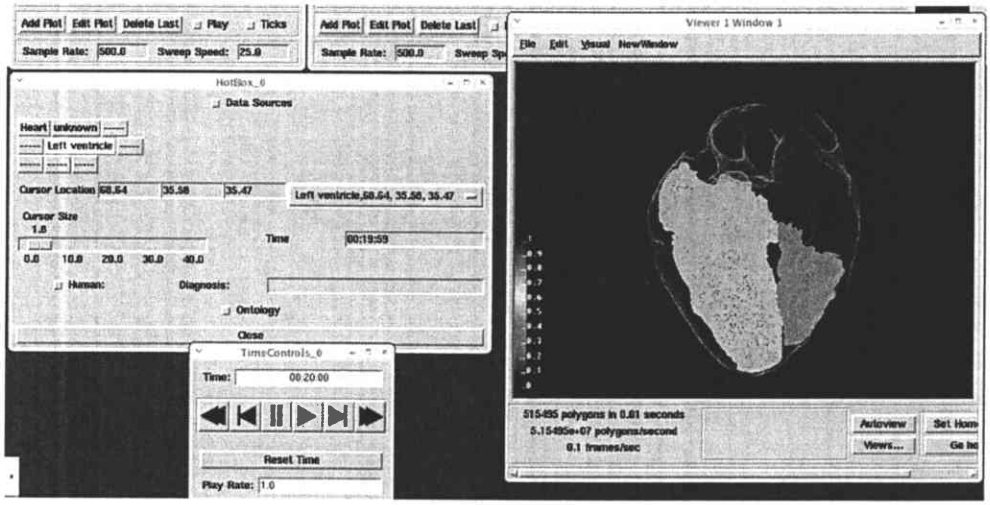

Figure 6: Hotbox (left) and Anatomy Display (right)

The Anatomy Display shows a 3D view that can be rotated, translated, and scaled to show the anatomical model that has been created from an individual's baseline CT scan. To this baseline image other post-injury information such as the wound track or an indication of specific injuries can be added based on either statistical or causal reasoning.

The HotBox is a user interface into the 3D anatomy and physiology of a specific individual (a porcine or a virtual human subject). It connects the visual anatomical model created from the CT to the Foundational Model of Anatomy, the wound's strain map, the injury list description of the wound, and the results of the high-level integrative physiological simulation. It works in combination with other SCIRun modules, the Physiology Display, and the 3D probe widget to display specific information selected by the medic, nurse, physician, or researcher.

Multiscale Modeling

Highly Integrated Physiology (HIP) Modeling

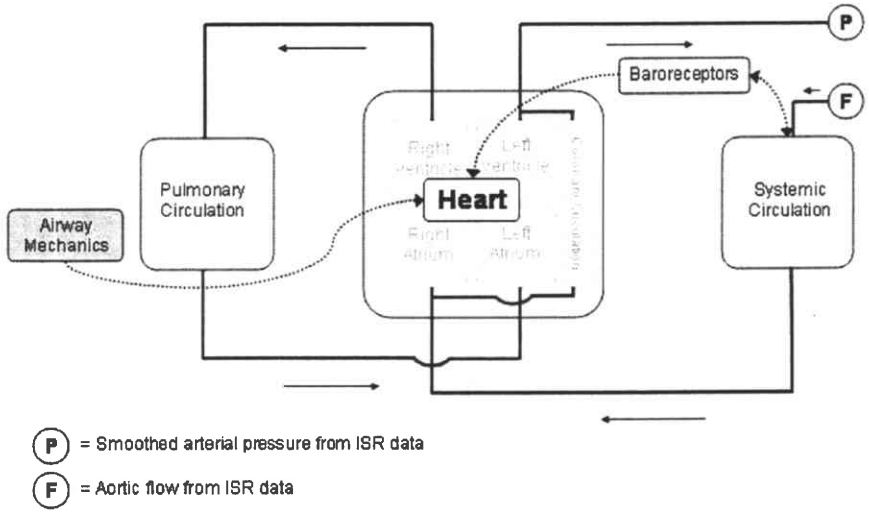

Figure 7: Highly Integrated Physiology (HIP) structure: open loop used for multiscale modeling

Outputs of HIP Model

- Pressures, volumes, forward flow and radial flow in:
  - Left atrium, Left ventricle, Proximal aorta, Distal aorta, Systemic arteries, Systemic arterioles, Systemic capillaries, Systemic veins, Vena cava, Right atrium, Right ventricle, Proximal pulmonary artery, Distal pulmonary artery, Small pulmonary arteries, Pulmonary capillaries, Pulmonary shunt, Pulmonary veins, Epicardial arteries, Coronary arteries, Coronary capillaries, and Coronary veins.
- Pressures, volumes, forward flow, and radial flow in:
  - Upper airways
  - Collapsible airways
  - Alveoli
- Heart and respiratory rates
- Heart chamber elastances
- Injury specifications
  - Blood lost from circulation
- ***Presently 150 variables, 40 ODEs***

3D Finite Element Model of Cardiac Electromechanics

- Geometry of porcine left and right ventricles scaled to match specific subjects acquired from porcine CT scans (ISR)
- Realistic myofiber architecture
- Nonlinear, anisotropic 3D passive and active material properties
- Local cellular properties based on detailed ionic-currents and realistic excitation-contraction coupling mechanisms
- Ventricular hemodynamics determined by highly integrated circulatory model initialized from and tuned to empirical data (ISR)
- Penetration wound modeled based on MPM results and coronary perfusion model (Auckland) by decoupling cells electrically, altering ionic currents and inhibiting active contraction around site of wound
- Reduction of contractility based on regional perfusion measurements (ISR)
- Real-time visualization done using a unique multi-mesh interpolation scheme triggered by the highly integrated circulatory model
- ECG simulated by solving the bioelectric forward solution in a 3-component model of the torso, heart, and lungs

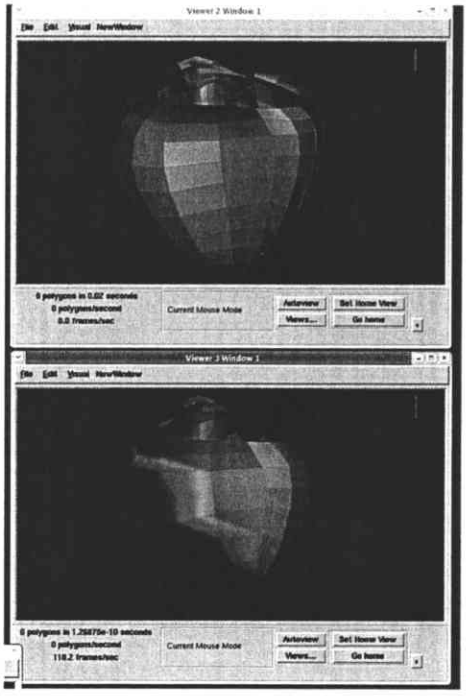

Figure 8: Mechanical (top) and electrical (bottom) Finite Element (FE) heart models

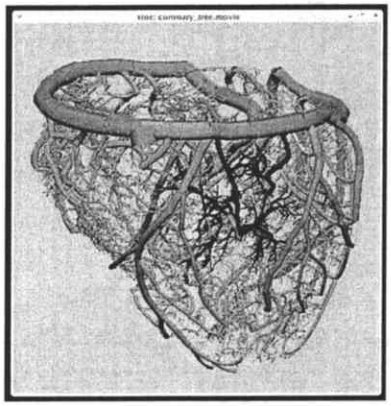

Figure 9: An animation of the results of the University of Auckland simulation showing changes in regional coronary blood flow at the time of injury

Material Point Method

- General particle-based multiphysics model
- Handles large deformations/tearing automatically
- Capable of modeling large scale **penetrating injuries** in arbitrarily complex geometries e.g. torso prototype
- Hi-fidelity/resolution tissue damage simulations
- Leverages 10yr DOE code investment
- Allows detailed validation of coarse-grain models
- Parallel computation of wound database possible

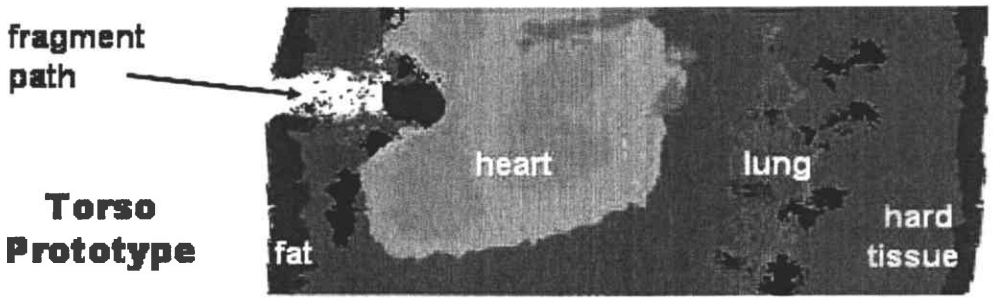

MPM Penetration Trauma of the Heart

- **Heart**
  - anatomically accurate porcine heart
  - discretized into ~1.5 mil material particles
  - modeled as a transversely isotropic hyperelastic material: an isotropic matrix reinforced by an elastic fiber family (fiber directions vary through the wall thickness)
  - a two-surface strain failure criteria is embedded in the model
- **Projected fragment (or shell casing)**
  - modeled to experiment specific geometry
  - elasto-plastic (metallic) material model
  - 76 ft/s initial speed
  - frictional contact enforced between tissue and probe

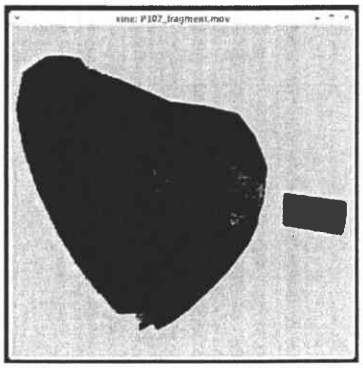

Figure 10: MPM movie showing a shell casing fragment injury

Anatomy from Anatomy Forecast and Comparison to Autopsy Findings

- Analyze postmortem image data, including:
  - porcine CT images from ISR,
  - postmortem isolated heart CT images from ISR,
  - manual segmentation by UW,
  - smoothed, segmented, and labeled anatomy from GE,
  - the Virtual Soldier Knowledge Base (VSKB) from UW, and
  - autopsy reports from UW
- Determine which anatomical structures are injured
- Display information for use by the medic/physician
- Compare forecast and autopsy results

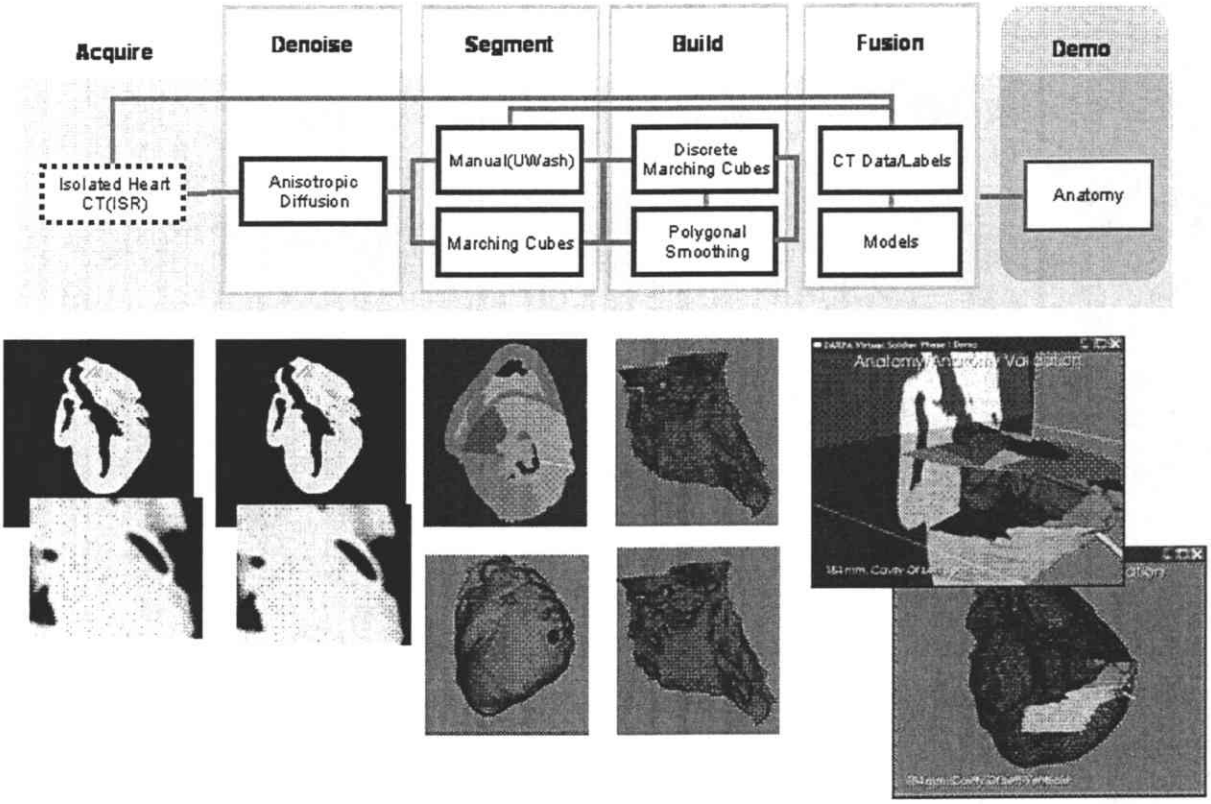

Figure 11: Anatomy from anatomy data flow diagram

Goals Demonstrated

- ✓ Diagnose heart wounds w/ accuracy >= 80%
- ✓ Predict likelihood of battlefield mortality, 93%
- ✓ Forecast time to death, 85%
- ✓ Estimate injury location, 83%
- ✓ Examine the utility of variables other than LVP and RVP including multivariate approaches
- ✓ Compare baseline data to post-injury data
- ✓ Make anatomy from anatomy forecast and compare to autopsy results
- ✓ Demonstrate organ and system level integration
- ✓ Extend and use global architecture
- ✓ Develop and use automatic segmentation
- ✓ Display results in visualizations simultaneously and synchronized with respect to time

Causal Reasoning Video

Main Aims:

1. One **Holomer instance** can represent and forecast the pathophysiological response of a specific soldier to a specific wound.
2. However, **multiple Holomer instances** are required to accommodate uncertainties of baseline conditions, damage assessment and pathological response as well as possible interventions.
3. **Multiple Holomer instances** can be automatically generated using deductive reasoning on symbolic representations of anatomy, physiology and pathology.

One premise of the Virtual Soldier Project:
Given battlefield circumstances and competition for scarce resources, a medic must make triage decisions based on outcome forecasts that depend on:

- Accuracy of damage assessment
  - Field-deployable scanner
- Medic's training and experience
  - Holomer forecasts from a hand-held device

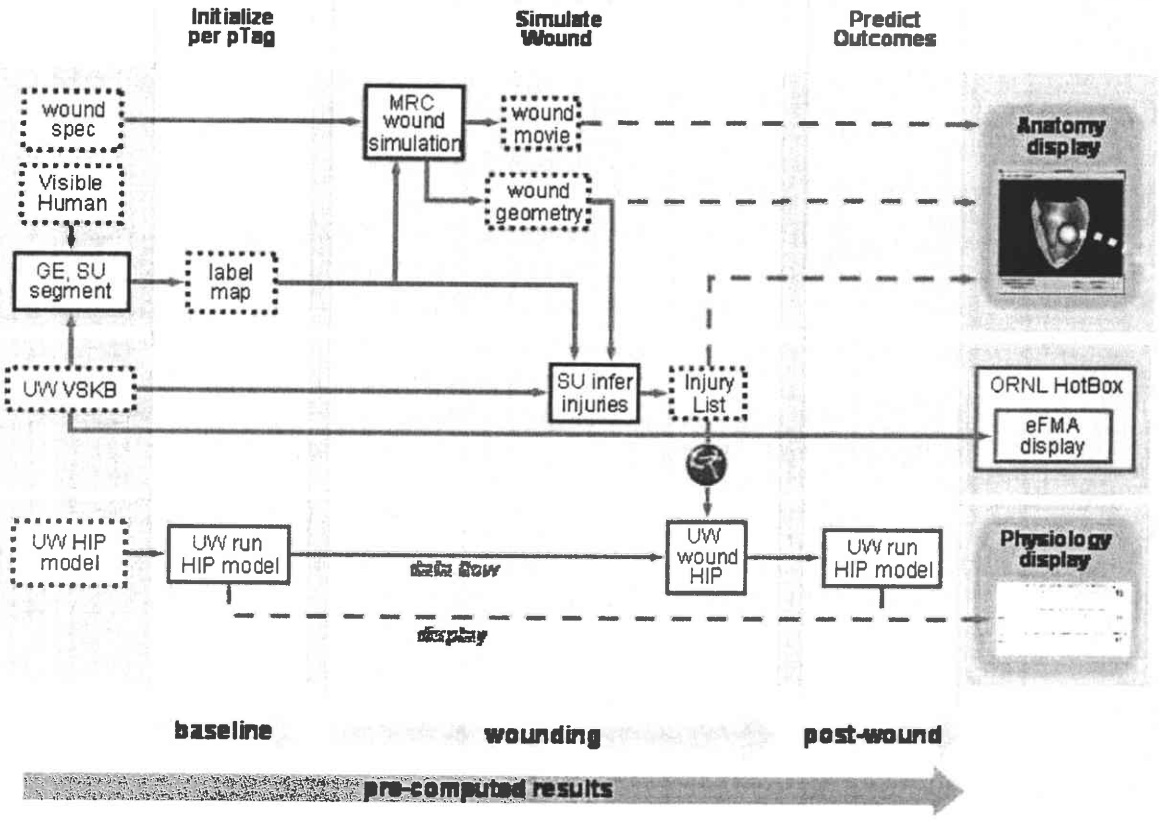

Figure 12: Causal Modeling data flow

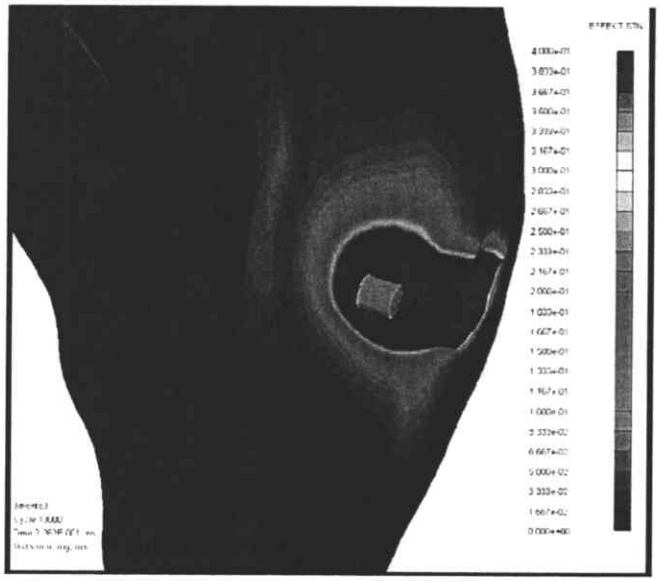

Movie Showing the results of the ATK-Mission Research ballistic simulation which is used together with baseline anatomy information to drive the rest of the Causal Modeling steps.

Figure 13: ATK-MRC ballistic model of LV wound

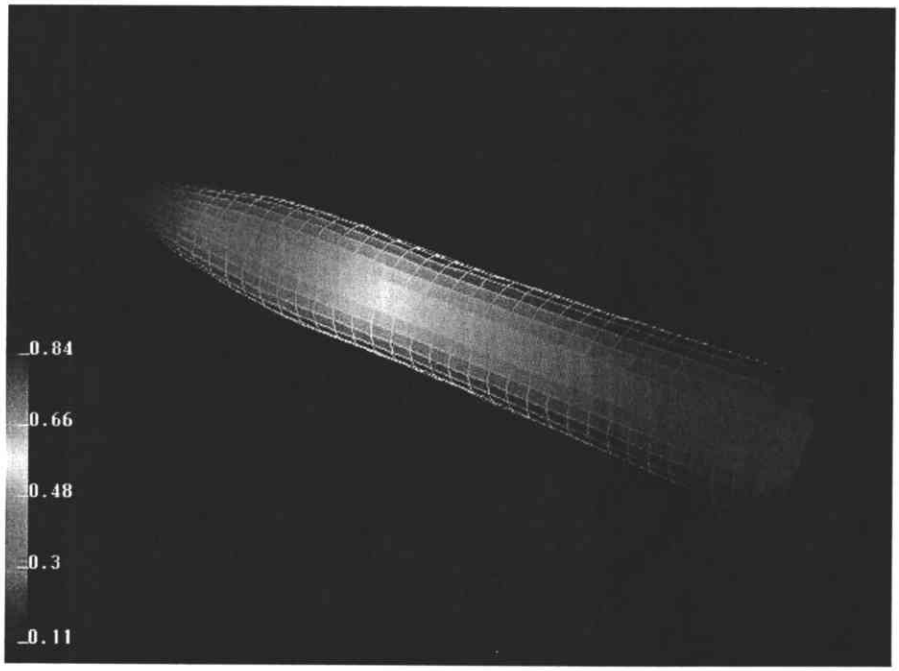

Figure 14: ATK-MRC circumferential strain model of wound track

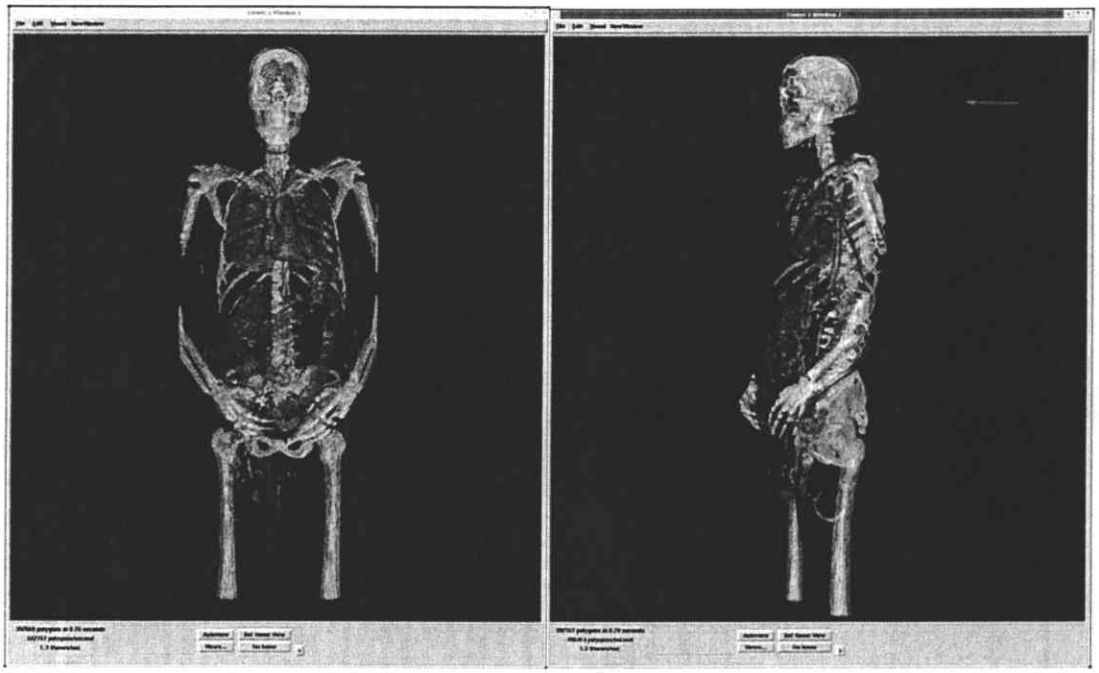

Figure 15: SCIRun anatomy display showing Visible Human anatomy as segmented by GE

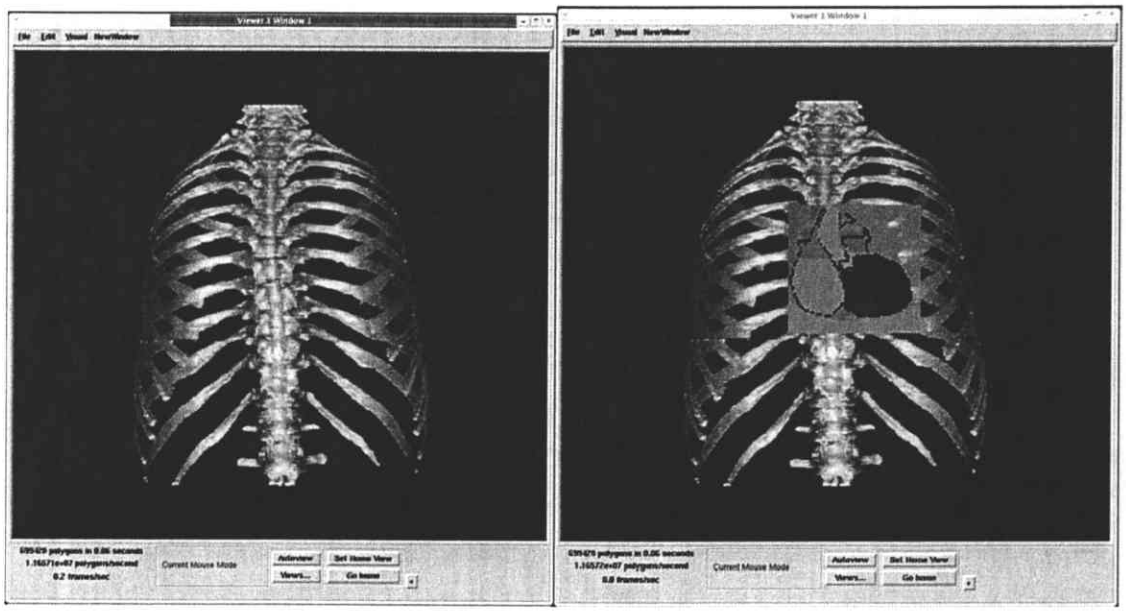

Figure 16: SCIRun Anatomy display (left) and SCIRun Anatomy display with heart section added (right)

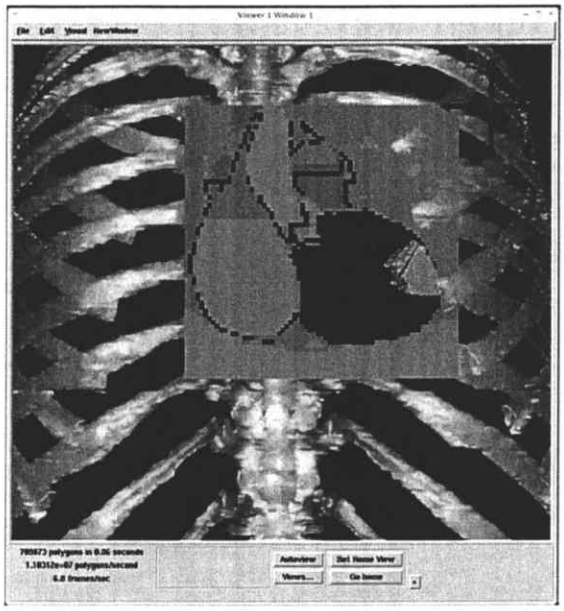

Figure 17: SCIRun anatomy display zoomed in with myocardial zone 12 highlighted to show a slice through the heart

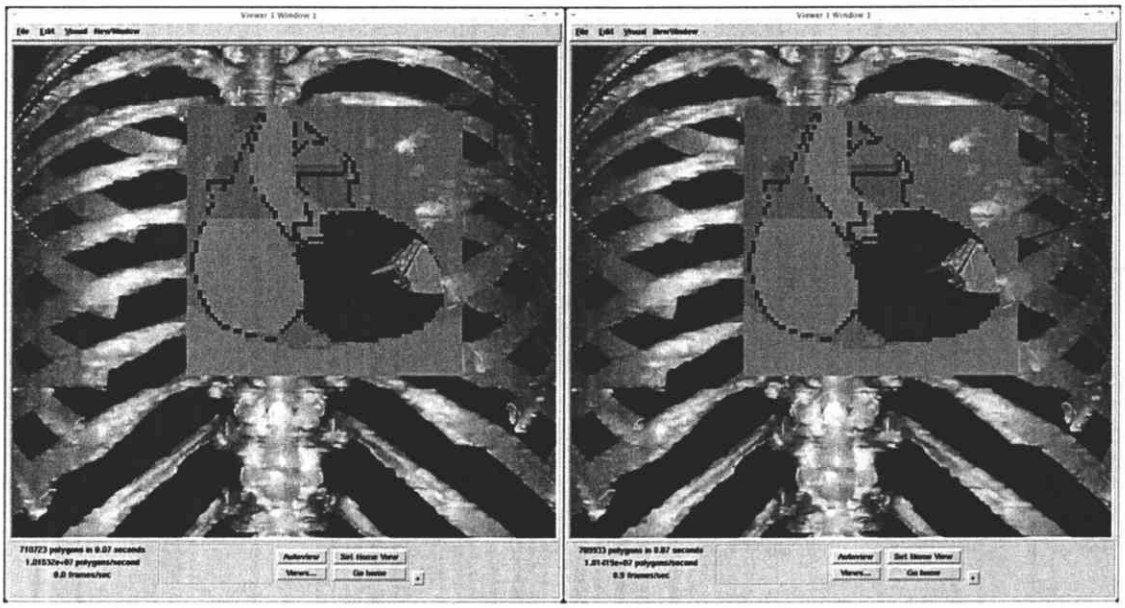

Figure 18: SCIRun anatomy display showing ATK-MRC wound track (left) and with primary injury displayed (right)

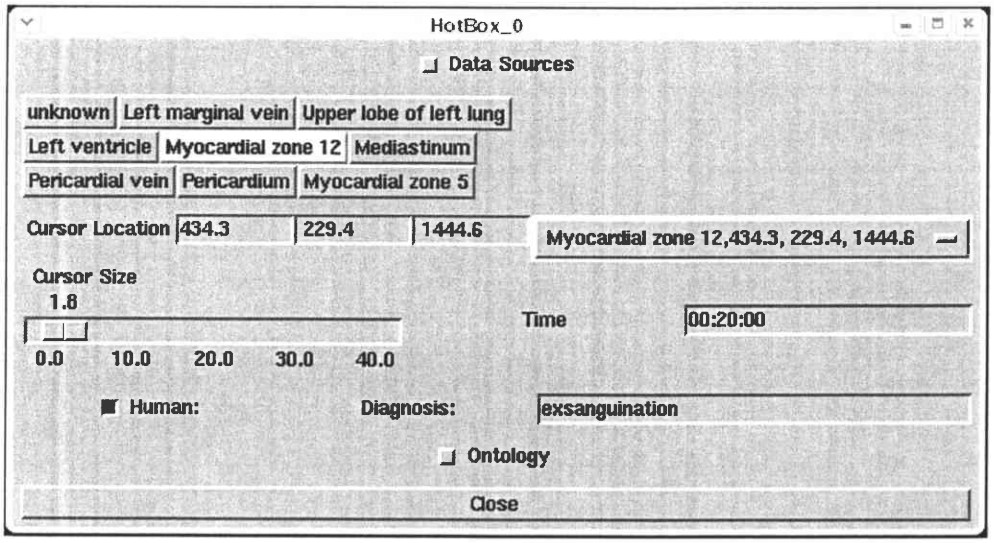

Figure 19: Hotbox showing information for the selected anatomic structure in the anatomy display (myocardial zone 12)

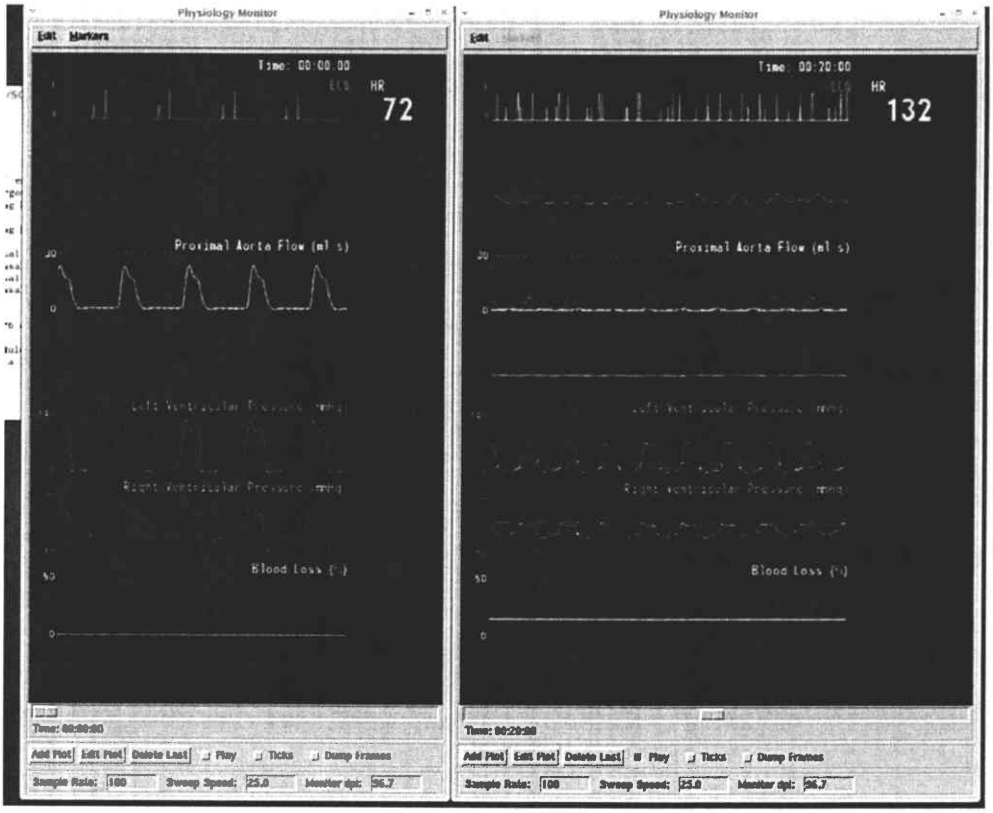

Figure 20: Physiology Monitor

Side-by-side displays allow comparison of baseline (left) and post-injury (right) information. Two traces for a single item show the results for exsanguination (gray) and tamponade (colored)

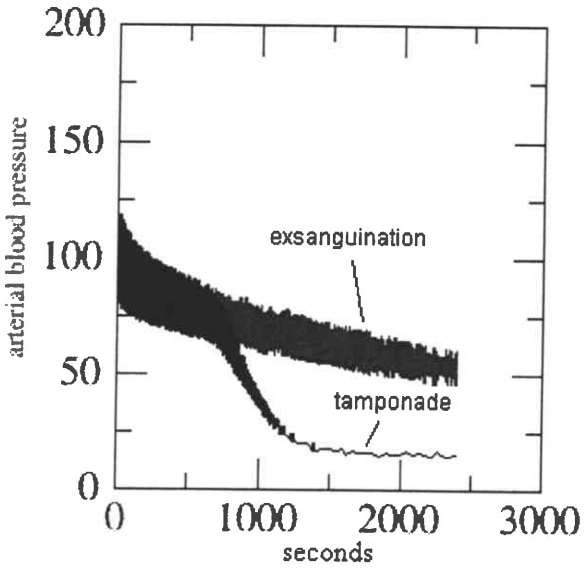

Figure 21: HIP model results showing LV penetration with and without tamponade

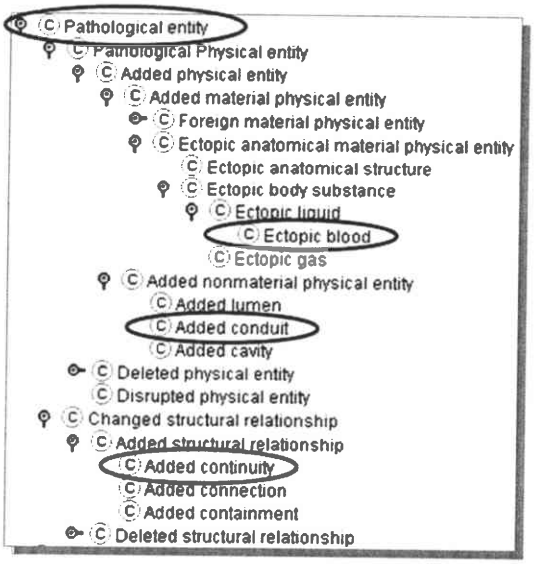

Figure 22: Excerpt from Pathology Reference Ontology

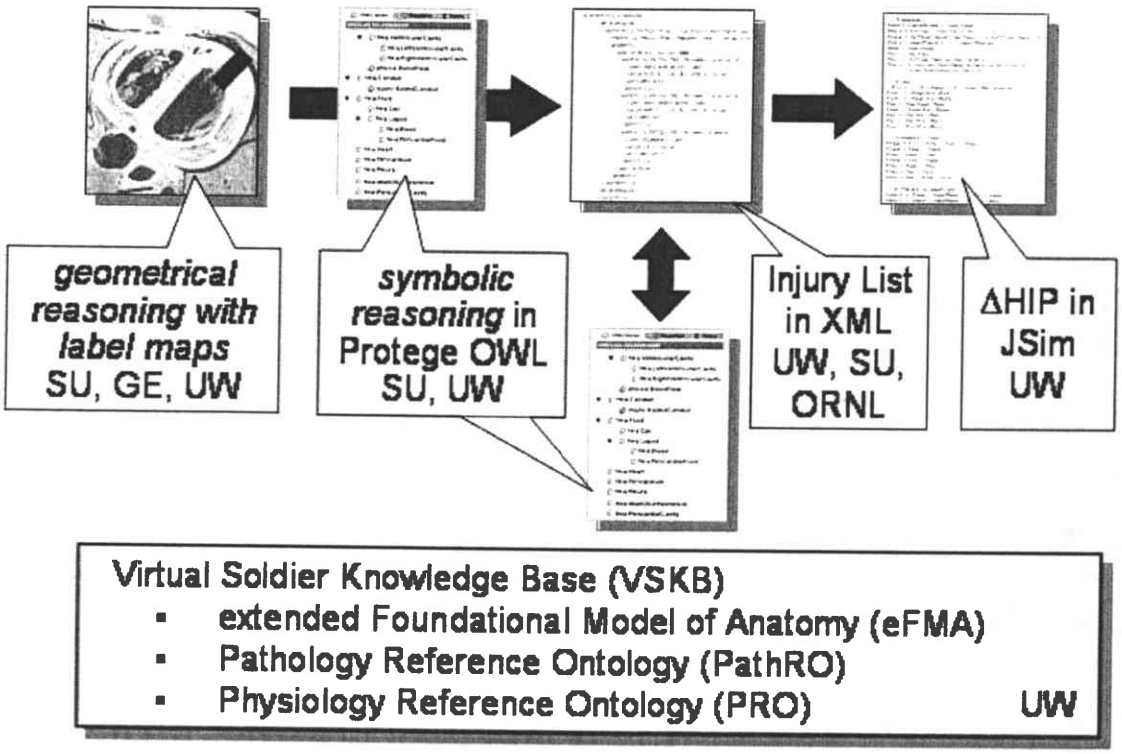

Figure 23: Generating multiple holomer models

Causal Reasoning Goals Demonstrated

- ✓ Diagnose heart wounds
- ✓ Compare baseline data to post-injury data
- ✓ Predict outcomes
- ✓ Demonstrate organ and system level integration
- ✓ Extend and use global architecture
- ✓ Develop and use automatic segmentation
- ✓ Develop and use Holomer display and interface

Appendix

Virtual Soldier Project Team Members

Academic and Not-for-Profit

University of Michigan (Prime Contractor)
Case Western Reserve University
Federation of American Scientists
Stanford University Medical School
University of California San Diego
    Subcontractor: University of Auckland
University of Utah, Scientific Computing and Imaging Institute
University of Washington, Bioengineering
University of Washington, Structural Informatics Group

Government

Defense Advanced Research Projects Agency
U.S. Army Telemedicine and Advanced Technology Research Center
U.S. Army Institute for Surgical Research
Oak Ridge National Laboratory
    Subcontractor: University of South Carolina

Corporate

ATK- Mission Research Corporation
Crowley Davis Research
    Gerry Higgins, Ph.D. (consultant)
    Howard Champion, M.D. (consultant)
    Lou D'Alecy, M.D., Ph.D (consultant)
General Electric Research
    Subcontractor: Brigham and Women's Hospital, Harvard University
Xtria

Use of Experimental Data

The following table summarizes the uses being made of the experimental data by different Phase I components

Portion of Demo	Image/CT Data	Physiology Data
Statistical Reasoning	Porcine	Porcine
Causal Reasoning	Visible Human	Simulated data only
Multiscale Modeling and Simulation	Porcine	Porcine
P-Tag, CODEC, Holomer Display	Porcine and Visible Human	Porcine and Simulated Human
Autostereoscopic / Holographic Display	Porcine and Human	None

Summary of ISR Experiments

Through April 28, 2005 a total of seventy seven (77) porcine animal experiments have been conducted at the U.S. Army's Institute for Surgical Research in San Antonio, Texas. Model development ended on November 12, 2004. The first experiment was conducted on November 30, 2004.

	Open Chest				Closed Chest				
	Frag		Probe		Frag		Probe		
Outcome	**LV**	**RV**	**LV**	**RV**	**LV**	**RV**	**LV**	**RV**	**Total**
TTD 11 to 120 mins.	8	-	2	1	-	-	-	-	11
TTD >120 mins. (survivor)	6	-	4	3	1	-	-	2	16
Analyzable sub-total	14	-	6	4	1	-	-	2	27
Quarantined	2		-	-	-	-	-	-	2
Death before injury	2				-	-	-	-	2
Short TTD (1 to 10 mins)	6	3	-	2	-	-	-	-	11
Incomplete data	3	-	-	-	-	-	-	1	4
Unanalyzable sub-total	16				1				17
Model development									31
Grand Total									77

Death is defined as a sustained MAP of 20 mmHg or less. Survival is defined as a time to death of more than 120 minutes. An "analyzable" experiment is an experiment with a time to death more than 10 mins. post injury and relatively complete data collection.

All deaths have been due to hemorrhage. No deaths due to ventricular fibrillation were observed due to the side effects of the drugs used during the experiment and the location of wounds. Death due to tamponade is not possible since during the open chest procedures much of the pericardium is removed before injury.

There are three analyzable closed chest experiments, but none of the three resulted in a particularly severe injury. A decision was made following the March 17th demonstration not to do additional closed chest experiments during Phase I.

Model Development, Training, and Test Sets

Sets of experimental data are often divided into model development, training, and test sets for statistical analysis. Dividing the Virtual Soldier Project's experimental data in this fashion is not always possible or appropriate. The alternative approaches used are described here.

The 31 model development experiments that ISR conducted before November 30th constitute the "model development" set that were used to develop and refine procedures and gain familiarity with the data.

The 46 experiments that ISR conducted between November 30, 2004 and April 28, 2005 were divided into three groups as follows:

25 analyzable open chest experiments (regular ECG and full instrumentation);
3 analyzable closed chest experiments (60+ lead ECG and limited instrumentation); and
18 experiments that were not analyzable according to criteria established in advance (incomplete or missing data, time to death of 10 minutes or less).

Data from the closed chest experiments is being used in a limited way by the University of Utah to help validate their cardiac electrical models, but is not being used for other aspects of the demonstrations or the statistical analysis report.

For the June 14th demonstration Dr. Satava that only data from the experiments conducted using fragments and no data from any of the experiments conducted using probes was to be used. Omitting the probe experiments leaves one quarantined and 14 other analyzable open chest fragment experiments.

For the June 14th demonstration one can think of the quarantined experiment as the "test set" and the 14 other experiments as the "training set".

For the separate *Report of Statistical Findings* the 14 available analyzable experiments are too few to be split into statistically meaningful "training" and "test" sets. Instead, we are using the technique of leave-out-one crossvalidation, a well-known, well-accepted alternative to separate "training" and "test sets" when data are scarce. One can view this technique as 14 crossvalidations where each experiment is treated as the "test subject" in

turn and the remaining 13 subjects become the "training set". In a sense this gives a "test set" of 14 and a "training set" of 182, but because each crossvalidation is done independently the required separation of "test" and "training" sets is maintained.

Even without the leave-out-one crossvalidation, the statistical results as represented in a standard scatterplot smoothing (see the last figure in section 6 of the Statistical Findings Report) for the dependence of time to death against its principal predictor (amplitude of ABP) along with an adjustment for the observance of the "alarm" are so strong that they are both powerful and suggestive without additional validation.

The discussion to this point applies to the statistical work done to detect "alarms", and to make survival or death and time to death forecasts. Because the fragment only "training set" includes no RV injuries, the forecasts of the location of the injury (LV vs. RV) is being done using the same criteria that were used for the March 17th demonstration. That approach used all of the analyzable experiments for which experimental data from ISR had been received on or before January 31, 2005 and includes both fragment and probe experiments. Due to the lack of analyzable data from RV fragment experiments, there was no choice but to use data from the probe experiments to make a statistical forecast of anatomy (injury location) from physiology.

The anatomy from anatomy forecasts for the June 14th demonstration are based on the CT images from fragment experiments and do not use data from probe experiments.

The approaches outlined above are entirely compatible with the standards of biological experimentation. There has been no "cherry picking" of the data.

Data Collected at ISR

The porcine animal experiments are performed according to DoD Animal Use Protocol number A-04-004: *Virtual Soldier Porcine Heart Injury Physiology Model* which was originally approved in May, 2004 and amended in September 2004, October 2004, and March 2005.

The following data items are collected for just the open chest experiments:

1. Aortic Flow in l/min @ 500 Hz
2. Pulmonary Artery Flow in l/min @ 500 Hz
3. Time Step Coronary Perfusion Studies @ baseline, 5 and 30 mins. post-injury (4 experiments)
4. Blood Volume @ baseline, 5 and 30 mins. post-injury (4 experiments)

The following data items are collected for just the closed chest experiments:

1. ECG 60+ leads @ 1000 Hz using equipment loaned to ISR by Utah
2. Cardiac Gated CT Scan pre-injury, post-instrumentation, 0.5mm slices, w/ contrast, reconstructions at systole and diastole, zoomed and unzoomed

The following data items are collected for both open and closed chest experiments:

1. Body Weight in kg @ start of experiment
2. Sex (always Female)
3. Times of Baseline CT Scan, Hemodynamic Data Collection Start, Injury, Blood Sample Collection, Death
4. Cardiac Gated CT Scan pre-injury, pre-instrumentation, 0.5mm slices, w/ contrast, reconstructions at systole and diastole, zoomed and unzoomed
5. Heart Rate (bpm) 5 sec.
6. Body temp. in deg. C @ 5 sec.
7. RV Pressure in mmHG @ 500 Hz
8. LV Pressure in mmHG @ 500 Hz
9. Central Venous Pressure in mmHG @ 500 Hz
10. Arterial Blood Pressure in mmHG @ 500 Hz
11. Pulse Oximetry (SPO2) in % @ 500 Hz
12. Plethysmograph (Pleth) @ 500 Hz (some experiments)
13. Respiratory Cycle @ 500 Hz (some experiments starting January 31, 2005)
14. Ventilator Settings including tidal volume (ml), breaths per min. @ 15 mins.
15. Respiratory CO2 in mmHg @ 500 Hz (not synchronized with other 500 Hz data)
16. ECG one lead @ 500 Hz
17. CT Scan postmortem isolated heart 0.5mm slices, w/o contrast (some experiments)
18. CT Scan postmortem in situ 0.5mm slices, w/o contrast (some experiments)
19. Blood Collection standard laboratory analysis @ baseline, 5, 15, 30, 60, 90, and 120 mins., or at death
20. Blood loss estimated by weight @ end of experiment
21. Description of injury (size, location, angle), cause of death, time to death
22. Digital photos of isolated heart w/ marker pins inserted @ end of experiment
23. Heart autopsy (conducted at University of Washington for some experiments)

Blood Collection Laboratory Analysis

Samples collected at baseline, 5, 15, 30, 60, 90, 120 mins. or at death.

Name	Abbreviation	Units
CBC		
White Blood Cell Count	WBC	10 3/mm^3
Red Blood Cell Count	RBC	
Hemoglobin	HGB	g/dl

Name	Abbreviation	Units
Hematocrit	HCT	%
Mean Corpuscular Volume	MCV	um^3
Mean Corpuscular Hemoglobin	MCH	pg
Mean Corpuscular Hemoglobin Concentration	MCHC	g/dl
Platelet	PLT	10 $3/mm^3$
Lymphocytes	LYM	%
Monocytes	MON	%
Neutrophils	NEU	%
Eosinophils	EOS	%
Basophils	BAS	%
Coagulation		
Prothrombin Time	PT	sec.
Activated Partial Thromboplastin Time	aPTT	sec.
Fibrinogen	FIB	mg/dl
Chemistry		
Urea Nitrogen		mg/dL
Creatine		mg/dL
Total Protein		g/dL
Albumin		dg/dL
Blood Gases		
Temperature At Time of Sample Collection	Temp	deg. C
Hydrogen Ion Activity	pH	
Partial Pressure of Carbon Dioxide	PCO2	mmHg
Partial Pressure of Oxygen	PO2	mmHg
pH Temperature Corrected	pHt	
PCO2 Temperature Corrected	PCO2t	mmHg
PO2 Temperature Corrected	PO2t	mmHg
Hematocrit	HCT	%
Total Hemoglobin Concentration	ctHb	g/dl
Oxyhemoglobin	O2Hb	%
Carboxyhemoglobin	COHb	%
Methemoglobin	MetHb	%
Sulfhemoglobin	SulfHb	%
Deoxyhemoglobin	HHb	%
Oxygen Concentration	ctO2	vol %
Oxygen Capacity	BO2	vol %
Functional Oxygen Saturation	SO2	%
Sodium	Na	mmol/l
Potassium	K	mmol/l
Chloride	Cl	mmol/l
Glucose	Glu	mmol/l
Lactate	Lac	mmol/l
Bicarbonate Concentration	cHCO3	mmol/l
Total Co2 Concentration in Blood	ctCO2(B)	mmol/l

Name	Abbreviation	Units
Base Excess in Blood	BE	mmol/l
Base Excess In Vivo	BEecf	mmol/l
Standard Bicarbonate	cHCO3st	mmol/l
Functional Oxygen Saturation	SO2	%
Half Saturation Tension of Oxygen in Partial Pressure of Oxygen	P50	mmHg

Preliminary Injury Device Characterization

GLB, Inc. in cooperation with ATK-MRC performed a preliminary characterization of the Modified Nail Gun (MNG) being used at ISR. A more complete characterization of the wounding device to be carried out by ISR was not funded.

GLB determined that the MNG probe travels at a velocity of between 76 and 92 feet per second (+-7%) and they estimate that a fragment would be released at a velocity of approximately 100 feet per second. See the table below. The device characterization may be too preliminary to draw firm conclusions, but it is possible that the ISR MNG delivers a fragment with a velocity and energy that is similar to .32 and .60 caliber projectiles.

Table 4 from *Physics of Penetrating Trauma*: *Examples of Missile Kinetic Energies on Different Tissues*, updated to include data on ISR MNG

Projectile	Mass (gm)	Velocity (ft/sec)	Impact Energy (Joules)	Tissue	Size of Temporary Cavity	Result
7.62 mm shell casing fragment	**5.0**	**~100**	**--**	**Heart**	**N/A**	**Varies by location of wound**
9 mm shell casing fragment	**3.075**	**~100**	**--**	**Heart**	**N/A**	**Varies by location of wound**
ATK-MRC 7 mm fragment	**4.1**	**~100**	**--**	**Heart**	**N/A**	**Varies by location of wound**
.32 caliber	0.27	87.4	1.0	Heart	None, only permanent cavity	Survived
.60 caliber	2.27	100.7	11.5	Liver	63.5 mm	Survived
40 mm Multi Pellet fragment	14	105.2	77.6	Heart	27mm	Cardiac avulsion - death
.25 Remington Rimfire	42	1180	154	Heart	N/A	Cardiac death

Projectile	Mass (gm)	Velocity (ft/sec)	Impact Energy (Joules)	Tissue	Size of Temporary Cavity	Result
12 gage shot bag	40.8	87.9	157.6	Heart	N/A	Ventricular avulsion - death
M16	3.6	3094	1416	Toe	2 mm	Minor wound repair
44 magnum	125	2340	1660	Heart	Not measurable as in solid tissue	Death
3006 Rifle	150	3779	2820	Heart	N/A	"Exploded thorax"
405 Winchester	75	3500	4489	Heart	N/A	Cardiac avulsion - death

References for the preceding table:

1. *Ballistic Trauma* (1997). (Eds. J.M. Ryan, N.M. Rich, R.F. Dale, B.T. Morgans and G.J. Cooper) Arnold Publishing, London.

2. *Textbook of Military Medicine, Part I, Warfare, Weaponry, and the Casualty, Volume 5 - Conventional Warfare: Ballistic, Blast and Burn Injuries*. (1990, *new update draft – 2004*) (R. Zajtchuk, D.P. Jenkins, R.F. Bellamy and M. Quick) Published by the Office of the Surgeon General, Department of the Army, United States of America.

3. Lyon, D.H., C.A. Bir and D. DuBay (1998) *Injury Evaluation Techniques for Non-Lethal, Kinetic Energy Munitions*. NTIS AQI98-11-2308.

4. Memo GBL-04-081 dated December 2, 2004 reporting qualified results of preliminary characterization of ISR MNG.

5. E-mail from Bob Eisler, ATK-MRC dated December 3, 2004, subject: *Quick and Dirty Checkout tests on ISR MNG*.

6. E-mail from Cpt. Eric Ansorge, USAISR dated January 7, 2005, subject: *fragment weights*.

7. E-mail from LTC James Fudge, USAISR dated April 20, 2005, subject: *fragment weight*.

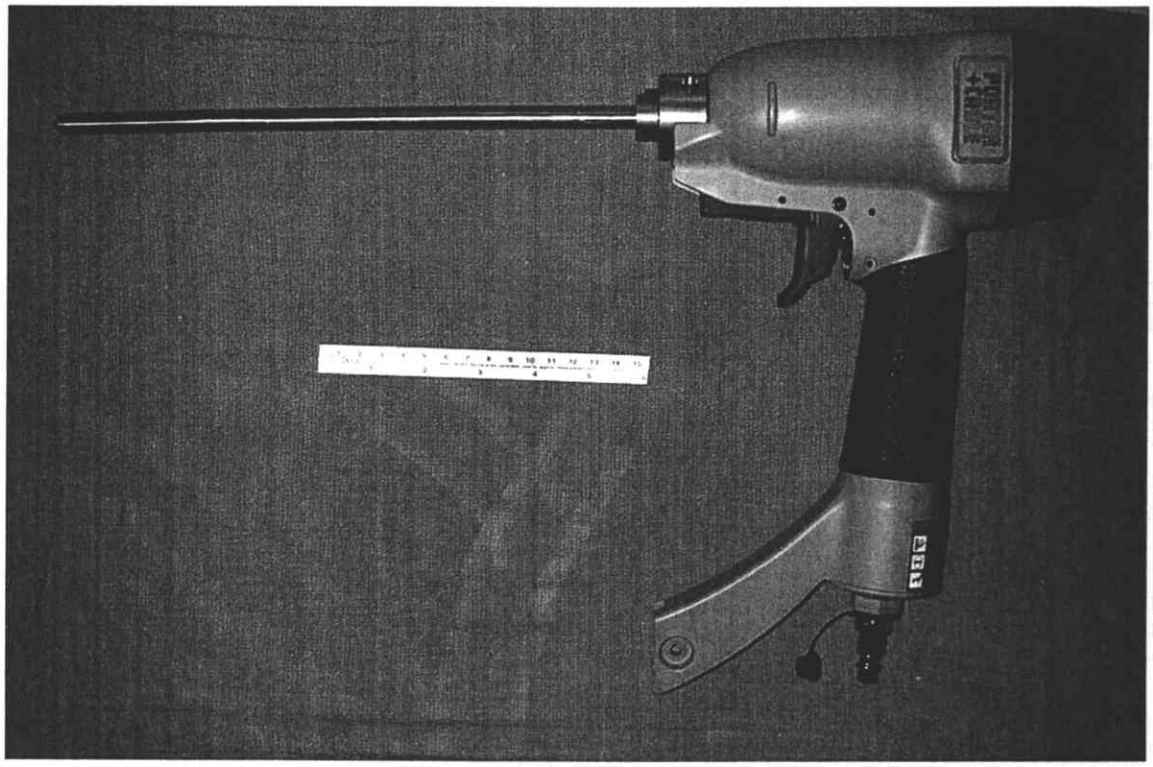

Figure 24: Modified Nail Gun with tip attached

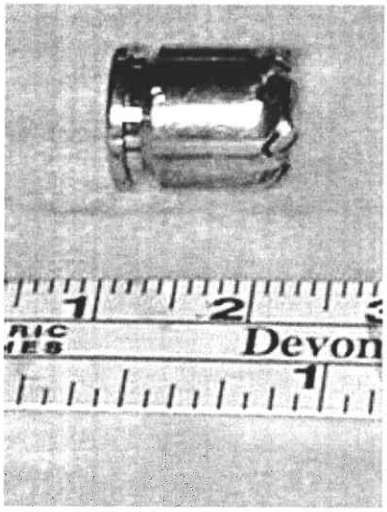

Figure 25: 9mm ISR shell casing fragment

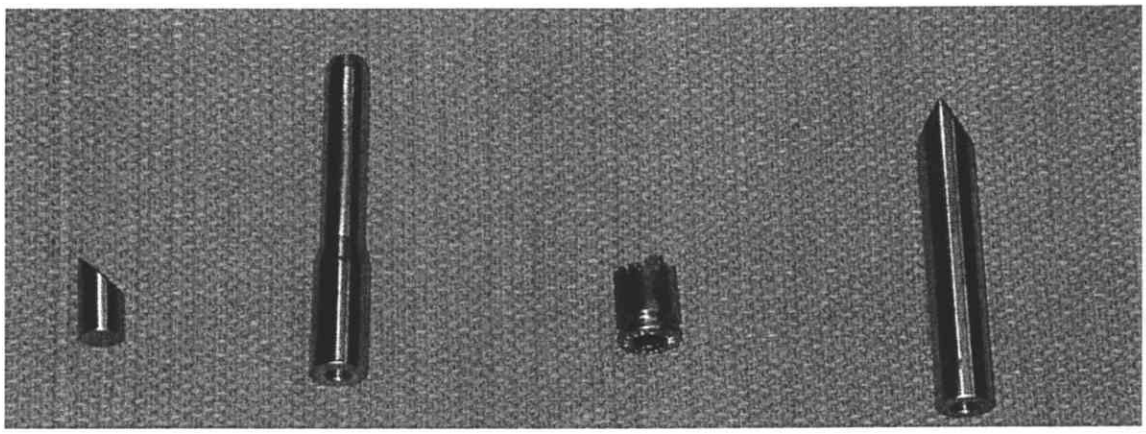

Figure 26: 7mm MRC fragment, 7mm blunt probe, 7.62mm ISR shell casing fragment, 10mm pointed probe

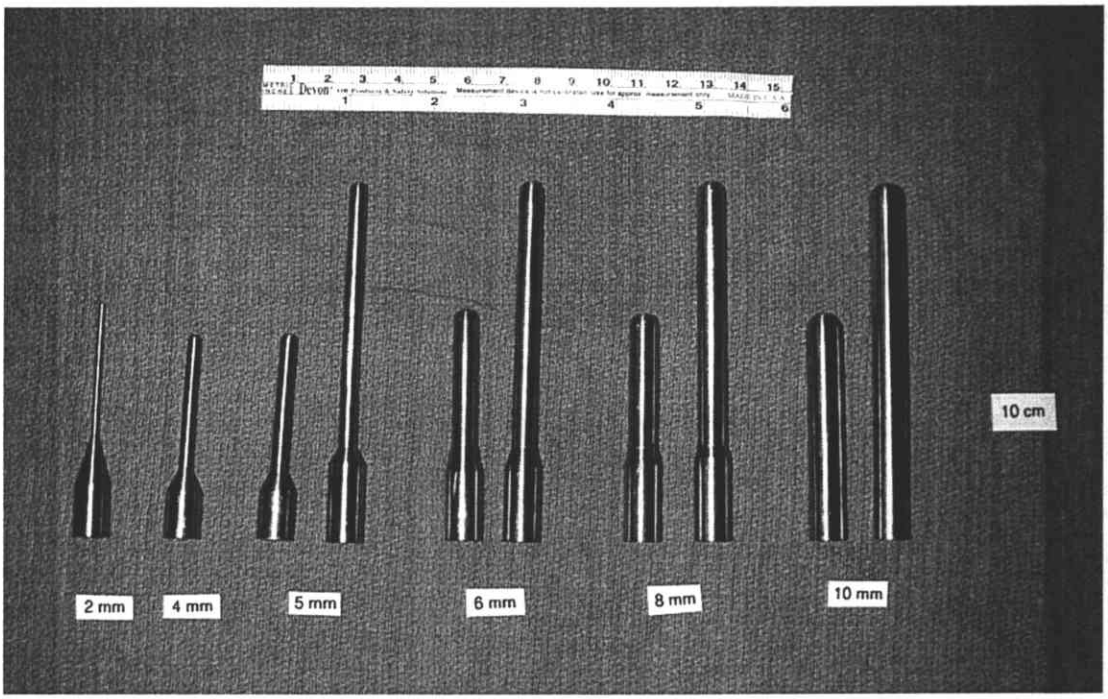

Figure 27: Blunt probes, long and short

Summary of Statistical Results

The table below shows the results for each of the 14 non-quarantined "analyzable" open chest fragment experiments conducted prior to the June 14th demonstration.

An analyzable experiment is one with a time to death longer than 10 minutes and relatively complete data collection. Death is defined as a sustained Mean Arterial Pressure (MAP) of 20 mmHg or less. Survival is defined as a time to death greater than 120 minutes.

For this class of animals we are able to:

- detect an alarm in all 8 non-survivors and no alarm in all 6 survivors (100%)
- correctly forecast death or survival for 13 of 14 (93%) at 4 minutes post injury
- forecast a time to death correlating 0.75 with actual time to death for the 7 non-survivors still alive at 20 minutes post-injury
- forecast a time to death of 21 minutes ±9 minutes at 20 minutes before actual death for the 6 non-survivors that lived for more than 25 minutes
- forecast a median time to death of 30 minutes
- from first alarm for all 8 non-survivors vs. the actual median time to death of 24 minutes

And within a test subset of 6 non-quarantined analyzable open chest fragment experiments we are able to:

- correctly identify injury location (LV vs. RV) for 5 cases with one ambiguous result (83%)

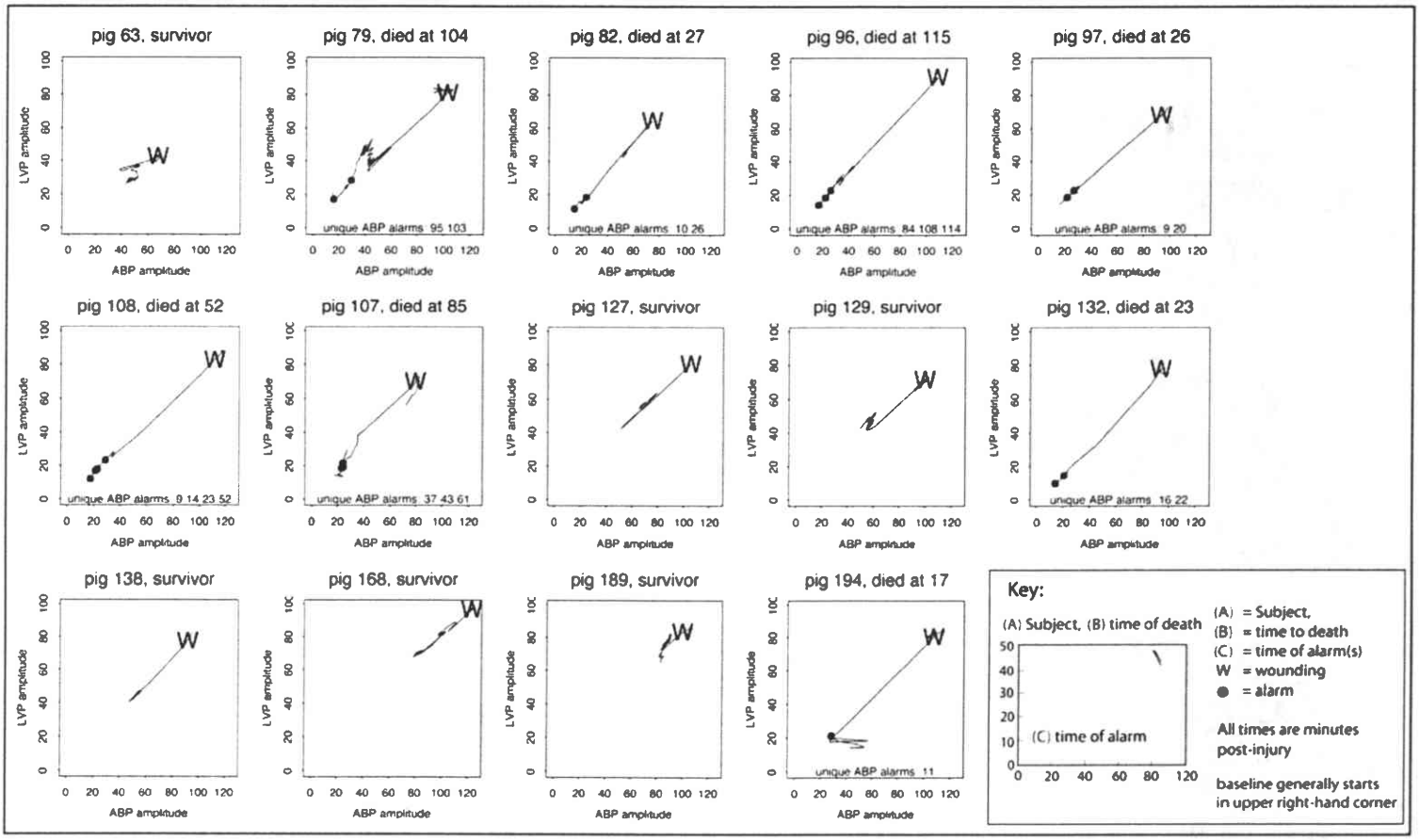

Figure 28: Decision Space Plots

Virtual Soldier Project Phase I: Summary of experimental data collected 30 November 2004 through 28 April 2005

Status: Quarantined (Q), Analyzable (A), Incomplete data (I), Short time to death (S), Died before injury (D)
Fragment or probe type: Fragments Shell Casing (FS), MRC (FM); Probes Regular Blunt (PR), Beveled (PB), Pointed (PP)
Experiment Type: Open Chest (O), Closed Chest (C); Location: RV or LV; **Cause of Death:** Hemorrhage (H), Euthanized (E)

Status	Date of Experiment	Data Received	Tag No.	Expt. Type	Frag. or probe type	Loc.	Size	Time of Death (mins)	Cause of Death	Forecast @ 10 mins. post-injury	Forecast @ 20 mins. post-injury	Forecast @ 20 mins. prior to death	Forecast @ time of 1st alarm	Time of 1st alarm
Quarantined Data:														
See the entry for P107 below as well. While not quarantined, P107 is available for use during the June 14th demo.														
Q	27Apr2005	3May2005	198	O	Fx	?	?	>10	?					
Quarantined data, will be used for statistical forecasts, HIP, FE, MPM, and Regional Bloodflow simulations, anatomy from anatomy forecasts and autopsy comparison during June 14, 2005 demonstration. APB signal interrupted when post injury blood samples are taken.														
Q, I	28Apr2005	3May2005	184	O	Fx	?	?	>10	?					
Partially quarantined data, will be used for anatomy from anatomy forecasts and autopsy comparison during June 14, 2005 demonstration. Instrumentation data from this experiments is judged to be unreliable due to problems with LVP, AOF, and PAF as well as concerns about zeros.														
Analyzable Open Chest Experiments Using Fragments:														
A	30Nov2004	8Dec2004	63	O	FM	LV	7	120+	E	Survival	Survival	Survival	n/a	n/a
ABP drop just before Injury, No Post injury CT														
A	4Jan2005	12Jan2005	79	O	FS	LV	7.62	104	H	99*	101*	93*	119*	77
***Initial forecast for this subject was incorrect (survival rather than death).** The near spherical wound occurred near the base of the left ventricle. Cause of death likely due to loss of blood volume after 104 minutes.														
A	12Jan2005	14Jan2005	82	O	FS	LV	7.62	27	H	31	58	27	24	4
Microsphere and blood volume analysis. Postmortem isolated heart CT. LVP catheter placed directly into LV. RVP catheter placed in RV. 0.5mm isolated heart reconstructions received 3/10/05.														
	18Jan2005	26Jan2005	96	O	FS	LV	7.62	115	H	53	76	117	52	9
LVP catheter placed directly into LV. 80% pre-injury CT missing from original data. Resent by ISR.														
	19Jan2005	26Jan2005	97	O	FS	LV	7.62	26	H	35	57	37	36	6
LVP catheter placed directly into LV.														
	25Jan2005	31Jan2005	108	O	FM	LV	7	52	H	41	59	50	43	7
LVP catheter placed directly into LV														
A	26Jan2005	31Jan2005	107	O	FM	LV	7	85	H	30	59	85	58	36
While not quarantined, the data will be used for statistical forecasts, HIP, FE, MPM, and Regional Bloodflow simulations, but not anatomy from anatomy forecasts or autopsy comparison during the June 14, 2005 demonstration. The data will also be included in the statistical analysis report. The notes for this experiment incorrectly report a 124 minute time to death, when the more detailed marker annotations show an 85 minute time to death. 85 minutes is correct. LVP and RVP catheters placed directly into LV and RV, respectively.														
A	16Feb2005	25Feb2005	127	O	FS	LV	7.62	120+	E	Survival	Survival	Survival	n/a	n/a
Post-injury data and outcome quarantined until March 17th demo. Some of the CT images have been skipped due to an irregular heart beat present at the time of the scan. The gated procedure cannot correctly process scans when the patient has an abnormal heart beat or rhythm. These results were also taken with a different filter convolution than normal. I tried to change it back to the normal filter convolution when I reconstructed the data, but I'm not sure if it will look the same. Postmortem CT done with 0.5mm slices.														
A	17Feb2005	8Mar2005	129	O	FS	LV	7.62	120+	E	Survival	Survival	Survival	n/a	n/a
Post-injury data and outcome quarantined until March 17th demo. LVP catheter placed directly into LV. The second marked time point that reads 15 min. is actually the 30 min time point.														
A	2Mar2005	17Mar2005	132	O	FM	LV	7	23	H	29	55	n/a	32	15
LVP catheter placed directly into LV.														
A	3Mar2005	17Mar2005	138	O	FM	LV	7	120+	E	Survival	Survival	Survival	n/a	n/a
LVP catheter placed directly into LV.														
A	31Mar2005	5Apr2005	168	O	FS	LV	7.62	120+	E	Survival	Survival	Survival	n/a	n/a
Bleeding appears to be mainly from the myocardium, not the chamber. Postmortem isolated heart CTs in air.														
A	13Apr2005	19Apr2005	189	O	FS	LV	7.62	120+	E	Survival	Survival	Survival	n/a	n/a
Bleeding appears from the myocardium only														
A	20Apr2005	26Apr2005	194	O	FS	LV	9	17	H	41	n/a	n/a	40	9
First use of a new "9mm" ISR fragment, somewhat larger than the ISR fragments previously used, but less severe than the 9mm ISR fragment used on 29March05. Injured the center portion of the Left Ventricle with 9mm shell casing. Subject started shivering after catheters were placed, at this time the EKG started to appear abnormal. Checked the pads and the wires for the EKG, all were fine, and the gross movement of the heart also appears normal. Femoral artery catheter line was clotted when drawing 5 min sample. Used ABP to draw samples. Measured ABP between samples, had to disconnect only in the minutes of drawing sample. Used ABP to draw 5 and 15 min sample. Agonao breathing pattern started at 10:36. Subjectively, clotting around the heart was a lot slower than usual.														

Figure 29: Statistical Summary of Analyzed Open Chest Fragment Experiments

Virtual Soldier Project Phase I: Summary of experimental data collected 30 November 2004 through 28 April 2005

Status: Quarantined (Q), Analyzable (A), Incomplete data (I), Short time to death (S), Died before injury (D)
Fragment or probe type: Fragments Shell Casing (FS), MRC (FM); Probes Regular Blunt (PR), Beveled (PB), Pointed (PP)
Experiment Type: Open Chest (O), Closed Chest (C); Location: RV or LV; **Cause of Death:** Hemorrhage (H), Euthanized (E)

Status	Date of Experiment	Data Received	Tag No.	Expt. Type	Frag. or probe type	Loc.	Size	Time of Death (mins)	Cause of Death	Forecast @ 10 mins. post-injury	Forecast @ 20 mins. post-injury	Forecast @ 20 mins. prior to death	Forecast @ time of 1st alarm	Time of 1st alarm
Analyzable Open Chest Experiments Using Probes:														
A	2Dec2004	8Dec2004	59	O	PR	RV	7	120+	E					
	AOF was not recorded until after the injury, NO Post Injury CT, AOF and PAF channels switched													
A	7Dec2004	6Jan2005	61	O	PR	LV	7	90	H					
	Original data sent unreadable. Data resent by ISR. No post injury CT													
A	16Dec2004	20Dec2004	78	O	PP	LV	7.62	120+	E					
	New flow probes used to correct for a large inballance between PAF and AOF using the older flow probes. No post injury CT.													
A	10Jan2005	14Jan2005	89	O	PP	LV	7.62	120+	E					
	Miscrosphere and blood volume analysis. Two wounds, first unsuccessful. LVP catheter placed directly into LV. 0.5mm isolated heart reconstructions received 3/10/05.													
A	11Jan2005	14Jan2005	87	O	PP	LV	7.62	120+	E					
	Microsphere and blood volume analysis. Postmortem isolated heart CT with 0.5mm slices. LVP catheter placed directly into LV.													
A	13Jan2005	26Jan2005	85	O	PR	RV	7.62	113	H					
	Microsphere and blood volume analysis. Postmortem isolated heart CT. LVP catheter placed directly into LV. 0.5mm isolated heart reconstructions received 3/10/05.													
A	14Feb2005	25Feb2005	124	O	PP	LV	10	76	H					
	Post-injury data and outcome quarantined until March 17th demo. 0.5mm postmortem reconstructions received 3/10/05.													
A	15Feb2005	25Feb2005	125	O	PP	LV	10	120+	E					
	Post-injury data and outcome quarantined until March 17th demo. Postmortem CT done with 0.5mm slices.													
A	8Mar2005	17Mar2005	146	O	PR	RV	7	120+	E					
	LVP catheter placed directly into LV. Mean CVP values were greater than would be expected. Flushed RVP line @ 1055 (6 min after injury). Adjusted RVP line @1057(8 min after injury).													
A	9Mar2005	17Mar2005	143	O	PR	RV	7	120+	E					
	LVP catheter placed directly into LV. First mark for injury was a mis-fire. Ketamine dose increased to 300 mcg/kg/min at 65 minutes. (Pig had a slight palpebral reflex.) Mean CVP values were greater than would be expected.													

Virtual Soldier Project Phase I: Summary of experimental data collected 30 November 2004 through 28 April 2005

Status: Quarantined (Q), Analyzable (A), Incomplete data (I), Short time to death (S), Died before injury (D)
Fragment or probe type: Fragments Shell Casing (FS), MRC (FM); Probes Regular Blunt (PR), Beveled (PB), Pointed (PP)
Experiment Type: Open Chest (O), Closed Chest (C); Location: RV or LV; **Cause of Death:** Hemorrhage (H), Euthanized (E)

Status	Date of Experiment	Data Received	Tag No.	Expt. Type	Frag. or probe type	Loc.	Size	Time of Death (mins)	Cause of Death	Forecast @ 10 mins. post-injury	Forecast @ 20 mins. post-injury	Forecast @ 20 mins. prior to death	Forecast @ time of 1st alarm	Time of 1st alarm
Analyzable Closed Chest Experiments:														
A	8Dec2004	20Dec2004	71	C	FM	LV	7	120+	E					
	Closed chest. Original data sent unreadable. Data resent. The fragment did not pierce / nor penetrate the pericardium or the LV, essentially there was no injury to the LV. No post injury CT.													
A	9Dec2004	15Dec2004	69	C	PR	RV	10	120+	E					
	Closed Chest, 60 lead ECG no flows, only baseline lab data, DICOM images of ECG sent, no post injury CT													
A	23Feb2005	8Mar2005	136	C	PP	RV	10	120+	E					
	Closed chest procedure. Extended ECG data collected. Two injuries because first was judged to be a miss or too minor. No postmortem CTs. spherical entry wound at the septum and an exit wound out the free wall of the left ventricle, just above the apex.													
Unanalyzable Experiments:														
S, I	1Dec2004	8Dec2004	58	O	FM	RV	7	4	H					
	LVP and AOF not measured No Post injury CT													
S	15Dec2004	20Dec2004	76	O	PR	RV	10	3	H					
	Subject died due to severe hemorrhage 3 min after injury. No post injury CT.													
S	5Jan2005	12Jan2005	80	O	FS	RV	7.62	7	H					
	The near spherical wound occurred near the base of the right ventricle. Cause of death severe hemorrhage approximately 7 min after injury.													
D	6Jan2005	12Jan2005	81	O	n/a	n/a	n/a	n/a	n/a					
	Died during instrumentation, pre and post validation 5 sec. And 500 Hz data only.													
I	20Jan2005	26Jan2005	95	O	FS	LV	7.62	15	H					
	LVP catheter placed directly into LV. Problems with anesthesia, RVP, AOF--see nts file for details.													
S	27Jan2005	31Jan2005	106	O	FM	RV	7	6	H					
	First experiment to include measured "breath rate" data. LVP catheter placed through the right common carotid artery. Arterial blood sampling catheter placed in the femoral artery													
I	1Feb2005	10Feb2005	105	O	FM	LV	7	120+	E					
	The animal lived for 120 min after being injured with the MRC fragment. LVP catheter placed in left ventricle. RVP trace appears to be consistent with CVP, suspect it has floated out of the ventricle. Data collection suspended from approx 1230 hrs until approx 1310hrs due to a hard drive failure. Hard drive recovered at approx 1310 hrs and data set continued as pig #105A. Heart sent to UW for analysis. Postmortem CT done. 0.5mm postmortem reconstructions received 3/10/05.													
D	8Feb2005	10Feb2005	117	O	n/a	n/a	n/a	n/a	n/a					
	Died during instrumentation													
S	9Feb2005	14Feb2005	120	O	FM	LV	7	7	H					
	Heart sent to UW, postmortem CT done, but wrong CT images originally sent–now corrected. 0.5mm postmortem reconstructions received 3/10/05.													

Virtual Soldier Project Phase I: Summary of experimental data collected 30 November 2004 through 28 April 2005

Status: Quarantined (Q), Analyzable (A), Incomplete data (I), Short time to death (S), Died before injury (D)
Fragment or probe type: Fragments Shell Casing (FS), MRC (FM); Probes Regular Blunt (PR), Beveled (PB), Pointed (PP)
Experiment Type: Open Chest (O), Closed Chest (C); Location: RV or LV; **Cause of Death:** Hemorrhage (H), Euthanized (E)

Status	Date of Experiment	Data Received	Tag No.	Expt. Type	Frag. or probe type	Loc.	Size	Time of Death (mins)	Cause of Death	Forecast @ 10 mins. post-injury	Forecast @ 20 mins. post-injury	Forecast @ 20 mins. prior to death	Forecast @ time of 1st alarm	Time of 1st alarm
S	10Feb2005	14Feb2005	116	O	FM	LV	7	4	H					
	LVP catheter placed directly into LV. 0.5mm postmorten reconstructions received 3/10/05.													
I	22Feb2005	4Mar2005	126	C	PP	RV	10	5	H					
	Closed chest procedure. Extended ECG data collected. Problems with pre-injury post-instrumentation CT data acquisition.													
S	10Mar2005	22Mar2005	145	O	PP	RV	10	10	H					
	LVP catheter placed directly into LV. RVP was not measured. Mean CVP values were greater than would be expected.													
S	29Mar2005	5Apr2005	179	O	FS	LV	9s	6	H					
	"Left cranial lung lobe 30-40% consolidated. Abmormal amount of fluid in pericardium. Postmortem isolated heart CTs in air. Used new larger sized (9mm) and more severly shaped fragment. The digital photos for this experiment show both a pair of white and a pair of green marker pins. We take this to indicate an entry wound (LV) and an exit wound (LV). To the best of our knowledge this is the 1st such outcome."													
S	30Mar2005	5Apr2005	155	O	FS	LV	7.62	2	H					
	Postmortem isolated heart CTs in air. This experiment resulted in a through and through injury with both an entry (LV) and exit (RV) wound. To the best of our knowledge this is only the 2nd such outcome.													
S	6Apr2005	19Apr2005	183	O	FS	LV	7.62	5	H					
	Time was changed due to daylight savings time after pre-validation calibrations were done and before the baseline [blood] sample was drawn.													
S	14Apr2005	19Apr2005	192	O	FS	LV	7.62	3	H					
	Subjectively the aorta was larger than usual. The largest size [flow] probe was used (20 mm), but it was a very tight fit. Digital photos show both an entrance (LV) and exit wound (apex) with the fragment still lodged in the exit wound.													
S	21Apr2005	26Apr2005	193	O	FS	LV	9	8	H					
	Injured Left Ventricle free wall, adjacent to apex of heart. Death blood sample had to be taken from ABP line, femoral artery line had clotted.													

Report of Statistical Findings
Virtual Soldier Project, Phase I

Fred L. Bookstein, Chief Statistician, Virtual Soldier Project
June 14, 2005

Summary. The hearts of 25 open-chest experimental pigs (anesthetized, respirated) were injured by projected fragments to the left or right ventricular wall. Fourteen of these animals survived for at least 10 minutes while continuously generating valid data 500 times per second in seven instrumented channels. Six of the fourteen were "survivors" that survived at least 120 minutes; we compared these to the 8 "nonsurvivors" that died before 120 minutes had elapsed. Gross effects of heart rate variation and respiratory cycle were removed from the original time series to produce smoothed *resampled waveforms* for each original instrument channel except ECG. From singular-value analysis of these waveforms over one-minute intervals were extracted predictors of survival minute by minute, predictors of time-to-death for the nonsurvivors, and an estimator of the side of the heart that was injured (LV or RV). The channels contributing to these computations, besides ECG, included LVP, RVP, and ABP, individually and in multivariate combinations. Other available data include various blood chemistries from draws at long intervals.

The best predictor of survivorship that we could find used the average of ABP and LVP power drop, minute by minute. This estimator accrues a total of **one error,** always for the same animal (a nonsurvivor), at any time after four minutes post-wound. The accuracy thus begins at 13/14 (93%) and dwindles with the passage of time to 8/9 (89%) as the pool of nonsurvivors shrinks. Classification is by the leave-one-out method, in which no animal's data contributes to the formula by which it itself is classified, using a standard maximum-likelihood classification rule on Gaussian normal models of different means and variances. Rise in blood lactate level, a chemical consequence of lowered cardiac output, also separates survivors from nonsurvivors well, though with lower temporal resolution.

Level of ABP alone predicts time to death (TTD) in the nonsurvivors by an essentially linear regression TTD $\sim$ 2(ABP–9), with a correlation of 0.65. An "alarm" triggered by a comparison of ABP power with its lagged values significantly improves the accuracy of the time-to-death forecast at the lowest range of ABP amplitudes, so that, for instance, by 20 minutes prior to death the associated prediction, exploiting the alarm where appropriate, is 21.3$\pm$9.3 min (85% of sum of squares explained by the mean). We believe this alarm makes considerable physiological and biomathematical sense, and look forward to opportunities to extend its logic in later studies of cardiopulmonary instabilities.

All experiments using fragments to cause RV injuries resulted in TTD of less than 10 minutes, and so no such injuries were available for analysis. Prediction of injury location relied on data collected earlier that included probe experiments as well as fragment experiments. Accuracy of the assessment of side of wound is five (83%) correct classifications, along with one ambiguity, for the set of 6 animals gathered after March 17, 2005 using the actual formulas already demonstrated on March 17.

In our view this combination of signal detection demonstrations substantially fulfills the statistical requirements of the original BAA under which we have been proceeding.

Introduction

A complete review of our statistical manipulations incorporates three components: a description of the experimental setting and the criteria for selecting analyzable data sets; a series of data conditioning steps supplying vectors of summary parameters suitable for statistical analysis; and the findings based on those few summary parameters. The experimental design and selection criteria are presented elsewhere in this Briefing Book. We have divided the remainder of the discussion here into seven subsections, three concerned with data conditioning or signal processing and the remaining four with detection of medically relevant signals within the conditioned data. Appendices convey a finding from a different channel (blood lactate) that did not require conditioning, and also set out the responses of a consultant critic, Prof. Kanti V. Mardia, to an earlier version of this report (March 17, 2005), along with our responses.

I. Data Conditioning and Signal Processing

Here we review three steps by which the 500Hz data are reduced to minute-by-minute parameters:

1. resampling the original 500 Hz data series to even spacing in the heartbeat;
2. smoothing to eliminate the strong cyclic effects of respiration;
3. conversion of resampled waveforms to minute-by-minute estimates of amplitude;

1. Resampling the original 500 Hz data

Heartbeats differ in duration even in healthy animals (the familiar "chaotic behavior" of this phenomenon), and of course they change drastically after the animal is wounded. The following plot indicates the typical amplitude of variation in the pre-wound state (not healthy, of course, because anesthetized and respirated in the open-chest condition). Following the wound, this rate will typically increase by some 50% to 70%, but then ordinarily stabilizes until the pig is clearly dying. A calibration is needed by which we can assess changes in net output over the cardiac cycle when the cycle is changing in length as drastically as this.

A suitable approach would resample beats of different length in such a way that a summary statistic, to be introduced in Sec. 3, can legitimately represent cardiac output already stabilized against changes of heart rate. A relatively simple approach is sufficient, as indicated in the second graphic following. Using a standard "R-wave detector" [ref.], we locate corresponding points on all of the "normal-looking" heartbeats of each animal's complete ECG measurement channel as originally recorded (500 Hz). [Heartbeats for which the R wave is too obscure to be reliably located, and heartbeats the duration of which falls outside a region of tolerance with respect to preceding and following heartbeats, are eliminated from the resampling, a decision that does not affect the signal-processing to follow. There is evidently a potential loss of information about the spacing of these irregularities, information that might be relevant to our clinical medical goals, but it is modest at worst and is ignored in what follows.]

Wherever the R-wave ictus is detected for two consecutive heartbeats, the instrument signal is resampled by linear interpolation between raw data points at 32 points distributed exactly evenly over the interictal interval. In the example here (see diagram on the next page), the heartrate is accelerating unrealistically (1 second, for the first "beat" shown; .9 second, for the second; .8 second, for the third), yet the resampling performs quite reasonably on a similarly accelerated simulated waveform (bottom panel). All subsequent analysis is in terms of these exactly evenly resampled waveforms, for which, of course, consecutive heartbeats never differ in duration by as much as the 10% of this diagram.

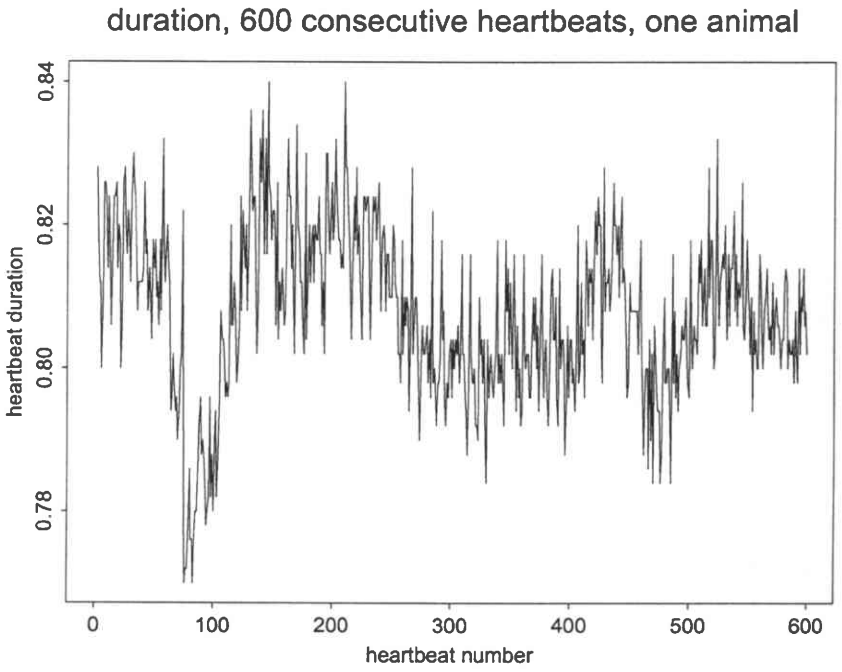

2. Eliminating effects of the respiratory cycle

In the resampled data record (see, for example, the second diagram on the next page), even under baseline conditions there are evidently temporal variations at relatively short time scales. Here we see about a minute's worth of resampled data (75 heartbeats) for five channels prior to wounding of one of the early experimental pigs. The cyclicity in these different traces appears to be synchronized, and analysis of the peaks proves it to be precisely synchronized with the respiratory cycle (which, for these animals, is controlled by an integer parameter, the number of breaths per minute explicitly dialed into the respirator).

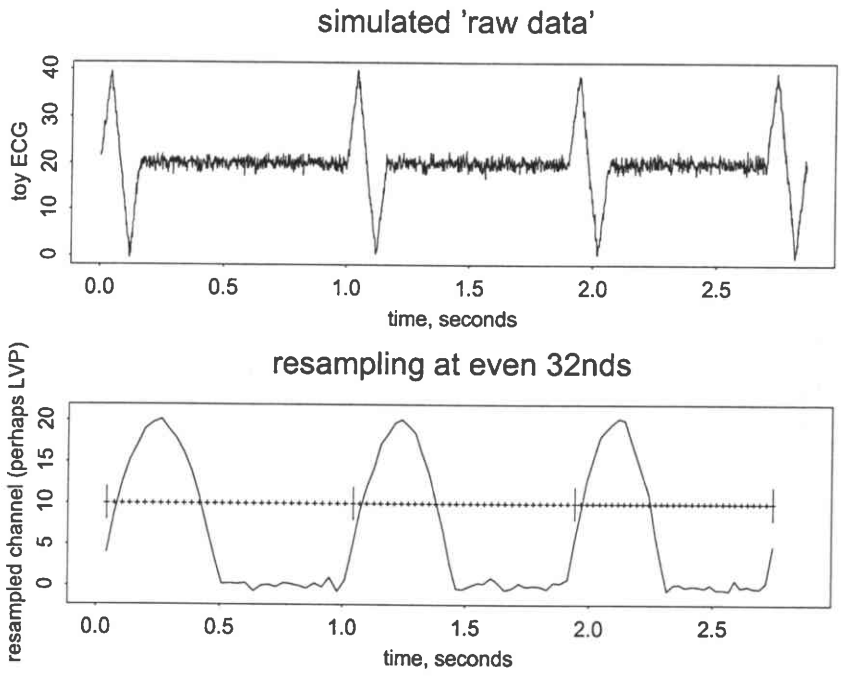

Resampled data continue to show respiratory effects.

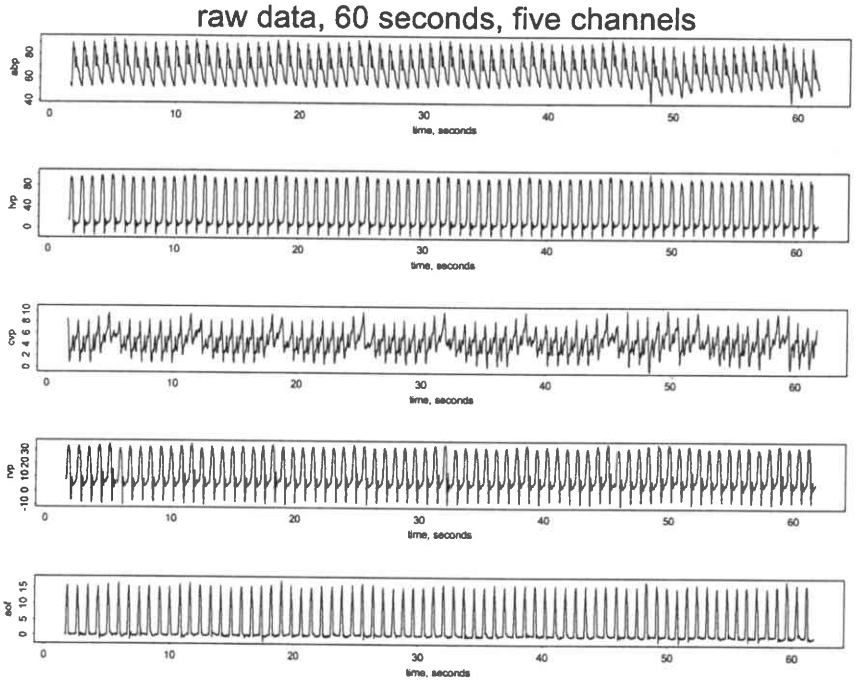

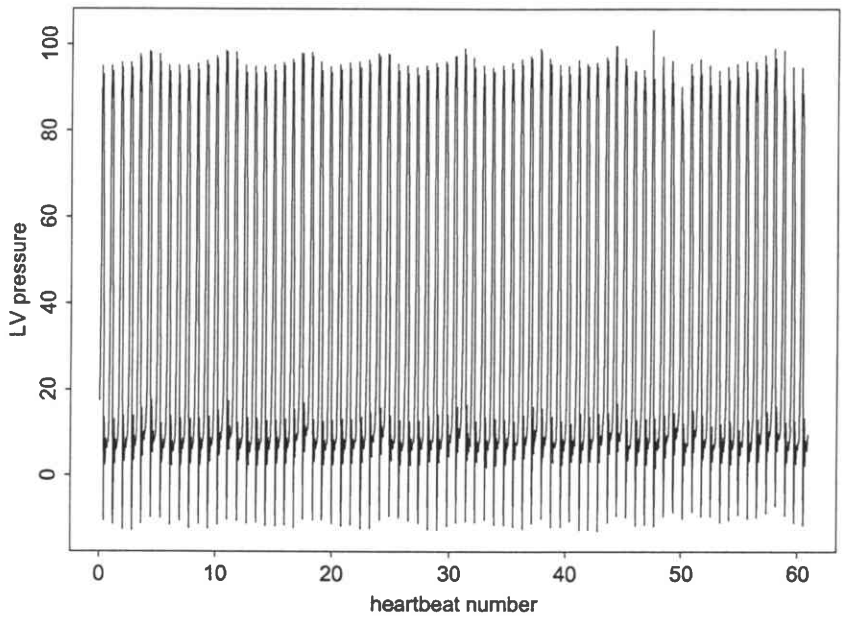

The net effect of this cycling is to produce a systematic periodicity in the surfaces we use in the course of extracting our waveforms. This systematic effect, if not suppressed, would swamp any attempt to find short-term signals of cardiovascular instability, such as those that actually turn out to sound the alarm in the data analysis to follow. *The cycle must be eliminated even though it is no artifact, but rather physiologically real.* In the figure following, the original resampled time series has been "folded" at each cycle of 32, rather like a book with only one line per page, so that corresponding phases of consecutive waveforms are aligned in the direction labelled "heartbeat."

For the purpose of filtering out this phenomenon we developed a filter that accommodates the lack of synchronization between the heartbeat and the respiratory cycle. The next diagram indicates the general idea. Among all sequences of consecutive heartbeats in the data set, from one to 99 in number, there will be some sequences that sum to within .005 seconds of an exactly integer duration of respiratory cycles. (As the diagram suggests, we are not presuming constancy of the heart rate over this interval, and we are ignoring phase information for both breathing and heartbeat.)

Approximately one-sixth of all the heartbeats in a typical experimental data set are embedded within an exactly integral system of respiratory cycles in this way. Because periodic terms of different wave numbers are orthogonal (i.e., $\int_0^1 \sin(2\pi ix)\sin(2\pi jx)dx = 0$ when $i \neq j$), the effect of the respiratory cycle is cancelled out almost exactly by this averaging.

In this way approximately one in every six of the original heartbeats is replaced by a centered local average of up to 99. *All the other resampled data are replaced by interpolations among these averages.* Plots not shown here indicate that the resulting time resolution, although itself smoothed, is quite adequate for the physiological signal processing yet to follow here.

original data, 60 seconds

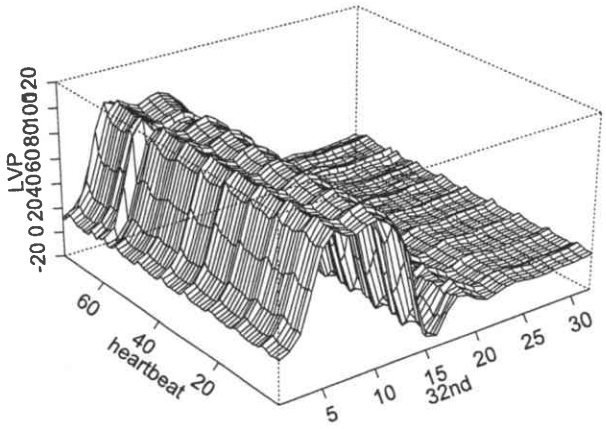

breathing correction (22 heartbeats = 3 breaths)

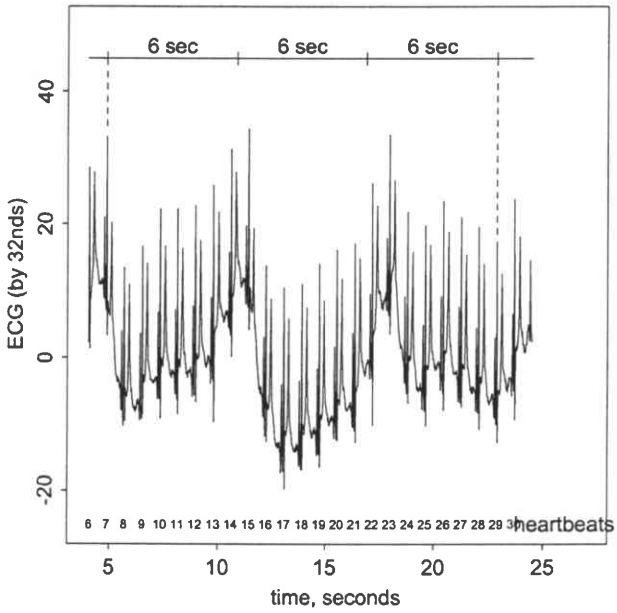

By comparing the plots of original and smoothed surfaces for the same 75 heartbeats, you can see the effect of this filter in greatly attenuating the amplitude of the respiratory component of this or any other physiological waveform under study. The example here is real (i.e., both surface diagrams apply to the same original 60 seconds of LVP data).

Around heartbeat 60 there is visible a smoothing domain of duration short enough that a certain amount of the original channel noise is still visible.

For field data, the fixed respiratory rate entailed in this algorithm would be replaced by intervals between consecutive detections of a phase-specific respiratory marker, leaving unchanged the other features of the diagram on page 6.

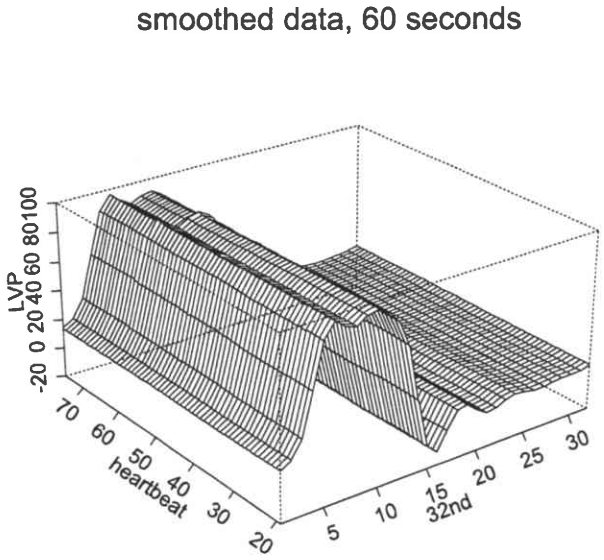

3. Converting waveforms to minute-by-minute amplitudes

The third step in the processing is the mathematical equivalent of what is already visible to your eye in the preceding diagram. Minute by minute, beginning at the start of the instrumented data record, each consecutive minute's worth of these smoothed derespirated resampled heartbeats is converted to the "average" for that minute in a specific technical sense. The average we are using, the *first singular vector* of the matrix displayed as a surface above, is the vector that best predicts all of the individual waveforms that accrued in the minute under study: the vector W (for "waveform") for which the observed surface is fit best (in the least-squares sense) by a product UW^t where U is a modified unit vector absorbing the effect of variation in the number of heartbeats observed minute by minute. The existence and uniqueness of such a decomposition is guaranteed by the celebrated *singular-value theorem*, and its computation is a standard feature of every sophisticated numerical analysis or statistical package.

The measure we are taking, "net" area under the dominant waveform, is in units of millimeters per heartbeat. In this report, that quantity will be called the **amplitude** of the measurement channel (LVP, ABP, RVP, etc.) As such, it compensates to a great extent for the tradeoff between shorter heartbeats (less time at this pressure) and more heartbeats per minute, and thus does not require any further calibration for variations in heart rate pre- or post-wound.

II. Detection of medically relevant signals in the conditioned data

Here we explain the strategies we followed and the formulas we used that converted the amplitudes introduced under I into the predictors of survival and time-to-death and the estimator of site of injury that were reported on page 1 and in various tabulations elsewhere in this Briefing Book. There are four steps in the analysis:

4. after examination of a range of bivariate choices, selection of ABP and LVP as carriers of the principal signals;
5. prediction of survival;
6. prediction of time until death, for nonsurvivors;
7. estimation of the side of the heart wounded.

4. Selection of ABP and LVP as predictor channels

Six data channels could be processed in this way once aggregated and de-respirated: ABP, LVP, CVP, RVP, AOF, and PAF.

With all valid data channels represented by one of these singular waveforms for each minute of experimental time, pre- or post-wound, we can now turn to the issue of what information to rely on for further statistical analysis. The following diagram provides a clear point of takeoff for this effort. The pair of ABP and LVP, uniquely among our pairs of measures, not only are measuring very similar physical quantities, in the same units, a few centimeters apart, but also correlate better than any other pair of measures from among our six.

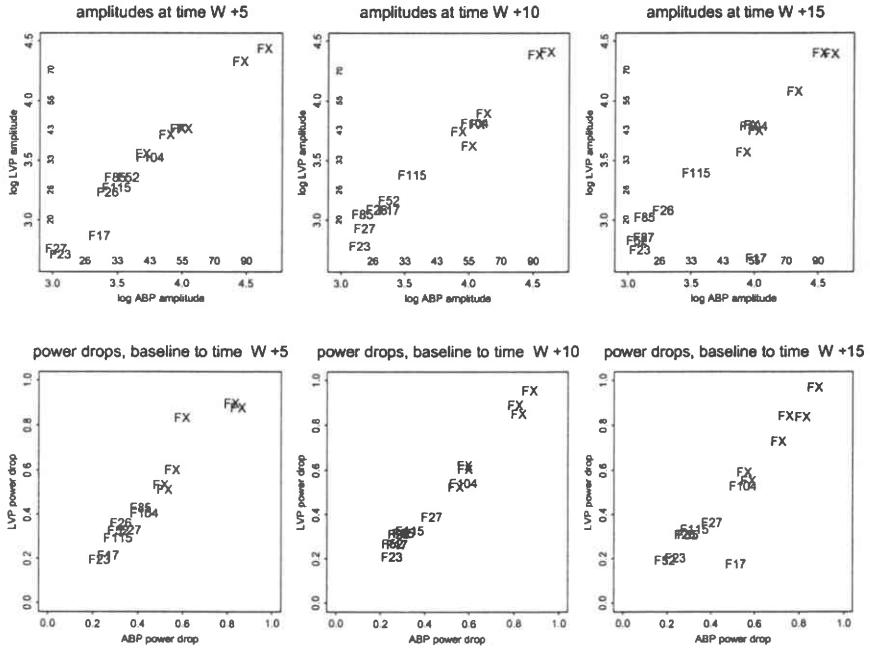

In the figure preceding, each plotted point corresponds to one animal wounded by a fragment device (the "F" of the plotting string). The animals plotted at "FX" survived; the others have a number corresponding to the number of minutes they survived post-wounding. Across the top are the waveform amplitude plots, ABP (horizontal) versus LVP (vertical), for 5, 10, and 15 minutes post-wounding (notice that at 15 minutes one animal is already fixing to die soon [at 17 minutes]). The plots of this top row are logged on both axes for legibility. (These are natural logs; the corresponding antilogs are printed in small type just inside the axes.) In the bottom row are the *relative* power values for these same two channels—the ratios, now no longer logged, of the post-wound amplitudes at the same three times to the "baseline" (anesthetized, open-chest) waveform amplitudes before the wound. These plots are generally straighter than those in the row above, but also, by 15 minutes post-wound (panel at lower right), the separation is perfect (although only just) along the diagonal of the plot—the average of LVP and ABP power loss.

When variables are correlated, as they are here, their linear combinations usually predict other quantities of interest more effectively than the separate components can. The next section relies on the combination of ABP and LVP to predict survival; but we revert to reliance on ABP alone in Sec. 6 for the time-to-death computations there.

We compare ABP to all five of the other possible choices (next plot) to indicate that this diagonality is not found (shown here, for ten minutes post-wound; other times are analogous) for any other pairing with ABP. The ABP–LVP combination is thus the optimal one.

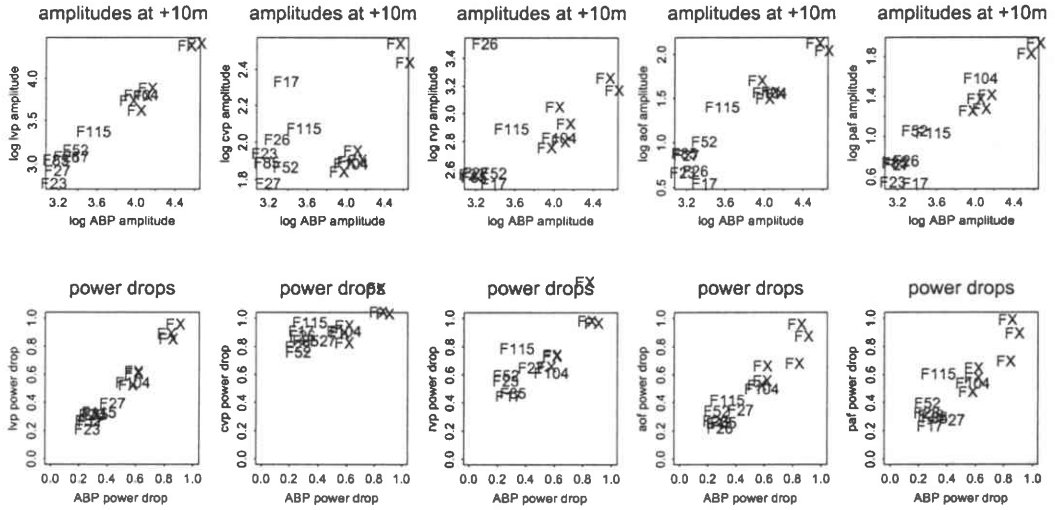

See Andy Boyd's addendum to this report for a discussion of additional potential predictor items from instrumentation collected less frequently than 500 Hz.

5. Predicting survival

There is nothing special about the tenth minute post-wound (or the fifth, or the 15th) selected for the preceding graphics. In the next display, the sum of ABP and LVP power, and also the sum of ABP and LVP relative power, are traced as curves for each of the 14 fragment animals separately. As the legend indicates, the 6 survivors are shown in dotted lines, and the eight nonsurvivors in solid lines that stop, of course, at the time of death of each of these animals. Hence the longest-living nonsurvivor dies at 115, and the shortest at just 17 minutes, as already noted.

It is clear that both the clustering of the survivors and the separation of survivors from nonsurvivors are better in the lower of these two diagram styles, the one that uses relative power loss. The separation that we saw in the preceding figure does indeed become perfect (14/14 correct) at just 15 minutes, and remains perfect throughout the entire remainder of the full data series, in spite of a real threat from the second longest-living nonsurvivor, who becomes so highly unstable around the 75th minute post-wound that the upward perturbations nearly overlap with the lowest-performing survivor.

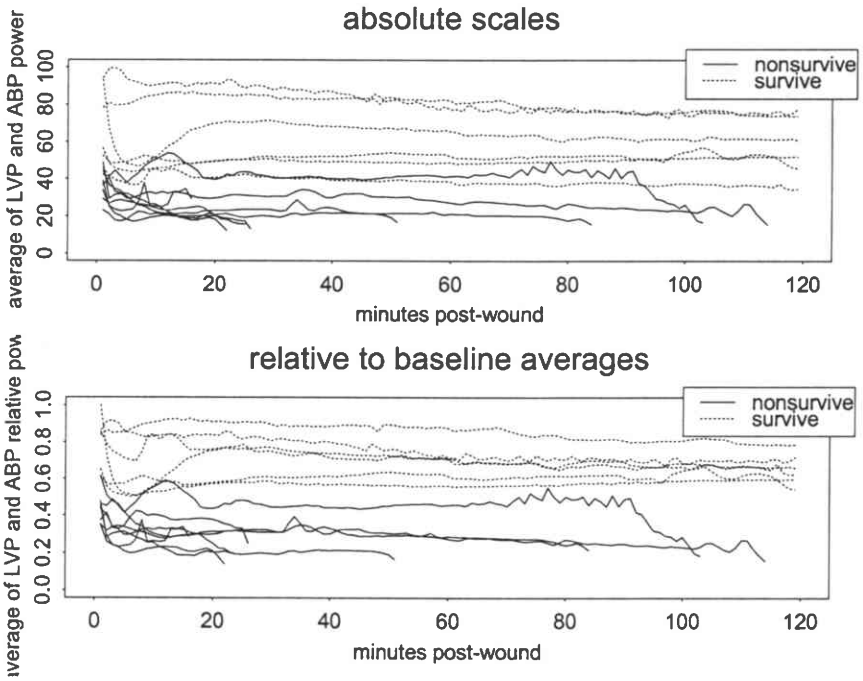

Of course, this "prediction" is biased; we are using our eyes to carefully draw a line up the middle of the plot that just manages to separate our groups even at their points of closest approach. The *honest* computation arriving at the same endpoint is reflected in the next diagram here, the diagram entitled "chance of survival, ABP + LVP, scaled." Plotted here are the posterior odds of membership in the survivor group for each of the fourteen animals, at each of its available post-wound data points, *computed solely with reference to the data from the other thirteen animals.* The computation is by classic likelihood-ratio[1] for imputed Gaussian distributions matching the observed means and variances of (i) all 6 survivors, together with (ii) as many of the nonsurvivors as have survived to the

[1] The chance of survival is LR/(1 + LR) where LR is the *likelihood ratio,* ratio of the probability of the datum on a Gaussian assumption presuming survival,

time at which we are testing, as long as there are at least two of them. [Hence the solid lines, representing the odds for the nonsurvivors, all stop at the 84th minute, at which time we no longer have "two other survivors" against which to calibrate.] As even three "surviving nonsurvivors" is many too few for the test we are using, the data generating the likelihoods are the cumulation of all the minute-by-minute amplitudes (or ratios) beginning just halfway from the wound to the minute in question. [The issue is not that there are only three survivors beyond the 52nd minute, but that two of them ar so clearly similar and one so strikingly different. Sec. 7 uses the same test in a comparison of 11 values against 2 without any paradox.]

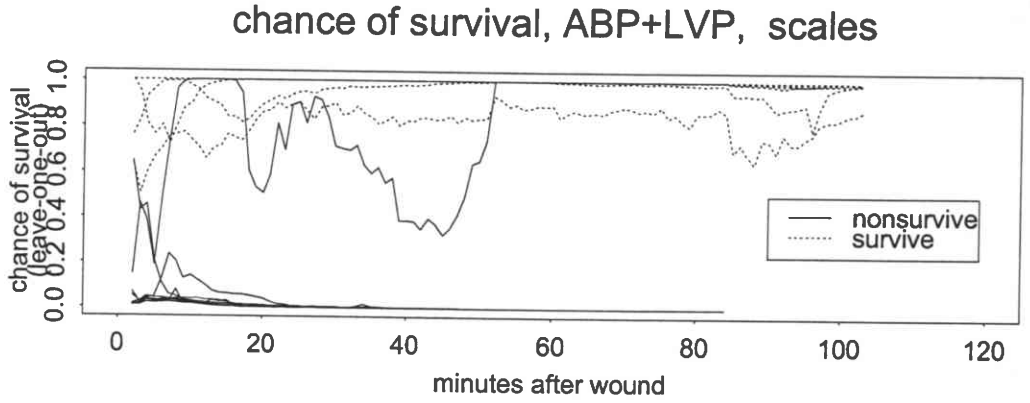

The finding here is *very* instructive. With one exception (the nonsurviving animal that approached so closely to the survivor group in the preceding plot), there is perfect separation of the survivors from the nonsurvivors at every minute past the fifth. Survivors do not vary much in their apparent "odds of survival"—they resemble one another a good deal—whereas the nonsurvivor riding high is often likelier to have emerged as a survivor instead of dying at minute 104, as it actually did. The long interval of apparent "certainty" of its survival, from minute 52 to minute 83 post-wound, is an artifact generated by the remarkable similarity of the two other pigs that survived past the 52nd minute. They are *so* similar in their data, and so relatively invariable over time, that any animal differing from them will be considered likelier to have arisen from the survivor group no matter

---

$$(\sqrt{2\pi}\sigma_S)^{-1}e^{-\frac{1}{2}((x_t-\mu_S)/\sigma_S)^2},$$

to the probability on a similar assumption presuming nonsurvival,

$$(\sqrt{2\pi}\sigma_{NS})^{-1}e^{-\frac{1}{2}((x_t-\mu_{NS})/\sigma_{NS})^2}.$$

Here x_t is the mean relative power drop from baseline at time t post-wound for the animal under consideration, μ_S and σ_S are the mean and standard deviation of the mean power drops for the survivors between times $t/2$ and t post-wound (deleting the animal under consideration if it is a survivor), and μ_{NS} and σ_{NS} are the same for the nonsurvivors.

whether its actual physiological level is higher or lower. This is just an accident of small sample sizes, of course, but nevertheless it counts as an error for purposes of this report. With the exception of that one persistent error, the classification of survival or not by relative ABP-LVP level is perfect, and in no case is an animal's own data involved in this classification, nor is there any parameter set by hand or by inspection.

It is of interest to examine the comparable plots based on the information from ABP power loss or LVP power loss alone. The figures below show that either analysis of the partial data resource is somewhat less reliable than the composite we've put forward here. The LVP-only analysis is inaccurate for one of the surviving pigs (i.e. predicts nonsurvival) beginning at time about 75 minutes post-wound; the ABP-only analysis is much more unreliable in predicting the nonsurvival of the nonsurviving animals between 5 and 15 minutes post-wounding. Neither avoids the persistent error for the highest-functioning longlived nonsurvivor, the single error for the composite criterion discussed above.

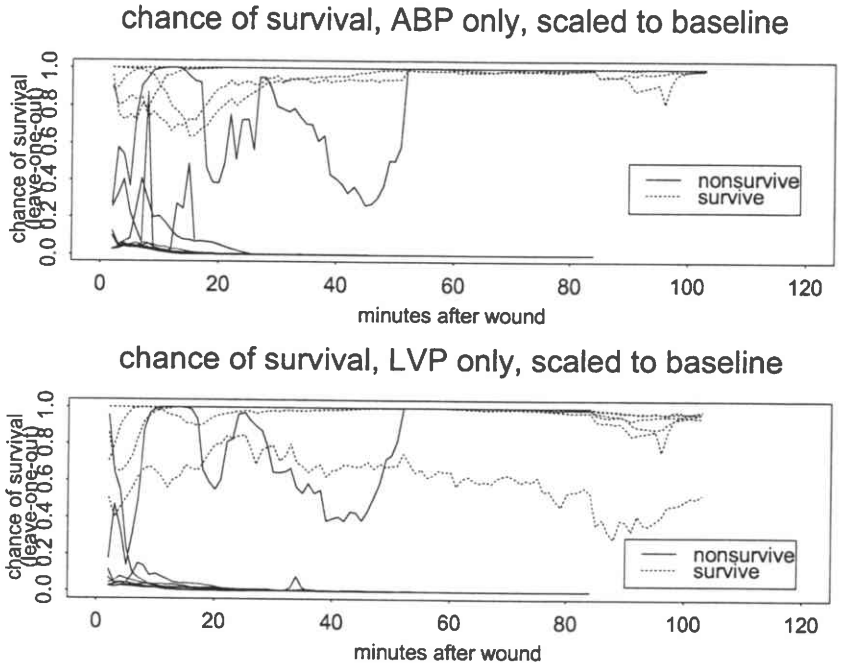

6. Prediction of time until death

The previous machinery produces a nearly perfect cross-validated classifier of survival/nonsurvival, but in doing so necessarily ignores the even more important consideration of predicting *time to death* (TTD). In the battlefield scenario, even more important than "triaging out" the pool of wounded likely to survive is the selection, among those "triaged in," of the subset who would truly benefit from early medical care. In the present experimental simulation, that is the subset of animals that would be predicted to die soon, and so we turn to the specific estimation of this remaining time. The estimate that follows is a purely statistical one, not based on any physiological model of the wounded animal's functioning per se. Nevertheless, it appears to be informative in the context of the present

data set.

As a first statistic for prediction of TTD, we considered a simple linear regression of the observed value against ABP waveform amplitude. The standard analysis, to be diagrammed a few pages further on, produces the prediction function TTD $\sim$ 2.1(ABP-9.3) with explained variance 0.427 (i.e. a correlation of 0.65 between predicted and actual TTD values).

As already introduced in our report for the March 17 demonstration, we are augmenting the previous time series of waveform amplitudes by a carefully tuned *second divided difference*. [Terminology: a "second difference" is something like a second derivative, but taken among points at finite separation rather than those "infinitely close together"; a *divided* difference is a derivative normalized to the level of the underlying variable—in a sense, a derivative "on a ratio scale."] Our data analysis of March indicated that we should be using differences at a unit lag of three minutes (hence second differences at a lag of six minutes), and we have continued to use that value for the data analysis here. Writing A_k for the amplitude of the ABP waveform at the k-th minute post-wound, the formula for the second divided difference is simply

$$\frac{A_k + A_{k-6}}{A_{k-3}} - 2,$$

and we will declare an **alarm** if this value falls below an empirical threshold of -0.05 (also set in March and not altered).

The reasoning behind this unfamiliar expression is at root biomathematical. The heartbeat of an animal destined to survive will not be beating with perfect regularity, any more than an unwounded animal's will. There will always be small variations in its system parameters arising from variations (sometimes periodic, sometimes not) in the animal's other systems: the active interaction of multiple controlled subsystems. In the survivor, these small perturbations are all *stable*, meaning that the heart will return from the perturbed value to the vicinity of its pre-perturbation cycle. If an animal cannot recover appropriately from such a perturbation—if a deviation downward is not compensated, in whole or in part, within a few minutes—it is fair to infer that the animal has exceeded the limits within which its own cardiovascular regulatory processes are capable of being stabilized, so that death is likely to follow sooner rather than later (as soon as sufficient additional irrecoverable perturbations have accumulated).

The following chart combines all the values of ABP waveform amplitude with the corresponding values of its second divided difference, connected by lines animal by animal, separately for survivors and nonsurvivors.

Clearly these distributions are very different. Every animal in whom the ABP waveform amplitude ever drops below 40 (mmHg) is a nonsurvivor; but, also, these are the animals for whom the second divided difference drops well below -0.05 (not counting the minutes just after the wounding, when the animal is trying to stabilize itself somehow in the presence of this unprecedented new regime of myocardial insult).

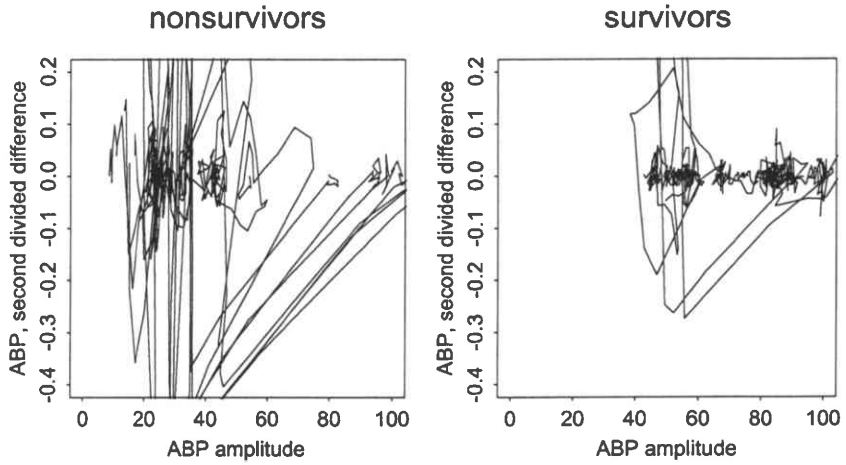

The corresponding plot for LVP (below) is much less effective at discriminating (notice that values for the survivors drop nearly to 20 mmHg, so that the lower limits for surviving and nonsurviving groups overlap much more extensively). We choose not to combine ABP with LVP for this prediction task, then, but to proceed with ABP alone. (We did not consider the other instrument channels for reasons already sketched in Sec. 4.)

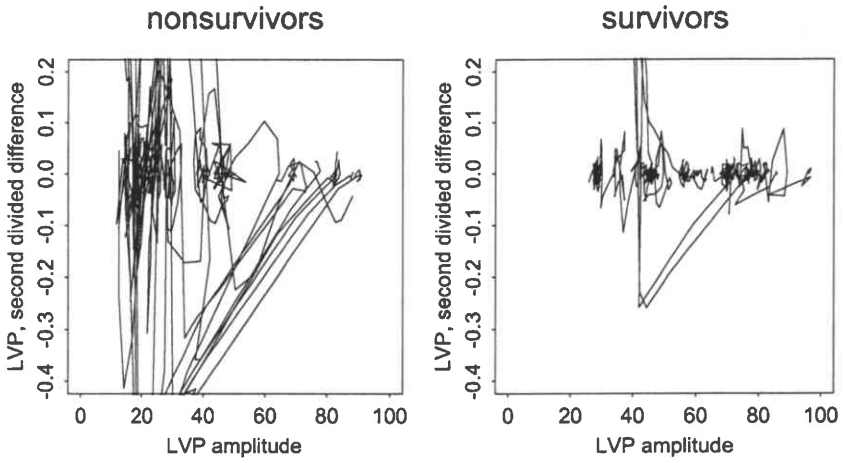

The left panels of the preceding two diagrams are of all the nonsurvivors together. To see how an alarm might work at the level of the individual subject, it is better to plot them separately, as in the next set of 14 panels. For every animal we have indicated the informative region—ABP under 40 and second divided difference under -0.05. As you see, the separation afforded by this classification is perfect; but, also, entry into this region supplies a criterion of time-to-death in a predictable form (because every animal that encounters this region is indeed a nonsurvivor). [Note that the gnomon is drawn at ABP 40 mmHg and relative second difference -0.05 on every plot; the difference in positioning owes to the difference in natural scales of these two variables pig by pig.]

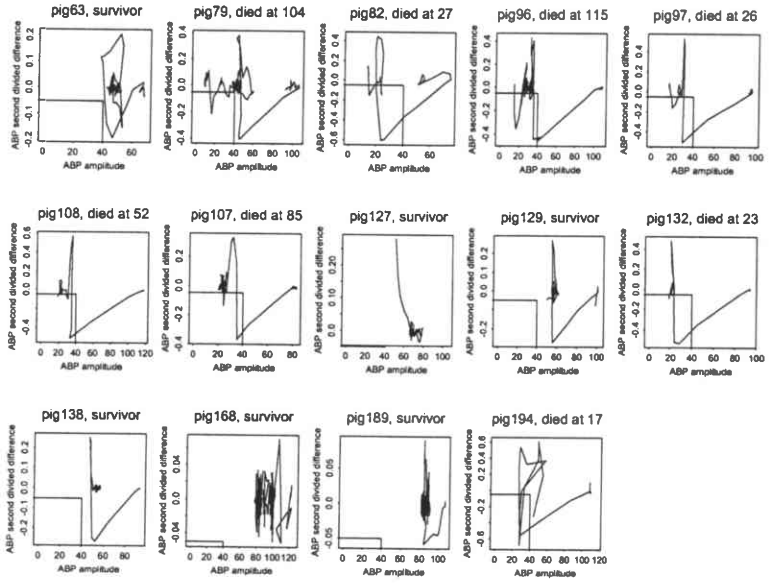

In the next, very instructive, plot we have printed the actual time to death for every point below the zero line in the preceding displays. (An "X" means that the point derives from a survivor, having no time-to-death.) There are some time-to-death values well below the axis at values of ABP waveform amplitude above 40, but actually very few; most of the animals that are destined to die spend most of their post-wound lifetimes at ABP's of 40 or below, as we already knew. The smaller TTD's clearly congregate toward the left of the plot (a restatement of the regression result set out near the beginning of this section).

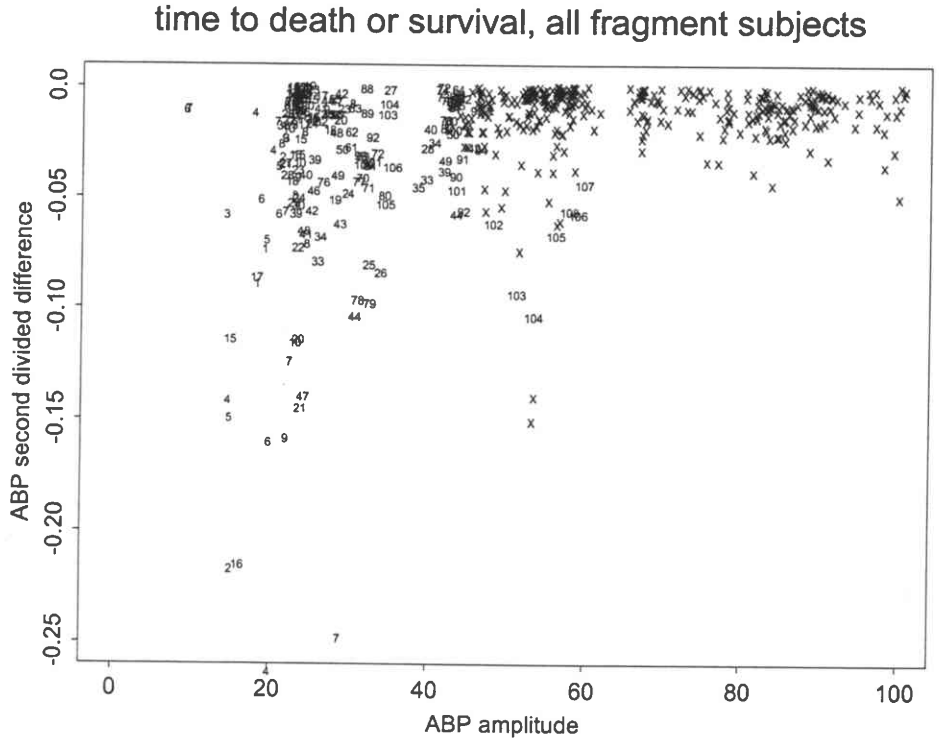

By clipping the vertical axis of the preceding plot near the proposed alarm setting (to wit, at -0.10, double the threshold of -0.05), we gain space for a clearer view (see next figure). A hint thereby emerges that the alarm in fact carries information – that the time-to-death estimate for any given value of ABP amplitude is separately affected by the value of the second divided difference at that same time. (Specifically, within the "typical" vertical row, the times to death near the bottom of the plot average less than those near the upper border.) A simple test for the additional informative value of the alarm is an ordinary comparison of mean time to death between those observations at which an alarm is present (i.e. those that are suddenly accelerating downward in cardiac performance) versus the others. The results of this mean comparison are highly significant, and in the hoped-for direction. Specifically, in the regime of ABP amplitude 30 or below, which is the domain within which death is relatively imminent, the time to death increases by about two minutes per mmHg of ABP amplitude, but drops by nearly 10 minutes when an alarm is present (these are the points plotted in big dots on the next page—note that most of them are below the straight line, the prediction by ABP); and the term for the alarm is statistically significant (at $p \sim 0.006$) by the standard t-test. (The best threshold for the alarm would actually be at -0.07, for which the mean TTD's differ by a full 14 minutes, $p \sim 0.0007$. In a larger sample of animals we might combine these Booleanly or at some time lag to increase sensitivity and specificity.)

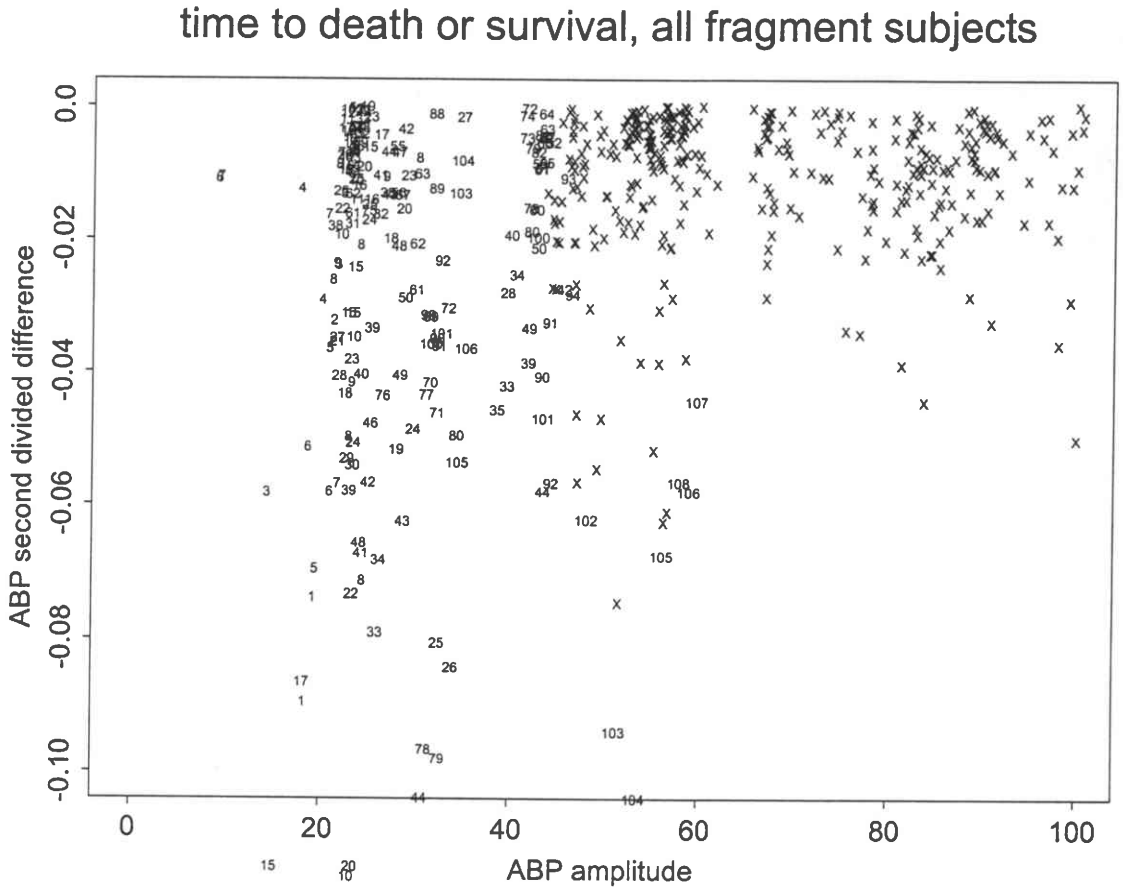

This combination of predictions can be presented jointly in the following scatterplot (our last). Here, we have plotted ABP level against time to death, but indicated (with big black dots) the points at which an alarm is triggered. The long pixellated line is the ordinary linear regression of time-to-death on ABP per se, the solid line is a nonlinear version of the same relationship (the function *lowess* in the statistical package `Splus`, labelled "smooth" in the diagram), and the short dashed line is the nonlinear regression of time-to-death on ABP for the minutes at which the alarm is sounding; this curve lies below or along the solid curve everywhere that it is defined. The comparison of curves here is computed independently for each small range of ABP values; the combination of the two observations (regression and mean shift) is more persuasive than either one would be separately. For example, at 20 minutes post-wound, the correlation between predicted and observed times to death for the seven animals surviving at least that long is 0.75; at 20 minutes prior to death, the mean predicted time to death for the six animals surviving at least 25 minutes, and hence having a forecast TTD twenty minutes before, has a mean of 21.3 minutes with standard deviation of 9.3 minutes (intraclass correlation η^2 around zero, 0.84).

In other words, **an ABP amplitude below 40 mmHg and an alarm signal are both nearly perfect predictors of death; but the combination signals death more imminently than does either one separately.** We believe the discovery of this alarm represents a substantial contribution of this project to battlefield medical care. Mean improvements in accuracy of 10 minutes or more in predictions of TTD are clearly of practical importance, and the alarm signal detector (that second divided difference) arises clearly from application of a familiar strategy of mathematical dynamics (the detection of transitions from generic stability to instability) in the context of known facts of the cardiac cycle (to wit, stability against perturbations as a characteristic of health). We very much hope that our sponsor sees this discovery as the impressive bridging phenomenon between biomedical signal processing and biomathematical modeling that we believe it to be.

When our Ann Arbor physiologist consultant Prof. L. G. D'Alecy was presented with these results, he commented further as follows:

> "There are many points or mechanisms of control in the cardiovascular system all of which ultimately function to enable survival. For example, heart rate is controlled largely by the sympathetic and parasympathetic nervous systems acting respectively to accelerate and decelerate the heart. Similar control is exerted on the strength of cardiac contraction and vascular resistance. These are modifiable effector pathways. Very few of the variables that we know of and can measure are sensed by the body. The importance of this that without being sensed, none can truly be considered a 'regulated variable.' Heart rate is not sensed and hence cannot be regulated.
>
> "Arterial blood pressure is sensed by peripheral nervous system sensors (baroreceptors) that send signals to the brain (central nervous system, CNS) where the information is broadly integrated with other sensed information and experiences. In addition to other pressure sensors throughout the body, we know of several variables that are regulated such as body temperature, chemical composition (pH, Na, osmolarity, etc.), body position, motor activity, etc., and this information is all relayed to the CNS for integration. The extent of information available to the CNS is barely beginning to be

appreciated. Needless to say, arterial blood presure and a myriad of other sensed variables allow the CNS to integrate all this information for the most survival-appropriate responses. The CNS responses use all of the controlled variables we know of (and numerous others) like heart rate and strength of cardiac contraction to affect a survival outcome.

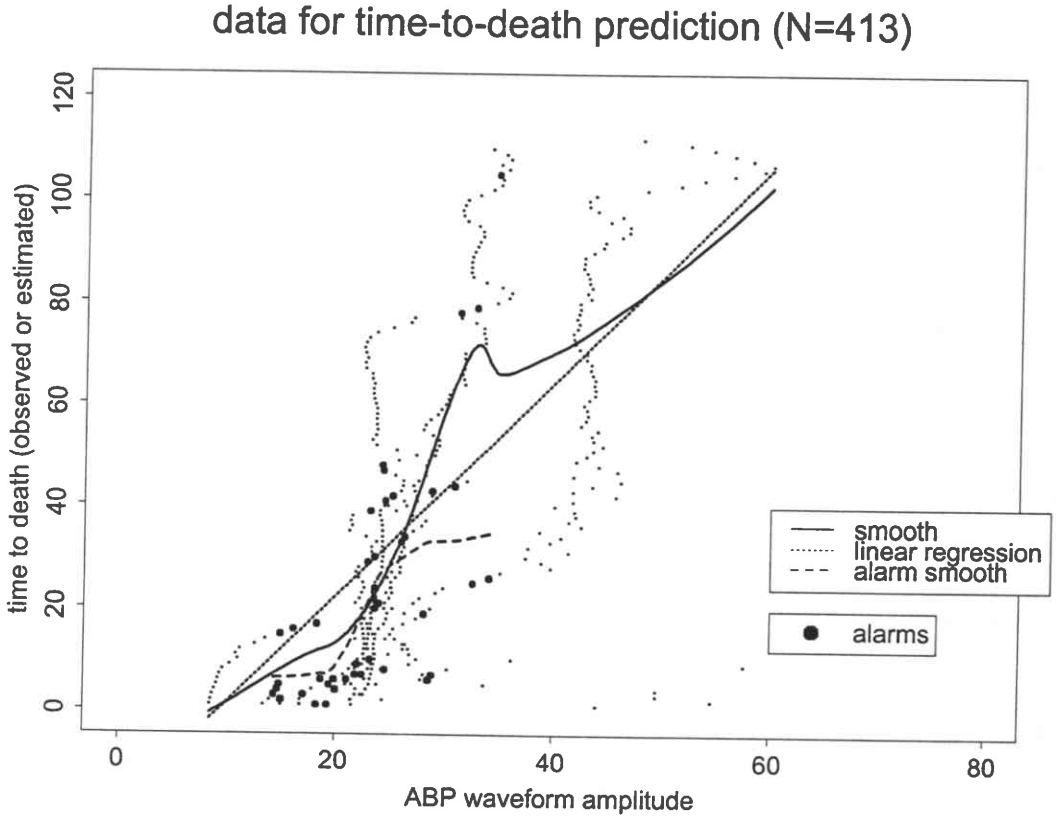

"I believe the alarm analysis evaluates the onset of failure of these combined and integrated responses. Looking at ABP, we are assessing the overall performance of the integrated survival system. the picture we see is the system searching for an appropriate arterial blood pressure. As the heart is injured and blood is lost, the system continues to compensate, adjusting a series of controlled variables and seeking a 'survivable' setpoint for pressure. As additional physiological information is processed by the CNS, the system maximizes and ultimately uses up all the major compensatory strategies. At some point (the 'alarm') the overall system can no longer maintain a compensatory strategy and begins to decompensate or fail. The second divided difference analysis finds this transition point and signals the beginning of decompensation and death."

7. Classifying wounds as to side

One topic remains, the determination of which ventricle, left or right, was wounded. There is a problem with the experimental design in the context of this purpose, since none

of the animals wounded by fragment in the RV survived beyond 10 minutes post wound and thus none contributed to our final data set. Nevertheless, a module carrying out this signal-detection task was demonstrated at the March 17 demonstration. A preliminary study of the experiments to that date indicated an apparently perfect discriminator of the side wounded in the sample as it was then, of 11 animals (7 fragment, 4 probe) with LV wounds and two (both probe) with RV wounds. The discriminator was a likelihood ratio (as for the survival odds prediction here) based on the deepest relative deficit of RV (vis-a-vis LV) over the first ten minutes after wounding (after which time any deficits in performance of either ventricle would have extended to the performance of both). We used the same data resource (11 cases, vs. two) as in the March demonstration, treating it as a "training data set" the decision rule from which was simply applied without change to the new "test data set" of the six additional fragment wounds accrued since then. The results were a detection of the LV wound in five of the six cases, at an odds ratio of at least 27:1, together with one case for which the odds are even. This is an accuracy of 5 correct and one ambiguous for the test data set of 6.

Report of Statistical Findings

Virtual Soldier Project, Phase I

Fred L. Bookstein, Chief Scientist, University of Michigan site

June 14, 2005

Addendum: Response to Comments by Prof. Kanti V. Mardia
on the earlier version of this report dated March 17, 2005

As part of our Scientific Report dated March 17, 2005, we included a short summary of the statistical work to that date. Following a suggestion by our DARPA management team, we sent that report to our consultant Prof. Kanti V. Mardia as well, inviting any criticisms he would care to convey. Prof. Mardia responded on April 28 of this year with several suggestions. In this addendum we précis those suggestions and indicate our responses for each. A nearly complete draft of the present Statistical Report was sent to Prof. Mardia late in May. His response to our responses reads as follows: "Since my [original] comments, Fred has now used the bivariate signals ABP and LVP effectively and I am of the opinion that this analysis cannot be improved."

1. "The valid or 'useful' data are messy with no experimental control, heterogeneous and no concomitant variables (which had been anticipated from the FE partners)."

Response. The data set for analysis is now slightly less heterogeneous, being restricted to only the animals wounded by the fragment device.

2. "The statistical data consists of 15 multiple time series—one for each animal. ... There were various channels and we will restrict our attention to LVP (left ventricle pressure) and ABP (Aortic Blood Pressure)."

Response. Following the March 17th demonstration, all of the 500Hz data channels were examined, along with some of the items collected less frequently. The new report explicitly lays out the reasoning according to which the multivariate analysis was focused on LVP and ABP.

3. "Out of the 15 valid experiments, the first 13 can be viewed as the training set which were in the Report. The last two can be regarded (queries to the data) as the test set ... ."

Response. We now clarify that, because we are exploiting leave-one-out techniques, the central prediction (survival/nonsurvival) can be construed as treating each fragment

animal, in turn, as the "test set" following a "training set" comprising all the others.

4. "Using excursion techniques, a powerful statistic A was developed to ascertain change points, i.e., setting an 'alarm.' The threshold for the alarm statistic A was constructed based on the training set."

Response. The threshold of the alarm, set based on a graphical comparison of survivors against nonsurvivors, was modified into a continuous choice in the course of the report. We do not have enough complete animal data to ascertain the reliability of the optimal setting, however, and so the report continues to exploit the value of -10% used in March (a value that is thus "a priori" as far as the June report is concerned).

5. The alarm seems to capture a magnification of perturbations rather than a damping, as would be healthy.

Response. This explanation [perhaps further improved by Lou] is now explicitly present in the text of the report.

6. "The semivariogram-plots before the wound (see the poster) indicate that there is complexity, but after the wound complexity is no longer evident."

Response. After our work on the chaotic structure of the cardiac cycle was substantially complete, we found primary literature indicating that anesthesia, per se, alters this structure. While the wound alters the variogram of the heartbeat duration, it is no longer tenable to interpret the pre-wound data as standing for a normal "baseline." We have thus chosen not to further pursue the interpretation of these spectra at this time.

7. "The statistic A is under some plausible null hypothesis has a Cauchy distribution. The data may give a clue to make the threshold adaptive."

Response. Upon closer examination, the formulas whose ratio yields the signal underlying the alarm are not of mean zero, and hence the ratio is the square root of a noncentral, not a central, F. The corresponding formulation is too complex to sustain feasible estimation in a sample this small.

8. "To use the variance cu-sum techniques (see for example D. Hsu, 1977, Appl. Statist.) once the variances are subject to fluctuations."

Response. The formulas suggested by Prof. Mardia were programmed and applied to individual data series. However, the shifts of variances proved not to be of the form modelled in the article cited or in others in its tradition: they are sporadic, not permanent. We are aware of no published statistic that would accommodate this

difficulty beyond the excursion approach that we are already using.

9. "To use the Mahalanobis cu-sum distance for LVP and RVP of a statistic like A to increase the discrimination power. The various plots show that the correlation is stronger for non-survivors than the survivors."

Response. While prediction of survival goes better in the multivariate context, as demonstrated in the June report, any alarm that takes the form of a divided difference needs to be in a univariate framework, owing to the need for a denominator for the ensuing dimensionless analysis. As the report notes, using ABP is by far the most powerful of these univariate options.

10. "Since the new directions require the alarm to be set before 20 minutes, the statistics can be fine tuned by adopting a suitable extrapolation, e.g., kriging could help since the behaviour of the semivariogram is known."

Response. New data accrued since the March demonstration include valid animals with much lower time to death, viz. 17 minutes and 23 minutes; indeed only half the nonsurvivors survive beyond thirty minutes post-wound. In the presence of so much heterogeneity of outcome it is unpromising to pursue additional constraints on the timing of candidate alarms; instead, we simply report the statistics (which are long-tailed) of the exemplar we have adopted.

Review of Additional Experimental Data Items

Andrew Boyd, MD, Research Fellow, University of Michigan

After the March 17th demonstration Dr. Satava asked for a review of additional experimental data items that are collected to see if any are potential candidates to predict survival vs. death. Our review of the additional data items collected at 500 Hz is included in Fred Bookstein's Report of Statistical Findings. In this addendum we report the results of reviewing data items collected at less frequent intervals (baseline, 5, 15, 30, 60, 90, and 120 minutes post-injury or at death). We evaluated the values from Temperature corrected pH (pHt), Hematocrit (Hct), White Blood Cell (WBC), Platelets (Plt), Prothrombin time (PT), Activated Partial Thromboplastin Time (aPTT), Creatine (Creat), Blood Urine Nitrogen (BUN), Total Protein, Albumin, Glucose, Lactate, Weight, and Blood Loss as a percent of total body weight.

In this data analysis we used 16 animals, which is two more than used in the previous analysis. The two additional animals had incomplete data collected at 500 Hz, but sufficient blood samples were collected to perform this analysis. The blood samples were drawn for all values at baseline (approximately 15 to 30 minutes before the injury), 5 minutes, 15 minutes, 30 minutes, 60 minutes, 90 minutes, and 120 minutes or at death. For some values we have a screening measurement performed days before the experiment, and a prebaseline measurement taken early in the morning of the experiment.

Of the 16 animals, 7 survived for more than120 minutes and 9 died within 120 minutes of injury. One non-surviving animal, died at exactly a15 minutes, so analysis of the lab values at 15 minutes are not included for this animal.

The most promising value showing separation between survival and death was lactate (see Figure 1).

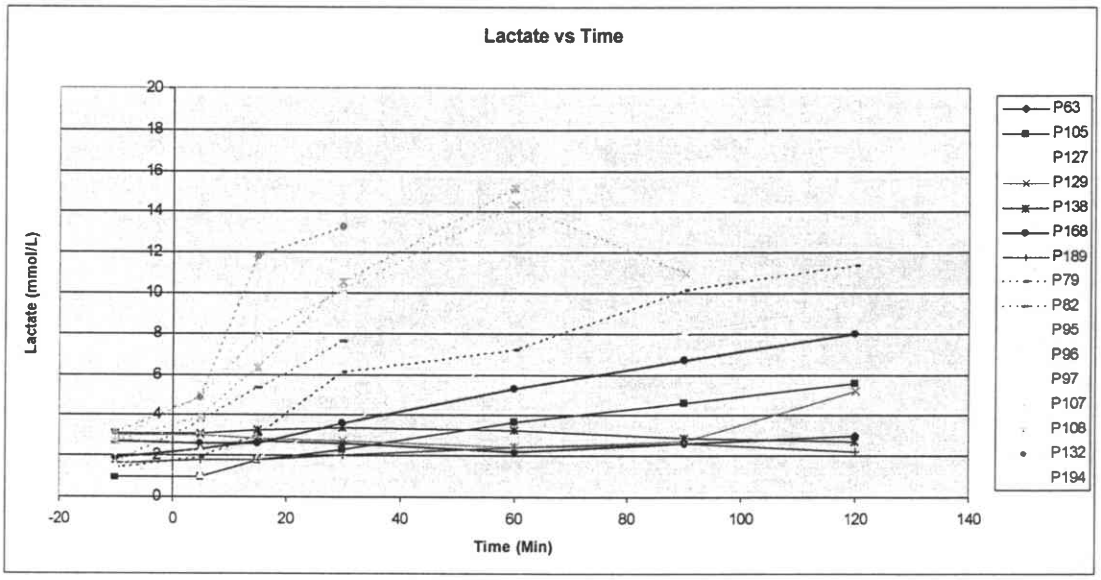

Figure 1: Lactate versus time. Solid Lines survivors, Dashed lines "non-survivors". Last value graphed for non survivors is the death value.

The difference between baseline lactate and lactate at 5 and 15 minutes after injury showed perfect discrimination between survivors and subjects who died (see Figure 2).

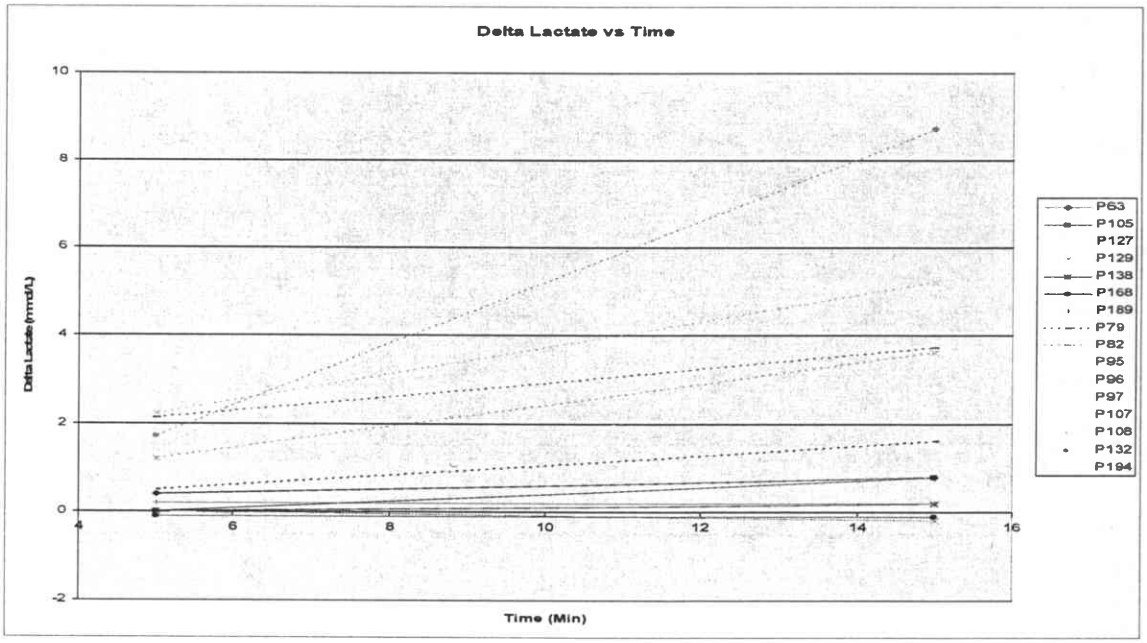

Figure. 2: Delta Lactate versus time. Solid lines are survivors, Dashed lines are "non-survivors"

Lactate can be measured in real time at the Point of Care with Accusport Lactate

Analyzer. This device currently costs $225.00 and weighs 3.75 ounces.

While lactate showed differences, pHt did not help discriminate between the survivors or the non-survivors. Lactate can vary over time with exercise. Additional studies under battlefield situations will be needed to demonstrate normal lactate variation.

Another value that showed initial promise in discriminating the survivors and non-survivors was protein. However, using just the protein values collected before the experiment allowed discrimination between survivors and non-survivors. To help explain the trend we look at Albumin, the most abundant protein in the blood, which did not demonstrate the same discriminating pattern. We looked at weight of the animals to see if the low protein was due to malnourishment. There was no difference in weight of the animals between survivors and non-survivors. And in additional analysis of the animals wounded using probes rather than fragments this trend disappears.

While most trauma protocols are concerned with total fluid loss of the individual, when comparing the measured total blood loss at the end of the experiment as a percentage of the body weight of the subject there was not good discrimination between survivors and subjects that died.

The other values examined, Hematocrit (Hct), White Blood Cell (WBC), Platelets (Plt), Prothrombin time (PT), Activated Partial Thromboplastin Time (aPTT), Creatine (Creat), Blood Urine Nitrogen (BUN), and Glucose, did not provide useful discrimination between survivors and non-survivors.

Virtual Soldier Project Publications

MMVR 2005 Abstracts and Posters

"Analytical Simulation of Penetrating Wounds to the Heart". *R. D. Eisler, S. F. Stone, A. K. Chatterjee*

"A Biologically Derived Computational Approach to Tissue Modeling". *Tim Andersen, Tim Otter, Cap Petschulat, Tom Menten*

"Representing the Holomer on Digital Media: Challenges and Opportunities for Data Representation and Compression". *Thomas G. Menten, Xiao Zhang, Lian Zhu. Abstract and Poster.*

"Creating Models from Segmented Medical Images". *Bill Lorensen, Jim Miller, Dirk Padfield, James Ross*

"Linking Human Anatomy to Knowledgebases: A Visual Front End for Electronic Medical Records". *Stewart Dickson, Line Pouchard, Richard Ward, Gary Atkins, Martin Cole, Bill Lorensen, Alexander Ade*

"A Middleware-based Computing Architecture for Virtual Medicine".
Line C. Pouchard, Richard C. Ward, Michael N. Huhns, Laura Zavala, Karthik Iyer

"A Web-Service Based Computational Environment for Biomedical Computing
Line C. Pouchard". Richard C. Ward, Michael N. Huhns, Laura Zavala, Karthik Iyer. Abstract and Poster.

"Using an Ontology of Human Anatomy to Inform Reasoning with Geometric Models".
Daniel L. Rubin, Yasser Bashir, David Grossman, Parvati Dev, and Mark A. Musen

"Three Dimensional Electromechanical Model of Porcine Heart with Penetrating Wound Injury". *Roy Kerckhoffs, Taras P. Usyk*

"Challenges of Presenting High Dimensional Data to aid in Triage in the Virtual Soldier Project". *Boyd AD, Wright ZC, Ade AS, Bookstein F, Ogden JC, Meixner W, Athey BD*

"The Cardiac Morphometric Markup: a Template for Experimental Cardiology". *Fred L. Bookstein, Ameed Raoof, William Green*

"Tracking Physiological Models by Kalman Filters", *Fred L. Bookstein, Daniel Cook, Jim Bassingthwaighte. Abstract and Poster.*

"Advanced Modeling and Visualization of Cardiothoracic Electrical Fields". *F. B. Sachse, M. Cole, R. M. Kirby, X. Tricoche, C. Johnson. Abstract and Poster.*

"Ontologies of Anatomy and Physiology - Basis for Causal Modeling Standards". Daniel Cook

"Computational Simulation of Penetrating Trauma in Biological Soft Tissues using the Material Point Method". *I Ionescu, J Guilkey, M Berzins, RM Kirby, J Weiss*

"Knowledge-based Anatomical Dynamic Scene Generation in XJ3D". *Wayne V. Warren, James F. Brinkley*

"Amending Dynamic Physiological Models to Represent Pathophysiological States". *Daniel Cook*

"A Highly Integrated Physiology (HIP) Cardiovascular/respiratory Model used to Simulate Cardiac Injury". *Maxwell Neal, James Bassingthwaighte, Taras Usyk, Andrew McCulloch, Roy Kerckhoffs*

MMVR 2005 Papers

Challenges of Presenting High Dimensional Data to aid in Triage in the Virtual Soldier Project. *A. D. Boyd, Z.C. Wright, A.S.Ade, F. Bookstein, J.C. Ogden, W. Meixner, B.D. Athey and T. Morris*

Computational Simulation of Penetrating Trauma in Biological Soft Tissues using the Material Point Method. *Irina Ionescu, Jameus Guilkey, Martin Berzins, Robert M. Kirby and Jeffrey Weiss*

Linking Human Anatomy to Knowledgebases: A Visual Front End for Electronic Medical Records. *Stewart Dickson, Line Pouchard, Richard Ward, Gary Atkins, Martin Cole, Bill Lorensen and Alexander Ade*

Compressing Different Anatomical Data Types for the Virtual Soldier. *Tom Menten, Xiao Zhang, Lian Zhu and Marc Footen*

Using an Ontology of Human Anatomy to Inform Reasoning with Geometric Models. *Daniel L. Rubin, Yasser Bahir, David Grossman, Parvati Dev and Mark Musen*

Three Dimensional Electromechanical Model of Porcine Heart with Penetrating Wound. *Taras Usyk and Roy Kerchoffs*

Journal/Conference Publications

Functionally and Structurally Integrated Computational Modeling of Ventricular Physiology.
Andrew D. McCulloch, Ph.D.
Japanese Journal of Physiology, Submitted 21 July, 2004, accepted.

Linking Ontologies with Three-Dimensional Models of Anatomy to Predict the Effects of Penetrating Injuries. *Rubin DL, Bashir Y, Grossman D, Dev P, Musen MA*
26th Annual International Conference IEEE Engineering in Medicine and Biology, Bethesda, MD, San Francisco, CA 2004.

Using Ontologies with geometric models to reason about penetrating injuries. *Rubin DL, Bashir Y, Grossman D, Dev P, Musen MA.*
Intelligent Data Analysis in Medicine and Pharmacology, Stanford, CA 2004.

Integrating Ontologies with Three-Dimensional Models of Anatomy. *Rubin DL, Bashir Y, Grossman D, Dev P, Musen MA*
Seventh International Protégé Conference, Bethesda, MD, 2004

Linking Ontologies with Three-Dimensional Models of Anatomy to Predict Physiological Effects of Penetrating Injuries.
Rubin DL, Bashir Y, Grossman D, Dev P, Musen MA
NASA Workshop on the Knowledge Integrating Virtual Iron Bird, Monterey, CA, 2004.

An Acoustic Model for Wave Propagation in a Weak Layer. *Michael El_Rahib, ATK-MRC*
Journal of Applied Mechanics, provisional acceptance pending revision.

Transient Waves in an Inhomogeneous Hollow Infinite Cylinder. *Michael El-Raheb,* ATK-MRC
International Journal of Solids and Structures, Accepted with Revision, Feb. 7, 2005

Wave Propagation in a Hollow Cylinder Due to Prescribed Velocity at the Boundary. *Michael El-Raheb*, ATK-MRC
International Journal of Solids and Structures, Accepted March 8, 2005

Transient Respose in a finite Hollow Cylinder from Time-delayed Prescribed Motion at the Boundary. *Michael El-Raheb*, ATK-MRC
Journal of Sound and Vibration, Accepted March 11, 2005

Other Posters and Conference Presentations

Computational Modeling of Tissue Damage from Penetrating Trauma: Linking Geometric Models to Anatomic and Biomechanical Knowledge.
Rubin DL, Bashir Y, Grossman D, Dev P, Musen MA. Invited presentation and poster, InfoRad Theater, Ninetieth annual scientific meeting of the RSNA, Chicago, IL, 2004.

Using 3-Dimensional Models as a Front End for Knowledge. *Gary Atkins (ORNL student intern)* Poster presented on Aug 11, 2004

The Development of Sophisticated Cardiac Models for Use in the Virtual Soldier Project. *Sarah Wing (ORNL student intern)* Poster at ORNL, presented on Aug 11, 2004

Cardiopulmonary Circuit Models for Predicting Injury to the Heart.
Richard Ward presentation at Southeast Section of the American Physical Society in Oak Ridge, November 11, 2004

A Web-based Computer Architecture for the Virtual Soldier
Line Pouchard, Richard Ward, Michael N. Huhns, Laura Zavala, Karthik Iyer
presentation to InterLab 2004 at Oak Ridge National Laboratory, Oct. 28, 2004

Visualization in the DARPA Virtual Soldier Project.
Stewart Dickson, Richard Ward, Alex Ade, Chris Johnson, Greg Jones, Martin Cole, Tom Menten
Abstract Submitted to Digital Human Modeling for Design and Engineering (DHM) meeting in Iowa City June 14-16, 2005

Challenges in Presenting High Dimensional Data to aid in Triage in the DARPA Virtual Soldier Project

Boyd AD, Wright ZC, Ade AS, Bookstein F, Ogden JC, Meixner W, Athey BD
University of Michigan
Morris T, *U.S. Army Medical Research & Material Command, Telemedicine & Advanced Technology Research Center (TATRC)*
adboyd@umich.edu

Abstract. One of the goals of the DARPA Virtual Soldier Project is to aid the field medic in the triage of a casualty. In Phase I, we are currently collecting 12 baseline experimental physiological variables and a cardiac gated Computed Tomography (CT) imagery for use in an prototyping a futuristic electronic medical record, the "Holomer". We are using physiological models and Kalman filtering to aid in diagnosis and predict outcomes in relation to cardiac injury. The physiological modeling introduces another few hundred variables. Reducing the complexity of the above into easy-to-read text to aid in the triage by the field medic is the challenge with multiple display solutions. A description of the possible techniques follows.

1. Problem:

Most battlefield first responders are not given advanced training for interpretation of physiologic parameters and imagery that could aid in the initial triage and treatment of casualties on the battlefield and far forward areas of care. In the DARPA Virtual Soldier Project (VSP), one of the goals is to prototype new capabilities to aid the battlefield medic in the triage of casualties. Twelve physiological variables, in addition to cardiac gated Computed Tomography (CT), will be used to fit physiological models and applied to Kalman filters to aid in diagnosis and predicting outcome. Detailed physiological modeling adds another few hundred variables to the data stream. In Phase I of the VSP, we are focusing on the consequences of injury on cardiac anatomy and physiology. Reducing the complexity of the models, data, and variables into an easy-to-read graphical user interface is the challenge we face to aid triage by the field medic. Creating a usable and informative interface will minimize health impacts by exploiting preventive measures and controls, by providing forward interim essential diagnosis and treatment of patients prior to strategic evacuation, and provide support to other critical health care support services in theater.

2. Methods:

Currently field medics are being trained in the art of casualty triage on a conventional battlefield. One of the underlining principals in this training is: "Triage establishes the order of treatment, not whether treatment is given" [1]. There are four priority classifications of treatment: Immediate, Delayed, Minimal, and Expectant. Immediate—casualties demand immediate treatment to save life, such as in the case of airway obstruction. Delayed—casualties have less risk of loss of life or limb: examples are

open chest wounds without respiratory distress. Minimal—casualties might be self treated, such as a sprain. The last category, Expectant—casualties is only used if resources are limited. This category of casualty includes those so critically injured that only complicated and prolonged treatment can improve life expectancy. This is meant to give a high level overview of the classifications of triage performed by the field medic; details are beyond the scope of this paper.

The other classification the field medics perform is the Medical Evacuation (MEDEVAC) priority of an individual casualty. The five classifications are Urgent, Urgent-Surgical, Priority, Routine, and Convenience. "Urgent" is a classification for casualties whose status cannot be controlled and have the greatest opportunity for survival. "Urgent-Surgical' are casualties needing far-forward surgical intervention to stabilize the patient "Priority" casualties are not stable and at risk of trauma-related complications. "Routine" casualties can be controlled without jeopardizing the patient's condition. The "Convenience" classification is for casualties who are evacuated for convenience, not for medical necessity. Further details of the classification of the MEDEVAC priorities of casualties are located in the 91 Whiskey combat medic training manual [1]. Appreciation of the complex decisions made by the field medic will help shape the following discussion of the possible techniques for the presentation of new material. Other variables not mentioned in the above description of field medic triage decision making which need to be taken into account when calculating time to definitive treatment are tactical and environmental situations, such as the number and location of the injured and the evacuation support capabilities available.

Compaq IPAQ handheld computers equipped with the Battlefield Medical Information System Tactical (BMIST) software are currently deployed world-wide in the field by the US Military Medical Corps [2]. These handhelds interface with an electronic dog-tag, or Personal Information Carrier (PIC), also known commercially as the P-TAG. These electronic dog-tags are capable of storing the soldier's entire electronic health record. BMIST is the point-of-care handheld software the field medic uses to record to initiate a field encounter. The data recorded to the PIC is also compatible with the Composite Health Care System II (CHCS II). CHCS II is the medical information system for the military health system. Since this technology is presently deployed with the field medic, we are limited in the presentation of the data listed above to the screen size of the IPAQ. While in the future the deployed handheld systems will have faster CPUs and more memory, portability and limited screen size will continue to be features of the system.

One goal of the VSP is to provide additional decision support information to the field medic to aid the decision making process. Another goal of the project is the creation of a personalized "Holomer structure" a compilation of all imaging and medical data, for each soldier and enable the transmission of this information to the field medic. Although currently all soldiers have a pre-deployment physical exam, additional measurements will need to be collected for the creation of the Holomer. In creating a Holomer, baseline physiological data of each individual will need to be collected These data are then used to populate the physiological and cardiac models designed by the VSP. Each subject also receives a Computed Tomography (CT) scan. The individual CT scan is processed through an automated segmentation process to define regions of the anatomy. Through the segmentation of the CT scan, personalized parameters of the model can be abstracted [3]. For example, an individual's left ventricular size can be determined through segmentation, and later the individual's left ventricular volume will be integrated into the computer models.

The level of detail and parameters used in the Highly Integrated Physiological (HIP) cardiac models (e.g. elasticity of the ventricle, valve pressure gradients, and baroreceptor firing interval) is beyond the knowledge of clinical care providers [4]. The field medic,

while trained in the triage definitions of blood pressure and heart rate, will probably not be familiar with the interplay of pressure gradients across the heart valves used in HIP model calculations. There are over 12 individual measurable parameters that can be fitted to the cardiac physiology models. The measurements the models require can all be obtained non-invasively. While these data may seem large, there are at least 300 outputs from the models, many of which change during a single heart beat cycle.

While the individual HIP models can accumulate experience by model fitting and model design, the VSP has taken an extended statistical approach to obtain population level trends. The method of reducing this high dimensional parameter space uses a Kalman filtering technique running multiple models with varying injury outcomes [5]. The initial number of validation training experiments is too small to be statistical persuasive, and so a Singular Value Decomposition (SVD) of an individual's physiological trends is being employed. A second validation data set will collect sufficient data to validate against a population, and this will provide confidence intervals and time to death estimates. During the whole process we are validating the trends of the expected injuries against test data. From the full data set we will attempt to make a forecast/prognosis of survival, ventricular fibrillation, and level of exsanguination.

In the above description of the VSP, there are several variables that could be of assistance to the field medic. The baseline physiological data of the individual soldier could be helpful for comparison purposes. The current physiological data on the battlefield could be helpful in triage. The HIP models of the individual's physiological state at the time of injury could also be helpful. For example, the outputs of the HIP models could simulate an ICU monitor, or a three dimensional graph of the SVD could be displayed to view the casualties' physiological states.

While all such displays might be relevant, the field medic must be provided with a display that is both useful and usable. The possible designs of these displays can range from simple color coding and a short text display describing the diagnosis and time to death to full functioning graphs and image displays.

Full functioning graphs and image displays of all of the above mentioned variables would provide the field medic with all of the information possible to make an educated decision on the triage and treatment of casualties (see Figure 1 for image of CT on handheld and see Figure 2 for the display of a few relevant variables from the HIP models of an individual). With more advanced training, the field medic might prefer such comprehensive display systems, but these options must always be balanced with the possibilities of information overload, lack of training, or insufficient time to assimilate the information due to battlefield conditions.

The method of displaying only the text of diagnosis, time to death, and confidence interval, relies heavily on the Kalman filter processing. This method would hide most of the models, physiological parameters, and images from the field medic, providing the field medic with just enough information to make informed triage decisions. Predictions become more confident as more data is collected. Alerts will be displayed on the BMIST handheld when a diagnosis reaches a threshold level of confidence (see Figure 3 for display of handheld of statistical results). The benefit of providing diagnosis and time to death allows the field medic to rapidly make critical decisions about a casualty's triage and treatment. However, introducing confidence intervals into a trauma scenario is an entirely new concept. Additional training would be needed to interpret the confidence intervals of the diagnosis, though this training would not be as extensive as that required for more comprehensive data displays.

The third method of displaying the results of the Virtual Soldier Project outputs (e.g. data, models, and predictions) is a simple color spectrum: Green - soldier normal, Yellow - soldier unstable, and Red would mean either severe physiological distress or death (Figure

4). This system has far less detail than the comprehensive system described above, and is similar to the physiological status monitoring research of the military using the classifications of "Alive," "Dead," or "Unknown" [6]. Reducing the data to a single value may reduce the utility of the interface for the complex decision making of a field medic, and may not provide much additional information beyond their current capabilities. For the specific wounds the VSP modeling, such as penetrating wounds to the heart, a field medic will MEDVAC the patient as "Urgent" or "Urgent-Surgical." In the unfortunate condition of "Expectant," the color system would provide limited additional information.

A Plethysmograph measurement of Heart Rate (HR) and Oxygen Saturation (SaO2) could being incorporated into the BMIST system. . From the data being recorded by the Warfighter Physiological Status Monitoring (WPSM) equipment, the additional data presented to the field medic might also include kilo Calorie (kCal) expenditure and respiration rate (RR) measurements (Figure 5). This screen shows how the data could be presented to the field medic (the area of injury is shown by the X on the body.) A pressure tracing of the arterial blood pressure is also shown in the lower left corner. This display is an example of how to integrate multiple data points into simple graphical user interface while providing enough data for the field medic to make an educated decision.

There are many other possible methods of data display, as well as additional combinations of the above descriptions and measurements that could be shown to the medic. Additional input and collaboration from physicians, medics, and interface/usability specialists will be needed to design the ultimate interface. Because of the critical nature of this software, careful analysis of the interface design by employing standard usability techniques such as GOMS (Goals, Operators, Methods, and Selection), cognitive walkthroughs, task analysis, and formal user testing will be necessary. These methods will ensure that the information and interface presented to the field medic is clear and intuitive, especially in the non-ideal and time-sensitive viewing situations that arise on the battlefield.

3.Results:

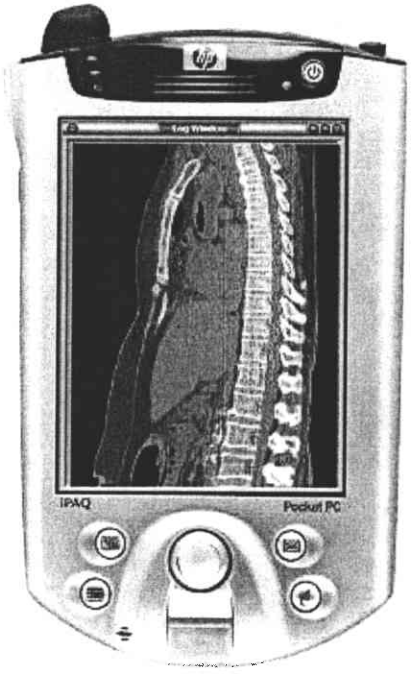

Figure 1. Saggital view of Torso CT Scan on handheld.

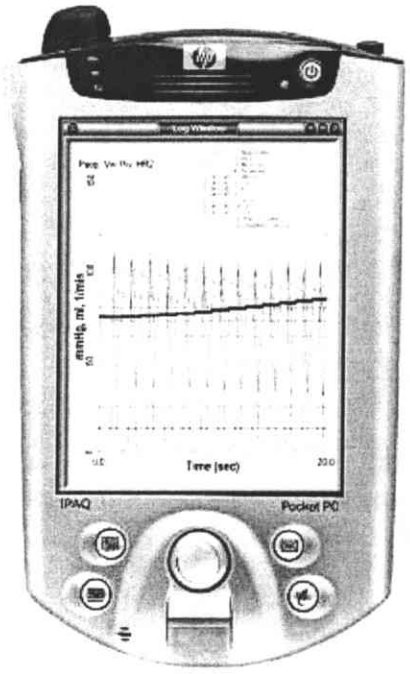

Figure 2. Graphing output of the Highly Integrated Physiological (HIP) models on handheld.

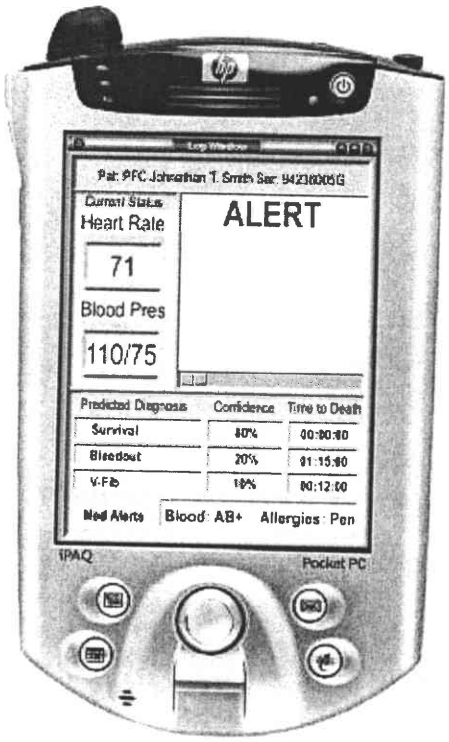

Figure 3. Text display of statistical forcast on handheld.

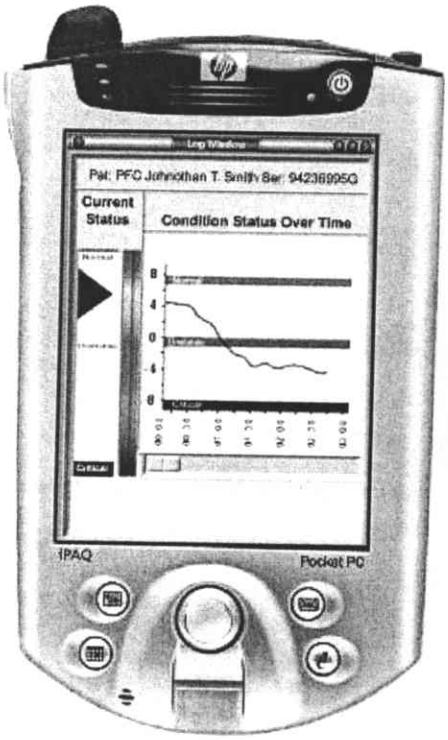

Figure 4. Color display of stability of casualty on handheld.

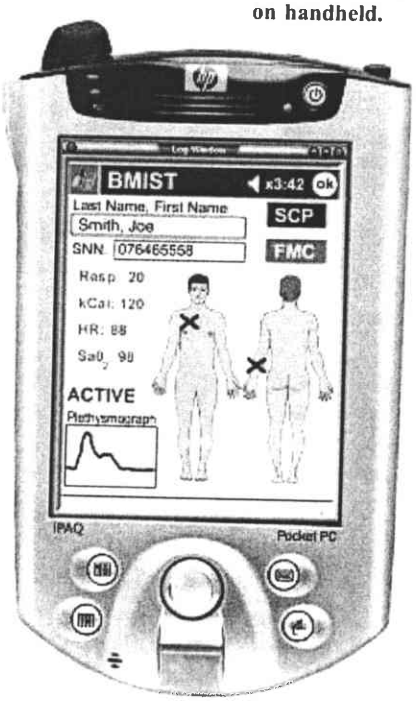

Figure 5. Display of the physiology to be collected in the field near term.

4. Conclusions/Discussion

The results generated by the DARPA Virtual Soldier Project are a good beginning; however, much of the physiology and statistical information generated to date is too abstract for use by the field medic to triage for treatment or MEDVAC priority. Providing the appropriate information, and an appropriate interface for rapid field use, while allowing the medic to incorporate their own judgment on triage decision-making, is the next step in user interface design. The deployment of this technology will need to be accompanied by additional field medic training This triage aid system and the additional information provided will need to be integrated into future triage protocols for the field medic's use. A more intuitive method of displaying the uncertainty of each result/prediction is also needed. While most of trauma protocol is binary decision making, allowing one to rapidly run through the triage protocol, the new information generated by the Virtual Soldier Project will need to be integrated in a careful and responsible manner into new protocols. The final system will have to assist the field medic in the critical decisions that will need to be made under difficult battlefield conditions, especially when multiple casualties require prioritization of evacuation. The experimental validation of this modeling and statistical approach will be published elsewhere.

This work was supported by a grant from DARPA, executed by the U.S. Army Medical Research and Materiel Command/TATRC Cooperative Agreement, Contract # W81XWH-04-2-0012.

Special thanks to Marty Cole from the University of Utah for assistance with figure 4.

5. References:

1. Triage Casualties on a Conventional Battlefield 081-833-0080.
2. Battlefield Medical Information System – Tactical, www.tatrc.org accessed July 14, 2004
3. Lorensen W, Miller J, Padfield D, Ross J, "Creating Models from Segmented Medical Images" MMVR 2005.
4. Neal M, Bassingthwaighte, Usyk T, McCulloch A, Kerckhoffs R, "A Highly Integrated Physiology (HIP) Cardiovascular/Respiratory Model Used to Simulate Cardiac Injury" MMVR 2005
5. Bookstein FL, Cook D, Bassingthwaighte J, "Tracking physiological models by Kalman Filters" MMVR 2005.
6. Savell CT, Borsotto M, Reifman J, Hoyt RW, "Life Sign Decision Support Algorithms" MEDINFO 2004, 2004, 1453-1460.

Computational Simulation of Penetrating Trauma in Biological Soft Tissues using the Material Point Method

Irina IONESCU*[+], James GUILKEY*[++], Martin BERZINS*[‡],
Robert M. KIRBY*[‡], Jeffrey WEISS*[+]
*Scientific Computing and Imaging Institute,
Departments of [+]Bioengineering, [++]Mechanical Engineering,
and [‡]School of Computing, University of Utah

Abstract. The objective of this research was to develop realistic computational models for soft tissues subjected to finite deformation and failure, and to test these models in the context of numerical simulations of penetrating trauma injuries. A transversely isotropic hyperelastic model with strain-based failure criteria was used to represent the behavior of anisotropic soft tissue. The constitutive model was implemented into an existing numerical code based on the Material Point Method (MPM). The penetration of a low-speed bullet through a myocardium material slab was simulated and several wounding scenarios were analyzed and compared. The material symmetry, the type of contact modeled between the bullet and the soft tissue and the bullet speed were shown to have a significant influence on the wound profile.

1. Introduction

Injuries due to penetrating trauma from bullet or knife wounds represent a significant healthcare problem [1]. An improved understanding of the factors that control the extent of tissue damage from these wounds can provide the means to improve diagnosis and treatment. Soft tissue failure (skeletal and cardiac muscle, ligament and tendon, nerve) typically represents a large part of the damage resulting from penetrating trauma [2]. However, the detailed three dimensional prediction of soft tissue failure is complicated by the highly anisotropic nature of the materials as well as the lack of appropriate failure models.

The objective of this research was to develop realistic computational models for soft tissues subjected to finite deformation and failure and to implement and test these models in the context of numerical simulations of penetrating trauma injuries.

2. Methods

The current research focused on modeling penetrating injuries to an analog of the myocardium. A "two-surface" strain-based failure criterion was incorporated into a hyperelastic constitutive model of the myocardium. The myocardium was represented as a composite of matrix and collagen fibers, each failing by different strain-driven failure mechanisms. Bullet penetration simulations of myocardial material slabs were performed using the Material Point Method (MPM) with explicit time integration [3].

2.1 Constitutive model and Failure Criteria

A strain-based failure model was developed for transversely isotropic hyperelastic soft tissues. The myocardium was modeled as a transversely isotropic hyperelastic material, comprised of an isotropic Mooney-Rivlin matrix reinforced by a single fiber family [4]. The local fiber direction was described by a unit vector $\mathbf{a}^0$ that changes direction and length as the material deforms, so that:

$$\boldsymbol{F} \cdot \boldsymbol{a}^0 = \lambda \boldsymbol{a}, \tag{1}$$

where λ denotes the local fiber stretch and $\boldsymbol{F}$ is the deformation gradient tensor. The strain energy function W was written in terms of the matrix and fiber response, respectively:

$$W = F_1(I_1, I_2) + F_2(\lambda), \tag{2}$$

where I_1 and I_2 are the first and second invariants of the right Cauchy-Green deformation tensor. The matrix was modeled using a Mooney-Rivlin model, while the elastic response of collagen fibers was considered exponential in the toe region and linear subsequently [5]:

$$F_1(I_1, I_2) = c_1(I_1 - 3) + c_2(I_2 - 3)$$
$$\lambda \frac{\partial F_2}{\partial \lambda} = \begin{cases} 0, & \lambda < 1 \\ c_3 e^{c_4(\lambda - 1))-1}, & \lambda \le \lambda^* \\ c_5 \lambda + c_6, & \lambda > \lambda^* \end{cases} \tag{3}$$

The five material coefficients to define the transverse isotropy of the above described material have been chosen as follows. The Mooney-Rivlin constants for the matrix were taken as c_1 = 2.1 KPa, c_2 = 0. The elastic fibers were characterized by a constant to scale the exponential stresses in the toe region c_3 = 0.14 KPa, the rate of fiber uncrimping c_3 = 22, and the modulus of the straightened collagen c_5 = 100 Kpa [4]. The stretch at which the collagen fibers straighten was assigned a value of λ^* = 1.4 [4]. The constant c_6 was determined from the condition that the collagen stress is continuous at λ^*. The material was considered as nearly incompressible, with a bulk:shear modulus ratio of 47.62. To represent the type of material symmetry exhibited by the myocardium, the fiber direction $\mathbf{a}^0$ was varied through the thickness of the slab so that fibers rotated clockwise 180° from epicardial to endocardial surface (Fig. 1a).

A strain-based failure criterion was developed to quantify failure resulting from the wounding. The myocardium can be seen as a composite material whose phases, matrix and fibers, have different ultimate strains, the collagen fibers withstanding a higher tensile strain than the matrix. Two modes of failure were represented: matrix failure under shear (Fig. 1b) and fiber failure under tension (Fig. 1c); hence the failure criterion was defined in terms of two failure surfaces. With these assumptions, the Cauchy stress was decomposed as:

$$\boldsymbol{\sigma} = \boldsymbol{\sigma}_{\text{volumetric}} + \boldsymbol{\sigma}_{\text{matrix}} + \boldsymbol{\sigma}_{\text{fibers}} \tag{4}$$

The matrix material was considered to fail locally if the maximum shear strain at a point exceeded 50% strain [6] and the matrix contribution to the stress was annulled:

$$\gamma_{\text{matrix}} > 50\% \quad \Rightarrow \quad \boldsymbol{\sigma}_{\text{matrix}} = 0, \ \boldsymbol{\sigma}_{\text{volumetric}} = 0 \tag{5}$$

If the fiber stretch λ exceeded 40% [5] strain at a point, the fiber was considered failed and its contribution to the total state of stress was annulled:

$$\varepsilon_{\text{fibers}} > 40\% \quad \Rightarrow \quad \sigma_{\text{fibers}} = 0 \tag{6}$$

If both of the above conditions were fulfilled locally, the material point exhibited total failure.

At each material point, the strains in the matrix and fibers were compared with the assigned failure values. A failure flag was defined at each of the particles in the model, to record if and what particular type of material failure may occur. The type of failure and the distribution of failed particles helped to interpret the wound profile.

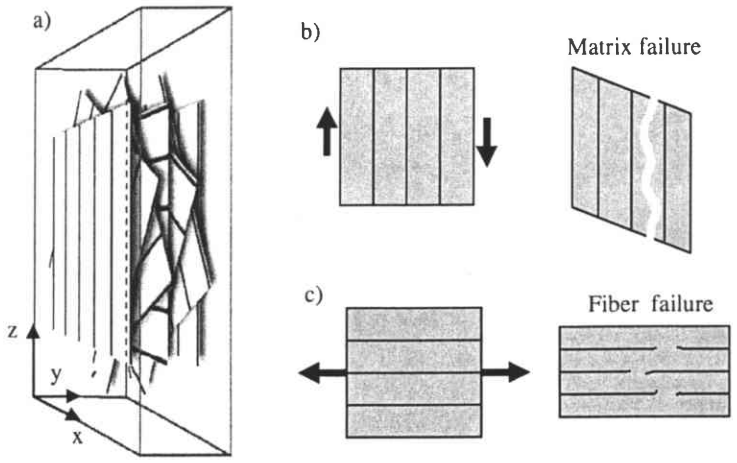

Fig. 1. a) Material symmetry of the myocardial slab. The local fiber direction rotated 180 degrees through thickness of the slab. Failure modes: b) matrix failure via shear strain and c) fiber failure via elongation along the fiber direction.

2.2 Numerical Discretization with Material Point Method

The equations of motion were discretized in space using the Material Point Method (MPM) [3]. Explicit time integration was used. MPM is a particle method for simulations in computational mechanics that is implemented within the Uintah computational framework, a software infrastructure for large-scale numerical simulations [7]. Like other quasi-meshless methods, MPM offers an attractive alternative to traditional finite element (FE) methods [8] because it simplifies the modeling of complex geometries, large deformations and fragmentations that are typical of penetrating trauma to the torso or its components.

2.3 Test problems

To test the failure model, the penetration of a bullet through a slab of myocardium was simulated. A 50×10×50 mm myocardial slab was considered (Fig. 1a). The *x*-*y* and *y*-*z* side boundaries were fixed, while the *x*-*z* faces were free of constraints. A 9 mm diameter bullet was modeled as an elastic-plastic material with neo-Hookean elastic material properties (properties used: bulk modulus K = 117 GPa, shear modulus μ = 53.8 GPa, yield stress 422.6 MPa, hardening modulus 53.8 MPa). The simulations consisted of $1.6 \cdot 10^6$ material points, distributed in a 4x4x4 spacing in each grid cell.

Simulations of a bullet wound to a myocardial tissue sample were performed using several material symmetry models and wounding scenarios. Simulations were performed for bullet velocities in the 'low-speed' range, i.e. less than 1000 ft/s. Low speed projectiles

have been shown to produce most of their damage by crushing the tissue, and almost no damage due to cavitation. Two initial bullet velocities were considered: 150 m/s and 50 m/s. To study the effects of anisotropy on wound profile, an isotropic material slab was also considered and results were compared to that obtained for the anisotropic case. Frictional contact with a coefficient of friction of 0.08 was considered between the bullet and the soft tissue. The matrix, fiber, or total tissue failure were recorded for the each of the simulations.

3. Results

The wound profile in each of the cases showed the damage from the bullet as it passed through the myocardial sample. The wound profile for the case of a bullet with an initial speed of 150 m/s and an anisotropic slab is presented in Fig. 2.

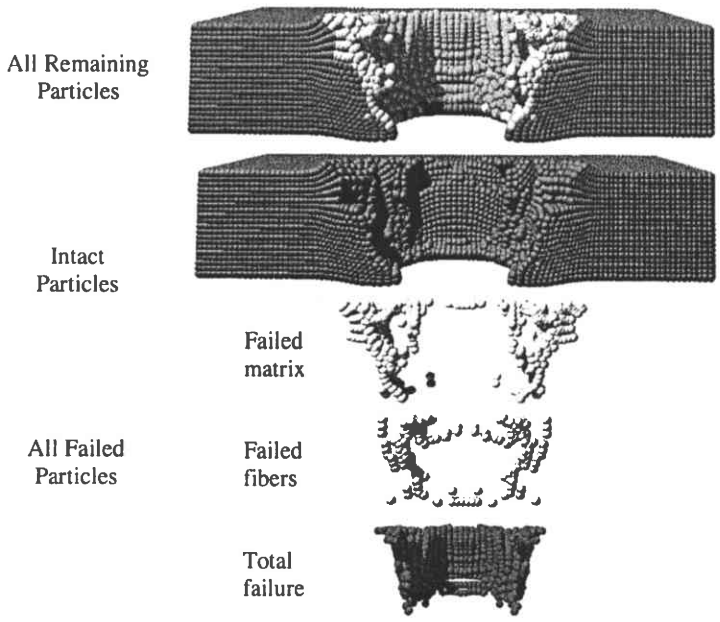

Fig. 2. Wound profile and failed particles for a myocardium slab in which material fibers rotate 180° through thickness. The failed particles are separated by the type of failure undergone: matrix, fiber or total tissue failure.

In all cases the entrance wound had a clean appearance and an approximate circular shape. Total tissue failure was observed in the immediate vicinity of the bullet tract, zones of matrix and fiber failure surrounding the inner total tissue failure zone (Fig. 2). The wound tract diameter increased uniformly from entrance to exit. The exit wound appeared to be elliptic, the fiber alignment in the slab outer layer perhaps influencing its regular shape. The phenomenon of cavitation of the bullet was not observed, due primarily to the small thickness of the slab.

The wound profiles and shape of the exits wounds were different between the anisotropic and isotropic cases (Fig. 3). The shape of the exit wound was elliptic for the case of anisotropic material symmetry (Fig. 3a) and circular for the case of isotropic material symmetry (Fig. 3b).

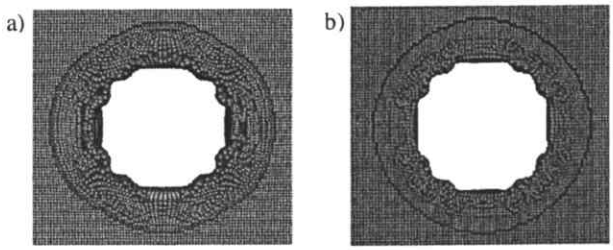

Fig. 3. Effects of anisotropy on the wound profile (exit wound view): a) anisotropic slab; b) isotropic slab (initial bullet speed 50 m/s).

4. Discussion

The results of the test problems are encouraging and can be interpreted in terms of the physics of the bullet penetration.

The wound profile (Fig. 2) showed an approximate circular central area of complete tissue disruption in the bullet path presenting a diameter increase from entrance to exit, as bullets were reported to produce [1]. The adjoining area of 'injured' soft tissue, presented a layered failed particle distribution. As the bullet penetrated the slab, it transferred its energy to the surrounding tissue producing damage. Closest to the wound tract, a layer of particles recording total tissue failure was observed, surrounded by a layer of particles with fiber failure and matrix failure. The damage dissipated with the distance from the bullet tract, as physically expected [1].

Fiber reinforcement was shown to make a difference even for very slow speeds (50 m/s) to the wound appearance (Fig. 3). The isotropic case presented a totally symmetric wound pattern, whereas in the anisotropic case the collagen fibers contribute to the asymmetry of the wound profile.

The jaggedness of the exit wound (Fig. 3) is most likely a result of projecting a circular object (the bullet) to a cartesian mesh. This artifact becomes less prominent with increasing grid resolution. Future work will investigate the use of higher order interpolation, which is also likely to improve the results.

It is understood that the predictions of failure from these simulations will clearly depend on the assumptions associated with the failure model. Future research will consider alternative myocardial material models [9] and failure properties. Beyond this, the approach of using MPM with constitutive models that explicitly represent failure in composites may be useful for large-scale simulations of injuries to the torso that affect multiple organs. Preliminary large-scale simulations of the entire torso, including bones and soft tissue organs, have yielded encouraging results. Others have reported on the use of MPM for modeling material failure and accommodating structural failure under impact [10]; this research demonstrates the feasibility of using MPM for computational modeling of soft tissue failure associated with penetrating wounds.

References

[1] Bartlett CS, *'Clinical Update: Gunshot Wound Ballistics'*: Clin Orth and Rel Research, 2003; 408:28-57

[2] Eisler RD, Chatterjee AK, Burghart GH, *'Simulation and modeling of penetrating wounds from small arms'*: Stud Health Technol Inform, 1996; 29:511-22.

[3] Sulsky D, Chen Z, Schreyer HL, *'A particle method for history dependent materials'*: Comp Meth Appl Mech Eng, 1994, 118:179-196.
[4] Humphrey JD, Strumpf RK, Yin FC, *'Determination of a constitutive relation for passive myocardium: II. Parameter estimation'*, J Biomech Eng., 1990; 112(3):340-346.
[5] Weiss JA, Maker BN, Govindjee S., *'Finite element implementation of incompressible, transversely isotropic hyperelasticity'*: Comp Meth Appl Mech Eng, 1996; 135:107-128.
[6] Hunter PJ, McCulloch AD, ter Keurs HE, *'Modelling the mechanical properties of cardiac muscle'*: Prog Biophys Mol Biol, 1998; 69:289-331.
[7] Parker S, *'A Component-based Architecture for Parallel Multi-Physics PDE Simulation'*: Intl Conf on Comp Science (ICCS2002) Workshop on PDE Software, 2002, April 21-24.
[8] Chen Z, Brannon R, *'An Evaluation of the Material Point Method'*: Sand Report, SAND2002-0482.
[9] Guccione JM, McCulloch AD, Waldman LK, *'Passive material properties of intact ventricular myocardium determined from a cylindrical model'*: J Biomech Engng, 1991; 113:42-55.
[10] Chen Z, Hu W, *'Recent Advances in First-Principle Simulation of the Transition from Continuous to Discontinuous Failure under Impact'*, 16th Eng Mech Conf of the ASCE, Seattle, Washington, 2003, July 16-18.

Acknowledgement

This work was supported by a grant from the DARPA, executed by the U.S. Army Medical Research and Materiel Command/TATRC Cooperative Agreement, Contract # W81XWH-04-2-0012.

Linking Human Anatomy to Knowledgebases: A Visual Front End for Electronic Medical Records*#

Stewart Dickson, Line Pouchard, Richard Ward
Oak Ridge National Laboratory
Gary Atkins, *Fisk University*
Martin Cole, *University of Utah*
Bill Lorensen, *GE Global Research*
Alexander Ade, *University of Michigan*

Abstract. A new concept of a visual electronic medical record is presented based on developments ongoing in the Defense Advanced Research Projects Agency Virtual Soldier Project. This new concept is based on the holographic medical electronic representation (Holomer) and on data formats being developed to support this. The Holomer is being developed in two different visualization environments, one of which is suitable for prototyping the visual electronic medical record. The advantages of a visual approach as a front end for electronic medical records are discussed and specific implementations are presented.

1. Introduction

The President's Information Technology Advisory Committee June 2004 report calls for federal leadership to create needed technological innovations "to enable development of 21st century electronic medical records" [1]. In July, Department of Health and Human Services Secretary Tommy Thompson and National Coordinator for Health Information Technology David Brailer announced a framework for strategic action for delivering "consumer-centric and information-rich" health care [2]. Concepts important to this vision for 21st century medical care include: medical information moves with consumers, care is delivered electronically as well as in person, medical care is provided with fewer medical errors and with less variation utilizing the electronic medical record. The report expresses the hope that "sophisticated decision-support tools that help identify treatments....best suited to a given patient would be available to help reduce unnecessary treatments and to ensure prevention procedures, both of which will result in better outcomes [2]." One component of that vision for future medical care is decision support tools to help the physician in diagnosis. Another component needed is a visual user interface that collects varied types of information, for example text, charts, imagery such as CT and MRI, and three-dimensional (3D) reconstructions. We refer to this component as the Visual Electronic Medical Record (VEMR).

The Defense Advanced Research Projects Agency (DARPA) Virtual Soldier Project (VSP) is working on these issues in the context of providing medical care on the battlefield. The

DARPA VSP is investigating methods to predict outcomes from wounding that will revolutionize medical care for the soldier. This research is expected to have a significant impact on civilian medical care. The goal of the VSP is prediction of outcomes of penetrating wounds, which will be based on comparison of results from complex mathematical models with experimental data. In the not too distant future, this will allow prediction of consequences of a wound using a soldier's post wound imaging along with pre-wound clinical data including baseline x-ray CT.

To provide a visual environment for encapsulating the results of this prediction, the VSP is developing a holographic medical representation (or Holomer) to be used to connect a 3D model of the soldier's body, based on x-ray CT, with anatomical and physiological information for purposes of improving medical diagnosis and treatment both on and off the battlefield. This visual-based prediction and medical record for the soldier can become, in the not too distant future, a first prototype for the VEMR, where a patient's vital signs, imagery, and other information is keyed to the locations in the anatomy of the medical complication. We discuss here the development of the VSP Holomer and its modifications for use in the civilian medical community as a VEMR.

2. Method

To address the problem of linking visual representation of the anatomy to a knowledgebase of information and prediction tools, the VSP is developing the Holomer. The Holomer will connect a 3D model of the soldier's body, based on X-ray CT, with anatomical and physiological information for purposes of improving medical diagnosis and treatment both on and off the battlefield. The Holomer coupled with predictive modeling software will facilitate a new level of integration in medical procedures and create a prototype for a truly interactive VEMR.

Figure 1. Thorax anatomy displayed in the SCIRun visualization environment. The blue sphere is the 3D widget (probe).

To demonstrate the Holomer concept, a 3D model was created from segmented and annotated National Library of Medicine Visible Human male photographic data [3]. The 3D model is displayed in SCIRun [4] using existing volume visualization techniques (Fig. 1), and is linked to knowledgebases using a specially developed module, referred to as the HotBox. The HotBox interacts with the geometric model via a 3D widget (the probe or blue sphere seen in Fig. 1) which is user controlled such that it can be moved to any location in the model. This provides the user with a means to input the location of interest. Given the location from the user controlled 3D widget, the HotBox implements the linkage to the 3D anatomy and the many levels of information provided in the knowledgebases.

Presently the information returned by the Hotbox is the tissue at the location of the probe and the adjacent tissues (see Fig. 2). In the future, this information could also include a list of a patient's allergic reactions to drugs or allergens, or records of visits to the physician, or vital signs recorded during a hospital stay.

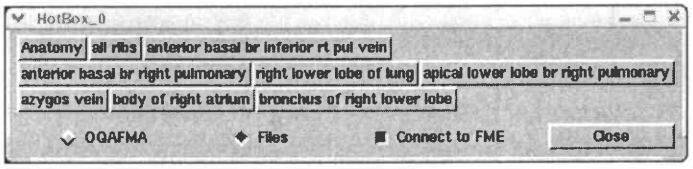

Figure 2. The Hotbox interface returns the tissue located at the 3D widget (probe), i.e. right lower lobe of the lung, and all adjacent tissues.

Different forms of information content from text-based to 3D imagery can be linked in the Holomer, thus providing a unique visual-based electronic medical record which the medic or physician can utilize for purposes of diagnosis and treatment. The specific focus of this unique visual approach to medical informatics in the VSP is penetrating wounds to the heart.

To develop the SCiRun-based Holomer, we have prototyped this concept using a visual front end developed using Visualization ToolKit (VTK) software [5]. The Visible Human (male) photographic data were used to create surface models and associated label maps for the thorax. For a soldier who has received a projectile wound, the wound is described using an Extensible Markup Language (XML) file standard based on a wound ontology developed by the VSP. Information in the wound ontology is used to show the regions of stunned and ablated tissue as the projectile enters the body and either lodges in an organ or exits the body. Information on the properties of the wounded tissue and various physiological and tissue material properties can be entered by the physician and stored in this XML file to control the display of the region of wounded tissue. Figure 3 demonstrates a wound to the left ventricle of the heart, where the wound track is shown as a series of concentric cylinders representing tissue which has been ablated or simply stunned by the projectile.

In the future the wound description could be obtained from comparison of post trauma ultra sound (US) with baseline US or X-ray CT imagery for this soldier. The combination of the comparison of the wounded region and the baseline would then be automatically encoded into the wound ontology instance or wound XML file that controls the visual interface. Existing XML standards for medical records (such as HL7) would also be used for integrating standard medical records data. We will demonstrate how this can be done in connection with the wound ontology XML developed under the VSP.

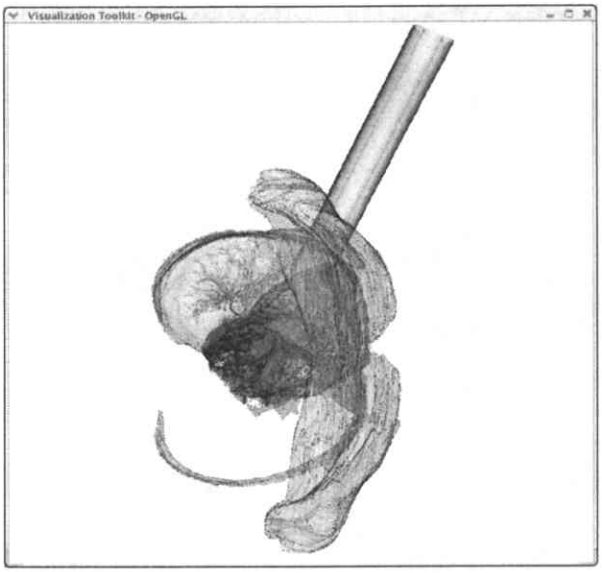

Figure 3. VTK-based visualization environment for prototype development. The wound has the projectile stopping in the left ventricle.

When applied to a patient in a hospital setting, the interface could capture and display the patient's vital signs, making it possible for the physician to keep a detailed record of the patient's physiological responses during surgery or during recovery. The visualization of the physiological data (see Fig. 4) is accomplished using standard ICU monitor software, which we demonstrate here with simple Tcl/Tk plotting program which interfaces with the original VTK Holomer.

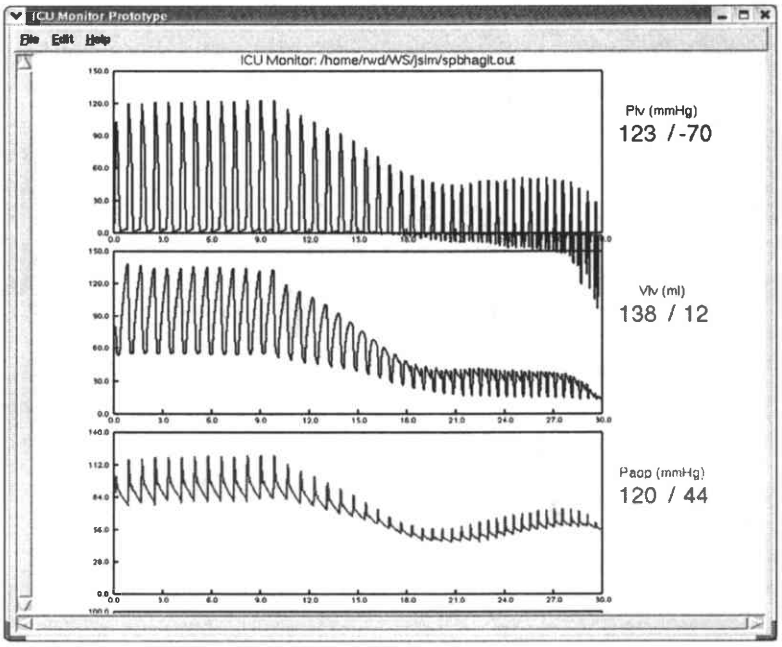

Figure 4. The prototype ICU Monitor screen displaying physiological results, in this case, for a model of the physiology in the thorax with injury to the left ventricle at 10 s. In clinical medical implementation, this display would show patient vital signs.

The advantage of this simple demonstration based on VTK is that it can be used to develop more sophisticated interfaces such as the SCIRun visualization interface being developed for the VSP and for prototyping a civilian VMER which is based on electronic medical record standards, yet incorporating new standards for the visual representation of information, such as the wound ontology XML and the physiological (vital signs) data format.

3. Results

A prototype of the HotBox has been developed within SCIRun. The HotBox, which comes from animation software [6], is a menu activated by placing the cursor at a particular point in the 3D space (anatomy). The menu provides the user with a multitude of options based on retrieving the anatomical structure at the spatial point from the "Master Anatomy" list created from segmenting and labeling the Visible Human data. For example, a menu item can be selected to invoke a connection, by Web services, to the Foundational Model of Anatomy [7] to provide the anatomical structures adjacent to the structure at the cursor location.

Physiological information from measured vital signs will also be available via the Web service from the HotBox menu. In addition, we have also developed an alternative approach for connecting to knowledgebases that is independent of SCIRun and can be run on PC platforms. In this approach the 3D images are created using VTK [5].

We have found that the VSP VTK-based Holomer concept has been useful in developing the more sophisticated visual Holomer based on SCIRun. It can also serve as a useful prototype development environment for a civilian version of the VEMR integrating significant new concepts such as the wound ontology XML and the physiological (vital signs) monitor with standard patient medical record. Further, the Holomer coupled with predictive modeling software will facilitate a new level of integration in medical procedures and create a prototype for a truly interactive VEMR.

4. Conclusions

We described the prototype concept of the HotBox, which can be integrated into the SCIRun Holomer to provide a link between 3D anatomy and knowledgebases of anatomical information, physiological response (vital signs) data and other standard medical records. We further describe a development environment based on VTK which has been used to prototype the SCIRun-based Holomer. The VTK-base visual interface is platform independent and has served well as a prototype for a new type of visual electronic medical record, one based on a 3D representation of the individual soldier or patient, providing unique visual access to the patient or soldier's condition, be it a wound or a disease.

The prototype Holomer being developed within the VSP is a unique demonstration of the concept of a "Visual Electronic Medical Record". Visual electronic medical records will improve the ease and use of medical records data by the physician, providing an interactive interface to records based on 3D anatomical reconstruction of the patient. Using the Holomer, a physician or medic will have access, at the touch of a button, to all available information about a patient or wounded soldier, greatly facilitating accurate and efficient diagnosis of medical conditions.

References

[1] President's Information Technology Advisory Committee (PITAC) Report, "Revolutionizing Health Care through Information Technology", June 2004 , (http://www.itrd.gov/pitac/reports/20040721_hit_report.pdf)

[2] Tommy G. Thompson and David J, Brailer, "The Decade of Health Information Technology: Delivering Consumer-centric and Information-rich Health Care: Framework for Strategic Action, July 2004, (http://www.hhs.gov/onchit/framework/).

[3] See: National Library of Medicine Web site: http://www.nlm.nih.gov/research/visible/.

[4] SCIRun: A Scientific Computing Problem Solving Environment, Scientific Computing and Imaging Institute (SCI), 2002 (http://software.sci.utah.edu/scirun.html)

[5] See: http://www.kitware.com/vtk.html

[6] Pouchard, LC, Dickson, SP (2004) "Ontology based three-dimensional Modeling for Human Anatomy" ORNL Technical Report ORNL/TM-2004/139

[7] Rosse, C. and Mejino, JLV. (2003) "Ontology for Bioinformatics: The Foundational Model o of Anatomy". *Journal of Biomedical Informatics 36*:478-500.

*This work was supported by a grant from the DARPA, executed by the U.S. Army Medical Research and Materiel Command/TATRC Cooperative Agreement, Contract # W81XWH-04-2-0012.

#The submitted manuscript has been authored by the U.S. Department of Energy, Office of Science of the Oak Ridge National Laboratory, managed for the U.S. DOE by UT-Battelle, LLC, under contract No. DE-AC05-00OR22725. Accordingly, the U.S. Government retains a non-exclusive, royalty-free license to publish or reproduce the published form of this contribution, or allow others to do so, for U.S. Government purpose.

Medicine Meets Virtual Reality 13
James D. Westwood et al. (Eds.)
IOS Press, 2005

Compressing Different Anatomical Data Types for the Virtual Soldier

Tom MENTEN, Xiao ZHANG, Lian ZHU and Marc FOOTEN
Crowley Davis Research, 280 South Academy Ave, Eagle, ID 83616

Abstract. The Virtual Soldier Project endeavors to represent the baseline physiology and anatomy of a soldier using disparate but linked digital data types (http://www.virtualsoldier.net). Processing these data for storage, transmission and encryption requires different capabilities than are typical in a single codec. These representation and coding issues are illustrated and future directions are indicated.

1. Challenges of Representing Disparate Data Types

The first generation of the "Virtual Soldier" makes use of multiple data components integrated by a common ontology. For example, physiological information may include electrocardiograms and other measurement data, while medical history may appear as ASCII or XML data. Computed Tomography (CT) data may be represented in DICOM format, while anatomical structures are represented by triangle mesh surface models (e.g. as VTK files.) Segmentation maps, indicating the anatomical structure of various regions of image files may be represented as PNG files. Thus the first generation of the Virtual Soldier incorporates many disparate data types that together encompass the baseline data. For machine readable data of this kind to be useful in the treatment of the individual, it must be easily and quickly accessible and interpretable by a variety of computational platforms and of immediate diagnostic use by a variety of medical personnel. No single compression method and thus no previously available codec (CODer/DECoder) can handle these various data types and requirements. A single integrated codec is being developed to more efficiently store and transmit these data components, and to respond to future more integrated data representations. We illustrate the progress of this effort with two different anatomical data types.

2. Coding of Whole Body Computed Tomography

A whole body CT scan of a person is represented by a series of about one thousand grey scale images that are typically stored in a DICOM, pixel based format. This representation permits direct imaging at a specified resolution, but typically these files are very large and slow to transmit. More efficient coding of these data is currently best achieved by wavelet transforms using the JPEG2000 standard [1]. Additional techniques such as Region of Interest (ROI) and scalable coding can greatly improve the storage and transmission of this kind of data.

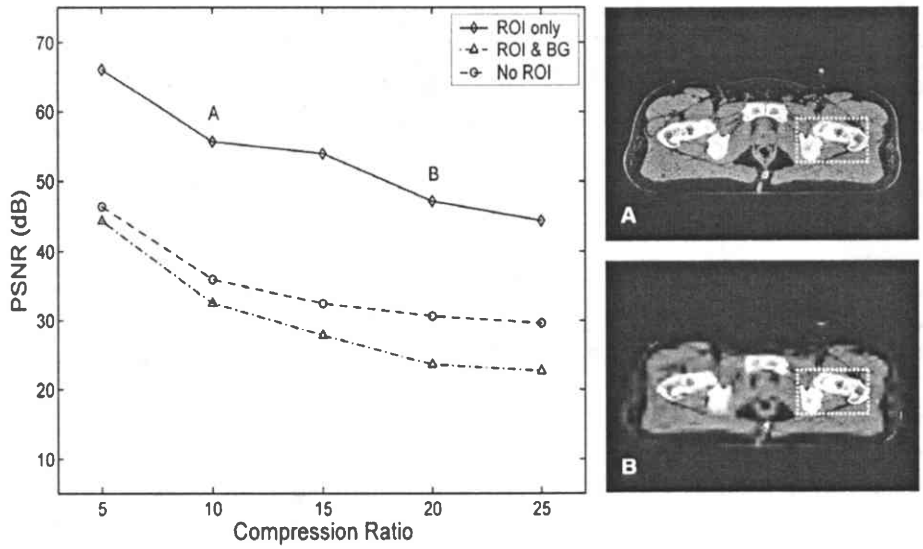

Figure 1. ROI Coding of Visible Human data (ROI, dashed boundary; PSNR, peak signal/noise ratio.) (A) CT scan whole body cross section, CR=10. (B) same image, CR=25. In (B) the image quality of the ROI (dashed boundary) is preserved while the surrounding area is degraded.

Region of Interest (ROI) coding [2] permits preferential allocation of storage or transmission resources to prioritized image regions. As a result, the observed image degradation is very modest in the Region of Interest, while the image quality of the non prioritized region is sacrificed. Figure 1 illustrates this benefit. 40db is widely considered to be a high fidelity representation (though this does NOT define "diagnostic image quality"). The ROI region never falls below 40db PSNR even at the high overall compression ratio (CR) of 25. In contrast, the PSNR of the non ROI coded image degrades rapidly to below 40 well before reaching a CR of 10. The ROI exhibits a gain of more than 20db from non ROI encoded format. ROI coding can be used to variously prioritize storage space or bandwidth. For example, using currently available project hardware, transmission of a whole body CT scan might require over 15 minutes. The use of ROI can facilitate the fast scan and selection of images and their subsequent transmission in less than 30 seconds.

3. Coding of 3D Anatomical Structures

Individualized anatomical structures derived from the computed tomography provide immediate visual and machine identification of anatomical structures [3]. For the Virtual Soldier project, the native format of these 3D triangle mesh geometry files is the VTK file. This very general data structure facilitates shape distortion, coloration and other manipulations but it is also inefficient for storage and transmission. In contrast, a much more efficient representation expands to yield the same structure [4]. Figure 2 illustrates the large reduction in file size (and correspondingly reduced transmission time) result-

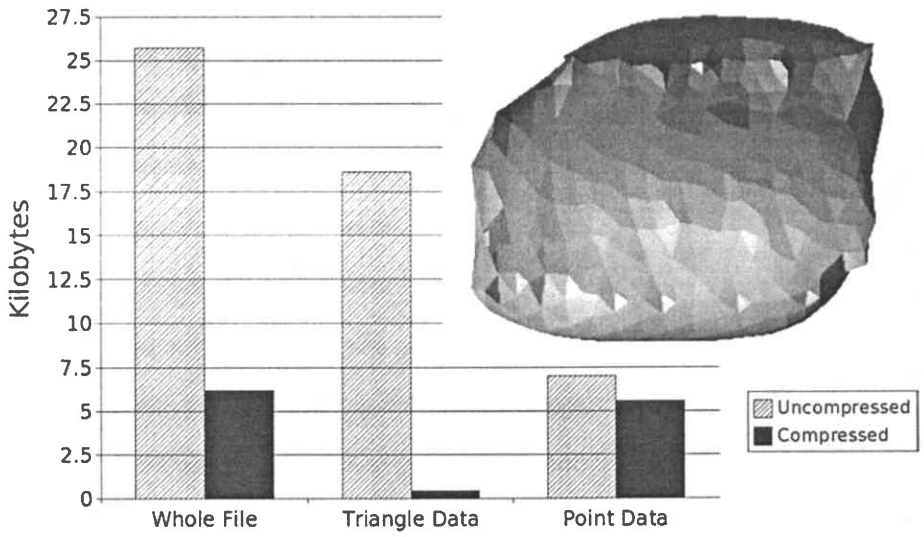

Figure 2. Compression of "right_nipple.vtk"; 3D model constructed from Visible Human dataset.

ing from efficient representation of the mesh geometry: the description of mesh topology was reduced losslessly by a factor of 46, leading to an overall compression ratio of 5:1. In another more extreme example, more efficient representation of a 90MB file, that would require more than 90 seconds to transmit, reduced the transmission time to less than 10 seconds.

4. Summary and Future Directions

We anticipate increasing complexity of data for the Virtual Soldier in terms of its anatomical and physiological scope, incorporation of encryption into the codec and an increasing level of integration of the baseline data components. While early focus has significantly emphasized the heart, we anticipate that future efforts will consider the human thorax more generally, incorporating still more data types while integrating others. Much of the value of the Virtual Soldier derives from preprocessing that identifies specific useful information in the basic data – inferred anatomical structure, for example. Future research will develop methods and tools to produce increasingly integrated and efficient representation of the basic and derived anatomical and physiological baseline information in ways that facilitate both human and automated use.

Acknowledgements

This work was supported by contract #W81XWH-04-2-0014 (DARPA) and DAMD17-02-2-0049 (TATRC).

Data used in figures were provided by the Visible Human Project of the National Library of Medicine, and by William Lorensen, General Electric Research.

References

[1] Adams, M. and F.Kossentini.(2000) Jasper: A Software-Based JPEG-2000 Codec Implementation, and Proceedings of ICIP 2000.

[2] Christopoulos,C.,Askelof,J. and M.Larsson (2000) Efficient Region of Interest Coding Techniques in the Upcoming JPEG2000 Still Image Coding Standard, Proceedings of IEEE, 2000 p41-p44.

[3] Lorensen,W., Miller,J., Padfield,D. and J. Ross (2004) Creating Models from Segmented Medical Images. Medicine Meets Virtual Reality 13. IOS Press, Amsterdam.

[4] Rosignac,J. (1999) Edgebreaker: Connectivity compression for triangle meshes IEEE Transactions on Visualization and Computer Graphics, Vol. 5, No. 1, pp. 47-61.

Medicine Meets Virtual Reality 13
James D. Westwood et al. (Eds.)
IOS Press, 2005

Using an Ontology of Human Anatomy to Inform Reasoning with Geometric Models

Daniel L. RUBIN, Yasser BASHIR, David GROSSMAN,
Parvati DEV and Mark A. MUSEN
Stanford Medical Informatics, Stanford, California 94305-5479 USA
e-mail: rubin@smi.stanford.edu

Abstract. The Virtual Soldier project is a large effort on the part of the U.S. Defense Advanced Research Projects agency to explore using both general anatomical knowledge and specific computed tomographic (CT) images of individual soldiers to aid the rapid diagnosis and treatment of penetrating injuries. Our goal is to develop intelligent computer applications that use this knowledge to reason about the anatomic structures that are directly injured and to predict propagation of injuries secondary to primary organ damage. To accomplish this, we needed to develop an architecture to combine geometric data with anatomic knowledge and reasoning services that use this information to predict the consequences of injuries.

1. Introduction

Medical assessment of penetrating injuries is a knowledge-intensive task. Rapid and effective medical intervention in response to civil and military-related injuries is crucial for saving lives and limiting disability [1]. Accurate assessment of penetrating injures is challenging because the spatial relationships among anatomic regions can be complex, and potential damage to some vital structures may not be recognized. Intelligent tools that can integrate patient-specific geometric data and anatomic knowledge to inform care providers about internal injuries could improve patient care and outcomes.

Dramatic advances have occurred in recent years in the quality and resolution of cross sectional imaging modalities such as computed tomography (CT), which now serve a critical role in evaluating an injured subject [2]. While these images contain detailed spatial information, they lack any knowledge of anatomy, such as the identity of anatomic structures and relationships among anatomic structures. To develop computerized tools to support diagnosis of traumatic injury, these tools need to be provided both with patient-specific geometric data and anatomic knowledge. Anatomic knowledge adds meaning to geometric data, labeling regions in space with particular organs, relating organ parts and subparts to other anatomic structures, and identifying critical structures that may affect patient prognosis and management.

The Virtual Soldier project is being undertaken by the U.S. Defense Advanced Research Projects agency to use both geometric data derived from images and canonical anatomic knowledge to aid the rapid diagnosis of penetrating injury [3]. The vision for the project is that each soldier would carry pre-injury CT images and other relevant base-

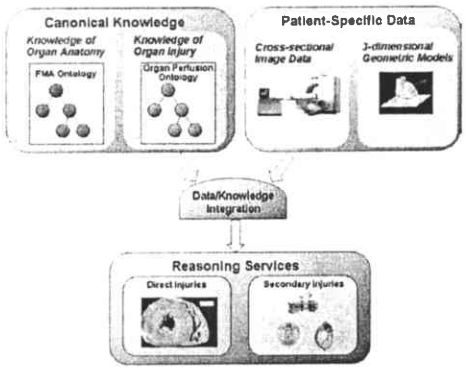

Figure 1. Architecture for integrating patient-specific data and canonical knowledge to reason about penetrating injury.

line clinical data on a small memory card. At the time of an injury, an information system would read the baseline data and offer advice about the nature of the wound, the patient's prognosis, and requirements for therapy.

Our goal is to develop a methodology to automate reasoning about penetrating injuries using canonical knowledge combined with specific subject image data. Our approach is to build three dimensional geometric models of subjects from segmented images. We link regions in this model to concepts in two knowledge sources: (1) a comprehensive ontology of anatomy containing organ identities, adjacencies, and other information useful for anatomic reasoning, and (2) an ontology of regional perfusion containing formal definitions of arterial anatomy and corresponding regions of perfusion. We are developing computerized reasoning services that can determine the organs that are injured given particular trajectories of projectiles, whether vital structures—such as a coronary artery—are injured, and can predict the propagation of injury ensuing after a vital structure is injured. This methodology may improve the speed and accuracy of rapid assessment of penetrating injury.

2. Methods

The architecture of our system to integrate patient-specific geometric data with anatomic knowledge in ontologies is shown in Figure 1. Canonical knowledge sources are ontologies containing detailed knowledge of organ anatomy as well as knowledge about structural anatomic dependencies that are important for predicting secondary injuries. Patient-specific data consist of cross-sectional imaging data and three dimensional geometric models that are built from these data. Data structures in our software architecture integrate the canonical knowledge and patient-specific geometric data, making both available to applications (reasoning services) that can perform intelligent tasks such as predicting direct and secondary injuries (Figure 1).

2.1. Knowledge of Anatomy

We use the Digital Anatomist Foundational Model of Anatomy (FMA) as our knowledge source of anatomy [4]. The FMA is a comprehensive ontology of human anatomy, con-

taining more than 70,000 concepts that describe the elements of canonical human morphology in a clear and consistent manner. It provides declarative descriptions of detailed anatomic structures in a computationally accessible format; it is modeled using the Protégé ontology-management environment (http://protege.stanford.edu), and it adheres to the conventions of the OKBC frame language [5].

Intelligent applications can be developed that use this representation to reason about anatomic relationships, such as inferring organ injuries related to a projectile trajectory. This is accomplished by reading anatomic concepts ("classes" in the ontology), and their attributes ("slots" on the class). Slots can be atomic types (such as integers, strings, etc.) or other classes (e.g., the "part-of" slot contains classes that have a partonomic relationship with the given class). Components in the FMA that we use in this project include organ names, compositionality (partonomy relationships), organ adjacencies, containment, and continuities. The FMA is particularly useful because it contains anatomic structures that may be too small to be visible on images, and thus may not be present in geometric models. This knowledge is useful for a reasoning service to deduce possible injury to small but vital structures that are adjacent to visible structures.

2.1.1. Knowledge of Organ Injury

While the FMA is an excellent knowledge source describing morphology and composition of anatomic structures, it lacks physiological knowledge. For example, it does not describe the regions of myocardium supplied by branches of the coronary arteries. Such knowledge is needed to reason about secondary organ damage—injury that occurs to particular anatomic structures as a result of damage to other structures.

We built an ontology of coronary artery anatomy and regional myocardial perfusion (Figure 2) using the Web Ontology Language (OWL) [6]. The OWL classes contain formal definitions, represented using logical statements, specifying the necessary and sufficient conditions ("assertions") for class inclusion. For example, the definition of the lateral wall of the left ventricle includes assertions specifying all of the branches of the coronary arteries that ordinarily supply it (Figure 2). This ontology specifies the segments and continuities in coronary arteries, the composition of myocardial regions (e.g., the left ventricle has anterior, lateral, posterior, apical, and septal parts), and it describes the myocardial regions supplied by particular coronary arterial branches. This ontology also defines the coronary arteries as being "critical" structures—anatomic structures that result in damage to other structures if they are injured.

The class definitions contained in the OWL ontology allow reasoning services to deduce important physiological consequences of arterial injury. First, the ontology encodes the knowledge that arterial branches downstream from an injured branch will be functionally impaired. Second, the ontology contains knowledge of all arterial branches feeding a myocardial region. There are also definitions about when a region is totally or partially ischemic (a region is totally ischemic if all arteries supplying it are impaired, and is partially ischemic if one ore more arteries are not impaired).

2.2. Geometric data sources and model

We obtained segmented images from the Visible Human project [7]. These comprise serial cross-sectional images from a cadaver, and they are analogous to reconstructed images available from CT on live patients. Each organ in these images was labeled,

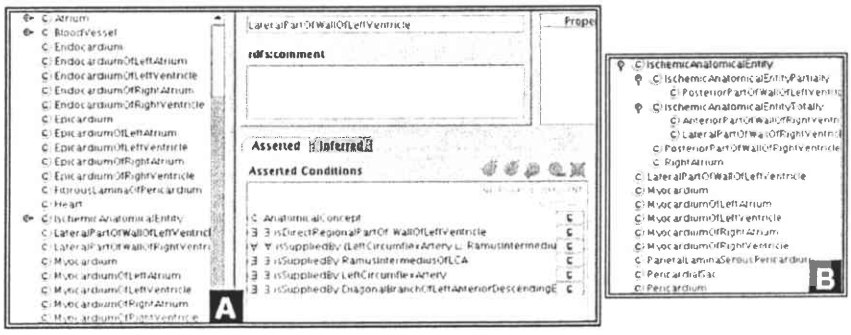

Figure 2. A) Ontology (in OWL) of coronary anatomy and regional myocardial perfusion. Classes of anatomic structures are shown on the left panel, and formal definitions of the concepts are shown on the right. The class "Lateral part of wall of left ventricle" is seen to be defined by six assertions, all necessary conditions for this class. Some of these assertions specify the coronary arterial branches that supply this structure. B) OWL ontology updated with the knowledge that the second segment of the right coronary artery has been injured. After automatic classification, new classes (light color) appear, suggesting the ischemic regions of myocardium that occur as a consequence of the right coronary artery injury.

and these labels were used to map these anatomic structures to corresponding anatomic classes in our ontologies.

The segmented two-dimensional images cannot be used directly for spatial anatomical reasoning; a three-dimensional representation of patient anatomy must be built from these images to reason with a three-dimensional projectile trajectory. We used the Insight Toolkit (ITK; http://itk.org) to build solid three-dimensional tetrahedral mesh models from the serial segmented images of the chest (Figure 3). These geometric mesh models created from the imaging data represented the three-dimensional coordinates of anatomic structures in space. Collections of vertices in the mesh model were labeled with FMA class names to identify the anatomic structures that they represent. Thus, the mesh model of patient-specific geometry is linked to canonical anatomic structures in the FMA (as well as the OWL ontology of myocardial perfusion). This provides a software architecture that makes patient-specific geometric data and canonical anatomic knowledge accessible to intelligent applications such as reasoning services.

We created a graphical visualization application that displays patient-specific geometric data models (Figure 3). Spatial objects comprising sets of tetrahedrons that represent particular organs or organ parts are displayed in different colors. A specified trajectory of penetrating injury can be incorporated into the geometric model as an additional spatial object. Rendering methods are applied to highlight the surface regions and internal volume of organs affected by the penetrating injury and area surrounding it.

2.3. Reasoning services

We have initially implemented two applications that use patient-specific geometric data and anatomic knowledge sources to perform useful reasoning capabilities: (1) a tool to determine which organs are injured by a penetrating injury ("Direct Injury Reasoner"), and (2) a tool that determines whether any vital structures are injured and the consequences of such injury ("Secondary Injury Reasoner").

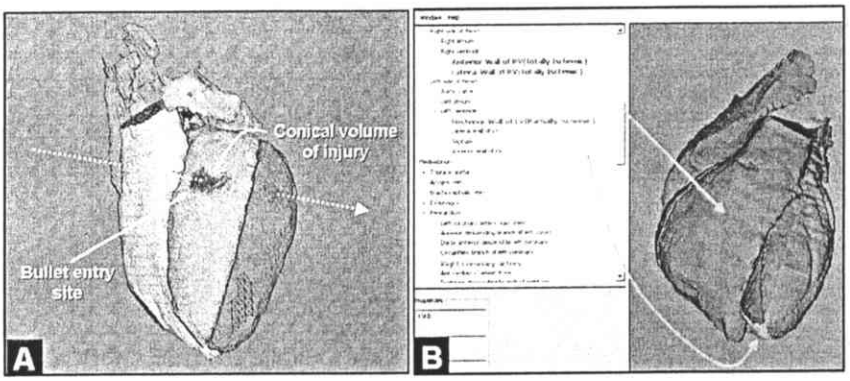

Figure 3. Three dimensional geometric model of the heart linked to FMA ontology of anatomy. A) A bullet path was described to traverse the patient, and predicted primary injuries are displayed (shaded conical region). B) Reasoning about secondary injury in graphical user interface display of patient anatomy and geometry. Shaded volumes in the geometric model (right) correspond to anatomic structure classes in the FMA ontology (left). An OWL reasoning service deduces parts of the myocardium that are injured consequent to a coronary artery injury, shown as highlighted structures in the FMA (left) and shaded parts of heart (right).

The Direct Injury Reasoner takes as input an entry wound and an exit wound on the patient, and it deduces the anatomic structures that have been injured by direct impact by the penetrating injury (or from shock waves in close proximity to the trajectory of injury). To accomplish this task, the Direct Injury Reasoner defines a parametric trajectory path of the penetrating injury using the observed wounds and three-dimensional tetrahedral mesh model of the patient derived from the image data. This trajectory is used to infer the organs that are injured by the projectile. The Secondary Injury Reasoner takes as input a list of anatomic structures that have been injured by the penetrating injury (deduced by the Direct Injury Reasoner) and it deduces additional tissue injury that are occurring or will occur as a consequence of the primary injuries. To accomplish this task, the Secondary Injury Reasoner uses the OWL ontology of anatomic knowledge to assert primary injuries and deduce secondary injuries by applying an automatic classifier to the ontology.

If any critical structures have been injured, the OWL ontology is updated with this information by creating new assertions (new subclasses indicating the structures that have been injured). For example, if the second segment of the right coronary artery (RCA) is injured, then a new subclass of the ontology class "functionally impaired blood vessel" would be created by the Secondary Injury Reasoner.

After the Secondary Injury Reasoner asserts the damaged critical structures, it calls a classification engine that updates the OWL ontology, inferring new classes and relationships given the asserted knowledge and pre-existing class definitions. In the case of the RCA injury above, new subclasses of the injury classes "IschemicAnatomicEntity-Totally" and "IschemicAnatomicEntityPartially" would be created, indicating that regions of myocardium are ischemic secondary to the RCA injury (Figure 2B). These secondary injuries would be deduced by the Secondary Injury Reasoner, and are used to update the graphical display of patient geometry (Figure 3B). In our example, the Secondary Injury Reasoner would deduce that most of the right ventricle and portions of

the left ventricle and right atrium were ischemic as a result of the injury to the second segment of the right coronary artery.

By combining the Direct and Secondary Injury Reasoners in series, we can begin with baseline patient imaging data and patient wounds and rapidly deduce the anticipated extent of direct and secondary injuries.

3. Discussion

Our goal is to develop intelligent applications to improve the ability of practitioners to assess and triage injured patients. Creating geometric models of internal anatomic structures alone is not adequate to solve this task. Images of patient anatomy may contain labels, but there is little knowledge in those labels beyond a name. By enhancing geometric models with anatomic knowledge, it is possible to build reasoning services that can predict the primary and secondary injures caused by a trajectory of injury that crosses different parts of the geometry. In the future we plan to add physiological knowledge to these models so that our reasoning services can inform practitioners about the physiological significance of injuries. Such information could be useful in developing decision support tools that assist practitioners prioritize treatment options for patients at the scene of injury.

Previous work on assessing penetrating injury focused on developing simulation environments and teaching aids to assist in assessing penetrating injuries [8]. Such teaching activity is valuable to give practitioners general experience managing trauma cases, but this differs from our approach which provides patient-specific information. Ogunyemi and colleagues developed a system that calculates the probabilities of organ injuries using a canonical geometric model of human anatomy [9]. This can be a helpful guide to typical injuries, but the geometric models are not specific to a particular patient. Our reasoning services operate on patient-specific representations of knowledge, an approach we believe is advantageous since there can be considerable variation in anatomy among people.

A limitation of our current approach is that it does not incorporate uncertainty relating to injuries. We are currently extending our representation to represent different possible trajectories, from which probabilities of organ injury can be calculated. Another limitation is that we have not yet performed a formal evaluation of our approach. We are now planning these evaluation studies.

Acknowledgments

This work was supported by a contract from DARPA, executed by the U.S. Army Medical Research and Materiel Command/TATRC Cooperative Agreement, Contract W81XWH-04-2-0012. We are grateful to Cornelius Rosse for many years of exciting discussion and collaboration. This work was also supported by the Protégé resource, under grant LM007885 from the U.S. National Library of Medicine.

References

[1] West JG, Trunkey DD, Lim RC. Systems of trauma care. A study of two counties. Arch Surg 1979;114(4):455-60.

[2] Alkadhi H, Wildermuth S, Desbiolles L, Schertler T, Crook D, Marincek B, et al. Vascular emergencies of the thorax after blunt and iatrogenic trauma: multi-detector row CT and three-dimensional imaging. Radiographics 2004;24(5):1239-55.

[3] Virtual Soldier Project. http://www.virtualsoldier.net/summary.htm. 2004.

[4] Rosse C, Mejino JL, Jr. A reference ontology for biomedical informatics: the Foundational Model of Anatomy. J Biomed Inform 2003;36(6):478-500.

[5] Noy NF, Musen MA, Mejino JLV, Rosse C. Pushing the envelope: challenges in a frame-based representation of human anatomy. Data & Knowledge Engineering 2004;48(3):335-359.

[6] Smith MK, Welty C, McGuinness D. OWL Web Ontology Language Guide, http://www.w3.org/TR/owl-guide/. 2004.

[7] Ackerman MJ, Yoo TS. The Visible Human Data Sets (VHD) and Insight Toolkit (ITk): Experiments in Open Source Software. Proc AMIA Symp 2003:773.

[8] Freeman KM, Thompson SF, Allely EB, Sobel AL, Stansfield SA, Pugh WM. A virtual reality patient simulation system for teaching emergency response skills to U.S. Navy medical providers. Prehospital Disaster Med 2001;16(1):3-8.

[9] Ogunyemi OI, Clarke JR, Ash N, Webber BL. Combining geometric and probabilistic reasoning for computer-based penetrating-trauma assessment. J Am Med Inform Assoc 2002;9(3):273-82.

Medicine Meets Virtual Reality 13
James D. Westwood et al. (Eds.)
IOS Press, 2005

Three Dimensional Electromechanical Model of Porcine Heart with Penetrating Wound Injury

Taras USYK and Roy KERCKHOFFS
Department of Bioengineering, The Whitaker Institute for Biomedical Engineering, University of California, San Diego, La Jolla, CA 92093-0412, USA
e-mail: taras@bioeng.ucsd.edu

Abstract. The aim of this study is development a prototype computational model of the pig heart that can be used to predict physiological responses to a penetrating wound injury. The pig has been chosen for this model studies because it shares many anatomical similarities with humans.

Three-dimensional cubic Hermite finite element meshes based on detailed measurements of porcine anatomy combined into an integrated anatomic model. The pig ventricular model includes detailed left and right ventricular geometry and myofiber and laminar sheet orientations throughout the mesh [1].

The cardiac mesh was refined and monodomain equations for action potential propagation solved using well-established collocation-Galerkin finite element methods [2]. The membrane kinetic equations for the action potential model was based on detailed cellular models of transmembrane ionic fluxes and intracellular calcium fluxes in canine ventricular myocytes and human atrial myocytes. We modified the anisotropic myocardial conductivity tensor on the endocardial surface of the ventricles by making use of a surface model fitted to measured of Purkinje fiber network anatomy.

The mechanical model compute regional three-dimensional stress and strain distributions using anisotropic constitutive laws referred to local material coordinate axes defined by local myofiber and laminar sheet orientations. Passive myocardial mechanics modeled using exponential orthotropic strain energy functions. Active systolic myocardial stresses computed from a multi-scale model that uses crossbridge theory to predict calcium-activated sarcomere length- and velocity-dependent tension filament tension.

Since the electrical and mechanical models use a common finite element mesh as the parent parametric framework and both models are solved within our custom finite element package, it is straightforward to couple these models, as we have recently done for a model of coupled ventricular electromechanics [3].

We apply the coupled electromechanical model to predict alterations in regional diastolic and systolic wall mechanics associated with rhythm disturbances and possible arrhythmias with decreased blood volume, tamponade, myocardial injury, and regional ischemia caused by a penetrating wound.

1. Introduction

The heart is a complex three-dimensional structure in which the biophysics of myocyte excitation and the mechanics of crossbridge interaction are coordinated to produce ven-

tricular pumping. Much is known about the cellular basis of the cardiac action potential and the uniaxial mechanics of cardiac muscle contraction, but relating these properties to the regional pattern of activation and mechanics in the intact ventricles remains a difficult problem. While some variables, such as regional strains and epicardial activation patterns have been measured in the intact heart [4], practical experimental methods for mapping three-dimensional distributions of other important variables such as stress, strain energy, or transmembrane potential are still not available.

The pig has been chosen for these model studies for the same reason that many investigators have used the pig as an experimental model system; namely that it is a well characterized experimental model for cardiovascular physiology and pathophysiology, and it shares many anatomical similarities with humans.

Cardiac function of the heart with penetrating wound injury causes regional alterations in stress strain and material properties, rhythm disturbances and possible arrhythmias with decreased blood volume.

A recent computational model of normal electromechanics [3] and the effects of ventricular pacing [5,6] showed good agreement with experimental measurements in anesthetized dogs. The goal of present study was to develop and validate a numerical electromechanical model of the pig heart and investigate how penetrating wound injury effect on global cardiac function and regional stress strain distribution during cardiac cycle. Such model will be useful tool in diagnostic and treatment soldiers with penetrating wound injury.

2. Methods

Three-dimensional model of porcine left and right ventricular anatomy with a detailed Purkinje fiber network, myofiber and sheet architecture was based on measurements [1]. The resulting 90 – element tricubic Hermite mesh was refined to obtain 720 – element mesh, which had 3042 degrees of freedom and was used as the computational domain for simulating passive inflation, electrical impulse propagation and active contraction of the left and right ventricles. The injured region was chosen at left ventricular free wall. The shape of this region was assumed cylindrical.

In the present analysis, the resting myocardium was modeled as a nonlinear, orthotropic and nearly incompressible material [7]. The passive properties of myocardium were taken from previous study [7] on the dog heart. Stiffness of injured region was increased by 20%, since we assume that passive property of the injury were stiffer, similar to severe ischemic region. We model penetrating wound injury similar to ischemic model described earlier by Mazhari et al [8]. Pressure boundary conditions were specified on the left and right ventricular endocardial surfaces, with left ventricular end diastolic pressure 11.0 mmHg, which was consistent with experimental observation.

Nonlinear membrane ionic kinetics was modeled using the two-variable modified FitzHugh-Nagumo [9,10] equations, and impulse propagation was modeled using a monodomain formulation [9,10]. The contribution of the Purkinje fiber network to ventricular conduction was modeled by adding an extra diagonal diffusion tensor, representing conductivity along the Purkinje fibers [3] on the lumenal surfaces of the endocardial elements. Electrical activation time was defined as the instant when transmembrane potential reached 40 mV and it was used to initiate regional systolic tension development

following a constant delay of 8.4 ms [11]. This latter time (electrical activation time plus 8.4 msec) we refer to as "contractile activation time". In order to model electrical propagation, we applied an initial stimulus at the left and right bundle brunch of Purkinje fiber network, located on the left and right ventricular side of the septum, similar to our earlier model of normal activation [3]. Diffusion coefficients were chosen same as in previous model [3], but we apply zero diffusion in injured region of the heart.

The model of active contraction includes length-, time- and calcium-dependent active contractile stresses with transverse active stress components [7]. To model active contraction in injured region myofiber calcium sensitivity was reduced with a step transition across the injured boundary [8,12].

A Windkessel model for arterial impedance was coupled to ventricular pressure and volume to compute the hemodynamic boundary conditions. Ventricular cavity volume constraints were imposed during the isovolumic phases [3]. The formulation and solution of the electromechanical model have been described in detail previously for the case of normal activation [3] and ventricular pacing [5,6].

3. Results

The calculation of the model of passive and active mechanics required 650 Mb of main memory and ran for approximately one hour and 8 hours respectively on a single processor of a Silicon Graphics Origin 2100. The model of electrical propagation required 1.76Gb of main memory and ran for approximately 12 hours on this platform.

The convergence of the reaction-diffusion problem for electrical impulse propagation is determined in part by the kinetics of the ionic model, which determines the sharpness of the wavefront upstroke. Hence, ionic models with faster kinetics than the FitzHugh-Nagumo model used by us do require additional spatial mesh refinement. Adopting a more detailed membrane kinetics, with a realistic upstroke rate, require approximately 96000 elements mesh, which increase calculation time approximately by 3000 times. To make such model practical it is necessary to parallelize the model code, which will require modifications to the algorithm such as imposing boundary conditions explicitly and using parallel solver.

The time for 90% activation of the left ventricle was 55 ms for normal activation after external simulation of the His bundle. Excitation spreads rapidly from the His bundle to the right and left bundle branches and significantly slower through the rest of the myocardial tissue. Wavefront progress around the cavity is much more rapid then the spread toward the epicardium. Those results agree with experimental activation data from long-axis sections of the human heart [13]. Figure 1 shows initial activation time during normal activation (*a*) and activation of the model with penetrating wound injury (*b*). In the model with penetrating wound injury activation time at septal and right ventricular wall are similar to normal activation. At left ventricular free wall excitation spreads around the injured region with no activation at the center of it.

Figure 2 shows that during mitral valve closure there were smaller fiber strains due to stiffer material properties of the injured region. During active contraction there were significantly larger fiber strains at the wounded region (See Figure 2). Computed strains show that the tissue shortened rapidly at the early activated regions and shortening was preceded by prestretching of the tissue. This prestretching was a result of passive stretch-

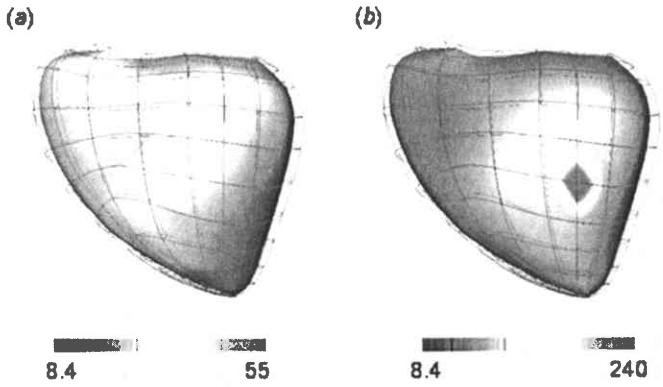

Figure 1. Initial activation time (ms) during normal activation (*a*); activation of the model with penetrating wound injury (*b*).

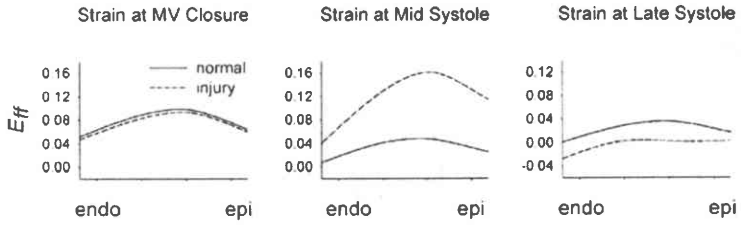

Figure 2. Fiber strains at left ventricular free wall at the location of injury during mitral valve (MV) closure, mid systole and late systole with reference state at the beginning of diastole.

ing of the late-activated regions in response to the contraction of the tissue activated earlier. At the injured region we found no contraction and passive stretching was significant due to contraction of surrounded tissue. Figure 3 represent circumferential, longitudinal and radial strain components during mitral valve closure, mid systole and late systole. At mid systole circumferential and longitudinal strain components were significantly larger for model with penetrating wound injury than for normal model, because of absent active forces at the wounded area.

4. Future work

A penetrating wound injury will most likely result in e.g. blood loss, tamponade, increasing heartbeat frequency, and a change in contractility. To account for these effects the finite element model will be integrated with a complex circulatory model, developed at the University of Washington [14], which contains the following sub-models: 1) varying elastance models for the atria (for a realistic preload) [15]; 2) pericardial load (for cardiac tamponade) [16]; 3) systemic and pulmonary circulations (for a realistic afterload) [17]; 4) baroreceptors (for the feedback on beating frequency/contractility) [16]; 5) ventilatory exchange (for pleural pressure acting on pericardium) [17] and 6)

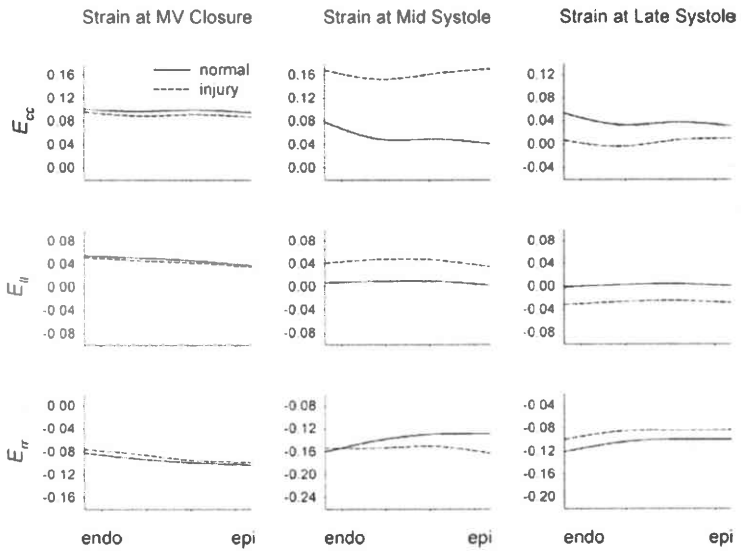

Figure 3. Circumferential, longitudinal and radial strains at left ventricular free wall at the location of injury during mitral valve (MV) closure, mid systole and late systole at the beginning of diastole.

blood/tissue gas exchange and blood O_2/CO_2/pH handling (for feedback on beating frequency/contractility).

The coupling between the finite element model and the circulatory model will take place through the right and left ventricular cavity pressures. Generally, throughout the whole cardiac cycle, cavity pressures will be estimated for each new timestep and prescribed both in the finite element model and circulatory model. When the difference in cavity volumes from the finite element model (V_{FE}) and the circulatory model (V_{circ}) is small enough, the next timestep will be entered. Otherwise, a new pressure will be estimated using dp/dV relations from both models. This iteration cycle will be repeated until V_{FE}–V_{circ} is small enough.

5. Conclusion

This study represent computational electromechanical model of the porcine left and right ventricles during normal conditions and with penetrating wound injury. Depending on the area and location of the injury such a model can define impact from penetrating wound on the cardiac function and can give prediction to physician how severe this impact is.

Acknowledgements

This work was supported by a grant from the DARPA, executed by the U.S. Army Medical Research and Materiel Command/TATRC Cooperative Agreement, Contract # W81XWH-04-2-0012.

References

[1] Stevens C, Hunter PJ. Sarcomere length changes in a model of the pig heart. Prog Biophys Molec Biol 82:229-241, 2003.

[2] Rogers JM, Courtemanche M, McCulloch AD. Finite element methods for modeling impulse propagation in the heart. In: Panfilov AV, Holden AV, editors. Computational Biology of the Heart. Sussex: John Wiley and Sons, Ltd.; 1996.

[3] Usyk TP, LeGrice IJ, McCulloch AD. Computational model of three-dimensional cardiac electromechanics. Comput Visual Sci. 4(4):249-257, 2002.

[4] Moore CC, Lugo-Olivieri CH, McVeigh ER, Zerchouni EA. Three-dimensional systolic strain patterns in the normal human left ventricle: characterization with tagged MR imaging. Radiology. 214: 453-466, 2000.

[5] Usyk TP, McCulloch AD. Electromechanical model of cardiac resynchronization in the dilated failing heart with left bundle branch block. Journal of electrocardiology. 36: 57-61, 2003.

[6] Usyk TP, McCulloch AD. Relationship between regional shortening and asynchronous electrical activation in a three-dimensional model of ventricular electromechanics. Journal of Cardiovascular Electrophysiology. 14:196-202, 2003.

[7] Usyk TP, Mazhari R. and McCulloch AD Effect of laminar orthotropic myofiber architecture on regional stress and strain in the canine left ventricle. J. Elasticity. 61: 143-164, 2000.

[8] Mazhari R., McCulloch AD. Integrative models for understanding the strucural basis of regional mechanical dysfunction in ischemic myocardium. Annals of Biomedical Engineering. 28: 979-990, 2000.

[9] Rogers JM, McCulloch AD. A Collocation-Galerkin finite element model of cardiac action potential propagation. Transactions on Biomedical Engineering. 41: 743-757, 1994.

[10] Rogers JM, McCulloch AD. Nonuniform muscle fiber orientation causes spiral wave drift in a finite element model of cardiac action potential propagation. Journal of Cardiovascular Electrophysiology. 5: 496-509, 1994.

[11] Wyman BT, Hunter WC, Prinzen FW, McVeigh ER. Mapping propagation of mechanical activation in the paced heart with MRI tagging. Am J Physiol. 276(3) (Heart Circ. Physiol): 881-891, 1999.

[12] Allen DG, Orchard CH. Myocardial contractile function during ischemia and hypoxia. Circ. Res. 60: 153-168, 1987.

[13] Durrer, D, van Dam RT, Freud GE, Janse MJ, Meijler FL, Arzbaecher RC: Total excitation of the isolated human heart. Circulation;41(6):899-912, 1970.

[14] Neal M, Bassingthwaighte J., Usyk T, McCulloch A, Kerchoffs R. A highly integrated physiology (HIP) cardiovascular/respiratory model used to simulate cardiac injury. MMVR13: The Magical Next Becomes the Medical Now. January 26-29, 2005 The Westin Long Beach Hotel Long Beach, California (in press).

[15] Rideout VC. Mathematical computer modeling of physiological systems. Englewood Cliffs, NJ: Prentice Hall, 1991, 261 pp.

[16] Sun Y, Beshara M, Lucariello RJ, Chiaramida SA. A comprehensive model for rightleft heart interaction under the influence of pericardium and baroreflex. Am J Physiol Heart Circ Physiol. 272: H1499H1515, 1997.

[17] Lu K, Clark JW, Ghorbel FH, Ware DL, Bidani A. A human cardiopulmonary system model applied to the analysis of the Valsalva maneuver. Am J Physiol Heart Circ Physiol. 281: H2661H2679, 2001.

Analytical Simulation of Penetrating Wounds To the Heart

R. D. Eisler, S. F. Stone, A. K. Chatterjee
rde18@columbia.edu

ATK Mission Research Corporation
Applied Mechanics and Material Sciences Group
Laguna Hills, California

Problem. The present effort develops an analytical simulation of a user prescribed low velocity fragment penetrating the heart. Three models corresponding to different generic fragment geometries are developed in which projectile kinematics during tissue penetration, dynamic pressure distributions about the projectile and transient tissue response in the wake of the projectile (along with the final wound tract geometry) are analytically modeled.

Analytic simulations are compared with ballistic experiments involving a subset of the projectiles modeled. Tissue displacement and disruption and more subtle forms of tissue response – e.g. transient ion gradient upset which affects cardiac bioelectric fields and heart contraction – are considered. Finally, the problem of conducting ballistic experiments and analytical models in surrogate materials and extrapolating model results to human tissue is discussed.

Method. The methodology entails using instrumented targets with surrogate materials that phenomenologically mimic physical processes evoked by projectile-tissue interaction during ballistic experiments. Surrogate material properties and constitutive relations are parametrically varied to determine effect on projectile terminal ballistics and target material response.

Hydrocode models are developed for the surrogate materials where material properties and constitutive relations are well understood. These models are developed to elaborate on the phenomenological details of ballistic experiments where measurements from in situ instrumentation are ambiguous or unavailable.

Analytical models are then developed to describe target response in terms of varied properties. These models are correlated with ballistic experiments and hydrocode models using material properties of the surrogate materials. The models are then exercised using available material properties of human tissue. Available tissue properties of interest include quasistatic Young's modulus, viscosity, and density of the tissue. These are different than the dynamic properties and constitutive models used in the parallel hydrocode studies.

The analytic models used to simulate the wound tract are fourfold and describe: (1) the motion of the projectile center-of-mass and projectile rotational kinematics, (2) the dynamic pressure distribution about the projectile, (3) propagation of the dynamic pressure distributions about the projectile to the wound tract boundary, and (4) transient response of the wound tract boundary, accumulation of inelastic strain, and the resting dimensions of the wound tract boundary – i.e., final wound tract geometry.

Conclusion. For low velocity penetration, much of the significant tissue damage and final wound tract dimensions are due to the radiated stress waves and transient tissue displacement occurring in the wake of the projectile, well after projectile passage, as opposed to the initial "cutting action" of the projectile which would, for example, tend to occur with a stab or puncture wound.

Acknowledgement. This work was supported by the DARPA *Virtual Soldier Program* and executed by the U.S. Army Medical Research and Materiel Command/TATRC Contract # W81XWH-04-C-0084 dated 1 March 2004.

A Biologically Derived Computational Approach to Tissue Modeling

Tim Andersen, Tim Otter, Cap Petschulat, Tom Menten; Crowley Davis Research
tim@cdres.com

Our approach to tissue modeling incorporates biologically-derived concepts into a computational framework. The general strategy is: 1) to construct rule sets containing biologically derived primitives that give rise to higher order properties; and 2) to evolve a synthetic genome capable of producing a target object using the biologically derived primitives.

In simulation, we have captured one of the most basic features of living organisms, the capacity for self-repair. A relatively simple encoded object, a 64-cell cube, can repair itself both during development (while the cube is being built) and after its phenotype has become fully formed, stabilized in an apparently static state. Once wounded, the cube reveals that the capacity for self repair remains a latent property, and the cube can recover fully from substantial damage (loss of ~30% of its cells). Our self-repairing cube demonstrates that it is possible to produce simulated biological function embedded within the corresponding simulated form, even though the encoding scheme does not include any specific instructions for maintenance of form. Instead, this capacity derives from the encoding rule set used to generate the cube.

We are extending these results to generate more complex self-repairing shapes and to explore other possible embedded properties such as mechanical deformability, excitability, and contraction.

This work was supported by a grant from the DARPA, executed by the U.S. Army Medical Research and Materiel Command/TATRC Cooperative Agreement, Contract # W81XWH-04-2-0014, and by a congressional award administered by TATRC Cooperative Agreement DAMD17-02-2-0049

Title: Representing the Holomer on Digital Media Challenges and opportunities for data representation and compression.

Thomas G. Menten, PhD; Xiao Zhang, BS, MS; Lian Zhu, PhD Crowley Davis Research, tom@cdres.com

The vision for the Virtual Soldier is an integrated, digital representation of the anatomy and physiology of an individual human. The Holomer is to be digitally represented on durable media to be worn on the soldier's person - an electronic "dog tag" similar to Personal Information Carrier's in use during "Desert Storm". This baseline "data", or model of the individual can be queried (probed) for information and forms the basis for treatment in the case of injury or illness.

As the supporting storage and bandwidth capabilities evolve, the challenges of representing the holomer in a way that can be used by a variety of platforms will also evolve. This paper illustrates the application of recent data compression technologies to these challenges and indicates possible future paths for increasingly biologically motivated solutions.

This work was supported by a grant from the DARPA, executed by the U.S. Army Medical Research and Materiel Command/TATRC Cooperative Agreement, Contract # W81XWH-04-2-0014

Creating Models from Segmented Medical Images

Bill Lorensen, Jim Miller, Dirk Padfield, James Ross GE Global Research
lorensen@research.ge.com

Problem Segmentation is the process of identifying objects in a scene. The goal of medical image segmentation is to distinguish anatomy contained within an image dataset. Often, the results of segmentation are represented masks of integers. Models created from these discrete volumes exhibit annoying step artifacts. This paper investigates several approaches to convert the results of segmentation into polygonal models that are suitable for visualization.

Method We investigate three approaches to model generation and compare the performance of the techniques.

Method 1: Convert the binary object labels into grayscale approximation using image smoothing filters and use standard isosurface techniques[1].

Method 2: Use the original grayscale data to constrain an evolving surface. Use the binary segmentation mask as an initial level set[2]. Once the evolution converges, extract the zero level set with standard isosurface techniques[1].

Method 3: Extract surfaces directly from the binary segmentation data using a discrete Marching Cubes algorithm. Smooth the resulting polygonal surface using a non-manifold variation of a surface fairing technique[3].

Results We applied the three methods to the segmentation labels contained in an atlas built from the 70mm film Visible Human Male physical cross-section images. The atlas covered the thorax and contained 407 labeled structures. For each method we selected large, medium and small representative structures. We evaluated the performance of each method using several objective and subjective measures. These included perceived smoothness, distance to the "true" surface, integrity of contact surfaces, time to create models and complexity of the method. For method 2, we evaluated several of the level set implementations in the Insight Toolkit (itk)[4]. We explored the methods' parameter spaces using a 256-node Linux cluster. For method 3 we developed a new variation of the Marching Cubes algorithm that operates directly on the binary labels. We also developed a new non-manifold surface-smoothing algorithm. Implementations of all algorithms used for each method are contained within the Visualization Toolkit (vtk)[5] and Insight Toolkit (itk)[4] open source software.

Discussion

Although the discrete models generated directly from the hand labeled data are the "truth", the resulting polygonal models are not suitable for visualization. Method 1 was the least complex of the three methods but produced inferior results. This method uses only the label of the structure being extracted without regard to the original image data or neighboring structures. Method 2 produced pleasing models but each of the level set techniques has several free parameters to adjust. Although the contact between adjacent structures was not maintained, the gaps were small since these methods are somewhat constrained by the original image data. Method 3, by design, maintained all of the contact surfaces, but produced slightly inferior models to those of method 2.

This topic has received little attention in the literature although many segmentation techniques produce discrete labeled data. The level set techniques show promise for creating high quality models, but automatic techniques must be developed to control the high dimension parameter space. The notion of maintaining contact between adjacent structures is a new research topic. Preliminary work has been done on multi-component level sets.

This work was supported by a grant from DARPA, executed by the U.S. Army Medical Research and Materiel Command/TATRC Cooperative Agreement, Contract # W81XWH-04-2-0012.

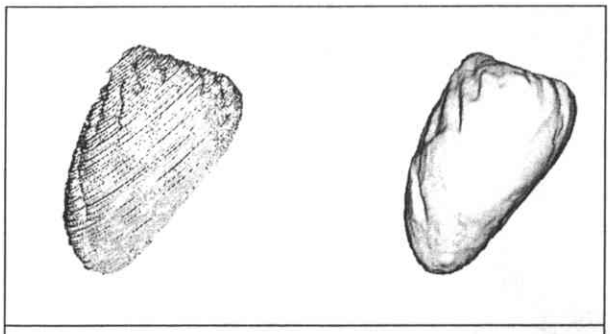

Figure 1. Discrete, Method 2 models of the left ventricle

References

[1]W.E. Lorensen and H.E. Cline. *Marching Cubes: A High Resolution 3D Surface Construction Algorithm,* Computer Graphics, vol. 21, no. 3, pp. 163-169, July 1987.

[2]J.A. Sethian. *Level Set Methods and Fast Marching Methods*. Cambridge University Press, 1996.

[3]G. Taubin, T. Zhang, and G. Golub . *Optimal Surface Smoothing as Filter Design,* Fourth European Conference on Computer Vision (ECCV'96), and IBM Research Technical Report RC-20404, March 1996.

[4]http://www.itk.org

[5]http://www.vtk.org

Linking Human Anatomy to Knowledgebases: A Visual Front End for Electronic Medical Records*

Stewart Dickson, Line Pouchard, Richard Ward, Oak Ridge National Laboratory; Gary Atkins, Fisk University
Martin Cole, University of Utah; Bill Lorensen, GE Global Research; Alexander Ade, University of Michigan

Problem

The Defense Advanced Research Projects Agency Virtual Soldier Project (VSP) is investigating methods to predict outcomes from wounding that will revolutionize medical care for the soldier, and in turn for civilian medical care. Prediction of outcomes of penetrating wounds will be made based on comparison of results from complex mathematical models, with experimental data, and (ultimately for the soldier) with clinical data including baseline X-ray CT and post wound imaging. The problem is to display this information in such a way as to capture the three-dimensional (3D) nature of the human body and to correlate that with extensive information about both the anatomy and the physiology of the wounded soldier.

Method

To address this problem, VSP has developed a holographic medical representation (or Holomer) to be used to connect a 3D model of the soldier's body, based on X-ray CT, with anatomical and physiological information for purposes of improving medical diagnosis and treatment both on and off the battlefield. The Holomer coupled with predictive modeling software will facilitate a new level of integration in medical procedures and create a prototype for a truly interactive visual electronic medical record.

To demonstrate the Holomer concept, a 3D model was created from segmented and annotated NLM Visible Human male photographic data [1]. The 3D model is displayed in SCIRun [2] using existing volume visualization techniques, and is linked to knowledgebases using a specially developed module, referred to as the HotBox. The HotBox interacts with the model via a 3D widget which is user controlled such that it can be moved to any location in the model. This provides the user input as to the location of interest. Given the location from the user controlled 3D widget, the HotBox implements the linkage to the 3D anatomy and the many levels of information provided in the knowledgebases. This provides a unique visual-based electronic medical record which the medic or physician can utilize for purposes of diagnosis and treatment. The specific focus of the VSP of this unique visual approach is for penetrating wounds to the heart.

Results

A prototype of the HotBox has been developed within SCIRun. The HotBox, which comes from animation software [3], is a menu activated by placing the cursor at a particular point in the 3D space (anatomy). The menu provides the user with a multitude of options based on retrieving the anatomical structure at the spatial point from the "Master Anatomy" list created from segmenting and labeling the Visible Human data. For example, a menu item can be selected to invoke a connection, by Web services, to the Foundational Model of Anatomy [4], to provide the anatomical structures adjacent to the structure at the cursor location. Physiological information from measured vital signs will also be available via the Web service from the HotBox menu. In addition, we have also developed an alternative approach for connecting to knowledgebases that is independent of SCIRun and can be run on PC platforms. In this approach the 3D images are created using the VTK [5].

Conclusion

We describe the prototype concept of the HotBox, which can be integrated into the SCIRun problem-solving environment to link between 3D anatomy and knowledgebases of anatomical information, physiological response (vital signs) data and other medical records. This design can serve as a prototype for a new type of electronic medical record, one based on a 3D representation of the individual soldier or patient, providing unique visual access to the condition, be it a wound or a disease, afflicting the individual.

Discussion

The prototype Holomer is a unique demonstration of the concept of a "Visual Electronic Medical Record", improving the ease and use of medical records data by the physician in an interactive setting. Using the Holomer, physician or medic will have access, at the touch of a button, to all available information about a patient or wounded soldier, greatly facilitating accurate and efficient diagnosis of medical conditions.

References

1) See: http://www.nlm.nih.gov/research/visible/.
2) "SCIRun: A Scientific Computing Problem Solving Environment. Scientific Computing and Imaging Institute (SCI), 2002 (software.sci.utah.edu/scirun.html)
3) Pouchard, LC, Dickson, SP (2004) "Ontology based three-dimensional Modeling for Human Anatomy" ORNL Technical Report ORNL/TM-2004/139
4) Rosse, C. and Mejino, JLV. (2003) "Ontology for Bioinformatics: The Foundational Model ofAnatomy". *Journal of Biomedical Informatics 36*:478-500.
5) See: http://www.kitware.com/vtk.html

*This work was supported by a grant from the DARPA, executed by the U.S. Army Medical Research and Materiel Command/TATRC Cooperative Agreement, Contract # W81XWH-04-2-0012.

The submitted manuscript has been authored by the U.S. Department of Energy, Office of Science of the Oak Ridge National Laboratory, managed for the U.S. DOE by UT-Battelle, LLC, under contract No. DE-AC05-00OR22725. Accordingly, the U.S. Government retains a non-exclusive, royalty-free license to publish or reproduce the published form of this contribution, or allow others to do so, for U.S. Government purpose.

A Middleware-based Computing Architecture for Virtual Medicine*

Line C. Pouchard, Richard C. Ward
Oak Ridge National Laboratory

Michael N. Huhns, Laura Zavala, Karthik Iyer
University of South Carolina

Problem

As the use of computer modeling spreads in medical research, smarter models of the human anatomy are needed in a broad range of applications, including clinical diagnosis, surgical planning, cancer treatment using radiation therapy, and other applications [1,2]. The Defense Advanced Research Projects Agency Virtual Soldier Project investigates methods to improve mathematical models of individual soldiers against in vivo experiments. Phase I focuses on coupling physiological, electro-mechanical, and anatomical properties of the heart in a single interactive 3D display that includes time series, a searchable semantic network and complex visualization of a virtual human heart. Large teams of researchers distributed nationwide among six universities, one national laboratory, and several companies collaborate. The complexity of the project requires a flexible, distributed, computing architecture that supports independent models for seamless integration of software components and ensuring interoperability.

Method

The architecture must support programmatic interaction in "near real-time" between the Integrator/Executive, an error prediction engine measuring the accuracy of the models [3] and the High-level Integrative Physiological Model (HIP) run through the JSIM batch program [4]. Additional requirements include accessing semantic concepts from the Foundation Model Anatomist [5], automating data movement, enabling programmatic interfaces between pre-computed simulation and experimental data stored in databases and file systems, and testing performance. "Near real-time" is defined by human perception and currently estimated as the rate of new data to be presented every second. We are building a middleware-based, flexible, computing architecture that provides services for bringing output data of one system to input of another upon request through programmatic interfaces. This architecture provides services for collecting, accessing, querying and presenting the data made available by models and experiments to the Executive. An inventory of producers and consumers of data were identified by iteration with members of each team. A consumer of data is a software system (typically designed by one team) that runs a program/model using the output data from another system. The same system can be both a producer and consumer of input and output data. Interactions were defined using the Unified Modeling Language [6] and data flow diagrams.

Results

A software component architecture was emphasized for adaptability and extensibility of the architecture in later phases of the project. Prototype services for programmatic access to the JSIM software that run a HIP simulation over the Web have been deployed. These services are implemented using the Simple Object Access Protocol, a Web Consortium standard recommendation for Web services. Other services have been designed but not yet implemented at the time of this writing: a file discovery service based on metadata, file requestor and locator services, and a file mapper service that parses logical to physical file names. Performance testing of the JSIM/FE model web service using the spheart model was done at USC. Timing tests for a single computation resulted in near real time performance including data transfer between client and server. Data volume for JSIM batch output was 936K per run.

Conclusion

Middleware services for running the HIP model over the Web have been implemented and tested, and can now serve as a blueprint for the planned services in the architecture.

Discussion

A large effort went into collecting project and system requirements in view of the Phase I demonstration. The effort will continue throughout the project as it evolves but the design of an architecture based on modules interacting through independent interfaces pays off as new model versions, access methods, and number of systems become available. The effort of migrating from a stand-alone to a distributed environment will also be reduced. An immediate benefit was to make available the computational and modeling capabilities of the HIP model to a wide audience through the Web while developers retain control of the model. While the performance is currently insufficient for serving the needs of the Integrator/Executive, a significant improvement must be made in the JSIM client as this appears to be a bottleneck. Service performance also needs to be improved.

References

[1] Satava, RM, "Cybersurgeon: Advanced simulation technologies for surgical education", *Medical Simulation and Training*, 1:6-9 (1996)

[2] Satava, RM, "Medical Virtual Reality", Medicine Meets Virtual Reality: 4 Health Care in the Information Age – Future Tools for Transforming Medicine, IOS Press, Amsterdam, pp. 100-105 (1996).

[3] Bookstein, F. et al. Tracking physiological models by Kalman filters. MMVR13, forthcoming.

[4] Kellen MR and Bassingthwaighte JB. An integrative model of coupled water and solute exchange in the heart. Am *J Physiol Heart Circ Physiol* 285: H1303-H1316, 2003.

[5] Rosse, C and Mejino, JLV. (2003) A Reference Ontology for Bioinformatics: The Foundational Model of Anatomy. *Journal of Biomedical Informatics* 36:478-500.

[6] Rumbaugh, J, Jacobson, I, Booch, G, *The Unified Modeling Language Reference Manual.* Addison-Wesley, 1999.

*This work was supported by a grant from the DARPA, executed by the U.S. Army Medical Research and Materiel Command/TATRC Cooperative Agreement, Contract # W81XWH-04-2-0012.

The submitted manuscript has been authored by the U.S. Department of Energy, Office of Science of the Oak Ridge National Laboratory, managed for the U.S. DOE by UT-Battelle, LLC, under contract No. DE-AC05-00OR22725. Accordingly, the U.S. Government retains a non-exclusive, royalty-free license to publish or reproduce the published form of this contribution, or allow others to do so, for U.S. Government purpose.

A Web-Service Based Computational Environment for Biomedical Computing*

Line C. Pouchard, Richard C. Ward; Oak Ridge National Laboratory
Michael N. Huhns, Laura Zavala, Karthik Iyer; University of South Carolina

Problem

The Defense Advanced Research Projects Agency Virtual Soldier Project (VSP) will investigate methods that will revolutionize medical care for the soldier. The project will produce complex mathematical models to create physiological representations of individual soldiers. These holographic medical representations (known as Holomers) can be used to improve medical diagnosis on and off the battlefield. The Holomers coupled with predictive modeling software, will facilitate a new level of integration in medical procedures.

A complex project such as this requires a flexible computational environment that, on the on hand, can support "real-time" prediction of outcomes of wounds and, on the other hand, support a large collaboratory of researchers in developing this capability. We are designing just such a flexible problem-solving environment, based at least partly on Web services, specifically to support the Virtual Soldier biomedical modeling, simulation, and prediction of outcomes to injuries.

Method

The focus of the project is on biomedical modeling of the heart. X-ray CT images of the heart will be segmented, and surface and volume models created. Individual-specific finite element (FE) mesh models of the heart will be created and computations performed using the Continuity program [1]. In addition, high-level integrative physiological models [2,3] will be constructed and validated against both experimental data and the higher resolution FE models for use in a "real-time" predictive capability.

The problem-solving environment we are developing consists of the following elements:

- Data storage for model and experimental results
- Web services to provide access to the high-level integrative models and their results
- Web services for access to anatomical and physiological ontologies
- Other services for file location, transfer, and conversion
- Support for visualization of the predictive results as well as their supporting model calculations.

Associated with this project is the development of a sophisticated predictive engine based on Kalman Filter processing. The various parts of the problem-solving environment must work smoothly with the prediction engine and associated control software (referred to as the Integrator) in "real time" response mode, where the prediction of the consequences of a wound will be nearly in step with the actual consequences, so that medic and medical professionals can make quick and decisive corrections. But it must also support the broad general needs for connectivity for the entire project. The Web service approach is flexible in that it can be scoped down to a single location if need be, yet can be distributed over a wide Internet. if so desired. We will demonstrate this capability at the meeting.

Conclusion

This talk focuses on the development of a problem-solving environment for biomedical modeling using Web services. The application of this approach to the Virtual Soldier Project is described. The services provide access to biomodeling simulations (using the JSim modeling environment [2,3]. This type of problem-solving environment plays an increasingly important role in biomedical computing, by providing large collaborations, such as the Virtual Soldier Project, with a single distributed computational environment.

Discussion

As the VSP problem-solving environment is developed in the future, additional areas of the body will be included. This will require the incorporation of additional computational and visualization capabilities into the problem-solving environment.

References

[1] Belik ME, Usyk TP, McCulloch AD (2003) Computational methods for cardiac electrophysiology. In Ayache N (Ed) Numerical Methods Handbook. Elsevier, 69 pages (in press)

[2]Kellen MR and Bassingthwaighte JB. An integrative model of coupled water and solute exchange in the heart. Am *J Physiol Heart Circ Physiol* 285: H1303-H1316, 2003.

[3]Bassingthwaighte JB and Vinnakota KC. The computational integrated myocyte. A view into the virtual heart.. In: Modeling in Cardiovascular Systems, edited by S. Sideman and R. Beyar. 2003. (In press Nov 03)

*This work was supported by a grant from the DARPA, executed by the U.S. Army Medical Research and Materiel Command/TATRC Cooperative Agreement, Contract # W81XWH-04-2-0012.

The submitted manuscript has been authored by the U.S. Department of Energy, Office of Science of the Oak Ridge National Laboratory, managed for the U.S. DOE by UT-Battelle, LLC, under contract No. DE-AC05-00OR22725. Accordingly, the U.S. Government retains a non-exclusive, royalty-free license to publish or reproduce the published form of this contribution, or allow others to do so, for U.S. Government purpose.

Using an Ontology of Human Anatomy to Inform Reasoning with Geometric Models

Daniel L. Rubin, Yasser Bashir, David Grossman, Parvati Dev, and Mark A. Musen
Stanford Medical Informatics, Stanford, California 94305-5479 USA
rubin@smi.stanford.edu

The Virtual Soldier project is a large effort on the part of the U.S. Defense Advanced Research Projects agency to explore using both general anatomical knowledge and specific computed tomographic (CT) images of individual soldiers to aid the rapid diagnosis and treatment of penetrating injuries. Our goal is to develop intelligent computer applications that use this knowledge to reason about the anatomic structures that are directly injured and to predict propagation of injuries secondary to primary organ damage. To accomplish this, we needed to develop an architecture to combine geometric data with anatomic knowledge and reasoning services that use this information to predict the consequences of injuries.

We used the Foundational Model of Anatomy (FMA), a well structured, comprehensive ontology of human anatomy. The FMA contains more than 70,000 concepts that describe the elements of canonical human morphology, and it provides formal definitions of detailed anatomic structures in a computationally accessible format.

The FMA is a symbolic model that lacks geometric information on organ shape, the absolute location of organs, and the specific surface relationships that organs and their components may share. To acquire and represent patient-specific spatial information, we developed a representation of 3-d spatial geometry using the Insight toolkit (ITK; http://itk.org). In this representation, 3-d tetrahedral mesh models are built from segmented images in which each anatomic structure is given a unique label. A geometric model of patient anatomy is constructed in ITK from the segmented images, and each geometric structure is linked to the FMA anatomic class that represents that structure. This architecture thus combines geometric data and anatomic knowledge, and it can be used for query, visualization, and reasoning (see Figure).

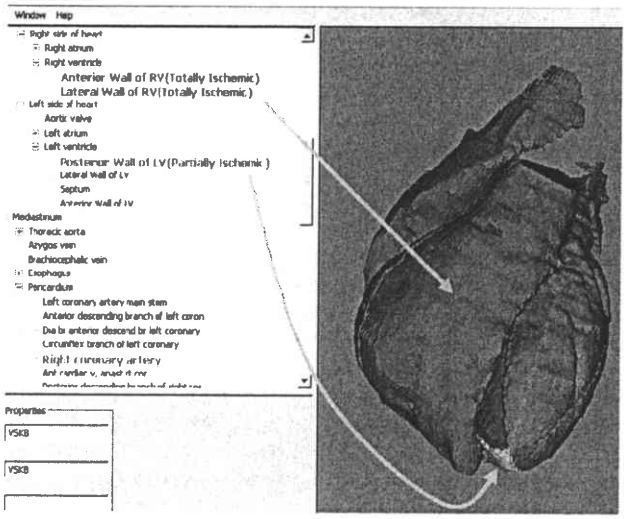

Figure. Reasoning application showing geometric model of the heart (right) integrated with anatomy ontology knowledge source (left). Each organ part has graphical and ontology representations. Ontology-based reasoning about organ injury (bold names in left panel) updates the geometric display, showing damaged regions of the heart (arrows).

We used serial axial segmented images from the Visible Human project to build 3-d models of the heart and its subparts (chambers and coronary arteries). The heart chambers have subdivisions that are not contained in the source segmented images. We used knowledge in the FMA (partonomy relationships) to inform a problem solving method that operates on the geometric model to automatically subdivide the heart chambers into their constituent subparts (see Figure). These chamber subparts correspond to coronary artery territories, and these subparts are used to reason about regions of the heart that are affected if a coronary artery is injured.

We have initially developed two reasoning services: (1) predict the organs directly injured by a projectile; and (2) predict propagation of injury if a feeding coronary artery is injured. Given an entry wound and an exit wound, the first problem solver defines a parametric trajectory path and uses the 3-d tetrahedral mesh model to infer the region of injury created by a projectile. The system identifies intercepted geometric elements and maps them to the corresponding classes in the FMA to infer the injured anatomic structures.

The second reasoning service uses a representation of the FMA in the Web Ontology Language (OWL) that we created to permit us to use automatic classification to implement this reasoning task. In the OWL representation, regions of the heart are defined in terms of the branches of coronary arteries supplying them. If a coronary artery segment is injured, the OWL ontology is updated with this information by making an assertion to the ontology, and the reasoning service infers regions of damaged myocardium by updating the ontology using a domain-independent description logic classifier.

We have implemented our architecture and reasoning services as an interactive application that links the FMA to a graphical display of the anatomy (see Figure). The user can specify a projectile trajectory and view the structures that are affected by direct and propagated injury. The display automatically updates as reasoning services deduce injuries.

By linking the geometric mesh model to the FMA, we take advantage of the FMA's rich set of relationships among anatomic concepts, allowing us to consider candidate paths of penetrating injuries in anatomic terms, to infer the organs that may be injured, and to deduce propagation of injury.

Acknowledgments
This work was supported by a grant from the DARPA, executed by the U.S. Army Medical Research and Materiel Command/TATRC Cooperative Agreement, Contract # W81XWH-04-2-0012. We are grateful to Cornelius Rosse for many years of exciting discussion and collaboration.

Three dimensional electromechanical model of porcine heart with penetrating wound injury

Roy Kerckhoffs and Taras P. Usyk

Department of Bioengineering, The Whitaker Institute for Biomedical Engineering, University of California, San Diego, La Jolla, CA 92093-0412, USA, e-mail: taras@bioeng.ucsd.edu

Introduction

The aim of this study is development a prototype computational model of the pig heart that can be used to predict physiological responses to a penetrating wound injury. The pig has been chosen for this model studies because it shares many anatomical similarities with humans.

Anatomy

Three-dimensional cubic Hermite finite element meshes based on detailed measurements of porcine anatomy combined into an integrated anatomic model. The pig ventricular model includes detailed left and right ventricular geometry and myofiber and laminar sheet orientations throughout the mesh [2].

Electrophysiology

The cardiac mesh was refined spatially to approximately 2.0 mm resolution, and monodomain equations for action potential propagation solved using well-established collocation-Galerkin finite element methods [1]. The membrane kinetic equations for the action potential model was based on detailed cellular models of transmembrane ionic fluxes and intracellular calcium fluxes in canine ventricular myocytes and human atrial myocytes. We modified the anisotropic myocardial conductivity tensor on the endocardial surface of the ventricles by making use of a surface model fitted to measured of Purkinje fiber network anatomy.

Mechanics

The mechanical model compute regional three-dimensional stress and strain distributions using anisotropic constitutive laws referred to local material coordinate axes defined by local myofiber and laminar sheet orientations. Passive myocardial mechanics modeled using exponential orthotropic strain energy functions. Active systolic myocardial stresses computed from a multi-scale model that uses crossbridge theory to predict calcium-activated sarcomere length- and velocity-dependent tension filament tension.

Coupled Electromechanical Model

Since the electrical and mechanical models use a common finite element mesh as the parent parametric framework and both models are solved within our custom finite element package, it is straightforfard to couple these models, as we have recently done for a model of coupled ventricular electromechanics [3]. The cellular model of ion fluxes includes the myoplasmic calcium transient and calcium binding to troponin-C. This model is then coupled to a model of length-dependent thin filament activation, which in turn allows the transition from non-permissive to permissive states for cross-bridge interaction. The crossbridge model includes nearest-neighbor cooperativity and force feedback to account for experimentally observed twitch prolongation with increased sarcomere length. The model recapitulates the major features of cardiac muscle mechanics as a function of activator calcium, sarcomere length history and shortening velocity. It also provides a framework to couple the mechanoenergetics of muscle contraction to the hydrolysis of ATP and flux balance models of purine nucleoside and nucleotide metabolism.

We apply the coupled electromechanical model to predict alterations in regional diastolic and systolic wall mechanics associated with rhythm disturbances and possible arrhythmias with decreased blood volume, tamponade, myocardial injury, and regional ischemia caused by a penetrating wound.

Acknowlegements

This work was supported by a grant from the DARPA, executed by the U.S. Army Medical Research and Materiel Command/TATRC Cooperative Agreement, Contract # W81XWH-04-2-0012

References

1. Rogers JM, Courtemanche M, McCulloch AD. Finite element methods for modeling impulse propagation in the heart. In: Panfilov AV, Holden AV, editors. Computational Biology of the Heart. Sussex: John Wiley and Sons, Ltd.; 1996.
2. Stevens C, Hunter PJ. Sarcomere length changes in a model of the pig heart. Prog Biophys Molec Biol 82:229-241, 2003.
3. Usyk TP, LeGrice IJ, McCulloch AD. Computational model of three-dimensional cardiac electromechanics. Comput Visual Sci 2002;4(4):249-257.

Challenges of Presenting High Dimensional Data to aid in Triage in the Virtual Soldier Project

Boyd AD, Wright ZC, Ade AS, Bookstein F, Ogden JC, Meixner W, Athey BD University of Michigan
adboyd@umich.edu

Problem:
In the Virtual Soldier Project, one of the goals is to aid the medic in triage of a wounded soldier. We are currently collecting a dozen physiological variables, including up to 60 ECG leads as well as CT and U/S imaging from experimental test subjects. We are using physiological models and Kalman filters to aid in diagnosis and predicting outcome. The physiological modeling adds another few dozen variables. Reducing the complexity of the above into easy-to-read text to aid in the triage of the field medic is the challenge.

Methods:
IPAQ handhelds are currently being deployed world-wide with the Battlefield Medical Information System-Tactical (BMIS-T)[1] software. These handhelds currently interface with the electronic dog tag (P-TAG) that stores a soldier medical record. BMIS-T is the point-of-care handheld on which the field medic records an encounter. Since this technology is currently deployed with the field medic, we are limited in the presentation of the data listed above to the screen size of the IPAQ.

The level of detail of the scientific models is beyond the knowledge of clinical care providers. The field medic while familiar with blood pressure and heart rate, will probably not be familiar with the intricate interplays of heart valve pressure gradients that are important for the models. Because it is essential that the field medic is presented with a display that is both useful and usable, we will be doing further careful analysis of the usability of the interface via standard techniques such as GOMS, cognitive walkthroughs, task analysis, and informal user testing. These methods will ensure the information and interface presented to the field medic are clear and intuitive, especially in the non-ideal viewing situations that may arise in the battlefield.

The baseline data of individual test subjects are measured before injury. These data are used to populate the physiological and cardiac models designed for the Project. Each subject also receives a CT scan, segmented to define regions of the anatomy. Through semi-landmarks and morphometric markup we also warp the models to the individual anatomy of the test subject.

The method of reducing the high dimensional data space uses a Kalman filtering technique running multiple models with the variable outcomes expected from the injury[2]. By validating the trends of the expected injuries against test data, we will estimate the probability of a specific diagnosis and make predictions of future data. Predictions become more confident as more data are collected on the test subject. Alerts will be displayed on the IPAQ handheld when a diagnosis reaches a threshold level of confidence.

For the wounds that we are modeling a field medic will triage the patient as Urgent or Urgent-Surgical. Currently there is no effort to distinguish between cardiac bleedout, ventricular fibrillation and survival. There is also no estimation of time to death or survival. We will provide this additional information to the field medic to aid their triage decision making.

Results:
"Expected Display"

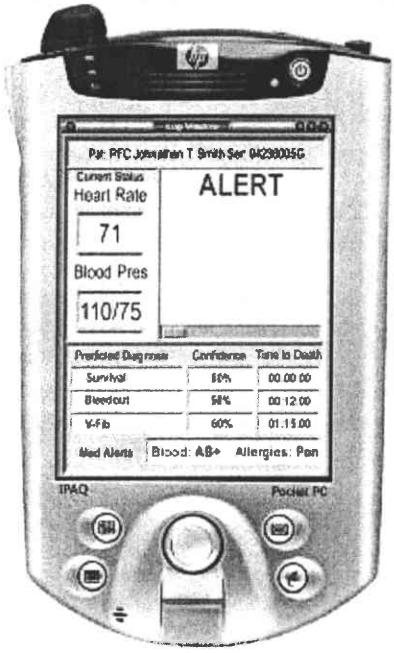

Conclusions/Discussion:
The results generated by the system (eg. diagnosis, confidence intervals, and time to death) is a good beginning, however this is more information than the field medic is familiar with in practice. The deployment of this technology will need to be accompanied by additional training for the field medic. We will need to integrate this additional information into future triage protocols that the field medics use in combat. We will also need to have a more intuitive method to display the uncertainty of each result. While most of a trauma protocol is binary decision making, allowing one to rapidly run through a protocol, new information will need to be integrated in a responsible manner to new protocols. This additional information will aid in deciding which soldiers need to be evacuated first when multiple causalities require prioritization.

This work was supported by a grant from DARPA, executed by the U.S. Army Medical Resaerch and Materiel Command/TATRC Cooperative Agreement, Contract # W81XWH-04-2-0012

References:

1. Battlefield Medical Information System – Tactical, www.tatrc.org accessed July 14, 2004
2. Bookstein FL, Cook D, Bassingthwaighte J, "Tracking physiological models by Kalman Filters" submitted to MMVR 2005

The Cardiac Morphometric Markup: a template for experimental cardiology

Fred L. Bookstein, Ameed Raoof, William Green, University of Michigan
fred@brainmap.med.umich.edu

Problem. Today there are spectacularly good "generic" biomechanical models of cardiac contraction, and very good segmentations of cardiac surfaces at diastole and systole (e.g., from gated CT), but fewer tools to support studies of the variation of these geometries or their covariation with causes (e.g., ischemia) or effects (e.g., hemodynamics). We sought a robust and flexible statistical method by which the variability of this shape change could be correlated to its causes or effects and by which biomathematical computations of perturbed heartbeats could be validated from ordinary CT images in a useful metric.

Method. Statistical methods now exist that can represent the form of the myocardium and its shape change over the cardiac cycle by a vector of *shape coordinates* corresponding to points with zero, one, or two geometric degrees of freedom in the original solid image. Ordinary *landmark points* are locations with three meaningful coordinates; these include the apex of the heart, the centers of the valves, and only a few others. *Semilandmarks* can arise on curves (one degree of freedom) or surfaces (two degrees of freedom). The heart is sampled fairly well by a scattering of curves: rings of all four principal valves, the creases at the bottom of the ventricles where they encounter the septum, the myocardial-membraneous junction at the top of the septum, and the principal coronary arteries upon the exterior surface. For purposes of correlation with biomathematical models or with cardiac physiology, the remainder of the necessary information is carried by a scheme of several hundred landmarks sliding on the myocardial surfaces outside and inside. These points have only one true coordinate. We call this the *Cardiac Morphometric Markup* (CMM). In subsequent statistical analysis, all coordinates corresponding to unspecified degrees of freedom (tangent lines or tangent planes of sliding) are explicitly ignored.

Results. New features of our interactive computer program package `Edgewarp` offer the digitizing features we need in the context of a general-purpose 3D image navigator/digitizer/warping engine. For the CMM, we built, entirely by hand, a representation combining these points and curves with intentionally undersampled surfaces based on the full-color image of the myocardium of the NLM's Visible Female, "Eve." This surface is deformed onto surface-enhanced CT scans of the heart at diastole and systole by a careful sequence of hand operations. On every novel image, first the selected discrete landmark points are located, and the template deformed (via thin-plate spline) to accord with them. Then the curves are traced by a suitable number of points jointly relaxed to match the given image at minimum bending from the template, and again the template is warped to correspond with this newly enriched information. Finally, in random sequence, points of the five surfaces (four chamber boundaries and the pericardial surface) are "pasted into place" and the warping updated. In practice, the number of points that need to be displaced is a small fraction of the total template point count.

At least in *Sus scrofa*, the species of interest to the project underwriting this work, variability of the myocardial surfaces appears to be adequately represented by a few hundred shape coordinate sets acquired in this way. Our MMVR13 presentation will show informative graphics of the variability of form at diastole, the geometry of contraction (deformation from diastole to systole), and their correlation.

Discussion. The method proposed here falls somewhere along the general continuum of methods for deformable template analysis. Dimensionality of the resulting dataset is intermediate between that of principal shapes or eigenshapes and the full representation by surface or volume displacement fields, and the information content of the representation appears to be adequate for the scientific applications intended.

This work was supported by a grant from the DARPA, executed by the U.S. Army Medical Research and Materiel Command/TATRC Cooperative Agreement, Contract # W81XWH-04-2-0012.

`An early digitizing stage (schematic).`

Tracking physiological models by Kalman filters

Fred L. Bookstein, University of Michigan
Daniel Cook, Jim Bassingthwaighte, University of Washington
fred@brainmap.med.umich.edu

Problem. *Highly integrated physiology* (HIP) models are a good testbed for investigations into circulatory system function at a variety of levels of lumping. However, tuning these models, and also confirming or disconfirming the dynamical assumptions that drive them, are limited by the finite dimension of correspondingly lumped instrumentation. A statistical technique is required for validating the high-dimensional HIP models by the lower-dimensional data streams accessible to the physiologist.

Method. A **Kalman filter** (KF) is a standard applied statistical tool for tracking complex processes. A KF is a special case of a hidden Markov model (HMM) for which all link functions are linear (or, in some cases, gently quasi-linear). The KF is generally applied to a vector time-series of observed data—here, a sequence of physiological measurements P_t observed with error. The measures are assumed to depend on a different vector of unobservable state variables D_t. The equations of the model combine two terms, one for the dynamics of the true (hidden) underlying state vector, and the other for the relation between that true state vector and the observed data:

$$D_{t+1} = AD_t + \xi_t,$$
$$P_t = CD_t + \eta_t.$$

In words: D, which we do not observe, is predicted by its own previous value, plus noise (and perhaps a trend term); P, which we *do* observe, is predicted by D at the same time, together with other noise.

The elegance of the Kalman filter inheres in the existence of optimal estimates of the values of D and P at any moment, along with their errors of estimate, in the form of an iterative procedure that does not increase in complexity as the observational data accrue over time. These estimates and errors of estimate can be expressed in terms of the link matrices A and C and error covariance structures for ξ and η. One form of this iteration is the so-called *predictor-corrector* form that compares the next data point P_t to what was expected given the data acquired prior to time t:

$$\hat{D}_{t|t} = \hat{D}_{t|t-1} + Kg_t(P_t - C\hat{D}_{t|t-1}),$$
$$\hat{D}_{t+1|t} = A\hat{D}_{t|t},$$

where Kg is the *Kalman gain matrix* relating the *innovation* $P_t - C\hat{D}_{t|t-1}$ to an updated estimate $\hat{D}$ of expected damage at the next time point.

Implementation. The University of Washington HIP models are coded at present in JSim, a Java-enabled simulation package in which they are expressed by a combination of identities and ordinary differential equations. The models currently run in "batch mode," producing entire vector time-series of simulated instrument readings over a time window of seconds to minutes.

Data will arise from measurements of several dozen normal specimens of *Sus scrofa*, the species of interest to the project underwriting this work. The measurements, every five seconds or so, are expected to include blood pressures at several sites of the circulatory system (systemic, venous, atrial, pulmonary, ventricular, aortic), aortic and pulmonary blood flow, heart rate, blood pH (arterial and venous), and oxygenation.

In an experimental context, validation of HIP models might hinge on their ability to accommodate changes in systemic boundary conditions (e.g., intrapleural pressure, systemic blood volume). In the nonexperimental context from which the data for this presentation arise, we will instead leverage the familiar *chaotic aspect* of the normal heartbeat, and so predict from one heartbeat to the next. From a very large number of JSim runs, the matrices A and C of the KF approach will be estimated whereby the dependence of one true state vector upon its predecessor is linearized and likewise the dependence of measurements (or, rather, their change scores) on the true state vector and *its* change scores.

Results. Our presentation at MMVR13 will explore the dimensions of the "state-of-the-art HIP model" that are most and least accurate for predictive purposes. We will also explore the extent to which the KF model is capable of tracking the chaotic state of the baseline circulatory physiology in these animals, or whether, instead, it needs to be treated as some sort of "ergodic" differential approximation that applies only over long intervals of temporal integration.

This work was supported by a grant from the DARPA, executed by the U.S. Army Medical Research and Materiel Command/TATRC Cooperative Agreement, Contract # W81XWH-04-2-0012.

Advanced Modeling and Visualization of Cardiothoracic Electrical Fields

F. B. Sachse (fs@cvrti.utah.edu)[1], M. Cole[2], R. M. Kirby[2], X. Tricoche[2], C. Johnson[2]
[1]Nora Eccles Harrison Cardiovascular Research and Training Institute,
[2]Scientific Computing and Imaging Institute, University of Utah, UT, USA

Problem. Major tools for clinical diagnosis of cardiac diseases are electrocardiographic techniques. Intra- and extracorporal electrical measurements are applied to gain knowledge concerning the activity of a patient's heart. The measurements deliver electrograms, which are commonly examined by medical experts and provide the basis for diagnosis. Promising techniques for clinical use are those, which apply methods of surface visualization to represent a large number of measured electrograms and derived quantities, e.g. body surface potential mapping [1], epicardial and endocardial mapping [2]. Furthermore, these techniques can be used in conjunction with computer-based anatomical and electrical models leading to principally new diagnosis methods.

In this abstract we will introduce several novel techniques for modeling and visualization of cardiothoracic electrical fields. The modeling techniques aim at improving accuracy and applicability of simulations, the visualization techniques at providing novel insights into results of simulations.

Methods. Numerical calculation of thoracic electrical fields created by cardiac sources, the so-called forward problem in electrocardiology, necessitates knowledge of the distribution of conductivity. Commonly, medical imaging data are applied to produce anatomical models, which are transformed to conductivity models.

Our framework for modeling (SCIRun/BioPSE [3], [4]) is based upon finite element techniques, which allow for inhomogeneity and anisotropy of conductivity in the thorax to be taken into account. We extended the framework by including high-order finite element techniques. Additionally, stochastic finite elements were developed for quantifying uncertainty in the forward problem. The underlying mathematical theory provides means of assessing statistical quantities such as mean and variance of a solution based upon known statistical moments of input data, e.g. mean and variance of potential on the heart and conductivity of the system.

We developed novel visualization techniques for representing electrical fields. An automated technique for placement of seed points to generate streamlines guarantees in a statistical sense that the density of electrical streamlines is proportional to the electrical current density. A streamsurface technique is used to capture the continuous behavior of the three-dimensional electrical current field through a curvilinear front integrated along the flow. An optimal resolution is adaptively determined to account for the local geometric characteristic of the field, resulting in smooth surfaces. A further technique extracts the topology of current fields constrained to the cardiac surface. This yields the global structure of tangential flow, segmenting the heart surface into regions, where streamlines exhibit homogeneous patterns.

Results. We provide examples of the utility of high-order finite element solutions for solving the forward problem. We present recent work on the use of stochastic finite elements. We applied the former described techniques to create exemplary visualizations.

Conclusion and Discussion. The presented techniques for modeling offer advances in comparison to the established methods. High-order elements emit exponential convergence behavior for smooth solutions. This translates to being able to solve forward problems more accurately with less degrees of freedom. Stochastic finite element techniques provide enhanced applicability of forward modeling in electrocardiology by quantifying uncertainty. A combination of both techniques will offer further numerical benefits.

The presented streamline and -surface techniques allow us to provide both intuitive and accurate visualizations of the interconnection between sinks and sources located on the cardiac surface through the current defined over the torso. The visualization of topological structure on the cardiac surface offers new insights into mechanisms of electrical field generation in the thorax and genesis of physiological and pathophysiological electrocardiograms.

Acknowledgments. This work was supported by a grant from the DARPA, executed by the U.S. Army Medical Research and Materiel Command/TATRC Cooperative Agreement, Contract # W81XWH-04-2-0012. This work was also supported by NSF Career award (RMK) CCF0347791, NIH NCRR award (CRJ) P41RR12553-05, and NSF award (CRJ) EIA0218721. Frank B. Sachse thanks for the support by the Richard A. and Nora Eccles Fund for Cardiovascular Research and the Nora Eccles Treadwell Foundation.

References

[1] B. Taccardi and B. B. Punske, "Body surface potential mapping," in *Cardiac Electrophysiology. From Cell to Bedside* (D. P. Zipes and J. Jalife, eds.), pp. 803–811, Philadelphia: W. B. Saunders Company, 4 ed., 2004.

[2] V. Markides, O. R. Segal, F. Tondato, and N. S. Peters, "Mapping," in *Cardiac Electrophysiology. From Cell to Bedside* (D. P. Zipes and J. Jalife, eds.), pp. 858–868, Philadelphia: W. B. Saunders Company, 4 ed., 2004.

[3] SCIRun: A Scientific Computing Problem Solving Environment. Scientific Computing and Imaging Institute (SCI), University of Utah, http://software.sci.utah.edu/scirun.html, 2002.

[4] BioPSE: Problem Solving Environment for modeling, simulation, and visualization of bioelectric fields. Scientific Computing and Imaging Institute (SCI), University of Utah, http://software.sci.utah.edu/biopse.html, 2002.

Knowledge-based Anatomical Dynamic Scene Generation in XJ3D

Wayne V. Warren and James F. Brinkley
Structural Informatics Group, Depts Biological Structure and Biomedical and Health Informatics,
University of Washington, Seattle (wvw@u.washington.edu)

Three-dimensional visualization of human anatomy is an effective way of describing appearances and spatial relationships within the human body. Toward this end, a knowledge-based Dynamic Scene Generator (DSG) has been created which constructs interactive three-dimensional scenes of human anatomy [1]. In this report we describe a next generation DSG, written in Java and using the XJ3D code library, which is portable, allows real-time interaction, and will serve as a framework for the visualization of biomedical data that relates directly to the scene generator's rendered structures.

Our concept of intelligent construction of 3-D interactive anatomical scenes requires contributions from three different areas: (1) anatomical semantic knowledge describing object names and relationships, (2) graphical/spatial models describing the shape, placement and appearance of the named objects, and (3) an architecture for integrating these components in an interactive scene. To meet these requirements, three components operate cooperatively within the DSG framework: a knowledge base, a 3-D model database, and a DSG client.

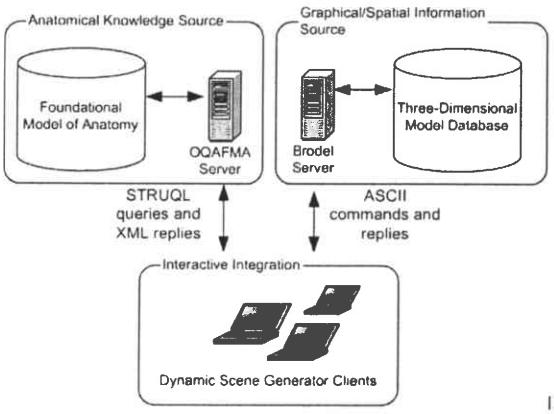

Figure 1 – The Architecture of the DSG

The knowledge base (Foundational Model of Anatomy, or FMA) which is accessed by the OQAFMA server, describes approximately 70,000 anatomical concepts and over 1.2 million relationships. The 3-D model database, which is accessed by the Brodel server, stores VRML graphics primitives describing the various anatomical structures. The DSG client constructs scenes by first obtaining a qualified set of anatomical object names from the FMA based on a user's criteria (e.g. all parts of the heart), and subsequently requests the corresponding VRML primitives from the 3-D Model Database. The DSG client is responsible for communicating with both the FMA and with the Model Database. The user builds the scene through interacting with a GUI which allows the adding, removing, and highlighting of specific anatomical structures by name or by hierarchical reference within the FMA.

The DSG client is implemented in Java and relies on VRML for its visual representation. EAI, or External Authoring Interface, is a standard API that allows for communication between external Java code and the VRML scene. The XJ3D library is used as the primary set of Java objects that implement the EAI standard. XJ3D is a project of the web 3D consortium to create a visualization toolkit that both renders the scene and handles the two-way event processing between the two technologies.

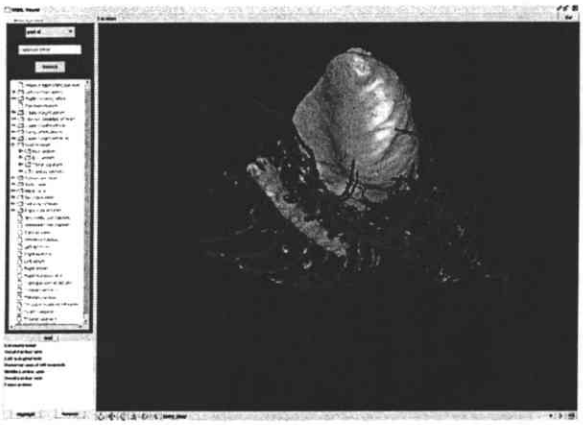

Fig 2. An Example Scene from the DSG

Whereas the DSG has obvious applications in the domain of medical-education, research is underway to use it as a structure-based information retrieval tool. In such an application, data queries are based on spatial information and a user's interaction with the scene, rather than text-based classical methods. Structure-based queries can solicit information regarding gene expression, tissue activity, or even patient information.

1. Wong, B. A. and Rosse, C. and Brinkley, J. F. (1999) Semi-Automatic Scene Generation Using the Digital Anatomist Foundational Model. In Proceedings, American Medical Informatics Association Fall Symposium, pages 637-641.

This work was funded in part by NLM Biomedical and Health Informatics Training Grant Program Number: 1 T15 LM07442 and by DARPA, executed by the U.S. Army Medical Research and Materiel Command/TATRC Cooperative Agreement, Contract # W81XWH-04-2-0012.

Amending dynamic physiological models to represent pathophysiological states

D. L. Cook[1], J. L.V. Mejino[2], C. Rosse[2,4] M. Neal[3], J. B. Bassingthwaighte[3]
Departments of [1]Physiology & Biophysics, of [2]Biological Structure, of [3]Bioengineering and of
[4]Medical Education and Bioinformatics, University of Washington, Seattle, WA, USA
contact: DLC, raintown@halcyon.com

Problem. An essential goal of the DARPA-sponsored Virtual Soldier Project (VSP) is to infer the nature and extent of battlefield damage and predict clinical outcomes for use in making triage decisions. Central to this task has been the development of sophisticated mathematical models of physiological function of specific individuals that provide the "predictor" models for statistical inferences by a Kalman filter. In addition, there is a recognized need to amend these dynamic models to reflect the pathophysiological consequences of different kinds of anatomical injuries sustained during wounding. For the highly constrained wound scenarios used in Phase I of the VSP, manual amendments to baseline models can readily generate alternative pathophysiological models. However, as the VSP entertains a wider range of injuries to a wider range of anatomical structures, there is a need to streamline the model amendment process in order to simulate the outcomes of different sets of hypothetical injuries.

Method. To solve this problem, the VSP teams at the University of Washington (UW) and Stanford University (SU) have prototyped a process consisting of: 1) inference of "initial" injuries from anatomical data (e.g., wound geometry), 2) "propagation" of these initial injuries to infer consequent injuries, and 3) translation of the symbolic representations of initial and propagated injuries into mathematical relationships that amend the normal physiological models.

As shown in the figure, the system for injury inference, propagation and model amendment is based on three key elements of the VSP Knowledge Base (VSKB; under development at the UW). The VSKB is anchored by the Foundational Model of Anatomy (FMA), a product of the Structural Informatics Group at the UW. It is a symbolic representation of some 70,000 anatomical entities (e.g., the heart, ventricles and coronary arteries) that are linked by over 1.7 million structural relationships (e.g., *is part of, is continuous with*). On top of the FMA is an Injury Taxonomy of things that can happen to anatomical entities (e.g., *penetrate* the left ventricular wall, *sever* a blood vessel). On top of both is a Physiology Ontology for representing, first, *properties* of anatomical entities (e.g., *mass*, *pressure*, *volume*) and, second, the kinds of physiological *actions* by which the *properties* of *role players* in the *action* are changed. Thus, blood in one location that *is continuous with* blood in another location implies that there is a *volume flow action* that represents the flow of blood between locations.

Independently, the UW simulation and modeling team (M.N. and J.B.B.) has built a Highly Integrated Physiology (HIP) model in the JSim simulation environment that is a dynamic mathematical model of normal cardiovascular and respiratory function. Using concepts from the Physiology Ontology, the mathematical HIP model can be cast into a symbolic form (as a "symbolic HIP model") in which each state variable and parameter is represented as a *property* and each flow equation as an *action*. Eventually, such symbolic HIP model will be used for both forward and backward inferences on cause-effect relationships in the system.

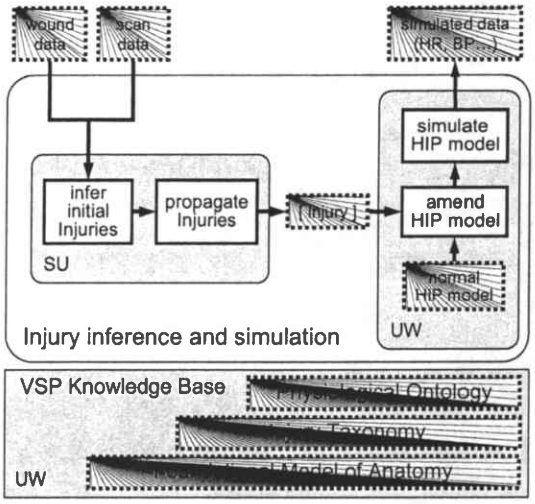

For VSP Phase I, the UW and SU team are developing symbolic reasoning methods (see figure) that combine the anatomical knowledge of the FMA with descriptions of normal anatomy and wound geometry to infer sets of initial injuries (e.g., *penetration* of the left ventricular wall). Initial injuries are then the basis for inferring subsequent injuries (i.e., pathophysiological processes). For instance, *penetration* of the left ventricle establishes *continuity* between fluid in the left ventricular cavity and fluid in the pericardial space. Such fluid *continuity* then implies a *volume flow action* relationship between these two fluids. Thus we see that it will be possible to amend the symbolic HIP model according to the symbolic representation of injuries and their corresponding pathophysiological *actions*. Then the symbolic representations of *injuries* in terms of new entities (blood in the pericardial space, *entity properties* (*volume*, *pressure* of the blood) and *action properties* (the *flow resistance* and *flow rate*) can be mapped directly to specific mathematical expressions that can amend normal HIP models for simulating pathophysiology.

Discussion. We are developing forward reasoning methods as VSP prototypes for a general approach to inferring the pathophysiological consequences of anatomical injuries. In the future, we expect that the symbolic representations and symbolic reasoning methods we are developing can be the basis for reverse reasoning (inferring the pathophysiological causes of abnormal clinical findings) in subsequent developments in the VSP.

Acknowledgement. This work was supported by a grant from the DARPA, executed by the U.S. Army Medical Research and Materiel Command/TATRC Cooperative Agreement, Contract # W81XWH-04-2-0012.

Computational Simulation of Penetrating Trauma in Biological Soft Tissues using the Material Point Method

I Ionescu*[+], J Guilkey*[++], M Berzins*[‡], RM Kirby*[‡], J Weiss*[+]
*Scientific Computing and Imaging Institute,
Departments of [+]Bioengineering, [++]Mechanical Engineering, and
[‡]School of Computing, University of Utah

INTRODUCTION: Injuries due to penetrating trauma from bullet or knife wounds represent a significant healthcare problem. An improved understanding of the factors that control the extent of tissue damage from these wounds can provide the means to improve diagnosis and treatment. Soft tissue failure (skeletal and cardiac muscle, ligament and tendon, nerve) typically represents a large part of the damage resulting from penetrating trauma [1]. However, the detailed three dimensional prediction of soft tissue failure is complicated by the highly anisotropic nature of the materials as well as the lack of appropriate failure models. The objective of this research was to begin to develop realistic computational models for soft tissues subject to finite deformation and failure and to implement and test these models in the context of numerical simulations of penetrating trauma injuries.

METHODS: The present research is based on the discretization of the equations of motion using the Material Point Method (MPM) [2]. MPM is a particle method for simulations in computational mechanics that is implemented in the Uintah computational framework that has been developed for large-scale numerical simulations at the University of Utah [3]. Like other meshless methods, MPM offers an attractive alternative to traditional finite element (FE) methods [4] because it simplifies the modeling of complex deformations and fragmentations that are typical of penetrating trauma to the torso or its components.

To apply MPM to penetrating trauma of soft tissue, a failure model was developed for anisotropic hyperelastic materials. The model represents the failure of anisotropic hyperelastic soft tissues in terms of dilatational strain, fiber strain and maximum shear strain.

To test the failure model, the penetration of a bullet through a myocardium material slab was simulated (Fig. 1, a)). The myocardium was modeled as a transversely isotropic hyperelastic material, comprised of a Mooney-Rivlin matrix reinforced by a single fiber family [5]. To represent the material anisotropy, the fiber direction was varied with location and the failure criterion was defined in terms of two-failure surfaces. The matrix material fails locally if the maximum shear strain at a point exceeds 50% strain [6]. If the fiber stretch exceeds 40% [5] strain at a point, the fiber is considered failed. If both of the above conditions are fulfilled locally, the material point exhibits total failure and the total Cauchy stress is zero. A failure tag was attached to each of the particles in the model, to record if and what type of material failure may occur.

For the ballistic simulation, a 50×10×50 mm myocardial slab was considered (Fig. 1). The xy and yz side boundaries were fixed, while the xz faces were free of constraints. A 9 mm bullet was modeled as an elastic-plastic material with neo-Hookean elastic material properties (specify material coefficients). The bullet was assigned an initial y-velocity of 369.2 m/s. Two cases of anisotropy were modeled: (i) a homogeneous fiber direction case (i.e. fibers perpendicular the bullet path) and (ii) an inhomogeneous case (i.e. fibers rotate 180 degrees through the slab thickness). The matrix, fiber, or total tissue failure were recorded for the each of the cases.

RESULTS: The wound profile in each of the cases showed the damage from the bullet as it passed through the myocardial sample (Fig. 1, b) and c)). In the inhomogeneous case (ii), the damage pattern shows less fiber failure owing to a better fiber reinforcement of the material, for approximately the same damaged areas.

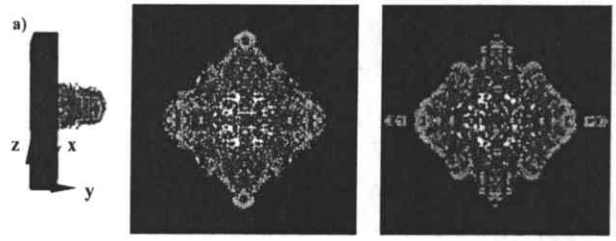

Fig. 1: Bullet penetration through a myocardium slab: a) bullet path view (ii); b) and c) cross sectional wound profile for (i) and (ii) at 0.7 distance through thickness (blue= undamaged tissue; green= failed matrix, yellow = failed fibers; red = total failure).

DISCUSSION: The present results are encouraging but clearly rely for their validity on the correctness of the material model and its accompanying failure model. Future research will consider alternative myocardial material models [7] and failure properties. Beyond this, MPM will also be used for the case of penetrating trauma to multiple torso organs. Exploratory studies in this area have yielded encouraging results.

This research demonstrates the feasibility of using MPM for computational modeling of soft tissue failure associated with penetrating wounds.

REFERENCES: [1] Eisler RD, et al.: Stud Health Technol Inform, 1996, 29:511-22. [2] Sulsky D, et al.: Comp Meth Appl Mech Eng, 1994, 118:179-196. [3] Parker S.: Intl Conf on Comp Science (ICCS2002) Workshop on PDE Software, 2002, April 21-24. [4] Chen Z, Brannon R: Sand Report, SAND2002-0482. [5] Weiss JA, et al.: Comp Meth Appl Mech Eng, 1996; 135:107-128. [6] Hunter PJ, et al.: Prog Biophys Mol Biol, 1998, 69:289-331. [7] Guccione JM, et al.: J Biomech Engng, 1991; 113:42-55.

ACKNOWLEDGEMENT: This work was supported by a grant from the DARPA, executed by the U.S. Army Medical Research and Materiel Command/TATRC Cooperative Agreement, Contract # W81XWH-04-2-0012.

A highly integrated physiology (HIP) cardiovascular/respiratory model used to simulate cardiac injury

Maxwell Neal (mneal@nsr.bioen.washington.edu) and James Bassingthwaighte (jbb@nsr.bioeng.washington.edu), Bioengineering, University of Washington, Seattle
Taras Usyk, Andrew McCulloch (amcculloch@ucsd.edu), Roy Kerckhoffs, Bioengineering, UCSD, San Diego

To provide an integrated model of the cardiovascular and respiratory system for the purposes of diagnosing and predicting the consequences of ballistic injuries to the heart, we used the JSim simulation environment (download at http://nsr.bioeng.washington.edu/PLN/Software) to build a model of: 1. a four-chamber heart[3] and pericardium[2,3,4], 2. systemic and pulmonary circulations [2], 3) baroreceptors[2,3,4], 4) ventilatory exchange[2,3] and 5) blood/tissue gas exchange and blood O_2 / CO_2 / pH handling[1]. In our UCSD/UW collaboration we link the relatively simple non-linear models described above to the UCSD finite element (FE) electro-mechanical cardiac models [5] The HIP model provides left and right ventricular cavity pressures to the FE model, while feedback to the HIP model is provided through the cavity volumes, adjusting varying elastance parameters through a control mechanism.

To extend the application of these multicomponent complex systems to pathological conditions, we provide a GUI for selecting various cardiac abnormalities or injuries, altering the model during a simulated run. To examine the effects of a ventricular septal defect, the user selects a radius for the defect (from 0 to 2 cm) and a time during the run at which the hole forms. The model then computes a conductance across the septum based on fluid dynamics, along with the time courses of circulatory pressures, flows, compliances, etc. Aside from penetrating injuries to the walls of the heart and the pericardium, reductions in ventricular elastance and various mitral/tricuspid valve maladies can be simulated, singly or in combination. A user may observe the physiologic effects of penetrating the pericardium, left ventricle wall and septum (Figure 1, top). If a clot closes the pericardial hole, then the result is cardiac tamponade (Figure 1, bottom), preventing the heart from filling.

The HIP system models and the electromechanical cardiac models, being of two different levels in the heirarchy of physiology, illustrate an application of a multiscale model. Also, in regards to our collaboration with the symbolic reasoning/knowledge representation teams at UW and Stanford, the physiologic stress module represents the first step toward linking the outputs of a cardiac injury symbolic reasoning engine with HIP model settings. When fully implemented, this integration would allow a HIP model to be automatically amended with specific injuries determined by an outside system. The overall result is improved predictive power with anticipated practical applications in medical care and teaching. Models are available at http://nsr.bioeng.washington.edu/PLN/Members/mneal/integrated_html/view.

This work was supported by a grant from the DARPA, executed by the U.S. Army Medical Research and Material Command/TATRC Cooperative Agreement, Contract # W81XWH-04-2-0012.

1) Dash RK and Bassingthwaighte JB. Blood HbO_2 and $HbCO_2$ dissociation curves at varied O_2, CO_2, pH, 2,3-DPG and temperature levels. Ann Biomed Eng 2004 (in press).
2) Lu K, Clark JW, Ghorbel FH, Ware DL, Bidani A. A human cardiopulmonary system model applied to the analysis of the Valsalva maneuver. Am J Physiol Heart Circ Physiol. 281: H2661-H2679, 2001.
3) Rideout VC. Mathematical computer modeling of physiological systems. Englewood Cliffs, NJ: Prentice Hall, 1991, 261 pp.
4) Sun Y, Beshara M, Lucariello RJ, Chiaramida SA. A comprehensive model for right-left heart interaction under the influence of pericardium and baroreflex. Am J Physiol Heart Circ Physiol. 272: H1499-H1515, 1997.
5) Usyk TP, LeGrice IJ, and McCulloch AD. Computational model of three-dimensional cardiac electromechanics. Comput Visual Sci 4: 249-257, 2002.

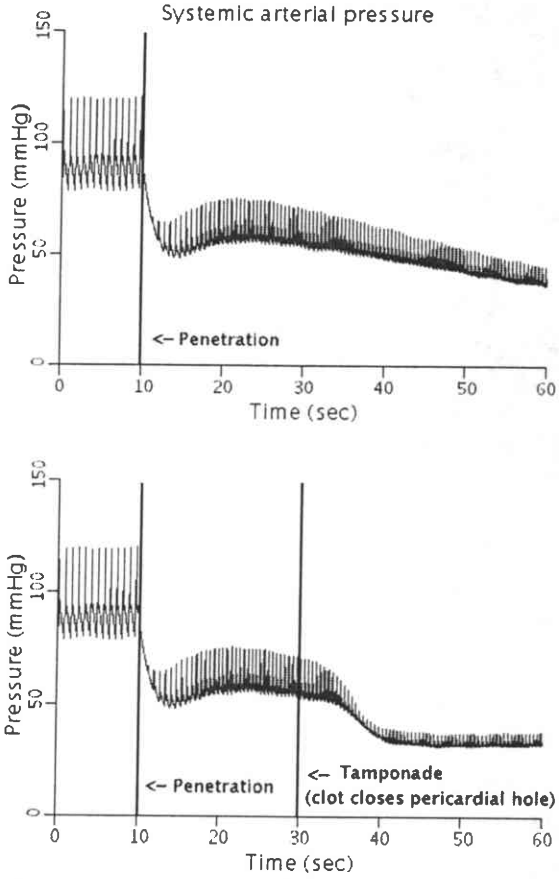

Figure 1- Systemic arterial pressure during cardiac penetration. Top: At 10 sec, a hole with a 2.5mm radius is created in the pericardium, left ventricle and septum. Bottom: Same injury with the pericardial hole closing at 30 sec.

Japanese Journal of Physiology. 2004 Dec; 54(6):531-9.

FUNCTIONALLY AND STRUCTURALLY INTEGRATED COMPUTATIONAL MODELING OF VENTRICULAR PHYSIOLOGY

Andrew D. McCulloch, Ph.D.

Department of Bioengineering

Whitaker Institute for Biomedical Engineering

University of California San Diego

9500 Gilman Drive

La Jolla, CA 92093-0412

Email: amcculloch@ucsd.edu

Fax: 858-534-5722

Tel: 858-534-2547

ABSTRACT

Computational biology is integrative in several ways. Functionally, computational models are valuable for integrating the many interacting processes within biochemical networks and the many interacting physiological subsystems within the cell. Structurally detailed models provide a means of integrating across scales of biological organization from molecule to organism. Data integration across diverse laboratory and clinical measurements is another unique strength of computational biology. We describe examples of all three categories of integration using recent advances in modeling cardiac excitation-contraction coupling and whole heart electromechanics in health and disease.

INTRODUCTION

A characteristic advantage of the use of computational tools in biomedical science is the ability to *integrate* scientific information. There are at least three distinct but interrelated ways in which computation in biology is integrative. Perhaps the most familiar is *data integration*: that is, the use of information technologies such as databases, web services, data management and analysis tools to archive, federate, search, query, match and integrate biological data from diverse sources from genomic and proteomic, metabolic and structural, to physiological and clinical data. This is the realm of *bioinformatics*.

Mathematical and statistical modeling provides the foundation for computational tools that facilitate *functional integration*: systems models of biological processes can compute functional consequences of interactions between individual components of cellular biochemical networks, or between functional subsystems within the cell, or between different cells and cell types within tissues, or between organs and organ systems within the whole body. Functionally integrated modeling is the domain of *systems biology and systems physiology*.

Finally, *structurally integrated* numerical models use physico-chemical first principles and detailed representations of three-dimensional biological structure to predict the function of proteins, cells, tissues or organs. This field is often referred to simply as *computational biology*. Whereas bioinformatics and systems biology are data-intensive, structurally integrated computational biology tends more often to be compute-limited.

Cardiac physiology is one biomedical application where functionally and structurally integrated computational modeling has made significant contributions. As data accumulate on the molecular and cellular mechanisms underlying cardiac physiology and pathophysiology, and as computational power continues to increase, the potential for increasingly sophisticated and predictive mechanistic models of the normal and diseased heart is growing rapidly. **Figure 1** shows a scheme for a functionally and structurally integrated computational model of the heart and circulation that has been developed as a result of two multi-institution collaborative research projects: the Integrated Human Function project supported by NASA through the National Biomedical Space Research Institute; and the Virtual Soldier Project, support by the U.S. Defense Advanced Research Projects Agency. These collaborative projects involve investigators from over a dozen institution including the University of Washington, the University of Michigan, Ann Arbor, the University of Utah, Oak Ridge National Laboratory, Stanford University, Loyola University of Chicago and Auckland University. We summarize here, some recent examples of new functionally and structurally integrated models of cardiac physiology and pathophysiology and point to new directions.

FUNCTIONALLY INTEGRATED MODELS OF CARDIAC MYOCYTES

Myocyte Ionic Models

The first cardiac myocyte models, published in 1960 (Fitzhugh, 1960; Noble, 1960), used the formalism developed by Hodgkin and Huxley (Hodgkin *et al.*, 1952) to model the contributions of sodium and potassium currents to the action potential and to investigate the mechanistic basis of the plateau of the cardiac action potential. As new experimental data on myocyte electrophysiology were obtained, the models were refined and extended, and their results in turn informed new experiments.

The latest generation of cardiac myocyte ionic models include upwards of 40 ordinary differential equations (Michailova *et al.*, 2001). They also include separate compartments representing the sarcoplasmic reticulum (SR), the narrow subsarcolemmel dyadic space between the sarcolemmal dihydropyridine receptor and the ryanodine receptor on the SR, and the bulk myoplasm (Winslow *et al.*, 1999). But these compartments are lumped, and these "common pool" models have no spatial structure. They are functionally integrated systems models.

The ionic models are valuable because they compute the interactions between numerous ion channels, pumps, transporters who properties have been painstakingly dissected experimentally. They have been used to perform a wide range of numerical experiments, even studies on the effects of single gene mutations associated with clinically observed arrhythmias. These latter models have typically been hybrids of classical Hodgkin-Huxley style models based on whole cell voltage clamp responses combined with more detailed Markov state-transition models based on single channel recordings. These models therefore represent some of the best and earliest examples of clinical disease phenotypes predicted in mathematical models from knowledge of single gene defects. One example is the study by Clancy and Rudy (Clancy *et al.*, 1999) demonstrating how the ΔKPQ mutation in the fast sodium channel can be pro-arrhythmic in patients with the LQT3 variant of long QT syndrome.

Excitation-Contraction Coupling

In addition to integrating across the cellular components responsible for ion fluxes and action potential generation, systems models have also been developed that integrate the functional components of cellular subsystems responsible for cardiac energy metabolism, muscle contraction, transport processes, and signal transduction. This then creates the opportunity to develop systems models that not only

integrate the components within a single sub-system but that also integrate the functions of two or more interacting sub-systems. Excitation-contraction coupling is one obvious such interaction, and the first mechanistic systems models of cardiac excitation-contraction coupling were published in the 1970's and 80's (Wong, 1981; Wong, 1970). Since then, more detailed models have been developed of myofilament activation by calcium and the effects of feedback from crossbridge binding (Michailova *et al.*, 1997; Rice *et al.*, 1999). Bluhm *et al* (Bluhm *et al.*, 1998) coupled the Luo-Rudy ionic model to a model of myofilament activation to predict the time-course of isometric tension development following an increase in sarcomere length. The model included the well-known Frank-Starling mechanism, but could not predict the slow component of the Frank-Starling response, which had first been described by von Anrep in 1912 and is thus often called the *Anrep effect*. By systematically perturbing all the components of the model at the time of the imposed stretch, the authors concluded that the mechanism of the slow increase in tension involves a sodium flux. At the time, available experimental data did not support this conclusion, but the following year, the first in a series of papers (Alvarez *et al.*, 1999) was published suggesting strongly a role for the sodium-proton antiporter and intracellular sodium accumulation in the cellular mechanisms of the Anrep effect.

Myocyte Metabolism and Metabolic Regulation of E-C Coupling

The field in which large-scale integrative systems models have arguably progressed the furthest is that of metabolic network modeling (Schilling *et al.*, 2000). The stoichiometry of biochemical reaction networks imposes constraints on their function. The use of metabolic flux balance analysis combined with comprehensive databases of metabolic networks such as the Kyoto Encyclopedia of Genes and Genomes[1] has led to the development of constraint-based methods capable of modeling metabolic networks at genome scale. Ramakrishna et al (Ramakrishna *et al.*, 2001) used flux-balance analysis to

[1] http://www.genome.ad.jp/kegg/

analyze the flux distributions for maximal mitochondrial production of adenosine triphosphate (ATP). The expected ATP yields for glucose, lactate, and palmitate were accurately predicted, and the effects of gene mutations on mitochondrial ATP production was simulated. Mitochondrial ATP production was severely affected by mutations in the tricarboxylic acid (TCA) cycle. In addition, the model predicted the secretion of TCA-cycle intermediates, which is observed clinically in mitochondriopathies such as those associated with fumarase deficiency.

This progress naturally suggests the integration of electrophysiological models with models of energy metabolism in the cardiac myocyte. The first comprehensive example was published by Ch'en and colleagues (Ch'en *et al.*, 1997). The analysis gave valuable insights into the arrhythmogenic mechanisms of ischemia, especially during the highly vulnerable reperfusion period. More recently, a comprehensive thermokinetic model by Cortassa and co-workers (Cortassa *et al.*, 2003) analyzed control of cardiac mitochondrial bioenergetics by combining equations for the TCA cycle, oxidative phosphorylation, and mitochondrial calcium handling. The model reproduced observations on mitochondrial bioenergetics, calcium dynamics, and respiratory control and demonstrated how calcium feedback provides a mechanism for matching mitochondrial energy production with the metabolic demand of the myocyte as workload changes. Michailova and McCulloch (Michailova *et al.*, 2001) extended the model of the ventricular myocyte by Winslow *et al.* (Winslow *et al.*, 1999) by incorporating equations for calcium and magnesium buffering and transport by ATP and ADP and equations for MgATP regulation of the sodium-potassium pump, and the sarcolemmal and sarcoplasmic calcium pumps. Under normal conditions, the model showed that calcium binding by low-affinity ATP and diffusion of CaATP may affect the amplitude and time course of intracellular calcium signals. Some of these predictions were subsequently supported by experimental observations

(Yang *et al.*, 2001). More recently, this model has also been used to study the effects of magnesium on ventricular excitation-contraction coupling (Michailova *et al.*, 2004).

Neurohormonal Regulation: Systems Models of Myocyte Signaling Pathways

While not yet as comprehensive as databases of metabolic networks, public data resources on cell signaling such as the Alliance for Cellular Signaling[2] (Papin *et al.*, 2004) are emerging. This is opening the way for more details systems models of signal transduction pathways. By integrating models of signaling networks with models of cardiac myocytes, it is now possible to investigate neurohormonal regulation of excitation-contraction coupling. Saucerman and colleagues (Saucerman *et al.*, 2003) developed a new model of β_1-adrenergic regulation of cardiac excitation-contraction coupling by combining a systems model of ionic currents and calcium handling in rat ventricular myocytes with a novel mechanistic model of cAMP-mediated cell signaling via β_1-adrenergic receptor that included the L-type calcium channel, phospholamban and inhibitor-1 as phosphorylation targets of protein kinase A (PKA). Later, they (Saucerman *et al.*, 2004) extended this model to include troponin-I and the ryanodine receptor (RyR) as additional PKA targets, though the analysis suggested that the controversial role of Ryr phosphorylation during adrenergic stimulation may be fairly insignificant under normal conditions in the intact cell owing to the effects of calcium autoregulation by the sarcoplasmic reticulum. This new class of models may be especially important for elucidating the pathogenesis of congestive heart failure, where dysregulated calcium handling in the myocyte is accompanied by down-regulation of β-adrenergic signaling. Another promising application of this new class of functionally integrated myocyte model is the subset of genetic arrhythmias (including a majority of individuals with the most prevalent of long QT syndromes, LQT1) that are associated with

[2] http://www.signaling-gateway.org/

stimulation of the sympathetic nervous systems during exercise and startle (Kass *et al.*, 2003; Marx *et al.*, 2002).

STRUCTURALLY INTEGRATED MODELS OF MYOCYTES, MYOCARDIUM AND WHOLE HEARTS

Myocyte Models

In contrast to functionally integrated systems models that are data intensive, spatially coupled structurally integrated models use physico-chemical principles to span scales of structural organization and therefore tend to be computationally intensive. Some examples of spatially coupled models of single cells include models of the diffusion of calcium and other ions in the cytoplasm. Michailova *et al.* (Michailova *et al.*, 2002) developed an axisymmetric model of calcium diffusion in the atrial myocyte, which lacks t-tubules in many mammalian species. The model incorporated radial calcium diffusion, binding to mobile and stationary calcium buffers, and subcellular compartments, including a subsarcolemmal space with restricted diffusion, a myofilament space, and the cytosol. Using measured L-type calcium currents as an input, the model computed local calcium signals that were qualitatively and quantitatively consistent with those imaged using the fluorescent calcium indicator Fluo-3 by laser-scanning confocal microscopy. In addition to steep concentration gradients in the subsarcolemmal region, the model showed the important effects of mobile intracellular calcium buffers including ATP (despite its low calcium affinity) and the indicator itself. In fact the effects of the buffering *per se*, and buffer mobility were not concordant. As the concentration of indicator in the model was decreased, the

magnitude of the calcium transient initially rose near the cell center as calcium buffering declined but then decreased as the contribution of the buffer to calcium diffusion was lost.

Another important modulator of myocyte physiology is intracellular pH, which is regulated by sarcolemmal proton transporters and stabilized by numerous intracellular buffers. Swietach *et al.* (Swietach *et al.*, 2003)investigated how the mobility of intracellular H^+ buffers affect proton diffusion by using two dimensional computational models to analyze the spatio-temporal distributions of H^+ concentration subject to local perturbations as a function of membrane proton-equivalent transport and cell geometry. As in the calcium diffusion models of Michailova *et al.* (Michailova *et al.*, 2002), confocal imaging using intracellular pH-sensitive dyes provided valuable data for model validation and hypothesis testing. By matching the model results to experimental data, the authors estimated an apparent intracellular H^+ diffusion coefficient in mammalian ventricular myocytes of 4.0×10^{-7} cm^2/s compared with around $1.2\times10^{-4}cm^2/s$ in free unbuffered solution at 37°C. Thus intracellular buffers decrease apparent cytosolic proton mobility by over two orders of magnitude.

Multicellular Models of Myocardium

Multicellular models come in three main varieties: cellular automata; resistively coupled networks and continuum models. Cellular automata and resistively coupled networks use physical properties or rules that approximate them to combine individual cells modeled as systems of ordinary differential equations as described earlier. These models are computationally tractable and have been particularly informative in elucidating the effects of electrical loading by neighboring cells on the propagation of the action potential from cell to cell via current flux through gap junctions. For example, Shaw and Rudy (Shaw *et al.*, 1997) used a multicellular model to explore the differences between conduction

slowing associated with decreased membrane excitability and that associated with reduced gap junction coupling. Whereas the "safety factor" for maintained conduction was decreased as membrane excitability decreased so that eventually conduction block occurred, decreased intercellular coupling actually increased the safety factor allowing very slow conduction to occur. Under these conditions the L-type calcium current became increasingly important in sustaining conduction as propagation was slowed, making it a potentially important mediator of reentrant activity during conditions of cellular uncoupling such as myocardial ischemia.

Continuum models of electrical impulse propagation typically use bi-domain or monodomain theory in which the intracellular and extracellular conductivities of the tissue are lumped into diffusion tensors, which are anisotropic and may differ between intracellular and extracellular domains (Trayanova *et al.*, 2002). Though they fail to account for the discreteness of myocardial properties, these well-established models are a three-dimensional extension of classical cable theory, and have been widely used for a large range of problems, including sophisticated large-scale analyses of the induction and stability of ventricular reentry and fibrillation in anatomically detailed whole heart models (Xie *et al.*, 2004) and the conversion of fibrillation to normal rhythm by an external shock.(Rodriguez *et al.*, 2003)..For a detailed derivation of these continuum theories see Belik et al (Belik *et al.*, 2004).

Continuum methods are also widely used for modeling regional biomechanics in the heart and other tissues (Usyk *et al.*, 2003). Within the continuum framework however, a constitutive model of the contributions of cellular and extracellular constituents is required to relate the passive and contractile stresses in the tissue to the state of deformation (strain). While many constitutive models are phenomenological relations, curved fitted to multiaxial experimental measurements of tissue

mechanical responses (Lin *et al.*, 1998), it is possible to apply micromechanical principles and quantitative histological measurements to derive microstructural constitutive relations. MacKenna and colleagues (MacKenna *et al.*, 1997) derived a microstructural model of the large coiled perimysial collagen fibers that run parallel to the layers of myocytes in the ventricular wall. By measuring the fiber diameter, number density and tortuosity and making use of measured properties of isolated collagen fibers, this model was able to explain the differences in tissue fiber stiffness seen between dogs and rats, and provided a mechanism that quantitatively explained the higher resting stiffness of myocardium parallel to than transverse to the mean muscle fiber direction. Costa and co-workers (Costa *et al.*, 2001) applied a microstructural approach to derive the anisotropic three-dimensional stress-strain properties of post-infarction myocardial scar tissue from detailed measured distributions of local collagen fiber orientations and numerical densities in different layers of the wall in transmural porcine infarct. The model suggested significant mechanical heterogeneities across the thickness of the infarct, and strains computed with the model under physiological loading showed good agreement with experimental measurements (Holmes *et al.*, 1994). Usyk and colleagues (Usyk *et al.*, 2000)developed a multi-scale model of three-dimensional active systolic myocardial mechanics that takes into account the orientation of crossbridges in the strongly bound state and the statistical dispersion of myofiber orientations within the tissue, which averages about 12° (Karlon *et al.*, 1998). The model was consistent with the experimental observation that tonically activated biaxial preparations of ventricular muscle generate a significant component of active stress perpendicular to the fiber axis, that can exceed 50% of the systolic fiber stress (Lin *et al.*, 1998)..

Detailed Models of Ventricular Anatomy

Models have been developed of the geometry and myofiber architecture of the dog (Nielsen *et al.*, 1991), rabbit (Vetter *et al.*, 1998) and pig (Stevens *et al.*, 2003) ventricles and human atria (Harrild *et al.*, 2000; Jacquemet *et al.*, 2003). The emergence of diffusion tensor magnetic resonance imaging as a non-destructive method for imaging myofiber architecture in fixed hearts (Hsu *et al.*, 1998; Scollan *et al.*, 1998). With interest in genetically engineered mouse models for studies of the molecular pathogenesis of inherited and acquired heart disease, there is increasing need for a model of the mouse ventricles. The small size of the mouse heart excludes reconstructions with the histological and dissection mechanisms, but opens up the possibility of serial section reconstructions at comparatively high resolutions approaching the diffraction limits of light.

Anatomically Detailed Models of Cardiac Electromechanics

The development of anatomically detailed models of cardiac geometry and muscle fiber architecture has enabled investigators to develop structurally integrated continuum models of cardiac electrical impulse propagation (Harrild *et al.*, 2000; Xie *et al.*, 2004) and wall mechanics (Stevens *et al.*, 2003) using finite volume, finite difference, or finite element methods. As cellular models become more biophysically detailed and functionally integrated, the opportunity is arising for structurally integrated models that are also functionally integrated, such as continuum models of coupled ventricular electromechanics (Kerckhoffs *et al.*, 2003; Kerckhoffs *et al.*, 2003; Usyk *et al.*, 2002; Usyk *et al.*, 2003; Usyk *et al.*, 2003)

Kerckhoffs *et al.* (Kerckhoffs *et al.*, 2003; Kerckhoffs *et al.*, 2003) use an eikonal curvature model of the anisotropic spread of electrical depolarization in the left ventricular wall and coupled the activation

time to the generation of systolic fiber tension via a constant time delay. Paradoxically, incorporating more physiological detail of ventricular electromechanics in the new model compared with earlier models in which mechanical activations was assumed to be regionally simultaneous, actually predicted regional transmural systolic fiber strain distributions that were unphysiologically inhomogeneous. Experimental studies in our laboratory and others have shown consistently that normal systolic fiber lengthening during filling and shortening during ejection tends to be transmurally uniform (Omens *et al.*, 1991; Takayama *et al.*, 2002; Waldman *et al.*, 1988)}. Computational models that take into account the fiber orientation, material anisotropy and geometry of the ventricular walls have shown excellent agreement with these measurements, and demonstrate that this regional homogeneity of fiber stress and strain is the combined consequence of the distribution of fiber orientation and myocardial torsional shearing (Usyk *et al.*, 2000). When simulating left ventricular mechanics with synchronous activation, myofiber strain was more homogeneous and in closer agreement with experimental observation than when the transmural activation delays associated with normal sinus rhythm were included in the model. Apparently, the assumption of a constant delay between depolarization and onset of crossbridge formation results in an unrealistic contraction pattern. The present finding may indicate that electromechanical delay times are heterogeneously distributed, such that a contraction in a normal heart is more synchronous than depolarization. Recent experimental evidence supports this conclusion. Cordeiro *et al.* (Cordeiro *et al.*, 2004) measured unloaded cell shortening, calcium transients, and inward L-type calcium currents in myocytes isolated from the canine left ventricular epicardial, endocardial, and midmyocardial layers. The onset and time to peak of contraction were longest in endocardial cells, shortest in epicardial myocytes and intermediate in midmyocardial cells. These authors concluded that regional difference in intracellular calcium handling were primarily responsible

for these transmural mechanical variations, which may provide a mechanism for maintaining transmural mechanical synchrony.

Usyk *et al.* coupled a model of action potential propagation in the left and right ventricles of the dog heart to investigate the mechanical effects of altered cardiac activation sequence during ventricular pacing. They used the three-dimensional Auckland canine anatomic model (Legrice *et al.*, 1997) incorporating a two-dimensional model of the endocardial Purkinje fiber network (Usyk *et al.*, 2002) to investigate the relationship between local electrical activation and the timing of fiber shortening. Asynchronous time-courses of regional fiber strains during contractions stimulated from the ventricular epicardium agreed well with MRI tagging measurements in dogs (Wyman *et al.*, 1999). When electrical activation in the model was coupled to the activation of local myofilament tension by a constant time delay of 8 ms, the mean delay from electrical activation to the onset of systolic fiber shortening was 14 ms. However, the delay between the onset of fiber tension and initial shortening varied substantially; being as late as 60 ms in some sites but as early as –50 ms in others, particularly the septum, and especially during right ventricular pacing. This large variation in activation-contraction delays was attributable to various factors, though the single greatest determinant appeared to be transmural coupling. For example, since most of the wall activated from endocardium to epicardium, even during epicardial pacing, longer delay times were seen on the endocardium than the epicardium, where endocardial unloading often caused passive epicardial shortening before epicardial depolarization.

Clinical Applications

One application of coupled ventricular electromechanical models is cardiac resynchronization therapy. Clinical and experimental evidence suggests that bi-ventricular pacing in patients with heart failure and widening of the QRS complex can improve hemodynamic pump function. However, the extent of QRS narrowing is not necessarily a good predictor of the hemodynamic improvement, and the optimal protocol for best functional improvement is not necessarily that which reduces QRS width the most (Leclercq *et al.*, 2002). Usyk and McCulloch (Usyk *et al.*, 2003) developed a computational model of ventricular electromechanics in the failing dog heart with left bundle branch block. The model was able to reproduce quite well experimentally observed improvements in mechanical synchrony associated with simultaneous bi-ventricular pacing in experimental animals (Leclercq *et al.*, 2002). The hemodynamic improvements were also consistent with experimental and clinical observations. Subsequently (**Figure 2**), the model has been used to simulate cardiac resynchronization with asynchronous left-right pacing. Consistent with some clinical observations, a 15 ms delay between left and right ventricular pacing further increased the hemodynamic improvement from an absolute increase in ejection fraction of 4.4% with synchronous bi-ventricular pacing to 7.5% with left-right sequential pacing.

ACKNOWLEDGEMENTS

The author thanks his colleagues and students Mary Ellen Belik, Sarah Healy, Anushka Michailova, Jeffrey Saucerman, and Taras Usyk and for their contributions to this article. The research described here was supported by the National Biomedical Computation Resource (NIH grant P41 RR08605), the National Science Foundation (BES-0086482), the National Biomedical Space Research Institute

(NASA CA00216), and a grant from the Defense Advanced Research Projects Agency (executed by the U.S. Army Medical Research and Materiel Command/TATRC Cooperative Agreement, Contract # W81XWH-04-2-0012.)

REFERENCES

Alvarez BV, Perez NG, Ennis IL, Camilion De Hurtado MC, Cingolani HE. Mechanisms underlying the increase in force and Ca(2+) transient that follow stretch of cardiac muscle : A possible explanation of the anrep effect. *Circ Res*. 1999;85:716-22.

Belik ME, Usyk TP, McCulloch AD. Computational methods for cardiac electrophysiology (in press). In: Ayache N, ed. *Computational Models for the Human Body*: Elsevier B.V.; 2004:1-69.

Bluhm WF, Lew WY, Garfinkel A, McCulloch AD. Mechanisms of length-history dependent tension in an ionic model of the cardiac myocyte. *American Journal of Physiology*. 1998;274:H1032-40.

Ch'en F, Clarke K, Vaughan-Jones R, Noble D. Modeling of internal pH, ion concentration, and bioenergetic changes during myocardial ischemia. In: Sideman S, Beyar R, eds. *Analytical and Quantitative Cardiology*. New York: Plenum; 1997:281-290.

Clancy CE, Rudy Y. Linking a genetic defect to its cellular phenotype in a cardiac arrhythmia. *Nature*. 1999;400:566-9.

Cordeiro JM, Greene L, Heilmann C, Antzelevitch D, Antzelevitch C. Transmural heterogeneity of calcium activity and mechanical function in the canine left ventricle. *Am J Physiol Heart Circ Physiol*. 2004;286:H1471-9.

Cortassa S, Aon MA, Marban E, Winslow RL, O'Rourke B. An integrated model of cardiac mitochondrial energy metabolism and calcium dynamics. *Biophys J*. 2003;84:2734-55.

Costa KD, Holmes JW, McCulloch AD. Modeling cardiac mechanical properties in three dimensions. *Phil Trans R Soc Lond A*. 2001;359:1233-1250.

Fitzhugh R. *J Gen Physiol*. 1960;43:867-896.

Harrild D, Henriquez C. A computer model of normal conduction in the human atria. *Circ Res*. 2000;87:E25-36.

Hodgkin AL, Huxley AF. A quantitative description of membrane current and its application to conduction and excitation in nerve. *J Physiol*. 1952;117:500-544.

Holmes JW, Yamashita H, Waldman LK, Covell JW. Scar remodeling and transmural deformation after infarction in the pig. *Circ*. 1994;90:411-420.

Hsu EW, Muzikant AL, Matulevicius SA, Penland RC, Henriquez CS. Magnetic resonance myocardial fiber-orientation mapping with direct histological correlation. *Am J Physiol*. 1998;274:H1627-34.

Jacquemet V, Virag N, Ihara Z, Dang L, Blanc O, Zozor S, Vesin JM, Kappenberger L, Henriquez C. Study of unipolar electrogram morphology in a computer model of atrial fibrillation. *J Cardiovasc Electrophysiol*. 2003;14:S172-9.

Karlon WJ, Covell JW, McCulloch AD, Hunter JJ, Omens JH. Automated measurement of myofiber disarray in transgenic mice with ventricular expression of ras. *Anatomical Record.* 1998;252:612-625.

Kass RS, Kurokawa J, Marx SO, Marks AR. Leucine/isoleucine zipper coordination of ion channel macromolecular signaling complexes in the heart. Roles in inherited arrhythmias. *Trends Cardiovasc Med.* 2003;13:52-6.

Kerckhoffs RC, Bovendeerd PH, Kotte JC, Prinzen FW, Smits K, Arts T. Homogeneity of cardiac contraction despite physiological asynchrony of depolarization: a model study. *Ann Biomed Eng.* 2003;31:536-47.

Kerckhoffs RC, Faris OP, Bovendeerd PH, Prinzen FW, Smits K, McVeigh ER, Arts T. Timing of depolarization and contraction in the paced canine left ventricle: model and experiment. *J Cardiovasc Electrophysiol.* 2003;14:S188-95.

Leclercq C, Faris O, Tunin R, Johnson J, Kato R, Evans F, Spinelli J, Halperin H, McVeigh E, Kass DA. Systolic improvement and mechanical resynchronization does not require electrical synchrony in the dilated failing heart with left bundle-branch block. *Circulation.* 2002;106:1760-3.

Legrice IJ, Hunter PJ, Smaill BH. Laminar structure of the heart: a mathematical model. *Am J Physiol.* 1997;272:H2466-76.

Lin DHS, Yin FCP. A multiaxial constitutive law for mammalian left ventricular myocardium in steady-state barium contracture or tetanus. *J Biomech Eng.* 1998;120:504-517.

MacKenna DA, Vaplon SM, McCulloch AD. Microstructural model of perimysial collagen fibers for resting myocardial mechanics during ventricular filling. *American Journal of Physiology.* 1997;273:H1576-86.

Marx SO, Kurokawa J, Reiken S, Motoike H, D'Armiento J, Marks AR, Kass RS. Requirement of a macromolecular signaling complex for beta adrenergic receptor modulation of the KCNQ1-KCNE1 potassium channel. *Science.* 2002;295:496-9.

Michailova A, Belik ME, McCulloch A. Effects of magnesium on cardiac excitation-contraction coupling. *Magnesium Research (in press).* 2004.

Michailova A, DelPrincipe F, Egger M, Niggli E. Spatiotemporal features of ca(2+) buffering and diffusion in atrial cardiac myocytes with inhibited sarcoplasmic reticulum. *Biophys J.* 2002;83:3134-51.

Michailova A, McCulloch A. Model study of ATP and ADP buffering, transport of Ca(2+) and Mg(2+), and regulation of ion pumps in ventricular myocyte. *Biophys J.* 2001;81:614-29.

Michailova A, Spassov V. Computer simulation of excitation-contraction coupling in cardiac muscle. A study of the regulatory role of calcium binding to troponin C. *Gen Physiol Biophys.* 1997;16:29-38.

Nielsen PMF, Le Grice IJ, Smaill BH, Hunter PJ. Mathematical model of geometry and fibrous structure of the heart. *Am J Physiol.* 1991;260:H1365-H1378.

Noble D. *Nature.* 1960;188:495-497.

Omens JH, May KD, McCulloch AD. Transmural distribution of three-dimensional strain in the isolated arrested canine left ventricle. *Am J Physiol.* 1991;261:H918-28.

Papin J, Subramaniam S. Bioinformatics and cellular signaling. *Curr Opin Biotechnol.* 2004;15:78-81.

Ramakrishna R, Edwards JS, McCulloch A, Palsson BO. Flux-balance analysis of mitochondrial energy metabolism: consequences of systemic stoichiometric constraints. *Am J Physiol Regul Integr Comp Physiol.* 2001;280:R695-704.

Rice JJ, Winslow RL, Hunter WC. Comparison of putative cooperative mechanisms in cardiac muscle: length dependence and dynamic responses. *Am J Physiol.* 1999;276:H1734-54.

Rodriguez B, Trayanova N. Upper limit of vulnerability in a defibrillation model of the rabbit ventricles. *J Electrocardiol.* 2003;36 Suppl:51-6.

Saucerman JJ, Brunton LL, Michailova AP, McCulloch AD. Modeling beta-adrenergic control of cardiac myocyte contractility in silico. *J Biol Chem.* 2003;278:47997-8003.

Saucerman JJ, McCulloch AD. Mechanistic systems models of cell signaling networks: a case study of myocyte adrenergic regulation. *Prog Biophys Mol Biol.* 2004;85:261-78.

Schilling CH, Edwards JS, Letscher D, Palsson BO. Combining pathway analysis with flux balance analysis for the comprehensive study of metabolic systems. *Biotechnol Bioeng.* 2000;71:286-306.

Scollan DF, Holmes A, Winslow R, Forder J. Histological validation of myocardial microstructure obtained from diffusion tensor magnetic resonance imaging. *Am J Physiol.* 1998;275:H2308-18.

Shaw RM, Rudy Y. Electrophysiologic effects of acute myocardial ischemia: A mechanistic investigation of action potential conduction and conduction failure. *Circ Res.* 1997;80:124-138.

Stevens C, Hunter PJ. Sarcomere length changes in a 3D mathematical model of the pig ventricles. *Prog Biophys Mol Biol.* 2003;82:229-41.

Swietach P, Zaniboni M, Stewart AK, Rossini A, Spitzer KW, Vaughan-Jones RD. Modelling intracellular H(+) ion diffusion. *Prog Biophys Mol Biol.* 2003;83:69-100.

Takayama Y, Costa KD, Covell JW. Contribution of laminar myofiber architecture to load-dependent changes in mechanics of LV myocardium. *Am J Physiol Heart Circ Physiol.* 2002;282:H1510-20.

Trayanova N, Eason J, Aguel F. Computer simulations of cardiac defibrillation: a look inside the heart. *Comput Visual Sci.* 2002;4:259-270.

Usyk TP, LeGrice IJ, McCulloch AD. Computational model of three-dimensional cardiac electromechanics. *Comput Visual Sci.* 2002;4:249-257.

Usyk TP, Mazhari R, McCulloch AD. Effect of laminar orthotropic myofiber architecture on regional stress and strain in the canine left ventricle. *J Elasticity.* 2000;61:143-164.

Usyk TP, McCulloch AD. Computational methods for soft tissue biomechanics. In: Holzapfel GA, Ogden RW, eds. *Biomechanics of Soft Tissue in Cardiovascular Systems.* Wien: Springer; 2003:273-342.

Usyk TP, McCulloch AD. Electromechanical model of cardiac resynchronization in the dilated failing heart with left bundle branch block. *J Electrocardiol.* 2003;36:57-61.

Usyk TP, McCulloch AD. Relationship between regional shortening and asynchronous electrical activation in a three-dimensional model of ventricular electromechanics. *Journal of Cardiovascular Electrophysiology.* 2003;14:S196-S202.

Vetter FJ, McCulloch AD. Three-dimensional analysis of regional cardiac function: a model of rabbit ventricular anatomy. *Progress in Biophysics and Molecular Biology.* 1998;69:157-183.

Waldman LK, Nossan D, Villarreal F, Covell JW. Relation between transmural deformation and local myofiber direction in canine left ventricle. *Circ Res.* 1988;63:550-562.

Winslow RL, Rice J, Jafri S, Marban E, O'Rourke B. Mechanisms of altered excitation-contraction coupling in canine tachycardia-induced heart failure, II: model studies. *Circ Res.* 1999;84:571-86.

Wong AY. A model of excitation-contraction coupling of mammalian cardiac muscle. *J Theor Biol.* 1981;90:37-61.

Wong AYK. A concentric layer model for estimating the energy expenditure of the left ventricle. *Bull Math Biophys*. 1970;32:581-598.

Wyman BT, Hunter WC, Prinzen FW, McVeigh ER. Mapping propagation of mechanical activation in the paced heart with MRI tagging. *Am J Physiol*. 1999;276:H881-91.

Xie F, Qu Z, Yang J, Baher A, Weiss JN, Garfinkel A. A simulation study of the effects of cardiac anatomy in ventricular fibrillation. *J. Clin. Invest*. 2004;113:686-693.

Yang Z, Steele DS. Effects of cytosolic ATP on Ca(2+) sparks and SR Ca(2+) content in permeabilized cardiac myocytes. *Circ Res*. 2001;89:526-33.

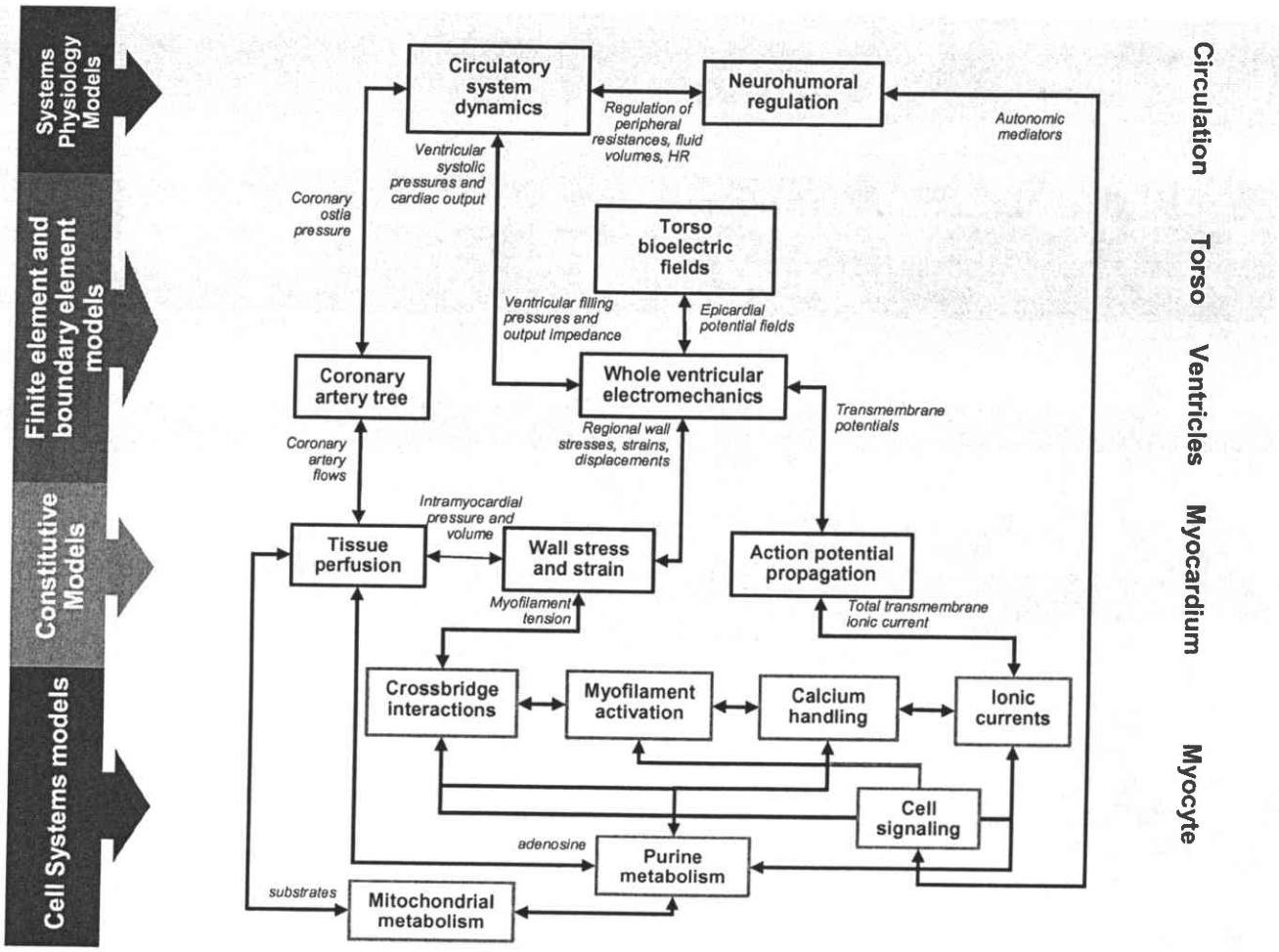

Figure 1: An integrative modeling scheme for the physiology of the heart and circulation adapted and extended from Bassingthwaighte's "Cardiome" concept. The model is both structurally and functionally integrated and requires both data- and compute-intensive analysis.

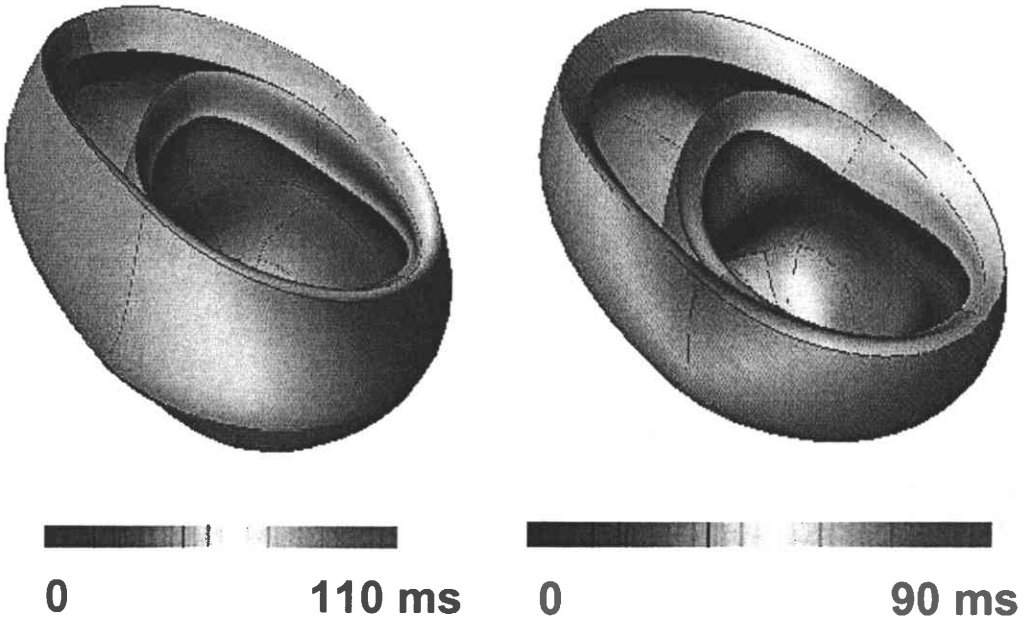

Figure 2: Color map of mechanical shortening onset times in a model of the failing canine ventricles with left bundle branch block (left) and during left-right sequential bi-ventricular pacing (right).

Linking Ontologies with Three-Dimensional Models of Anatomy to Predict the Effects of Penetrating Injuries

Rubin, D.L. Bashir, Y. Grossman, D. Dev, P. Musen, M.A.
Stanford Medical Informatics, Stanford University, Stanford, CA;

This paper appears in: **Engineering in Medicine and Biology Society, 2004. IEMBS '04. 26th Annual International Conference of the IEEE**
Publication Date: 1-5 Sept. 2004
Volume: 2, On page(s): 3128- 3131
ISBN: 0-7803-8439-3
Posted online: 2005-03-14 08:32:40.0

Abstract
Rapid diagnosis of penetrating injuries is essential to increased chance of survival. Geometric models representing anatomic structures could be useful, but such models generally contain only information about the relationships of points in space as well as display properties. We describe an approach to predicting the anatomic consequences of penetrating injury by creating a geometric model of anatomy that integrates biomechanical and anatomic knowledge. We created a geometric model of the heart from the Visible Human image data set. We linked this geometric model of anatomy with an ontology of descriptive anatomic knowledge. A hierarchy of abstract geometric objects was created that represents organs and organ parts. These geometric objects contain information about organ identity, composition, adjacency, and tissue biomechanical properties. This integrated model can support anatomic reasoning. Given a bullet trajectory and a parametric representation of a cone of tissue damage, we can use our model to predict the organs and organ parts that are injured. Our model is extensible, being able to incorporate future information, such as physiological implications of organ injuries.

Linking Ontologies with Three-Dimensional Models of Anatomy to Predict Physiological Effects of Penetrating Injuries

Daniel L. Rubin, Yasser Bashir, David Grossman, Parvati Dev, and Mark A. Musen
Stanford Medical Informatics, Stanford, CA

Motivation:
We are interested in predicting the anatomic and physiological effects of penetrating injury. The underlying technology will need to link segmented 3-d geometrical models
with anatomical models, in order to simulate both the direct and indirect effects of a projectile injury.

Methods:
Anatomic knowledge, such as which organs are in a region of the body and how they relate to other components, can be represented in an ontology. Ontologies provide formal definitions of concepts and relationships among concepts. One source of anatomic knowledge is the Digital Anatomist Foundational Model (FMA), a domain ontology that represents a coherent body of explicit declarative knowledge about human anatomy. The FMA provides formal definitions of detailed anatomical concepts and relationships of anatomic structures in a computationally-accessible format. However, it lacks information on organ shape and absolute location.

Conversely, geometric knowledge regarding the location and shape of organs is represented in a 3-d geometric model. These models may be segmented to identify organ parts and sub-parts. While geometric models contain detailed information on organ *location and shape*, the anatomical knowledge about the segmented structures remains in the head of the viewer.

Geometric and ontologic models of anatomy exist in largely disjoint worlds.

We are developing methods to integrate these two worlds so that software can relate geometry to anatomic structures in the FMA. For example, software could reason about remote consequences of a localized injury by identifying the site of injury in the geometrical model, referencing the anatomic entities associated with that site, and working through relationships in the FMA to establish the other anatomic structures that are also likely affected because they are related to the injured organs.

Our approach is based on developing an ontology of various geometric models that are used by many groups to represent an organism from segmented volumetric image data. This ontology allows components within a geometric model to be annotated with terms in the FMA in order to link geometry and anatomy. A path of destruction can be specified in the geometrical model, and a set of intercepted geometrical elements can be deduced. These geometrical elements can be mapped to the FMA to infer the organs that are injured.

Results:
We have developed a 3-d geometry ontology and will show how it can be used to add anatomic information to geometric models. Our geometry ontology represents a spectrum of primitive geometric elements used to construct 3-d geometrical models, such as points, cells, meshes, and

simplexes. These geometric elements relate to various attributes needed to simulate the effect of penetrating injury, such as boundary features, externality, and physical properties.

From a volumetric image data set of the chest, we produced 3-d geometric models of the heart. The anatomic structures, such as the ventricles and aorta, are labeled in the geometry. We have superimposed a projectile trajectory and deduced the path of injury and produce a list of damaged structures (Figure 1). We will discuss how we are developing and using ontologies to reason about what structures are adjacent to the path of injury so that we can predict the extent of organ damage.

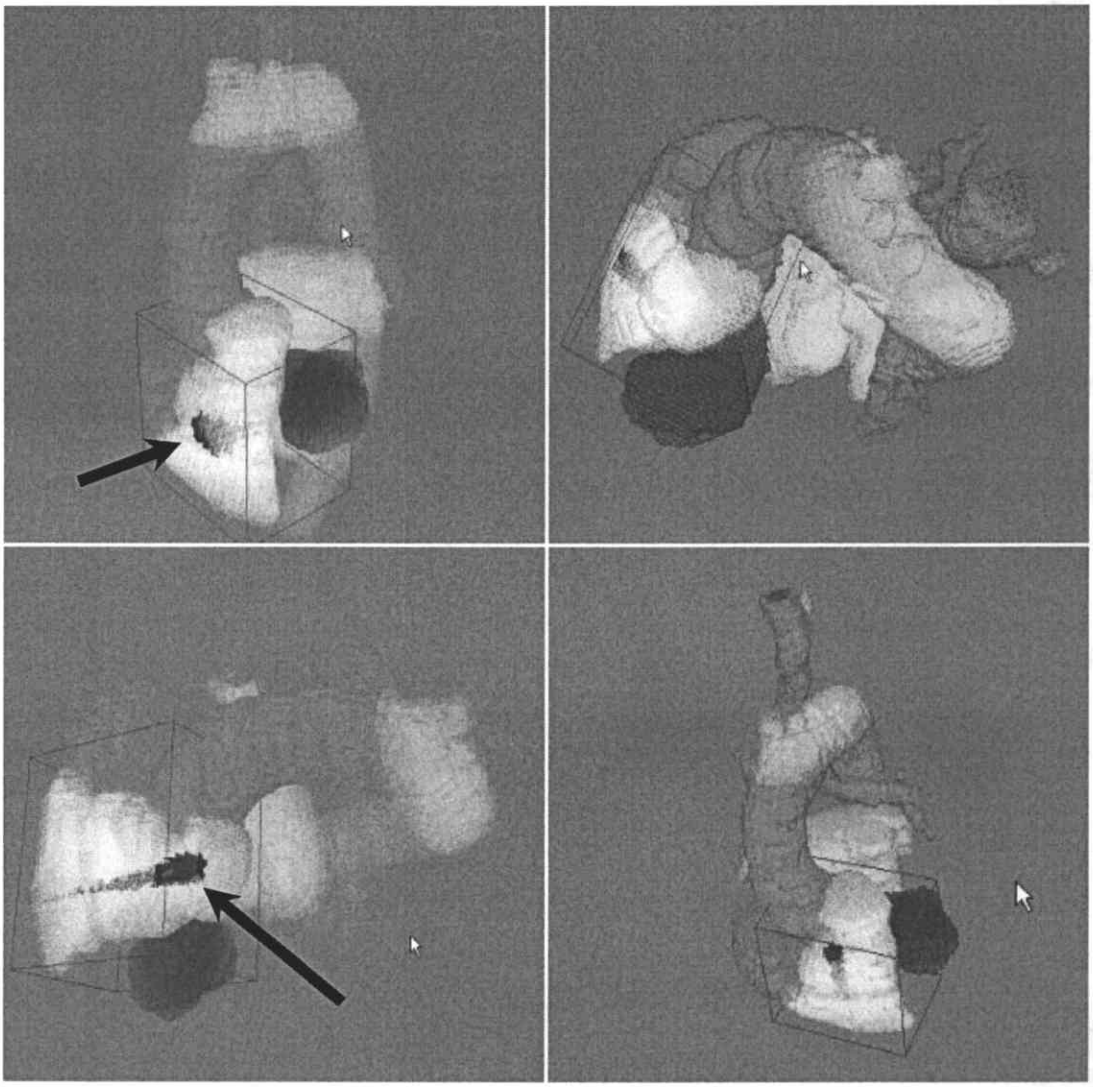

Figure 1: Four views of a three dimensional geometric model of the heart with anatomic structures labeled (shaded structures in the geometric model correspond to anatomic structure classes in the FMA ontology). A trajectory of penetrating injury was superimposed, and regions of tissue injury are predicted and demonstrated in the geometrical model (conical region shown by arrow). We can determine the identities of injured anatomic structures and infer the possibly injured adjacent structures using knowledge in the FMA ontology.

Computational Modeling of Tissue Damage from Penetrating Trauma: Linking Geometric Models to Anatomic and Biomechanical Knowledge

Daniel L Rubin, MD, MS[1,2] Yasser Bashir[1] David Grossman, PhD[1] Parvati Dev, PhD[1] Mark Musen, MD, PhD[1]

[1]Stanford Medical Informatics and [2]Department of Radiology, Stanford University

INTRODUCTION

Detailed geometric models of anatomy can be created from CT and MRI images. These 3-dimensional models are generally used in visualizations for physicians, but they are not directly computer-interpretable. We are interested in using geometric models of patient anatomy for computerized prediction of organ injury after trauma. We make these models computable by augmenting them with explicit anatomic and biomechanical knowledge. We can then develop computer programs that operate on these augmented models. We describe an approach to predicting the consequences of penetrating injury by integrating geometry with anatomic and biomechanical knowledge.

OBJECTIVES

(1) Develop a computer representation of patient anatomy that links models spatial geometry with anatomic knowledge.
(2) Create computer reasoning services that use geometric models integrated with anatomic knowledge to predict consequences of penetrating injuries:
- Direct injury
- Propagation of injury (injuries secondary to the primary injury)

(3) Develop an application to visualize patient spatial geometry and anatomic knowledge, and results of computer reasoning.

METHODS

There are four components to our approach:
(1) Generation of geometric models
(2) Computer representation of anatomic knowledge
(3) Linking geometry to anatomic and biomechanical knowledge
(4) Computer reasoning (making inferences from the available data).

Generation of Geometric Models

We create 3-dimensional geometric mesh models of patient anatomy using conventional segmentation-based approaches. A volumetric imaging study of the heart is segmented to separate and label points in space corresponding to the major anatomic structures, such as chambers of the heart, coronary arteries, etc. We have used the Visible Human data in this work; CT data could be used instead.

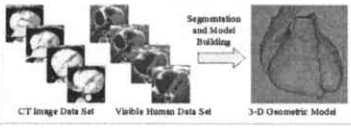

Computer Representation of Anatomic Knowledge

Anatomic knowledge is stored in ontologies, representations of knowledge that can be read by people and processed by machines. Ontologies provide a declarative representation of the concepts, properties, and relationships among the concepts of a domain, and are very useful in building intelligent computer applications.

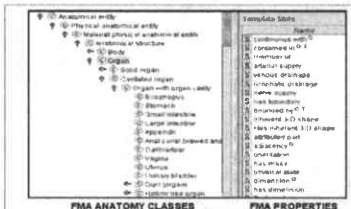

We use the Foundational Model of Anatomy (FMA [1]), a comprehensive ontology of human anatomy containing more than 70,000 concepts that describe the elements of canonical human morphology in a clear and consistent manner. In addition to enumerating anatomic structures, it describes adjacencies, part-whole relationships, continuities, and other information relevant to inferring injuries.

We use symbolic knowledge from the FMA to define what we mean by "functionally impaired blood vessel", "severed blood vessel", "ischemia" and "partial ischemia."

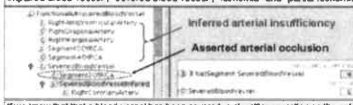

If we know that that a blood vessel has been severed, a classifier operating on the ontology can determine the vessels *continuous with* the injured vessel that are "functionally impaired."

Linking Geometry to Anatomic and Biomechanical Knowledge

We build a three-dimensional representation of patient anatomy from spatial mesh models using the Insight Toolkit (ITK [2]). We create a conceptual hierarchy of anatomic data structures (ADS) in ITK representing organs and organ parts present in the geometry. Each ADS contains information about organ identity, composition, adjacency, and biomechanical properties and links to a portion of the geometry.

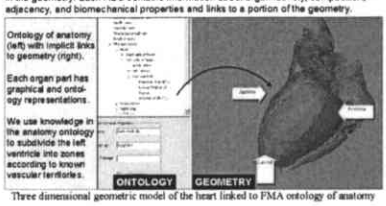

Three dimensional geometric model of the heart linked to FMA ontology of anatomy

RESULTS

We have used our integrated geometry/knowledge models to implement two computer reasoning services to evaluate a trajectory of penetrating injury: (1) Direct injury reasoning and (2) Injury propagation reasoning. Both rely on combining geometric data and anatomic knowledge.

Computer Reasoning about Direct Injuries

- Given a path of injury in the patient, the computer can predict and display primary injuries.
- Every point along injury trajectory is intersected with geometric model to determine regions of direct injury.
- Organs that are directly injured are intersected by the trajectory.
- Tissue biomechanical properties stored with each organ are used to estimate the volume of tissue injury.
- Identity of directly injured organs is established by lookup in anatomy ontology, since geometry model links spatial regions to the ontology.

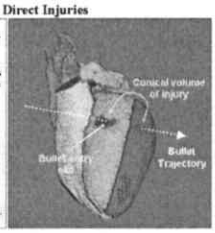

Computer Reasoning about Injury Propagation

Injuries occurring secondary to the primary injuries are inferred by the computer using the ontology of anatomy. The ontology contains knowledge about organs and organ parts supplied by different arterial branches.

- Ontology-based reasoning about secondary tissue damage after coronary artery injury, updating the geometric display to show damaged regions of the heart.
- The computer uses knowledge about myocardial perfusion to infer secondary myocardial damage (gray regions) from a right coronary artery injury.
- The computer can differentiate total and partial ischemic regions.

Shaded volumes in the geometric model (right) correspond to anatomic structure classes in the anatomy ontology (left). A computer reasoning service uses the ontology to deduce parts of the myocardium that are injured consequent to a coronary artery injury, shown as highlighted structures in the FMA (left) and shaded parts of heart (right).

CONCLUSION

We have demonstrated a methodology to automate computerized reasoning about penetrating injuries using canonical knowledge combined with image data. A key element is our use of a comprehensive ontology of anatomy containing organ identities, adjacencies, and other information useful for anatomic reasoning, and an ontology of regional perfusion containing formal definitions of arterial anatomy and corresponding regions of perfusion. Our integrated knowledge/geometry model supports computerized anatomic reasoning. Given an injury path, we can determine the organs that are injured, whether vital structures—such as a coronary artery—are injured, and can predict the propagation of injury ensuing after a vital structure is injured. Our approach is extensible and can incorporate future information, such as physiological implications of organ injuries. This methodology may be useful in teaching and simulation applications.

Acknowledgements

This work was supported by a contract from DARPA, executed by the U.S. Army Medical Research and Materiel Command/TATRC Cooperative Agreement, Contract W81XWH-04-2-0012. This work was also supported by the Protégé resource, under grant LM007885 from the U.S. National Library of Medicine.

References

1. Rosse C, Mejino JL, Jr. A reference ontology for biomedical informatics: the Foundational Model of Anatomy. J Biomed Inform 2003;36(6):478-500.
2. The Insight Toolkit, http://www.itk.org.
3. Rubin DL, Bashir Y, Grossman D, Dev P, Musen MA: Linking Ontologies with Three-Dimensional Models of Anatomy to Predict the Effects of Penetrating Injuries, 26th Annual International Conference IEEE Engineering in Medicine and Biology, Bethesda, MD, San Francisco, CA 2004.

An Acoustic Model for Wave Propagation in a Weak Layer

Michael El-Raheb
ATK Mission Research,
23052 Alcade Drive,
Laguna Hills, CA 92653

An acoustic model is developed for transient wave propagation in a weak layer excited by prescribed pressure or prescribed acceleration at the boundary. The validity of the acoustic model is investigated for the two excitations. A comparison of transient response from the acoustic model and a 3D axisymmetric elastic model reveals that for prescribed acceleration the acoustic model fails to capture important features of the elastic model even as Poisson ratio ν approaches 1/2. However for prescribed pressure, the two models agree since shear stress is reduced. For prescribed acceleration adopting the modal approach, the mixed boundary-value problem on the excited boundary is converted to a pure traction problem utilizing the influence method. To validate the elaborate modal approach a finite difference model is also developed. [DOI: 10.1115/1.1988367]

1 Introduction

Laboratory simulation of blunt trauma in living tissue relies on measuring propagation of stress waves from low velocity impact in a weak viscoelastic material such as ordnance gelatin. It has acoustic impedance close to that of water yet living tissue dissipates energy from viscoelasticity and possesses shear rigidity controlling transverse propagation. It has been widely assumed that gelatin is similar to water because it has approximately the same density and bulk speed of sound. In a weak solidlike gelatin, effects of the free surface and lateral propagation of a forcing pulse are controlled by shear modulus G and the speed of shear waves, respectively. These types of propagation are independent of a loss mechanism like viscoelasticity. Loss produces an attenuation of the pulse over and above that from dispersion. It reduces the participation of high frequency modes by smoothing the average response and its gradients.

In a fluid like water, propagation is mostly volumetric, with shear related to dissipation that is proportional to velocity gradient and kinematic viscosity. At the free surface a different kind of wave develops controlled by gravity and depth of the fluid. It can be argued that although water and gelatin have very similar acoustic impedances, shear rigidity of gelatin may control how a stress wave propagates laterally and its character at and close to the free surface. If gelatin is like water then it can be treated as an acoustic fluid governed by the wave equation. In this work the wave equation is derived as a limiting case of the linear elastodynamic equations of a homogeneous solid. In fact when Poisson ratio assumes the value of 1/2, the elastic field converts to the acoustic field. One issue addressed in this work is the sensitivity of the solution to Poisson ratio close to 1/2.

To measure transmission of stress waves produced by low velocity impact on gelatin, a layer is bonded onto a metallic substrate instrumented by sensitive carbon gauges. Upon impact, stress waves propagate across the layer reaching the substrate with substantial reduction in intensity from dispersion and viscous losses. Measuring impact and transmitted pressures are needed to construct the material's constitutive model. Carefully controlled experiments with sufficient accuracy reproducing transient histories for correlation with computed results are very hard to execute. The problem lies in the weakness of the material. Gauges cannot be placed inside the material while gauges at the interface between material and metal substrate suffer from lack of cohesion adding uncertainty to measured data. This difficulty forces investigators to rely on sensitivity studies from analysis and general purpose discretization programs in order to understand phenomena. Moreover, literature in this field addresses quasistatic measurements of elongation omitting important dynamic effects such as strain-rate dependence in the microsecond regime. The simulation of these experiments led to the realization that approximating gelatin as a viscous fluid is valid only for unrealistic impact conditions when pressure over the footprint is uniform.

Acoustic wave propagation governed by the Helmholtz equation has been treated extensively in the literature. Solution techniques range from the analytical for simple geometries to numerical for problems with complicated geometry, medium inhomogeneity, and nonlinearity. Theil [1] treats the 1D viscoelastically damped wave equation analytically. Yserentant [2] shows how a consistent discretization of the acoustic equation can be recovered from the particle model of compressible fluids (see Ref. [3]). Sina and Khashayar [4] solve the 3D wave equation analytically for arbitrary nonhomogeneous media adopting the differential transfer matrix. Sujith et al. [5] present an exact solution to 1D transient waves in curvilinear coordinates adopting transformation of variables suggested by the WKB approximation. Hamdi et al. [6] present exact solitary wave solutions of the 1D wave propagation in nonlinear media with dispersion. Yang [7] solves numerically the wave equation with attenuation from linear friction utilizing grid modification to track wave fronts accurately. Narayan [8] solves the 3D transient acoustics in inhomogeneous media by finite difference and Schemann and Bornemann [9] apply the adaptive Rothe integrator. Bailly and Juve [10] present a numerical solution to the 2D acoustic propagation from transient sources using the dispersion-relation-preserving scheme in space and a fourth-order Runge-Kutta in time. Wagner et al. [11] and Gaul and Wenzel [12] use a hybrid boundary element method for frequency and transient acoustic response in bounded and unbounded regions. Mehdizadeh and Paraschivoiu [13] develop a spectral element method to solve the 3D Helmholtz equation retaining accuracy for large wave numbers. None of the references above addresses 3D transient propagation from impact analytically.

Acoustic wave propagation in a free disk is developed here adopting a modal analysis validated by a finite difference method. Transient response to prescribed pressure and prescribed acceleration at the boundary is analyzed. Since the primary goal of this work is to investigate the validity of the established belief that

Contributed by the Applied Mechanics Division of THE AMERICAN SOCIETY OF MECHANICAL ENGINEERS for publication in the ASME JOURNAL OF APPLIED MECHANICS. Manuscript received by the Applied Mechanics Division, December 21, 2004; final revision, February 7, 2005. Associate Editor: O. M. O'Reilly. Discussion on the paper should be addressed to the Editor, Prof. Robert M. McMeeking, Journal of Applied Mechanics, Department of Mechanical and Environmental Engineering, University of California-Santa Barbara, Santa Barbara, CA 93106-5070, and will be accepted until four months after final publication in the paper itself in the ASME JOURNAL OF APPLIED MECHANICS.

 Copyright © 2005 by ASME

tissue can be treated as a fluid, the acoustic equation is derived from the elastic equations of a solid in the limit when Poisson ratio and shear stresses vanish (Appendix).

Section 2 develops the acoustic model utilizing the modal approach for both prescribed pressure and prescribed acceleration. In the modal approach, the forcing function at the boundary is treated adopting the static-dynamic superposition method (see Berry and Naghdi [14]). The solution is expressed as a superposition of a static term satisfying the inhomogeneous boundary conditions, and a dynamic solution in terms of the eigenfunctions satisfying homogeneous boundary conditions.

Since the projectile's strength and acoustic impedance are much greater than those of tissue, the excitation transmitted over the boundary at the projectile-tissue interface can be approximated as a given time dependent prescribed motion in contrast to an unknown pressure excitation. However, this type of excitation would lead to a mixed boundary condition; i.e., pressure gradient prescribed over part of the boundary and zero pressure prescribed over the remaining part. This difficulty can be overcome by the influence method which superimposes response from a set of unit pressures with time-dependent weights prescribed on annular portions of the footprint. These weights are updated at each time step from the condition that combined acceleration at the center of each ring over the footprint equals the prescribed instantaneous acceleration. In this way, the forcing function is converted to pure traction with time-varying spatial dependence.

Section 3 develops the finite difference approach. Radial and axial dependence are discretized by central differences while time dependence is integrated by the Kutta-Runge method.

Section 4 compares acoustic histories from the two approaches validating the modal approach. Histories of the acoustic model are compared to those from a 3D axisymmetric elastic model demonstrating the inadequacy of the acoustic model when applied to a solid with Poisson ratio near 1/2 and forced by applied acceleration. Sensitivity of the acoustic histories to type of excitation and to parameters of the prescribed acceleration profile is also presented. The effect of Poisson ratio ν on peak elastic stress is evaluated confirming that for prescribed acceleration mismatch of acoustic and elastic results is not caused by small deviations in Poisson ratio ν from 1/2 in the elastic model. Finally, results from the two models are compared for prescribed uniform pressure revealing that the mismatch diminishes when shear stress is reduced.

2 Modal Analysis

In the analysis to follow, all variables are independent of circumferential angle due to the assumption of axisymmetry. This condition applies for a cylindrical projectile at normal incidence. Consider a traction-free disk with radius r_d and length h bonded to a rigid substrate. Appendix A derives the acoustic equation in the limit when shear stress vanishes in the linear elastodynamic equations of a solid. In the analysis to follow, r and z denote radial and axial coordinates. Acoustic propagation in the disk is governed by the acoustic equation

$$(\partial_{rr} + 1/r\partial_r + \partial_{zz})p_d - 1/c_h^2\partial_{tt}p_d = 0 \tag{1a}$$

with the following boundary conditions:

$$p(r_d,z;t) = 0 \tag{1b}$$

$$\left.\begin{aligned} p(r,0;t) &= [H(r) - H(r-r_p)]f(t) && \text{prescribed pressure} \\ \partial_z p(r,0;t) &= -\rho\ddot{f}_w(t) \quad 0 \le r \le r_p \\ p(r,0;t) &= 0 \qquad\qquad r_p < r < r_d \end{aligned}\right\} \text{prescribed acceleration} \tag{1c}$$

$$\partial_z p(r,h;t) = 0, \quad \text{fixed face, or alternatively}$$

$$p(r,h;t) = 0, \quad \text{free face} \tag{1d}$$

where $H(r)$ is the Heaviside function, r_p is footprint radius of the external excitation which is projectile radius, $f(t)$ is time dependence of prescribed pressure, and $\ddot{f}_w(t)$ is time dependence of prescribed acceleration. Express $p(r,z;t)$ as a superposition of two terms (see Berry and Naghdi [14])

$$p(r,z;t) = \begin{cases} p_s(r,z)f(t) + p_d(r,z;t), & \text{prescribed pressure} \\ -p_s(r,z)\rho\ddot{f}_w(t) + p_d(r,z;t), & \text{prescribed acceleration} \end{cases} \tag{2}$$

where $p_s(r,z)$ is the static solution of Eq. (1a) with inhomogeneous boundary conditions (1b)–(1d) assuming $f(t)=1$ or $\ddot{f}_w(t) = 1/\rho$, and $p_d(r,z;t)$ is a dynamic solution of Eq. (1a) satisfying the homogeneous boundary conditions (1b)–(1d) with $f(t)=0$ or $\ddot{f}_w(t)=0$.

The prescribed acceleration boundary condition in Eq. (1c) is mixed. In other words, part of the boundary has prescribed pressure gradient and the other part has prescribed pressure. This difficulty can be overcome by dividing the circle bounding the footprint into $n+1$ equidistant radial stations with increment Δr_p

$$0, r_1, r_2, \ldots, r_{n-1}, r_n, \quad r_k - r_{k-1} = \Delta r_p = \text{const}$$

where $r_n = r_p$. Assume a uniform pressure of unit intensity acting over each annular segment $r_{k-1} \to r_k$ that is termed source segment. Where subscript z denotes partial derivative with respect to z, evaluating the pressure gradient $P_{z,lk}(r,z;t)$ from the kth source segment at the center of the lth segment $r_{cl} = (r_l + r_{l-1})/2$ that is termed target point and following the expansion in (2) yields

$$P_{z,lk}(r_{cl},0;t) = -p_{zs,lk}(r_{cl},0)\rho\ddot{f}_w(t) + p_{zd,lk}(r_{cl},0;t) \tag{3}$$

where $p_{zs,lk}(r_{cl},0;t)$ and $p_{zd,lk}(r_{cl},0)$ are static and dynamic pressure gradients at the lth target point due to the kth source segment. Enforcing the condition of prescribed pressure gradient $p_{zf}(t)$ over the footprint at each time step yields a set of simultaneous equations in the weights $c_k(t)$

$$\sum_{k=1}^{n} P_{z,lk}(r_{cl},0;t)c_k(t) = p_{zf}(t), \quad 1 \le l \le n \tag{4}$$

The combined pressure from all annular source segments is the superposition of $P_{lk}(r,z;t)$ factored by time dependent weights $c_k(t)$

$$p(r,z;t) = \sum_{k=1}^{n} P_{lk}(r,z;t)c_k(t), \quad 1 \le l \le n$$

$$P_{lk}(r,z;t) = -p_{s,lk}(r,z)\rho\ddot{f}_w(t) + p_{d,lk}(r,z;t) \tag{5a}$$

Solutions of $p_{s,k}(r,z;t)$ and $p_{d,k}(r,z;t)$ for each unit source segment are outlined in what follows. The static solution for the kth source segment $p_s(r,z)$ takes the form

$$p_{s,k}(r,z) = \sum_{m=1}^{m_r} \psi_{sm,k}(z)J_0(k_{rm}r)$$

$$\psi_{sm,k}(z) = \alpha_{mk}\sinh(k_{rm}z) + \beta_{mk}\cosh(k_{rm}z) \tag{5b}$$

where $J_0(k_{rm}r)$ is the Bessel function of the first kind and zeroth order. Substituting (5b) in the boundary conditions (1b)–(1d) and enforcing orthogonality of $J_0(k_{rm}r)$ yields

$$J_0(k_{rm}r_d) = 0, \quad 1 \le m \le m_r \tag{6a}$$

$$\beta_{m,k} = \frac{2(r_k J_1(k_{rm}r_k) - r_{k-1}J_1(k_{rm}r_{k-1}))}{r_d^2 J_1^2(k_{rm}r_d)k_{rm}} \tag{6b}$$

$$\alpha_{m,k}=\begin{cases}-\beta_{m,k}\tanh(k_{rm}h), & \text{fixed face, or alternatively}\\ -\beta_{m,k}/\tanh(k_{rm}h), & \text{free face}\end{cases} \tag{6c}$$

Note that in (3), $p_{zs,lk}(r_{cl},0)=\partial_z p_{s,k}(r_{cl},0)$.

The dynamic solution $p_{d,k}(r,z;t)$ satisfies

$$(\partial_{rr}+1/r\partial_r+\partial_{zz})p_{d,k}-1/c_b^2\partial_{tt}p_{d,k}=0 \tag{7}$$

and the homogeneous boundary conditions in (1*b*)–(1*d*). Expand $p_d(r,z;t)$ in terms of its orthogonal eigenfunctions

$$p_{d,k}(r,z;t)=\sum_m\sum_n a_{mn,k}(t)\psi_{dn}(z)J_0(k_{rm}r) \tag{8}$$

Applying the homogeneous boundary conditions in (1*b*)–(1*d*) to $J_0(k_{rm}r)$ and $\psi_{dn}(z)$ produces

$$J_0(k_{rm}r_d)=0, \quad 1\leq m\leq m_r \tag{9a}$$

$$\psi_{dn}(z)=\begin{cases}\cos(k_{zn}z),\cos(k_{zn}h)=0\rightarrow k_{zn}h=\dfrac{1}{2}(2n-1)\pi, & \text{fixed face}\\ \sin(k_{zn}h),\sin(k_{zn}h)=0\rightarrow k_{zn}h=n\pi, & \text{free face}\end{cases}, \quad 1\leq n\leq n_z \tag{9b}$$

$$k_{zn}^2+k_{rm}^2=k_{mn}^2, \quad \omega_{mn}=c_b k_{mn} \tag{9c}$$

where ω_{mn} is the eigenfrequency corresponding to mode (m,n). Substituting (3) in (1*a*) with use made of (5*a*), (5*b*), (6), (8), and (9) and enforcing orthogonality of $\psi_{dn}(z)$ and $J_0(k_{rm}r)$ yields

$$\ddot{a}_{mn,k}(t)+\omega_{mn}^2 a_{mn,k}(t)=-N_{sd\ mn,k}\rho f_w^{IV}(t); \quad f_w^{IV}(t)=\partial^4 f_w(t)/\partial t^4$$

$$N_{sd\ mn,k}=\frac{2}{h}\int_0^h \psi_{sm,k}(z)\psi_{dn}(z)dz, \quad 1\leq m\leq m_r, \quad 1\leq n\leq n_z \tag{10}$$

In deriving Eq. (10) the term $\nabla_0^2(-p_s)\rho\ddot{f}_w(t)$, $(\nabla_0^2\equiv\partial_{rr}+1/r\partial_r)$ vanishes since static pressure $p_s(r,z)$ satisfies the equation $\nabla_0^2 p_s=0$. Acoustic displacements $(w,u)_k$ are determined from (A4)

$$\partial_z p_{d,k}=-\rho\partial_{tt}^2 w_k$$

$$\partial_r p_{d,k}=-\rho\partial_{tt}^2 u_k \tag{11}$$

The solution to (10) is expressed as a Duhamel integral

$$a_{mn,k}(t)=-\frac{\rho N_{sd\ mn,k}}{\omega_{mn}}\int_0^t \sin\omega_{mn}(t-\tau)f_w^{IV}(\tau)d\tau \tag{12}$$

Note that in (11) $\partial_z p_{d,k}(r_{cl},0;t)=p_{zd,lk}(r_{cl},0;t)$ as defined in (3). Once histories of $\partial_z p_{d,k}$ and $\partial_r p_{d,k}$ are determined from solving (10), histories of w_k and u_k are found by integrating (11) numerically.

3 Finite Difference

Consider a disk with traction-free boundaries satisfying the conditions

$$\partial_r p(0,z;t)=0 \tag{13a}$$

$$p(r_d,z;t)=0 \tag{13b}$$

$$\partial_z p(r,0;t)=0 \tag{13c}$$

$$p(r,h;t)=[H(r)-H(r-r_p)]f(t) \quad \text{prescribed pressure} \tag{13d}$$

$$\left.\begin{aligned}&\partial_z p(r,h;t)=-\rho\ddot{f}_w(t), && 0\leq r\leq r_p\\ &p(r,h;t)=0, && r_p<r\leq r_d\end{aligned}\right\} \quad \text{prescribed acceleration}$$

where ( ) denotes time derivative. Unlike the analysis in Sec. 2 where z has its origin at the excited boundary, in the finite difference scheme z has its origin at the nonexcited boundary. Condition (13*a*) is symmetry about the axis of revolution $r=0$, (13*b*) is traction-free boundary at $r=r_d$, (13*c*) is fixed boundary at $z=0$, and (13*d*) is prescribed acceleration for $0\leq r\leq r_p$ and traction-free boundary for $r_p\leq r\leq r_d$ at $z=h$. Form the rectangular grid

$$\begin{aligned}&i=1\rightarrow n_r, \quad d_r\leq r\leq r_d-d_r, \quad d_r=r_d/(n_r+1)\\ &j=1\rightarrow n_z, \quad d_z\leq z\leq h-d_z, \quad d_z=h/(n_z+1)\end{aligned} \tag{14}$$

In this grid, nodes do not include points on the boundaries. Expressing Eq. (1*a*) in central difference to first order yields the following relations depending on position:

(a) Internal points $d_r<r<r_d-d_r$, $d_z<z<h-d_z\Rightarrow 2\leq i\leq n_r-1$, $2\leq j\leq n_z-1$

$$\alpha_1 p_{i+1,j}+\alpha_2 p_{i-1,j}+\alpha_3 p_{i,j}+\alpha_4(p_{i,j+1}+p_{i,j-1})=1/c_b^2\ddot{p}_{i,j}$$

$$\alpha_1=\left(\frac{1}{d_r^2}+\frac{1}{2r_i d_r}\right), \quad \alpha_2=\left(\frac{1}{d_r^2}-\frac{1}{2r_i d_r}\right), \quad \alpha_3=-2\left(\frac{1}{d_r^2}+\frac{1}{d_z^2}\right), \quad \alpha_4=\frac{1}{d_z^2} \tag{15a}$$

(b) Corner point at $r=d_r$, $z=d_z\Rightarrow i=1$, $j=1$

$$\alpha_1 p_{i+1,j}+(\alpha_2+\alpha_3+\alpha_4)p_{i,j}+\alpha_4 p_{i,j+1}=1/c_b^2\ddot{p}_{i,j} \tag{15b}$$

(c) Points along axis $r=d_r$, $d_z<z<h-d_z\Rightarrow i=1$, $2\leq j\leq n_z-1$

$$\alpha_1 p_{i+1,j}+(\alpha_2+\alpha_3)p_{i,j}+\alpha_4(p_{i,j+1}+p_{i,j-1})=1/c_b^2\ddot{p}_{i,j} \tag{15c}$$

(d) Corner point at $r=d_r$, $z=h-d_z\Rightarrow i=1$, $j=n_z$

For prescribed pressure

$$\alpha_1 p_{i+1,j}+(\alpha_2+\alpha_3)p_{i,j}+\alpha_4 p_{i,j-1}-1/c_b^2\ddot{p}_{i,j}=\alpha_4 f(t) \tag{15d}$$

For prescribed acceleration

$$\alpha_1 p_{i+1,j}+(\alpha_2+\alpha_3+\alpha_4)p_{i,j}+\alpha_4 p_{i,j-1}-1/c^2\ddot{p}_{i,j}=-\rho\ddot{f}_w(t)/d_z$$

(e) Points along boundary $d_r<r<r_d-d_r$, $z=d_z\Rightarrow 2\leq i\leq n_r-1$, $j=1$

$$\alpha_1 p_{i+1,j} + \alpha_2 p_{i-1,j} + (\alpha_3 + \alpha_4) p_{i,j} + \alpha_4 p_{i,j+1} = 1/c_b^2 \ddot{p}_{i,j} \tag{15e}$$

(f) Points along boundary $d_r < r < r_d - d_r$, $z = h - d_z \Rightarrow 2 \leq i \leq n_r - 1$, $j = n_z$

For $0 \leq r \leq r_p$ and prescribed pressure

$$\alpha_1 p_{i+1,j} + \alpha_2 p_{i-1,j} + \alpha_3 p_{i,j} + \alpha_4 p_{i,j-1} - 1/c_b^2 \ddot{p}_{i,j} = \alpha_4 f(t) \tag{15f}$$

For $0 \leq r \leq r_p$ and prescribed acceleration

$$\alpha_1 p_{i+1,j} + \alpha_2 p_{i-1,j} + (\alpha_3 + \alpha_4) p_{i,j} + \alpha_4 p_{i,j-1} - 1/c_b^2 \ddot{p}_{i,j} = -\rho \ddot{f}_w(t)/d_z$$

For $r_p < r \leq r_d$

$$\alpha_1 p_{i+1,j} + \alpha_2 p_{i-1,j} + \alpha_3 p_{i,j} + \alpha_4 p_{i,j-1} - 1/c_b^2 \ddot{p}_{i,j} = 0$$

(g) Corner point at $r = r_d - d_r$, $z = d_z \Rightarrow i = n_r$, $j = 1$

$$\alpha_2 p_{i-1,j} + (\alpha_3 + \alpha_4) p_{i,j} + \alpha_4 p_{i,j+1} = 1/c^2 \ddot{p}_{i,j} \tag{15g}$$

(h) Points along boundary $r = r_d - d_r$, $d_z < z < h - d_z \Rightarrow i = n_r$, $2 \leq j \leq n_z - 1$

$$\alpha_2 p_{i-1,j} + \alpha_3 p_{i,j} + \alpha_4 (p_{i,j+1} + p_{i,j-1}) = 1/c_b^2 \ddot{p}_{i,j} \tag{15h}$$

(i) Corner point at $r = r_d - d_r$, $z = h - d_z \Rightarrow i = n_r$, $j = n_z$

$$\alpha_2 p_{i-1,j} + \alpha_3 p_{i,j} + \alpha_4 p_{i,j-1} = 1/c_b^2 \ddot{p}_{i,j} \tag{15i}$$

In (15*a*)–(15*i*), the differential equation is satisfied only at internal points of the grid modified by constraints on the boundaries.

Applying (15*a*)–(15*i*) at all internal points in the grid (14) produces a set of ordinary differential equations in $p_{i,j}(t)$ cast in the form of tridiagonal blocks as follows:

$$\ddot{\mathbf{p}} = c_b^2 (\mathbf{M}_p \mathbf{p} - \mathbf{F}(t))$$

$$\mathbf{M}_p = \begin{bmatrix} \mathbf{A}_1 & \mathbf{C}_1 & & & \\ \mathbf{B}_2 & \mathbf{A}_2 & \mathbf{C}_2 & & \\ & \square & \square & \square & \\ & & \mathbf{B}_{n_r-1} & \mathbf{A}_{n_r-1} & \mathbf{C}_{n_r-1} \\ & & & \mathbf{B}_{n_r} & \mathbf{A}_{n_r} \end{bmatrix} \tag{16}$$

$\mathbf{B}_i$ and $\mathbf{C}_i$ are $(n_z \times n_z)$ diagonal matrices, $\mathbf{A}_i$ is the $(n_z \times n_z)$ banded matrix with bandwidth 3, and $\mathbf{F}$ is the global vector of the forcing function in (15*d*) and (15*f*). For each point $j \ni (1 \leq j \leq n_z)$ along an i line in the grid, coefficients of $p_{i,j}$ in the Laplacian define $\mathbf{A}_i$, coefficients of $p_{i-1,j}$ define $\mathbf{B}_i$, and coefficients of $p_{i+1,j}$ define $\mathbf{C}_i$. The time derivative is expressed in the central difference to first order allowing integration in time.

Viscous damping is included following the approximate equation (A12)

$$(1 + \tilde{\nu}/c_b^2 \partial_t)(\partial_{rr} + 1/r\partial_r + \partial_{zz}) p - 1/c_b^2 \partial_{tt} p = 0 \tag{A12}$$

This modifies (16) to the first order system

$$\dot{\mathbf{p}} = \mathbf{q}$$

$$\dot{\mathbf{q}} = c_b^2 \mathbf{M}_p \mathbf{p} + \tilde{\nu} \mathbf{M}_p \mathbf{q} - c_b^2 \mathbf{F}(t) \tag{17}$$

4 Results

The numerical experiments to follow assume a traction-free gelatin disk 12.7 mm (=0.5 in.) thick and 25.4 mm (=1 in.) radius with the boundary $z = h$ bonded to a rigid surface. In the elastic model the gelatin properties are (Eisler [16]):

$$E = 3.1 \times 10^9 \text{ dyn/cm}^2 (= 4.5 \times 10^4 \text{ lb./in.}^2),$$

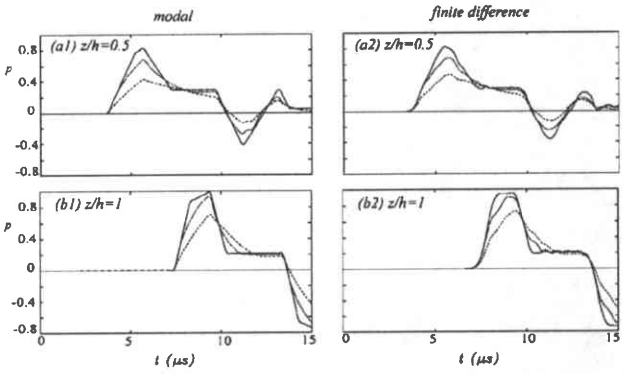

Fig. 1 Acoustic histories from prescribed pressure: —, $r=0$; ---, $r=0.5r_p$; – – –, $r=0.9r_p$. (*a*1), (*b*1) modal; (*a*2), (*b*2) finite difference.

$$\rho = 0.93 \text{ g/cm}^3 (= 8.7 \times 10^{-5} \text{ lb. s}^2/\text{in.}^4), \quad \nu = 0.48 \tag{18a}$$

The data in (13*a*) yield a small ratio of *Lame'* constants $\mu/\lambda = (1-2\nu)/(2\nu) \approx 0.0417$ resulting in reduced shear stresses and in turn large displacements. In the acoustic model, bulk modulus E_b, density ρ, and speed of sound c_b are then

$$E_b = E/(3(1-2\nu)) = 2.73 \times 10^{10} \text{ dyn/cm}^2 (= 3.95 \times 10^5 \text{ lb./in.}^2)$$

$$\rho = 0.93 \text{ g/cm}^3 (= 0.87 \times 10^{-4} \text{ lb. s}^2/\text{in.}^4)$$

$$c_b = \sqrt{E_b/\rho} = 1.71 \text{ km/s} (= 6.74 \times 10^4 \text{ in./s}) \tag{18b}$$

E_b is determined from experimental measurements of c_b.

To confirm the implementation of the complicated analytical approach adopting time dependent influence coefficients, results are first compared to those from the more straightforward numerical finite difference approach derived in the Appendix. Figure 1 compares acoustic pressure histories from the two approaches for a layer forced by a prescribed trapezoidal pressure pulse of unit intensity lasting 8 μs with 2 μs rise and fall times and 4 μs plateau applied over a circular footprint with radius $r_p = 6.35$ mm (=0.25 in.). Figures 1(*a*1), 1(*a*2) plots histories at $z = 0.5h$ and Figs. 1(*b*1), 1(*b*2) at $z = h$. For each z, histories at 3 radial stations $r/r_p = 0$, 0.5, and 0.9 are superimposed. Figures 1(*a*1) and 1(*b*1) show that the prescribed pressure pulse quickly changes profile as the wave travels along z. The flat plateau of the profile acquires a discontinuity in intensity after an interval $\Delta t_1 = 3.5$ μs from the wavefront equal to travel time of the wave over r_p. Over this interval intensity diminishes smoothly with z, while over the remaining interval $\Delta t_2 = 4.5$ μs intensity diminishes steeply with z. At $z = h$, intensity over Δt_1 rises from reflections at the rigid boundary. Histories from the two distinctly different approaches agree confirming the implementation of the analytical model.

The difference in response between the acoustic model and the 3D axisymmetric elastic model is discussed in what follows. Figures 2(*a*) and 2(*b*) plot the eigenfrequency Ω (kHz) versus radial wave number $\lambda_m/\pi = k_{rm} r_d/\pi$ with axial wave number n as parameter for the elastic and acoustic models. For each mode (m,n), Ω of the acoustic model is 5 times higher than that of the elastic model. The reason is that in the acoustic model Ω is proportional to c_b while in the elastic model it is proportional to the flexural phase velocity c_p that is bounded by the shear speed $c_s = \sqrt{E/(2(1+\nu)\rho)}$. For $\nu = 0.48$, $c_b/c_s = 4.97$ consistent with the ratio observed in Fig. 2. This is the fundamental difference distinguishing the two models. Furthermore, the acoustic model cannot capture transverse wave propagation as no shear is included in the model. Although in the elastic model extensional modes exist with frequencies proportional to c_b nevertheless flexural modes dominate the response because of their lower frequencies.

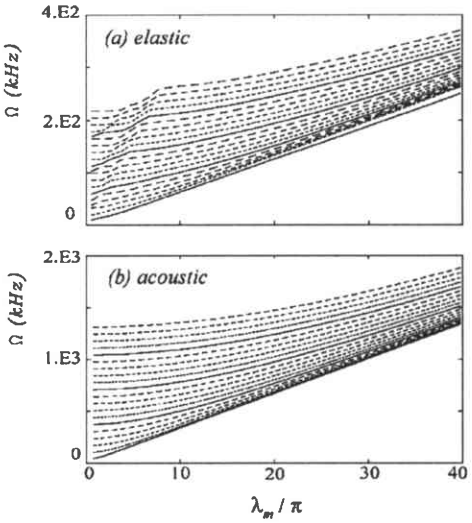

Fig. 2 Frequency spectra of elastic and acoustic models. (*a*) Elastic model; (*b*) acoustic model.

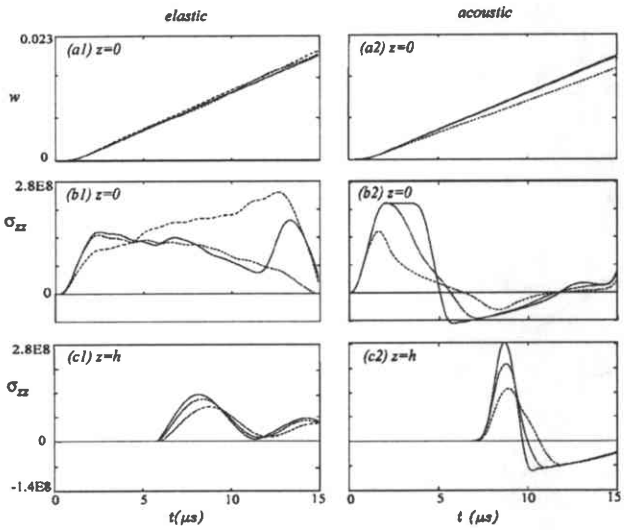

Fig. 4 Comparison of elastic and acoustic histories for prescribed acceleration: —, $r=0$; ---, $r=0.5r_p$; – – –, $r=0.9r_p$. Elastic model: (*a*1) $w(r,0)$, (*b*1) $\sigma_{zz}(r,0)$, (*c*1) $\sigma_{zz}(r,h)$; acoustic model: (*a*2) $w(r,0)$, (*b*2) $\sigma_{zz}(r,0)$, (*c*2) $\sigma_{zz}(r,h)$.

Figure 3 plots prescribed motion $\ddot{f}_w(t)$, $\dot{f}_w(t)$, and $f_w(t)$ when acceleration is prescribed at the footprint. $\ddot{f}_w(t)$ is made of 4 linear segments

(1) Linear acceleration: $\ddot{f}_{w1}(t)=\alpha_1 t$, $0\leqslant t\leqslant t_1$
(2) Constant acceleration: $\ddot{f}_{w2}(t)=\alpha_1 t_1$, $t_1\leqslant t\leqslant t_2$
(3) Linear deceleration: $\ddot{f}_{w3}(t)=\ddot{f}_{w2}(t_2)-\alpha_2(t-t_2)$, $t_2\leqslant t\leqslant t_3$
(4) Constant velocity: $\ddot{f}_{w4}(t)=0$, $\dot{f}_{w4}(t_3)=U_0$, $t_3\leqslant t\leqslant t_4$

Assuming that the first three time intervals are equal ($\Delta t_1=\Delta t_2=\Delta t_3$, $\Delta t_i=t_i-t_{i-1}$) and $\alpha_2=\alpha_1$, then α_1 is determined by assigning the constant velocity U_0 to $\dot{f}_{w4}(t_3)$. In the analysis to follow

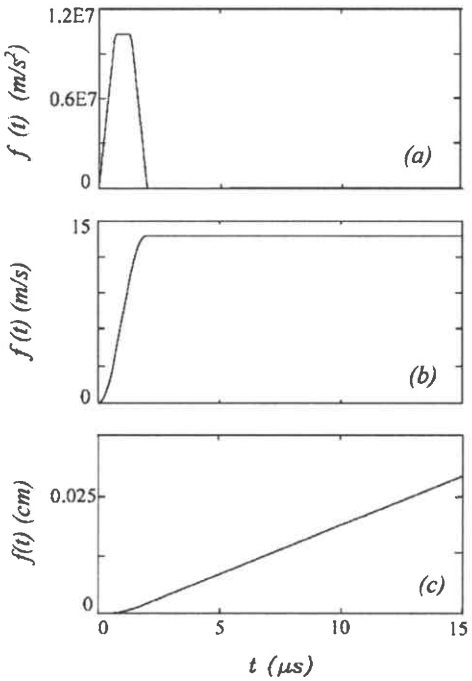

Fig. 3 Prescribed motion at footprint. (*a*) Acceleration; (*b*) velocity; (*c*) displacement.

$$\Delta t_{1,3}\equiv\Delta t_1+\Delta t_2+\Delta t_3=2\ \mu\text{s},\quad U_0=14\ \text{m/s}(\equiv 46\ \text{ft./s}) \tag{19}$$

Figure 4 compares histories of the elastic and acoustic models from prescribed acceleration. Displacement at $z=0$ (Figs. 4(*a*1), 4(*a*2)) conforms to the prescribed value in Fig. 3(*c*). At $z=0$, Figs. 4(*b*1), 4(*b*2) compare histories of axial stress $-\sigma_{zz}$ from the elastic model to pressure p from the acoustic model. Peak stress, pulse duration, distribution of p over the footprint, and shape differ substantially between the two models. At $z=h$, Fig. 4(*c*1) and 4 (*c*2) compare $-\sigma_{zz}$ to p histories. There, magnitude and pulse width also differ. It is evident from this comparison that the two models differ appreciably in spite of the fact that in the elastic model $\nu=0.48$ is close to the transition value 1/2.

The difference between the two models in response from uniform prescribed pressure and prescribed acceleration is demonstrated in the example to follow. A uniform pressure pulse duplicating that at $r=0$ in Fig. 4(*b*2) is applied at $z=0$ (see Fig. 5(*b*)). The resulting histories of displacement w and pressure p at $z=h$ are shown in Figs. 5(*a*) and 5(*c*). Comparing histories in Figs. 4(*a*2) and 4(*c*2) to those in Figs. 5(*a*) and 5(*c*) reveals the sensitivity of response to p distribution over the footprint. Further evidence of this sensitivity appears when comparing p and w profiles at $z=0$ of the two cases. For prescribed acceleration p (Fig. 6(*a*1)) is not uniform while w (Fig. 6(*b*1)) is almost constant for $r<r_p$ and discontinuous at $r=r_p$. For prescribed pressure, p (Fig. 6(*a*2)) duplicates the external pulse while w (Fig. 6(*b*2)) increases with r reaching a maximum at $r=r_p$ with a discontinuity even stronger than that in Fig. 6(*b*1).

The parameters characterizing the applied acceleration profile are the final constant velocity U_0, and time interval $\Delta t_{1,3}$ of acceleration and deceleration to reach U_0 smoothly from rest. Figure 7 plots $p_{\max}$ against U_0 with $\Delta t_{1,3}$ as the parameter and vice versa. As expected, $p_{\max}$ is linear with U_0 (Figs. 7(*a*1) and 7(*a*2)). In contrast, $p_{\max}$ is nonlinear with $\Delta t_{1,3}$ (Figs. 7(*b*1), 7(*b*2)) following a relation $p_{\max}\propto U_0\Delta t_{1,3}^{-\alpha}$, where the α depends on z. $p_{\max}$ approaches a constant value as $\Delta t_{1,3}\to 0$ when slope of the acceleration profile in Fig. 3(*a*) becomes infinite. This is the limiting case when U_0 is applied instantaneously. For $\Delta t_{1,3}<3$ μs, $p_{\max}$ goes through a transition when its value at $z=h$ exceeds that at $z=0$. The transition $\Delta t_{1,3}$ is almost independent of U_0.

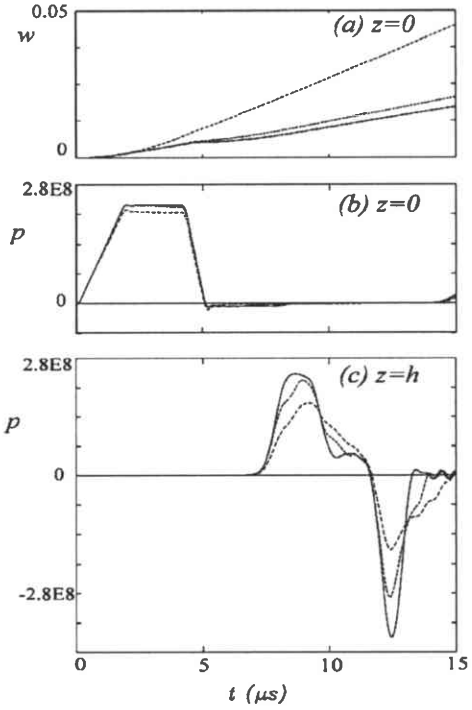

Fig. 5 Acoustic histories from prescribed pressure: —, $r=0$; ---, $r=0.5r_p$; – – –, $r=0.9r_p$. (*a*) $w(r,0;t)$; (*b*) $p(r,0;t)$; (*c*) $p(r,h;t)$.

Figure 8(a) shows deformed shapes at $t=8$ μs from the elastic model for $\nu=0.470$ and 0.495 keeping bulk modulus E_b the same. This requires expressing the constitutive law in terms of E_b and ν as in Eq. (A2b). Note that bulging of material near the perimeter is more pronounced for $\nu=0.495$ than for $\nu=0.470$. As ν approaches 1/2, material compressibility diminishes followed by a reduction in phase velocity along r near the free surface which delays propagation of the wavefront. In turn, conservation of volume and pressure release beyond the perimeter $r>r_p$ explains the formation and intensification of the bulge. Indeed, the closer ν gets to 1/2 the steeper the displacement gradient $\partial_r w$ along the perimeter reminiscent of the acoustic w profile in Fig. 6($b1$). The effect on peak elastic stress $(\sigma_{zz})_{\max}$ of ν in the range $0.47\leqslant\nu\leqslant0.498$ is shown in Fig. 8(b). Although $(\sigma_{zz})_{\max}$ at $z=0$ is insensitive to ν for $\nu<0.495$, its value at $z=h$ drops by 76% due to a 6% increase in

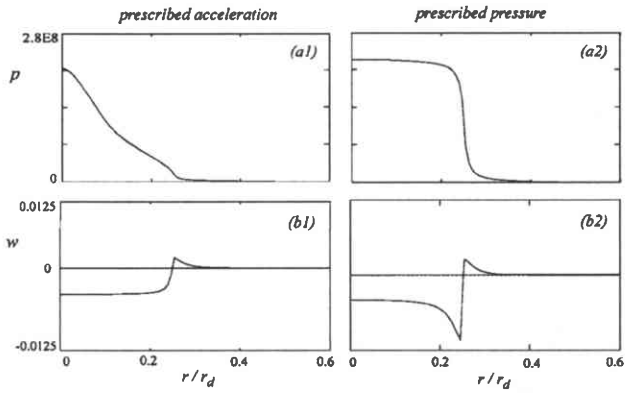

Fig. 6 Acoustic pressure and displacement profiles at $z=0$ and $t=4$ μs. (*a*1), (*b*1) Prescribed acceleration; (*a*2), (*b*2) prescribed pressure.

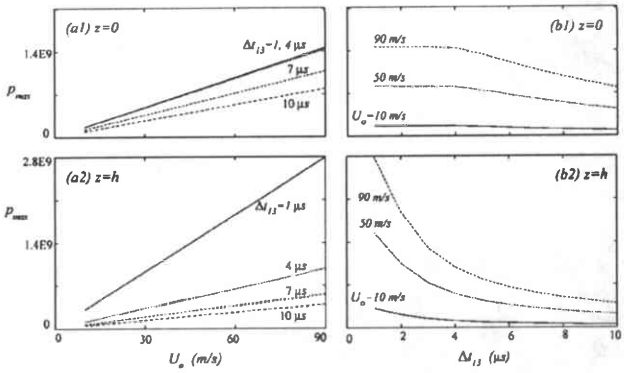

Fig. 7 Variation of p_{mx} with acceleration parameters U_0 and Δt_{13}. (*a*1), (*b*1) $z=0$; (*a*2), (*b*2) $z=h$.

ν. Unfortunately for attempts to use the acoustic model to capture elastic features, this makes the discrepancy between acoustic and elastic results even larger than that in Figs. 4($c1$) and 4($c2$).

Convergence of the elastic model with number of modes is paramount in the comparison between elastic and acoustic results. This is especially important since in the elastic model shear drops modal frequencies substantially (see Fig. 2). A larger modal set in the elastic model may be needed for its results to agree with the acoustic model that includes volumetric modes only. To verify convergence of the elastic model, histories from the analysis that produced results in Fig. 4($b1$) and Fig. 8(b) are compared to those from the finite volume model employed by El-Raheb [15] that couples projectile and disk with 40,000 nodes. Properties and geometry of the projectile are

$$E_p = 1.21\times10^{11}\ \text{dyn/cm}^2\ (=1.76\times10^6\ \text{lb./in.}^2),$$

$$\rho_p = 1\ \text{g/cm}^3\ (=9.3\times10^{-5}\ \text{lb. s}^2/\text{in.}^4),\quad \nu_p = 0.3$$

$$r_p = 6.35\ \text{mm}\ (=0.25\ \text{in.}),\quad h_p = 25.4\ \text{mm}\ (=1\ \text{in.}),$$

$$U_p = 20\ \text{m/s}\ (=65\ \text{ft./s})$$

$$c_{bp} = (E_p(1-\nu_p)/((1+\nu_p)(1-2\nu_p)\rho_p))^{1/2}$$
$$= 4.1\ \text{km/s}\ (=1.6\times10^5\ \text{in./s})$$

r_p, h_p are projectile radius and length, U_p is striking velocity, and c_{bp} is dilatational speed of sound. Properties of gelatin are given in (13a) and (13b). Based on the acoustic impedances (ρc_b) of projectile and gelatin, the velocity of gelatin at the footprint following impact is approximately $U_0=14$ m/s (=45 ft./s). Histories of axial displacement w at the footprint from the two models coincide (Figs. 9($a1$), 9($a2$)) since the asymptotic velocity U_0 at the footprint is the same for both models. Figures 9($b1$) and 9($b2$) compare histories of axial stress σ_{zz} at the footprint from the two models. In the finite volume model, the drop in σ_{zz} 4 μs after impact (Fig. 9($b2$)) corresponds to $t_{pr}=c_{bp}/2r_p$ the arrival time at

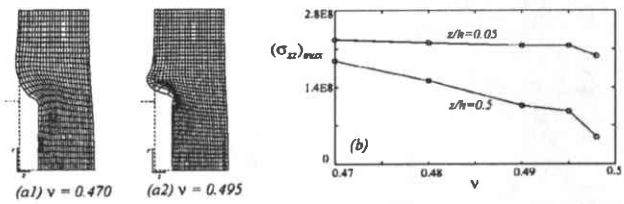

Fig. 8 Effect of Poisson ratio ν on (*a*) deformation snapshots at $t=8$ μs: (*a*1) $\nu=0.470$, (*a*2) $\nu=0.495$; (*b*) variation of peak stress with ν

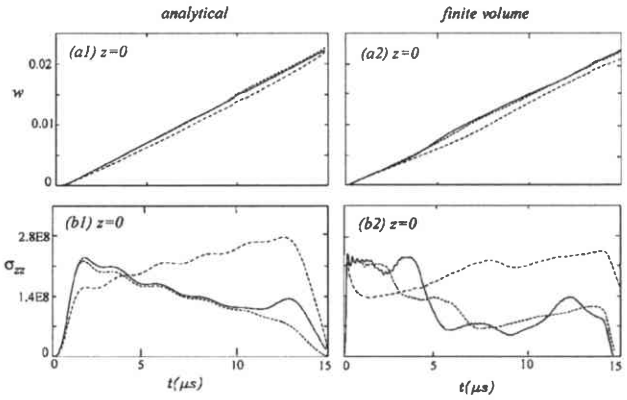

Fig. 9 Comparison of analytical and finite volume elastic models: —, $r=0.02r_p$; ---, $r=0.5r_p$; – – –, $r=0.96r_p$. (*a*1), (*b*1) *w*, σ_{zz} analytical.

$r=0$ of tensile reflections from the projectile's lateral boundary. This is evidenced by the deviation from linearity of the w histories at t_{pr} in Fig. 9($a2$). In general, magnitude and shape of the σ_{zz} histories agree suggesting convergence of the analytical elastic model.

For prescribed uniform pressure, w histories from elastic and acoustic models agree (Figs. 10($b1$) and 10($b2$)) except at the footprint $z=0$ (Figs. 10($a1$) and 10($a2$)). In Fig. 11, the lead pulse in the σ_{zz} histories from the two models is followed by a plateau with lower magnitude. The wave reflected from the constrained face at $z=h$ appears as a peak following the plateau. In the elastic model,

(i) Risetime is longer;
(ii) History is modulated by a periodic oscillation;
(iii) Magnitude of the reflection dip is reduced.

For prescribed uniform pressure, the two models agree better than for prescribed acceleration implying that mismatch between the two models increases with magnitude of shear stress in the elastic model. Indeed, near the perimeter of the footprint shear stress is lower for prescribed uniform pressure than it is for prescribed acceleration because in the later pressure distribution is not uniform (Ref. [15]).

5 Conclusion

Acoustic wave propagation in a weak layer is treated adopting both a modal and a finite difference approach. The acoustic equation derives from the elastodynamic equations when shear stress vanishes. Two types of excitations are considered at the boundary, prescribed pressure, and prescribed acceleration. In the modal approach, the external excitation is modeled by the static-dynamic superposition method. Noteworthy results are

(1) Acoustic histories from the modal and finite difference approaches coincide.
(2) For prescribed acceleration, histories from the acoustic and elastic models disagree both in magnitude and shape because the resulting pressure is not uniform. However the two models show agreement for prescribed uniform pressure because shear stress is reduced.
(3) Employing the elastic model reveals that remote from the footprint $(\sigma_{zz})_{\max}$ drops sharply as ν approaches 1/2 making the discrepancy between acoustic and elastic results even larger.
(4) Convergence of the elastic model with number of modes is verified by comparing its histories with those from a finite volume model coupling projectile and disk.
(5) For prescribed acceleration at the boundary, rise time in pressure history is proportional to $\Delta t_{1.3}$ while $p_{\max}$ is proportional to $U_0\Delta t_{13}^{-\alpha}$.
(6) Histories from prescribed pressure and prescribed acceleration differ because of nonuniform pressure distribution over the footprint.
(7) For $\Delta t_{1.3}<(\Delta t_{1.3})_T$, $p_{\max}$ goes through a transition when its value at the boundary $z=h$ exceeds that at the footprint $z=0$. $(\Delta t_{1.3})_T$ is a function of E_b and ρ but is almost independent of U_0.

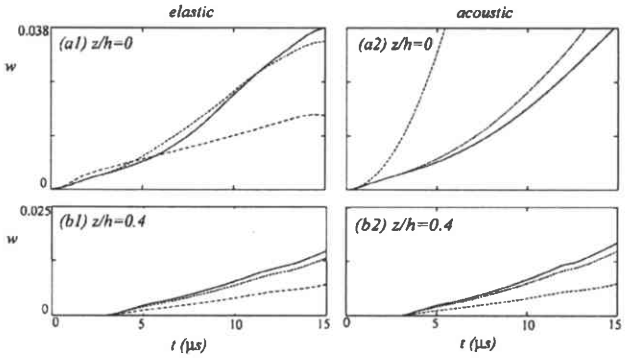

Fig. 10 Comparison of *w* histories from elastic and acoustic models with prescribed pressure: —, $r=0$; —, $r=0.5r_p$; – – –, $r=0.9r_p$

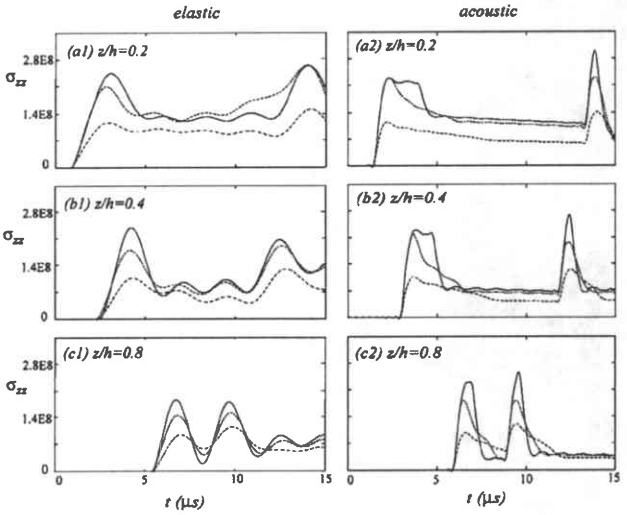

Fig. 11 Comparison of σ_{zz} histories from elastic and acoustic models with prescribed pressure: —, $r=0$; —, $r=0.5r_p$; – – –, $r=0.9r_p$

Acknowledgment

This work was supported by a grant from DARPA, executed by the U.S. Army Medical Research and Materiel Command/TATRC Contract No. W81XWH-04-C-0084.

Appendix: Acoustic Equation in the Limit of Elasto-Dynamic Equations

Consider the linear axisymmetric elasto-dynamic equations in cylindrical coordinates

$$\partial_r\sigma_{rr}+(\sigma_{rr}-\sigma_{\theta\theta})/r+\partial_z\tau_{rz}=\rho\partial_{tt}u$$

$$\partial_z \sigma_{zz} + \partial_r \tau_{rz} + \tau_{rz}/r = \rho \partial_{tt} w \tag{A1}$$

where $(\sigma_{rr}, \sigma_{\theta\theta}, \sigma_{zz}, \tau_{rz})$ are radial, circumferential, axial, and shear stresses, and (u, w) are radial and axial displacements. Bulk modulus E_b relates average normal stress σ_V to volumetric strain ε_V

$$\sigma_V = E_b \varepsilon_V \equiv \rho c_b^2 \varepsilon_V, \quad E_b = (3\lambda + 2\mu)/3 \equiv E/(3(1-2\nu))$$

$$\sigma_V = (\sigma_{rr} + \sigma_{\theta\theta} + \sigma_{zz})/3$$

$$\varepsilon_V = \varepsilon_{rr} + \varepsilon_{\theta\theta} + \varepsilon_{zz} \equiv \nabla \cdot \mathbf{u} = \partial_r u + u/r + \partial_z w \tag{A2a}$$

where (λ, μ) are *Lame'* constants and c_b is bulk speed of sound. In terms of E_b and ν, the constitutive law takes the form

$$\sigma_{ij} = \frac{3\nu}{(1+\nu)} E_b \varepsilon_V \delta_{ij} + \frac{3(1-2\nu)}{(1+\nu)} E_b \varepsilon_{ij} \tag{A2b}$$

As $\nu \to 1/2$, $\sigma_{ij} \to \sigma_V = E_b \varepsilon_V$ recovering the bulk relation in (A2*a*)

$$\nu \to 1/2 \Rightarrow \tau_{rz} = 0, \quad \sigma_{rr} = \sigma_{\theta\theta} = \sigma_{zz} \equiv -p_d \tag{A3}$$

where δ_{ij} is Dirac's delta function. Substituting (A3) in (A1) produces the linear Euler equation

$$\rho \partial_{tt} \mathbf{u} = -\nabla p_d \tag{A4}$$

where $\mathbf{u}$ is the displacement vector. For a homogeneous fluid, conservation of mass takes the form

$$\partial_t \rho + \rho \partial_t (\nabla \cdot \mathbf{u}) = 0 \tag{A5}$$

The equation of state is

$$\frac{dp_d}{d\rho} = c_b^2 \tag{A6}$$

implying that

$$\partial_t p_d = c_b^2 \partial_t \rho \tag{A7}$$

Unlike the elastic solid where deviatoric or shear stresses contribute to material stiffness and reversible strain energy, in a viscous fluid these stresses are dissipative and irreversible. They are related to acoustic velocity by a constitutive law resembling that of an elastic solid

$$\begin{aligned} \tau_{ij} &= (\zeta - 2/3\,\eta)\delta_{ij}\partial_t \varepsilon_{ll} + \eta \partial_t \varepsilon_{ij} \\ &= (\zeta - 2/3\,\eta)\delta_{ij}\partial_t \partial_{x_l} u_l + \eta \partial_t (\partial_{x_i} u_j + \partial_{x_j} u_i) \end{aligned} \tag{A8}$$

x_i, x_j are independent variables and $(\zeta - 2/3\,\eta)$ and η are coefficients of viscosity for dilatational and deviatoric stains (see Landau and Lifshitz [17], p. 48). Equation (A8) resembles the constitutive relation (A2*b*) where $3\nu/(1+\nu)E_b$ and $3(1-2\nu)/(1+\nu)E_b$ are replaced by $(\zeta - 2/3\,\eta)$ and η. The linearized Navier-Stokes equations simplify to

$$\rho \partial_{tt} \mathbf{u} = -\nabla p_d + \partial_t [(\zeta - 1/6\,\eta)\nabla(\nabla \cdot \mathbf{u}) + (\eta/2)\nabla^2 \mathbf{u}] \tag{A9}$$

Conservation of mass and the equation of state are given by (A5) and (A6). Substituting for $\partial_t \rho$ from (A7) into (A5) yields

$$\partial_t [p_d + \rho c_b^2 (\nabla \cdot \mathbf{u})] = 0 \tag{A10}$$

Equation (A10) is the time derivative of (A2*a*) with σ_V replaced by $-p$. For a nonviscous fluid, taking the divergence of (A4), then eliminating $\mathbf{u}$ using (A10) determines the acoustic equation

$$(\partial_{rr} + 1/r\partial_r + \partial_{zz}) p_d - 1/c_b^2 \partial_{tt} p_d = 0 \tag{A11}$$

Equation (A11) is purely hyperbolic nondispersive.

For a viscous fluid, adopting the procedure that led to (A11) on (A9) and assuming that $\zeta = 1/6\,\eta$ yields the approximate viscous acoustic equation

$$(1 + \tilde{\nu}/c_b^2 \partial_t)(\partial_{rr} + 1/r\partial_r + \partial_{zz}) p_d - 1/c_b^2 \partial_{tt} p_d = 0 \tag{A12}$$

where $\tilde{\nu} = \eta/(2\rho)$ (cm^2/s) is kinematic viscosity.

References

[1] Theil, F., 1998, "Young-Measure Solutions for a Viscoelastically Damped Wave Equation with Nonmonotone Stress-Strain Relation," Arch. Ration. Mech. Anal., **144**, pp. 47–78.

[2] Yserentant, H., 2001, "The Propagation of Sound in Particle Models of Compressible Fluids," Numer. Math., **88**, pp. 581–601.

[3] Yserentant, H., 1997, "A Particle Model of Compressible Fluids," Numer. Math., **76**, pp. 111–142.

[4] Sina, K., and Khashayar, M., 2002, "Analytical Solution of Wave Equation for Arbitrary Non-Homogeneous Media," Proceedings of SPI, The International Society of Optical Engineering 4772, pp. 25–36.

[5] Sujith, R., Bala Subrahmanyam, P. T., and Lieuwen, P., 2003, "Propagation of Sound in Inhomogeneous Media: Exact Solutions in Curvilinear Geometries," ASME J. Vibr. Acoust., **125**, pp. 133–136.

[6] Hamdi, S., Enright, W., Schiesser, W., and Gottlieb, J., 2003, "Exact Solutions of the Generalized Equal Width Wave Equation," Lect. Notes Comput. Sci., **266**, pp. 725–734.

[7] Yang, D., 1994, "Grid Modification for the Wave Equation with Attenuation," Numer. Math., **67**, pp. 391–401.

[8] Narayan, J., 1998, "2.5-D Numerical Simulation of Acoustic Wave Propagation," Pure Appl. Geophys., **151**, pp. 47–61.

[9] Schemann, M., and Bornemann, F., 1998, "An Adaptive Rothe Method for the Wave Equation," Computing and Visualization in Science, **3**, pp. 137–144.

[10] Bailly, C., and Juve, D., 2000, "Numerical solution of acoustic propagation problems using linearized Euler equations," AIAA J., **38**, pp. 22–29.

[11] Wagner, G., Wenzel, M., and Dumont, W., 2001, "Numerical treatment of acoustic problems with the hybrid boundary element method," Int. J. Solids Struct., **38**, pp. 10–13; , **38**, pp. 1871–1888.

[12] Gaul, L., and Wenzel, M., 2001, "Acoustic calculations with the hybrid boundary element method in the time domain," Eng. Anal. Boundary Elem., **25**, pp. 259–265.

[13] Mehdizadeh, O., and Paraschivoiu, M., 2003, "Investigation of a Three-Dimensional Spectral Element Method for Helmholtz's Equation," Lect. Notes Comput. Sci., **2668**, pp. 819–825.

[14] Berry, J., and Naghdi, P., 1956, "On the Vibration of Elastic Bodies Having Time Dependent Boundary Conditions," Q. Appl. Math., **14**, pp. 43–50.

[15] El-Raheb, M., 2004, "Wave Propagation in a Weak Viscoelastic Layer Produced by Prescribed Velocity on the Boundary," J. Sound Vib., **275**(1–2), pp. 89–106.

[16] Eisler, R., 2003, (private communication, Mission Research Corporation, Laguna Hills, CA).

[17] Landau, L., and Lifshitz, E., 1959, *Fluid Mechanics*, 1st English Ed., Pergamon Press, Addison-Wesley, New York.

Intelligent Data Analysis in Medicine and Pharmacology (IDAMAP04), Stanford, CA 2004.

Using ontologies linked with geometric models to reason about penetrating injuries

Daniel L. Rubin, Olivier Dameron, Yasser Bashir, David Grossman, Parvati Dev, and Mark A. Musen

Stanford Medical Informatics, Stanford University, Stanford, CA

Abstract

Medical assessment of penetrating injuries is a difficult and knowledge-intensive task. Physical examination and computed tomographic (CT) imaging data must be combined with detailed anatomic, physiologic, and biomechanical knowledge to assess the injured subject. We are developing a methodology to automate reasoning about penetrating injuries using canonical knowledge combined with specific subject image data. We build a three dimensional geometric model of a subject from segmented images. We link regions in this model to concepts in two knowledge sources: (1) a comprehensive ontology of anatomy containing organ identities, adjacencies, and other information useful for anatomic reasoning, and (2) an ontology of regional perfusion containing formal definitions of arterial anatomy and corresponding regions of perfusion. We developed problem solvers that can determine the organs that are injured given particular trajectories of projectiles, whether vital structures—such as a coronary artery—are injured, and can predict the propagation of injury ensuing after a vital structure is injured. This methodology may improve the speed and accuracy of rapid assessment of penetrating injury.

Introduction

Rapid and effective medical intervention in response to civil and military-related injuries is crucial for saving lives and limiting disability [1]. Assessing penetrating injuries is a complex task, requiring both geometric data and anatomic knowledge. Accurate assessment of these injures is challenging because the spatial relationships among anatomic regions can be confusing, and potential damage to certain vital structures may not be recognized. Intelligent tools that can integrate patient-specific geometric data and anatomic knowledge to inform care providers about internal injuries can be valuable to patient care.

Geometric data are specific to the patient, usually obtained from volumetric CT images, and they contain spatial information about the size and location of visible structures in the body. Anatomic knowledge adds meaning and insight to geometric data, labeling regions in space with particular organs, relating organ parts and subparts to other anatomic structures, and identifying critical structures that may affect patient prognosis and management.

Geometric data alone are insufficient to assess penetrating injury. The resolution of imaging modalities is limited, and small anatomic structures may not be visible in the images. Certain organs are known to be adjacent to others, but this knowledge is not contained in the images—an expert interpreter of the images is needed. Injuries to some regions of anatomy (such as an artery supplying the heart) will result in damage to other organs that were not directly injured by a projectile (the wall of the heart that is supplied by the injured artery). Such knowledge is not contained in the geometric data, but is known to domain experts.

A project to use both geometric data derived from images and canonical anatomic knowledge to aid the rapid diagnosis of penetrating injury called the Virtual Soldier project is being undertaken by the U.S. Defense Advanced Research Projects agency [2]. The vision for the project is that each soldier could wear a "dog tag" containing both with pre-injury CT images and other relevant baseline clinical data. At the time of an injury, an information system would read the images off the dog tag and offer advice about the nature of the wound, the patient's prognosis, and requirements for therapy.

In order to fulfill the vision of this project, we need to develop a method to integrate patient-specific geometric data and anatomic knowledge and use that knowledge to reason about penetrating injuries. In this paper, we describe our approach to this integration problem and our development of problem solving services to use anatomic knowledge to reason about penetrating injuries.

Material and Methods

The architecture of our system to integrate patient-specific geometric data with anatomic knowledge in ontologies is shown in Figure 1. Canonical knowledge sources contain detailed knowledge of organ anatomy as well as knowledge about structural anatomic dependencies that are important for predicting secondary injuries. Patient-specific data comprise cross-sectional imaging data and three dimensional geometric models that are built from these data. Data structures in our software architecture integrate the canonical knowledge and patient-specific geometric data, making both available to applications (reasoning services) that can perform intelligent tasks such as predicting direct and secondary injuries (Figure 1).

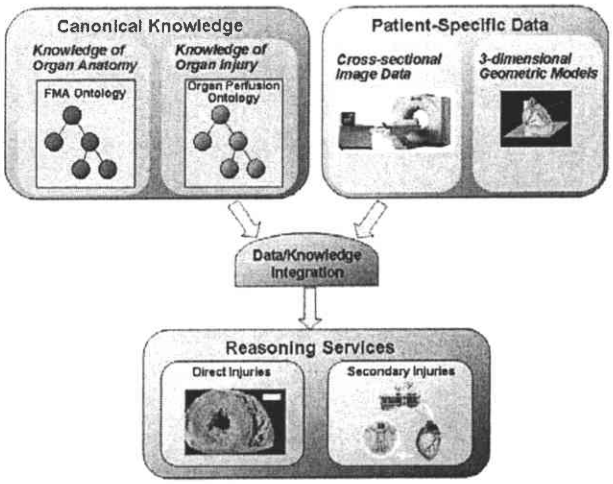

Figure 1 – Architecture for integrating patient-specific data and canonical knowledge to reason about penetrating injury.

Knowledge sources

Ontology of Canonical Anatomy

Rosse and colleagues [3] have developed a comprehensive ontology of human anatomy known as the Digital Anatomist Foundational Model of Anatomy (FMA). The FMA contains more than 70,000 concepts that describe the elements of canonical human morphology in a clear and consistent manner (Figure 2). The ontology is modeled using the Protégé ontology-management environment (http://protege.stanford.edu), and it adheres to the conventions of the OKBC frame language [4]. With this representation, reasoning services access knowledge in the FMA by locating the pertinent anatomic concepts ("classes" in the ontology), and reading their attributes ("slots" on the class). Slots can be atomic types (such as integers, strings, etc.) or other classes (e.g., the "part-of" slot contains classes that have a partonomic relationship with the given class).

The FMA provides declarative descriptions of detailed anatomic structures in a computationally accessible format. Knowledge in the FMA that we use in this project includes organ names, compositionality (partonomy relationships), organ adjacencies, containment, and continuities (Figure 2).

The FMA is particularly useful because it contains anatomic structures that may be too small to be visible on images, and thus may not be present in geometric models. This knowledge is useful for a reasoning service to deduce possible injury to small structures that are adjacent to visible structures.

Ontology of coronary anatomy and regional perfusion

While the FMA is an excellent knowledge source describing morphology and composition of anatomic structures, it lacks physiological and pathophysiological knowledge. In particular, it does not describe the regions of myocardium supplied by branches of the coronary arteries. Such knowledge is needed to reason about secondary organ damage—injury that occurs to particular anatomic structures as a result of damage to other structures.

We built an ontology of coronary artery anatomy and regional myocardial perfusion (Figure 3) using the Web Ontology Language (OWL) [5]. The OWL classes contain formal definitions, represented using logical statements, specifying the necessary and sufficient conditions ("assertions") for class inclusion. For example, the definition of the lateral wall of the left ventricle includes assertions specifying all of the branches of the coronary arteries that ordinarily supply it (Figure 3). This ontology specifies the segments and continuities in coronary arteries, the composition of myocardial regions (e.g., the left ventricle has anterior, lateral, posterior, apical, and septal parts), and it describes the myocardial regions supplied by particular coronary arterial branches. This ontology also defines the coronary arteries as being "critical" structures—

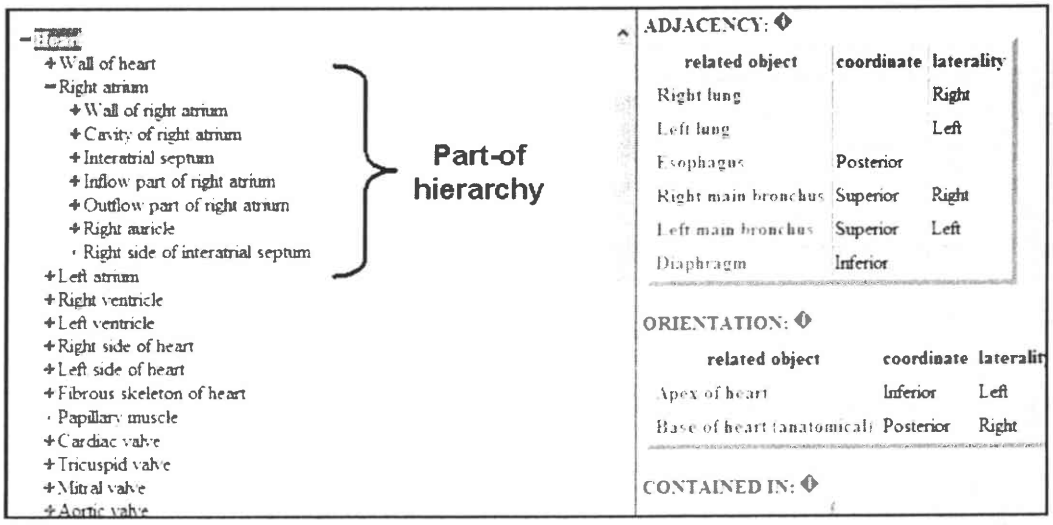

Figure 2 – The Foundational Model of Anatomy (FMA). A portion of the FMA ontology is displayed using a Web interface, showing structures related to the heart. Organs and organ parts are shown in the hierarchy on the left (a "partonomy" display). Knowledge about individual organs or organ parts is shown in the panel on the right, and includes information such as adjacencies, orientation, and containment. The ontology is stored in Protégé.

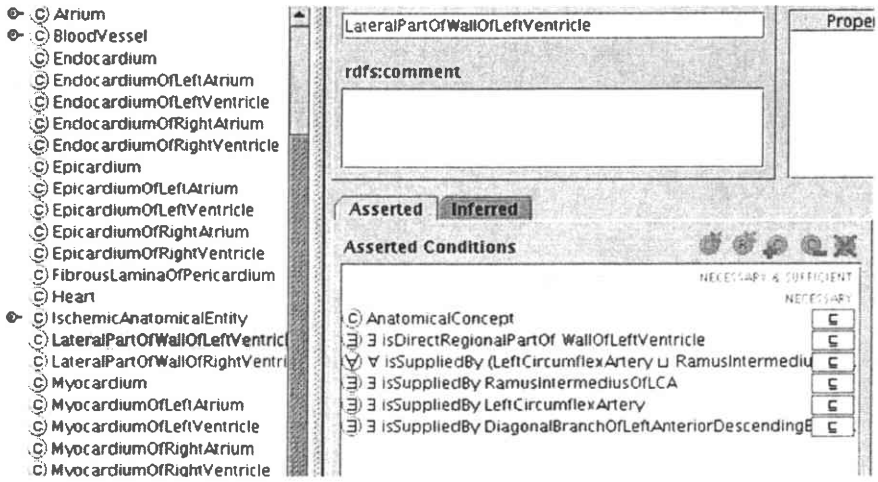

Figure 3 – Ontology (in OWL) of coronary anatomy and regional myocardial perfusion. Classes of anatomic structures are shown on the left panel, and formal definitions of the concepts are shown on the right. The class "Lateral part of wall of left ventricle" is seen to be defined by six assertions, all necessary conditions for this class. Some of these assertions specify the coronary arterial branches that supply this structure.

anatomic structures that result in damage to other structures if they are injured.

The class definitions contained in the OWL ontology permit reasoning services to deduce important physiological consequences of arterial injury. First, the ontology encodes the knowledge that arterial branches downstream from an injured branch will be functionally impaired. Second, the ontology contains knowledge of all arterial branches feeding a myocardial region. There are also definitions about when a region is totally or partially ischemic (a region is totally ischemic if all arteries supplying it are impaired, and is partially ischemic if one ore more arteries are not impaired).

Protégé provides support for OWL development, so we were able to coordinate the development of the OWL ontology of cardiac perfusion with the FMA in the same ontology development environment.

Geometric data sources and model

We obtained segmented images from the Visible Human project [6]. These comprise serial cross-sectional images from a cadaver, and they are analogous to reconstructed images available from CT on live patients. The images had been manually segmented, a process in which non-overlapping geographic regions in the raw images are assigned labels identifying anatomic structures. These labels were used to map these anatomic structures to corresponding anatomic classes in our ontologies.

The segmented two-dimensional images cannot be used directly for spatial anatomical reasoning; a three-dimensional representation of patient anatomy must be built from these

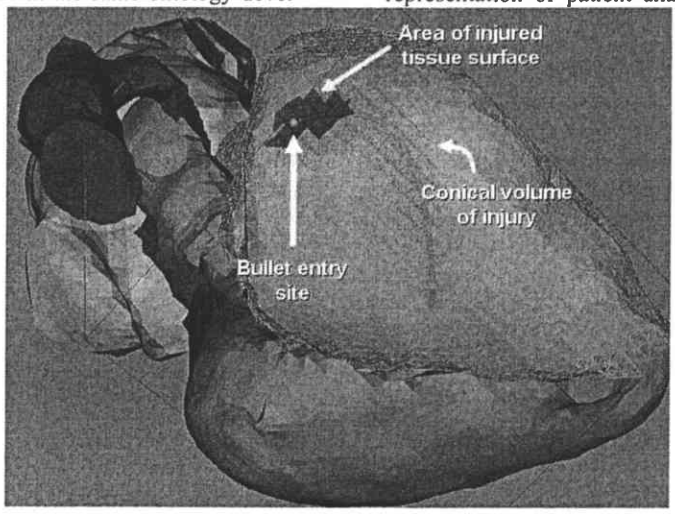

Figure 4: Three dimensional geometric model of the heart with labeled anatomic structures (shaded volumes in the geometric model correspond to anatomic structure classes in the FMA ontology). A trajectory of penetrating injury is superimposed (curved tubular shaded area). A conically-shaped region of tissue injury is predicted and displayed in the geometrical model (conically-shaped shaded region shown by arrow). We can determine the identity of injured anatomic structures and the volume of damaged organs from this geometric model. We can infer possible injuries to adjacent structures using knowledge in the FMA ontology.

images to reason with a three-dimensional projectile trajectory. We used the Insight Toolkit (ITK; http://itk.org) to build solid three-dimensional tetrahedral mesh models from the serial segmented images of the chest (Figure 4). These geometric mesh models created from the imaging data represented the three-dimensional coordinates of anatomic structures in space. Collections of vertices in the mesh model were labeled with FMA class names to identify the anatomic structures that they represent. This is accomplished in ITK by creating data structures that contain collections of vertices representing particular structures (called "spatial objects"). The spatial objects were extended to include the name of the FMA class of the anatomic structure represented by the spatial object. In this manner, the mesh model of patient-specific geometry is linked to canonical anatomic structures in the FMA (as well as the OWL ontology of myocardial perfusion). This provides a software architecture that makes patient-specific geometric data and canonical anatomic knowledge accessible to intelligent applications such as reasoning services.

We created a graphical visualization application that displays patient-specific geometric data models. Spatial objects comprising sets of tetrahedrons that represent particular organs or organ parts are displayed in different colors. A specified trajectory of penetrating injury can be incorporated into the geometric model as an additional spatial object. Rendering methods are applied to highlight the surface regions and internal volume of organs affected by the penetrating injury and area surrounding it (Figure 4).

Reasoning services

We have initially implemented two applications that use patient-specific geometric data and our canonical knowledge sources to perform useful reasoning capabilities: (1) a tool to determine which organs are injured by a penetrating injury ("Direct Injury Reasoner"), and (2) a tool that that determines whether any vital structures are injured and the consequences of such injury ("Secondary Injury Reasoner").

The Direct Injury Reasoner takes as input an entry wound and an exit wound on the patient, and it deduces the anatomic structures that have been injured by direct impact by the penetrating injury (or from shock waves in close proximity to the trajectory of injury). To accomplish this task, the Direct Injury Reasoner defines a parametric trajectory path of the penetrating injury using the observed wounds and three-dimensional tetrahedral mesh model of the patient derived from the image data. This trajectory is added to the geometric model, and it is used to infer the region of injury created by a projectile (Figure 4). The Direct Injury Reasoner deduces the anatomic structures that have been hit by the projectile by identifying the set of geometric elements intercepted by the trajectory and mapping them to the corresponding concepts in the FMA. It also creates a parametric representation of a region of tissue damage in the vicinity of the trajectory due to shock waves and tissue strain. The Direct Injury Reasoner can only infer damage to structures that are visible in the segmented images that were used to build the geometric model of the patient.

By linking the geometric mesh model to the FMA, the FMA's rich set of relationships among anatomic concepts become accessible to the Direct Injury Reasoner so that it can deduce injury to structures not visible in the segmented images. The FMA includes complex adjacency relationships (noting, for each structure, other structures that may be superior, inferior, anterior, posterior, left, or right), orientation relationships (e.g., that the apex of the heart is inferior and to the left), and contained-in relationships (e.g., that the heart is contained in the middle mediastinum). The linkage between the geometric model and the FMA allows the Direct Injury Reasoner to consider the path of a penetrating injury in anatomic terms and to deduce which adjacent anatomic structures not visible in the image data may have also been injured.

The Secondary Injury Reasoner takes as input a list of anatomic structures that have been injured by the penetrating injury (deduced by the Direct Injury Reasoner) and it deduces additional tissue injury that are occurring or will occur as a consequence of the primary injuries. To accomplish this task, the Secondary Injury Reasoner first examines the injured organs to identify critical anatomic structures structures. At this point in our work, we have modeled coronary arteries as the only critical structures. The Secondary Injury Reasoner can recognize which of the structures are critical by querying our OWL ontology, because it defines which anatomic structures are critical (Figure 3).

If any critical structures have been injured, the OWL ontology is updated with this information by creating new assertions (new subclasses indicating the structures that have been injured). For example, if the second segment of the right coronary artery (RCA) is injured, then a new subclass of "functionally impaired blood vessel" would be created by the Secondary Injury Reasoner (Figure 5).

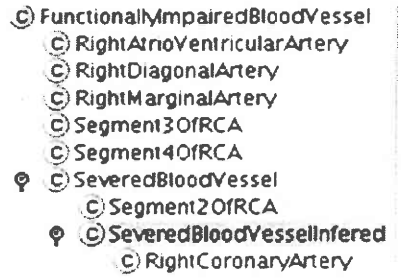

Figure 5 – OWL ontology of coronary anatomy and regional myocardial perfusion, with a new assertion that the second segment of the right coronary artery has been injured (a new class, "Segment2OfRCA" was created under "FunctionallyImpairedBloodVessel"). After automatic classification, additional impaired blood vessels are deduced (classes in light color), such as segments 3 and 4 of RCA, which are downstream from the injured segment 2 RCA.

After the Secondary Injury Reasoner asserts the damaged critical structures, it calls a classification engine that updates the OWL ontology, inferring new classes and relationships given the asserted knowledge and pre-existing class definitions. Finally, the Secondary Injury Reasoner examines the updated OWL ontology to determine if there is new knowl-

edge about injured organs as a consequence of the critical organ injury previously asserted. It accomplishes this task by looking for new subclasses of the OWL ontology that contain classes representing secondary injury (Figure 6). In our example, the Secondary Injury Reasoner would deduce that most of the right ventricle and portions of the left ventricle and right atrium were ischemic as a result of the injury to the second segment of the right coronary artery.

By combining the Direct and Secondary Injury Reasoners in series, we can begin with baseline patient imaging data and patient wounds and rapidly deduce the anticipated extent of internal direct and secondary injuries.

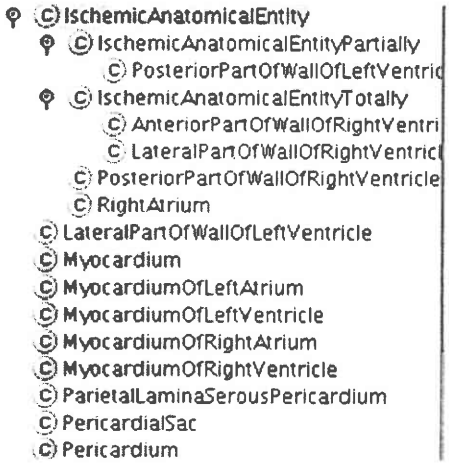

Figure 6 – OWL ontology of coronary anatomy and regional myocardial perfusion, updated with the knowledge that the second segment of the right coronary artery has been injured. After automatic classification, new classes (light color) appear as subclasses of "IschemicAnatomicalEntity," suggesting that regions of the left ventricle, right ventricle, and right atrium are ischemic as a result of the right coronary artery injury previously asserted (Figure 5).

Discussion

Timely and accurate assessment of penetrating injury is challenging. Inexperienced providers may be hampered in performance when faced with the demands of stabilizing casualties not frequently encountered. Multiple injury cases can be particularly complex to diagnose, requiring the integration and processing of complex data. Furthermore, the task in integrating anatomic knowledge and geometric data can be challenging, especially under the pressure of stabilizing the acutely injured patient.

Our goal is to develop intelligent applications to improve the ability of practitioners to assess and triage injured patients. Creating geometric models of internal anatomic structures from volumetric images alone is not adequate to solve this task. Images of patient anatomy may contain labels, but there is little knowledge in those labels beyond a name. Furthermore, vital anatomic structures may not be visible on the imaging modality used to create the geometric models, in which case there will be no label in the model

In order to create intelligent applications that can assist with tasks such as evaluating penetrating injury, they need to have reasoning capabilities. In our context, reasoning means inferring new knowledge from knowledge asserted in the ontologies that are used in the reasoning task. Reasoners are tools that use ontologies and patient data and perform reasoning with it.

To support reasoning about the consequences of organ injury, we needed to go beyond annotating geometric models with organ names and take advantage of the knowledge encoded in ontologies such as the FMA. This permits us to develop reasoning services such as the Direct Injury Reasoner that identifies structures adjacent to injured organs that may be injured. It also allows these services to suggest other anatomic structures that may have been injured but that are not visible in the patient images.

We use two different types of ontologies to support reasoning services. The first ontology is the FMA, which encodes a breadth of anatomic knowledge in a declarative format consisting of concept classes and numerous informative relationships and attributes. Ontologies like the FMA specify the concepts in the domain and the relationships among them, providing a domain of discourse that is meaningful to both humans and intelligent computer applications.

Some of the tasks of evaluating penetrating injury require additional anatomic and physiological knowledge not contained in the FMA, such as inferring additional anatomic injury secondary to primary injuries. Thus, we developed a second ontology to represent cardiac arterial anatomy and myocardial perfusion, encoded using OWL. OWL is a language for defining Web ontologies. In OWL, an ontology is a set of definitions of classes and properties, and constraints on the way those classes and properties can be employed [5]. In this representation, we formally specify the meaning of certain anatomic concepts and capture their anatomic semantics (we define regions of cardiac myocardium in terms of the coronary artery branches that supply them). Representing this knowledge in OWL makes it accessible to intelligent reasoning such as automatic classification based on Description Logics.

Classification is used to infer specialization relationships between classes from their formal definitions. A domain-independent classifier takes an input class hierarchy and the logical expressions it contains, and returns a new class hierarchy, which is logically equivalent to the input hierarchy. In our work, we use this classification approach to infer new knowledge: by asserting a new fact in our OWL representation of coronary anatomy, such as the presence of injury to the second segment of the right coronary artery, we can discover after automatic classification that several regions of the myocardium will be ischemic. Regions of myocardium that are perfused by other arteries that are not occluded are not inferred to be ischemic (Figure 6). By taking this knowledge modeling approach, we can use the power of automatic classification to cast the problem of reasoning about the consequences of arterial injury as a classification problem.

We used the Protégé suite of tools (http://protege.stanford.edu) in this work to manage and ac-

cess the ontologies. A benefit of using Protégé for ontology management in this project is that it supports both OKBC and OWL representations, and it can invoke automated classification engines. It also provides a Java API for developing applications such as our reasoning services.

Previous work related to assessing penetrating injury has focused on developing simulation environments and teaching aids to assist in assessing penetrating injuries [7]. While such teaching activity is valuable to give practitioners experience managing such trauma cases, it does not replace the need to have specific knowledge about the particular constellation of injuries in the particular patient being cared for.

In other related work, Ogunyemi and colleagues developed a system that calculated the probabilities of organ injuries using a canonical geometric model of human anatomy, and used a Bayesian network to classify particular combinations of injuries [8]. While this can be a helpful guide to typical injuries, its geometric models were not specific to the particular patient. In addition, the reasoning capability is a hard-coded classifier. In our work, we adopt ontological representations of knowledge and create reasoning services that use these ontologies and patient-specific geometric models. These reasoning services can be extended or modified without having to re-engineer the underlying knowledge or data representations. For example, Direct Injury Reasoner identifies anatomic structures that intersect the trajectory path of the projectile, and are directly injured. Subsequently, we created the Secondary Injury Reasoner that uses the ontology of myocardial perfusion in OWL to recognize coronary artery segments in the list of injured structures and reason about myocardial ischemic damage that occur as a result of coronary artery injury.

A limitation of our work is that our knowledge sources are canonical, while particular patient anatomy can be variable. Our knowledge sources were designed to be "canonical," meaning that they represent the typical entities and relationships that are observed. This limitation can be overcome if by extending our ontologies to model anatomic variation. We are currently adding the balanced and right dominant patterns of coronary arterial supply to our myocardial perfusion ontology. In this way, the patient-specific geometric model can be associated with a more appropriate anatomic knowledge source.

Another limitation is that are reasoning is focused on the chest, and particularly on the heart. In particular, heart and coronary artery injuries due to penetrating injury are uncommon compared to other organ damage, such as lung injury. However, our approach can be generalized to other anatomic regions by adding the necessary knowledge to the supporting ontologies. The FMA already includes comprehensive anatomic knowledge in the trunk, and the Direct Injury Reasoner could be extended to identify penetrating injury to other parts of the trunk. In a similar manner, the Secondary Injury Reasoner could be extended to reason about other types of injuries by creating the appropriate ontology class definitions and assertions. For example, the pleura of the lung could be defined as a vital structure, and the normal pleural space could be defined as absence of air in this space. A puncture of the pleura could be defined as allowing air into the pleural space; then a penetrating injury of the chest wall could be recognized to produce pneumothorax using automatic classification with this ontology.

Conclusion

We have demonstrated methods of augmenting spatial geometric models of injured subjects with anatomic knowledge sources in ontologies to develop intelligent reasoning services. Detailed anatomic knowledge, usually only available to an expert, can be encoded in ontologies and exploited by computer applications to reason about the consequences of penetrating injury. The knowledge used by these applications is in a declarative format that can be maintained by domain experts and interpreted by machines. These knowledge-based tools may help reduce the complexity and potential confusion associated with assessing these injuries.

Acknowledgments

This work was supported by a contract from DARPA, executed by the U.S. Army Medical Research and Materiel Command/TATRC Cooperative Agreement, Contract W81XWH-04-2-0012. We are grateful to Cornelius Rosse for many years of exciting discussion and collaboration. This work was also supported by the Protégé resource, under grant LM007885 from the U.S. National Library of Medicine.

References

[1] West JG, Trunkey DD, Lim RC. Systems of trauma care. A study of two counties. Arch Surg 1979;114(4):455-60.

[2] Virtual Soldier Project. http://www.virtualsoldier.net/summary.htm. 2004.

[3] Rosse C, Mejino JL, Jr. A reference ontology for biomedical informatics: the Foundational Model of Anatomy. J Biomed Inform 2003;36(6):478-500.

[4] Noy NF, Musen MA, Mejino JLV, Rosse C. Pushing the envelope: challenges in a frame-based representation of human anatomy. Data & Knowledge Engineering 2004;48(3):335-359.

[5] Smith MK, Welty C, McGuinness D. OWL Web Ontology Language Guide, http://www.w3.org/TR/owl-guide/. 2004.

[6] Ackerman MJ, Yoo TS. The Visible Human Data Sets (VHD) and Insight Toolkit (ITk): Experiments in Open Source Software. Proc AMIA Symp 2003:773.

[7] Freeman KM, Thompson SF, Allely EB, Sobel AL, Stansfield SA, Pugh WM. A virtual reality patient simulation system for teaching emergency response skills to U.S. Navy medical providers. Prehospital Disaster Med 2001;16(1):3-8.

[8] Ogunyemi OI, Clarke JR, Ash N, Webber BL. Combining geometric and probabilistic reasoning for computer-based penetrating-trauma assessment. J Am Med Inform Assoc 2002;9(3):273-82.

Address for correspondence

Daniel L. Rubin, Stanford Medical Informatics, MSOB X-215, 251 Campus Drive, Stanford, CA 94305. rubin@smi.stanford.edu

Integrating Ontologies with Three-Dimensional Models of Anatomy

Daniel L. Rubin, Yasser Bashir, David Grossman, Parvati Dev, and Mark A. Musen
Stanford Medical Informatics, Stanford, CA

Introduction:
Three dimensional geometric models have been used in a variety of application areas, such as surgical simulation, planning, visualization, and teaching. In nearly all such domains, these models encode detailed spatial geometric information, but usually contain little additional information, such as knowledge about the structures these models contain or properties of those structures.

In some application domains, such as predicting the effects of penetrating injury on a victim, it is necessary to know about the internal anatomy in addition to the spatial geometry. Anatomic knowledge in 3-d geometric models is generally in the head of the viewer. Thus, this knowledge is inaccessible for computer applications such as decision support, or reasoning about the physiological and anatomic consequences of penetrating injury.

The goal of our work is to link an ontology containing anatomic knowledge with 3-d geometric models in order to support anatomic reasoning about the effect of a projectile on an inured subject. In can be difficult to determine the extent of internal organ damage after a person suffers a penetrating injury. One can observe external trauma, but internal damage cannot be seen without an imaging test such as CT, which is not available at the time the injured person is first examined in the field. Our hypothesis is that we can predict the anatomic and physiological effects of penetrating injury using 3-d geometric models that contain anatomic knowledge. The goal of our work is to develop methodology to link 3-d geometrical models derived from segmented image data with logical anatomic knowledge in order to simulate both the direct and indirect effects of a projectile injury.

Methods:
In this project, we are developing and linking representations (or "models") of two kinds of knowledge: anatomic knowledge and geometric knowledge. Anatomic knowledge, such as which organs are in a region of the body and how they relate to other components, can be represented in an ontology. Ontologies provide formal definitions of concepts and relationships among concepts. One source of anatomic knowledge is the Digital Anatomist Foundational Model (FMA, [1]), a domain ontology that represents a coherent body of explicit declarative knowledge about human anatomy. The FMA provides formal definitions of detailed anatomical concepts and relationships of anatomic structures in a computationally-accessible format. However, as the FMA is a logical representation of canonical anatomy, it lacks information on organ shape and absolute location.

Conversely, geometric knowledge regarding the location and shape of organs is represented in a 3-d geometric model. These models may be segmented to identify organ parts and sub-parts. We developed an ontology in Protege to represent the entities in that are common to most geometric modeling approaches in which source data are derived from segmented volumetric images. We call this a "canonical" ontology of geometry, as it is meant to capture generic geometric notions common to most geometric models. This ontology specifies the particular data members present in geometric models that are instantiated according to its class design.

We created code classes in C++ using the Insight Toolkit (ITK; [2, 3]). These classes were designed according to the classes in our geometry ontology. The ITK classes provide the geometric representation of anatomic structures in 3-d space. The ontology allows components within a geometric model to be annotated with terms in the FMA in order to link geometry and anatomy. The geometric objects created in the ITK ("abstract geometric objects") were created as a hierarchy of objects using knowledge in the FMA ontology to structure the relationships among these objects.

Programmatic access to Protégé from C++ was accomplished using a C++/Java interface layer implemented using JACE,[1] a public domain tool to access the Java JNI. We built C++ proxy classes to transparently access corresponding Protégé Java classes (e.g., KnowledgeBase.cpp, Cls.cpp, Slot.cpp, etc.). The advantage of this approach is that the C++ code to access Protégé methods and link our ITK classes with the FMA ontology was nearly transparent.

We used the Visible Human data set [4] as a source for anatomic image data. Anatomic structures, such as the chambers of the heart, were labeled in the segmented images from this data set. From volumetric images of the chest, we produced 3-d geometric models of the heart. We used the Insight Toolkit to load the segmented images and build 3-d tetrahedral mesh models.

A path of destruction can be specified in our geometrical model, and a set of intercepted geometrical elements can be deduced. These geometrical elements can be mapped to the FMA to infer the organs that are injured.

Results:

Our ontology represents a spectrum of primitive geometric elements used to construct 3-d geometrical models. It has sufficient generality to allow either images or meshes. It includes such entities as points, cells, meshes, and simplexes. These geometric elements relate to various attributes of the organism from which the geometry is derived (organ name and biomechanical properties) as well as attributes needed to simulate the effect of penetrating injury, such as boundary features, externality, and physical properties.

Our ontology of 3-d geometry enables us to add anatomic information to geometric models. Each voxel or vertex in our geometric models contains information about the organ to which that element belongs. Anatomic structures such as the ventricles and aorta are labeled in the geometry, and can be displayed using different color shadings (Figure 1).

We have superimposed a projectile trajectory and deduced the path of injury and produce a list of damaged structures. For example, assuming a linear path for the bullet and a parameterized region of tissue injury (decreasing tissue destruction along the bullet path), we can describe and display a conically-shaped region of tissue injury (Figure 1). In addition to displaying the injured region, a user can query the model by selecting points. Because we have linked the 3-d model to the FMA, we can identify which organs or organ parts are injured, and quantify percentage of an organ that is damaged.

We are also developing and using the FMA ontology to reason about which structures are adjacent to the path of injury so that we can predict the extent of organ damage. The FMA contains information about which organs are adjacent to other organs. Using this adjacency information, it is possible to suggest organs adjacent to the path of injury that are nearby and possibly damaged.

The FMA is also useful in order to answer questions that require anatomic abstraction. For example, we would predict from our geometric model that the left ventricle has been injured, but by reasoning from the FMA based on partonomic relationships, we would also know that the pericardial sac has been penetrated and that the left side of the heart has been injured (since the left ventricle is contained in the left side of the heart).

Conclusion

We have demonstrated an approach to integrate geometric models with ontologies of anatomic knowledge so that software can help deduce the anatomic consequences of injury. The utility of our methodology is that software can reason about remote consequences of a localized injury. This entails identifying the site of injury in the geometrical model, finding the corresponding structure in the FMA, and reason about relationships in the FMA to establish the other anatomic structures that are also likely affected by their proximity to the projectile path.

---

[1] http://sourceforge.net/projects/jace/

Our methodology is extensible, and we can include additional information in our models to permit their use in other application domains.

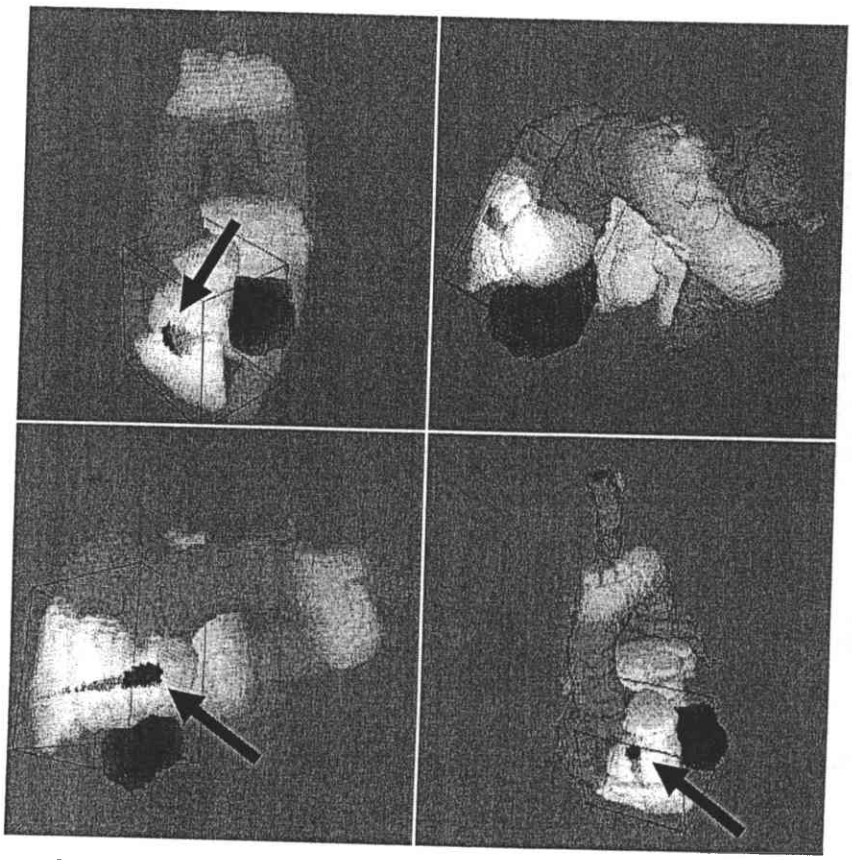

Figure 1: Four views of a three dimensional geometric model of the heart with anatomic structures labeled (shaded structures in the geometric model correspond to anatomic structure classes in the FMA ontology). A trajectory of penetrating injury was superimposed (top left image), and regions of tissue injury are predicted and demonstrated in the geometrical model (conically-shaped region shown by arrow). We can determine the identities of injured anatomic structures and infer the possible injuries to adjacent structures using knowledge in the FMA ontology.

References:

1. Rosse C, Mejino JL, Jr. A reference ontology for biomedical informatics: the Foundational Model of Anatomy. J Biomed Inform 2003;36(6):478-500.
2. The Insight Toolkit. http://itk.org. In.
3. Ackerman MJ, Yoo TS. The Visible Human Data Sets (VHD) and Insight Toolkit (ITk): Experiments in Open Source Software. Proc AMIA Symp 2003:773.
4. Ackerman MJ. The Visible Human Project: a resource for anatomical visualization. Medinfo 1998;9 Pt 2:1030-2.

Conf Proc IEEE Eng Med Biol Soc. 2004;5:3128-31

Linking Ontologies with Three-Dimensional Models of Anatomy to Predict the Effects of Penetrating Injuries

Daniel L. Rubin, Yasser Bashir, David Grossman*, Parvati Dev, and Mark A. Musen
Stanford Medical Informatics, Stanford University, Stanford, CA

Abstract—**Rapid diagnosis of penetrating injuries is essential to increased chance of survival. Geometric models representing anatomic structures could be useful, but such models generally contain only information about the relationships of points in space as well as display properties. We describe an approach to predicting the anatomic consequences of penetrating injury by creating a geometric model of anatomy that integrates biomechanical and anatomic knowledge. We created a geometric model of the heart from the Visible Human image data set. We linked this geometric model of anatomy with an ontology of descriptive anatomic knowledge. A hierarchy of abstract geometric objects was created that represents organs and organ parts. These geometric objects contain information about organ identity, composition, adjacency, and tissue biomechanical properties. This integrated model can support anatomic reasoning. Given a bullet trajectory and a parametric representation of a cone of tissue damage, we can use our model to predict the organs and organ parts that are injured. Our model is extensible, being able to incorporate future information, such as physiological implications of organ injuries.**

Keywords—**Geometric models, ontologies, simulation**

I. Introduction

In can be difficult to determine the extent of internal organ damage after a person suffers a penetrating injury. One can observe external trauma, but internal damage cannot be seen without an imaging test such as a CT scan, which is not available at the time the injured person is first examined in the field. Since survival depends on rapid diagnosis of the nature and extent of organ injury in penetrating trauma, methods to determine this information rapidly are needed.

We are interested in using geometric models to predict the anatomic and physiological effects of penetrating injury. But geometric models alone are insufficient because they lack anatomic knowledge. The underlying technology we are developing will link three dimensional (3-d) geometrical models derived from segmented image data with descriptive anatomical models (in ontologies) in order to simulate both the direct and indirect effects of a penetrating injury. Such methodology may be useful for triage of injured subjects by field medics.

In this project, we are developing and linking representations (or "models") of two kinds of knowledge: anatomic knowledge and geometric knowledge. Anatomic knowledge, such as which organs are in a region of the body and how they relate to other components, can be represented in an ontology. Ontologies provide formal definitions of concepts and relationships among concepts. One source of anatomic knowledge is the Digital Anatomist Foundational Model of Anatomy (FMA) [1], a domain ontology that represents a coherent body of explicit declarative knowledge about human anatomy (Figure 1). The FMA provides formal definitions of detailed anatomical concepts and relationships of anatomic structures in a computationally-accessible format. However, as it is a descriptive model of anatomy, it lacks precise information on organ shape and absolute location.

Conversely, geometric knowledge regarding the location and shape of structures is represented in a 3-d geometric model. A geometric model is a spatial representation of objects using vertices and edges as modeling primitives. They are generally used to create visualizations of body regions or organs, or to provide spatial coordinate information in biomechanical simulations. While geometric models contain detailed spatial information, they generally contain no anatomic knowledge. Knowledge about the organs contained in geometric models remains in the head of the viewer. Thus, geometric and ontologic models of anatomy currently exist in largely disjoint worlds.

An early effort to explore the relationship between anatomy and geometry was undertaken by intersecting 3-d models with a wound path [2], but the geometric model contained no knowledge other than organ names. We are developing methods to integrate the two worlds of geometry and anatomy so that software can relate geometry to anatomic structures in the FMA. For example, software could reason about remote consequences of a localized injury by identifying the site of injury in the geometrical model, referencing the anatomic entities associated with that site, and working through relationships in the FMA to establish the other anatomic structures that are also likely affected because they are related to the injured organs.

II. Methodology

We developed an ontology to represent the entities that are common to most geometric modeling approaches for which source data is derived from segmented volumetric images. We call this a "canonical" ontology of geometry, as

*IEEE Fellow

it is meant to capture generic geometric notions common to most geometric models. This ontology specifies the particular data members present in geometric models that are instantiated according to its class design.

We created C++ classes (called "abstract geometric objects") in the Insight Toolkit (ITK; [3, 4]) The ITK provides a large library of data structures and algorithms for working with imaging data and models derived from these data. The abstract geometric objects were designed according to the classes in our geometry ontology, and they are the data structures that we use to produce a geometric representation of anatomy in 3-d space. The ontology allows components within a geometric model to be annotated with class names in the FMA in order to link geometry and anatomy. Abstract geometric objects represent not only the spatial geometric data, but also include additional knowledge such as the organ location (named FMA class), boundary features, biomechanical properties, and tissue damage attributes.

Starting with leaf classes in the FMA (representing the smallest organ sub-parts in the geometric models), we use the FMA to build a hierarchy of abstract geometric objects, linking these objects with anatomic knowledge in the FMA (Figure 1).

We used the Visible Human data set [5] as a source for anatomic images. Anatomic structures, such as the chambers of the heart, were labeled in the segmented images from this data set (Figure 2). From volumetric images of the chest, we produced 3-d geometric models of the heart. We used ITK to load the segmented images and build 3-d solid tetrahedral mesh models. A hierarchy of abstract geometric objects was created and populated with knowledge from the FMA.

A path of destruction can be specified in our geometrical model, and a set of intercepted geometrical elements can be deduced. We described the region of damage commonly associated with penetrating injuries by creating a conically-shaped parametric region around the projectile path, and we designated this region a "conical region of tissue damage." Geometrical elements within the conical region of damage can be mapped to the FMA to infer the organs that are injured.

III. Results

A. Geometry ontology

Our ontology represents a spectrum of primitive geometric elements used to construct 3-d geometrical models. It has sufficient generality to allow either images or meshes. It includes such entities as points, cells, meshes, and simplexes (Figure 3). These geometric elements relate to various attributes of the organism from which the geometry is derived (organ name and biomechanical properties) as well as attributes needed to simulate the effects of penetrating injury, such as boundary features, externality, and physical properties.

Our ontology of 3-d geometry enables us to add anatomic information to geometric models. Each voxel or vertex in our geometric models contains information about the organ to which that element belongs ("in_organ" attributes in Figure 3). Anatomic structures such as the ventricles and aorta are labeled in the geometry, and they can be displayed using different color shadings (Figure 4). The display parameters for each organ are stored in the corresponding abstract geometric object. The path of penetrating injury and its surrounding region of tissue damage can be similarly

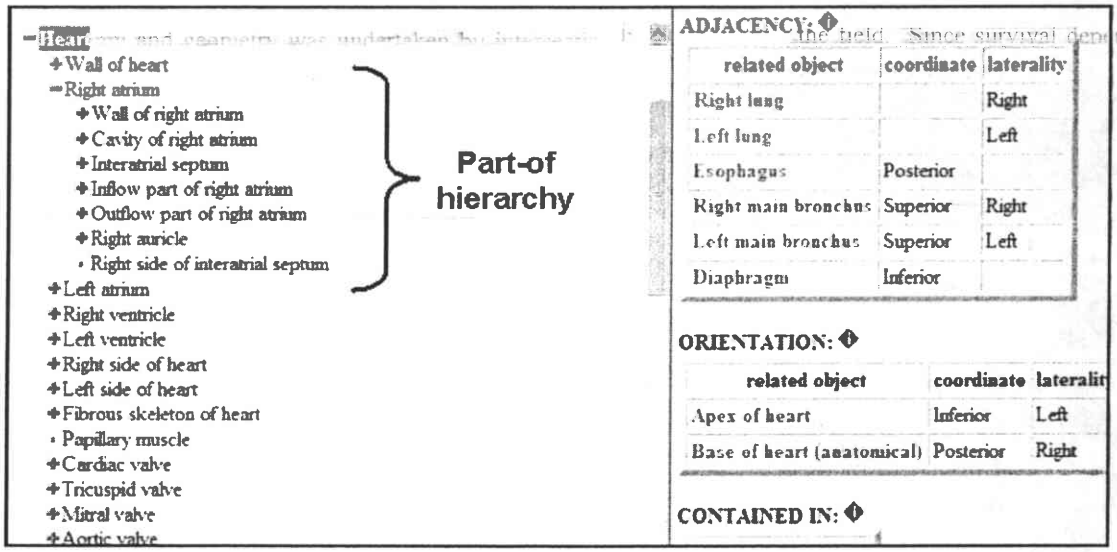

Figure 1: The Foundational Model of Anatomy (FMA). A portion of the FMA ontology is shown here, focused on the heart. Organs and organ parts are shown in the hierarchy on the left (a "partonomy"). Knowledge about individual organs or organ parts is shown in the panel on the right, and includes information such as adjacencies, containment, and vascular supply.

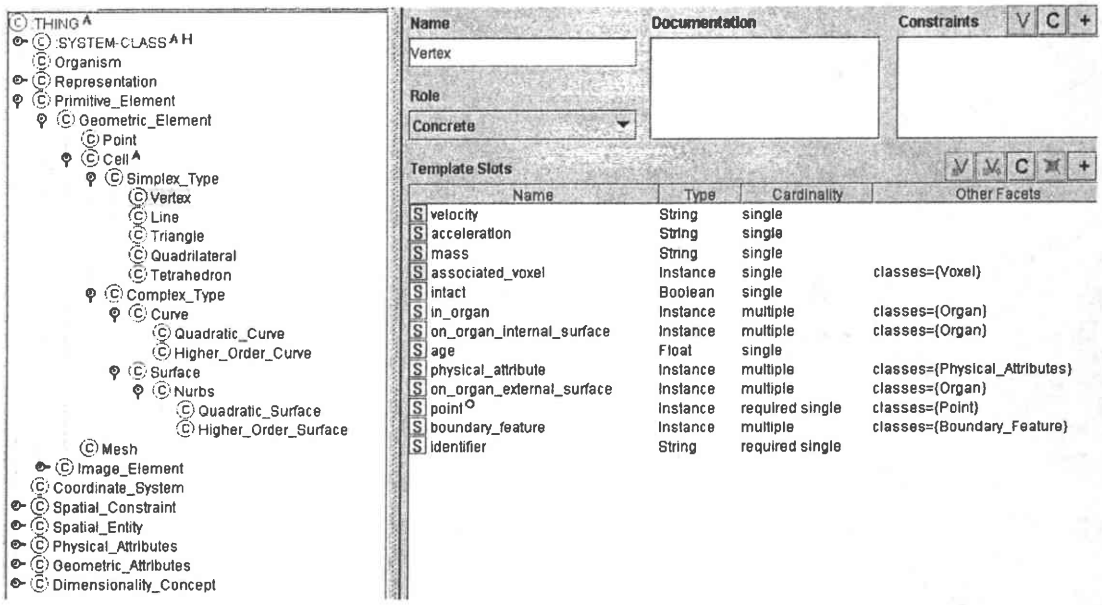

Figure 3: Screen shot of ontology of geometry developed for building canonical geometric models of anatomy.

represented in the same geometric model (Figure 4).

B. Reasoning with the model

We have superimposed a projectile trajectory, deduced the path of injury, and produced a list of damaged structures. For example, assuming a curved path for the bullet and decreasing tissue damage as the projectile decelerates, a conically-shaped region of tissue injury results (Figure 4). While we have assumed a simple parametric description of tissue damage, in practice, our modeling approach is flexible enough to accommodate more complex descriptions of regions of tissue injury. In addition to displaying the injured region, a user can query the model by selecting points. Because we have linked the 3-d model to the FMA, we can identify which organs or organ parts are injured, and quantify percentage of an organ that is damaged.

We are also developing methods for using the FMA ontology to reason about which structures are adjacent to the path of injury so that we can predict the extent of organ damage. The FMA contains information about which organs are adjacent to other organs (Figure 1). Using this adjacency information, it is possible to suggest organs adjacent to the path of injury that are nearby and possibly damaged.

The FMA is also useful for answering questions that require anatomic abstraction. For example, if we predict from our geometric model that the left ventricle has been injured, by reasoning from the FMA based on partonomic relationships, we would also know that the pericardial sac has been penetrated and that the left side of the heart has been injured (since the left ventricle is contained within the pericardium and is in the left side of the heart).

IV. Discussion

This work addresses the issue of linking two kinds of knowledge: geometrical knowledge about 3-d shape and locations of coordinates of objects in space, and anatomical knowledge about organ composition and spatial relationships to other organs. By representing anatomical knowledge in an ontology, it is possible to reason about how particular organs relate to other organs or organ parts. For example, we can infer from the FMA that the left side of the heart is composed of the left atrium and left ventricle, and that both are contained in the pericardial sac.

Geometrical knowledge is usually stored in the form of

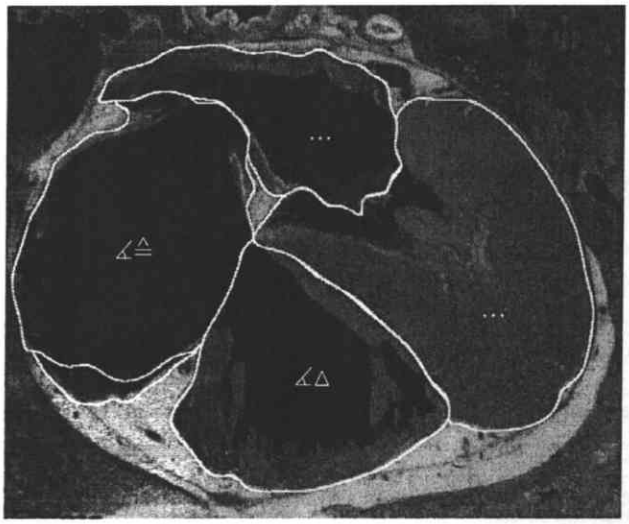

Figure 2: Cross sectional image of the heart from the Visible Human project. The chambers of the heart are segmented from the rest of the image using hand-drawn boundaries (lines in white).

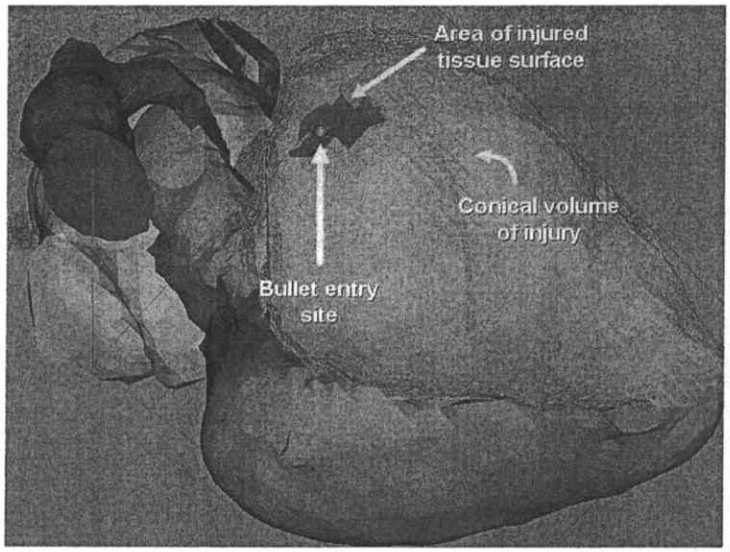

Figure 4: Three dimensional geometric model of the heart with labeled anatomic structures (shaded volumes in the geometric model correspond to anatomic structure classes in the FMA ontology). A trajectory of penetrating injury was superimposed (curved tubular shaded area). A conically-shaped region of tissue injury was predicted and displayed in the geometrical model (conically-shaped shaded region shown by arrow). We can determine the identity of injured anatomic structures and the volume of damaged organs from this geometric model. We can infer possible injuries to adjacent structures using knowledge in the FMA ontology.

models comprising images or meshes. Meshes usually contain color values for display but little if any other knowledge. Geometric models contain detailed information on organ location and shape, but much knowledge such as anatomical knowledge is in the head of the observer, not explicitly in the model. In order to develop intelligent computer applications that use geometrical models, ways to link them with ontologies are needed.

We have demonstrated an approach to integrating these two worlds so that software can relate geometry to anatomic structures in the FMA. The utility of our methodology is that software can reason about remote consequences of a localized injury by identifying the site of injury in the geometrical model, finding the corresponding structure in the FMA, and reasoning about relationships in the FMA to establish other anatomic structures that are also likely affected based on their proximity to injured organs.

While our current work has focused on predicting effects of a penetrating injury, we believe our approach can be generalized to other application areas. Because our abstract geometrical objects are extensible, we can add other information, such as spring constants, tissue material properties, etc. Such augmented models then could be useful in dynamic simulation of projectiles in motion. Alternatively, our models could incorporate information such as tissue radiosensitivity, and then they could be used in radiation therapy treatment planning to predict the effect of radiation beam energy or beam direction on tissues.

Currently, we are developing graphical interface displays to allow users to explore these complex geometrical models and interrogate different regions of 3-d space in the context of anatomical knowledge. We are also developing ways to integrate navigation of the FMA ontology with exploration of geometrical models so that a user can simultaneously browse the FMA and geometry as two different "views" of the same structures.

ACKNOWLEDGMENT

This work has been supported in part by a contract supported by the Defense Advanced Research Projects Agency (DARPA). This work was conducted using the Protégé resource, which is supported by grant LM007885 from the United States National Library of Medicine.

REFERENCES

[1] C. Rosse and J. L. Mejino, Jr., "A reference ontology for biomedical informatics: the Foundational Model of Anatomy," *J Biomed Inform*, vol. 36, pp. 478-500, 2003.

[2] O. Ogunyemi, B. L. Webber, and J. R. Clarke, "Probabilistically predicting penetrating injury for decision support.," presented at 11th Annual IEEE Symposium on Computer-Based Medical Systems, Lubbock, Texas, 1998.

[3] "The Insight Toolkit. http://itk.org.."

[4] M. J. Ackerman and T. S. Yoo, "The Visible Human Data Sets (VHD) and Insight Toolkit (ITk): Experiments in Open Source Software," *Proc AMIA Symp*, pp. 773, 2003.

[5] M. J. Ackerman, "The Visible Human Project: a resource for anatomical visualization," *Medinfo*, vol. 9 Pt 2, pp. 1030-2, 1998.

An Acoustic Model for Wave Propagation in a Weak Layer

Michael El-Raheb
ATK Mission Research,
23052 Alcade Drive,
Laguna Hills, CA 92653

An acoustic model is developed for transient wave propagation in a weak layer excited by prescribed pressure or prescribed acceleration at the boundary. The validity of the acoustic model is investigated for the two excitations. A comparison of transient response from the acoustic model and a 3D axisymmetric elastic model reveals that for prescribed acceleration the acoustic model fails to capture important features of the elastic model even as Poisson ratio ν approaches 1/2. However for prescribed pressure, the two models agree since shear stress is reduced. For prescribed acceleration adopting the modal approach, the mixed boundary-value problem on the excited boundary is converted to a pure traction problem utilizing the influence method. To validate the elaborate modal approach a finite difference model is also developed. [DOI: 10.1115/1.1988367]

1 Introduction

Laboratory simulation of blunt trauma in living tissue relies on measuring propagation of stress waves from low velocity impact in a weak viscoelastic material such as ordnance gelatin. It has acoustic impedance close to that of water yet living tissue dissipates energy from viscoelasticity and possesses shear rigidity controlling transverse propagation. It has been widely assumed that gelatin is similar to water because it has approximately the same density and bulk speed of sound. In a weak solidlike gelatin, effects of the free surface and lateral propagation of a forcing pulse are controlled by shear modulus G and the speed of shear waves, respectively. These types of propagation are independent of a loss mechanism like viscoelasticity. Loss produces an attenuation of the pulse over and above that from dispersion. It reduces the participation of high frequency modes by smoothing the average response and its gradients.

In a fluid like water, propagation is mostly volumetric, with shear related to dissipation that is proportional to velocity gradient and kinematic viscosity. At the free surface a different kind of wave develops controlled by gravity and depth of the fluid. It can be argued that although water and gelatin have very similar acoustic impedances, shear rigidity of gelatin may control how a stress wave propagates laterally and its character at and close to the free surface. If gelatin is like water then it can be treated as an acoustic fluid governed by the wave equation. In this work the wave equation is derived as a limiting case of the linear elastodynamic equations of a homogeneous solid. In fact when Poisson ratio assumes the value of 1/2, the elastic field converts to the acoustic field. One issue addressed in this work is the sensitivity of the solution to Poisson ratio close to 1/2.

To measure transmission of stress waves produced by low velocity impact on gelatin, a layer is bonded onto a metallic substrate instrumented by sensitive carbon gauges. Upon impact, stress waves propagate across the layer reaching the substrate with substantial reduction in intensity from dispersion and viscous losses. Measuring impact and transmitted pressures are needed to construct the material's constitutive model. Carefully controlled experiments with sufficient accuracy reproducing transient histories for correlation with computed results are very hard to execute. The problem lies in the weakness of the material. Gauges cannot be placed inside the material while gauges at the interface between material and metal substrate suffer from lack of cohesion adding uncertainty to measured data. This difficulty forces investigators to rely on sensitivity studies from analysis and general purpose discretization programs in order to understand phenomena. Moreover, literature in this field addresses quasistatic measurements of elongation omitting important dynamic effects such as strain-rate dependence in the microsecond regime. The simulation of these experiments led to the realization that approximating gelatin as a viscous fluid is valid only for unrealistic impact conditions when pressure over the footprint is uniform.

Acoustic wave propagation governed by the Helmholtz equation has been treated extensively in the literature. Solution techniques range from the analytical for simple geometries to numerical for problems with complicated geometry, medium inhomogeneity, and nonlinearity. Theil [1] treats the 1D viscoelastically damped wave equation analytically. Yserentant [2] shows how a consistent discretization of the acoustic equation can be recovered from the particle model of compressible fluids (see Ref. [3]). Sina and Khashayar [4] solve the 3D wave equation analytically for arbitrary nonhomogeneous media adopting the differential transfer matrix. Sujith et al. [5] present an exact solution to 1D transient waves in curvilinear coordinates adopting transformation of variables suggested by the WKB approximation. Hamdi et al. [6] present exact solitary wave solutions of the 1D wave propagation in nonlinear media with dispersion. Yang [7] solves numerically the wave equation with attenuation from linear friction utilizing grid modification to track wave fronts accurately. Narayan [8] solves the 3D transient acoustics in inhomogeneous media by finite difference and Schemann and Bornemann [9] apply the adaptive Rothe integrator. Bailly and Juve [10] present a numerical solution to the 2D acoustic propagation from transient sources using the dispersion-relation-preserving scheme in space and a fourth-order Runge-Kutta in time. Wagner et al. [11] and Gaul and Wenzel [12] use a hybrid boundary element method for frequency and transient acoustic response in bounded and unbounded regions. Mehdizadeh and Paraschivoiu [13] develop a spectral element method to solve the 3D Helmholtz equation retaining accuracy for large wave numbers. None of the references above addresses 3D transient propagation from impact analytically.

Acoustic wave propagation in a free disk is developed here adopting a modal analysis validated by a finite difference method. Transient response to prescribed pressure and prescribed acceleration at the boundary is analyzed. Since the primary goal of this work is to investigate the validity of the established belief that

Contributed by the Applied Mechanics Division of THE AMERICAN SOCIETY OF MECHANICAL ENGINEERS for publication in the ASME JOURNAL OF APPLIED MECHANICS. Manuscript received by the Applied Mechanics Division, December 21, 2004; final revision, February 7, 2005. Associate Editor: O. M. O'Reilly. Discussion on the paper should be addressed to the Editor, Prof. Robert M. McMeeking, Journal of Applied Mechanics, Department of Mechanical and Environmental Engineering, University of California-Santa Barbara, Santa Barbara, CA 93106-5070, and will be accepted until four months after final publication in the paper itself in the ASME JOURNAL OF APPLIED MECHANICS.

 Copyright © 2005 by ASME

Downloaded 02 Jul 2007 to 141.214.17.5. Redistribution subject to ASME license or copyright, see http://www.asme.org/terms/Terms_Use.cfm

tissue can be treated as a fluid, the acoustic equation is derived from the elastic equations of a solid in the limit when Poisson ratio and shear stresses vanish (Appendix).

Section 2 develops the acoustic model utilizing the modal approach for both prescribed pressure and prescribed acceleration. In the modal approach, the forcing function at the boundary is treated adopting the static-dynamic superposition method (see Berry and Naghdi [14]). The solution is expressed as a superposition of a static term satisfying the inhomogeneous boundary conditions, and a dynamic solution in terms of the eigenfunctions satisfying homogeneous boundary conditions.

Since the projectile's strength and acoustic impedance are much greater than those of tissue, the excitation transmitted over the boundary at the projectile-tissue interface can be approximated as a given time dependent prescribed motion in contrast to an unknown pressure excitation. However, this type of excitation would lead to a mixed boundary condition; i.e., pressure gradient prescribed over part of the boundary and zero pressure prescribed over the remaining part. This difficulty can be overcome by the influence method which superimposes response from a set of unit pressures with time-dependent weights prescribed on annular portions of the footprint. These weights are updated at each time step from the condition that combined acceleration at the center of each ring over the footprint equals the prescribed instantaneous acceleration. In this way, the forcing function is converted to pure traction with time-varying spatial dependence.

Section 3 develops the finite difference approach. Radial and axial dependence are discretized by central differences while time dependence is integrated by the Kutta-Runge method.

Section 4 compares acoustic histories from the two approaches validating the modal approach. Histories of the acoustic model are compared to those from a 3D axisymmetric elastic model demonstrating the inadequacy of the acoustic model when applied to a solid with Poisson ratio near 1/2 and forced by applied acceleration. Sensitivity of the acoustic histories to type of excitation and to parameters of the prescribed acceleration profile is also presented. The effect of Poisson ratio ν on peak elastic stress is evaluated confirming that for prescribed acceleration mismatch of acoustic and elastic results is not caused by small deviations in Poisson ratio ν from 1/2 in the elastic model. Finally, results from the two models are compared for prescribed uniform pressure revealing that the mismatch diminishes when shear stress is reduced.

2 Modal Analysis

In the analysis to follow, all variables are independent of circumferential angle due to the assumption of axisymmetry. This condition applies for a cylindrical projectile at normal incidence. Consider a traction-free disk with radius r_d and length h bonded to a rigid substrate. Appendix A derives the acoustic equation in the limit when shear stress vanishes in the linear elastodynamic equations of a solid. In the analysis to follow, r and z denote radial and axial coordinates. Acoustic propagation in the disk is governed by the acoustic equation

$$(\partial_{rr} + 1/r\partial_r + \partial_{zz})p_d - 1/c_b^2\partial_{tt}p_d = 0 \tag{1a}$$

with the following boundary conditions:

$$p(r_d,z;t) = 0 \tag{1b}$$

$$\left.\begin{aligned} p(r,0;t) &= [H(r) - H(r-r_p)]f(t) && \text{prescribed pressure} \\ \partial_z p(r,0;t) &= -\rho\ddot{f}_w(t) \quad 0 \le r \le r_p \\ p(r,0;t) &= 0 \qquad\qquad r_p < r < r_d \end{aligned}\right\} \text{prescribed acceleration} \tag{1c}$$

$$\partial_z p(r,h;t) = 0, \quad \text{fixed face, or alternatively}$$

$$p(r,h;t) = 0, \quad \text{free face} \tag{1d}$$

where $H(r)$ is the Heaviside function, r_p is footprint radius of the external excitation which is projectile radius, $f(t)$ is time dependence of prescribed pressure, and $\ddot{f}_w(t)$ is time dependence of prescribed acceleration. Express $p(r,z;t)$ as a superposition of two terms (see Berry and Naghdi [14])

$$p(r,z;t) = \begin{cases} p_s(r,z)f(t) + p_d(r,z;t), & \text{prescribed pressure} \\ -p_s(r,z)\rho\ddot{f}_w(t) + p_d(r,z;t), & \text{prescribed acceleration} \end{cases} \tag{2}$$

where $p_s(r,z)$ is the static solution of Eq. (1a) with inhomogeneous boundary conditions (1b)–(1d) assuming $f(t)=1$ or $\ddot{f}_w(t) = 1/\rho$, and $p_d(r,z;t)$ is a dynamic solution of Eq. (1a) satisfying the homogeneous boundary conditions (1b)–(1d) with $f(t)=0$ or $\ddot{f}_w(t)=0$.

The prescribed acceleration boundary condition in Eq. (1c) is mixed. In other words, part of the boundary has prescribed pressure gradient and the other part has prescribed pressure. This difficulty can be overcome by dividing the circle bounding the footprint into $n+1$ equidistant radial stations with increment Δr_p

$$0, r_1, r_2, \ldots, r_{n-1}, r_n, \quad r_k - r_{k-1} = \Delta r_p = \text{const}$$

where $r_n = r_p$. Assume a uniform pressure of unit intensity acting over each annular segment $r_{k-1} \to r_k$ that is termed source segment. Where subscript z denotes partial derivative with respect to z, evaluating the pressure gradient $P_{z,lk}(r,z;t)$ from the kth source segment at the center of the lth segment $r_{cl} = (r_l + r_{l-1})/2$ that is termed target point and following the expansion in (2) yields

$$P_{z,lk}(r_{cl},0;t) = -p_{zs,lk}(r_{cl},0)\rho\ddot{f}_w(t) + p_{zd,lk}(r_{cl},0;t) \tag{3}$$

where $p_{zs,lk}(r_{cl},0;t)$ and $p_{zd,lk}(r_{cl},0)$ are static and dynamic pressure gradients at the lth target point due to the kth source segment. Enforcing the condition of prescribed pressure gradient $p_{zf}(t)$ over the footprint at each time step yields a set of simultaneous equations in the weights $c_k(t)$

$$\sum_{k=1}^{n} P_{z,lk}(r_{cl},0;t)c_k(t) = p_{zf}(t), \quad 1 \le l \le n \tag{4}$$

The combined pressure from all annular source segments is the superposition of $P_{lk}(r,z;t)$ factored by time dependent weights $c_k(t)$

$$p(r,z;t) = \sum_{k=1}^{n} P_{lk}(r,z;t)c_k(t), \quad 1 \le l \le n$$

$$P_{lk}(r,z;t) = -p_{s,lk}(r,z)\rho\ddot{f}_w(t) + p_{d,lk}(r,z;t) \tag{5a}$$

Solutions of $p_{s,k}(r,z;t)$ and $p_{d,k}(r,z;t)$ for each unit source segment are outlined in what follows. The static solution for the kth source segment $p_s(r,z)$ takes the form

$$p_{s,k}(r,z) = \sum_{m=1}^{m_r} \psi_{sm,k}(z)J_0(k_{rm}r)$$

$$\psi_{sm,k}(z) = \alpha_{mk}\sinh(k_{rm}z) + \beta_{mk}\cosh(k_{rm}z) \tag{5b}$$

where $J_0(k_{rm}r)$ is the Bessel function of the first kind and zeroth order. Substituting (5b) in the boundary conditions (1b)–(1d) and enforcing orthogonality of $J_0(k_{rm}r)$ yields

$$J_0(k_{rm}r_d) = 0, \quad 1 \le m \le m_r \tag{6a}$$

$$\beta_{m,k} = \frac{2(r_k J_1(k_{rm}r_k) - r_{k-1}J_1(k_{rm}r_{k-1}))}{r_d^2 J_1^2(k_{rm}r_d)k_{rm}} \tag{6b}$$

Downloaded 02 Jul 2007 to 141.214.17.5. Redistribution subject to ASME license or copyright, see http://www.asme.org/terms/Terms_Use.cfm

$$\alpha_{m,k}=\begin{cases}-\beta_{m,k}\tanh(k_{rm}h), & \text{fixed face, or alternatively}\\ -\beta_{m,k}/\tanh(k_{rm}h), & \text{free face}\end{cases} \tag{6c}$$

Note that in (3), $p_{zs,lk}(r_{cl},0)=\partial_z p_{s,k}(r_{cl},0)$.

The dynamic solution $p_{d,k}(r,z;t)$ satisfies

$$(\partial_{rr}+1/r\partial_r+\partial_{zz})p_{d,k}-1/c_b^2\partial_{tt}p_{d,k}=0 \tag{7}$$

and the homogeneous boundary conditions in (1*b*)–(1*d*). Expand $p_d(r,z;t)$ in terms of its orthogonal eigenfunctions

$$p_{d,k}(r,z;t)=\sum_m\sum_n a_{mn,k}(t)\psi_{dn}(z)J_0(k_{rm}r) \tag{8}$$

Applying the homogeneous boundary conditions in (1*b*)–(1*d*) to $J_0(k_{rm}r)$ and $\psi_{dn}(z)$ produces

$$J_0(k_{rm}r_d)=0, \quad 1\leq m\leq m_r \tag{9a}$$

$$\psi_{dn}(z)=\begin{cases}\cos(k_{zn}z),\cos(k_{zn}h)=0\rightarrow k_{zn}h=\dfrac{1}{2}(2n-1)\pi, & \text{fixed face}\\ \sin(k_{zn}h),\sin(k_{zn}h)=0\rightarrow k_{zn}h=n\pi, & \text{free face}\end{cases}, \quad 1\leq n\leq n_z \tag{9b}$$

$$k_{zn}^2+k_{rm}^2=k_{mn}^2, \quad \omega_{mn}=c_b k_{mn} \tag{9c}$$

where ω_{mn} is the eigenfrequency corresponding to mode (m,n). Substituting (3) in (1*a*) with use made of (5*a*), (5*b*), (6), (8), and (9) and enforcing orthogonality of $\psi_{dn}(z)$ and $J_0(k_{rm}r)$ yields

$$\ddot{a}_{mn,k}(t)+\omega_{mn}^2 a_{mn,k}(t)=-N_{sd\ mn,k}\rho f_w^{IV}(t); \quad f_w^{IV}(t)=\partial^4 f_w(t)/\partial t^4$$

$$N_{sd\ mn,k}=\frac{2}{h}\int_0^h \psi_{sm,k}(z)\psi_{dn}(z)dz, \quad 1\leq m\leq m_r, \quad 1\leq n\leq n_z \tag{10}$$

In deriving Eq. (10) the term $\nabla_0^2(-p_s)\rho\ddot{f}_w(t)$, $(\nabla_0^2\equiv\partial_{rr}+1/r\partial_r)$ vanishes since static pressure $p_s(r,z)$ satisfies the equation $\nabla_0^2 p_s=0$. Acoustic displacements $(w,u)_k$ are determined from (A4)

$$\partial_z p_{d,k}=-\rho\partial_{tt}^2 w_k$$

$$\partial_r p_{d,k}=-\rho\partial_{tt}^2 u_k \tag{11}$$

The solution to (10) is expressed as a Duhamel integral

$$a_{mn,k}(t)=-\frac{\rho N_{sd\ mn,k}}{\omega_{mn}}\int_0^t \sin\omega_{mn}(t-\tau)f_w^{IV}(\tau)d\tau \tag{12}$$

Note that in (11) $\partial_z p_{d,k}(r_{cl},0;t)=p_{zd,lk}(r_{cl},0;t)$ as defined in (3). Once histories of $\partial_z p_{d,k}$ and $\partial_r p_{d,k}$ are determined from solving (10), histories of w_k and u_k are found by integrating (11) numerically.

3 Finite Difference

Consider a disk with traction-free boundaries satisfying the conditions

$$\partial_r p(0,z;t)=0 \tag{13a}$$

$$p(r_d,z;t)=0 \tag{13b}$$

$$\partial_z p(r,0;t)=0 \tag{13c}$$

$$p(r,h;t)=[H(r)-H(r-r_p)]f(t) \quad \text{prescribed pressure} \tag{13d}$$

$$\left.\begin{aligned}\partial_z p(r,h;t)&=-\rho\ddot{f}_w(t), & 0\leq r\leq r_p\\ p(r,h;t)&=0, & r_p<r\leq r_d\end{aligned}\right\} \text{ prescribed acceleration}$$

where ( ) denotes time derivative. Unlike the analysis in Sec. 2 where z has its origin at the excited boundary, in the finite difference scheme z has its origin at the nonexcited boundary. Condition (13*a*) is symmetry about the axis of revolution $r=0$, (13*b*) is traction-free boundary at $r=r_d$, (13*c*) is fixed boundary at $z=0$, and (13*d*) is prescribed acceleration for $0\leq r\leq r_p$ and traction-free boundary for $r_p\leq r\leq r_d$ at $z=h$. Form the rectangular grid

$$\begin{aligned}&i=1\rightarrow n_r, \quad d_r\leq r\leq r_d-d_r, \quad d_r=r_d/(n_r+1)\\ &j=1\rightarrow n_z, \quad d_z\leq z\leq h-d_z, \quad d_z=h/(n_z+1)\end{aligned} \tag{14}$$

In this grid, nodes do not include points on the boundaries. Expressing Eq. (1*a*) in central difference to first order yields the following relations depending on position:

(a) Internal points $d_r<r<r_d-d_r$, $d_z<z<h-d_z\Rightarrow 2\leq i\leq n_r-1$, $2\leq j\leq n_z-1$

$$\alpha_1 p_{i+1,j}+\alpha_2 p_{i-1,j}+\alpha_3 p_{i,j}+\alpha_4(p_{i,j+1}+p_{i,j-1})=1/c_b^2\ddot{p}_{i,j}$$

$$\alpha_1=\left(\frac{1}{d_r^2}+\frac{1}{2r_i d_r}\right), \quad \alpha_2=\left(\frac{1}{d_r^2}-\frac{1}{2r_i d_r}\right), \quad \alpha_3=-2\left(\frac{1}{d_r^2}+\frac{1}{d_z^2}\right), \quad \alpha_4=\frac{1}{d_z^2} \tag{15a}$$

(b) Corner point at $r=d_r$, $z=d_z\Rightarrow i=1$, $j=1$

$$\alpha_1 p_{i+1,j}+(\alpha_2+\alpha_3+\alpha_4)p_{i,j}+\alpha_4 p_{i,j+1}=1/c_b^2\ddot{p}_{i,j} \tag{15b}$$

(c) Points along axis $r=d_r$, $d_z<z<h-d_z\Rightarrow i=1$, $2\leq j\leq n_z-1$

$$\alpha_1 p_{i+1,j}+(\alpha_2+\alpha_3)p_{i,j}+\alpha_4(p_{i,j+1}+p_{i,j-1})=1/c_b^2\ddot{p}_{i,j} \tag{15c}$$

(d) Corner point at $r=d_r$, $z=h-d_z\Rightarrow i=1$, $j=n_z$

For prescribed pressure

$$\alpha_1 p_{i+1,j}+(\alpha_2+\alpha_3)p_{i,j}+\alpha_4 p_{i,j-1}-1/c_b^2\ddot{p}_{i,j}=\alpha_4 f(t) \tag{15d}$$

For prescribed acceleration

$$\alpha_1 p_{i+1,j}+(\alpha_2+\alpha_3+\alpha_4)p_{i,j}+\alpha_4 p_{i,j-1}-1/c^2\ddot{p}_{i,j}=-\rho\ddot{f}_w(t)/d_z$$

(e) Points along boundary $d_r<r<r_d-d_r$, $z=d_z\Rightarrow 2\leq i\leq n_r-1$, $j=1$

Downloaded 02 Jul 2007 to 141.214.17.5. Redistribution subject to ASME license or copyright, see http://www.asme.org/terms/Terms_Use.cfm

$$\alpha_1 p_{i+1,j} + \alpha_2 p_{i-1,j} + (\alpha_3 + \alpha_4) p_{i,j} + \alpha_4 p_{i,j+1} = 1/c_b^2 \ddot{p}_{i,j} \tag{15e}$$

(f) Points along boundary $d_r < r < r_d - d_r$, $z = h - d_z \Rightarrow 2 \leq i \leq n_r - 1$, $j = n_z$

For $0 \leq r \leq r_p$ and prescribed pressure

$$\alpha_1 p_{i+1,j} + \alpha_2 p_{i-1,j} + \alpha_3 p_{i,j} + \alpha_4 p_{i,j-1} - 1/c_b^2 \ddot{p}_{i,j} = \alpha_4 f(t) \tag{15f}$$

For $0 \leq r \leq r_p$ and prescribed acceleration

$$\alpha_1 p_{i+1,j} + \alpha_2 p_{i-1,j} + (\alpha_3 + \alpha_4) p_{i,j} + \alpha_4 p_{i,j-1} - 1/c_b^2 \ddot{p}_{i,j} = -\rho \ddot{f}_w(t)/d_z$$

For $r_p < r \leq r_d$

$$\alpha_1 p_{i+1,j} + \alpha_2 p_{i-1,j} + \alpha_3 p_{i,j} + \alpha_4 p_{i,j-1} - 1/c_b^2 \ddot{p}_{i,j} = 0$$

(g) Corner point at $r = r_d - d_r$, $z = d_z \Rightarrow i = n_r$, $j = 1$

$$\alpha_2 p_{i-1,j} + (\alpha_3 + \alpha_4) p_{i,j} + \alpha_4 p_{i,j+1} = 1/c^2 \ddot{p}_{i,j} \tag{15g}$$

(h) Points along boundary $r = r_d - d_r$, $d_z < z < h - d_z \Rightarrow i = n_r$, $2 \leq j \leq n_z - 1$

$$\alpha_2 p_{i-1,j} + \alpha_3 p_{i,j} + \alpha_4 (p_{i,j+1} + p_{i,j-1}) = 1/c_b^2 \ddot{p}_{i,j} \tag{15h}$$

(i) Corner point at $r = r_d - d_r$, $z = h - d_z \Rightarrow i = n_r$, $j = n_z$

$$\alpha_2 p_{i-1,j} + \alpha_3 p_{i,j} + \alpha_4 p_{i,j-1} = 1/c_b^2 \ddot{p}_{i,j} \tag{15i}$$

In (15*a*)–(15*i*), the differential equation is satisfied only at internal points of the grid modified by constraints on the boundaries.

Applying (15*a*)–(15*i*) at all internal points in the grid (14) produces a set of ordinary differential equations in $p_{i,j}(t)$ cast in the form of tridiagonal blocks as follows:

$$\ddot{\mathbf{p}} = c_b^2 (\mathbf{M}_p \mathbf{p} - \mathbf{F}(t))$$

$$\mathbf{M}_p = \begin{bmatrix} \mathbf{A}_1 & \mathbf{C}_1 & & & & \\ \mathbf{B}_2 & \mathbf{A}_2 & \mathbf{C}_2 & & & \\ & \square & \square & \square & & \\ & & \mathbf{B}_{n_r-1} & \mathbf{A}_{n_r-1} & \mathbf{C}_{n_r-1} & \\ & & & \mathbf{B}_{n_r} & \mathbf{A}_{n_r} \end{bmatrix} \tag{16}$$

$\mathbf{B}_i$ and $\mathbf{C}_i$ are $(n_z \times n_z)$ diagonal matrices, $\mathbf{A}_i$ is the $(n_z \times n_z)$ banded matrix with bandwidth 3, and $\mathbf{F}$ is the global vector of the forcing function in (15*d*) and (15*f*). For each point $j \ni (1 \leq j \leq n_z)$ along an i line in the grid, coefficients of $p_{i,j}$ in the Laplacian define $\mathbf{A}_i$, coefficients of $p_{i-1,j}$ define $\mathbf{B}_i$, and coefficients of $p_{i+1,j}$ define $\mathbf{C}_i$. The time derivative is expressed in the central difference to first order allowing integration in time.

Viscous damping is included following the approximate equation (A12)

$$(1 + \tilde{\nu}/c_b^2 \partial_t)(\partial_{rr} + 1/r \partial_r + \partial_{zz}) p - 1/c_b^2 \partial_{tt} p = 0 \tag{A12}$$

This modifies (16) to the first order system

$$\dot{\mathbf{p}} = \mathbf{q}$$

$$\dot{\mathbf{q}} = c_b^2 \mathbf{M}_p \mathbf{p} + \tilde{\nu} \mathbf{M}_p \mathbf{q} - c_b^2 \mathbf{F}(t) \tag{17}$$

4 Results

The numerical experiments to follow assume a traction-free gelatin disk 12.7 mm (=0.5 in.) thick and 25.4 mm (=1 in.) radius with the boundary $z = h$ bonded to a rigid surface. In the elastic model the gelatin properties are (Eisler [16]):

$$E = 3.1 \times 10^9 \text{ dyn/cm}^2 (= 4.5 \times 10^4 \text{ lb./in.}^2),$$

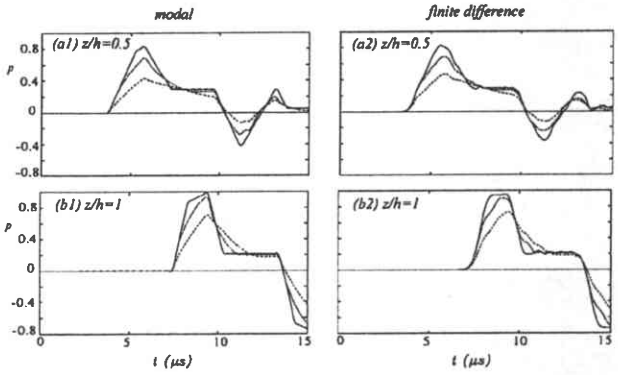

Fig. 1 Acoustic histories from prescribed pressure: —, $r=0$; —, $r=0.5r_p$; – – –, $r=0.9r_p$. (*a*1), (*b*1) modal; (*a*2), (*b*2) finite difference.

$$\rho = 0.93 \text{ g/cm}^3 (= 8.7 \times 10^{-5} \text{ lb. s}^2/\text{in.}^4), \quad \nu = 0.48 \tag{18a}$$

The data in (13*a*) yield a small ratio of *Lame'* constants $\mu/\lambda = (1-2\nu)/(2\nu) \approx 0.0417$ resulting in reduced shear stresses and in turn large displacements. In the acoustic model, bulk modulus E_b, density ρ, and speed of sound c_b are then

$$E_b = E/(3(1-2\nu)) = 2.73 \times 10^{10} \text{ dyn/cm}^2 (= 3.95 \times 10^5 \text{ lb./in.}^2)$$

$$\rho = 0.93 \text{ g/cm}^3 (= 0.87 \times 10^{-4} \text{ lb. s}^2/\text{in.}^4)$$

$$c_b = \sqrt{E_b/\rho} = 1.71 \text{ km/s} (= 6.74 \times 10^4 \text{ in./s}) \tag{18b}$$

E_b is determined from experimental measurements of c_b.

To confirm the implementation of the complicated analytical approach adopting time dependent influence coefficients, results are first compared to those from the more straightforward numerical finite difference approach derived in the Appendix. Figure 1 compares acoustic pressure histories from the two approaches for a layer forced by a prescribed trapezoidal pressure pulse of unit intensity lasting 8 μs with 2 μs rise and fall times and 4 μs plateau applied over a circular footprint with radius $r_p = 6.35$ mm (=0.25 in.). Figures 1(*a*1), 1(*a*2) plots histories at $z = 0.5h$ and Figs. 1(*b*1), 1(*b*2) at $z = h$. For each z, histories at 3 radial stations $r/r_p = 0$, 0.5, and 0.9 are superimposed. Figures 1(*a*1) and 1(*b*1) show that the prescribed pressure pulse quickly changes profile as the wave travels along z. The flat plateau of the profile acquires a discontinuity in intensity after an interval $\Delta t_1 = 3.5$ μs from the wavefront equal to travel time of the wave over r_p. Over this interval intensity diminishes smoothly with z, while over the remaining interval $\Delta t_2 = 4.5$ μs intensity diminishes steeply with z. At $z = h$, intensity over Δt_1 rises from reflections at the rigid boundary. Histories from the two distinctly different approaches agree confirming the implementation of the analytical model.

The difference in response between the acoustic model and the 3D axisymmetric elastic model is discussed in what follows. Figures 2(*a*) and 2(*b*) plot the eigenfrequency Ω (kHz) versus radial wave number $\lambda_m/\pi = k_{rm} r_d/\pi$ with axial wave number n as parameter for the elastic and acoustic models. For each mode (m,n), Ω of the acoustic model is 5 times higher than that of the elastic model. The reason is that in the acoustic model Ω is proportional to c_b while in the elastic model it is proportional to the flexural phase velocity c_p that is bounded by the shear speed $c_s = \sqrt{E/(2(1+\nu)\rho)}$. For $\nu = 0.48$, $c_b/c_s = 4.97$ consistent with the ratio observed in Fig. 2. This is the fundamental difference distinguishing the two models. Furthermore, the acoustic model cannot capture transverse wave propagation as no shear is included in the model. Although in the elastic model extensional modes exist with frequencies proportional to c_b nevertheless flexural modes dominate the response because of their lower frequencies.

Downloaded 02 Jul 2007 to 141.214.17.5. Redistribution subject to ASME license or copyright, see http://www.asme.org/terms/Terms_Use.cfm

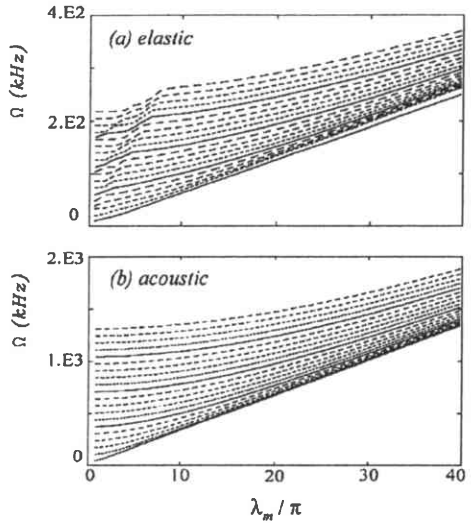

Fig. 2 Frequency spectra of elastic and acoustic models. (*a*) Elastic model; (*b*) acoustic model.

Figure 3 plots prescribed motion $\ddot{f}_w(t)$, $\dot{f}_w(t)$, and $f_w(t)$ when acceleration is prescribed at the footprint. $\ddot{f}_w(t)$ is made of 4 linear segments

(1) Linear acceleration: $\ddot{f}_{w1}(t)=\alpha_1 t$, $0\leq t\leq t_1$
(2) Constant acceleration: $\ddot{f}_{w2}(t)=\alpha_1 t_1$, $t_1\leq t\leq t_2$
(3) Linear deceleration: $\ddot{f}_{w3}(t)=\ddot{f}_{w2}(t_2)-\alpha_2(t-t_2)$, $t_2\leq t\leq t_3$
(4) Constant velocity: $\ddot{f}_{w4}(t)=0$, $\dot{f}_{w4}(t_3)=U_0$, $t_3\leq t\leq t_4$

Assuming that the first three time intervals are equal ($\Delta t_1=\Delta t_2=\Delta t_3$, $\Delta t_i=t_i-t_{i-1}$) and $\alpha_2=\alpha_1$, then α_1 is determined by assigning the constant velocity U_0 to $\dot{f}_{w4}(t_3)$. In the analysis to follow

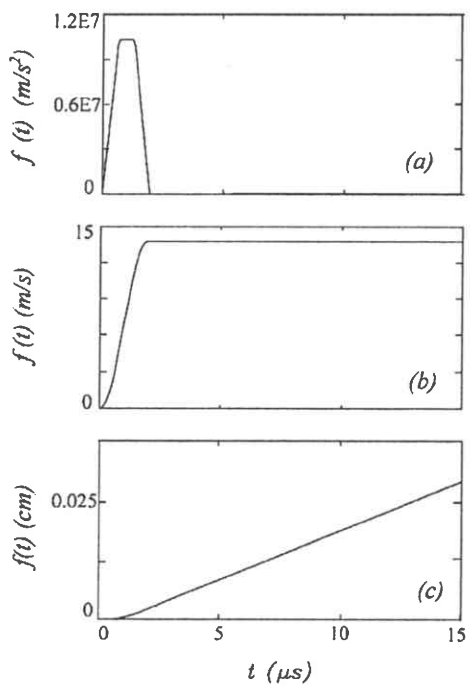

Fig. 3 Prescribed motion at footprint. (*a*) Acceleration; (*b*) velocity; (*c*) displacement.

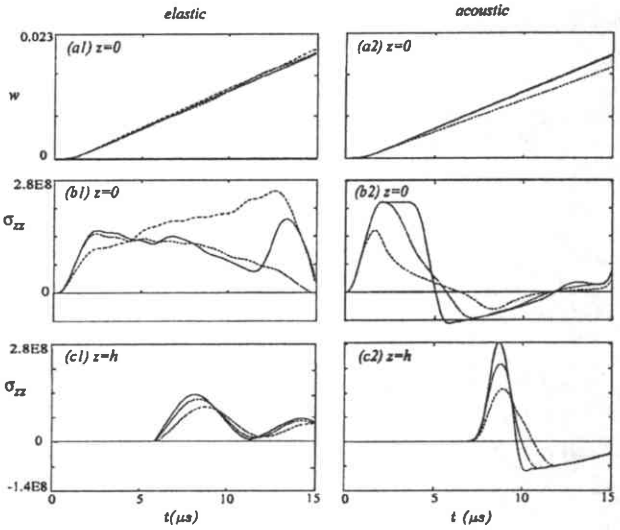

Fig. 4 Comparison of elastic and acoustic histories for prescribed acceleration: —, $r=0$; —, $r=0.5r_p$; – – –, $r=0.9r_p$. Elastic model: (*a*1) $w(r,0)$, (*b*1) $\sigma_{zz}(r,0)$, (*c*1) $\sigma_{zz}(r,h)$; acoustic model: (*a*2) $w(r,0)$, (*b*2) $\sigma_{zz}(r,0)$, (*c*2) $\sigma_{zz}(r,h)$.

$$\Delta t_{1,3}\equiv\Delta t_1+\Delta t_2+\Delta t_3=2\ \mu s,\quad U_0=14\ \text{m/s}(\equiv 46\ \text{ft./s}) \tag{19}$$

Figure 4 compares histories of the elastic and acoustic models from prescribed acceleration. Displacement at $z=0$ (Figs. 4(a1), 4(a2)) conforms to the prescribed value in Fig. 3(c). At $z=0$, Figs. 4(b1), 4(b2) compare histories of axial stress $-\sigma_{zz}$ from the elastic model to pressure p from the acoustic model. Peak stress, pulse duration, distribution of p over the footprint, and shape differ substantially between the two models. At $z=h$, Fig. 4(c1) and 4 (c2) compare $-\sigma_{zz}$ to p histories. There, magnitude and pulse width also differ. It is evident from this comparison that the two models differ appreciably in spite of the fact that in the elastic model $\nu=0.48$ is close to the transition value 1/2.

The difference between the two models in response from uniform prescribed pressure and prescribed acceleration is demonstrated in the example to follow. A uniform pressure pulse duplicating that at $r=0$ in Fig. 4(b2) is applied at $z=0$ (see Fig. 5(b)). The resulting histories of displacement w and pressure p at $z=h$ are shown in Figs. 5(a) and 5(c). Comparing histories in Figs. 4(a2) and 4(c2) to those in Figs. 5(a) and 5(c) reveals the sensitivity of response to p distribution over the footprint. Further evidence of this sensitivity appears when comparing p and w profiles at $z=0$ of the two cases. For prescribed acceleration p (Fig. 6(a1)) is not uniform while w (Fig. 6(b1)) is almost constant for $r<r_p$ and discontinuous at $r=r_p$. For prescribed pressure, p (Fig. 6(a2)) duplicates the external pulse while w (Fig. 6(b2)) increases with r reaching a maximum at $r=r_p$ with a discontinuity even stronger than that in Fig. 6(b1).

The parameters characterizing the applied acceleration profile are the final constant velocity U_0, and time interval $\Delta t_{1,3}$ of acceleration and deceleration to reach U_0 smoothly from rest. Figure 7 plots p_{max} against U_0 with $\Delta t_{1,3}$ as the parameter and vice versa. As expected, p_{max} is linear with U_0 (Figs. 7(a1) and 7(a2)). In contrast, p_{max} is nonlinear with $\Delta t_{1,3}$ (Figs. 7(b1), 7(b2)) following a relation $p_{max}\propto U_0\Delta t_{1,3}^{-\alpha}$, where the α depends on z. p_{max} approaches a constant value as $\Delta t_{1,3}\to 0$ when slope of the acceleration profile in Fig. 3(a) becomes infinite. This is the limiting case when U_0 is applied instantaneously. For $\Delta t_{1,3}<3\ \mu s$, p_{max} goes through a transition when its value at $z=h$ exceeds that at $z=0$. The transition $\Delta t_{1,3}$ is almost independent of U_0.

Downloaded 02 Jul 2007 to 141.214.17.5. Redistribution subject to ASME license or copyright, see http://www.asme.org/terms/Terms_Use.cfm

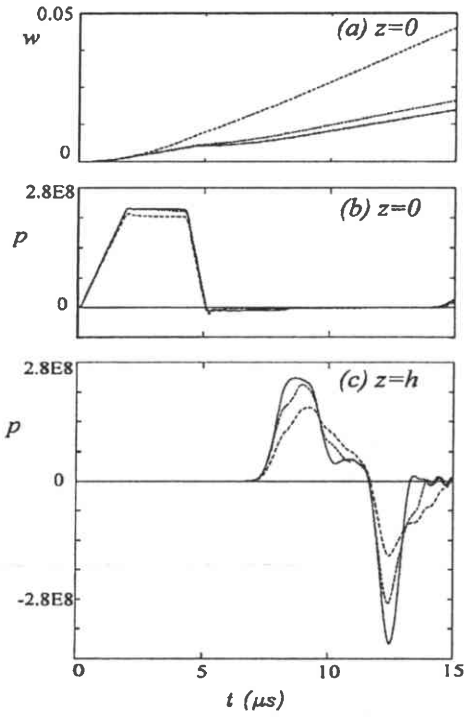

Fig. 5 Acoustic histories from prescribed pressure: —, r=0; – – –, r=0.5r_p; – – –, r=0.9r_p. (*a*) $w(r,0;t)$; (*b*) $p(r,0;t)$; (*c*) $p(r,h;t)$.

Figure 8(*a*) shows deformed shapes at t=8 μs from the elastic model for ν=0.470 and 0.495 keeping bulk modulus E_b the same. This requires expressing the constitutive law in terms of E_b and ν as in Eq. (A2*b*). Note that bulging of material near the perimeter is more pronounced for ν=0.495 than for ν=0.470. As ν approaches 1/2, material compressibility diminishes followed by a reduction in phase velocity along r near the free surface which delays propagation of the wavefront. In turn, conservation of volume and pressure release beyond the perimeter $r>r_p$ explains the formation and intensification of the bulge. Indeed, the closer ν gets to 1/2 the steeper the displacement gradient $\partial_r w$ along the perimeter reminiscent of the acoustic w profile in Fig. 6(*b*1). The effect on peak elastic stress $(\sigma_{zz})_{\max}$ of ν in the range $0.47 \leq \nu \leq 0.498$ is shown in Fig. 8(*b*). Although $(\sigma_{zz})_{\max}$ at z=0 is insensitive to ν for $\nu < 0.495$, its value at z=h drops by 76% due to a 6% increase in

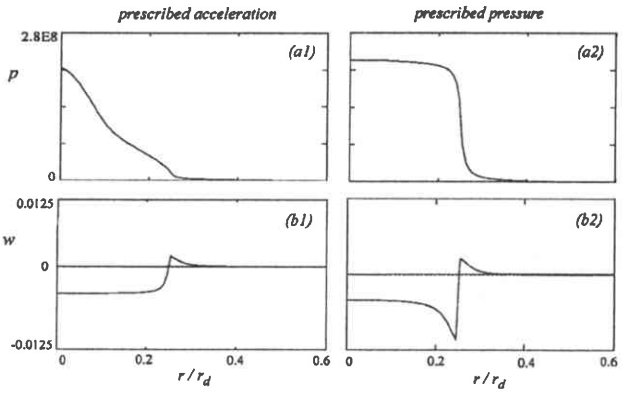

Fig. 6 Acoustic pressure and displacement profiles at z=0 and t=4 μs. (*a*1), (*b*1) Prescribed acceleration; (*a*2), (*b*2) prescribed pressure.

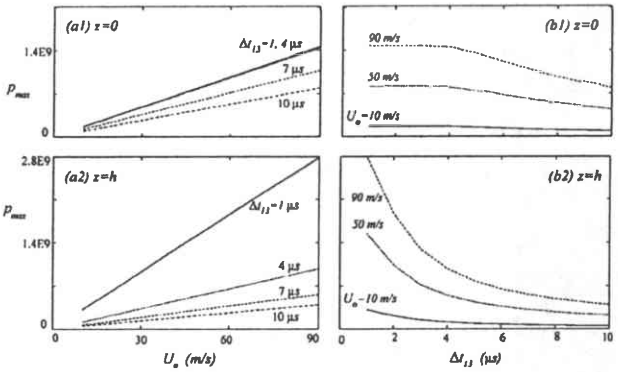

Fig. 7 Variation of p_{mx} with acceleration parameters U_0 and Δt_{13}. (*a*1), (*b*1) z=0; (*a*2), (*b*2) z=h.

ν. Unfortunately for attempts to use the acoustic model to capture elastic features, this makes the discrepancy between acoustic and elastic results even larger than that in Figs. 4(*c*1) and 4(*c*2).

Convergence of the elastic model with number of modes is paramount in the comparison between elastic and acoustic results. This is especially important since in the elastic model shear drops modal frequencies substantially (see Fig. 2). A larger modal set in the elastic model may be needed for its results to agree with the acoustic model that includes volumetric modes only. To verify convergence of the elastic model, histories from the analysis that produced results in Fig. 4(*b*1) and Fig. 8(*b*) are compared to those from the finite volume model employed by El-Raheb [15] that couples projectile and disk with 40,000 nodes. Properties and geometry of the projectile are

$$E_p = 1.21 \times 10^{11}\ \text{dyn/cm}^2\ (=1.76 \times 10^6\ \text{lb./in.}^2),$$

$$\rho_p = 1\ \text{g/cm}^3\ (=9.3 \times 10^{-5}\ \text{lb. s}^2\text{/in.}^4), \quad \nu_p = 0.3$$

$$r_p = 6.35\ \text{mm}\ (=0.25\ \text{in.}), \quad h_p = 25.4\ \text{mm}\ (=1\ \text{in.}),$$

$$U_p = 20\ \text{m/s}\ (=65\ \text{ft./s})$$

$$c_{bp} = (E_p(1-\nu_p)/((1+\nu_p)(1-2\nu_p)\rho_p))^{1/2}$$
$$= 4.1\ \text{km/s}\ (=1.6 \times 10^5\ \text{in./s})$$

r_p, h_p are projectile radius and length, U_p is striking velocity, and c_{bp} is dilatational speed of sound. Properties of gelatin are given in (13*a*) and (13*b*). Based on the acoustic impedances (ρc_b) of projectile and gelatin, the velocity of gelatin at the footprint following impact is approximately U_0=14 m/s (=45 ft./s). Histories of axial displacement w at the footprint from the two models coincide (Figs. 9(*a*1), 9(*a*2)) since the asymptotic velocity U_0 at the footprint is the same for both models. Figures 9(*b*1) and 9(*b*2) compare histories of axial stress σ_{zz} at the footprint from the two models. In the finite volume model, the drop in σ_{zz} 4 μs after impact (Fig. 9(*b*2)) corresponds to t_{pr}=$c_{bp}/2r_p$ the arrival time at

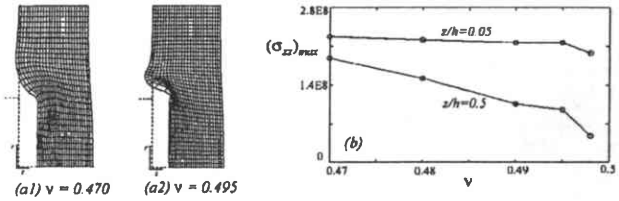

Fig. 8 Effect of Poisson ratio ν on (*a*) deformation snapshots at t=8 μs: (*a*1) ν=0.470, (*a*2) ν=0.495; (*b*) variation of peak stress with ν

Downloaded 02 Jul 2007 to 141.214.17.5. Redistribution subject to ASME license or copyright, see http://www.asme.org/terms/Terms_Use.cfm

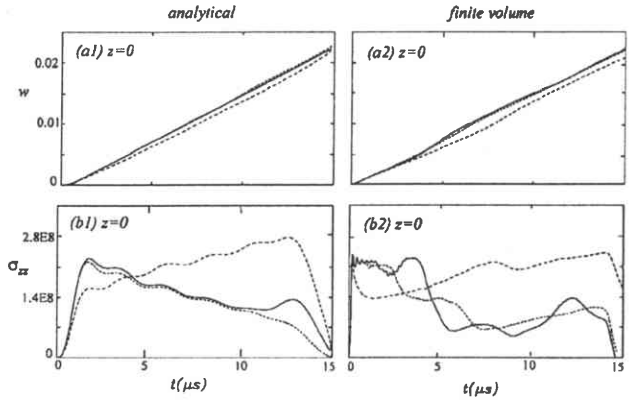

Fig. 9 Comparison of analytical and finite volume elastic models: —, $r=0.02r_p$; —, $r=0.5r_p$; – – –, $r=0.96r_p$. (*a*1), (*b*1) *w*, σ_{zz} analytical.

$r=0$ of tensile reflections from the projectile's lateral boundary. This is evidenced by the deviation from linearity of the w histories at t_{pr} in Fig. 9(a2). In general, magnitude and shape of the σ_{zz} histories agree suggesting convergence of the analytical elastic model.

For prescribed uniform pressure, w histories from elastic and acoustic models agree (Figs. 10(b1) and 10(b2)) except at the footprint $z=0$ (Figs. 10(a1) and 10(a2)). In Fig. 11, the lead pulse in the σ_{zz} histories from the two models is followed by a plateau with lower magnitude. The wave reflected from the constrained face at $z=h$ appears as a peak following the plateau. In the elastic model,

(i) Risetime is longer;
(ii) History is modulated by a periodic oscillation;
(iii) Magnitude of the reflection dip is reduced.

For prescribed uniform pressure, the two models agree better than for prescribed acceleration implying that mismatch between the two models increases with magnitude of shear stress in the elastic model. Indeed, near the perimeter of the footprint shear stress is lower for prescribed uniform pressure than it is for prescribed acceleration because in the later pressure distribution is not uniform (Ref. [15]).

5 Conclusion

Acoustic wave propagation in a weak layer is treated adopting both a modal and a finite difference approach. The acoustic equation derives from the elastodynamic equations when shear stress vanishes. Two types of excitations are considered at the boundary, prescribed pressure, and prescribed acceleration. In the modal approach, the external excitation is modeled by the static-dynamic superposition method. Noteworthy results are

(1) Acoustic histories from the modal and finite difference approaches coincide.
(2) For prescribed acceleration, histories from the acoustic and elastic models disagree both in magnitude and shape because the resulting pressure is not uniform. However the two models show agreement for prescribed uniform pressure because shear stress is reduced.
(3) Employing the elastic model reveals that remote from the footprint $(\sigma_{zz})_{\max}$ drops sharply as ν approaches 1/2 making the discrepancy between acoustic and elastic results even larger.
(4) Convergence of the elastic model with number of modes is verified by comparing its histories with those from a finite volume model coupling projectile and disk.
(5) For prescribed acceleration at the boundary, rise time in pressure history is proportional to $\Delta t_{1,3}$ while $p_{\max}$ is proportional to $U_0\Delta t_{13}^{-\alpha}$.
(6) Histories from prescribed pressure and prescribed acceleration differ because of nonuniform pressure distribution over the footprint.
(7) For $\Delta t_{1,3}<(\Delta t_{1,3})_T$, $p_{\max}$ goes through a transition when its value at the boundary $z=h$ exceeds that at the footprint $z=0$. $(\Delta t_{1,3})_T$ is a function of E_b and ρ but is almost independent of U_0.

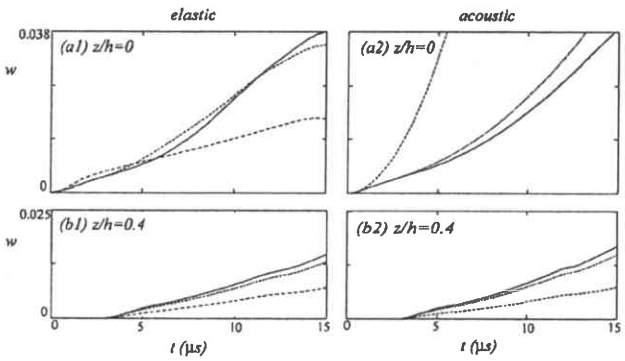

Fig. 10 Comparison of *w* histories from elastic and acoustic models with prescribed pressure: —, $r=0$; —, $r=0.5r_p$; – – –, $r=0.9r_p$

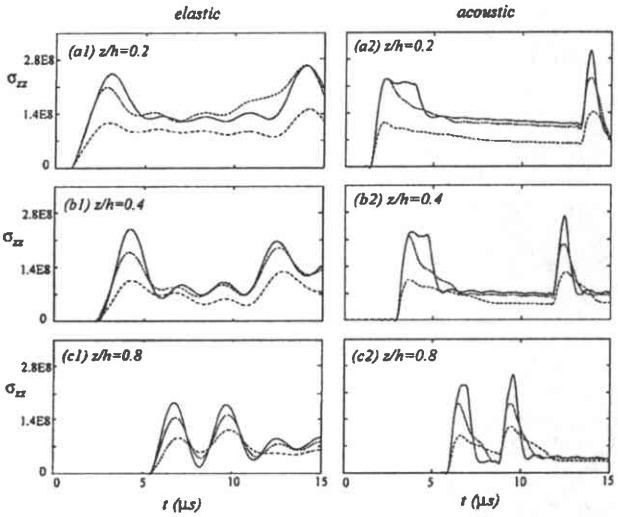

Fig. 11 Comparison of σ_{zz} histories from elastic and acoustic models with prescribed pressure: —, $r=0$; —, $r=0.5r_p$; – – –, $r=0.9r_p$

Acknowledgment

This work was supported by a grant from DARPA, executed by the U.S. Army Medical Research and Materiel Command/TATRC Contract No. W81XWH-04-C-0084.

Appendix: Acoustic Equation in the Limit of Elasto-Dynamic Equations

Consider the linear axisymmetric elasto-dynamic equations in cylindrical coordinates

$$\partial_r\sigma_{rr}+(\sigma_{rr}-\sigma_{\theta\theta})/r+\partial_z\tau_{rz}=\rho\partial_{tt}\mu$$

Downloaded 02 Jul 2007 to 141.214.17.5. Redistribution subject to ASME license or copyright, see http://www.asme.org/terms/Terms_Use.cfm

$$\partial_z \sigma_{zz} + \partial_r \tau_{rz} + \tau_{rz}/r = \rho \partial_{tt} w \tag{A1}$$

where $(\sigma_{rr}, \sigma_{\theta\theta}, \sigma_{zz}, \tau_{rz})$ are radial, circumferential, axial, and shear stresses, and (u, w) are radial and axial displacements. Bulk modulus E_b relates average normal stress σ_V to volumetric strain ε_V

$$\sigma_V = E_b \varepsilon_V \equiv \rho c_b^2 \varepsilon_V, \quad E_b = (3\lambda + 2\mu)/3 \equiv E/(3(1-2\nu))$$

$$\sigma_V = (\sigma_{rr} + \sigma_{\theta\theta} + \sigma_{zz})/3$$

$$\varepsilon_V = \varepsilon_{rr} + \varepsilon_{\theta\theta} + \varepsilon_{zz} \equiv \nabla \cdot \mathbf{u} = \partial_r u + u/r + \partial_z w \tag{A2a}$$

where (λ, μ) are *Lame'* constants and c_b is bulk speed of sound. In terms of E_b and ν, the constitutive law takes the form

$$\sigma_{ij} = \frac{3\nu}{(1+\nu)} E_b \varepsilon_V \delta_{ij} + \frac{3(1-2\nu)}{(1+\nu)} E_b \varepsilon_{ij} \tag{A2b}$$

As $\nu \to 1/2$, $\sigma_{ij} \to \sigma_V = E_b \varepsilon_V$ recovering the bulk relation in (A2*a*)

$$\nu \to 1/2 \Rightarrow \tau_{rz} = 0, \quad \sigma_{rr} = \sigma_{\theta\theta} = \sigma_{zz} \equiv -p_d \tag{A3}$$

where δ_{ij} is Dirac's delta function. Substituting (A3) in (A1) produces the linear Euler equation

$$\rho \partial_{tt} \mathbf{u} = -\nabla p_d \tag{A4}$$

where $\mathbf{u}$ is the displacement vector. For a homogeneous fluid, conservation of mass takes the form

$$\partial_t \rho + \rho \partial_t (\nabla \cdot \mathbf{u}) = 0 \tag{A5}$$

The equation of state is

$$\frac{dp_d}{d\rho} = c_b^2 \tag{A6}$$

implying that

$$\partial_t p_d = c_b^2 \partial_t \rho \tag{A7}$$

Unlike the elastic solid where deviatoric or shear stresses contribute to material stiffness and reversible strain energy, in a viscous fluid these stresses are dissipative and irreversible. They are related to acoustic velocity by a constitutive law resembling that of an elastic solid

$$\begin{aligned} \tau_{ij} &= (\zeta - 2/3\eta)\delta_{ij}\partial_t \varepsilon_{ll} + \eta \partial_t \varepsilon_{ij} \\ &= (\zeta - 2/3\eta)\delta_{ij}\partial_t \partial_{x_l} u_l + \eta \partial_t (\partial_{x_i} u_j + \partial_{x_j} u_i) \end{aligned} \tag{A8}$$

x_i, x_j are independent variables and $(\zeta - 2/3\eta)$ and η are coefficients of viscosity for dilatational and deviatoric stains (see Landau and Lifshitz [17], p. 48). Equation (A8) resembles the constitutive relation (A2*b*) where $3\nu/(1+\nu)E_b$ and $3(1-2\nu)/(1+\nu)E_b$ are replaced by $(\zeta - 2/3\eta)$ and η. The linearized Navier-Stokes equations simplify to

$$\rho \partial_{tt} \mathbf{u} = -\nabla p_d + \partial_t [(\zeta - 1/6\eta)\nabla(\nabla \cdot \mathbf{u}) + (\eta/2)\nabla^2 \mathbf{u}] \tag{A9}$$

Conservation of mass and the equation of state are given by (A5) and (A6). Substituting for $\partial_t \rho$ from (A7) into (A5) yields

$$\partial_t [p_d + \rho c_b^2 (\nabla \cdot \mathbf{u})] = 0 \tag{A10}$$

Equation (A10) is the time derivative of (A2*a*) with σ_V replaced by $-p$. For a nonviscous fluid, taking the divergence of (A4), then eliminating $\mathbf{u}$ using (A10) determines the acoustic equation

$$(\partial_{rr} + 1/r\partial_r + \partial_{zz}) p_d - 1/c_b^2 \partial_{tt} p_d = 0 \tag{A11}$$

Equation (A11) is purely hyperbolic nondispersive.

For a viscous fluid, adopting the procedure that led to (A11) on (A9) and assuming that $\zeta = 1/6\eta$ yields the approximate viscous acoustic equation

$$(1 + \tilde{\nu}/c_b^2 \partial_t)(\partial_{rr} + 1/r\partial_r + \partial_{zz}) p_d - 1/c_b^2 \partial_{tt} p_d = 0 \tag{A12}$$

where $\tilde{\nu} = \eta/(2\rho)$ (cm^2/s) is kinematic viscosity.

References

[1] Theil, F., 1998, "Young-Measure Solutions for a Viscoelastically Damped Wave Equation with Nonmonotone Stress-Strain Relation," Arch. Ration. Mech. Anal., **144**, pp. 47–78.

[2] Yserentant, H., 2001, "The Propagation of Sound in Particle Models of Compressible Fluids," Numer. Math., **88**, pp. 581–601.

[3] Yserentant, H., 1997, "A Particle Model of Compressible Fluids," Numer. Math., **76**, pp. 111–142.

[4] Sina, K., and Khashayar, M., 2002, "Analytical Solution of Wave Equation for Arbitrary Non-Homogeneous Media," Proceedings of SPI, The International Society of Optical Engineering 4772, pp. 25–36.

[5] Sujith, R., Bala Subrahmanyam, P. T., and Lieuwen, P., 2003, "Propagation of Sound in Inhomogeneous Media: Exact Solutions in Curvilinear Geometries," ASME J. Vibr. Acoust., **125**, pp. 133–136.

[6] Hamdi, S., Enright, W., Schiesser, W., and Gottlieb, J., 2003, "Exact Solutions of the Generalized Equal Width Wave Equation," Lect. Notes Comput. Sci., **266**, pp. 725–734.

[7] Yang, D., 1994, "Grid Modification for the Wave Equation with Attenuation," Numer. Math., **67**, pp. 391–401.

[8] Narayan, J., 1998, "2.5-D Numerical Simulation of Acoustic Wave Propagation," Pure Appl. Geophys., **151**, pp. 47–61.

[9] Schemann, M., and Bornemann, F., 1998, "An Adaptive Rothe Method for the Wave Equation," Computing and Visualization in Science, **3**, pp. 137–144.

[10] Bailly, C., and Juve, D., 2000, "Numerical solution of acoustic propagation problems using linearized Euler equations," AIAA J., **38**, pp. 22–29.

[11] Wagner, G., Wenzel, M., and Dumont, W., 2001, "Numerical treatment of acoustic problems with the hybrid boundary element method," Int. J. Solids Struct., **38**, pp. 10–13; , **38**, pp. 1871–1888.

[12] Gaul, L., and Wenzel, M., 2001, "Acoustic calculations with the hybrid boundary element method in the time domain," Eng. Anal. Boundary Elem., **25**, pp. 259–265.

[13] Mehdizadeh, O., and Paraschivoiu, M., 2003, "Investigation of a Three-Dimensional Spectral Element Method for Helmholtz's Equation," Lect. Notes Comput. Sci., **2668**, pp. 819–825.

[14] Berry, J., and Naghdi, P., 1956, "On the Vibration of Elastic Bodies Having Time Dependent Boundary Conditions," Q. Appl. Math., **14**, pp. 43–50.

[15] El-Raheb, M., 2004, "Wave Propagation in a Weak Viscoelastic Layer Produced by Prescribed Velocity on the Boundary," J. Sound Vib., **275**(1–2), pp. 89–106.

[16] Eisler, R., 2003, (private communication, Mission Research Corporation, Laguna Hills, CA).

[17] Landau, L., and Lifshitz, E., 1959, *Fluid Mechanics*, 1st English Ed., Pergamon Press, Addison-Wesley, New York.

Downloaded 02 Jul 2007 to 141.214.17.5. Redistribution subject to ASME license or copyright, see http://www.asme.org/terms/Terms_Use.cfm

The DARPA Virtual Soldier Program

"Computational and Informatics Approaches to Understanding Physiological and Anatomical Changes During Acute Ballistic Trauma"

Department of Anesthesiology
Research Discussion
16 May 2007

Presented by
Brian D. Athey, Ph.D.
Associate Professor
Bioinformatics and Computational Biology
University of Michigan Medical School

Principal Investigator, DARPA Virtual Soldier Project
Principal Investigator, NIH National Center for Integrative Biomedical Informatics

Director, Michigan Center for Biological Information (MCBI)
Office of the Vice President for Research (OVPR)
The University of Michigan

DARPA Virtual Soldier Project Objectives

Build a Virtual Soldier on an Electronic "Dog Tag" to Diagnose and Predict Combat Injury

WHY?

Quickly & Accurately diagnose internal combat injury (Heart)

HOW?

Build Predictive models from total body scan on "Dog Tag"

(3-D Anatomy & Physiology)

Compare to data acquired on the battlefield after wounding

(CT, Physiology, and other key data)

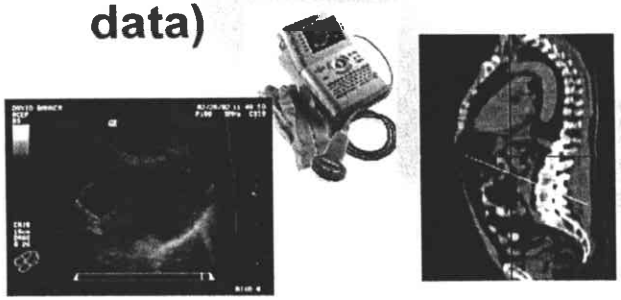

Predict likelihood of battlefield mortality

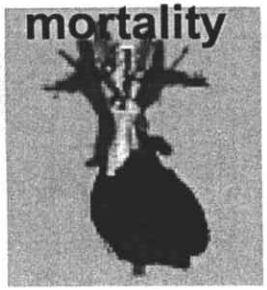

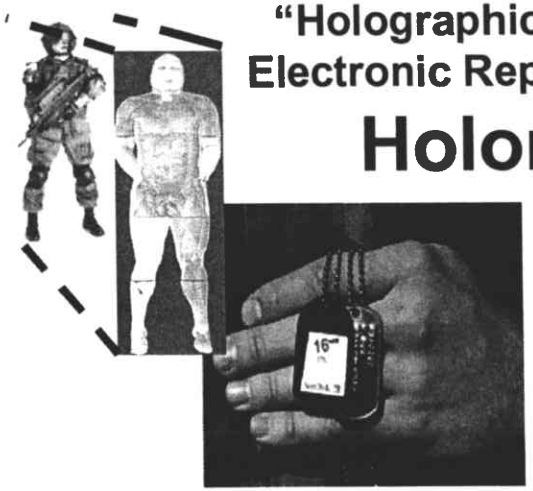

"Holographic" Medical Electronic Representation

Holomer

Accurate Diagnosis & Treatment Saves Lives

FOR THE INDIVIDUAL SOLDIER THIS MEANS:

Empowering the individual medic <u>at the point of wounding</u> to make a diagnosis of an injury with the same expertise as having an expert surgeon on site.

Functional Overview of the DARPA Virtual Soldier Project

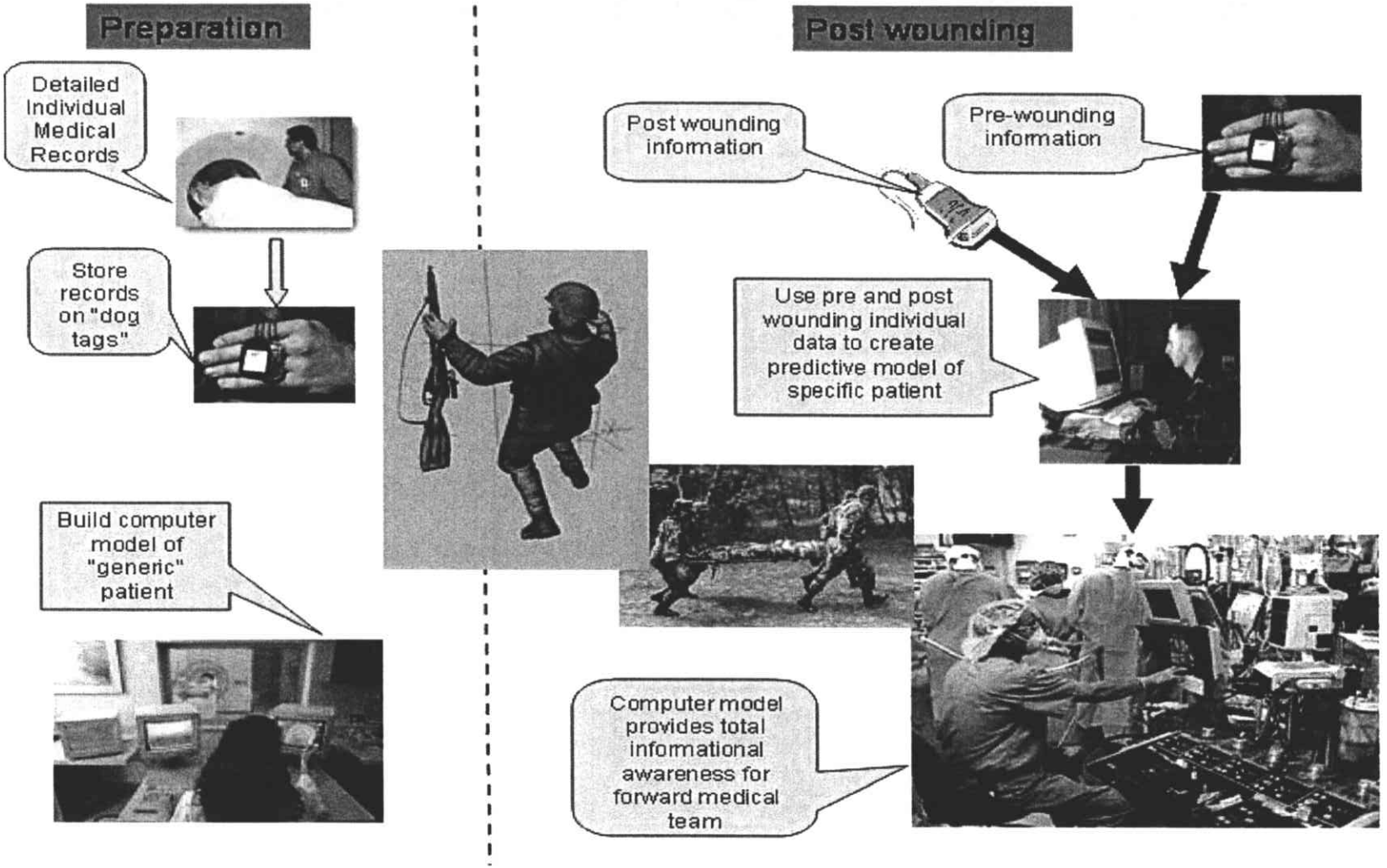

DARPA Program Manager Goals for Virtual Solider Project (as interpreted by PI)

- Develop a 21st Century medical record for the soldier that is not print-based, but instead instantiates a full hierarchal model representation of the patient: "The Holomer"
- Provide support for the Medic at the time of wounding (improve ability to assess warfighter status—triage)
- Provide support for "downstream" surgery team: "practice" on a virtual representation of the injured soldier
- Jump-start the Digital Human Project for transfer back to NIH by establishing a "dream team" of researchers from academia, industry, and government labs

DARPA Virtual Soldier Team

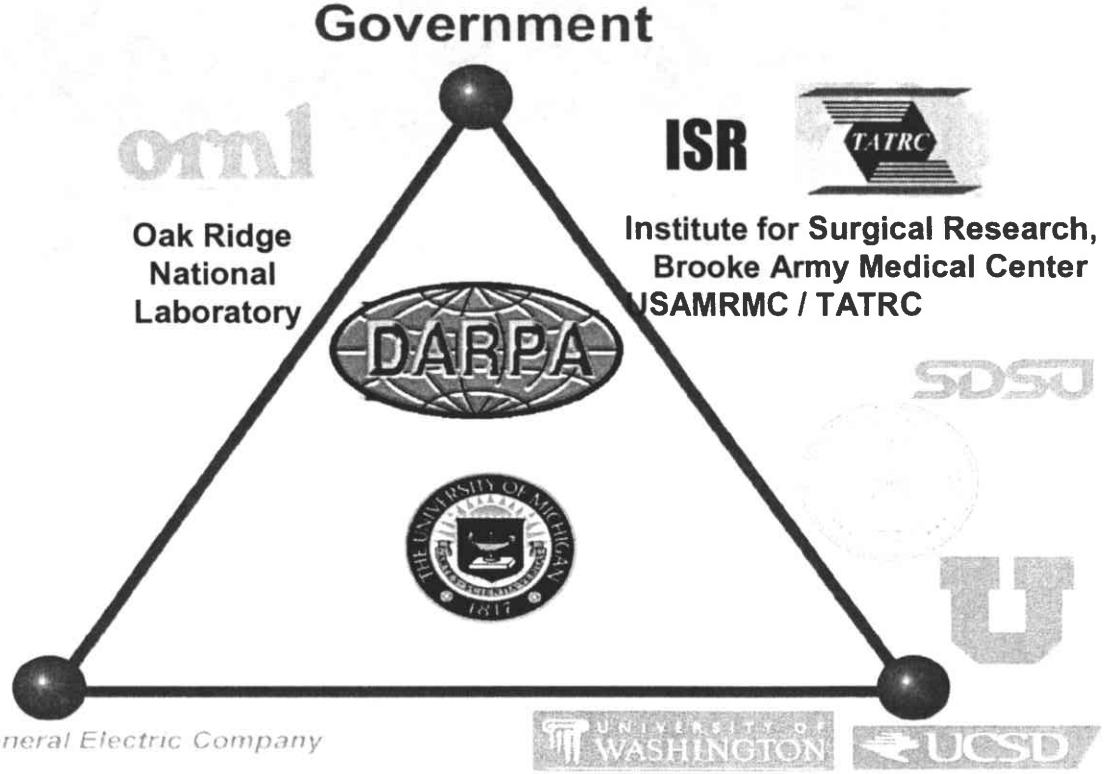

General Electric Corporation
ATK Mission Research Corporation
Crowley Davis Research
Xtria, LLC
SanDisk, Corp.

University of Michigan
Stanford University
University of Washington
University of Utah
UCSD
San Diego State University
University of South Carolina
Harvard University

Integrative Informatics Challenge: Synthesis of Knowledge at Multiple Levels (Spatial and Temporal)

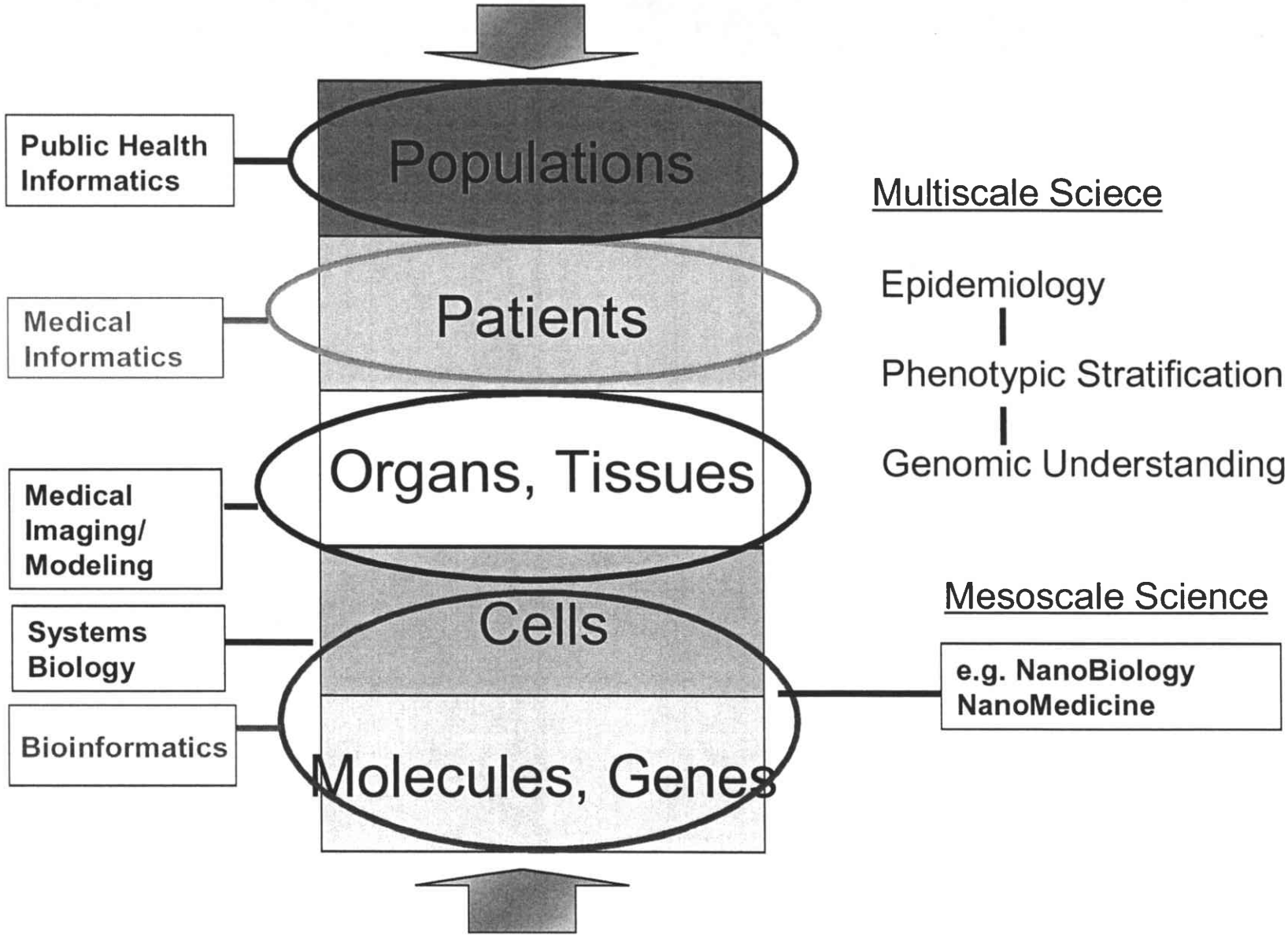

How best to move from the Macroscopic to the Microscopic

Top-down vs. Bottom-up

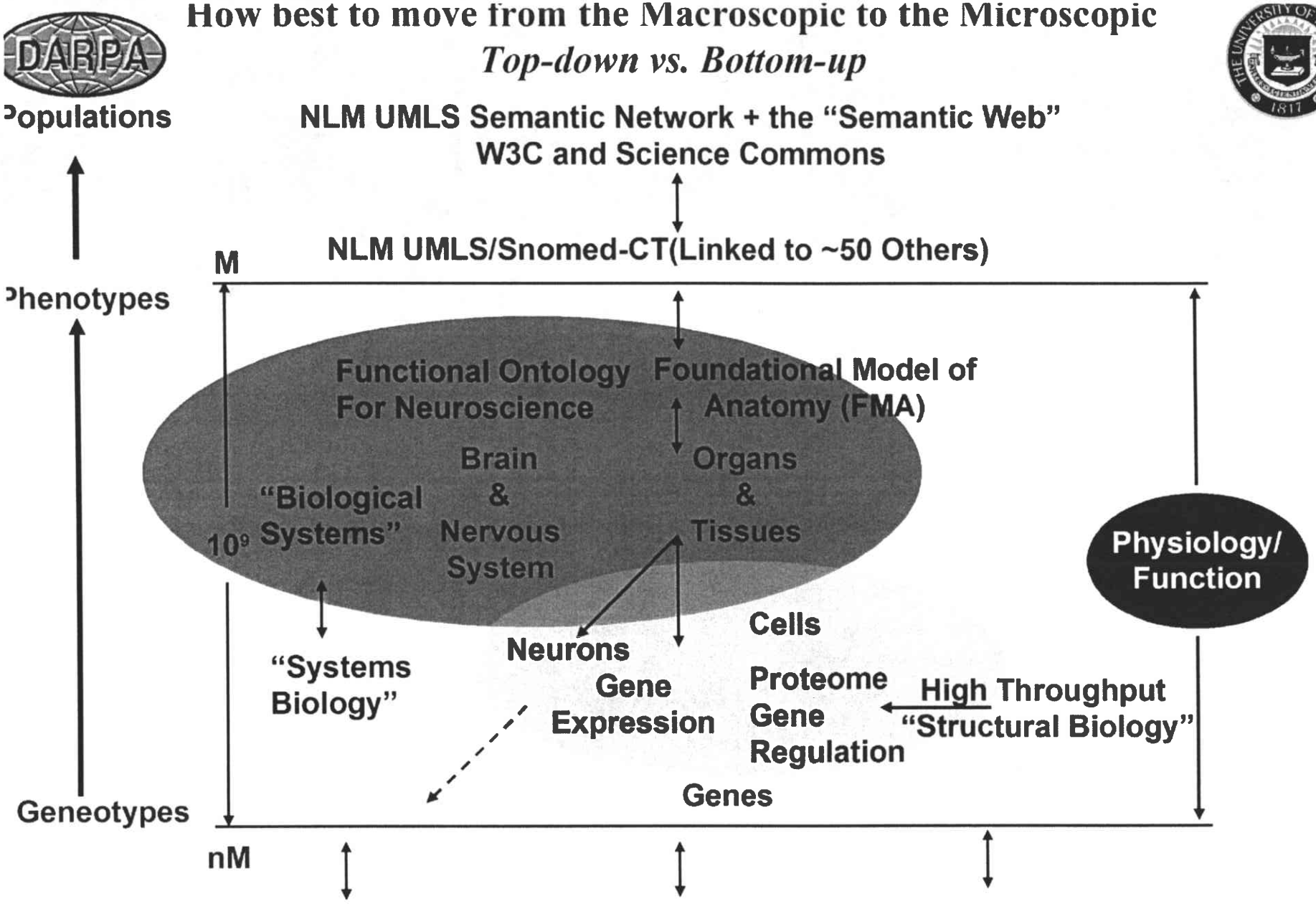

Background: The Visible Human Project in the 1990's

Medical Teaching Theatre to Internet Collaboratory

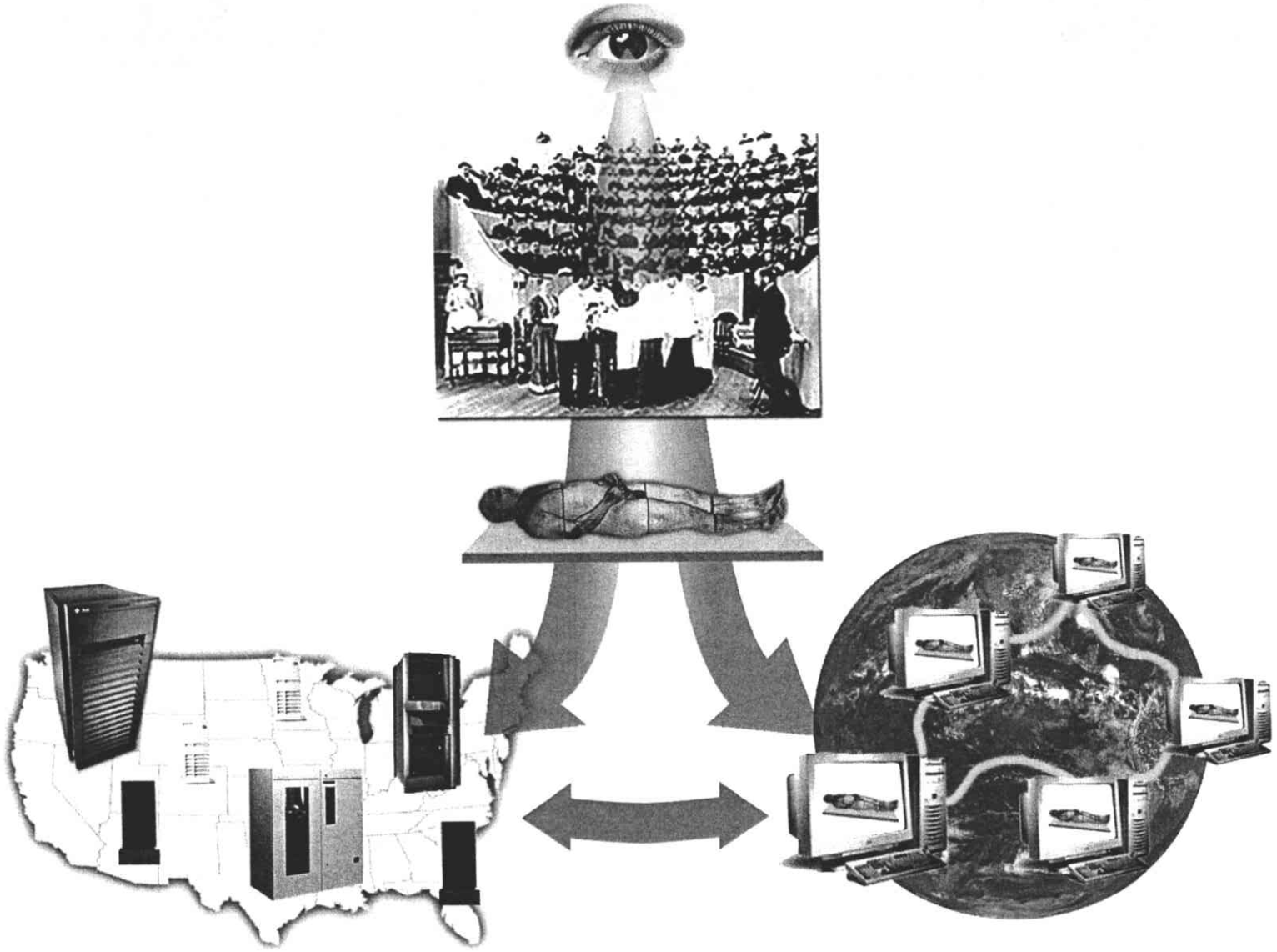

Visible Human Project: Linking Rendering and Labeling enabled Web-based "Navigation" in the late 1990s

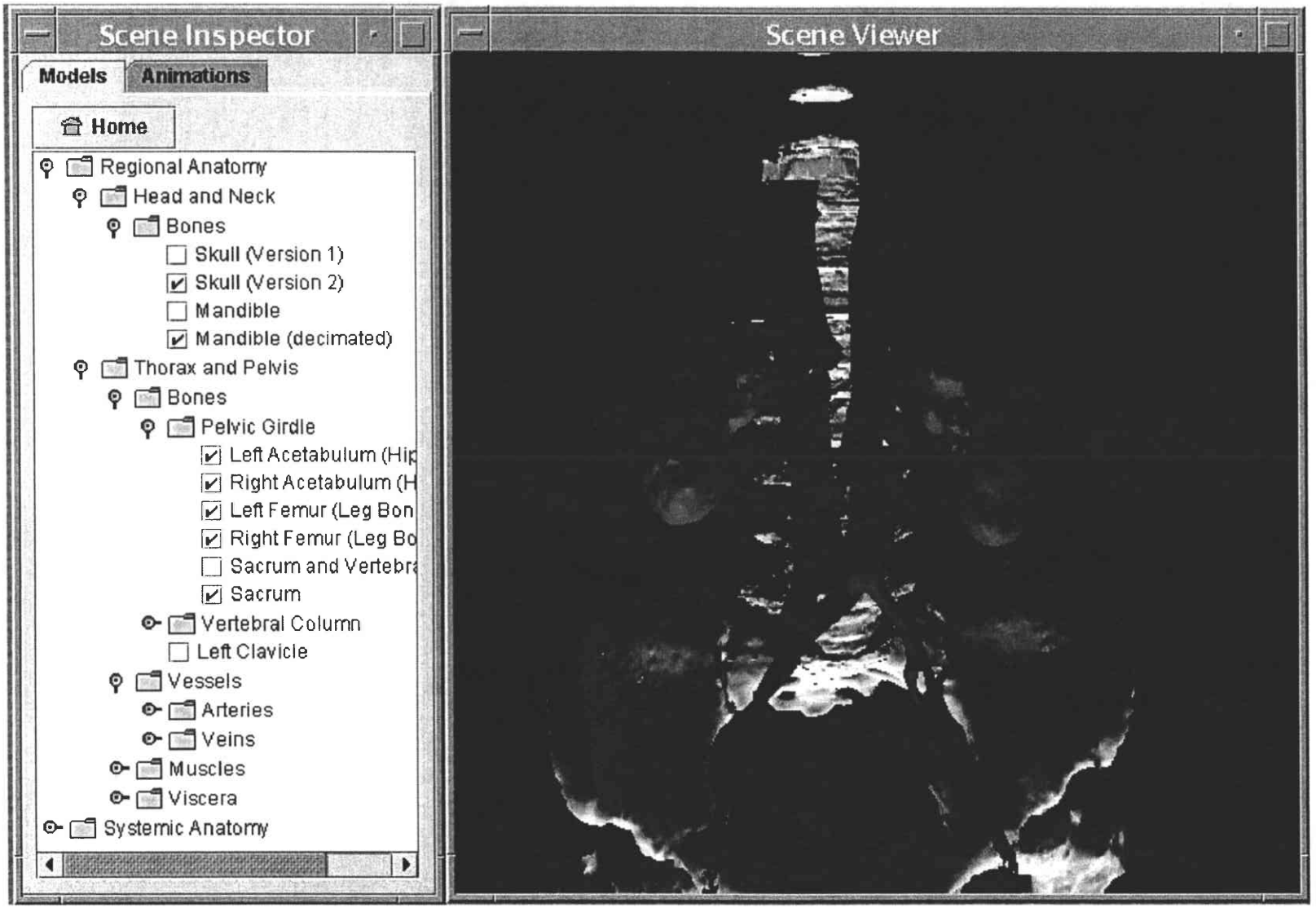

Multi-scale Human Anatomy is Described by the Foundational Model of Anatomy (FMA)

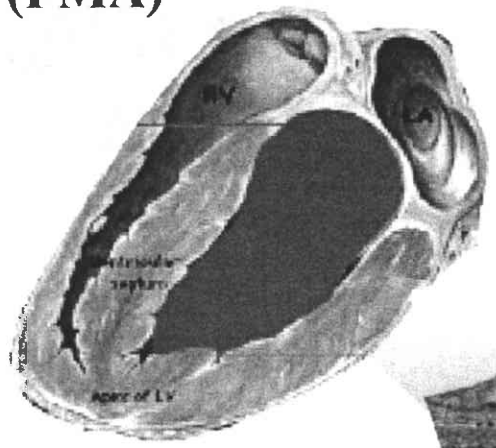

- Heart
  - Right atrium
  - Right ventricle
  - Left atrium
  - Left ventricle
    - Cavity of left ventricle
    - Wall of left ventricle
      - Myocardium of left ventricle
        - Cardiac muscle fasciculus of ventricle
          - Cardiac myocyte
            - Protoplasm of cardiac muscle cell
              - Myofibril
                - Myofilament
                  - Actin
                  - Myosin

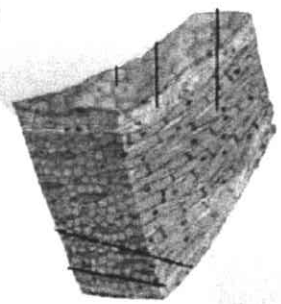

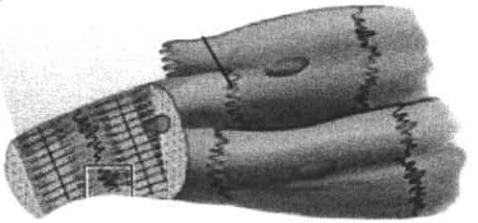

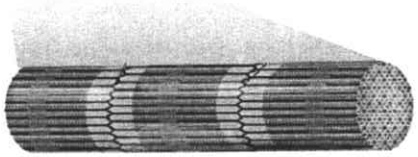

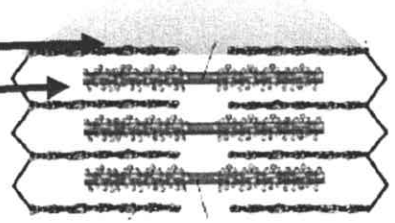

University of Washington, Michigan and Stanford University

Highly Integrated Physiology (HIP) Models Provide Global Context (University of Washington)

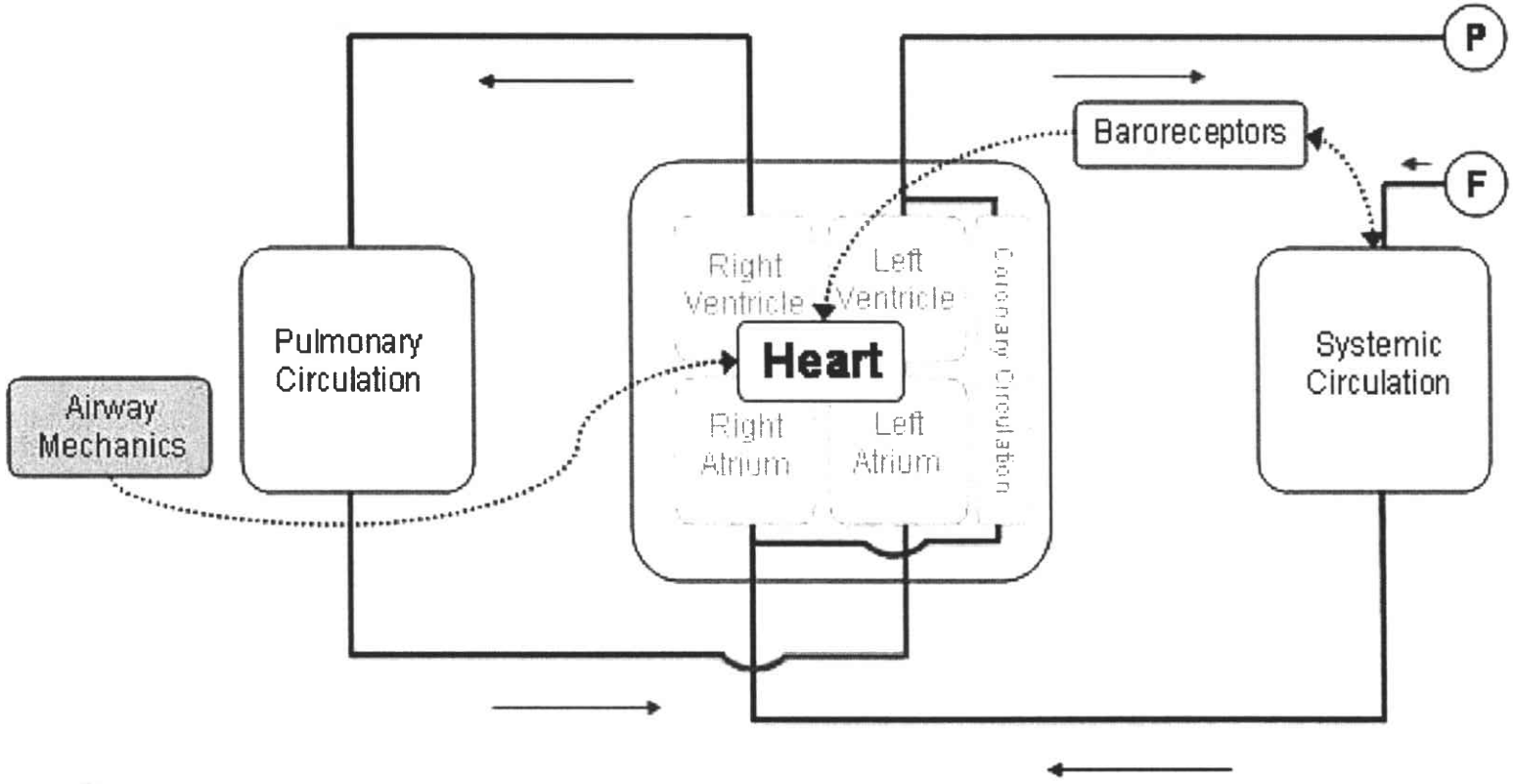

(P) = Smoothed arterial pressure from ISR data

(F) = Aortic flow from ISR data

James Bassingsthwaite

Highly Integrated Physiology (HIP) Modeling Objectives

- Create ordinary differential equation (ODE)-based whole body models for simulating clinically relevant human and porcine physiology.
- Use UW's *JSim* simulation system to code models, provide system and models to other institutions (ORNL, UCSD, U. Michigan, Stanford)
- Parameterize model to reflect normal resting human physiology
- Enable simulation of cardiovascular penetrating injuries to the heart
- Parameterize model to match specific baseline and post-injury data gathered from porcine experiments at ISR
- Use model simulations in conjunction with statistical methods at the University of Michigan to aid in prediction/simulation of battlefield wounds
- Support UW knowledge representation team by providing HIP model as a collection of entities that will help inform the structure of the Virtual Soldier Knowledge Base (VSKB)

Highly Integrated Physiology (HIP) Model Outputs were Expanded to:

Pressures, volumes, forward flow and radial flow in the:

- Left atrium, Left ventricle, Proximal aorta, Distal aorta, Systemic arteries, Systemic arterioles, Systemic capillaries, Systemic veins, Vena cava, Right atrium, Right ventricle, Proximal pulmonary artery, Distal pulmonary artery, Small pulmonary arteries, Pulmonary capillaries, Pulmonary shunt, Pulmonary veins, Proximal epicardial arteries, Distal epicardial arteries, Large coronary arteries, Small coronary arteries, Coronary capillaries, Small coronary veins, Large coronary veins, Epicardial veins, and Pericardium (injury flow)

Pressures, volumes, forward flow, radial flow, [O2], [CO2], and [N2] in:

- Upper airways, collapsible airways and alveoli
- pO2, pCO2, pH, [HCO3] and [Carbaminohemoglobin] in the aorta and pulmonary artery
- Diffusion capacity of O2, CO2 and N2 across the alveolar membrane
- Heart and respiratory rates
- Heart chamber elastances

Injury specifications:

- Conductances of penetrating "wounds"
- Blood in pericardial space
- Blood lost from circulation

363 variables and 75 Ordinary Differential Equations were included in the HIP models

Subject P87 data curves (thick) and corresponding HIP model fits (thin)

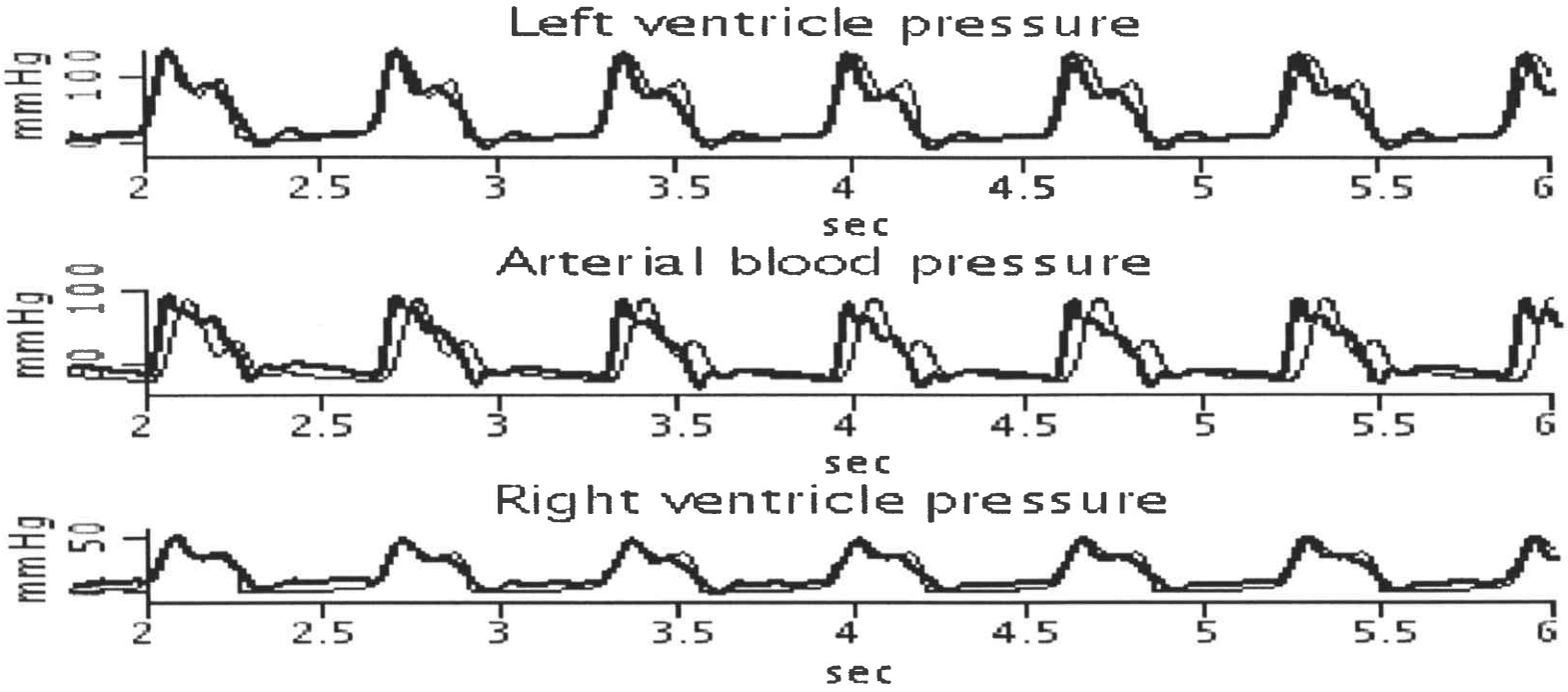

Physiological Status Monitor Displays Baseline Data and Response

- Store/replay (forward and backward) physiological response
- Developed to understand comparison of modeled with real data
- Developed by Visualization team: U Utah, U Michigan, and ORNL

3D Finite Element & Multiscale Models provided by UCSD, the University of Auckland, and the University of Utah

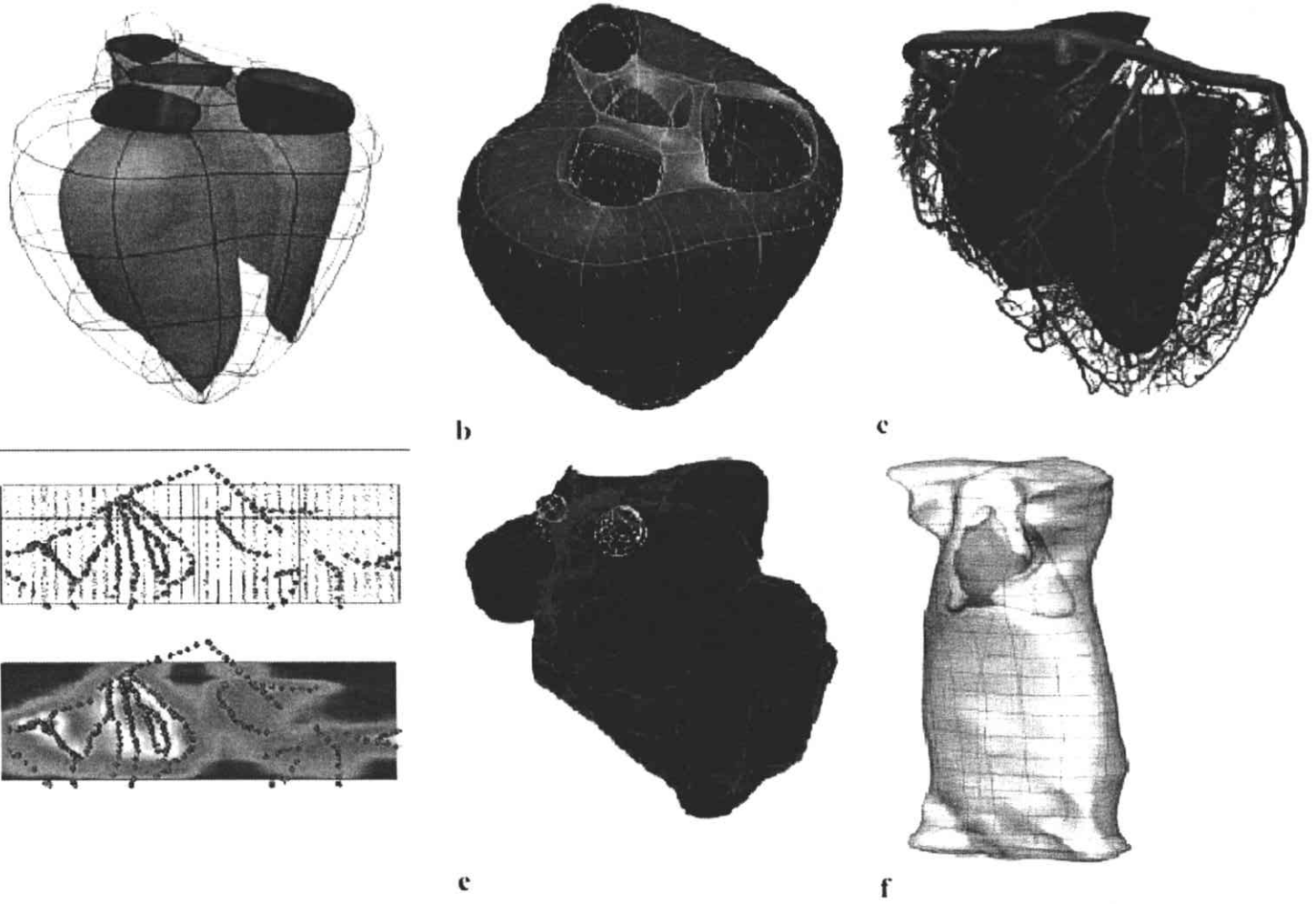

3-D Finite Element Model of Cardiac Electromechanics I
University of California, San Diego

Scientific: Developed and validated anatomically and biophysically detailed 3D models of ventricular electromechanics in interaction with functionally integrated comprehensive models of circulatory physiology to model trauma.

- An accurate finite element geometry of porcine left and right ventricle with a realistic myofiber orientation from Auckland University was used to solve cardiac electromechanics. General Electric provided porcine-specific geometries.
- Modeling of excitation-contraction and mechano-electrical feedback by coupling cellular ionic models to models of myofilament activation and crossbridge formation in combination with a mono- or bi-domain formulation of propagation.
- Simulated transmembrane potentials were used by University of Utah to calculate potentials on the porcine torso. Torso potentials are measurable and served as a means of tuning and validation.
- Complete integration of ventricular electromechanics and circulatory model from University of Washington, such that the FE model is the driving force of the circulation.

3D Finite Element Model of Cardiac Electromechanics II
University of California, San Diego

- Geometry of porcine left and right ventricles scaled to match specific subjects acquired from porcine CT scans (ISR)
- Realistic myofiber architecture: spans scales of cells, tissue and organ
- Local cellular properties based on detailed ionic-currents and realistic excitation-contraction coupling mechanisms
- ECG simulated by solving the bioelectric forward solution in a 3-component model of the torso, heart, and lungs
- Nonlinear, anisotropic 3D passive and active material properties
- Ventricular hemodynamics determined by highly integrated circulatory model initialized from and tuned to empirical data (ISR)
- Penetration wound modeled based on MPM results and coronary perfusion model (Auckland) by decoupling cells electrically, altering ionic currents and inhibiting active contraction around site of wound
- Reduction of contractility based on regional perfusion measurements (ISR)
- Real-time visualization done using a unique multi-mesh interpolation scheme triggered by the highly integrated circulatory model

Algorithm for 3-D Electromechanical integration

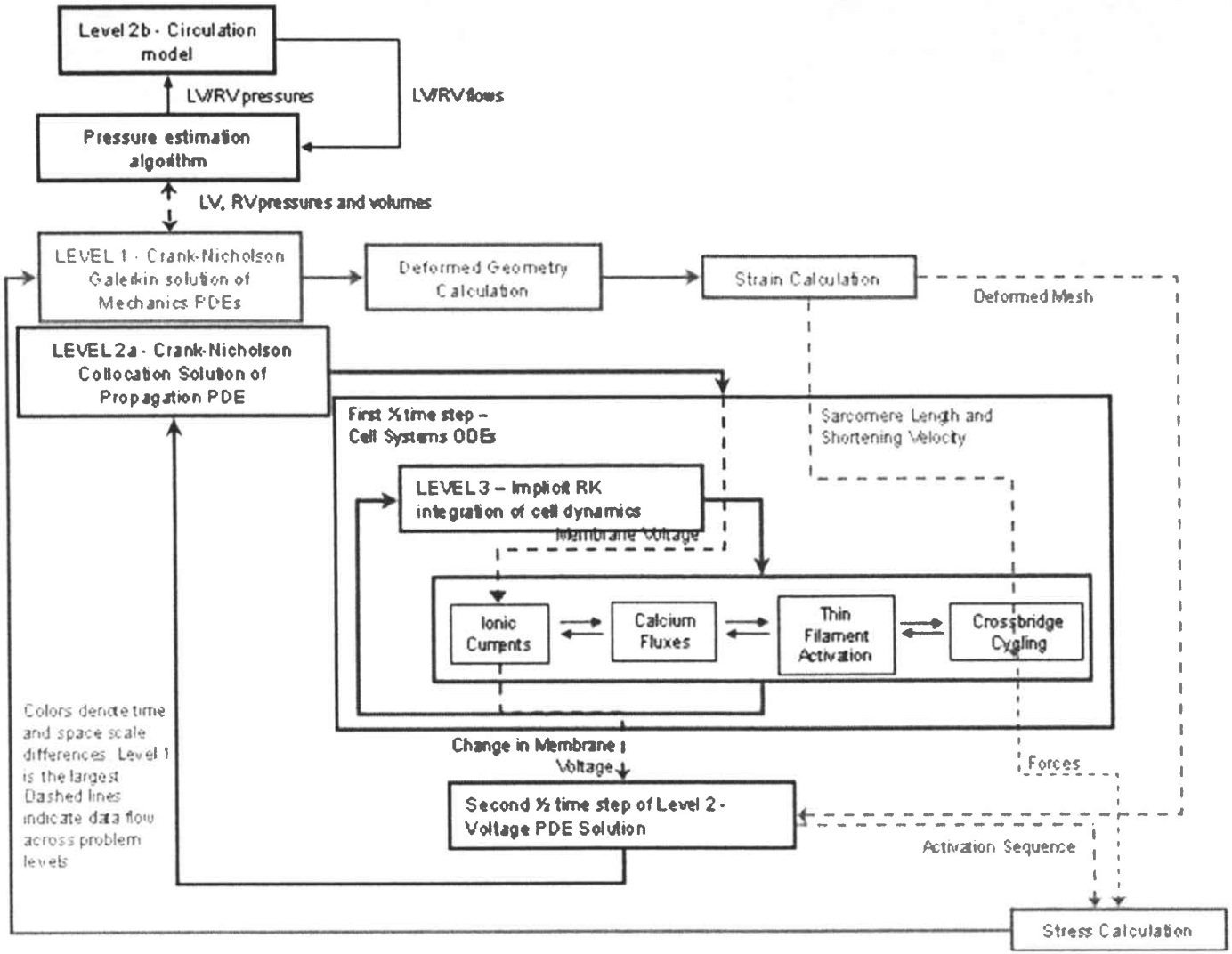

ATK/Mission Research Corporation
Ballistic Modeling I

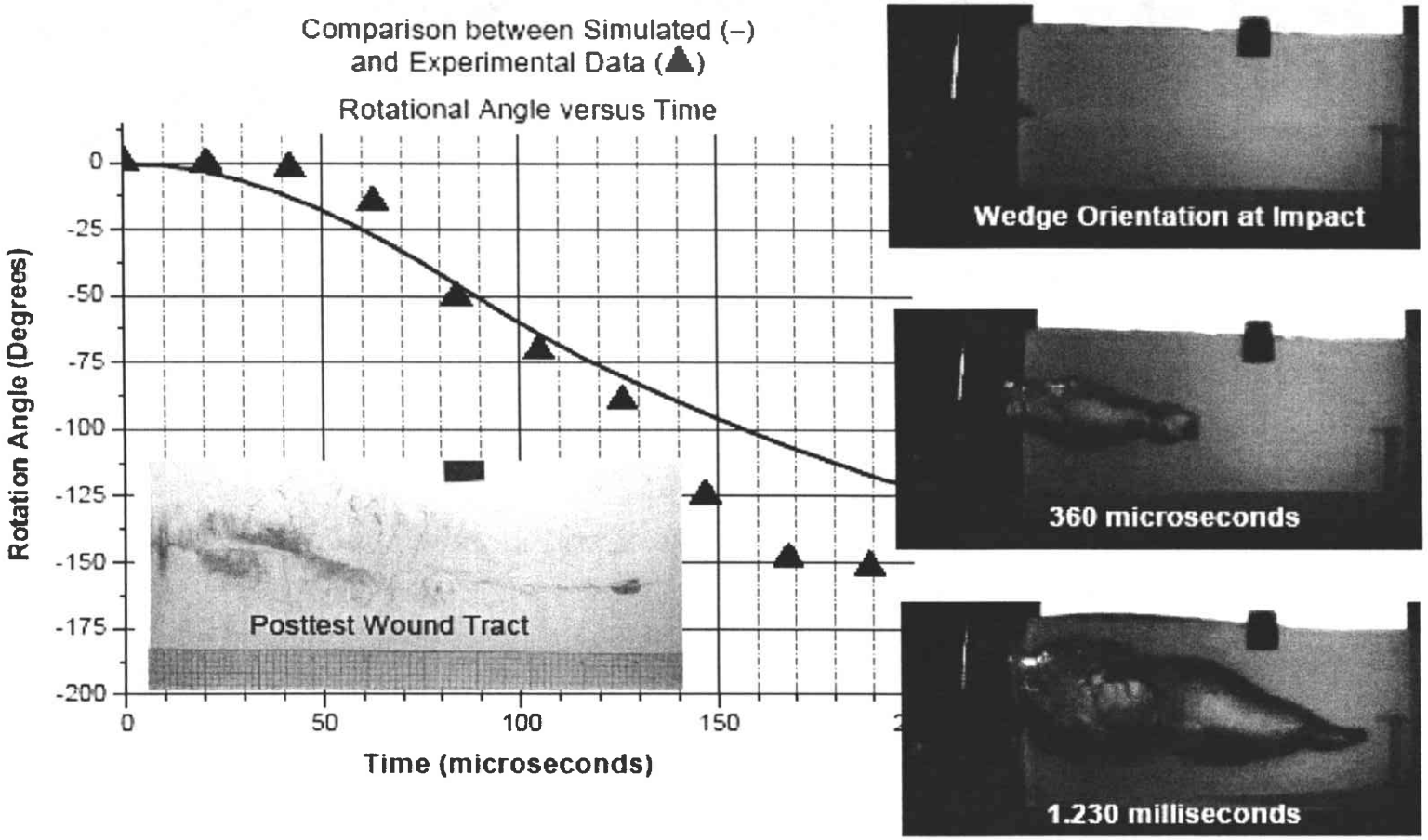

ATK/Mission Research Corporation
Ballistic Modeling II

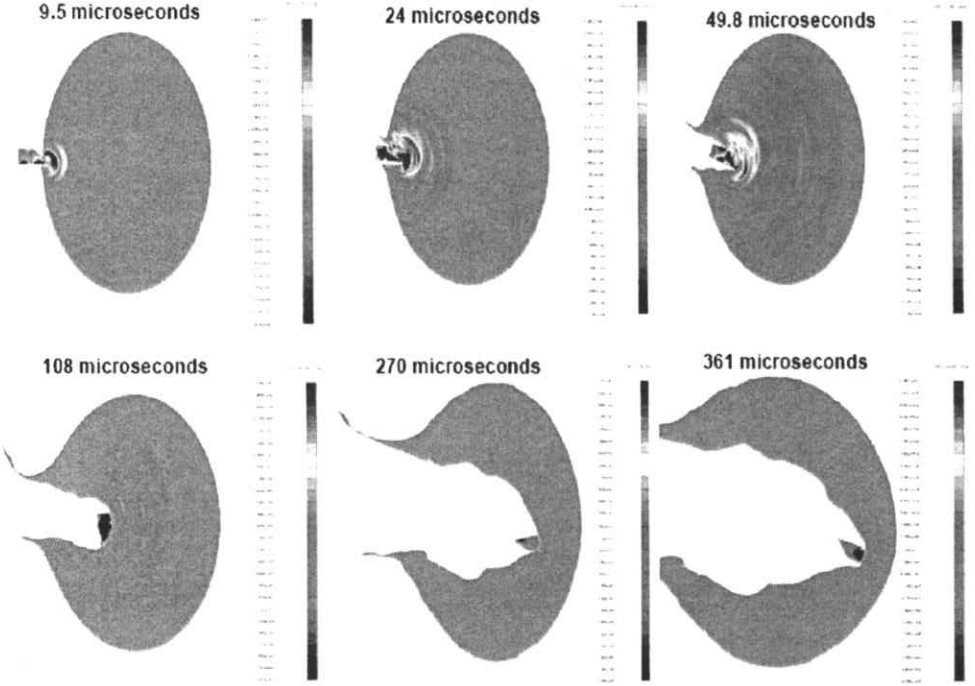

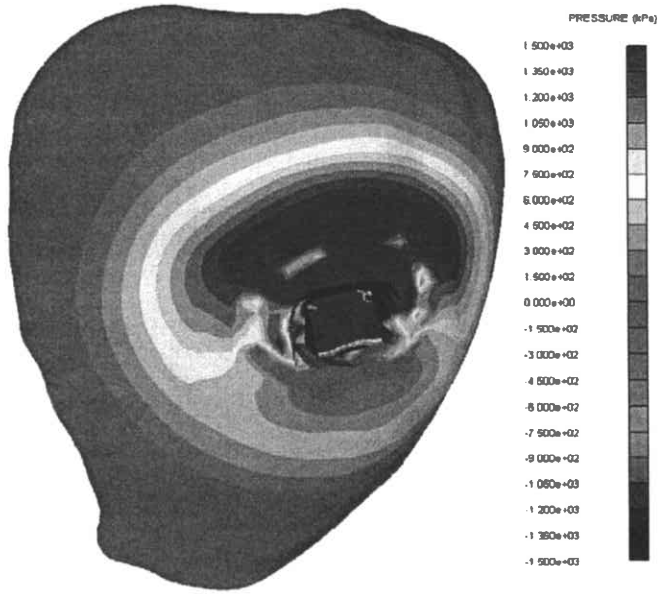

Stress Contours on LV Surface at 95 milliseconds after impact. Peak stress is 20 bars.

Total Penetration Depth vs Striking Velocity

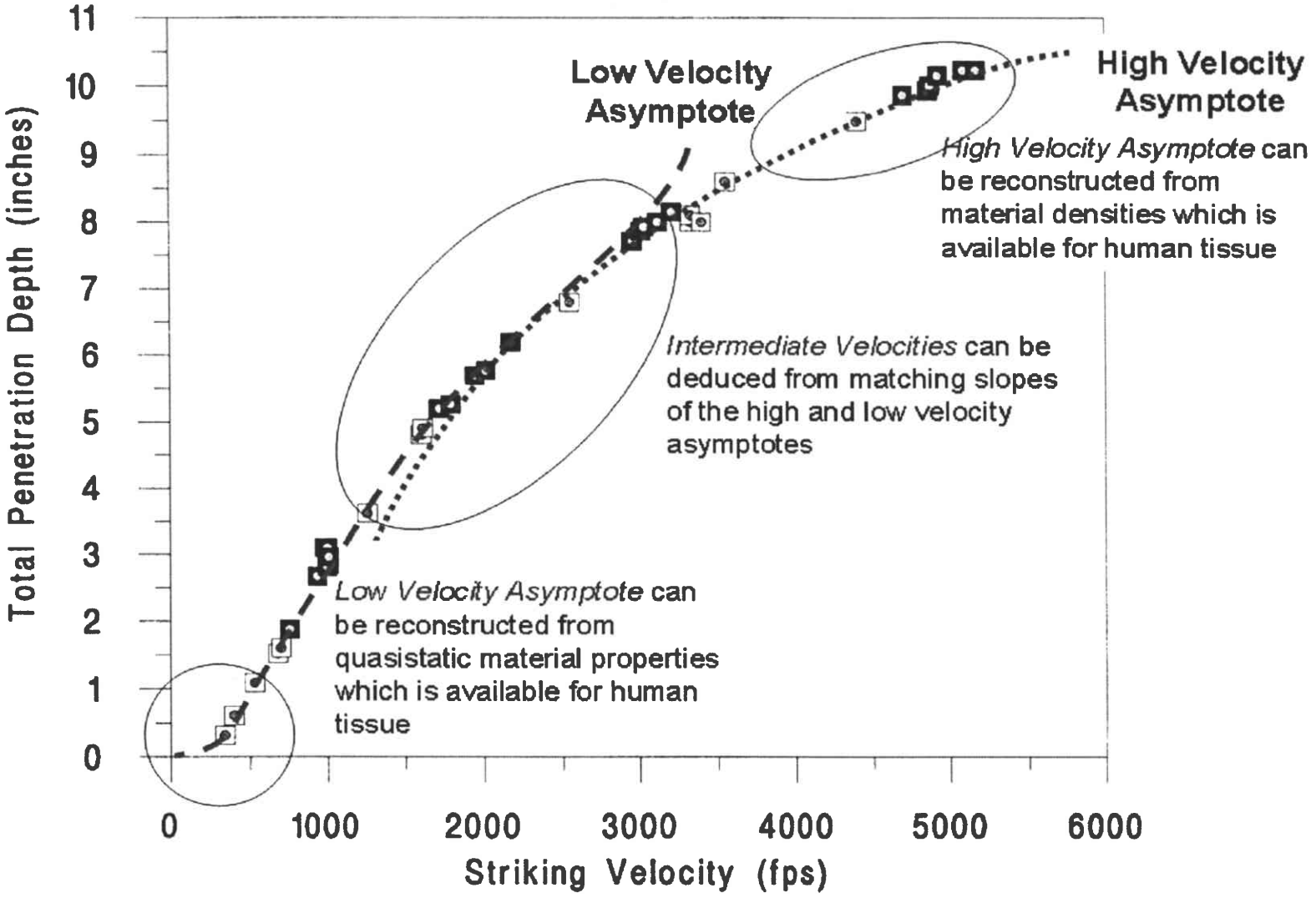

Material Point Method Penetration Trauma of the Heart
The University of Utah

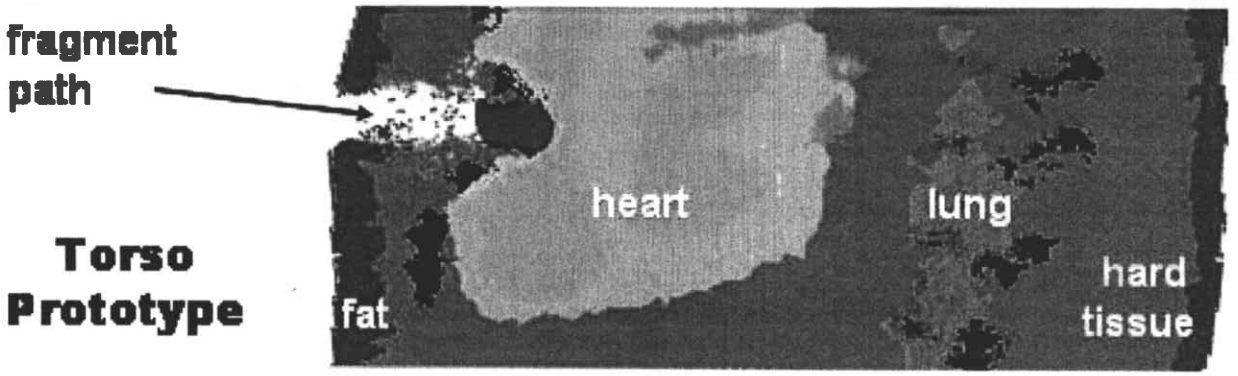

Heart

- Anatomically accurate porcine heart
- Discretized into ~1.5 mil material particles
- Modeled as a transversely isotropic hyperelastic material: an isotropic matrix reinforced by an elastic fiber family (fiber directions vary through the wall thickne
- A two-surface strain failure criteria is embedded in the model

Projected fragment (or shell casing)

- Modeled to experiment specific geometry
- Elasto-plastic (metallic) material model
- 76 ft/s initial speed
- Frictional contact enforced between tissue and probe

Holomer Wounding Location based on SCIRun Visualization Environment

HotBox Interface

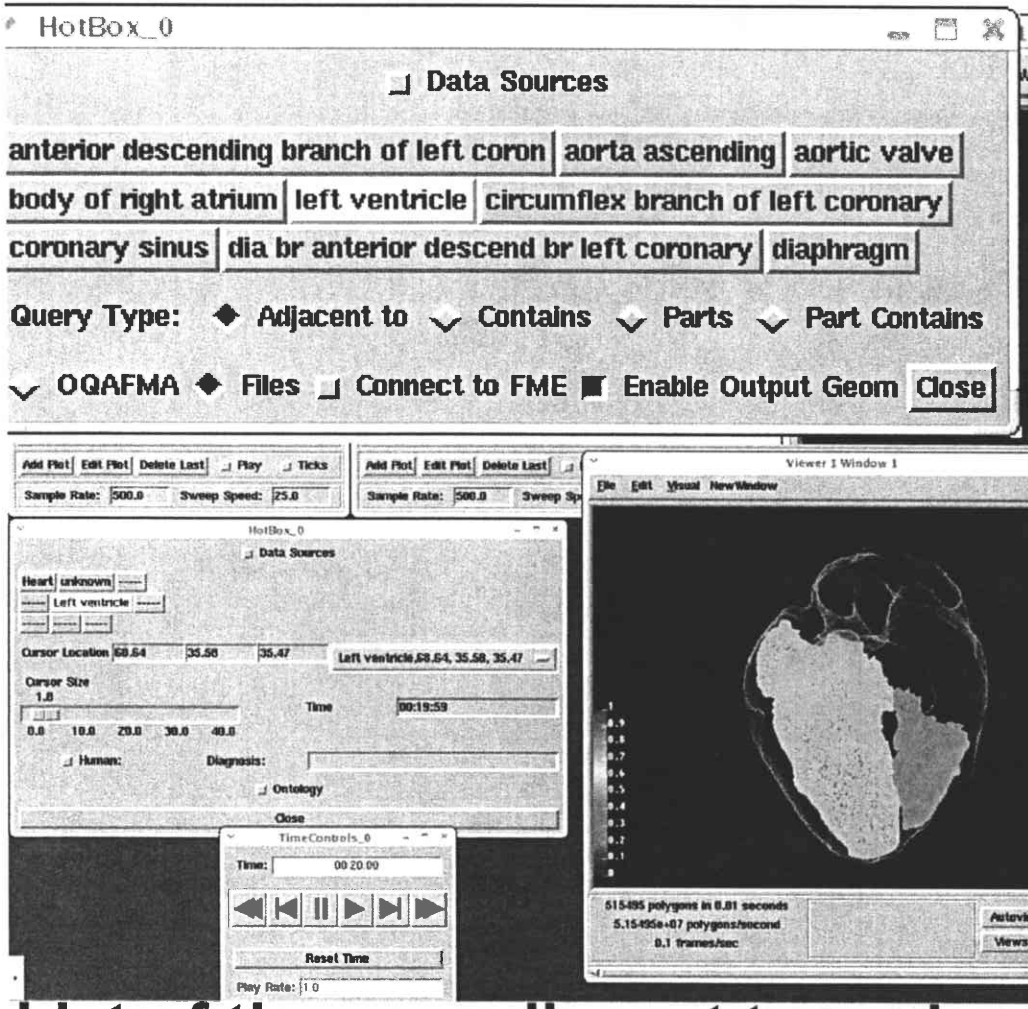

List of tissues adjacent to probe (arrow) in lower right lobe of lung

SCIRun display of thorax model

Model Development, Training, and Test Sets

The 31 model development experiments ISR conducted before November 30th 2004 constitute the "model development" set used to develop and refine procedures and gain familiarity with the data.

The 46 experiments ISR conducted between November 30, 2004 and April 28, 2005 were divided into the following three groups:

- 25 analyzable open chest experiments (regular ECG and full instrumentation);
- 3 analyzable closed chest experiments (60+ lead ECG and limited instrumentation); and
- 18 experiments un-analyzable according to criteria established in advance (incomplete or missing data, time to death of 10 minutes or less).

Phase Space Representation of Experimental Data

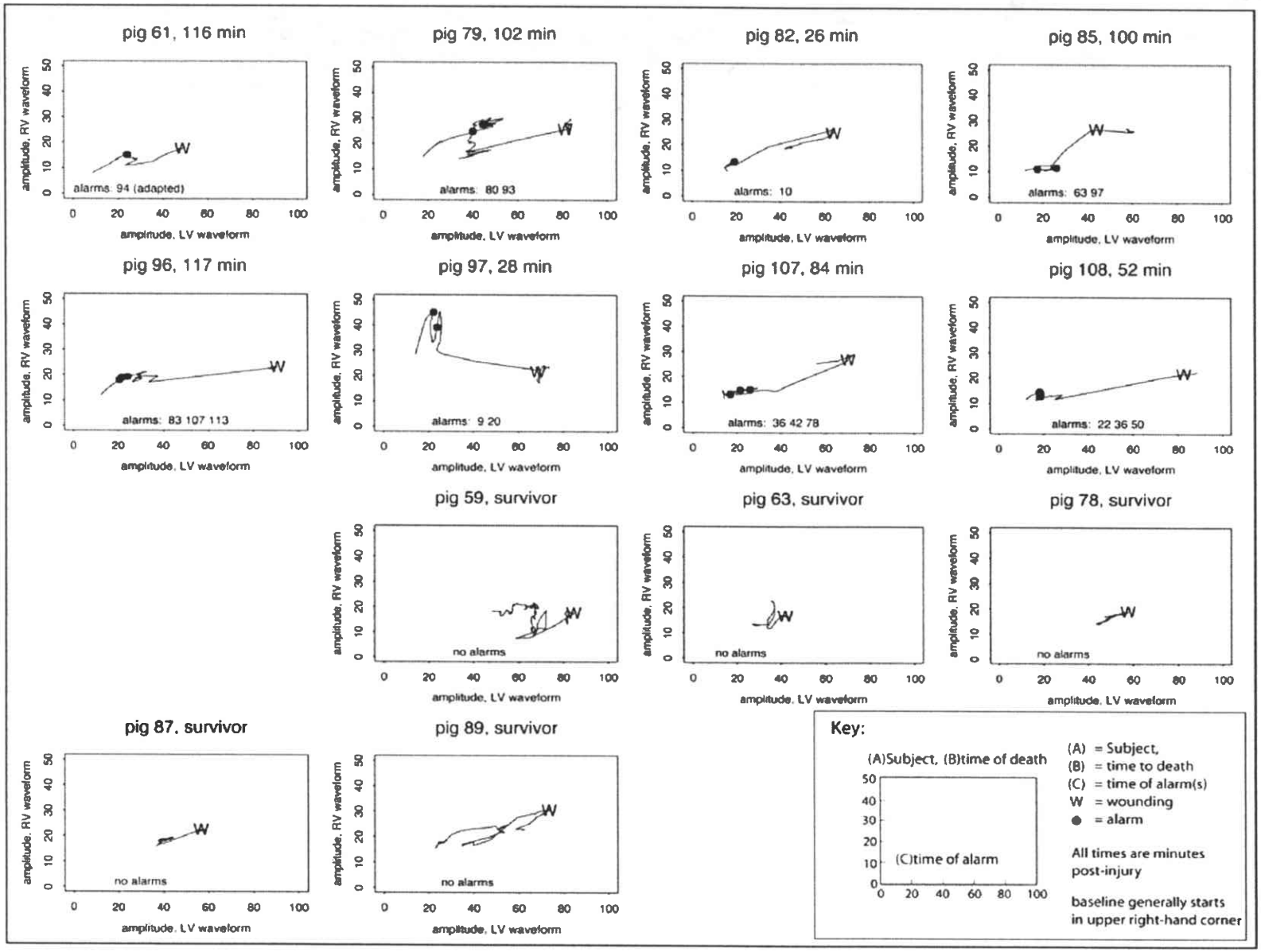

Kalman Filter-based Statistical Prediction Engine

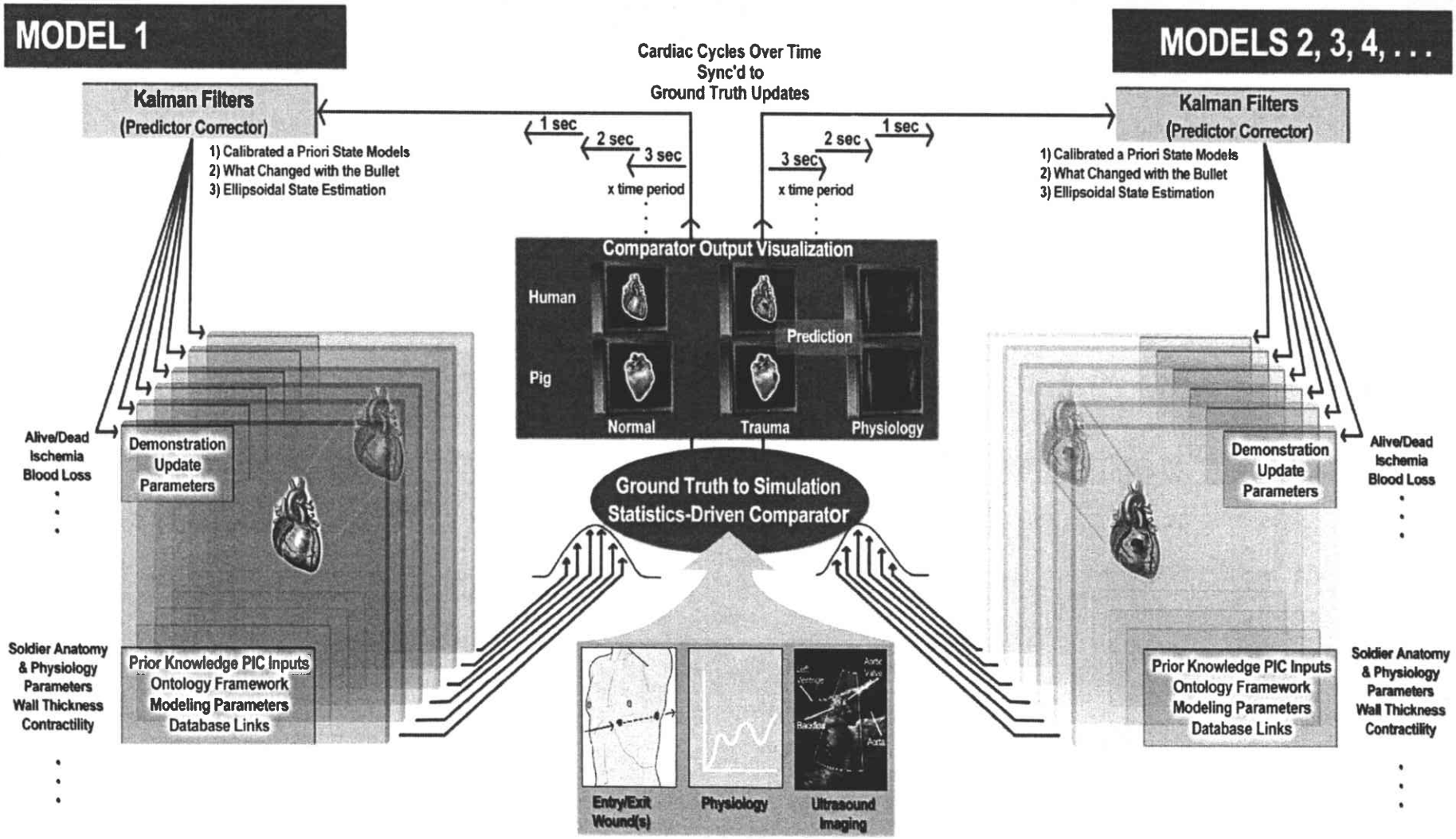

Statistical Reasoning Data Flows

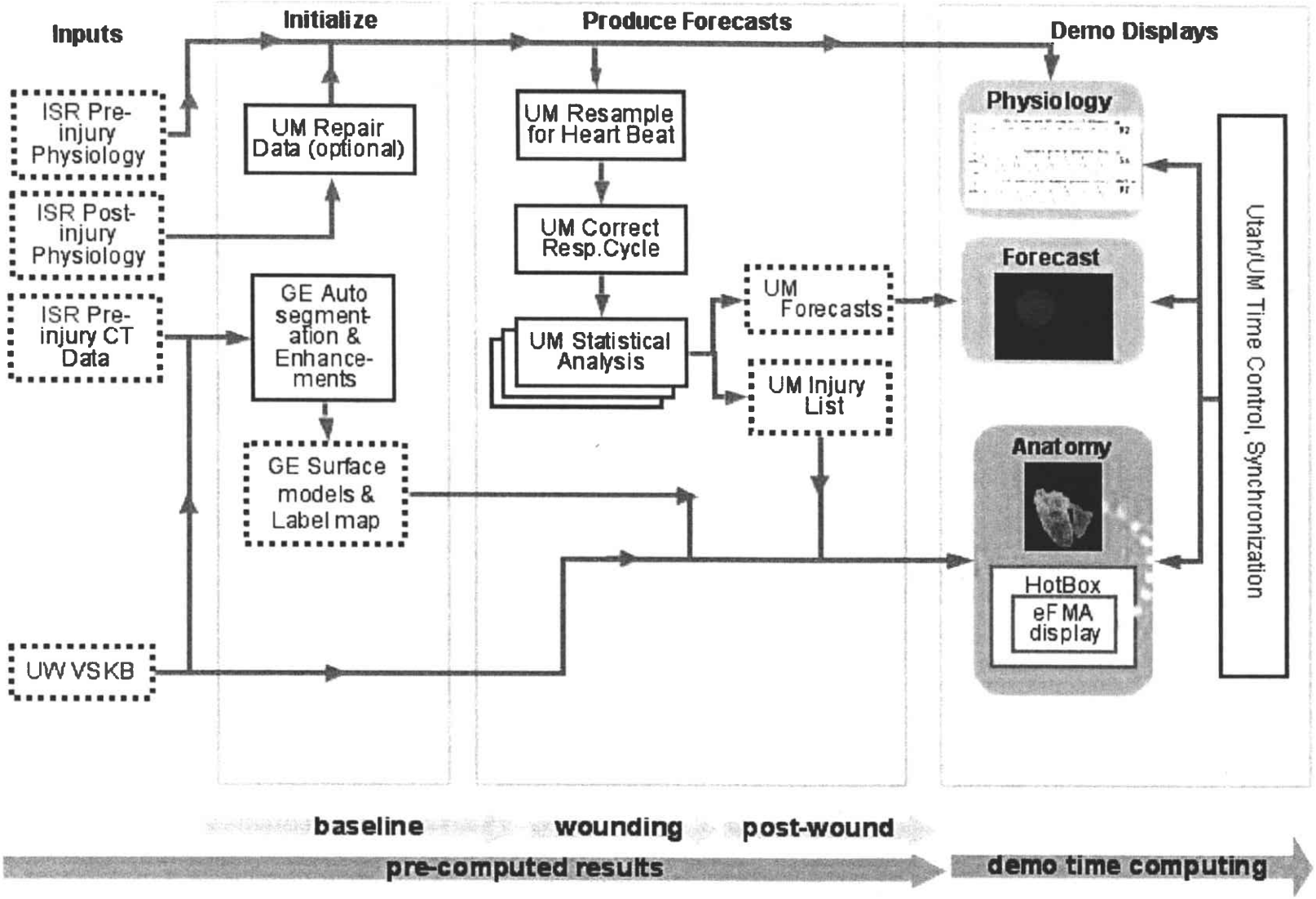

Statistical Display Details

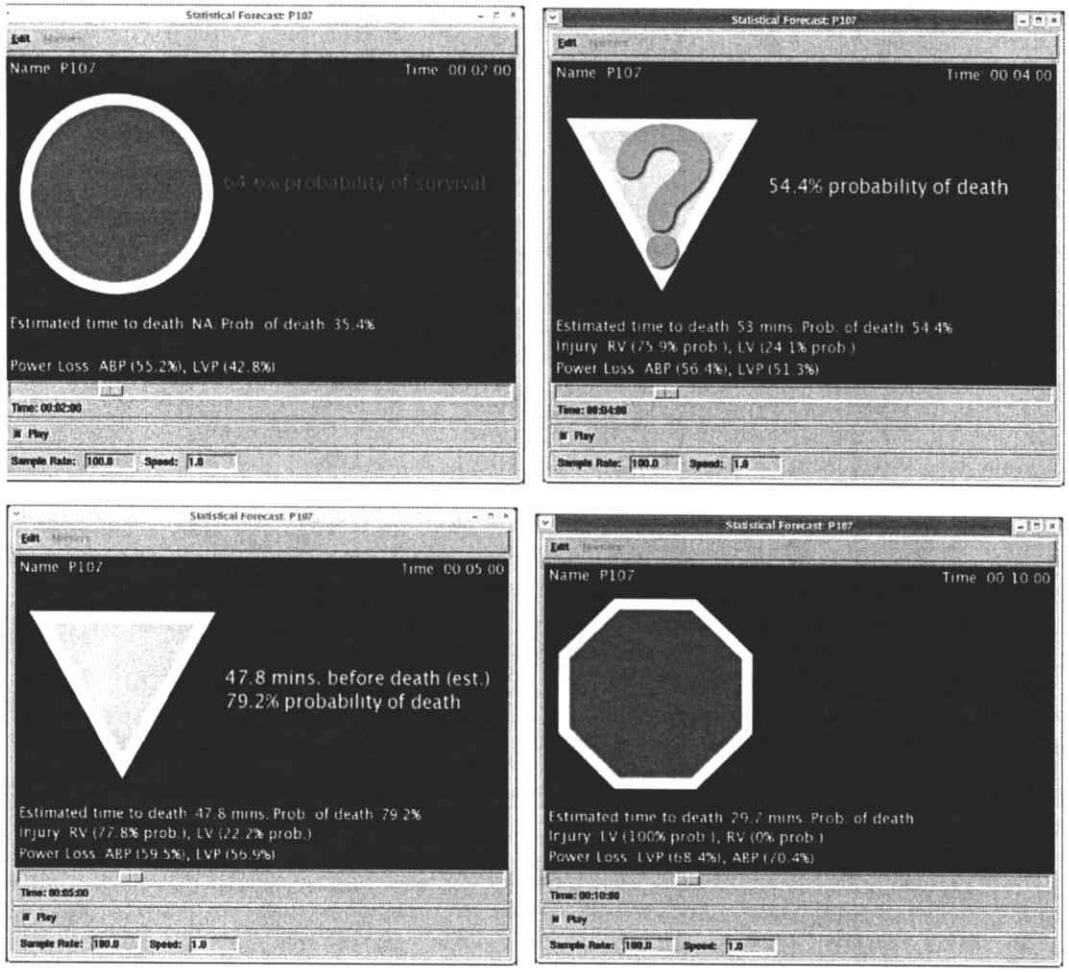

- A green circle indicates that the subject is expected to survive

- A red octagon indicates that the subject is expected to die within a relatively short period of time and there is no time for interventions to change the outcomes

- A yellow triangle indicates that the subject is expected to die, but there is time to intervene to change the outcome

- To the right of the icons text gives the percentage probability of survival or death and if death is the forecast an estimate of time to death in minutes.

Within the set of 14 non-quarantined analyzable open chest fragment experiments the Statistical Analysis showed:

- Detected an alarm in all 8 non-survivors and no alarm in all 6 survivors (100%)
- Correctly forecast death or survival for 13 of 14 (93%) at 4 minutes post-injury
- Forecast a TTD correlating 0.75 with actual TTD for the 7 non-survivors still alive at 20 mins. post-injury
- Forecast a TTD of 21 mins. ±9 mins. at 20 mins. before actual death for 6 non-survivors that lived >25 mins.
- Forecast a median TTD of 30 mins. from first alarm for all 8 non-survivors vs. the actual median TTD of 24 mins.
- Within a test subset of 6 non-quarantined analyzable open chest fragment experiments:
- Correctly identified injury location (LV vs. RV) for 5 cases with one ambiguous result (83%)

VSP Causal Reasoning Model

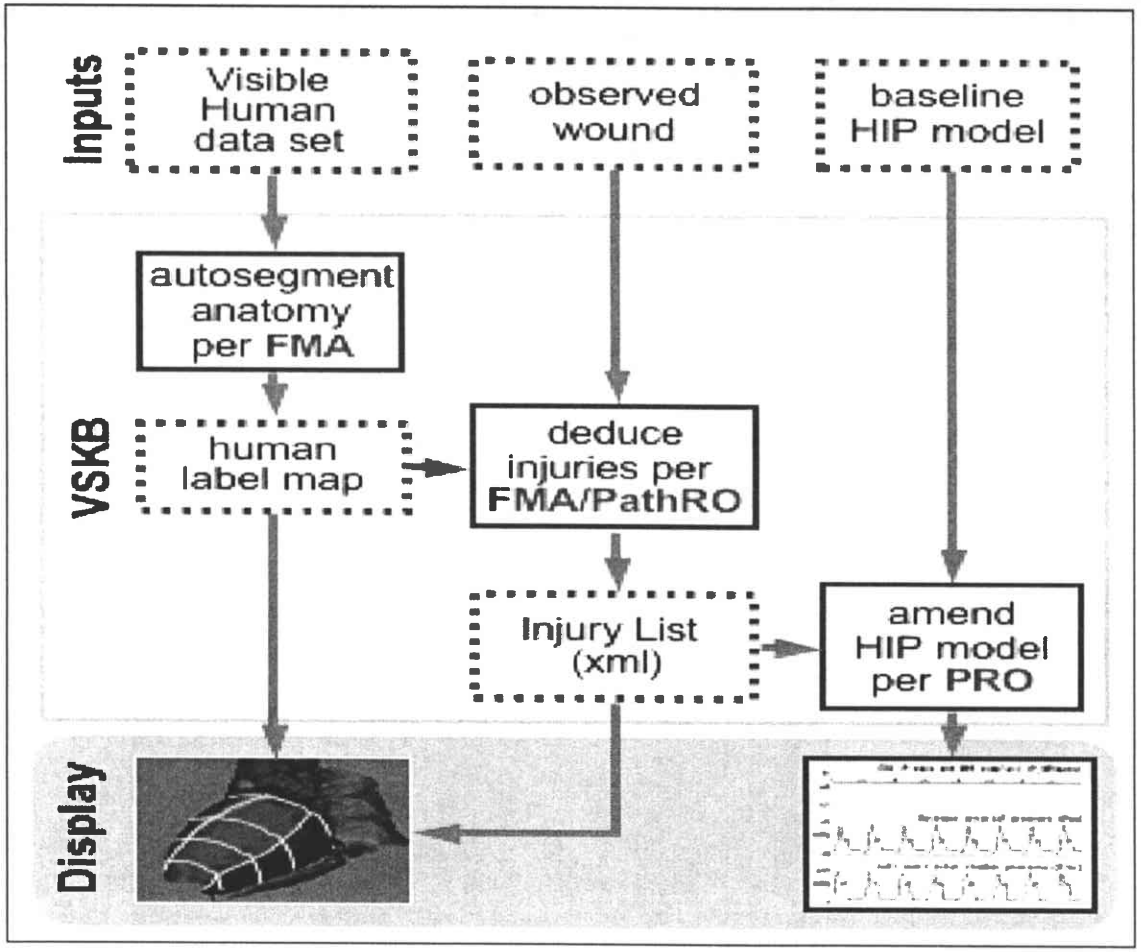

Machine readable ontologies enable reasoning which can provide the ability to ask "what if?"

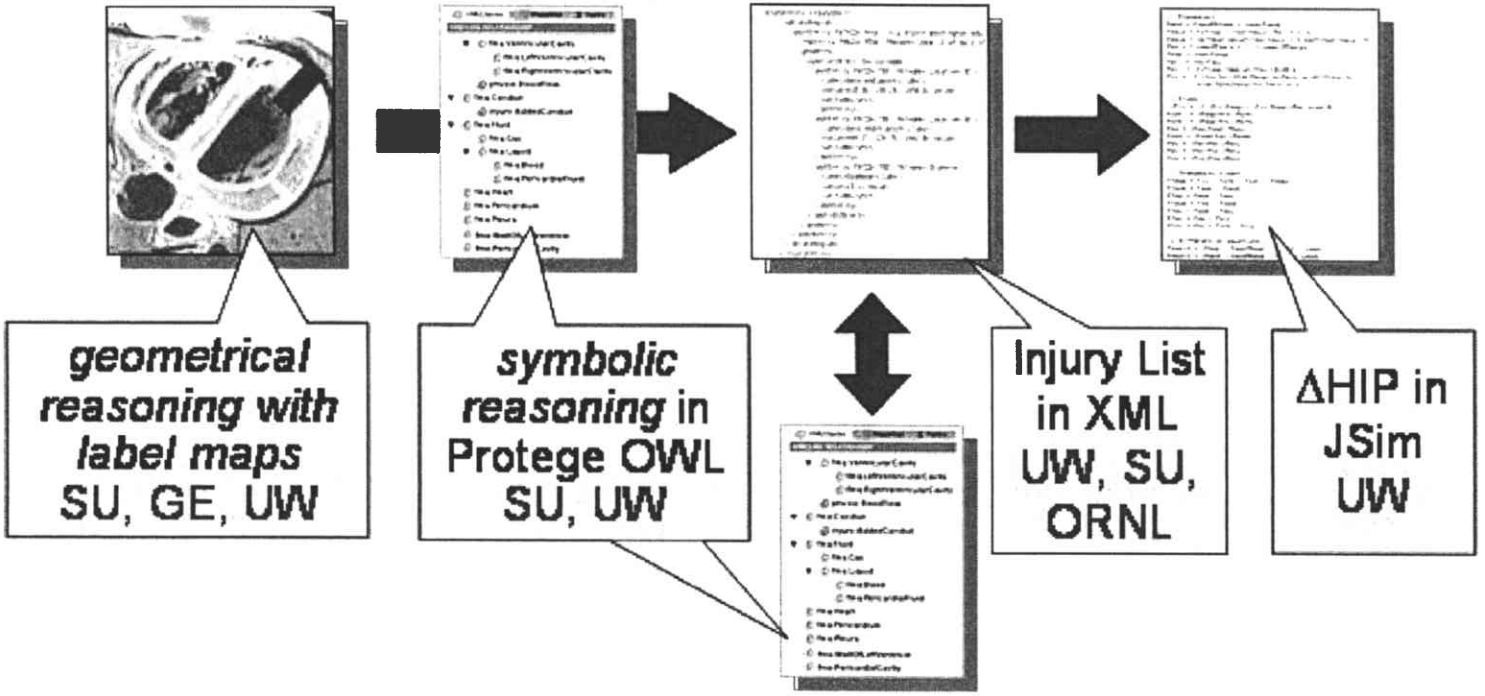

Virtual Soldier Knowledge Base (VSKB)

- extended Foundational Model of Anatomy (eFMA)
- Pathology Reference Ontology (PathRO)
- Physiology Reference Ontology (PRO) UW

Symbolic Reasoning in Final Demonstration

- Inference of damaged anatomic structures (both primary injuries and injury propagation) based on a wound description or spatially-oriented patterns of tissue strains. Raw data tell the field medic little about the war fighter's internal injuries. Stanford reasoning services provide the field medic with needed insights.

- Developed a software platform to integrate anatomic knowledge with geometry data from image label maps. We created reasoning services using OWL, an emerging standard in knowledge representation that permits automatic classification, to deduce primary and propagated injuries.

- Created a system to demonstrate our reasoning capability. A user specifies the trajectory of the projectile, and the application infers the anatomic structures that are directly injured as well as secondary injuries.

- These reasoning services can be used to provide the field medic decision support, and they can be combined with patient physiological and anatomical data to enhance triage and increase survivability of battlefield casualties.

Anatomy from Anatomy Forecast and Comparison to Autopsy Findings

- Analyze postmortem image data, including:
  - porcine CT images from ISR,
  - postmortem isolated heart CT images from ISR,
  - manual segmentation by UW,
  - smoothed, segmented, and labeled anatomy from GE,
  - the Virtual Soldier Knowledge Base (VSKB) from UW, and
  - autopsy reports from UW
- Determine which anatomical structures are injured
- Display information for use by the medic/physician
- Compare forecast and autopsy results
- Results of comparison show ability to predict injury from segmented image

Anatomy from Anatomy Data Flow Diagram

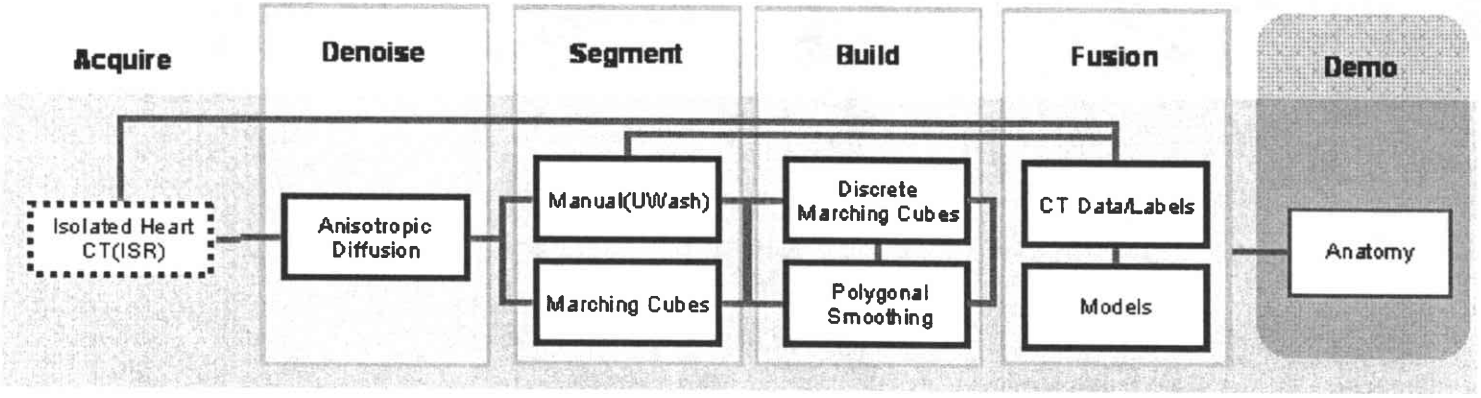

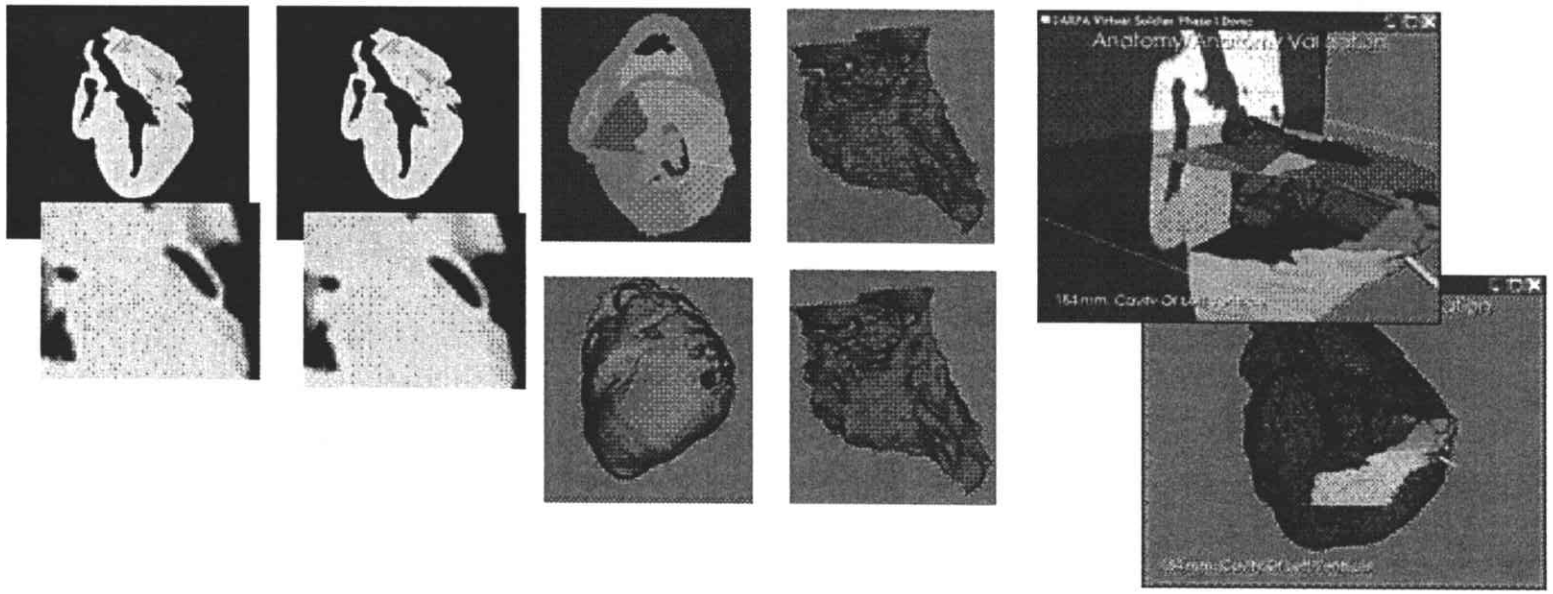

General Electric Corporation
Automatic Segmentation

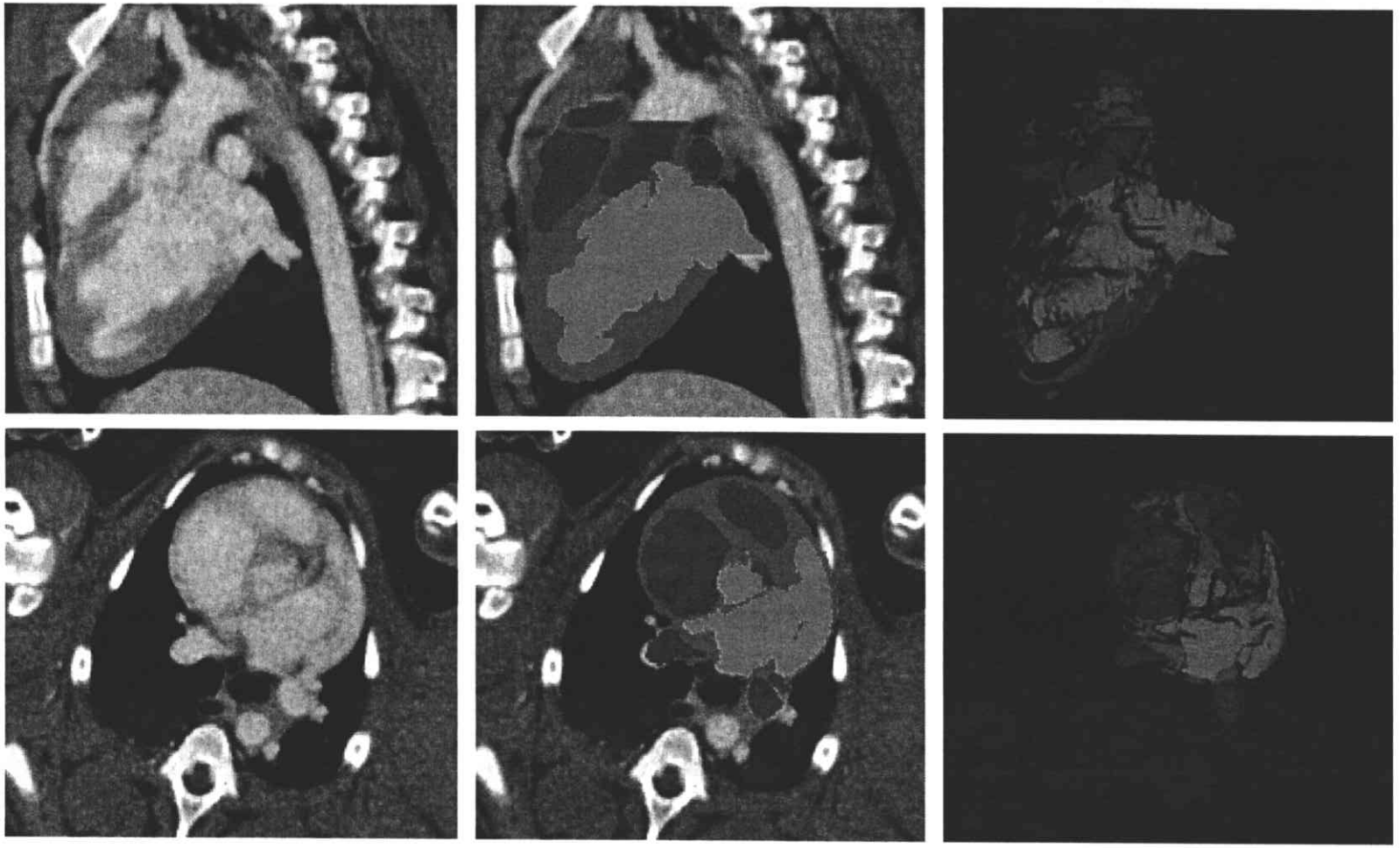

Autopsy Example Image

Data Compression and Transfer Rates onto DoD B-MIST Platform

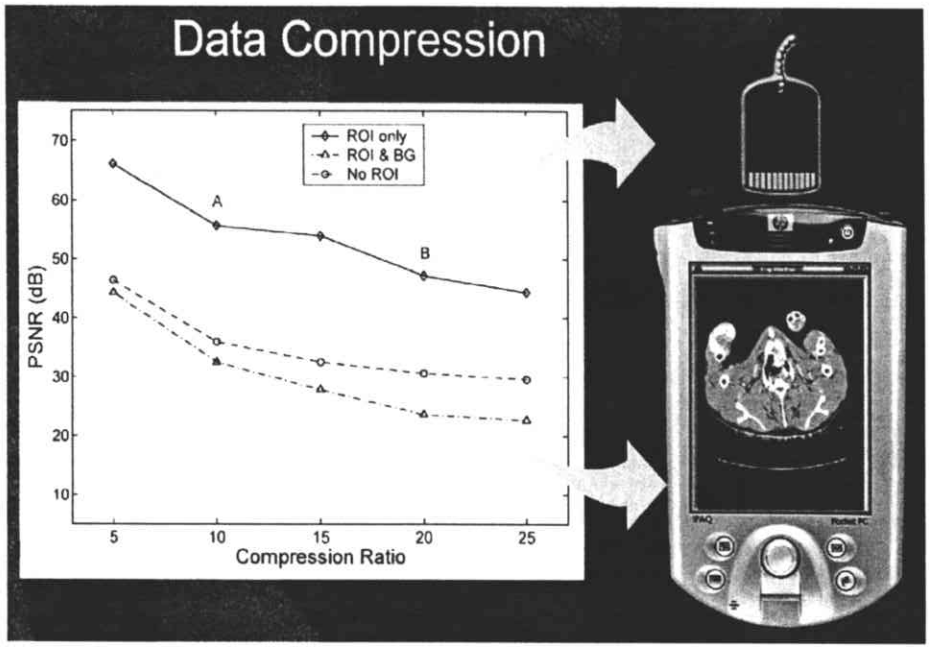

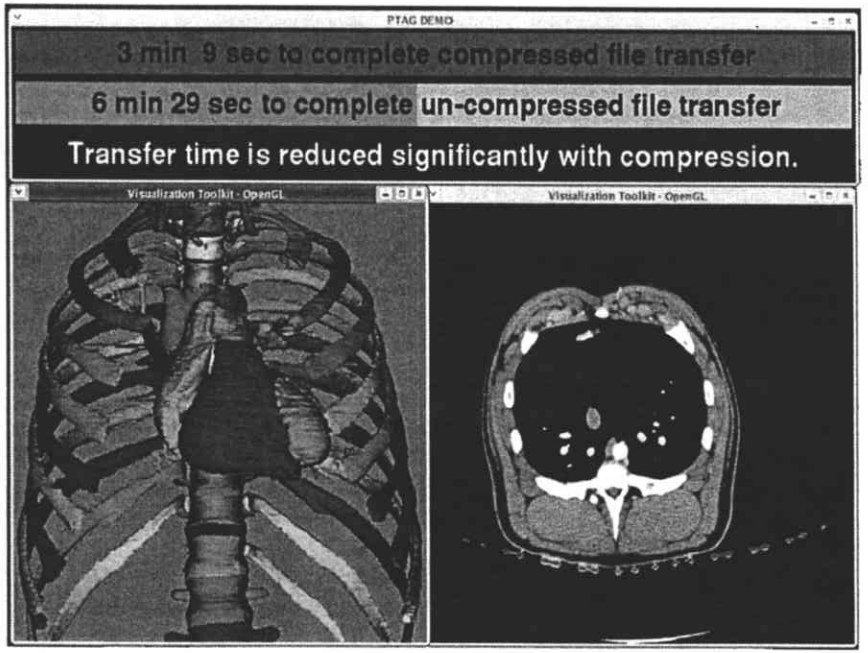

Multiscale Modeling Data Flows

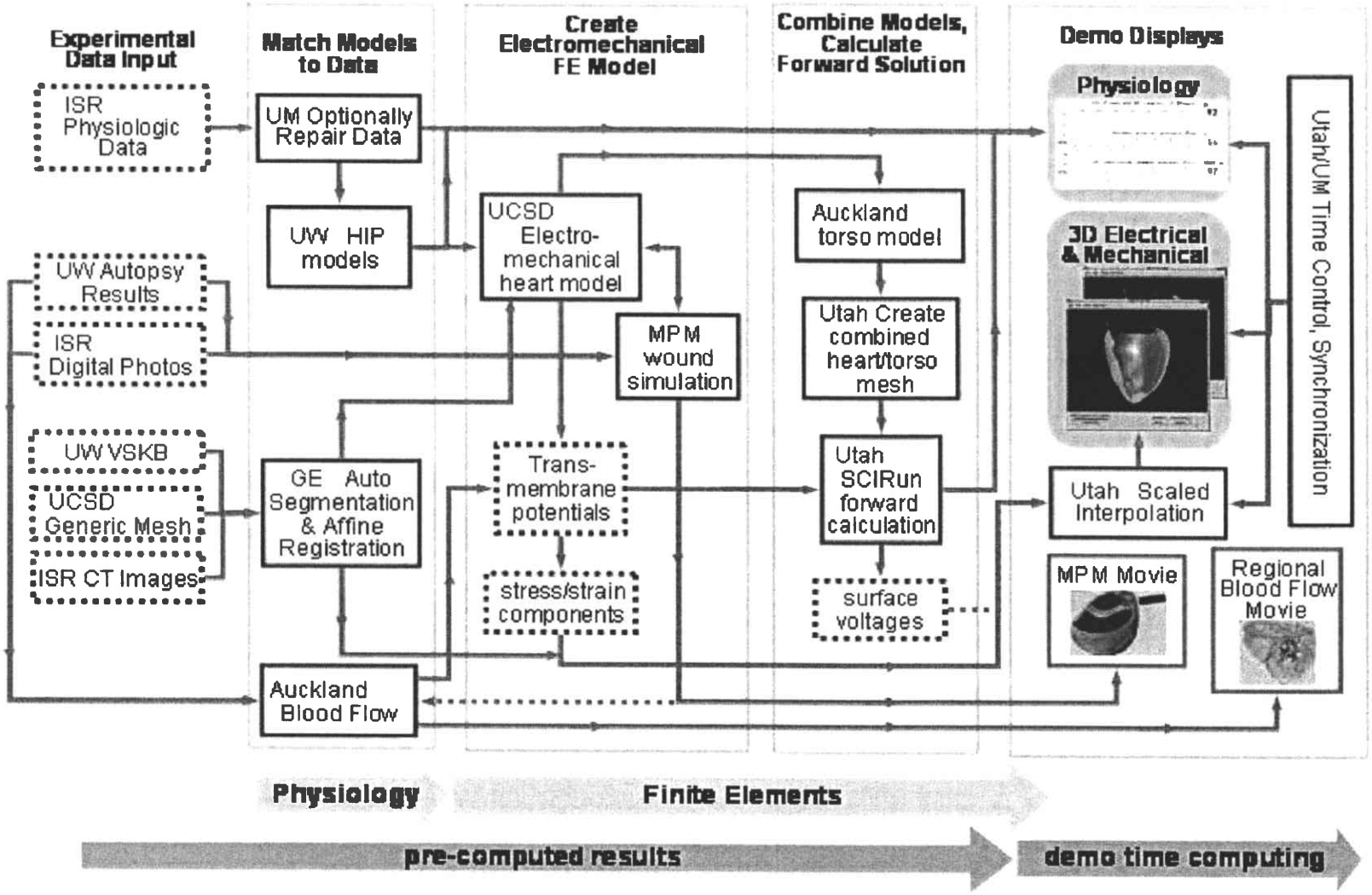

Models of Electrophysiological Responses to Regional Injury

UCSD and University of Auckland

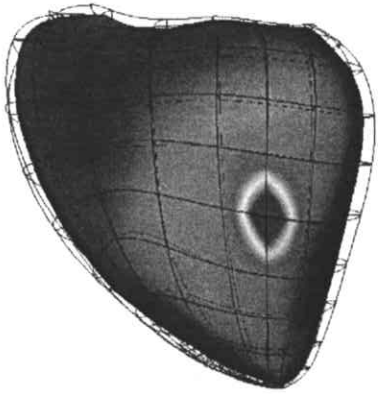

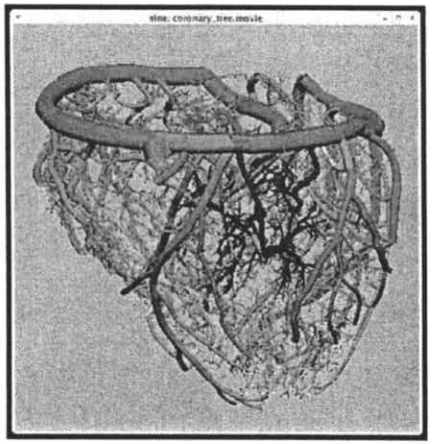

Regional coronary blood flow

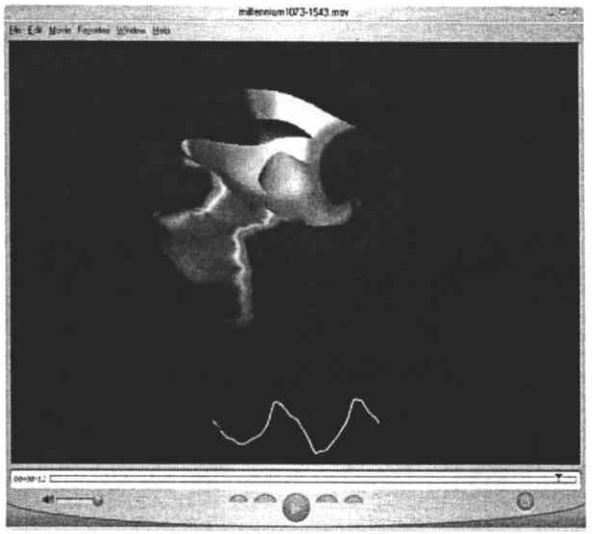

3D visualization of the Electrical Finite Element results

3D visualization of the Mechanical Finite Element results

Demonstration Movie Overview

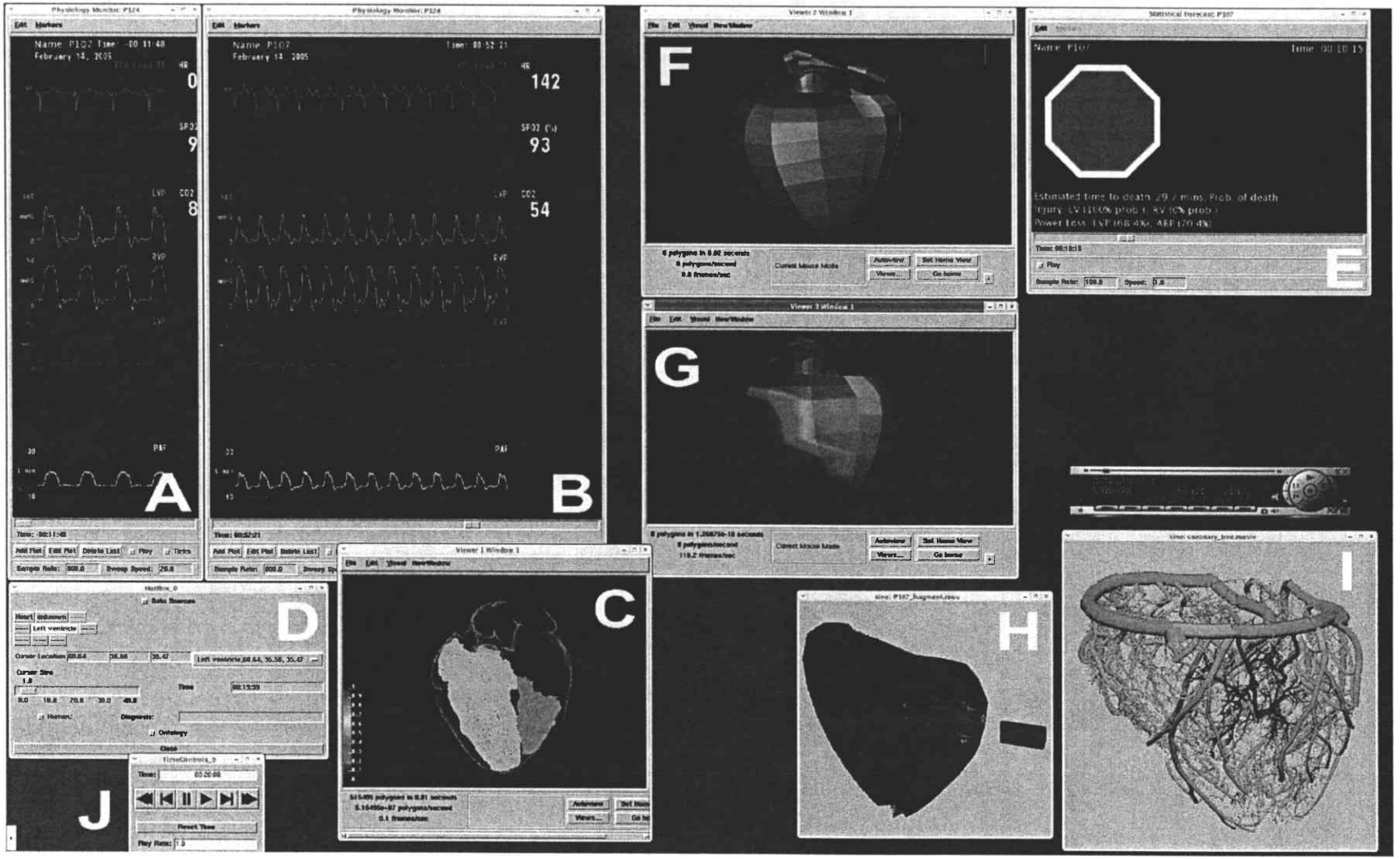

Conclusions

- A new statistical methodology to predict injury progression. Best predictor of survivorship using the average of ABP and LVP power drop.
- The indication of a simple measurable physiology parameter, lactate concentrations, can assist in determining an injury state and its progression.
- Mapping of atlas-based imagery and volume data to individuals by semi-automated segmentation and registration.
- Communication protocols between anatomy ontology databases, medical imagery, and mathematical physiology models.
- Extension of the Highly Integrated Physiology, Finite Element and Electrophysiology models to more closely mimic human medical conditions.
- Compression algorithms for rapid retrieval of regions of interest.
- A Virtual Soldier Knowledge Base which integrated the functionalities of the Foundational Model of Anatomy, the new HotBox display concept, and Protégé.

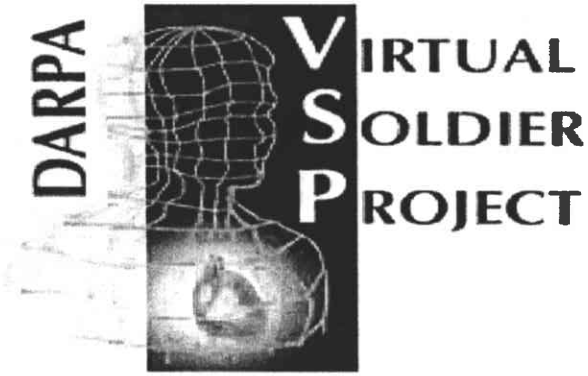

Phase I Final Demonstration

Ann Arbor, Michigan
June 14, 2005

90 Second Video

DARPA
U.S. Army MRMC/TATRC
University of Michigan
ATK-Mission Research
Brigham and Women's Hospital
Case Western Reserve University
Crowley Davis Research
Federation of American Scientists
General Electric Research
Oak Ridge National Laboratory
Stanford University
University of Auckland
University of California San Diego
University of South Carolina
University of Utah
University of Washington
U.S. Army Institute of Surgical Research
Xtria LLC

Cardiopulmonary Circuit Models for Predicting Injury to the Heart

Richard C. Ward
Oak Ridge National Laboratory

Sarah Wing
Davidson College

James Bassingthwaighte, Maxwell Neal
University of Washington

This work was supported by a grant from the DARPA, executed by the U.S. Army Medical Research and Materiel Command/TATRC Cooperative Agreement, Contract # W81XWH-04-2-0012.

DARPA Virtual Soldier Project

- The Virtual Soldier Project will improve treatment of American soldiers on the battlefield.
- Virtual Soldier is a completely computerized mathematical model of the human body
- All body systems incorporated into model
- Developing and testing cardiopulmonary models at ORNL and at the University of Washington
- Goal of Phase I: To demonstrate capability to:
  - Predict the consequences of a wound
  - Display (in 3D) anatomy, wound track and both baseline (unstressed) and injured (stressed) physiological state
  - Relate anatomy and physiology using innovative graphical user interface

To accomplish the goals of the DARPA Virtual Soldier Project

- Develop both high-level integrative physiological (HIP) cardiopulmonary models and 3D Finite Element models
- Validate computational models so that outcome of injury can be predicted
- Focus is on injuries to the heart
- Utilize individual segmented X-ray CT for anatomy and vital signs (HR, BP, O_2) for physiology
- Goal of high-resolution display of prediction in interactive visualization environment

Holographic Medical Electronic Record: HOLOMER

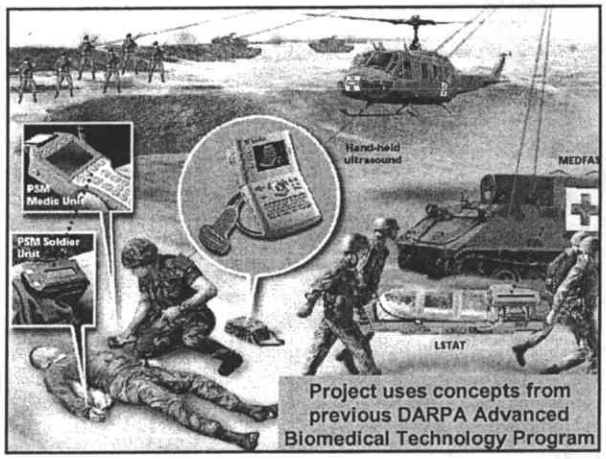

Virtual Human Computational Environment

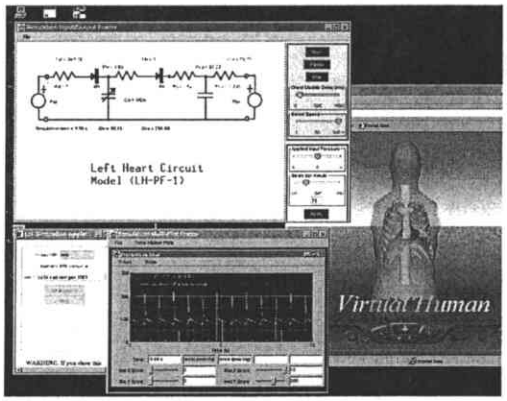

Heart Anatomy / Heart Electrophysiology

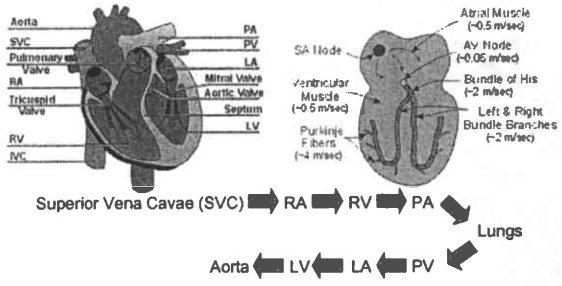

Notes: The LV is larger than the RV.
Atrium pressures: P_{LA} 6-10 mmHg; P_{RA} 0-3 mmHg.

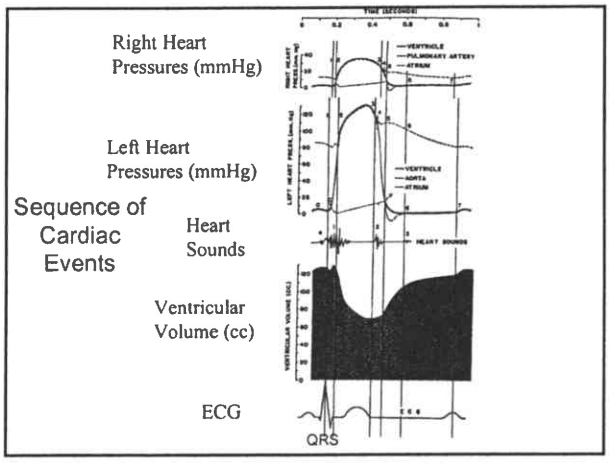

What's Involved with Heart Modeling

- SYSTEMS LEVEL
  - Cardiovascular flow
  - Cardiopulmonary flow
- ORGAN LEVEL
  - Mechanical model
  - Electrophysiology
- CELLULAR LEVEL
  - Muscle models
- Others?

electrophysiology

Cardiovascular model of the left heart (LF-PF1)

Reference: Vincent Rideout, *Mathematical and Computer Modeling of Physiological Systems* (1991)

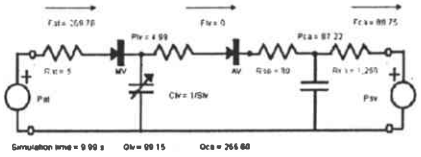

Left Atrium | Left Ventricle | Rest of the Body

Left Heart Circuit Model (LH-PF-1)

Mathematics Behind the Cardiovascular Model

- Circuit Equivalents
  - Current = Blood flow (e.g., F_{LV})
  - Voltage = Pressure (e.g., P_{LV})
  - Charge = Blood volume (e.g., Q_{LV})
  - Resistance = Resistance to flow (e.g., R_{LV})
  - Capacitance = Compliance (e.g., C_{LV})

    Note: C_{LV} is a variable capacitor, simulates the heart beat
- Two coupled differential equations for the volume of blood in the left ventricle (Q_{LV}) and small capillaries (Q_{CA})

Mathematics Behind the Cardiovascular Model

- Two coupled differential equations for left ventricle volume (Q_{LV}) and small capillaries volume (Q_{CA})
- $I = \Delta V/R$

or Blood Flow = Change in Pressure/ Resistance

LV Pressure: $P_{LV} = Q_{LV} * S_{LV}(t)$; $S_{LV} = 1/C_{LV}$ is square wave

Atrial flow: $F_{AT} = \text{Valve}[(P_{AT} - P_{LV}) / R_{AT}]$

Cap flow: $F_{CA} = (P_{CA} - P_{VE}) / R_{SA}$ where $P_{CA} = Q_{CA}/C_{CA}$

Ven flow: $F_{LV} = \text{Valve}[(P_{LV} - P_{CA}) / R_{SA}]$

where Valve is an on/off function (or step function) of time

- $dQ_{LV}/dt = F_{AT} - F_{LV}$
- $dQ_{CA}/dt = F_{LV} - F_{CA}$

Monitor Cardiovascular Function (P_{LV} and P_{CA})

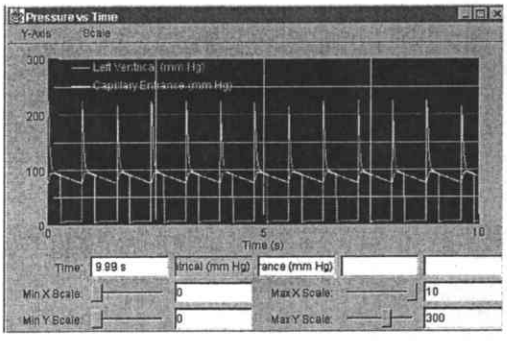

13

"Phase Space" Diagram: Plot P_{LV} vs. Q_{LV}

From cvphysiology.com

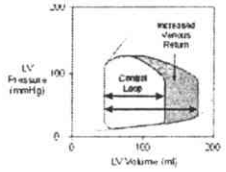

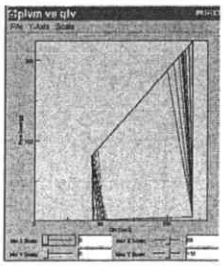

LH-PF-1 Model is too simple!

14

Next Level of Left Heart Model in Rideout

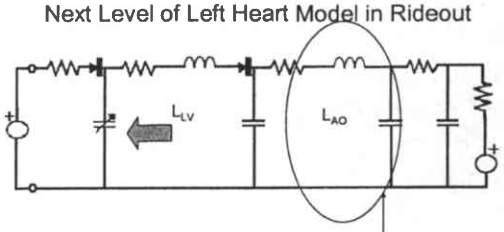

Left Heart Circuit Model
(LH-PF-3)

Introduce inductors L_{LV} and L_{AO} and better model for aortic valve

Use Sine wave rather than square wave for variable capacitor

15

DARPA Virtual Soldier Team

Corporate

GE Global Research
Mission Research Corporation
Crowley Davis Research
Xtria

Academic

University of Michigan
Stanford University
University of Washington
University of Utah
UCSD

16

Virtual Solider Cardiopulmonary Model

- The most complex model to date consists of
  - Systemic circulation
  - Pulmonary circulation
  - A four-chamber heart sub-model
  - Baroreceptor feedback
  - Airway mechanics
  - Gas exchange
  - Pleural pressure influence on the circulation

  Model represented by complex circuit!

Model Development

model name	systemic circulation	pulmonary circulation	4 chamber varying-elastance	baro-receptor feedback	airway mechanics	gas exchange	blood gas handling	pleural pressure influence	pericardium selectable injunct
spheart	✓	✓	✓						
spbheart	✓	✓	✓	✓					
spbha	✓	✓	✓	✓	✓				
spbhag	✓	✓	✓	✓	✓	✓			
spbhagt	✓	✓	✓	✓	✓	✓	✓	✓	
spbhagit	✓	✓	✓	✓	✓	✓	✓	✓	✓

18

SPHEART Model

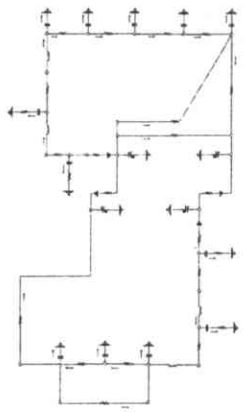

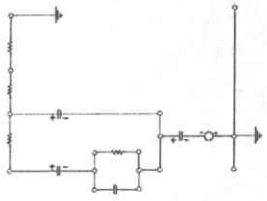

Airway Mechanics

Cardiovascular/Pulmonary flow

19

For Cardiopulmonary Modeling Virtual Soldier uses JSim Software

- JSim (for Java Simulator) is a software environment for scientific modeling
- Provides tools for development of models, for their run-time control, and for analysis of their behavior
- Developed at the University of Washington
  - Eric Butterworth (programmer)
  - Max Neal (biomedical engineer, analyst)
  - James Bassingthwaighte

http://nsr.bioeng.washington.edu/PLN/Software

20

JSim Screenshot of Unstressed Model

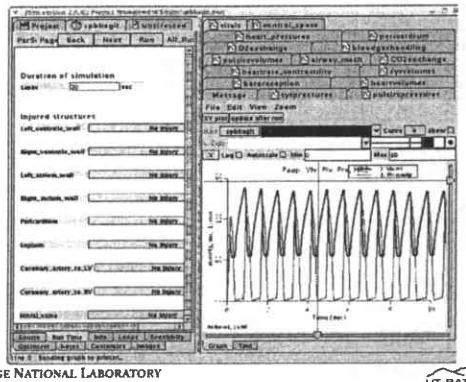

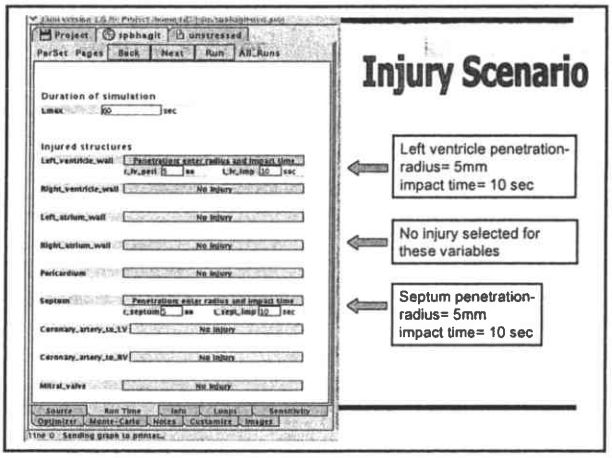

22

Injury to LV and Pericardium

2.5mm hole at 10s

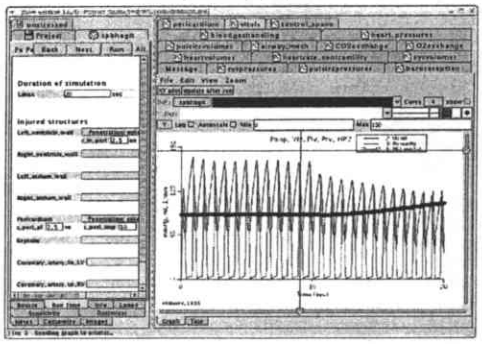

Phase Space Plot for Injury

to LV and Pericardium

2.5mm hole at 10s

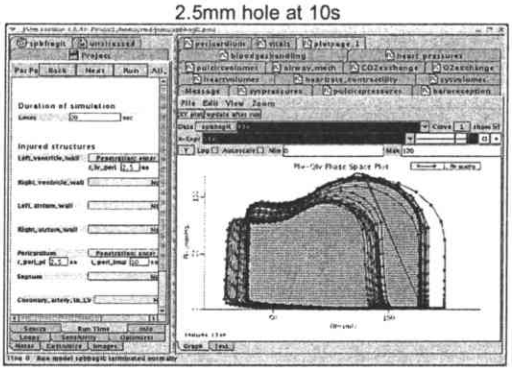

24

Remote Computational Method

- Download the input file from University of Washington
- Run model using JSim to ensure it contains no errors
- Send file to Web service at the University of South Carolina, where the model is run using the batch processing engine of JSim and results are sent back
- Manipulate parameters of the model using the command line for the Web service
- Plot results using Tcl/Tk "ICU Monitor"

25

Unstressed Results from Web Service

Left Ventricle Pressure

Left Ventricle Volume

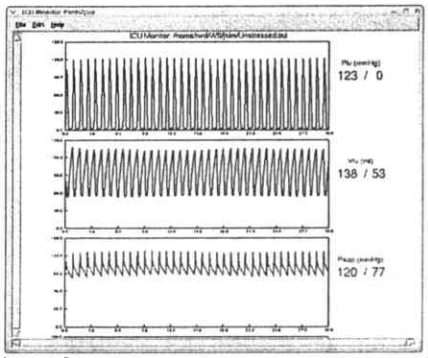

26

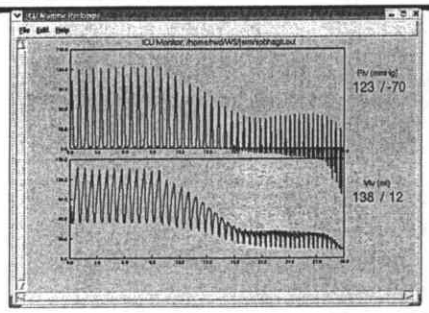

Results of Web service plotted using Tcl/Tk

Model: spbhagit Injury: left ventricle injury 2.5mm at 10s

27

Comparison of injury with baseline

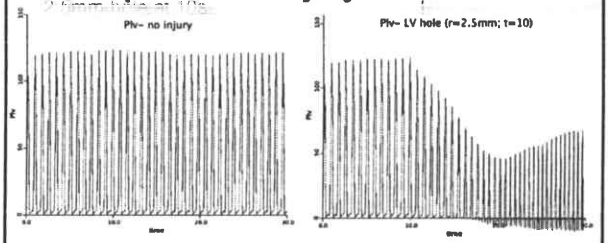

- Pressure in the LV remains consistent in the uninjured case
- In the injured case, a hole with radius 2.5mm occurs in the LV at time 10s.
- LV pressure for the injured case shows a dramatic decrease following the injury

Integrating Applications

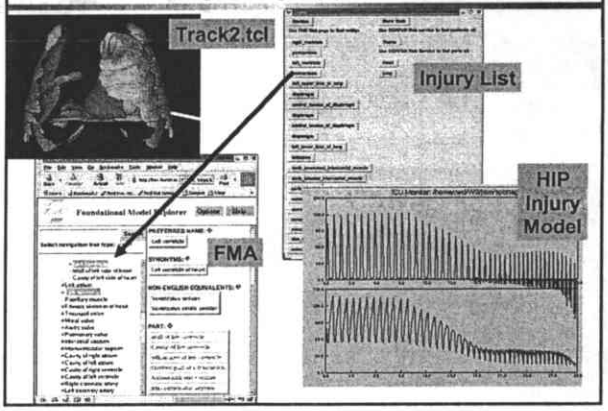

29

Future Work

- Complete validation of the injury model
- Examine various injury scenarios
- Complete implementation of the Web service
- Prepare for Phase I demonstration (March 1)
- Expand cardiopulmonary models for Phase II
  - Add pulmonary and vascular networks
  - Develop new injury scenarios such as Pneumothorax
  - Further develop the description of the wound

30

Visual Display of Circuit Diagram using VH Environment

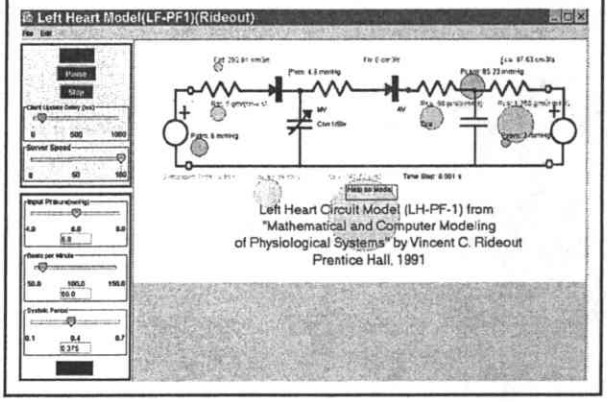

Left Heart Circuit Model (LH-PF-1) from "Mathematical and Computer Modeling of Physiological Systems" by Vincent C. Rideout Prentice Hall, 1991

Connectivity between geometric model and anatomical ontology in SCIRun Visualization Environment

HotBox Interface

SCIRun display of thorax model

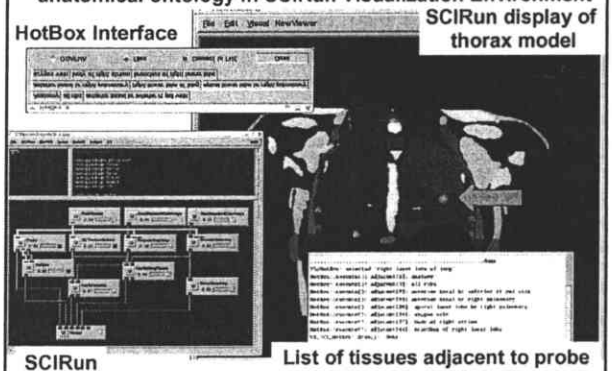

SCIRun network

List of tissues adjacent to probe (arrow) in lower right lobe of lung

Java Code for Mathematics

`u[0], u[1]`: volumes for previous time step

```
qlv = u[0];              // Left ventricle volume
qca = u[1];              // Small arteries volume
plv = qlv*calcSlv (t);   // Left ventricle pressure

fatx = (pat - plv)/rat;  // Atrial flow with no valve
fat = calcFat (fatx);    // Atrial flow with valve

pca = qca/cca;           // Capillary entrance
fca = (pca - pve)/rca;   // Capillary entrance

flvx = (plv - pca)/rsa;  // Left ventricle flow, no valve
flv = calcFlv (flvx);    // Left ventricle flow, with valve

v[0] = fat - flv;        // ODE for left ventricle volume
v[1] = flv - fca;        // ODE for small arteries volume

return v;
```

`v[0], v[1]`: new RHS for this time step. These are passed to the solver to integrate to obtain new volumes qlv, qca.

Vital Signs Data Used for Validation

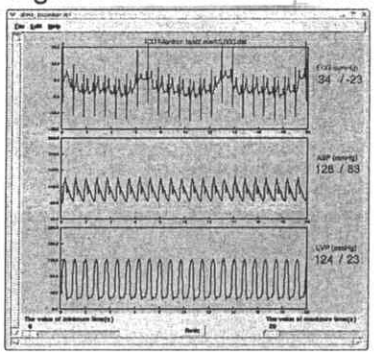

Cardiopulmonary Circuit Models for Predicting Injury to the Heart

Richard C. Ward, Oak Ridge National Laboratory, Oak Ridge, TN
Sarah Wing, Davidson College, Davidson, NC
James Bassingthwaighte, Maxwell Neal, University of Washington, Seattle, WA

Circuit models have been used extensively in physiology to describe cardiopulmonary function. Such models are being used in the DARPA Virtual Soldier (VS) Project* to predict the response to injury or physiological stress. The most complex model consists of systemic circulation, pulmonary circulation, and a four-chamber heart sub-model. This model also includes baroreceptor feedback, airway mechanics, gas exchange, and pleural pressure influence on the circulation. As part of the VS Project, Oak Ridge National Laboratory has been evaluating various cardiopulmonary circuit models for predicting the effects of injury to the heart. We describe, from a physicist's perspective, the concept of building circuit models, discuss both unstressed and stressed models, and show how the stressed models are used to predict effects of specific wounds.

This work was supported by a grant from the DARPA, executed by the U.S. Army Medical Research and Materiel Command/TATRC Cooperative Agreement, Contract # W81XWH-04-2-0012.

The submitted manuscript has been authored by the U.S. Department of Energy, Office of Science of the Oak Ridge National Laboratory, managed for the U.S. DOE by UT-Battelle, LLC, under contract No. DE-AC05-00OR22725. Accordingly, the U.S. Government retains a non-exclusive, royalty-free license to publish or reproduce the published form of this contribution, or allow others to do so, for U.S. Government purpose.

APS Membership #: WA667980

Why a Web Services approach for the Virtual Soldier Project?

- Six universities, one lab, several companies.
- A web-based distributed approach is advantageous to expose a programmatic interface for running services, programs, and software components between the different teams.
- Developers own their code: each version or change in the service does not affect the client: ex JSIM updated 30 times a year.
- New data can be automatically available.
- An underlying principle of making these services and data available to Web users in the future.

A Web-based Computer Architecture for the Virtual Soldier

Line C. Pouchard, Richard C. Ward
Oak Ridge National Laboratory
Michael N. Huhns, Laura Zavala, Karthik Iyer
University of South Carolina

http://www.virtualsoldier.net

OAK RIDGE NATIONAL LABORATORY
U. S. DEPARTMENT OF ENERGY

Defining Requirements for Integrating Project Components

A Provider/Consumer table

- Who provides data or a service that another will use?
  - Human users, other software components, APIs.
- What is the required functionality of the necessary interactions within the project?
- What data formats and platforms are likely to exist?
- **VSKB**: The Virtual Soldier Knowledge Base, an ontology of anatomy (Digital Anatomist Foundation Model).
  - approximately 70,000 concepts and over 110,000 terms; 168 relationship types; over 1.5 million relationship instances

PROVIDER	SERVICE NAME	CONSUMER
VSKB Knowledge Base	MIDDLEWARE Knowledge Update Services	HIP Model Simulation (JSim)
VSKB Namespace	MIDDLEWARE Ontology Query Services	VTK Visualization
HIP Model Simulation (JSim)	MIDDLEWARE Dynamic Invocation Services	VTK Visualization
FE Heart and Thorax Simulation	MIDDLEWARE Data Location Services	SCIRun Visualization

- **HIP**: High-level Interactive Physiological model run by JSim.
  - **JSIM**: component that runs the model.

OAK RIDGE NATIONAL LABORATORY
U. S. DEPARTMENT OF ENERGY

What is the Virtual Soldier Project?

- Develop methods that will revolutionize medical care for the soldier in the battlefield and elsewhere.
- Phase I:
  - Coupling physiological, electro-mechanical, and anatomical properties of the heart to predict chances of survival after injury.
  - An interactive 3D display that includes time series, a searchable semantic network and complex visualization of a virtual human heart.
- http://www.virtualsoldier.net

OAK RIDGE NATIONAL LABORATORY
U. S. DEPARTMENT OF ENERGY

Identifying Necessary Web Services

- Services for collecting, accessing, querying and presenting the data made available by models and experiments to others within the project.
- Process diagrams identifying the web services supporting requirements.
  - Locate
  - Update
  - Query
  - Run

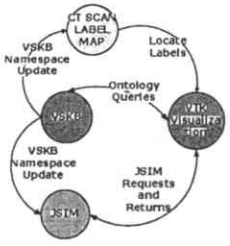

OAK RIDGE NATIONAL LABORATORY
U. S. DEPARTMENT OF ENERGY

What is the project trying to do?

Build a Virtual Soldier on an Electronic "dog tag" From Which to Diagnose and Predict Combat Injury

Why?
Instantly & Accurately diagnose internal combat injury (heart)

How?
3-D model from total body scan on "dog tag" (anatomy & physiology)

Compare to data acquired on the battlefield after wounding (Ultrasound)

Predict likelihood of battlefield mortality

Holographic Medical Electronic Representation
Holomer

ORNL mandate:

- **Develop a middleware computer architecture in view of a demonstration of the Holomer.**
- **Includes a graphical representation of human anatomy enriched with medical indicators obtained in physiological modeling.**
- **Seamlessly integrate components provided by six universities, one lab, and several companies.**

WS Integration of components

Initiating the service

- Running the spheart model with a batch input file corresponding to an injury scenario invoking the JSim web service
- The batch input file also invokes a vtk visualization

VSP Web Service Architecture

- Display: a Web or other graphical front-end
  - Independent from the WS
- Universal Data Format
  - XML
- Service Description Language
  - WSDL
- Service Interaction
  - SOAP
- Communication
  - http, tcp/ip

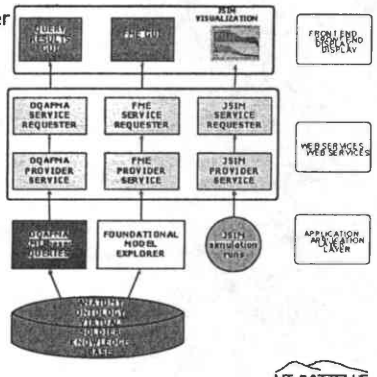

WS Integration of components

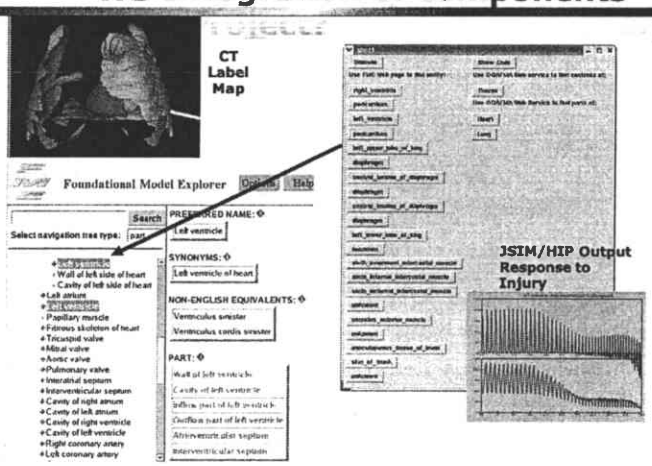

High-level Interactive Physiological Model (U. Washington)

Goal: simulate a patient monitor with heartbeat, ventricular pressure, blood flow. Run by JSim software

```
t = { 0 0.01 0.02 0.03 0.04 0.05 0.06 0.07 0.08...} mmHg*sec*ml^-1
Rvc(t) = { (0,0.03192521) (0.01,0.03192828) (0.02,0.03193117)...} mmHg*sec*ml^-1
Plv(t) = { (0,5) (0.01,14.28506947) (0.02,28.02342933))...} mmHg
Paop2(t) = { (0,65.10416667) (0.01,65.0309892) (0.02,64.90119688)...} mmHg
Paop(t) = { (0,65.10416667) (0.01,65.0309892) (0.02,64.90119688)...} mmHg
   etc...
```

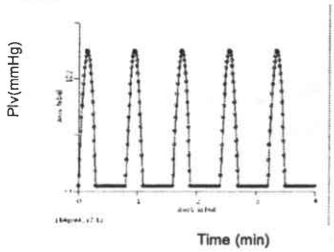

Performance of JSim WS

- Conditions
  - The Web services installed on a Web server located at USC
  - Compared WS to direct invocation of JSim for several values of the simulation parameters.
  - Measurements, which included latency and throughput, made both locally and remotely.
- Results show that use of Web services adds relatively small overhead.
- In some cases, running the batch program directly with JSim is slower than running it through WS.

Output of HIP/JSIM model

Plv (mmHg)

Qlv (ml)

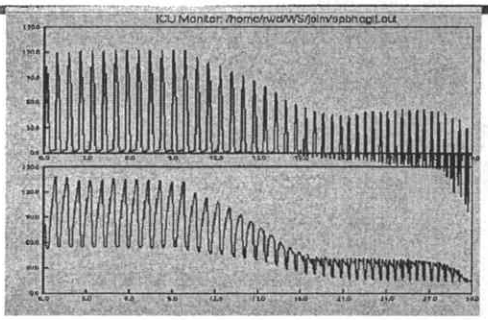

Left ventricle pressure (mmHg) & volume of blood (ml) for injury model (spbhagit) with a 2.5 mm hole in the left ventricle at 10s.

Performance of JSim WS

- Each case involves running JSim for 30 seconds of simulation time using the spheart.mod model and a batch input file.
- 1.8 GHZ CPU, with 512 MB RAM.
- LAN for case #4 is 1 Gigabit Ethernet

- The Java VM has to be loaded into memory every time **jsbatch** runs, whereas Tomcat is always up and running.
- **jsbatch** will read from and write to files, whereas the data for the Web service resides in data structures in memory.

Running jsbatch only	26.75 s	31.08 s	27.14 s	
Running jsbatch wrapped as a WS	23.89 s	22.15 s		
Running jsbatch as a WS, from a client residing on the server machine	31.173s			
Running jsbatch as a WS, from a client residingon a remote machine	29.30 s	32.28 s		

Where do we go from here?

- Continue development of services (location, metadata look-up, VSP data retrieval).
- Refine the JSim web service based on componentization of JSim code.
- Integrate with SCIRun visualization environment.
- Build a grid portal for the Virtual Soldier Application (Phase II).

Acknowledgements

- DARPA
  - Rick Satava, MD, Program Manager.
- USArmy Medical Research and Materials Command
  - Gerry Moses, PhD.
- University of South Carolina, Center for Information Technology
  - Pr. Mike Huhns, Laura Zavala, Karthik Iyer
- University of Washington
  - Jim Bassingthwaighte
  - Cornelius Rosse, Daniel Cook (Structural Informatics)

OAK RIDGE NATIONAL LABORATORY
U. S. DEPARTMENT OF ENERGY

A Web-based Computer Architecture for the Virtual Soldier

Line C. Pouchard, Richard C. Ward
Oak Ridge National Laboratory
Michael N. Huhns, Laura Zavala, Karthik Iyer
University of South Carolina

Abstract

The Defense Advanced Research Projects Agency Virtual Soldier Project (DARPA-VSP) investigates methods that will revolutionize medical care for the soldier. The project will produce complex mathematical models to create physiological and anatomical representations of individual soldiers. It currently focuses on coupling physiological, electro-mechanical, and anatomical properties of the heart in a single interactive 3D display that includes time series, a searchable semantic network and complex visualization of a virtual human heart. Large teams of researchers distributed nationwide among six universities, one national laboratory, and several companies collaborate. The complexity of the project requires a flexible, distributed, computing architecture that supports independent models and seamless integration of software components.

We present a Web-based, flexible, computing architecture that provides services for bringing output data of one system to input of another upon request through programmatic interfaces. This architecture provides services for collecting, accessing, querying and presenting the data made available by models and experiments. As an example we present a Web service for physiological modeling software (JSIM) developed by the University of Washington. We also present the results of performance tests on the Web service developed for JSIM.

The Development of Sophisticated Cardiac Models for Use in the Virtual Soldier Project

Sarah Wing
Davidson College
Richard Ward, Mentor

Introduction

- The Virtual Soldier Project will maximize the efficiency of medical services to American soldiers on the battlefield.
- Virtual Soldier = a completely computerized mathematical model of the human body
- All body systems incorporated into model
- At ORNL and at the University of Washington- developing and testing cardiac models
- Goal of this stage: to create an ICU-type monitor that scrolls the graphical results from the models across the screen

Methods

- Download the ".mod" input file[1] (from http://nsr.bioeng.washington.edu) and enter tuned parameters in JSim
- Run model to ensure that it contains no errors
- Send file to Web service at the University of South Carolina, where the model is run using the batch processing engine of JSim and results are sent back[2]
- Sending the model via the Web means that doctors would be able to manipulate certain parameters of the model, using the command line as input for the Web ervice
- In the most sophisticated model to date, specific injuries to the heart can be entered into the model[3]

[1] See Figure 1 to the left
[2] See Figure 2 to the left
[3] See Figure 3 to the left

Model Development

model name	systemic circulation	pulmonary circulation	4 chamber varying-elastance	baro-receptor feedback	airway mechanics	gas exchange	blood gas handling	pleural pressure influence	cardiac selectable injuries
sphsart	✓	✓	✓						
spbheart	✓	✓	✓	✓					
spbha	✓	✓	✓	✓	✓				
spbhag	✓	✓	✓	✓	✓	✓			
spbhagt	✓	✓	✓	✓	✓	✓	✓	✓	
spbhagll	✓	✓	✓	✓	✓	✓	✓	✓	✓

Figure 1 (left)

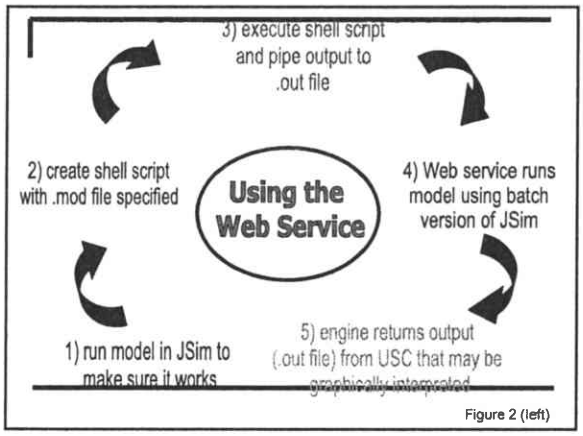

Figure 2 (left)

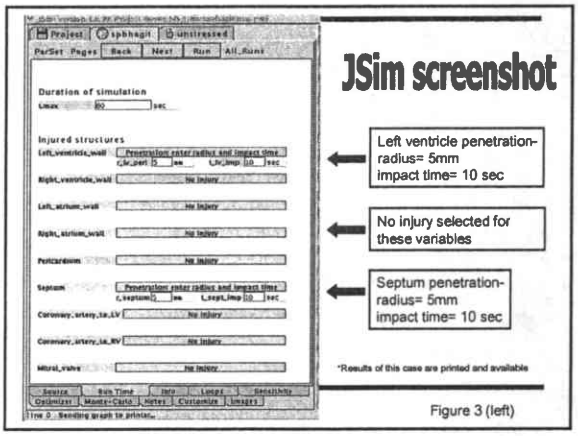

Figure 3 (left)

Results

- The goal of this stage is to create an ICU-type monitor that scrolls the graphical results from the models across the screen[1]
- Once data is received from the web service, it can be plotted graphically using Tcl software[2]
- While data can be displayed, it has been difficult to get the results of a specified variable to scroll across the screen as a function of time, and this part of the project is not yet complete
- It is possible to see graphical distinctions in certain variables between an injured heart and a healthy heart[3]

[1] See Figure 1 to the right
[2] See Figure 2 to the right
[3] See Figure 3 to the right

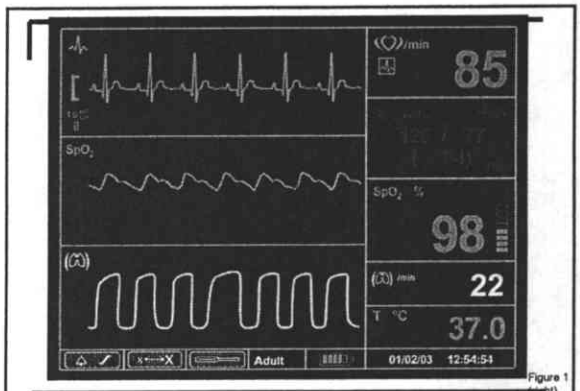

Figure 1 (right)

Goal: make data scroll to appear like an ICU monitor

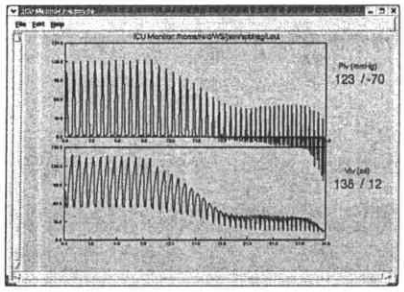

Results of Web service data, plotted using Tcl

Model spbhagit, left ventricle injury as below

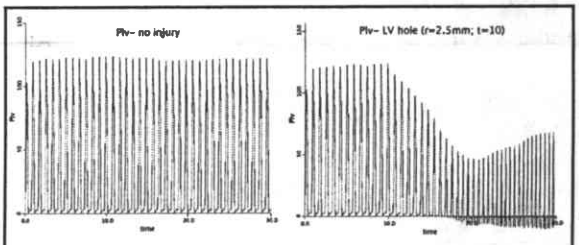

- Pressure in the left ventricle remains consistent in the uninjured case
- In the injured case, a hole with radius 2.5mm appears in the left ventricle at time 10 sec.
- Left ventricular pressure for the injured case shows a dramatic decrease following the injury

Figure 3 (right)

Discussion

- The most recent model, spbhagit, is the best illustration so far of the ultimate goal of this project
- Spbhagit allows the user to enter a specific injury and view the graphical effect on specific variables
- Ultimately, a doctor would be able to look at graphical models of specific injuries and compare them to graphical data they may acquire from a soldier
- Such capabilities will allow for faster diagnosis on the battlefield and more efficient treatment once a diagnosis is determined
- Ultimately, these models will be of use not only on the battlefield, but also in our hospitals, advancing healthcare for everyone

Acknowledgements

- This work was supported by a grant from the DARPA, executed by the U.S. Army Medical Research and Materiel Command/TATRC Cooperative Agreement, Contract # W81XWH-04-2-0012.
- Work was also supported by the DOE SULI (Science Undergraduate Laboratory Internship) program.

Computational Modeling of Tissue Damage from Penetrating Trauma: Linking Geometric Models to Anatomic and Biomechanical Knowledge

Daniel L Rubin, MD, MS[1,2] Yasser Bashir[1] David Grossman, PhD[1] Parvati Dev, PhD[1] Mark Musen, MD, PhD[1]

[1]Stanford Medical Informatics and [2]Department of Radiology, Stanford University

INTRODUCTION

Detailed geometric models of anatomy can be created from CT and MRI images. These 3-dimensional models are generally used in visualizations for physicians, but they are not directly computer-interpretable. We are interested in using geometric models of patient anatomy for computerized prediction of organ injury after trauma. We make these models computable by augmenting them with explicit anatomic and biomechanical knowledge. We can then develop computer programs that operate on these augmented models. We describe an approach to predicting the consequences of penetrating injury by integrating geometry with anatomic and biomechanical knowledge.

OBJECTIVES

(1) Develop a computer representation of patient anatomy that links models spatial geometry with anatomic knowledge.
(2) Create computer reasoning services that use geometric models integrated with anatomic knowledge to predict consequences of penetrating injuries:
- Direct injury
- Propagation of injury (injuries secondary to the primary injury)

(3) Develop an application to visualize patient spatial geometry and anatomic knowledge, and results of computer reasoning.

METHODS

There are four components to our approach:
(1) Generation of geometric models
(2) Computer representation of anatomic knowledge
(3) Linking geometry to anatomic and biomechanical knowledge
(4) Computer reasoning (making inferences from the available data).

Generation of Geometric Models

We create 3-dimensional geometric mesh models of patient anatomy using conventional segmentation-based approaches. A volumetric imaging study of the heart is segmented to separate and label points in space corresponding to the major anatomic structures, such as chambers of the heart, coronary arteries, etc. We have used the Visible Human data in this work; CT data could be used instead.

Computer Representation of Anatomic Knowledge

Anatomic knowledge is stored in ontologies, representations of knowledge that can be read by people and processed by machines. Ontologies provide a declarative representation of the concepts, properties, and relationships among the concepts of a domain, and are very useful in building intelligent computer applications.

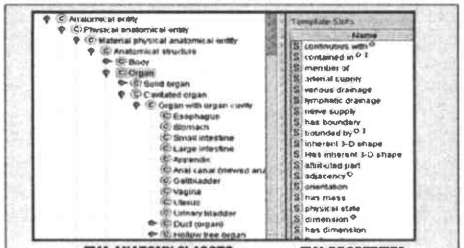

We use the Foundational Model of Anatomy (FMA [1]), a comprehensive ontology of human anatomy, containing more than 70,000 concepts that describe the elements of canonical human morphology in a clear and consistent manner. In addition to enumerating anatomic structures, it describes adjacencies, part-whole relationships, continuities, and other information relevant to inferring injuries.

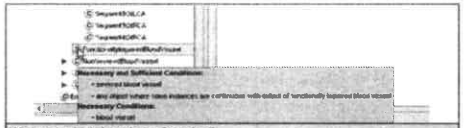

We use symbolic knowledge from the FMA to define what we mean by "functionally impaired blood vessel", "severed blood vessel", "ischemia" and "partial ischemia."

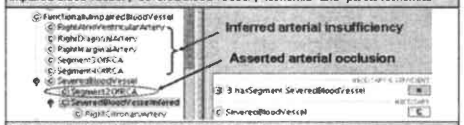

If we know that that a blood vessel has been severed, a classifier operating on the ontology can determine the vessels *continuous with* the injured vessel that are "functionally impaired."

Linking Geometry to Anatomic and Biomechanical Knowledge

We build a three-dimensional representation of patient anatomy from spatial mesh models using the Insight Toolkit (ITK [2]). We create a conceptual hierarchy of anatomic data structures (ADS) in ITK representing organs and organ parts present in the geometry. Each ADS contains information about organ identity, composition, adjacency, and biomechanical properties and links to a portion of the geometry.

Ontology of anatomy (left) with implicit links to geometry (right).

Each organ part has graphical and ontology representations.

We use knowledge in the anatomy ontology to subdivide the left ventricle into zones according to known vascular territories.

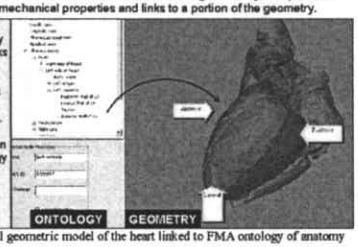

Three dimensional geometric model of the heart linked to FMA ontology of anatomy

RESULTS

We have used our integrated geometry/knowledge models to implement two computer reasoning services to evaluate a trajectory of penetrating injury: (1) Direct injury reasoning and (2) Injury propagation reasoning. Both rely on combining geometric data and anatomic knowledge.

Computer Reasoning about Direct Injuries

- Given a path of injury in the patient, the computer can predict and display primary injuries.
- Every point along injury trajectory is intersected with geometric model to determine regions of direct injury.
- Organs that are directly injured are intersected by the trajectory.
- Tissue biomechanical properties stored with each organ are used to estimate the volume of tissue injury.
- Identity of directly injured organs is established by lookup in anatomy ontology, since geometry model links spatial regions to the ontology.

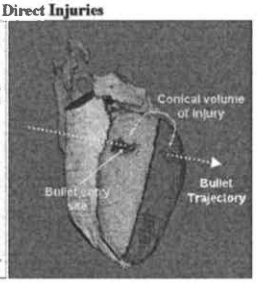

Computer Reasoning about Injury Propagation

Injuries occurring secondary to the primary injuries are inferred by the computer using the ontology of anatomy. The ontology contains knowledge about organs and organ parts supplied by different arterial branches.

- Ontology-based reasoning about secondary tissue damage after coronary artery injury, updating the geometric display to show damaged regions of the heart.
- The computer uses knowledge about myocardial perfusion to infer secondary myocardial damage (gray regions) from a right coronary artery injury.
- The computer can differentiate total and partial ischemic regions.

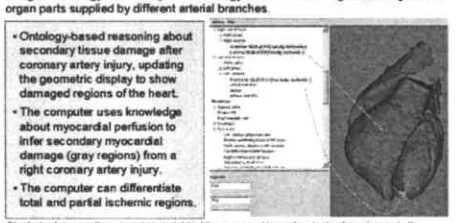

Shaded volumes in the geometric model (right) correspond to anatomic structure classes in the anatomy ontology (left). A computer reasoning service uses the ontology to deduce parts of the myocardium that are injured consequent to a coronary artery injury, shown as highlighted structures in the FMA (left) and shaded parts of heart (right).

CONCLUSION

We have demonstrated a methodology to automate computerized reasoning about penetrating injuries using canonical knowledge combined with image data. A key element is our use of a comprehensive ontology of anatomy containing organ identities, adjacencies, and other information useful for anatomic reasoning, and an ontology of regional perfusion containing formal definitions of arterial anatomy and corresponding regions of perfusion. Our integrated knowledge/geometry model supports computerized anatomic reasoning. Given an injury path, we can determine the organs that are injured, whether vital structures—such as a coronary artery—are injured, and can predict the propagation of injury ensuing after a vital structure is injured. Our approach is extensible and can incorporate future information, such as physiological implications of organ injuries. This methodology may be useful in teaching and simulation applications.

Acknowledgements

This work was supported by a contract from DARPA, executed by the U.S. Army Medical Research and Materiel Command/TATRC Cooperative Agreement, Contract W81XWH-04-2-0012. This work was also supported by the Protégé resource, under grant LM007885 from the U.S. National Library of Medicine.

References

1. Rosse C, Mejino JL, Jr. A reference ontology for biomedical informatics: the Foundational Model of Anatomy. J Biomed Inform 2003;36(6):478-500.
2. The Insight Toolkit, http://itk.org.
3. Rubin DL, Bashir Y, Grossman D, Dev P, Musen MA: Linking Ontologies with Three-Dimensional Models of Anatomy to Predict the Effects of Penetrating Injuries, 26th Annual International Conference IEEE Engineering in Medicine and Biology, Bethesda, MD, San Francisco, CA 2004.

Abstract ID: 4411395
Public ID: 9430 IMA-i
Submission Type: infoRAD
Submission Status: Accepted

Contact:
Daniel Rubin
Stanford University
Medical Informatics

Phone: 650-725-5693
E-Mail: rubin@smi.stanford.edu

Primary Category: 9400 - Image Manipulation / Analysis

Computational Modeling of Tissue Damage from Penetrating Trauma: Linking Geometric Models to Anatomic and Biomechanical Knowledge

D L Rubin, MD, MS, Stanford, CA; Y Bashir; D Grossman, PhD; P Dev, PhD; M A Musen, MD, PhD (daniel.l.rubin@stanford.edu)

LEARNING OBJECTIVES

1. To learn how to integrate anatomic and biomechanical knowledge into geometric models of anatomy created with imaging data sets.
2. To demonstrate how penetrating injuries can be modeled and predicted with these tools.

ABSTRACT

Detailed geometric models of patient anatomy can be generated from CT and MRI images. However, these models cannot be used for computer prediction of organ injury after trauma because they lack anatomic and biomechanical knowledge. We describe an approach to predicting the consequences of penetrating injury by integrating geometry with anatomic and biomechanical knowledge. This knowledge is stored in ontologies, constructs which facilitate computer reasoning. We created a geometric model of the heart from Visible Human data. A hierarchy of geometric objects was created using the Insight Toolkit to represent organs and organ parts. These objects contain information about organ identity, composition, adjacency, and biomechanical properties. This integrated model can support computerized anatomic reasoning. Given an injury path, we can predict the extent of organ damage. Our model is extensible and can incorporate future information, such as physiological implications of organ injuries.

Disclosures:

No Disclosure: Daniel Rubin, Yasser Bashir, David Grossman, Parvati Dev, Mark Musen

Questions:

1. **AV**: The meeting rooms and info**RAD** theater will be furnished with a PC computer (Pentium-4/1.3 GHz, 256MB RAM), video/data projector with 1024x786 resolution, mouse access for presenters at lectern, and a 15" flat LCD monitor next to lectern.

The RSNA-supplied computers in the Speaker Ready Rooms and meeting rooms will be Window-based PC's with Microsoft PowerPoint (Office XP installed); the latest versions of Adobe Acrobat Reader, Windows Media Player, Quick Time for Windows, Internet Explorer and Netscape Navigator. Other presentation programs will not be available.

For audiovisual guidelines and Speaker Ready Room information, please go to the RSNA web site at www.rsna.org. Click on the annual meeting logo, then click on information for speakers or visit the above help menu.

DO YOU REQUIRE ANY SPECIAL REQUIREMENTS, SUCH AS SOUND FOR YOUR PRESENTATION, INTERNET, ETC?

No

If yes, please describe. NOTE: All special requirements are subject to review for approval.

No response

125.15